A286625

AGARD-CP-549

AGARD

ADVISORY GROUP FOR AEROSPACE RESEARCH & DEVELOPMENT
7 RUE ANCELLE, 92200 NEUILLY-SUR-SEINE, FRANCE

AGARD CONFERENCE PROCEEDINGS 549

Impact of Acoustic Loads on Aircraft Structures

(Impact des sollicitations acoustiques
sur les structures d'aéronefs)

A-1

This publication was prepared at the request of the Structures
and Materials Panel (SMP) of AGARD. Papers presented
at a Symposium held in Lillehammer, Norway, May 1994

North Atlantic Treaty Organization
Organisation du traité de l'Atlantique Nord

Best Available Copy

The Mission of AGARD

According to its Charter, the mission of AGARD is to bring together the leading personalities of the NATO nations in the fields of science and technology relating to aerospace for the following purposes:

— Recommending effective ways for the member nations to use their research and development capabilities for the common benefit of the NATO community;

— Providing scientific and technical advice and assistance to the Military Committee in the field of aerospace research and development (with particular regard to its military application);

— Continuously stimulating advances in the aerospace sciences relevant to strengthening the common defence posture;

— Improving the co-operation among member nations in aerospace research and development;

— Exchange of scientific and technical information;

— Providing assistance to member nations for the purpose of increasing their scientific and technical potential;

— Rendering scientific and technical assistance, as requested, to other NATO bodies and to member nations in connection with research and development problems in the aerospace field.

The highest authority within AGARD is the National Delegates Board consisting of officially appointed senior representatives from each member nation. The mission of AGARD is carried out through the Panels which are composed of experts appointed by the National Delegates, the Consultant and Exchange Programme and the Aerospace Applications Studies Programme. The results of AGARD work are reported to the member nations and the NATO Authorities through the AGARD series of publications of which this is one.

Participation in AGARD activities is by invitation only and is normally limited to citizens of the NATO nations.

The content of this publication has been reproduced
directly from material supplied by AGARD or the authors.

Published September 1994

Copyright © AGARD 1994
All Rights Reserved

ISBN 92-836-0001-0

Printed by Canada Communication Group
45 Sacré-Cœur Blvd., Hull (Québec), Canada K1A 0S7

Best Available Copy

BEST

AVAILABLE

COPY

Preface

With the rapid development and introduction of new technologies in modern aircraft design and structures, such as powered lifting systems with blown flaps or deflected jets, supersonic configurations with their well-known problematic thermo-acoustical phenomena, the promising advances in the field of nonmetallic materials (CFRP, ceramics), there is a strong need to concentrate on the wide band of "new structural fatigue problems" resulting therefrom and to ascertain state-of-the-art expertise in the fatigue area.

Meeting contributions focus on topics dealing with the acoustic environment in sub-, super- and hyper-sonic flow regimes, innovative structural design techniques and materials allowing the layout of fatigue resistant structures as well as with experimental and analytical tools for evaluation of the behaviour of structures in an acoustically and thermally adverse environment.

An additional session of the Meeting is dedicated to topics related to the field of structural-acoustics. Thereby a broad band of different activities is addressed, e.g. the prediction of noise in closed compartments, the identification of structural-borne noise paths as well as the acoustic diagnosis of aircraft disasters.

Préface

Avec le développement et la mise en application rapides des nouvelles technologies pour la conception et les structures des aéronefs modernes, telles que les systèmes hypersustentateurs à volets soufflés ou à jets à poussée orientable, les configurations supersoniques avec leur phénomènes thermoacoustiques problématiques bien connus, et les progrès prometteurs réalisés dans le domaine des matériaux non-métalliques (CFRP, céramiques), il est important de se concentrer sur le secteur très large des «nouveaux problèmes de la fatigue structurale» qui en résultent et de faire le point de l'état de l'art de l'expertise dans le domaine de la fatigue.

Les contributions à la réunion concernent en particulier les questions relatives à l'environnement acoustique en régime d'écoulement subsonique, supersonique et hypersonique, les techniques ainsi qu'aux matériaux de conception structurale innovateurs permettant la conception de structures résistantes à la fatigue, ainsi que les aides expérimentales et analytiques à l'évaluation du comportement des structures dans un environnement acoustiquement et thermiquement hostile.

Une session supplémentaire est consacrée à certaines questions relatives au domaine de l'acoustique structurale. Ainsi, une large gamme d'activités est examinée, entre autres la prédiction du bruit dans les cellules closes, l'identification de trajets du bruit acheminé par les structures, le diagnostic acoustique des catastrophes aériennes et les avancées dans le domaine du contrôle actif du bruit.

Dr R. FREYMANN
Sub-Committee Chairman

Structures and Materials Panel

Chairman: Mr. R. Labourdette
Directeur Scientifique des Structures
ONERA
29 Av. de la Div. Leclerc
92322 Châtillon Cedex
France

Deputy Chairman: Dr. O. Sensburg
Chief Engineer
Deutsche Aerospace AG
Militaerflugzeuge
Postfach 80 11 60
81663 Munich
Germany

SUB-COMMITTEE MEMBERS

Chairman: Dr. R. Freymann (Ministère de la Force Publique, Luxembourg)
Bahnhofstrasse 27
85386 Eching
Germany

Members:

D. Chaumette	FR	R. Potter	UK
L. Chesta	IT	E. Sanchiz	SP
M. Curbillon	FR	N. Sandsmark	NO
H. Forsching	GE	O. Sensburg	GE
A.R. Humble	UK	D.L. Simpson	CA
R. Labourdette	FR	J.P. Watterson	UK
H.H. Ottens	NE	R. Zwaan	NE
D. Paul	US		
H. Perrier	FR		
C. Perron	CA		

PANEL EXECUTIVE

Dr. Jose M. CARBALLAL, Spain

Mail from Europe:
AGARD-OTAN
7, rue Ancelle
92200 Neuilly sur Seine
France

Mail from US and Canada:
From USA and Canada
AGARD-NATO/SMP
PSC 116
APO AE 09777

Tel: (1) 4738 5790 & 5792
Telefax: (1) 4738 5799
Telex: 610176F

Contents

Page

Preface/Préface iii

Structures and Materials Panel iv

Technical Evaluation Report T
by I.J. Kacprzynski

SESSION I : OVERVIEW

Current and Future Problems in Structural Acoustic Fatigue 1
by P.D. Green

Helicopter Internal Noise 2
by G. Niesl and E. Laudien

Dimensionnement et qualification aéroacoustique des tuiles HERMES 3
Aeroacoustic Qualification of Hermes Shingles
by C. Petiau and A. Paret

SESSION II : ENVIRONMENT

Weapons Bay Acoustic Environment 4
by L.L. Shaw and R.M. Shimovetz

Impact of Noise Environment on Engine Nacelle Design 5
by R. Giuzio, E. Dalle Mura and G. Giuffrè

Impact of Dynamic Loads on Propulsion Integration 6
by J.M. Seiner

High Temperature Acoustic Test Facilities and Methods 7
by J. Pearson

Design and Operation of a Thermoacoustic Test Facility 8
by G. Bayerdorfer and L. Freyberg

Nonlinear Dynamic Response of Aircraft Structures to Acoustic Excitation 9
by H.F. Wolfe and R.G. White

Acoustics of Space Structures 9A
by F. Morganti, R. Giovannucci and P. Santini

Prediction of Fluctuating Pressure and Power Spectra in Attached and Separated Compressible Flow 10
by A.L. Laganelli, K.R. Wentz and H.F. Wolfe

Modelling Structurally Damaging Twin-Jet Screech 11
by Mary K. Lockwood, S.H. Walker and A.B. Cain

Application of the PSD Technique to Acoustic Fatigue Stress Calculations in Complex Substructures 12
by H. Climent and J. Casalengua

SESSION III : MATERIALS AND STRUCTURAL DESIGN TECHNIQUES

Acoustic Fatigue Testing on Different Materials and Skin-Stringer Elements 13
by K. König

Acoustic Fatigue Characteristics of Advanced Materials and Structures 14
by J.H. Jacobs and M.A. Ferman

Acoustic Fatigue of Carbon Fibre Structures 15
by G. Müller and M. Grünewald

Brite-Euram Programme : Acoufat
Acoustic Fatigue and Related Damage Tolerance of Advanced Composite and Metallic Structures 16
by D. Tougard

Acoustic Fatigue Behaviour of GLARE Composites 17
by P.T. Elangovan, H. Ottens and G. Bayerdorfer

Thermo-Acoustic Fatigue Design for Hypersonic Vehicle Skin Panels 18
by K.R. Wentz, R.D. Blevins and I. Holehouse

Application of Superplastically Formed and Diffusion Bonded Structures in High Intensity Noise Environments 19
by R.J. Cummins and J.P.C. Wong

SESSION IV : STRUCTURAL ACOUSTICS

An Overall Approach of Cockpit Noise Verification in a Military Aircraft 20
by R. Giuzio and M. Norese

Noise Transmission and Reduction in Turboprop Aircraft 21
by D.G. MacMartin, G.L. Basso and B. Leigh

Paper 22 withdrawn

Advanced Statistical Energy Analysis 23
by K.H. Heron

Identification and Analysis of Air- and Structure-borne Noise and Vibration Paths 24
by H. Van der Auweraer, K. Wyckaert, P. Van der Linden and D. Otte

Paper 25 withdrawn

Spectrogram Diagnosis of Aircraft Disasters 26
by F.W. Slingerland

TECHNICAL EVALUATION REPORT

J.J. Kacprzynski
Institute for Aerospace Research
National Research Council of Canada

Introduction

The AGARD Structures and Materials Panel has been concerned with activities in acoustic fatigue since 1960 and had achieved a considerable success in coordinating and encouraging acoustic fatigue research in the NATO countries. By 1968 Panel's Specialists group on Design in Acoustic Fatigue identified six subject areas in which sufficient research results had been accumulated of suitable kind to warrant their immediate consolidation and presentation in design data sheet form. Arising from this a project was initiated under which Engineering Science Data Unit (ESDU) revised and extended the existing data sheets with the support and collaboration of AGARD. The subjects chosen for this project were:

- jet noise near field prediction;
- stress response of flat stiffened panels;
- stress response of curved stiffened panels;
- natural frequencies of flat and curved honeycomb panels;
- stress response of honeycomb panels;
- random S-N curves for light alloys.

The data sheets covering the above topics were issued in 1972 as AGARDograph 162 Part I and II (Ref. 29) and as ESDU Data Sheets. A symposium on Acoustic Fatigue was held during the 35th SMP Meeting, in Toulouse, France in September 1972 (Ref. 30).

Since that time the acoustic aircraft loads became more severe and the developed in the sixties and seventies methods for solution of acoustic problems became not longer adequate. Therefore the Structures and Materials Panels organized the present Specialists Meeting on the Impact of Acoustic Loads on Aircraft Structures, which was held on May 2 - 4, 1994 in Lillehammer, Norway.

During the meeting 25 papers were presented, in four sessions, covering the general review of the state-of-the-art, Acoustic Environment, Materials and Structure Design Techniques and Structural Acoustics.

The developed in the late sixties and mid seventies methods (Ref. 28 and 31) were based on simple methods for response predictions, using fundamental mode approximation for estimation of induced stress and strain caused by acoustic excitation. These methods assuming linear behaviour and normal mode approach, validated for simple aluminium structures, are still used extensively. For the present state-of-the-art military aircraft and particularly for the short take off and vertical landing (STOVL) aircraft, the acoustic impact on the structure becomes more severe. Also new materials are being used and therefore the data of References 28 and 31 are not longer adequate. Since the mid seventies a significant progress has been made in the evaluation of acoustic effects, both in America and in Europe where a large cooperative activity dealing with acoustic effects has been organized in a form of collaboration on Acoustic Fatigue and Related Damage Tolerance of Advance Composite and Metallic Structures, called ACOUFAT, has been organized. This programme is described in Reference 16. In spite of the achieved progress, the present Specialists Meeting demonstrated, that the currently available methods still do not allow for accurate fatigue life assessment (Ref. 1).

Although the acoustic generated strains/stresses are relatively small comparing to strains/stresses induced by other aircraft's loads, they are for more numerous and usually at high frequency. In consequence, the acoustic fatigue cracking (or delamination) may occur after a very short period of aircraft usages.

To avoid fatigue damage caused by the acoustic loads, the design process should be able to tackle the following problems:

- evaluation of acoustic loads (acoustic environment);
- estimation of structural response to acoustic loads;
- estimation of the fatigue life under the acoustically induced strains (stresses).

Acoustic Environment

During the meeting ten papers were presented in the session on Acoustic Environment (Ref. 4 - 12 and 24). The acoustic loads from engine and aerodynamic sources depend on aircraft

Presented at a Symposium on 'Impact of Acoustic Loads on Aircraft Structures' held in Lillehammer, Norway, May 1994.

flight conditions. It appears that the most critical aerodynamic acoustic loads are due to flow separation and due to shock waves. There are still difficulties in accurate predictions of the aerodynamic acoustic data. The state-of-the-art numerical analyses are still very costly and their reliability is questionable. The results depend on the used turbulence models, mathematical flow models and the idealisation of the aircraft geometry. During a project development and design phases, when the flight test data are available, loads estimates are obtained based on experimental procedures, past experience and read-across from other aircrafts with similar mission and performances.

The wind tunnel results, although very useful, due to a different than in flight turbulence level, do not predict correctly the acoustic loads. The PWT (Progressive Wave Tubes) also do not represent correctly flight conditions. Hence, almost inevitable, the flight measurement of acoustic loads, are required for a verification of the predicted acoustic fatigue life.

One paper (Ref. 4) was devoted to Acoustic Environment of weapons bay. The definition of the cavity types was made, together with the description of the phenomenon. The predictions of acoustic loads, their frequency and amplitude have been made both with the simple empirical equations and with the complex numerical flow analyses. Both active and passive suppression concepts have been discussed. It appears that the passive suppression systems are effective only over the small range of Mach numbers. Thus in the future, some type of active control will be needed to be adaptive over the entire speed range.

Transfer path analysis methods presented in paper (24) allows to investigate the contribution of individual sources and source transmission paths. The current research focusses on validating the accuracy of this method for the solution of industrial problems and on extending it to other problems. The extensions of the method include the use of reciprocity techniques to measure vibro-acoustic effects, the qualification of air-borne source contributions, the transfer of structure-borne sound though connected substructures and the physical interpretation of the transmission path phenomena.

Paper (10) gives a review of engineering prediction techniques for power intensity (rms fluctuating pressure) and power spectral density (PSD) for attached and separated flow. Recent results of the test of shock wave/turbulent boundary layer interaction are included. A technique is presented, based on the Houbolt spectra assumption, that appears to provide engineering solutions to the design resolution of complex flow problem.

Paper (5) describes the general philosophy and methodology in engine nacelle acoustic design, particularly intake and exhaust ducts, necessary to satisfy the noise certification requirements. A general description of conventional acoustic liners, currently in service, and being developed innovative liners is also enclosed. The Alenia developed software package (ALNOIS) for complete engine nacelle acoustic design and acoustic panel manufacturing was presented.

Aircraft dynamic loads produced by engine exhaust plumes were examined (Ref. 6) for a class of configuration of fighters and bombers in model and full scale. The presented results are for USAF F-15 and B-1B aircraft and for US F-18 HARV (High Alpha Research Vehicle) and ASTOVL (Advanced Short Take-off and Vertical Landing) programs.

Currently USAF F-15 aircrafts are flying without external nozzle flaps (Ref. 11), due to the continuous structural fatigue experienced by the flaps and the cost of replacing them. Although the aft region of the aircraft is known to experience high aerodynamic loads due to massive unsteady flow separation, there is the evidence, that the severe acoustic loads contribute to the observed structural damage. These acoustic loads are attributed to a phenomenon known as jet screech - it is essentially a resonance feedback loop in the jet flowfield, that can set up between the nozzle tip and the jet shock cells. It is most severe for medium spaced twin jet aircraft and can occur during subsonic flight with non-perfectly expanded supersonic jet. Screech has been measured at levels of 160 dB, high enough to exceed the fatigue limit for metallic aircraft structures. Paper (11) describes an initial engineering workstation tool to predict occurrence of screech, ultimately allowing the design of configurations which will not result in screech.

Three papers gave the description of thermoacoustic test facilities (Ref. 7, 8 and 14). The American facility (Ref. 7) is designed to operate at temperatures from -250 °F to 3000 °F at sound pressure levels up to 180 dB and heat flux of 1000 Btu per square foot per second. The German facility (Ref. 8) have maximum sound pressure level of 160 dB with surface temperature of 1300 °C and heat flux of 100 W/sec.

Paper (14) describes thermo-acoustic test facility capable of 171 dB acoustic loading with simultaneous cross flow.

Structural Response

For the former approach (Ref. 28, 31) the structure was idealised to determine the fundamental mode frequency. Stress levels were predicted at the critical stress location, assuming uniform static pressure loading of the panel and that the static deflected shape and mode shape were identical. All these assumptions contributed to the significant difference (by as much as a factor of 2) between stress predictions and measurements (Ref. 32).

Finite element analysis methods enable more complex structures, with detailed acoustic loading characteristics, to be analyzed. Higher order modes, in addition to the fundamental, can also be included. The analysis process involves assessing the frequency response of the structure across the relevant frequency range to derive the power spectral densities of stress response. The probability density function of stress levels involved are usually represented by a single equivalent rms (root means square) level.

Two presented papers (Ref. 12 and 14) discussed in details finite element analysis of the response of the structure to acoustic loads. Paper (12) describes the Power Spectral Density (PSD) technique for acoustic fatigue evaluation. The sound pressure levels are converted to acoustic pressures PDS and applied to a finite element model representation of the substructure. The technique can cover complex structural geometries and contribution of several normal modes.

The method based on NASTRAN for the linear analysis and on specially developed code TAPS (Thermal Acoustic Response and Fatigue of Pre-Buckled and Post-Buckled Structureal) for nonlinear analysis were presented in paper (14). TAPS contains extensive material data base (including composites) and automated flight profile fatigue life prediction.

The effects of nonlinearity on the dynamic response of aircraft structures to acoustic excitation were studied in paper (9).

The main objective of this paper was to develop a method for prediction nonlinear response of simple structures. Both aluminum alloy plates and CFRP plates were studied.

Acoustic Fatigue

Stress levels in rms form for particular flight cases are used together with rms stress endurance data to estimate fatigue damage for each case. These damages are then accumulated, assuming Miner's rule, according to the mix and duration of flight cases in the life of the particular aircraft. Overall damage can then be used to estimate the fatigue life of the component. Life estimates have not been particularly accurate - there are several reasons for these discrepancies, and particularly:

- the use of rms levels in the damage analysis (they do not represent properly the more complex behaviour of the range of stresses they are representing);
- the presence of other loads acting simultaneously with acoustic loads;
- the limitation of endurance data to simple geometries.

Acoustic Testing

Acoustic fatigue testing is performed for two reasons:

- to provide design acoustic data from test coupons;
- to test the complete structure or the component for design verification/certification.

The design data are usually obtained under random loading but at constant input rms acceleration levels using shaker tables exciting the simple coupon test pieces at resonance. Usually there are tested plain coupons or simple elements representing structure, skin fasteners, lay-up, changing in sections or joints.

The endurance life is usually taken as the time to when cracks or delamination are first detected or when the degradation in the fundamental frequency falls by a specific amount.

The usefulness of the coupon testing is somehow limited. Firstly, it is questionable how representative of real structures are simple coupons under inertial loading. The correct mode shapes are not represented. The point of failure is difficult to determine and estimating the duration to that point often requires the somewhat dubious practice of allowing a time for "setting in" of the coupon - particularly for composites.

Four papers were dealing with coupon/material testing (Ref. 13, 14, 15 & 17). Paper (13) describes a comparative study of 29 different coupons covering eight different designs and six different materials tested by excitation of 30 g^2/Hz on a shaker. It concluded that although the scatter of results was very large, the tests showed clear tendencies. All the new materials allow lighter structures with higher eigenfrequencies. Most of the damping values found were smaller than values given in ESDU. It concluded that deeper investigations for the definition of qualified failure or safety criteria are necessary.

Paper (15) describes some of the problems of acoustic fatigue of carbon fibre structures investigations obtained within ACOUFAT program. The investigation have been carried out with respect to:

- nonlinealities in the measurements for the calibration of the different transducers;
- effect of residual strength for the coupons;
- effects of moisture and temperature in the material due to storage and testing in humid environment.

The sum of these effects for one tested coupon required the reduction of the allowable strain in the range of high cycles by a factor -4 compared to the value obtained originally at room temperature with 2% failure criteria.

Paper (17) describes the acoustic fatigue behaviour of GLARE composites. The influence of the laminate lay-up and temperature on the acoustic fatigue was investigated from the shaker tests. The test included also stiffened GLARE skin panels showing the importance of the secondary structure in the acoustic environment.

Qualification Testing

Unlike the conventional fatigue testing, the full scale acoustic fatigue testing is normally not performed. Aerodynamic and engine acoustic environment would need to be generated simultaneously by wind tunnel and engine sources, or in flight conditions, to represent interactions. Instead the acoustic test are performed on relatively small components or assemblies where the localized acoustic pressure field can be simulated in a more practical manner. No papers were presented on this topic.

Internal Aircraft Noise

Paper (20) describes the applicable concepts for cockpit noise verification in military aircrafts. A design-to-noise procedure is outlined and the overall requirements for medical, intelligibility and operational aspects are discussed. Guidelines for cockpit noise control, to be applied during aircraft design phase, are given together with the expected benefits. Advanced noise control measures and noise measuring techniques are also dealt and cockpit noise verification is described.

A new reciprocal technique for study of noise transmission and reduction in turboprop aircraft is described in paper (21). A capacitive scanner is used to measure the fuselage response due to an internal noise source. The approach is validated by comparing this reciprocal noise measurement with the direct measurement. The fuselage noise transmission information is then combined with computer predictions of the propeller pressure field data to predict the internal noise.

Helicopter Internal Noise

Helicopter internal noise (Ref. 2) contains a high amount of discrete tones which are more annoying than a broadband noise spectrum. This is mainly due to discrete frequencies by the main transmission system, and also from other components like main and tail rotor, engines and cooling fans. Up to now, mainly passive systems have been used for interior noise reduction with high weight penalties, particularly in the low frequency range. The active panel noise control, having mechanical actuators exciting the cabin walls and active control of gearbox struts with actuators in the load path between gearbox and fuselage are potentially useful techniques for reduction of the internal noise to a level of about 85 dB or even lower. The paper describes RHINO project (Reduction of Helicopter Interior Noise) of Commission of European Communities. For contemporary composite laminate structures of helicopters the noise problem is more severe than for metallic structures.

Impact on Space Structures

Some difficulties of the solutions of problems of the acoustic load of space structures are presented in paper (3), where as an example, the study of the Hermes

Space shuttle shingles is presented. The qualification of shingles was based on aeroelasticity analyses and on ground testing in wind tunnels, propessive wave tubes and on shakers. It was demonstrated, that none of these means can alone satisfy the needs of structural dimensioning and qualification. Particularly the calculation of the turbulent flow is not reliable. The simulation of the actual loads of the structural parts in ground testing is very difficult. A strategy for aeroacoustic dimensioning and qualification of structural space parts is proposed.

Thermo-acoustic fatigue design of hypersonic vehicles skin panels is discussed in paper (18). Aerothermal analysis shows, that impingement of the bow shock wave on the vehicle and engine noise produce high fluctuating pressures and local heat fluxes. The maximum temperatures will exceed 1500 °C at the top of the ascent trajectory and engine sound levels will exceed 170 dB at takeoff. As a result, loads due to engine acoustics and shock impingement dominate the design of many transatmospheric vehicle skin panels. The paper contains results of NASTRAN analysis and high temperature (980 °C) shaker tests to establish high cycle fatigue allowable of material coupons and joint subelements under random loading.

A method simulating the acoustic vibration effects, in terms of peak and rms accelerations response of the spacecraft external panels is presented in paper (27). It allows to identify the suitable design solutions. By using modal approach in the frequency domain, the structure has to be described through a finite element model and the acoustic field through Green's function. The presence of air leads to addition to the mass matrix and to the damping matrix. The transfer function is then applied to the case of random inputs, for which an analytical expression is provided. Some numerical examples show the effect of the additional terms on the spectral distribution and on the relevant rms value.

Advanced Statistical Energy Analysis (ASEA)

Paper (23) describes Advanced Statistical Energy Analysis - ASEA, which does not contain some drawbacks of the known Statistical Energy Analysis (SEA). It is shown that the errors, that sometimes occur when predictive SEA is applied to complex structural assemblies are mainly due to not modelled power transport mechanism. This "tunnelling" mechanism occurs when direct coupling exists between two SEA sub-systems that are physically separated from each other by other SEA sub-systems. ASEA is interpreted as a series of mathematical models, the first of which is identical to standard SEA and subsequent higher order models are convergent to the desired results. The real structure will have to be broken up into the subsystems available within ASEA, possibly requiring hundreds of subsystems similar like the elements in finite element methods codes.

The usefulness of ASEA methods will be determined by availability of the transmission and reflection coefficients. ASEA method will hopefully guarantee accurate predictions, but is usefulness may be limited by the magnitude of computations needed.

Acoustic Study of Aircraft Disasters

A spectrogram diagnosis method of examination of aircraft disasters is presented in paper (26). It is known, that impulsive forces applied to an aircraft fuselage generate radial vibration waves. It has been found, that these waves are detected by the cockpit area microphone, and that spectrogram analysis of the microphone recording can provide information on the nature, origin and strength of the source, whether an explosion or a sudden decompression. Results of analysis of several aircraft crashes were presented.

Superplastically Formed and Diffusion Bonded Components

The application of superplastically formed and diffusion bonded components in high intensity noise environments is discussed in paper (19). Two specimens, representing aircraft control surface and an access door, have been manufactured and tested under high intensity acoustic excitation. The access door was also subjected to an elevated temperature of 150 °C. These specimens were manufactured as multi-cell box configurations by superplastic forming and diffusion bonding (SPFDB) to a similar structural weight as existing aircraft components produced by alternative means of construction. The influence of the spandrel-shaped void, formed at the skin/stinger intersection on acoustic fatigue performance was examined.

General Discussion and Recommendations

It appears, that much development needs to be done to achieve proficient acoustic fatigue design for the future. All aspects of the process have to be improved and particularly:

- Development of more efficient and more accurate methods for prediction of fluctuating pressure levels and associated spectral content for engine afflux, boundary layer and separated aerodynamic flow.
- Improving the methods for accurately predicting the structural response to acoustic loads, covering more complex structures and also non-linear effects.
- Investigation of the representation of acoustically induced strain/stress spectra (rms) leading to more accurate fatigue analysis.
- Development and investigation of methods for assessing of the fatigue under combined acoustic and manoeuvre induced loads.
- Investigate the application of acoustic fatigue endurance date across a wide range of structural geometries.
- Development and investigation of improved methods for non-destructive damage detection in severe acoustic environments.
- Investigate and improve the use and validity of accelerated testing.
- Development and investigation of rules for zoning the aircraft to identify areas for detailed acoustic analyses (e.g. regions with loads higher than 150 dB).
- Development of techniques to determine the thermal acoustic response of damaged and repaired structures.
- Development of mechanisms for absorbing thermal acoustic energy.
- Collection of endurance data for new materials and acoustically resilient sandwich panels.

References

The Meeting papers in the order of presentation.

1. Current and Future Problems in Structural Acoustic Fatigue, P.D. Green

2. Helicopter Interior Noise, G. Niesl and E. Laudien

3. Aeroacoustic Qualification of Hermes Shingles, C. Petiau and A. Paret

4. Weapons Bay Acoustic Environment, L.L. Shaw and R.M. Shimovetz.

5. Impact of Noise Environment on Engine Nacelle Design, R. Giuzio, E. Dalle Mura and G. Giuffre.

6. Impact of Dynamic Loads on Propulsion Integration, J.M. Seiner.

7. High Temperature Acoustic Test Facilities and Methods, J. Pearson.

8. Design and Operation of a Thermoacoustic Test Facility, G. Bayerdoerfer and L. Freyberg.

9. Nonlinear Dynamic Response of Aircraft Structures to Acoustic Excitation, H.F. Wolfe and R.G. White.

10. Prediction of Fluctuating Pressure and Power Spectra in Attached and Separated Compressible Flow, A.L. Laganelli, K.R. Wentz and H.W. Wolfe.

11. Modelling Structurally Damaging Twin-Jet Screech, Mary K.A.E. Lockwood, S.H. Walker and A.H. Cain.

12. Application of the PSD Technique to Acoustic Fatigue Stress Calculations in Complex Substructures, H. Climent and J. Casalengua.

13. Acoustic Fatigue Testing on Different Materials and Skin-Stringer Elements, K. Konig.

14. Acoustic Fatigue Characteristics of Advanced Materials and Structures, J.H. Jacobs and M.A. Ferman.

15. Acoustic Fatigue of Carbon Fibre Structures, G. Mueller and M. Gruenewald.

16. Brite-Euram Programme: Acoustic Fatigue and Related Damage Tolerance of Advanced Composite and Metallic Structures - Acoufat, D. Tougard.

17. Acoustic Fatigue Behaviour of GLARE Composites, P.T. Elangovan, H. Ottens and G. Bayerdoerfer.

18. Thermo-Acoustic Fatigue Design for Hypersonic Vehicle, R.D. Blevins and I. Holehouse.

19. Application of Superplastically Formed and Diffusion Bonded Structures in High Intensity Noise Environments, R.J. Cummins and J.P.C. Wong.

20. An Overall Approach of Cockpit Noise Verification in a Military Aircraft, R. Giuzio and M. Norese.

21. Noise Transmission and in Turboprop Aircraft, D.G. MacMartin, G.L. Basso and B. Leigh.

23. Advanced Statistical Energy Analysis, K H. Heron.

24. Identification and Analysis of Air- & Structure-borne Noise and Vibration Transfer Paths, H. Van der Auweraer, K. Wyckaert, P. Van der Lindon and D. Otte.

26. Spectrogram Diagnosis of Aircraft Disasters, F.W. Slingerland.

27 Acoustics of Space Structures, F. Morganti, R. Giovannucci and P. Santini.

Additional references:

28. Acoustic Fatigue Sub-series Volumes Incorporating Royal Aeronautical Data Sheets - Engineering Science Data Unit (ESDU).

29. AGARDograph No. 162, Part I & II, 1972.

30. AGARD Conference Proceedings on Symposium on Acoustic Fatigue, 1972

31. Sonic Fatigue Design Guide for Military Aircraft, F.F. Rudder and H.E. Plumlee, AFFDL-TR-74-112, Feb. 1975.

32. Stresses in Skin Panels Subjected to Random Acoustic Loading, B. Clarkson, Aeronautical Journal of the Royal Aeronautical Society, Vol. 72, No. 695, 1968.

CURRENT AND FUTURE PROBLEMS IN STRUCTURAL ACOUSTIC FATIGUE

P.D.Green
British Aerospace Defence Limited,
Military Aircraft Division,
Warton Aerodrome, Preston
Lancashire, England

1. SUMMARY

Acoustic fatigue failures can be caused by the dynamic response of aircraft structures to unsteady pressure loading from aerodynamic and engine acoustic sources. The life of structures is often difficult to assess accurately and may be greatly affected by steady thermal, in-plane and out-of-plane panel loads. Furthermore, currently available methods do not enable fatigue life assessments of the substructure to be made, despite these failures occurring regularly in service.

This paper discusses current problems associated with structural acoustic fatigue and extends upon this to account for likely clearance philosophies and configurations for future aircraft.

2. INTRODUCTION

In the late 60's to mid 70's, aerospace companies and research establishments were involved in the development of dynamic response methods and generation of endurance data, culminating in the publication of the ESDU data sheets[1] and AFFDL design guide[2].

A major part of the work was based on simple methods for response prediction, using fundamental mode approximation, for the estimation of induced stress or strain under the action of random acoustic excitation. Such methods assume linear behaviour and a normal mode approach. These methods, validated for simple aluminium alloy structures, are still extensively used today.

However, the airframe manufacturer is required to meet ever more stringent performance and mass targets, being achieved through developments in optimised and efficient design of structures, and the introduction of new materials. There is a corresponding need for development in acoustic fatigue design methods and data. The need becomes particularly acute with current STOVL (short take off and vertical landing) developments which tend to increase the severity of acoustic loads.

Such is the interest in this subject across both the military and civil aerospace sectors, that many European airframe manufacturers and research bodies recently collaborated on the subject of Acoustic Fatigue and Related Damage Tolerance of Advanced Composite and Metallic Structures[3]. However, despite producing an immense amount of extremely valuable data, the programme has probably raised more questions than it has answered.

This paper surveys acoustic design practice as it is today, seeking to identify current shortcomings, and goes on to look forward towards the likely requirements that will be introduced by future aircraft projects.

3. ACOUSTIC FATIGUE - CURRENT DESIGN RULES

3.1 The Phenomenon of Acoustic Fatigue

Engine efflux, boundary layer and separated aerodynamic flow are all typical sources of acoustic pressure fields. Any structure along the path of this broad frequency range, random load, environment will respond by vibrating. Although the cycles of stress so produced are small, often much smaller than the stresses induced by aircraft manoeuvres, they are far more numerous and usually at high frequency. In consequence, fatigue cracking can occur after a very short period of time.

Presented at a Symposium on 'Impact of Acoustic Loads on Aircraft Structures' held in Lillehammer, Norway, May 1994.

Acoustic fatigue damage may be evident in various forms, e.g., cracking or delamination of skin, stringer, rib or frame, or inter-connecting cleat elements. Typically, damage is found at the edges of panels, bays and cleats, emanating from fastener holes and changes in section.

3.2 Basic Design Process

To avoid acoustic fatigue cracking, it is clear that a design process must be able to tackle the following aspects:

(i) evaluation of the magnitude and character of the acoustic environment;

(ii) estimation of the structural response to that environment;

(iii) estimation of the fatigue life under the induced stresses.

To support design prediction, suitable testing must be carried out both to derive the design data from which the predictions are made and to confirm the final design.

An efficient process also requires rules defining where complete and detailed analysis must be undertaken (e.g. covering critical structure in close proximity to acoustic sources) and where it can be omitted, i.e. zoning.

These aspects are dealt with in more detail below.

3.3 Acoustic Environment

Acoustic pressure levels from engine or aerodynamic sources obviously depend on engine settings and aircraft flight conditions. Currently, where there is no appropriate data for future projects, empirical or semi-empirical methods[1] are used to estimate the levels, which are accumulated over the range of conditions needed to represent the life of the aircraft.

These methods, although adequate for simple situations, are increasingly found to be insufficiently accurate for modern optimised design at high jet pressure ratios and temperature. In addition, occasionally, factors have to be added where uncertainty exists as to whether predicted levels are large enough to reflect actual aircraft conditions. Almost inevitably, predictions have to be refined at a later stage by flight measurements. The consequent risk of demonstrating the inadequacy of the design at this stage is obviously undesirable.

3.4 Structural Response

Once the acoustic environment has been defined, the response of the structure to it is currently evaluated using simple equations or proprietary finite element codes.

In the former approach, e.g. ESDU or AFFDL, the structure is idealised to determine the fundamental mode frequency; this involves taking into consideration the effective size of the panel, edge fixity and curvature. Stress levels are predicted at the critical stress location, assuming uniform static pressure loading on the panel, with the assumption that the static deflected shape and the mode shape are identical. It is further assumed that the pressure field is in-phase across the panel and there is little difference between maximum response levels at normal and grazing incidence to the panel in the fundamental mode, and that the damping is small. Further, analysis is confined to very simple idealisations.

With all these assumptions, it is not entirely unexpected that significant differences (by as much as a factor of 2) emerge between stress predictions and test measurements[4].

Finite element analysis methods enable more complex structural features, with detailed acoustic loading characteristics, to be analysed. Higher order modes, in addition to the fundamental, can also be determined. The process involves assessing the frequency response of the structure across the relevant frequency range to derive the power spectral densities of stress response. The probability density function of stress levels involved are usually represented by a single equivalent rms (root-mean-square) level.

However, for both the above methods, the stress prediction assumes that the response of the structure is linear; from tests performed on thin metallic and composite panels at high sound pressure levels[3,5], non-linear membrane effects are evident.

3.5 Acoustic fatigue life estimation

Derived stress levels in rms form for particular flight cases, are used together with rms stress endurance data[1,2] to estimate fatigue damage for each case. These 'unit' damages are then accumulated, assuming Miner's Rule, according to the mix and duration of the flight cases which go together to reflect the complete life of the aircraft. Overall damage can then be used to estimate the fatigue life of the component.

However, life estimates have not been particularly accurate and factors correlating prediction with test have occasionally been large. Of the possible reasons for these discrepancies, three stand out as being particularly important. The first is the use of rms levels in the damage analysis; they cannot be expected to reflect the more complex behaviour of the range of stresses they are representing. The second concerns the presence of other sources of loading acting simultaneously with the acoustic loads. At present, there is no satisfactory way of introducing these effects into the analysis. Thirdly, the applicability of available endurance design data to cover a wide range of geometries is questionable.

3.6 Acoustic testing

Acoustic fatigue testing is performed for two quite distinct reasons. The first is to provide data, usually from tests on coupons, from which design curves can be generated. The second is to confirm the design, by test on a complete component or assembly.

Data for design curves are usually obtained, under random loading but at a constant input rms acceleration levels, using shaker tables exciting the simple coupon test pieces at resonance. Plain coupons or simple elements representing, for example, substructure, skin, fasteners, lay-up, changes in section or jointing compounds can be tested in this way. The endurance life is usually taken as the time to when cracks or delaminations are first detected or when degradation in the fundamental frequency falls by a specified amount.

A number of problems have been encountered with shaker table testing. Firstly, it is questionable how representative of real aircraft structure under acoustic loading, are the simple coupons tested under inertial loading. The ability to induce correct mode shapes and types of failure is fairly limited. The point of failure is also very difficult to determine, and estimating the duration to that point often requires the somewhat dubious practice of allowing a time for 'settling in' of the coupon.

Qualification testing - proving the design - involves the use of noise ducts and reverberation rooms as well as shaker tables, depending on component size, the characteristics of acoustic pressure field and magnitude of levels required. Unlike conventional fatigue testing, full scale acoustic fatigue testing is not normally performed; it is both impractical and costly. Aero- or engine-acoustic environments would need to be generated by wind tunnel and engine sources, acting simultaneously to enable interactions to be simulated. Instead, testing is performed on relatively small components or assemblies where the required localised acoustic pressure field can be simulated in a more practical manner.

Noise ducts employ electro-pnuematic transducers to generate the acoustic pressure field, exciting the component at grazing or direct incidences. Problems with this type of testing include unrepresentative non-linearity of the pressure field at high acoustic levels, limitations in simulating the correct pressure variations within the duct, together with the potential unwanted interactions with the acoustic behaviour of the duct itself.

A reverberation room would tend to be used where acoustic excitation is expected to be extremely diffuse (i.e. where the excitation is random in direction). So far, these have not been extensively used within BAe MAD and experience is limited.

The use of shaker tables for qualification testing is beset with the same problems as noted in the previous section.

Whichever method is used, the testing situation is complicated still further by the impracticability of applying a full life time of typical aircraft acoustic loads. The test time is usually shortened to a more realistic duration by factoring up the acoustic levels. However, there are obvious questions as to how large the factor should be and whether the resulting accelerated testing induces the correct stress levels and modes of failure.

3.7 Zoning

It is not practical to perform detailed acoustic fatigue analysis for all parts of the airframe. At present, those parts of structure near the source, or along the path of significant acoustic pressure field intensity are given particular attention.

At present, for guidance in military applications, BAe consider detailed analysis essential in areas where acoustic levels are 150dB (OASPL) or above. This does not prevent attention being given in other zones if the specific situation demands it. In fact, there is still some doubt as to whether the level of 150dB is sufficiently low to identify all significant problem areas.

4. ACOUSTIC FATIGUE - FUTURE REQUIREMENTS

It is highly likely that in future, specific military projects will require STOVL capabilities. Whatever the form of propulsion chosen to produce this, it is inevitable that the system will exhaust closer to the structure when compared with more traditional designs. Structure will have to withstand much higher levels of acoustic and thermal loading, and for longer periods.

In this respect, a great deal of experience has derived from the Harrier programme not only in setting out the rules for design but also assessing where rules have been insufficient and identifying aspects of acoustic fatigue which could not have been foreseen. But it is fair to say that the future aircraft will be more advanced in terms of performance and a more severe thermal acoustic environment is likely to exist.

Deployment of stores from internal cavities, buried engines, and panel designs with higher response characteristics all increase the aggressiveness of thermal acoustic environment acting on the structure.

In addition, higher performance requires more optimised structure where compromises between weight and material and structural properties lead to more marginal clearance. There is also an increased emphasis towards structures which are damage tolerant and durable. At present, thermal acoustic methods and data are not sufficiently developed to provide confidence in clearing such critically designed structure.

5. WAY FORWARD

It is apparent from the previous sections that much development needs to be done to achieve proficient acoustic fatigue design for the future. It is important that all aspects of the process are improved. Some under active investigation are given below.

In particular:

- development and investigation of improved methods of accurately predicting fluctuating pressure levels and associated spectral content for engine efflux, boundary layer and separated aerodynamic flow;

- development and investigation of improved methods of accurately predicting the structural response to acoustic environments, covering more complex structure and also non-linear effects;

- investigation of the representation of acoustically induced stress spectra (rms) leading to more accurate fatigue analysis;

- development and investigation of satisfactory means of assessing the fatigue performance under combined acoustic and manoeuvre induced structural loads;

- investigate the application of acoustic fatigue endurance data across a wide range of structural geometries;

- investigate and improve the understanding, applicability, together with the manipulation and use of results from shaker, noise duct and reverberation room tests;

- development and investigation of improved methods of non-destructive damage detection in severe acoustic environments;

- investigate and improve the use and validity of accelerated testing techniques;

- development and investigation of rules for zoning the aircraft to identify areas for detailed acoustic analysis;

- development and investigation of techniques to deal confidently with the thermal acoustic environments associated with STOVL or features which induce more severe acoustic environments.

Developments listed above will provide the basic tools for thermal acoustic fatigue design. Many other issues are involved to extend this capability and to investigate methods of reducing damage. Some of the more important include:

- continued development of acoustically resilient sandwich panel structural design to meet high stiffness to weight requirements;

- optimisation of substructure design to meet the integration of the above panels and satisfy types of panel edge fixation and minimise vibration transmission;

- development of techniques to determine the thermal acoustic response of damaged and repaired structure;

- development of mechanisms for absorbing thermal acoustic energy.

6. CONCLUSIONS

This paper has reviewed current acoustic fatigue design practise and identified current shortcomings. Further, it has identified the areas where development and improvement is required, to meet future aircraft requirements, some of which are being addressed today.

REFERENCES:

1. "Acoustic Fatigue Sub-series Volumes incorporating Royal Aeronautical Society data sheets", Engineering Science Data Unit.

2. Rudder, F.F; and Plumlee H.E., "Sonic Fatigue Design Guide for Military Aircraft", AFFDL-TR-74-112, Feb 1975.

3. Commission of the European Communities, Brite/Euram programme: "Acoustic Fatigue and Related Damage Tolerance of Advanced Composite and Metallic Structures (ACOUFAT)"

4. Clarkson B.L., "Stresses in Skin Panels Subjected to Random Acoustic Loading", Aeronautical Journal of the Royal Aeronautical Society Vol 72 No. 695 1968.

5. White R.G., "A Comparison of some Statistical Properties of Responses of Aluminium Alloy and CFRP Plates to Acoustic Loading", Composites Journal Oct 1978.

HELICOPTER INTERNAL NOISE

G. Niesl
EUROCOPTER Deutschland
München, Germany

E. Laudien
Daimler-Benz AG
Postfach 80 04 65
81663 Munchen
GERMANY

Summary

Compared to fixed wing aircraft, helicopter interior noise is higher, and subjectively more annoying. This is mainly due to discrete frequencies by the main transmission system, and also from other components like main and tail rotor, engines, or cooling fans. Up to now, mainly passive measures have been used for interior noise reduction. Despite intensive experimental and theoretical investigation to improve acoustic treatment, their weight penalties remain high especially in the low frequency range.

Here, active noise control offers additional capacities without excessive weight efforts. Loudspeaker based systems are sufficiently well developed for implementing a prototype system in the helicopter. Two other principles are in development: Active panel control which introduces mechanical actuators to excite the cabin walls, and active control of gearbox struts with actuators in the load path between gearbox and fuselage.

1. Introduction

Helicopters serve many markets and perform various functions; from military and police missions to oil rig supply, emergency tasks, executive transports and commuter operations. Therefore, unlike for commercial fixed wing aircraft, the helicopter design has to meet many functional, and economic requirements and is not optimized for single use. The interior noise of existing helicopters is unacceptable high and may even affect the hearing integrity of passengers without ear defenders. The effect of noise on passengers and pilots is reflected in spontaneous complaints reported to the manufacturers or as results of physiological studies.

In light helicopters, major noise sources are near the passengers' heads. However, the effectiveness of noise control measures such as sound absorbing materials and damping sheets, is limited not only by weight but also by space constraints, especially at the ceiling. The weight penalty of conventional acoustic treatment is severe, it degrades performance and in most cases, the residual noise levels still remain relatively high. In contrast to other aircraft, for example propeller driven aircraft, the helicopter interior noise contains a high amount of discrete tones which are more annoying than a broadband noise spectrum.

In addition to pure tones, there are interactive effects of noise and vibrations which cause an even more stressful environment for passengers [1]. Especially in rescue helicopters it is often not possible to wear ear protection for medical personnel and injured persons because of communication reasons. For pilots and medical personnel, performing responsible and high sophisticated work, a suitable environment with acceptable levels of noise and vibrations is necessary.

2. Status of Helicopter Internal Noise

Most flying helicopters are in general not designed for low interior noise levels. Therefore, all existing helicopter with low interior noise are penalized by the additional weight of the interior trim.

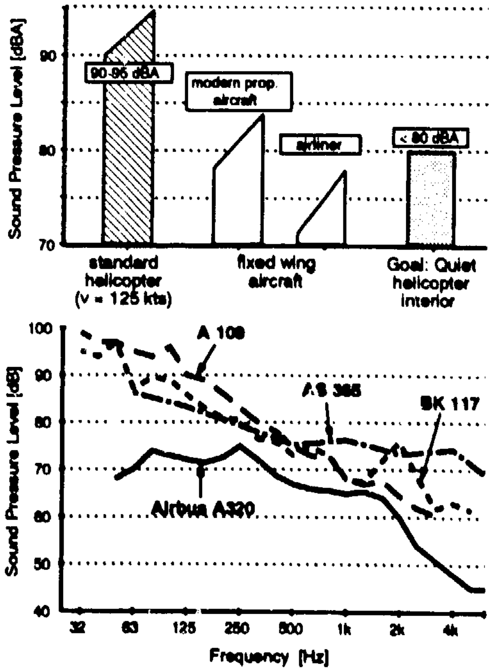

Figure 1: Interior Noise Levels of VIP-sound-proofed Helicopters Compared to Fixed Wing Aircraft

---

presented at the 78th meeting of the AGARD Structural and Material Panel, Lillehammer, Norway, May 1994

Presented at a Symposium on 'Impact of Acoustic Loads on Aircraft Structures' held in Lillehammer, Norway, May 1994.

Cabin noise levels for untreated helicopters are higher than 100 dBA, although this level varies between helicopters of different size, performance, gearbox construction, etc. Most standard helicopters with minimum noise requirements have levels of about 90 to 95 dBA. Soundproofed versions for passenger transport show interior noise levels of about 85 dBA, in some cases like VIP helicopters even lower. The weight of the additional treatment is at least 2% of the helicopter take-off weight.

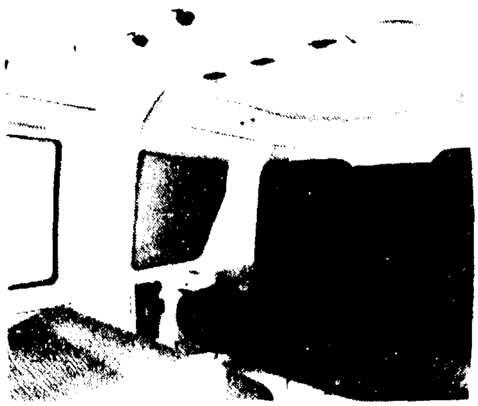

Figure 2: Typical Interior Treatment for High Comfort Passenger Transport

Figure 1 provides a general overview of interior noise levels inside soundproofed helicopter cabins compared to fixed wing aircraft. The main difference to the noise spectrum of an airliner, here represented by an Airbus A320, is given in the frequency range below 1000 Hz.

Figure 2 shows an example of a high insulating interior treatment for VIP transport. For comfort and design considerations, the interior panelling is very heavy to ensure adequate transmission loss.

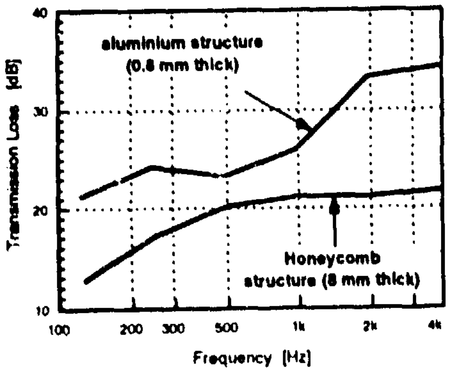

Figure 3: Transmission Loss of Pure Aluminium Structure and Honeycomb Structure (8 mm)

The internal noise problem will even increase, when new composite materials are introduced to helicopter design. Figure 3 shows transmission loss measurements of a conventional aluminium structure and a honeycomb structure, both in a configuration as used in helicopters. The poor performance of the composite panel is caused by the lower weight of the structure itself and due to the reduced number of stringers and spars necessary to provide the same stiffness. It can be foreseen that new helicopter designs with composite materials will be faced with increased interior noise problems.

3. Requirements for Interior Noise

Often noise considerations during helicopter cabin design are of no necessity, since part of the helicopter missions does not require exceptional low interior noise levels. On the other hand, interior noise reduction plays an important role in passengers' acceptance for future helicopter transport.

Nowadays helicopter design takes care of acoustic constraints already in the early design stage. The design goal of an advanced helicopter with low interior noise level has to include the following considerations:

- Human hearing characteristics including hearing risk criteria: Up to now there is no generally accepted limit which defines the comfort threshold. In some countries, there is an requirement for a maximum noise level inside the cabin which should not exceed an 8 hr equivalent continuous noise level L_{eq} of 85 dBA.

  The interior noise level of passenger transport helicopters is more and more oriented towards fixed wing aircraft. However, to reach this goal the level must be considerably reduced compared to existing helicopters. The airliner standard is about 75 dBA. Modern turboprop aircraft also show noise levels below 80 dBA.

- Speech Interference Level (dB(SIL)): The method commonly used to estimate speech intelligibility is based on the measurement of the noise at the listener's ear and a comparison of this value with maximum allowable noise levels for undistorted speech. Hereby, only the frequency range from 350 to 5600 Hz is considered. Modern helicopters are aiming to a SIL value below 75 dB(SIL) which allows communication with normal or slightly increased voice effort.
- Comfort considerations (frequency analysis): More than the integral noise level, pure tone components degrade the comfort inside the helicopter. Especially, as the main gearbox is attached

directly to the cabin deck of the helicopter, a large amount of discrete frequency components are emitted into the cabin.

As the A-weighted dB-sound pressure level often does not represent the subjective impression of noise as accurately as necessary (Figure 4), alternative noise measurement systems are recommended which model the noise reception of the human ear more realistically. An example is the Zwicker method for calculating loudness levels ([2], [3]), based on frequency noise spectra measured in 1/3-octave bands. This calculation method is also used by ECD.

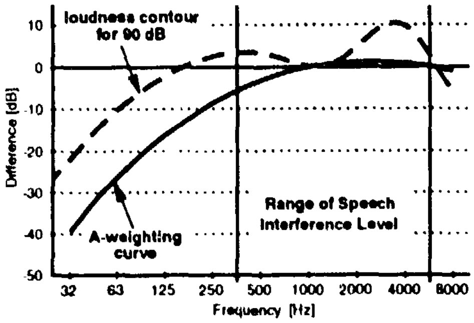

Figure 4: Comparison of A-weighted Curve with Loudness Sensitivity Curve for 90 dB(A)

More advanced measurement systems use artificial heads with a detailed modelling of the human ear. Existing systems include

- modulation of tonal effects
- relation of higher frequency parts of the spectrum to lower frequency parts
- harmony (relation of tonal components)
- masking effects of the human ear
- directivity of the human ear

4. Helicopter Noise Sources

There are numerous sources which contributes to the noise level observed in the helicopter cabin. The main sources and their location with respect to the passengers is given in Figure 5. Those which dominate a typical spectrum (see Figure 6), are both rotors, the engine and auxilliary equipment, airframe noise, and the main transmission. Generally spoken, the spectrum of helicopter cabin noise comprises a complex series of harmonically related discrete tones, superimposed to broadband noise. The sound is transmitted into the cabin either by airborne or structure-borne paths and in some cases by both.

The rotor noise in the cruise flight regime is generated mainly by two mechanisms. The first one is a monopol source called thickness noise, which is due to the fluid volume displacement of the moving rotor blade and becomes a major contribution at high advancing blade Mach numbers. This component is highly directionally. The second type is a dipole source named rotational noise which is generated by the aerodynamic lift and drag forces excerted by the rotor blade on the surrounding fluid. Due to the relative low frequency range, the rotational noise has very little influence on the A-weighted noise level inside the cabin.

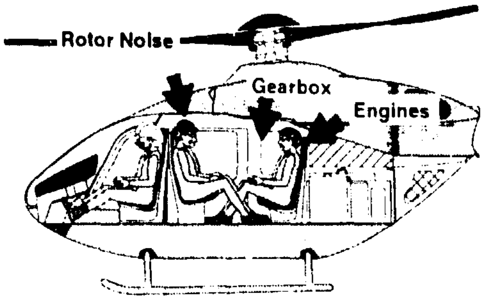

Figure 5: Helicopter Internal Noise Sources

The most annoying rotor noise is blade slap. This highly impulsive sound is generated by blade vortex interaction and is emitted due to its impulsiveness at higher rotor harmonics. Thus, it can become a major contributor to helicopter interior noise as shown in fluctuating surface pressure measurements on the roof of a BO 105 helicopter conducted by the DLR [4]. During blade slap condition, the surface pressure levels were 20-30 dB higher compared to normal horizontal flight. Furthermore, the measurement showed for this specific helicopter type, that the transmission loss of the cabin wall is a minimum in the frequency range of highest rotor induced noise levels.

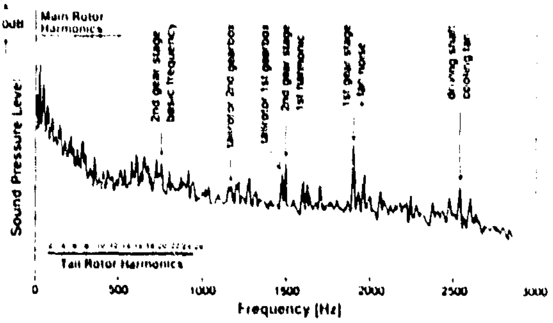

Figure 6: Typical Interior Noise Spectrum in an Untreated Small Size Helicopter

Another aerodynamic source is the boundary layer noise along the fuselage. Especially in the door region, the sound level increases with flight speed because of broadband noise generated by the air streaming along the helicopter fuselage. Further sources for internal noise are auxilliary power units, heating systems, pumps and fans which contribute more or less to a frequency spectrum, depending on the type of helicopter. In the BK 117, for instance, it is the oil cooling fan which transmits a discrete tone at 1900 Hz into the cabin by an airborne path.

The most annoying noise source, however, is the gear noise of the main transmission which propagates on a structure-borne as well as airborne path into the cabin. The meshing frequency, giving rise to high level discrete tones, is equal to the number of gear teeth times the rotational speed. The sound enters the cabin directly by acoustic transmission of airborne noise through the cabin wall and also due to structural radiation by the gearbox struts, the airframe, and finally the interior surfaces such as the floor, doors, windows, and trim panels (Figure 7). The frequency of this noise ranges from about 500 to 3000 Hz and matches exactly the peak responses of the human ear. The narrow band sound is subjectively more annoying than broadband noise of the same sound pressure level.

The position of the main transmission relative to the passengers is a major factor regarding the magnitude of annoyance. The worst case is, when the gearbox is located on top of the cabin above the passengers seats. In small helicopters, effective noise reduction measures are often limited at the ceiling due to the head clearance of the passengers (see Figure 5).

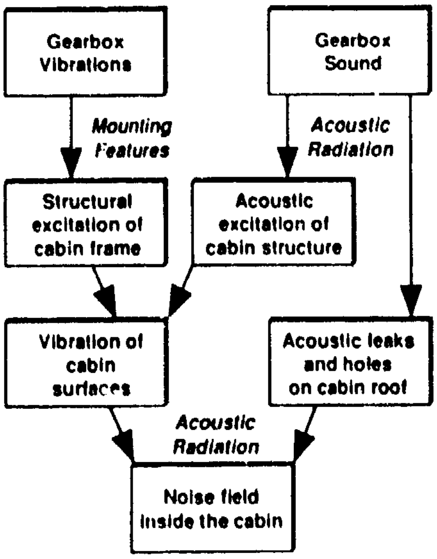
Gearbox Vibrations
Gearbox Sound
Mounting Features
Acoustic Radiation
Structural excitation of cabin frame
Acoustic excitation of cabin structure
Vibration of cabin surfaces
Acoustic leaks and holes on cabin roof
Acoustic Radiation
Noise field inside the cabin

Figure 7: Noise Transmission Paths from the Gearbox to the Cabin

5. Reduction of Interior Noise

Noise reduction at the source of existing helicopters offer some specific problems because each modification is associated with performance penalties and safety reasons. The palliative measures for passive noise reduction are dependant on the transmission paths. If the structure-borne path dominates, structural modifications at the airframe/cabin interface become necessary. If, however, the air-borne path is shown to be dominant, a soundproofing scheme is necessary with the target to concentrate these treatments where they are needed most in order to keep the weight penalties as low as possible.

For future helicopter development, the reduction of interior noise is one of the major challenges. There were several company related interior noise reduction efforts over the last decade ([5], [6] and [7]). A promising programme for interior noise reduction is seen in the current BRITE/EURAM project RHINO (Reduction of Helicopter Interior NOise). The project is supported by the Commission of the European Communities (CEC), Directorate for Science, Research and Development. Based on the experience of the ASANCA (Advanced Study of Active Noise Control of Aircraft) project RHINO represents a balanced and integrated approach to the solution of the closely linked problem of noise and weight control [8]. The noise control strategy within RHINO deals with four different areas:

- noise reduction at the source: Gearbox noise source strength description, and reduction of gearbox noise,
- noise transmission path: Identification of the noise transmission paths and reduction of structure-borne gearbox noise by an active strut,
- propagation of noise to the receiver: Optimization of passive noise reduction, active panel control, and active control by loudspeakers,
- development of an interior noise prediction code.

5.1 Interior Noise Prediction

Theoretical prediction of internal noise is an essential prerequisite for the design and optimization of noise reduction measures of future helicopters. Besides Finite Element (FEM) and Boundary Element Methods (BEM) for the lower frequency range, the Statistical Energy Analysis (SEA) is a prediction tool useful for the higher frequency range.

A new approach to SEA is currently developed under the BRITE/EURAM Research programme RHINO in an attempt to overcome the difficulties in the gearbox related frequency range where the other prediction methods are impracticable. This Advanced Statistical Energy Analysis (ASEA) is based on a travelling wave approach which allows a consistent mathematical description for the vibrational and acoustic energy flow into different coupled subsystems avoiding as much as possible empirical coupling coefficients required by conventionally SEA methods. So far the mathematical subsystems consist out of plates and beams and plates with beams for which the reflexions and the transmission coefficients can be calculated exact for ideal connections. Eventually the real helicopter structure will be broken up into the subsystems available within ASEA possibly requiring hundreds of subsystems similar like the elements for present FEM codes.

In the context the effect of sound absorption in porous media is investigated for to include suitable physical/mathematical models in the ASEA environment. Sound absorption measures will influence the dynamic and acoustic behaviour of a complex structure like a helicopter cabin in different ways. For a foam fixed to a homogeneous panel the increase in weight and stiffness can be taken into account by modifying the elastic parameters of the plate. Acoustic effects of the foam are changed to the radiation efficiency for the plate and changes to the reflexion of incident sound waves from the panel. This will influence the calculated sound pressure levels for cavities as well as the transmitted sound through double walls containing absorption foam, which is common construction for helicopter cabins with trim panels.

In general the acoustic effects are taken into account by replacing the porous medium by a fluid layer with effective compressibility describing the energy loss for the sound wave traversing the layer. Common models are based on a number of empirical parameters related to pore shapes, tortuosity, friction loss, etc increasing the difficulty to calculated the absorption and the transmission of sound with a consistent model.

A new model for the absorption of sound has been developed [9] requiring only geometrical parameters of foams with open cells which can be determined completely from microscopic pictures. The geometrical parameters required are the pore size, the area of connection between the pores and the statistical distribution of these parameters within the foam. The model basically consists out of two steps. One step is the mathematical description of the sound propagation within the pores and the other step is the statistical model to derive effective medium parameters taking into account the variation of pore sizes and connection areas within the foam.

The basic physical model for the porous medium is a three dimensional grid of spherical Helmholtz-Resonators which are interconnected. The pore size determines the volume of the resonators and the connection areas correspond to the neck areas of the resonators. Energy losses are due to the frictional losses of the compressed air to the walls consisting of foam material. Both effects can be calculated for the assumed geometry without empirical assumption.

In the second step the effective frequency dependent sound velocity is calculated by a numerical integration over the statistical fluctuating geometrical parameters of the pores. To determine the effective medium parameters a method is adapted which allows to calculates the effective impedance for three dimensional networks with local disturbances. Applied to the foam in general the result differs from calculating the sound velocity for average pore size.

Figure 8 shows a comparison between measured absorption coefficients for the impedance tube and calculated ones for the new model. Compared to conventional models the agreement is reasonable well enough to take advantage from the fact that only geometrical parameters of the foam were used for the calculation and no additional empirical parameters had to be introduced.

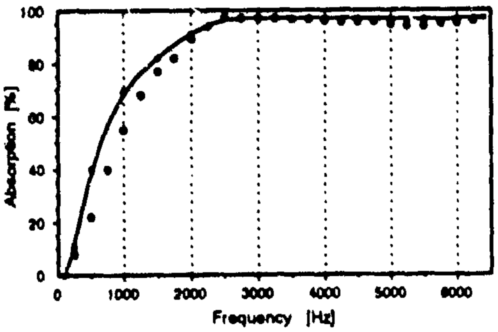

Figure 8: Comparison of Measured (●) and Calculated (*) Absorption Coefficients

5.2 Noise Transmission Path Identification

The noise reduction strategy which is most effective for internal noise, depends fundamentally on whether the acoustic energy is transmitted to the cabin mainly by an airborne or a structure-borne path. Up to now, only experimental path identification methods are feasible to answer this fundamental question for each individual helicopter.

DRA has developed a method for the identification of the noise transmission paths [10]. During flight tests, the acoustical and vibratory excitations are measured with a number of differently oriented interface response transducers which register the magnitude as well as the phase. In a subsequent ground test, mechanical exciters are used at the gearbox to reproduce the in-flight response. Finally, a linear superposition is done to numerically simulate the in-flight response at the interface by using an adequate fitting process.

5.3 Optimization of Soundproofing

In the development of any new aircraft, it is necessary to optimize the interior trim in order to meet noise and weight targets. In the past, this has been accomplished by using sound pressure measurements and a combination of experience and ad-hoc modifications which often ended in an iteration process of measurement and modification. This can be costly and inefficient, and the final solution is not necessarily the optimum one.

Irrespectative of the potential benefits of active noise control, there will always be a requirement for passive measures, especially since many of the active noise control systems are restricted to certain frequency ranges or merely to some discrete frequencies. With regard to the surface area and due to structural considerations, this trim will be a substantial proportion of any noise control strategy. To ensure a maximum of noise reduction with a minimum of additional weight, it is important to achieve an optimum trim distribution. This is of special importance for modern fuselages made out of reinforced composites, since these helicopters are facing severe noise problems compared with conventional aluminium structures.

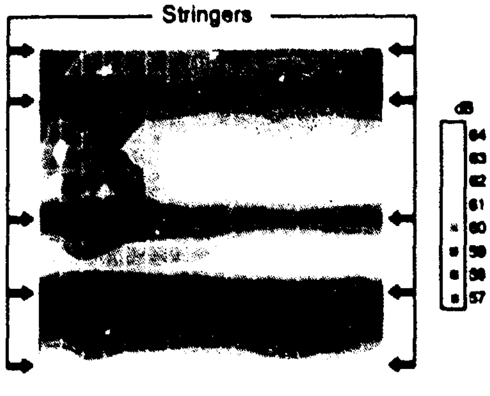

Figure 9: Sound pressure level of the RHINO test structure (238 points, 2000 Hz 1/3 octave band)

Within the RHINO programme, the potential of sound intensity is investigated as a measurement technique to optimize a typical helicopter trim package for minimum noise and weight. Sound intensity measurement is used to calculate the sound power radiated from discrete trim areas fitted into a curved helicopter test structure. It will be subjected to a combination of mechanical and/or acoustic excitations. Interior trim panels coated with various damping layers will be tested. Ranking the radiated sound power will enable a localized trim distribution and thus a weight minimisation. The capabilities of the sound intensity method to determine local noise radiation and acoustic leakage can be seen from Figure 9.

Other subjects for application of sound intensity are feasible and would increase the knowledge of the acoustics of helicopter cabins:

- detailed analysis of the amplitudes and phases of the sound pressure inside the cabin.
- analysis of noise transmission pathes by measurement of the sound intensity inside and outside the cabin combined with vibration intensity flow measurements
- real time source location with a three dimensional vector probe.

5.4 Passive Means for Interior Noise Reduction

Within the scope of optimized passive noise reduction, multilayer trim panels were tested with respect to global and discrete frequency damping. Several test structures, similar to helicopter structural components, were arranged in a test window between reverberation room (excitation) and anechoic room (measurement).

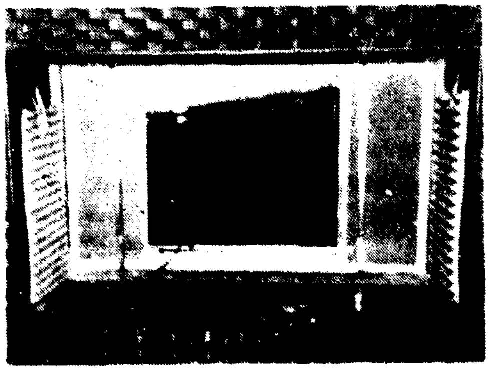

Figure 10: Test Set-up for Improvement of Cabin Door Transmission Loss

Figure 10 shows as an example the test set-up for the BO 108 (EC 135) cabin door improvement programme. In addition, a flat and a curved honeycomb structure, and an aluminium structure were tested. All the test structure were manufactured similar to real helicopter structural parts. The sound field data acquired with the intensity measurement technique was used to determine the distributions of radiated sound power.

The transmission loss of the BO 108 (EC 135) door components - window, spars and honeycomb structure - was measured at 31 points. Based on the local sound power radiation, modifications to the cabin door were implemented in order to reach an adequate damping characteristic of all door components. Figure 11 shows the transmission loss values before and after modification.

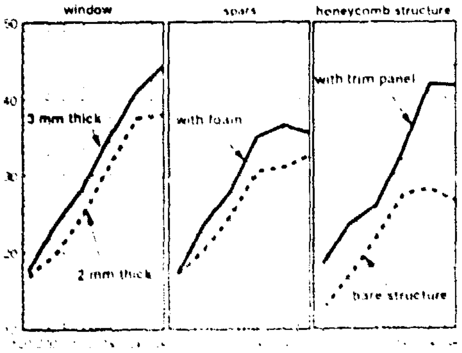

Figure 11: Sound Transmission Loss of the BO 108 cabin door before and after Modification

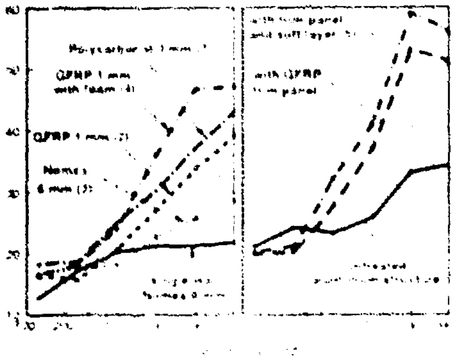

Figure 12: Investigation of transmission loss of different trim panel configurations

Figure 12 shows measurements of the transmission loss of various trim panels. The materials were different in thickness, mass and stiffness. The transmission loss increases with weight, as expected. Normalized to the same weight, the Polycarbonat (PC) plate (1) and the Glass-fibre-reinforced-composite (GFRP) plate (2) show the same transmission loss, whereas the 6 mm Nomex honeycomb plate (3) has significantly lower values.

An increase in transmission loss was achieved by filling the 25 mm space between fuselage structure and panel with foam (4). The transmission loss increased by 3 to 10 dB at frequencies above 250 Hz. A further noise reduction is achieved by adding of a light-weight third soft layer (Nr. 5 of Figure 12).

5.5 Resonators for Additional Absorption

In the lower frequency range, the sound energy can not be absorbed sufficiently due to the relative large wave lengths compared to the thickness of absorption materials. Here, resonance absorber systems offer an additional sound reduction, especially for light helicopters which normally cannot provide the space required for conventional measures.

Resonance absorbers like the Helmholtz resonator are mass-spring systems. The air in the hole of the resonator can be regarded as the oscillating mass. The chamber volume located behind, is equivalent to the spring. The attenuation bandwidth of a these resonators is relatively narrow. By selecting differently tuned resonators, the bandwidth can be spread to a broader characteristic. Modern helicopter fuselage designs imply more and more honeycomb structures which can easily be converted to Helmholtz resonators (Figure 13). By perforating the cover layer of the honeycomb wall, frequentially tuned resonators are obtained.

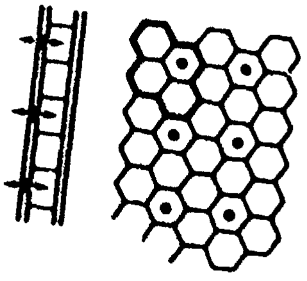

Figure 13: Honeycomb Cores Converted to Helmholtz Resonators (25% of the Cores)

A honeycomb panel was tested with 6, 12, and 25% of the honeycomb chambers used as resonators. They were tuned to the most annoying gearbox frequency of 1900 Hz. The absorption coefficient of the wall without resonators is lower than 0.12 at 1900 Hz. As can be seen in Figure 14, absorption and bandwidth increased strongly with the resonator density. An absorption degree of 0.98 has been achieved if every forth honeycomb core was converted to a resonator. It should be noted, that this kind of absorption inside the cabin requires no additional weight.

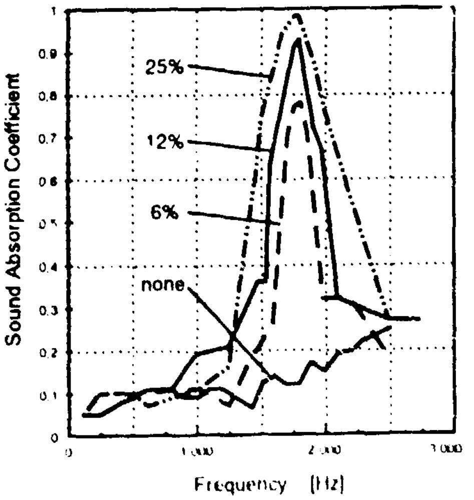

Figure 14: Absorption of the Honeycomb Plate with Different Number of Cores Converted to Resonators (6%, 12%, 25%)

Resonators are also able to reduce noise at the source, for example at an oil cooling fans. Fan noise may be divided into a rotational and a vortex component. The rotational part is a series of discrete tones at the fundamental blade passage frequency and its harmonics. Because of the constant rotation provided by the main gearbox, resonators are appropriate means for reducing the rotational noise component.

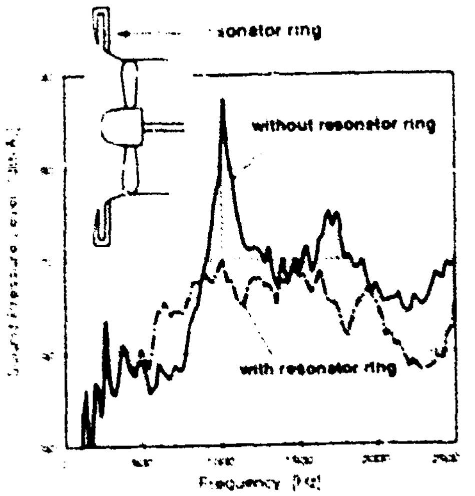

Figure 15 Noise Reduction by a Resonators Ring on an Oil-cooling Fan

For investigations with a 8 bladed radial fan, a ring was fixed to the air inlet containing three rows of Helmholtz resonators, which were tuned to different frequencies. The frequency spectrum with open and closed resonators is shown in Figure 15. This design of an inlet silencer provides a rather broadband and not only a discrete frequency damping characteristic with considerable high sound pressure level reductions. As the volume flow of the fan changed only by 1%, the efficiency of the fan will not be influenced. By a close arrangement of the resonator layers, it is possible to integrate the resonator ring in the air inlet structure.

5.6 Gearbox Noise

The transmission system of a helicopter generates a discrete frequency noise which is mainly transmitted into the cabin by the gearbox struts. In general, there is very little structure-borne noise attenuation through any path between gearbox and cabin because there are only small impedance changes to cause major losses. As an example, in Figure 16, a simultaneously measured gearbox vibration and a cabin sound spectrum is shown. The transfer of the acceleration levels into the cabin is very impressively illustrated in this Figure.

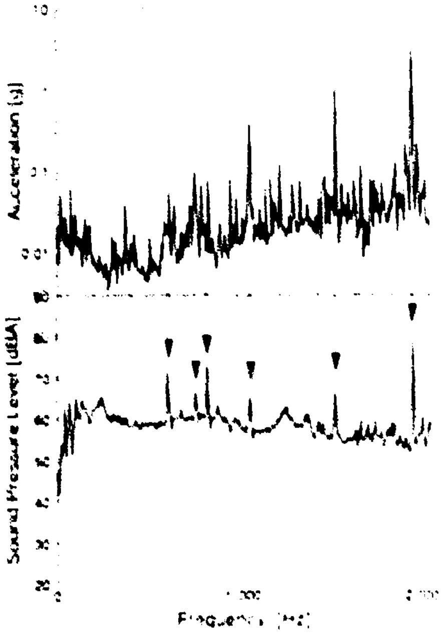

Figure 16 Acceleration at the Gearbox Mount and Cabin Sound Levels Measured in the BK 117

It is highly desireable to decrease the noise emission of the gearbox itself because a reduction at the source is more effective and less weight consuming than passive measures in the cabin. The major design goal of a helicopter gearbox is minimum weight combined with high reliability and an adequate service life. Consequently, the toothing and bearing characteristic of the gearbox is optimized in a way which is often acoustically unfavourable.

A significant noise reduction was achieved by EUROCOPTER France (former Aerospatiale helicopter) in the modification of a Dauphin SA 365 gearbox. Hereby the input spiral bevel gear toothing were redesigned to ensure a better meshing continuity, which led to a reduction of the gearbox meshing noise by about 15 dB and the internal noise by 6.5 dB SIL (Speech Interference Level) Furthermore, the noise transmission characteristic of the gearbox mounts have been modified by adding local weights to the bars. The comparable low weight penalty of 1.3 kg resulted in a reduction of the internal noise by 4.2 dB(SIL)

A further reduction is expeced by a noise oriented layout of the gearbox casing. By adding damping materials to the casing or, even better, by using casing materials that offer a large internal damping, the vibration itself and the coupling effects between the transmission excitation and the casing response will be reduced.

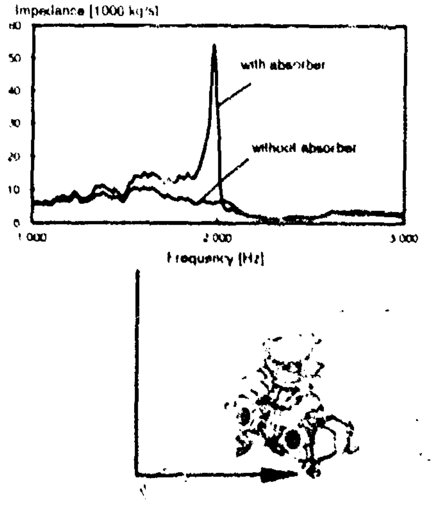

Figure 17: Impedance Measurements on one of the Four Vertical Gearbox Levers With and Without Absorbers

Since design changes of the gearbox itself are often impossible, it is convenient to change the transmission characteristics of the gearbox struts. An adjustable resonance vibration absorber fixed to the struts and tuned to the gearbox frequency absorbs some of the acoustic energy. As an example, Figure 17 shows the point impedance measurement of one gearbox strut with and without absorbers. All four vertical struts show similar frequency responses.

With absorbers - each one weighs about 0.8 kg - the impedance increased dramatically. The position where the absorber is fixed to the helicopter, is essential for its design. The schematic diagram of the test set-up is shown in Figure 18. Figure 19 shows the acceleration transmitted by the gearbox lever with and without absorber during ground tests. The excitation (by shaker) was at the gearbox side while the acceleration was measured at the attachment point of the gearbox strut to the cabin structure. The vibration transmission was decreased by a factor of 1000 at the desired discrete frequency.

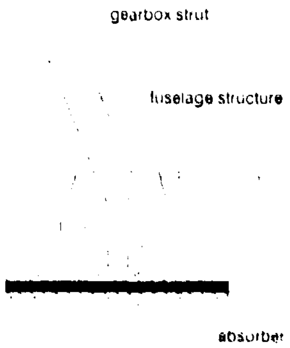

Figure 18: Schematic Diagram of the Test Arrangement Inside the Helicopter

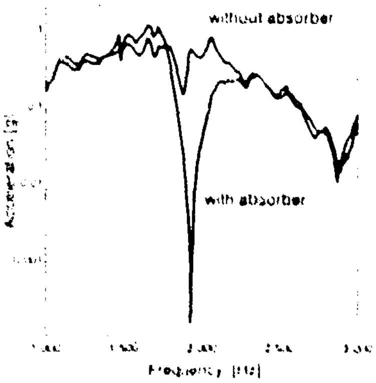

Figure 19: Vibration Transmission Frequency Response of a Gearbox Strut With and Without Absorber

6. Noise Reduction by Passive Measures on Helicopters

As an example of an improvement of the interior noise without large weight penalty, a BK 117 has been equipped with some of the previously examined damping and absorptive measures (improved double wall system with additional soft layer, improved door and window sealing, resonators). Compared with the original equipment which also represents a noise treated interior standard, the noise level could be considerably decreased (Figure 20). At a flight speed of 110 kts, the noise level reduction was 5 dBA. At a higher flight speed, the internal noise level is dominated more and more by boundary layer noise especially in the cabin door region which limited the noise reduction to 4 dBA at 130 kts. Still, these values do not reflect the real improvement in comfort, since very annoying discrete tones in the 2000 Hz 1/3-octave band were reduced by 12 dB at 110 kts and 7 dB at 130 Hz.

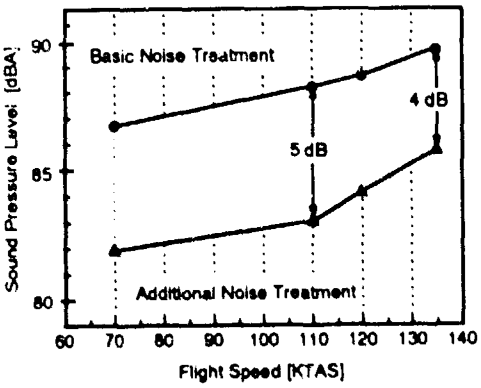

Figure 20: BK 117 Measurement Results Before and After Additional Passive Noise Treatment

7. Isolated Inner Shell

The problem of reducing structural radiation can be solved to a certain extent by use of an isolated inner cabin. This concept consists essentially in limiting the number of vibration transmission pathes by using a separate frame for the cabin, which is mounted vibrationally isolated to the airframe by use of high mass transmission barriers. The correct method of mounting is essential to ensure that the high vibration levels of the airframe are not transmitted to this inner cabin. This isolated inner cabin concept was successfully applied by Westland Helicopter on a VIP Commando [11]. However, the inner shell concepts realized up to now were a very weight intensive and expensive solution.

8. Active Control of Noise and Vibrations

Conventional passive noise reduction methods for interior noise like constructive modification of the fuselage, gearbox mounting, or additional damping and absorption often lead to an impairment with respect to other design goals. Especially at low frequencies, passive measures are inadequate (heavy and space consuming) to provide the required acoustic effect for low noise levels in the helicopter cabins. Here, active noise or vibration control may contribute significantly if discrete tones deteriorate the passengers comfort. Active vibration control can be applied to the gearbox itself, at the interface between gearbox and cabin, and at the radiating interior trim panels itself. Active noise control directly by loudspeakers is applied to the interior noise field.

Active Gearbox Strut

In the past, active gear box struts were developed by several manufacturers in order to reduce the 4/rev cabin vibration levels. These systems were based on hydraulic actuators and therefore restricted to low frequencies. Figure 21 shows a principle scheme of an active gearbox vibration control system. Active systems with application to noise relevant frequency ranges will use electrodynamic or magneto-restrictive actuators.

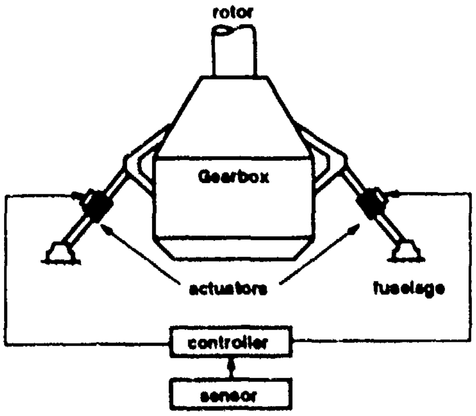

Figure 21. Functional Scheme of an Active Gear box Strut

Even in case of small helicopters, fluctuating forces on the gearbox struts are extremely high. The energetic disadvantage by compensation of these forces is obvious. Furthermore, the gearbox is connected to the cabin by several elements to transmit forces and moments. All of them transmit structure-borne noise and therefore must be provided with by an active system.

Active Noise Control by Loudspeakers

Active noise control uses an array of loudspeakers to minimize the sound pressure level at a number of error microphones inside the cabin. The technology has been successfully applied to cars and propeller airplanes [12], [13]. With respect to the first three propeller blade passage frequencies, a reduction potential of 10 to 20 dB were indicated. Active sound control systems may be configured to produce noise reductions at local regions or globally throughout the entire cabin volume. The necessary effort of the system is dependant on the complexity and extension of the sound field. Feasible systems include one loudspeaker and two microphones for each passenger seat.

For helicopters, active noise control by loudspeakers is thought to reduce the discrete frequencies of the main and tail rotor up to 200 or 300 Hz at the maximum. However, the system is not able to cope with tonal components of the main transmission which start to be significant above 300 Hz. Active vibration control is here a more promising method to reduce cabin noise.

Active Control of Panels

Within the BRITE/EURAM project RHINO, active panel control will be investigated to reduce structurally radiated sound by application of active forces directly to vibrating panels. Figure 22 shows a principal scheme of an active panel control system. Basic investigation of the global layout of an active panel control prototype and the control algorithm development will be performed on a flat honeycomb sandwich structure. The implication of an active panel control system by interaction of helicopter fuselage, panels, actuators and sensors will be evaluated by use of a realistic helicopter test structure.

Both tests will be used for the definition of appropriate sensors and actuators. The test structures will be excited with airborne and structure-borne noise. The resulting structural vibrations will be suppressed by directly applying active forces to the panels. High noise reduction is expected for single modes by using point force actuators like electrodynamic shakers. As these actuators are heavy, voluminous, and need a supporting structure, distributed actuators based on piezo-electric materials will also be taken into consideration. The main disadvantage of piezoelectrical materials is their small displacement, however, research on new materials like piezo-electric materials based on bimorph principle are expected to overcome this disadvantage.

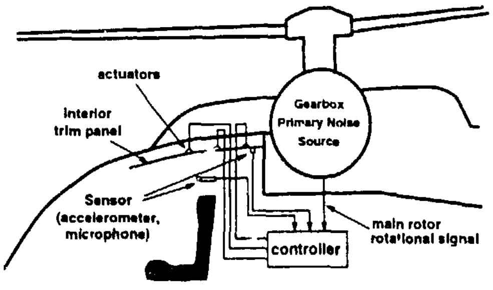
actuators
interior trim panel
Gearbox Primary Noise Source
Sensor (accelerometer, microphone)
controller
main rotor rotational signal

Figure 22: Principle Scheme of Active Panel Control

The theoretical and experimental investigation will lead to an adapted instrumentation for active control experimentation. The resulting prototype system will be applied and tested on the laboratory test structure. The embedding conditions and the excitation sources will be chosen in a way to simulate as close as possible to real helicopter flight conditions.

Conclusions

In the past, cabin noise was often judged only by its A-weighted sound pressure level. The result was a global noise reduction strategy, but in many cases only with minor improvement in annoyance level. In order to optimize the relation of noise reduction to weight of the interior trim, subjective noise measurement systems are very helpful to specify the most annoying spectral components of the cabin noise.

The cabin noise level of passenger transport helicopters must be considerable reduced if they are oriented towards fixed wing aircraft. However new helicopter design with composite materials are facing even more noise problems which are caused by the lower surface weight itself as well as the reduced number of stringer and spars necessary to provide the same stiffness. Consequently, additional soundproofing material is required to compensate for it.

Passive soundproofing design is mainly based on past experience. However, there are possibilities of improving the existing interior trim. The sound intensity mapping technique does help to find acoustic leaks and thus enabling a localized trim distribution with a minimum of weight. Acoustic resonators and absorbers as well as an optimized double wall system should be included in a fully integrated passive installation.

Active noise control systems offer advantages in the low frequency range, where passive measures are limited in efficiency. A careful analysis of the performance of the active system on the global noise reduction and annoyance improvement must be conducted.

Acknowledgements:

Part of the research described in this paper has been supported by the BRITE/EURAM project RHINO.

The authors would like to thank Dr. M. Grünewald for his contribution and helpful comments to this paper.

References:

/1/ Kryter, K. D., "Exposure to steady state noise and impairment of hearing", JASA 35 (1963)

/2/ ISO-Recommendation R532 - 1966: "Method for Calculating Loudness Levels"

/3/ Eberhard Zwicker, "What is a Meaningful Value for Quantifying Noise Reduction?", Institute for Electroacoustic, Technical University München, presented at the Internoise 85, München, 18-20 September 1985

/4/ K.-J. Schultz, W.R. Splettstößer, "Fluctuating Surface Pressure Characteristics on a Helicopter Fuselage Under Hover and Forward Flight Conditions", DLR, presented at the 4th European Rotorcraft Forum, Stresa/Italy, Sept. 1978, Paper 59

/5/ P. Bellavita, J. Smullin, "Cabin Noise Reduction for the AGUSTA A-109 Helicopter", 4th. European Rotorcraft Forum, Stresa, Italy, 1978

/6/ H.J. Marze and F.N. d'Ambra, "Helicopter Internal Noise Treatment - Recent Methodologies and Practical Applications", 11th. European Rotorcraft Forum, London, England, 1985

/7/ E. Laudien, G. Niesl, "Noise Reduction Inside Helicopter Cabins", 16th. European Rotorcraft Forum, Glasgow, United Kingdom, 1990

/8/ G. Vignati, K. Heron, M. Ohlrich, G. Niesl, S. Marulo, "Research on Helicopter Interior Noise: A Survey on Current Activities in Helicopter Industries", pres. at the AERODAYS 1993 in Naples

/9/ M. Grünewald, G. Engel, W. Schirmacher, "Schallabsorption in porösen Medien", 20th German Acoustic Conference - DAGA 94, Dresden, Germany, 1994

/10/ K. Heron, C. Davies, "A New Path Identification Method in Structural Acoustic", Royal Aerospace Establishment, Technical Report No. 89060

/11/ J. S. Pollard, J. W. Leverton, "Cabin Noise Reduction - Use of Isolated Inner Cabins", 2nd. European Rotorcraft Forum. Sept. 1976, Germany

/12/ S. J. Elliot, P.A. Nelson, I. M. Stothers, C. C. Boucher, "In-flight Experiments on the Active Control of Propeller-induced Cabin Noise", Journal of Sound and Vibration, 1990, 140(2)

/13/ I. U. Borchers et al, "Advanced Study for Active Noise Control in Aircraft (ASANCA)", DLRG/AIAA 14th Aeroacoustic Conference, May 1992, Aachen, Germany

DIMENSIONNEMENT ET QUALIFICATION AEROACOUSTIQUE DES TUILES HERMES

AEROACOUSTIC QUALIFICATION OF HERMES SHINGLES

par

C. PETIAU[*]
et
A. PARET[**]
Dassault Aviation

RESUME

Les problèmes généraux de l'analyse aéroacoustique sont présentés ici en prenant exemple de l'étude des tuiles de la Navette Spatiale HERMES Le dessin particulier des tuiles et leur environnement aéroacoustique très sévère rendaient là cette analyse particulièrement difficile.

Les outils d'analyse disponibles sont passés en revue
- Moyens de calcul, qui sont globalement ceux de l'aéroélasticité,
- Moyens d'essais au sol (souffleries, tubes à ondes progressives, tables vibrantes,...).

Aucun de ces moyens ne peut être suffisant, à lui seul, pour valider le dimensionnement des structures ; en particulier la modélisation des sources turbulentes n'est pas possible aujourd'hui et la simulation expérimentale de leurs effets sur les structures semble très difficile

En dépit de ces difficultés, en s'appuyant sur les calculs et les essais préliminaires des tuiles HERMES, une stratégie rationnelle est proposée pour le dimensionnement et la qualification vis-à-vis de l'aéroacoustique

On aboutit à un enchaînement d'essais dont les conditions sont déterminées par calcul, les modèles de calcul étant eux-mêmes validés par comparaison aux résultats d'essais

ABSTRACT

General problems of aeroacoustic analysis are presented here, taking as an example shingle studies of HERMES space shuttle. Analysis of shingle behaviour meets this problem in a particularly difficult way (very hard environment, specific difficulties due to design of shingles).

Available analysis tools are listed
- Calculation means, which are mainly those of aeroelasticity,
- Ground test means (wind tunnel, progressive wave tubes, shakers, ..).

None of these means can alone satisfy the needs of structural dimensioning and qualification ; in particular the calculation of turbulent sources is not possible today, and they are very difficult to simulate with ground test of actual structural parts

In spite of these difficulties, and referring to the preliminary tests and calculations of HERMES shingles, a rational strategy is proposed for aeroacoustic dimensioning and qualification of structural parts

This leads to a succession of tests, the conditions of which are determined by calculations, calculation models being themselves validated by comparison with test results

---

[*] DASSAULT AVIATION - Cedex 300 - 92552 St Cloud Cedex - Tel 33(1)47 11 31 89 - Fax 33(1)47 11 34 00

[**] DASSAULT AVIATION - Direction Technique Espace B P 23 - 31701 BLAGNAC Cedex

Presented at a Symposium on 'Impact of Acoustic Loads on Aircraft Structures' held in Lillehammer, Norway, May 1994.

1. INTRODUCTION

On appelle phenomenes "aeroacoustiques" l'ensemble des fluctuations de pressions et des vibrations de structure engendrees par les écoulements aérodynamiques turbulents et les mouvements d'onde de choc Pour les avions le plus classique des phenomenes aeroacoustique est le tremblement (Buffeting)

Dans la gamme des moyennes frequences (quelques dizaines a quelques centaines de Hertz), les phenomenes aeroacoustiques peuvent être source de dommages divers pour les structures et les equipements des avions fissures de fatigue, voire ruptures statiques Ils sont aussi sources d'inconfort pour les pilotes et les passagers

Les problemes aeroacoustique peuvent se rencontrer de façon plus ou moins aigue pour tous les types d'avion, les exemples les plus classiques sont liés aux sillages d'aerofrein et de charges exterieures Cependant c'est avec l'etude des tuiles de protection thermique de la navette HERMES que nous avons rencontre les problemes d'aeroacoustique avec le maximum d'acuite, cela du fait de l'environnement tres severe du vehicule au lancement, de sa forme aerodynamique peu propice et de la specificité structurale des tuiles

Nous allons exposer ici les grandes lignes des problemes poses par l'analyse aeroacoustique en general, ils sont principalement liés aux difficultes d'effectuer des calculs precis et de trouver des moyens d'essais au sol representatifs Nous présentons les solutions utilisables actuellement et les développements qu'on proposerait a partir des leçons tirees de l'etude des tuiles HERMES, ils sont globalement transposables pour la conception et la qualification de cellules d'avions plus classiques

2. AEROACOUSTIQUE DES TUILES HERMES

Pour le projet de navette spatiale HERMES l'environnement aeroacoustique le plus severe etait prevu pendant les phases transsoniques du lancement (voir planche 2), cela tant du fait d'une pression dynamique relativement elevee (0,45 bar), qu'en raison de la forme très emoussee de l'avion (voir planche 1) Cette forme est necessaire pour limiter l'echauffement cinetique de rentree, mais elle est peu propice pour eviter les decollements d'ecoulement et les instabilites d'onde de choc

Dans certaines zones les niveaux acoustiques globaux peuvent atteindre 162 db auxquels peuvent se rajouter des fluctuations de pression de l'ordre de 300 mb a basse fréquence (~ 10 hz) dues aux mouvements d'ondes de choc

Les éléments les plus sollicités par cet environnement aéroacoustique sont les tuiles de protection thermique auxquels nous nous intéressons ici, elles couvrent l'ensemble de l'intrados du véhicule et la partie avant du fuselage (voir planche 1) Elles sont constituées de panneaux minces (épaisseur environ 1 mm) en composite céramique C-SiC protégeant un bloc d'isolant ultra leger fait de multiples écrans réflecteurs séparés par des feutres isolant, les principales caracteristiques sont résumées planche 3

Cette conception de tuile, dont on demontre par ailleurs tous les avantages par rapport a d'autres solutions, notamment par rapport au système de "Pave" choisi pour l'Orbiter US (voir référence 1), presente des spécificites compliquant, s'il était besoin, l'analyse aéroacoustique par rapport à celle des structures classiques, ce sont

- Le materiau C-SiC dont la rheologie est très non-linéaire (voir planche 4), mais qui par contre presente une résistance mécanique interessante (au-delà de 200 MPa) et une très faible sensibilité à la fatigue et aux effets d'entaille (ce materiau supporte par ailleurs des températures superieures a 1300°C en restant très faiblement sensible a l'oxydation)
- La non-linearite d'effet de membrane tres prononcee du panneau (voir planche 4 la courbe de flèche en fonction de la pression statique) Cela se traduit aussi par une tres forte sensibilite de la frequence des modes de vibration à la pression statique
- Le comportement complexe des joints et de l'isolant interne (raideur non lineaire, hysteresis,)
- L'effet de raideur "pneumatique" important susceptible d'être creé par l'air de la cavité sous tuile (~ 20 % d'augmentation de frequence fondamentale entre une tuile non etanche et une tuile etanche, voir planche 10)
- Les effets de couplage aeroelastique importants dus à la faible épaisseur relative du panneau, qui conduisent a une sensibilite au Flutter dont l'analyse est un préalable à celle de l'aeroacoustique (voir planche 11)

Ces comportements complexes compliquent certes les calculs, mais, ils sont tres favorables pour le comportement aéroacoustique des tuiles, en créant des dissipations d'énergie importantes et des cycles limites qui réduisent les amplitudes des vibrations.

3. PANOPLIE DES OUTILS D'ANALYSE ET DE VERIFICATION DISPONIBLE

3.1. OUTILS DE CALCUL

La base de la panoplie d'outils de calcul utilisable aujourd'hui pour l'aéroacoustique est globalement celle de l'aéroélasticité ; on en trouvera les détails dans les références 2, 3 et 4 ; les grandes lignes sont les suivantes :

- Modélisation de l'aérodynamique instationnaire dans le domaine fréquence, à partir des équations de potentiel résolues par méthode de singularité, sources et doublets (voir références 5 et 6).

  Dans cette approche les zones d'écoulement turbulent sont représentées par une certaine densité de source répartie dans le fluide.

  On obtient en sortie les opérateurs de transfert complexes reliant les pressions de paroi aux variations d'incidence de ces parois et à l'intensité des sources turbulentes, soit :

  1 $P = \frac{1}{2} P V^2 [A(\omega,V)]\alpha + \frac{1}{2} P V^2 [B(\omega,V)]$

  I.s tur

  La difficulté est que nous n'avons aujourd'hui aucun moyen d'appréhender le 2ème terme de cette équation, ne sachant en pratique calculer ni la position ni l'intensité des sources turbulentes.

  On contourne ce problème en constatant que ce 2ème terme a la signification des pressions engendrées sur une paroi rigide par les sources turbulentes , on doit alors obtenir ces pressions expérimentalement, l'équation 1 devient alors .

  2 $P = \frac{1}{2} P V^2 [A(\omega,V)]\alpha + \mathrm{Pr}$

  Ce type de modèle se prolonge naturellement à Mach = 0 et V = 0 en un modèle acoustique.

  Les maillages surfaciques de ces modèles aérodynamiques comportent de quelques centaines à quelques milliers de facette, ce qui est le rang de la matrice de coefficients d'influence complexe à construire et inverser pour chaque fréquence de calcul.

  Quand on ne s'intéresse qu'à l'aéroacoustique extérieur (pas de réverbération d'onde acoustique) les opérateurs calculés sont relativement continus en fonction de la fréquence. Ce qui autorise à ne faire le calcul complet que pour un nombre limité de fréquences (quelques dizaines au plus), entre lesquels les résultats sont interpolés.

  Il en résulte un calcul relativement peu coûteux aujourd'hui.

  Le défaut évident de la méthode est de ne pas calculer les sources turbulentes. Ceci nécessiterait, dans l'absolu, la résolution de l'équation de Navier Stokes instationnaire au nombre de Reynolds du vol des avions. Ce problème, cible de la "Computer Fluid Dynamic" (C.F.D.) est assez loin d'être résolu industriellement. En attendant, certains proposent des techniques intermédiaires basées sur des modèles semi-empiriques de distribution de source turbulente calibrés sur des essais (voir référence 7).

- Modélisation structurale

  Elle est généralement obtenue par technique d'Eléments Finis. Le plus souvent, en linéaire on utilise comme degré de liberté les modes propres structuraux. On calcule ainsi les termes de l'équation de la dynamique structurale

  3 $[M]x'' + [C]x' + [K]x = [T]P$

  Cela à l'exception des termes de la matrice d'amortissement structurale dont on ne connaît généralement pas les bases physiques qui permettraient de les calculer. Les amortissements structuraux sont donc soit dérivés d'essais, soit négligés (si la dissipation d'énergie par rayonnement acoustique ou par amortissement aeroélastique est jugée prépondérante).

- Modélisation acoustique interne

  La méthode de singularité utilisée pour l'acoustique externe serait utilisable avec la difficulté que l'existence de mode acoustique de cavite crée des pics aux fonctions de transfert acoustique interne, ce qui nécessite donc de très nombreux points de calcul en fréquence (quelques centaines à quelques milliers) contrairement au cas de l'acoustique externe On préfère utiliser une modélisation des cavités internes par Elément Fini tridimensionnel adaptée à l'équation d'Helmoltz (voir planche 7), associée à une réduction modale "acoustique" (voir référence 8).

- Couplage des modèles

Les équations couplées entre les 3 types de modèle sont établies en considérant la compatibilité des déplacements, l'équilibre des forces et la conservation des travaux virtuels à leurs interfaces ; la difficulté principale vient de la non coïncidence géométrique à la frontière des maillages de chaque modèle à coupler (adapté prioritairement aux spécificités de sa discipline), nous en détaillons la technique dans les références 3 et 4.

Il en résulte le système d'équation couplé formulé dans le domaine fréquence de la forme :

$$\left(-\omega^2[M]+i\omega[C]+[K]-\frac{1}{2}\rho V^2[A(\omega,v)]\right)x=[T]\mathrm{Pr} \tag{4}$$

ou

$$[D(\omega,V]x=[T]\mathrm{Pr} \tag{4'}$$

La matrice [D (ω,V)] est l'opérateur classique de l'analyse du Flutter (sa singularité correspond à la vitesse de Flutter).

Les modèles de chaque discipline fournissent les opérateurs permettant de passer des degrés de liberté aux paramètres qu'on veut suivre (accélérations, déformations, contraintes, efforts internes, pression dans les fluides, etc...) soit :

$$s=[L]x$$

On déduit la fonction de transfert entre les pressions de la turbulence sur paroi rigide et les paramètres suivis , soit :

$$s=[L][D(\omega,V)]^{-1}[T]\mathrm{Pr}$$

ou

$$s=[H(\omega,V]\mathrm{Pr}$$

On en déduit les spectres de puissance des paramètres suivis en fonction des spectres et interspectres* des composantes du vecteur soit :

$$S(s_i,s_i)=\sum_m\sum_n H_m H_n S(\mathrm{Pr}_m,\mathrm{Pr}_n)$$

de là on passe au nombre moyen de dépassements d'un niveau donné de ces paramètres suivis par la formule de Rice (voir référence 9) soit :

$$N(a)=N(o)e^{\,a^2\;2(RMS(s))^2}$$

avec

$$N(o)=\frac{1}{\Pi}RMS(s')/RMS(s)$$

ce qui permet d'effectuer les prédictions statistiques de durée de vie aussi bien vis-à-vis de la résistance statique que de la fatigue (à partir des abaques expérimentales de résistance en fatigue cyclique et en admettant la règle de cumul de dommage de Miner).

Pour prendre en compte les non-linéarités structurales (telles qu'on les rencontre sur les tuiles HERMES) on dispose de 2 techniques :

- La linéarisation du modèle autour de l'équilibre statique calculé en non-linéaire (voir référence 10) et l'utilisation dans l'équation de la dynamique structurale 3 de la matrice de rigidité "tangente" à l'équilibre.

- Le calcul structural dynamique non-linéaire (grands déplacements, plasticité et rhéologie non linéaire, contact) par intégration directe dans le domaine temps.

Pour ce calcul non linéaire couplé la difficulté est de disposer d'un modèle aérodynamique dans le domaine temps. Pour cela nous utilisons généralement une procédure simple, homogène à la rusticité globale du modèle aérodynamique, où l'opérateur de couplage aérodynamique est identifié par lissage dans le domaine fréquence avec des effets de raideur, amortissement et de masse ajoutées, après

---

* qu'il faut donc obtenir par mesure

transposition dans le repère des degrés de liberté E.F., ces termes de couplage aérodynamiques sont ajoutés aux termes correspondants de l'équation différentielle du mouvement en non-linéaire.
Le champ de pression d'excitation dans le domaine temps est soit dérivé directement des mesures brutes en soufflerie en fonction du temps, soit "reconstitué" à partir des matrices de spectres de pression (ceci permet des prolongements statistiques pour obtenir les cas limites).

Avec l'outil ELFINI dont dispose DASSAULT AVIATION les procédures de calculs linéaires et linéarisés évoquées ici sont aujourd'hui peu coûteuses en temps de calcul ; il n'en va pas de même pour le non-linéaire "complet", surtout si les modèles structuraux sont importants et si on veut accéder aux caractéristiques statistiques de la réponse non-linéaire. (Nécessité de disposer d'échantillons de réponse dans le temps longs ou nombreux). Ceci nous a amené pour les tuiles HERMES à réserver cette analyse non linéaire complète à la compréhension qualitative des phénomènes et à la reconnaissance des limites de validités des approches linéaires et linéarisés.

3.2. MOYENS EXPERIMENTAUX

Nous avons mis en oeuvre ou envisagé les types d'essais suivants pour les tuiles HERMES.

3.2.1. Essais en soufflerie sur maquette rigide

Ils ont été effectués principalement dans les souffleries HST et SST du NLR entre Mach 0,7 et Mach 3 sur des maquettes au 1/30ème et 1/40ème instrumentées d'une quarantaine de capteurs de pression instationnaire

Ils ont visé à établir :

- Une compréhension des phénomènes aérodynamiques (positions et mouvement des chocs, décollements turbulents, etc par visualisation strioscopique, voir planche 6).

- La mesure des spectres et de quelques interspectres aux points estimés les plus critiques, qui ont servi de base à l'établissement des charges aéro-acoustiques

Les questions qu'on se pose pour exploiter les résultats de ces essais sont :

- Sont-ils extrapolables à l'échelle 1 du fait de la non-similitude de Reynolds.

- Sait-on a priori implanter aux points les plus pertinents les capteurs dont on dispose (du fait de leur encombrement et de leur nombre limité).

3.2.2. Essais en soufflerie avec éléments structuraux réels en paroi (tuile réelle ou maquette d'étude dynamique à échelle 1)

Ils sont été effectués en plaçant les éléments à tester en paroi de la soufflerie HST du NLR (Mach 0,8 à Mach 1,2), voir planche 7.

Un déflecteur amovible crée un sillage turbulent en amont de la tuile. L'épaisseur de couche limite est partiellement réglable.

Ce type d'essais avait 2 buts :

- Vérifier le comportement au Flutter des tuiles et valider les modèles de calcul (déflecteur enlevé).

- Vérifier le comportement aéroacoustique. On s'est heurté là à la difficulté d'estimer la représentativité vis-à-vis du vol de l'écoulement extrêmement complexe créé par le déflecteur.

3.2.3. Essais acoustiques en tube à ondes progressives (T.O.P.) (effectués dans l'installation de l'IABG, voir planche 8)

Ils ont l'avantage d'être beaucoup moins coûteux que les précédents mais ils présentent un problème inhérent de représentativité.

Le couplage aéroélastique est remplacé par un couplage acoustique pur avec la cavité du T.O.P. et les longueurs de corrélation des pressions sont beaucoup plus importantes qu'en vol. Les comportements des tuiles en T.O.P. sont différents de ceux observés en paroi de soufflerie (voir planche 9); ce type de constatation a aussi été fait avec l'opération ACOUFAT de la C.E.E., (voir référence 7)

On peut cependant arriver dans ce type d'essais à régler l'excitation pour obtenir approximativement un spectre de réponse donné (accélération, effort ou contrainte interne) en un point choisi (le plus critique en principe).

3.2.4. Essais sur table vibrante

Ils sont encore moins coûteux que les précédents, et comme eux ils ne peuvent être représentatifs que si on règle le montage et l'excitation pour obtenir une réponse interne ponctuelle justifiée par ailleurs.

3.2.5. Essais partiels élémentaires sur vibreurs ou machines de fatigue "statiques"

On les utilise pour vérifier la résistance des différents détails structuraux critiques (exemple attaches, dépliement local des bordures du panneau, etc...), cela à partir de spectres de charges locales estimés par ailleurs.

3.2.6. Essais en vol

Les mesures en vol sont les moyens les plus fiables pour apprécier les effets des phénomènes aéroacoustiques sur les structures ou sur les équipements (mesures par jauges de contrainte ou accéléromètres), cela à condition d'avoir su placer les capteurs aux endroits pertinents (ce qu'on sait faire sur les avions classiques quand on a découvert des fissures de fatigue aéroacoustique).

Pour HERMES cette approche a l'inconvénient de ne fournir des informations qu'après le premier vol, ce qui laisse ouvert le problème de la qualification pour ce premier vol.

4. STRATEGIE D'ANALYSE ET DE DEMONSTRATION, EXEMPLES

On doit viser successivement 2 objectifs

- Supporter les choix de conception du véhicule et donner une méthode de dimensionnement initiale
- Permettre la démonstration de qualification de la solution choisie

Compte tenu des limites de la précision et de la représentativité des moyens de calcul et d'essais disponibles nous sommes conduits à gérer au mieux un compromis entre :

- des surspécifications, donc un surdimensionnement, plus ou moins importants
- la complexité, donc des surcoûts, des procédures de calcul et d'essais

Nous avons proposés les 3 phases suivantes :

A. Phase préparatoire

Elle doit se dérouler normalement pendant la phase de conception initiale du véhicule, voire la précéder ; ses objectifs sont :

- La reconnaissance des phénomènes.
- La mise au point des méthodes de calcul et de leur règle d'emploi.
- La mise au point des méthodes d'essais.
- La démonstration de faisabilité du concept de tuile choisi vis-à-vis de l'aéroacoustique, les niveaux d'excitation aéroacoustique supportables (taux d'échange entre les niveaux d'excitations et la masse des tuiles).
- La détermination de la stratégie à appliquer pour les phases suivantes (dimensionnement et qualification).

Les calculs et les essais sont effectués sur des dessins génériques de structures, permettant des études paramétriques.

Parmi les travaux réalisés dans cette phase sur les tuiles HERMES citons :

- L'identification des charges aéroacoustiques sur maquette rigide (cf § 3.2.1), on en tire aussi les régles pour adapter l'implantation des capteurs en fonction des phénomènes découverts et pour permettre la mesure des corrélations spatiales des champs de pression.

  Il faut vérifier que la différence de nombre de Reynolds avec le vol n'influe pas trop sur la position des chocs et des décollements :
  - Par essais (en faisant varier la pression dynamique dans la soufflerie)
  - Par calcul (type Euler stationnaire + couche limite).
- Essais de tuiles en paroi de soufflerie transsonique (cf § 3.2.2), calculs correspondants linéaires, linéarisés et non linéaires (cf § 3.1)

  On présente sur la planche 11 une synthèse de comparaisons relativement satisfaisante entre essais et calcul pour l'analyse du Flutter.

On a essayé des tuiles volontairement amincies pour rencontrer l'instabilité de Flutter ; du fait de la non-linéarité de membrane, elle se traduit par des cycles limites ; on remarque aussi qu'elle est très sensible à la surpression statique (la référence 11 présente ces expériences plus en détail).

Les essais et les calculs de la même configuration avec une turbulence aéroacoustique créée par un déflecteur sont présentés planche 9.

L'écoulement aérodynamique réalisé est très complexe, on arrive cependant à recouper passablement par calcul les réponses structurales mesurées, en partant des pressions mesurées sur un élément de paroi rigide.

- Essais en tube à ondes progressives et calculs correspondants.

  On présente des mesures de réponses planche 9. On constate que la réponse de la même tuile diffère sensiblement entre le T.O.P. et la soufflerie pour des puissances d'excitation similaire dans les octaves sensibles.

  Ceci est expliqué surtout par la différence de forme spatiale des champs de pression ; dans le T.O.P. ils sont pratiquement en phase sur toute la surface d'une tuile et les modes "antisymétriques" ne sont pas excités. (Lors des essais en soufflerie avec turbulence ces modes anti-symétriques étaient fortement excités, créant notamment des dommages de fatigue sur les attaches de tuiles dans certains cas)

  Ces essais et calculs aéroacoustiques complets ont été précédés d'analyse et d'essais plus simples servant à valider les modèles élastiques et dynamiques des tuiles et à examiner l'influence de tous leurs paramètres de conception (exemples courbure du panneau, nature du bloc d'isolant, perméabilité du système d'étanchéité,), citons parmi ces études

  - la réponse sous chargement statique (flèche, déformation, fréquence, cf planche 4)
  - les mesures des fréquences et des formes modales (a servi en particulier à déterminer les amortissements structuraux).

Quand le projet HERMES a été abandonné nous avions globalement atteint la fin de cette phase préparatoire pour l'analyse aéroacoustique des tuiles.

L'organisation proposée pour les étapes suivantes résulte de l'expérience acquise.

B. Support de la conception du dimensionnement et de la qualification avant les premiers vols inhabités*

On propose l'organisation des travaux schématisée planche 12 ; elle est fondée sur les principes suivants :

- Etablissement des charges aéroacoustiques de dimensionnement :
  - Mesure en soufflerie des pressions aéroacoustiques sur maquette rigide à échelle réduite, à la forme "finale" ; vérification de l'influence du nombre de Reynolds par essais et par calcul de couche limite.
  - Interprétation des mesures pour obtenir des spécifications de "charges limites" aéroacoustiques sur toutes les zones du véhicule. Elles sont définies sous forme de combinaisons de spectres (et d'interspectres, voir § 5) de fluctuation de pressions, de surpressions statiques locales, et de cas de charges "généraux" déformant la sous-structure.

    On doit démontrer (par calcul) que ces cas de charges, base du dimensionnement, enveloppent de façon raisonnablement conservative la réalité.

    Si les spécifications aéroacoustiques se révèlent trop pénalisantes il faut étudier des modifications des formes générales du véhicule.
- Dimensionnement d'ensemble des tuiles et de la structure adjacente

---

* Dernier scénario de la logique de développement du projet Hermes

Il paraît souhaitable que le dimensionnement corresponde à des spécifications vérifiables en essais au sol, ce qui conduit aux travaux suivants :

- Définition d'éprouvettes et de procédures d'essais de qualification au sol.
  Ce sont, pour plusieurs zones de l'avion des caissons représentatifs de la sous-structure revêtus par des tuiles qui subiront simultanément ou successivement un ensemble de sollicitations mécaniques et thermiques. L'environnement aéroacoustique devrait être justifié là par des essais sur table vibrante et/ou en T.O.P.
  On doit rechercher, en se basant sur les calculs, des conditions d'essais majorant au plus juste les conditions de vol.
  Le dimensionnement des tuiles et de la structure adjacente correspondra à ces conditions conservatives des essais au sol.

- Dimensionnement des composants des tuiles

  Pour limiter les risques de découvertes tardives de difficulté lors des essais d'ensembles, on propose une approche similaire à la précédente :

  - Définition de conditions d'essais élémentaires (essais de fatigue quasi statique, pot vibrant, T.O.P.) pour les composants des tuiles (panneau, isolant, joints, attaches, etc.), qui deviennent des spécifications de dimensionnement

  Ces conditions d'essais élémentaires sont établies par calculs comparatifs avec celles des essais d'ensemble

  Le retour des essais élémentaires permet des itérations de dimensionnement , les essais d'ensemble sont plutôt prévus pour ne participer qu'à la qualification pour les premiers vols (inhabités) et à la démonstration de validité a posteriori des modèles de calcul ayant servi à les définir

B. Qualification finale pour les vols habités, dérivée des essais en vol

Cet approche relativement complexe de qualification par imbrication de calcul et d'essais s'autovalidant sur plusieurs niveaux comporte des risques de défaillance qu'on peut ne juger acceptable que pour un vol inhabité

Pour qualifier finalement le véhicule pour les vols habités il paraît hautement souhaitable de valider la conservativité de l'ensemble de la procédure de dimensionnement, et surtout celle du modèle de charges aéroacoustiques, par recoupement avec les mesures effectuées pendant les premiers vols automatiques.

L'étude de l'implantation de l'installation d'essais pertinente (accéléromètres, jauges de contraintes, capteur de pression,...) est un problème difficile qui doit être supporté par des techniques de calcul inverse.

5. RECHERCHES ET DEVELOPPEMENTS A MENER

Au-delà de l'achèvement de la mise au point de la procédure d'analyse aéroacoustique présentée, il est souhaitable de mener un certain nombre de recherches et de développements pour en compenser les lacunes, citons entre autre :

- Le perfectionnement de l'analyse des charges

  A long terme il pourrait résulter de la résolution de l'équation de Navier Stokes instationnaire (à coût admissible). A plus court terme, on souhaiterait l'établissement d'une banque de donnée de modèles empiriques de distribution de source turbulente en aval de défauts de forme typiques , ces modèles semi-analytiques seraient calibrés sur les essais en soufflerie par calcul inverse

  Ces modèles fourniraient directement la distribution spatiale et l'intensité des sources turbulentes, ce qui éviterait les mesures complexes et le maniement très délicat des champs de pression à la paroi.

  Ces procédures de calcul inverse, permettant de remonter aux charges aéroacoustiques, à partir des mesures de réponses structurales, sont aussi à mettre au point pour exploiter les mesures en vol (comme nous le faisons pour les charges quasi-statique, voir référence 12)

- La recherche de procédés pour créer en soufflerie des excitations représentatives des charges aéroacoustiques réelles, dans le cas des essais d'éléments structuraux à échelle 1

- Le perfectionnement des modèles structuraux , il est en particulier indispensable si on s'intéresse à la propagation des vibrations dans l'ensemble du véhicule ; on trouvera là toutes les difficultés des modélisations structurales dans la gamme des moyennes fréquences (voir référence 4) ; un des problèmes majeurs est la compréhension exacte puis la modélisation des phénomènes de dissipation de l'énergie qu'on cache derrière le mot "Matrice d'Amortissement Structural".

6. CONCLUSIONS

Le début d'expérience qu'on a acquis avec les études aéroacoustiques HERMES montre :

- qu'on ne dispose aujourd'hui d'aucun moyen de calcul ou d'essais permettant, à lui seul, de justifier la résistance structurale aux effets aéroacoustiques avant les essais en vol
- que certaines approches classiques comme la qualification exclusivement par essais en chambre réverbérante ou en T.O.P. sont illusoires, du fait de l'absence d'un couplage aéroélastique correcte et surtout à cause d'une représentation erronée des champs de pression aeroacoustiques
- qu'une procedure de dimensionnement et de qualification rationnelle est cependant possible avec les moyens actuels, en enchainant, comme on l'a montre les essais et les calculs et en acceptant d'eventuels surdimensionnements locaux dus aux marges prises pour garantir la conservativite de la procedure
- que les moyens d'analyse et l'experience actuelle permettent d'evaluer les risques dès le debut du projet, a condition de disposer de mesures des charges aéroacoustiques par essais en soufflerie. En cas de difficultés il est alors possible de traiter le probleme à sa source en "travaillant" les formes aerodynamiques de l'avion

Nous constatons que ces conclusions rejoignent celles de l'operation ACOUFAT menees par la C.E.E. (voir reference 7), on y voit en particulier les grosses differences de comportement d'une même structure placee successivement en paroi de soufflerie et en T.O.P. avec des spectres d'excitation acoustique en principe equivalents

REFERENCES

1. **C. PETIAU,** The challenge of the HERMES TPS shingles
Proc. Internat. Conf. "Spacecraft Structures and Mechanical Testing", Noorwijk, The Netherlands, 24-26 April 1991 (ESA SP-321, October 1991)

2. **R.L. BISPLINGHOFF, H. ASHLEY,** Principles of Aeroelasticity - Joyn Wiley and Sons Inc - New York 1962

3. **C. PETIAU, S.BRUN,** Tendances actuelles de l'analyse aeroélastique des avions militaires AGARD conference proceedings N° 403 - Athènes 1986

4. **C. PETIAU,** Aeroelasticite et vibration des structures
Etat de l'art et tendances
Forum International d'Aéroelasticite et de Dynamique des structures 93, Edition AAF

5. **ALBANO, E., and RODDEN, W.P.,** "A Doublet Lattice Method for Calculating Lift Distribution on Oscillating Surfaces in Subsonic Flows" AIAA Paper N° 68-73, 1968

6. **R. DAT,** Vibration Aeroelastique, Cours de l'Ecole Nationale Superieure de l'aeronautique et de l'espace 1978

7. **D. TOUGARD,** Brite-Euram Programme ACOUFAT-Acoustic Fatigue and Related Damage Tolerance of Advanced Composite and Metallic Structures - AGARD 78th SMP Meeting - Impact of acoustic loads on aircraft structures

8. **P. LAMARY,** Une methode de couplage Elasto-Acoustique par operateur de grille frontiere pour discretisation acoustique et structure non coincidentes - These de l'Universite de Compiegne - Decembre 1992

9. **D.E. NEWLAND,** An introduction to random vibrations and spectral analysis - LONGMAN Group limited Ed 1986

10. **C. PETIAU, C. CORNUAULT,** Algorithmes efficaces pour les calculs en post-flambement. 5eme colloque tendaces actuelles en calcul de structure - Edition Pluralis Paris 1985

11. **A.L. GEORGES,** Aeroelastic non linear study for HERMES Shingle
Forum International d'Aeroelasticite et de Dynamique des structures 93, Edition AAF

12. **C. PETIAU, M. DE LAVIGNE,** Analyse aeroelastique et identification des charges en vol, Agard conferences proceeding n° 375 "Operational loads data", Sienne 1984

Planche 1
Forme générale de la Navette Hermès

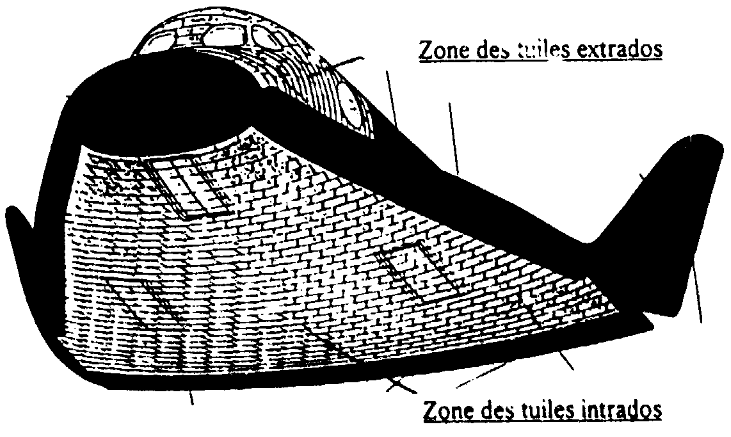
Zone des tuiles extrados
Zone des tuiles intrados

Planche 2
Niveaux de bruit aéroacoustique maximum

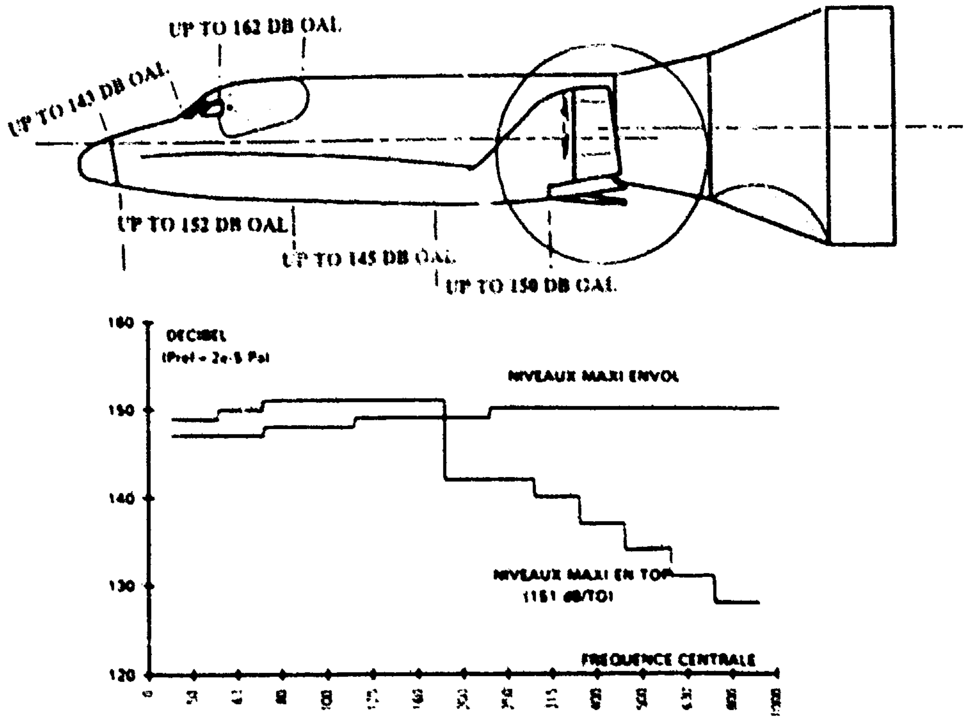

Planche 3
Présentation des tuiles

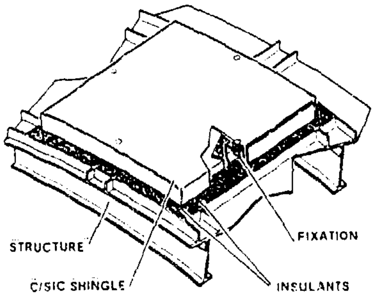
STRUCTURE
C/SIC SHINGLE
FIXATION
INSULANTS

Tuile extrados

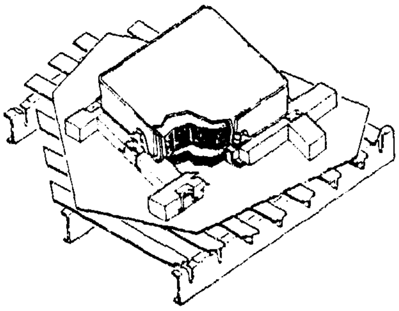

Tuile intrados

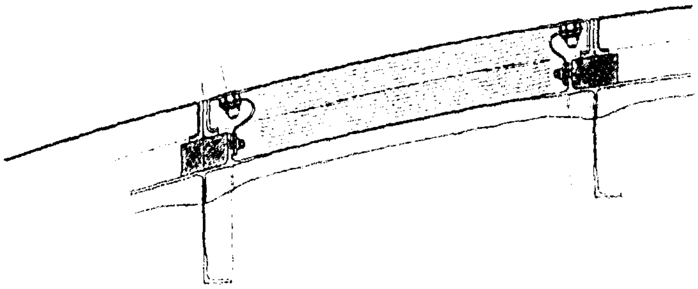

Tuiles intrados

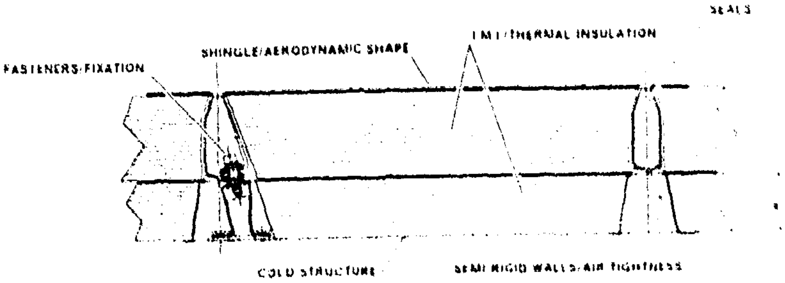
SEALS
IMI/THERMAL INSULATION
SHINGLE/AERODYNAMIC SHAPE
FASTENERS/FIXATION
COLD STRUCTURE
SEMI RIGID WALLS/AIR TIGHTNESS

Tuiles extrados

Planche 4

Comportement non linéaire des tuiles
Effet de membrane, influence de la pression statique

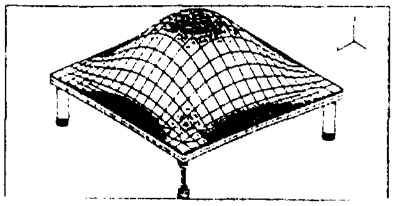

Calcul linéaire

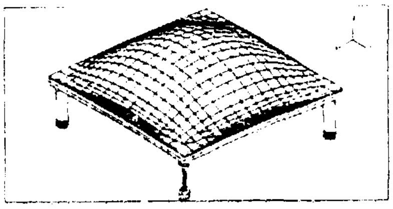

Calcul non linéaire

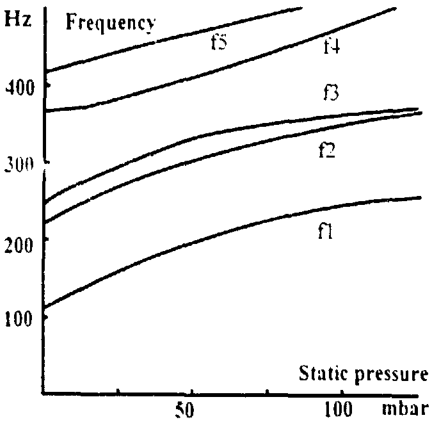

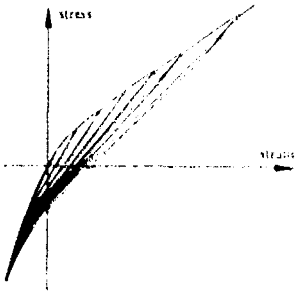

Rhéologie non linéaire du matériau C-SIC

Comparaison Calcul-essais
(Pression statique)

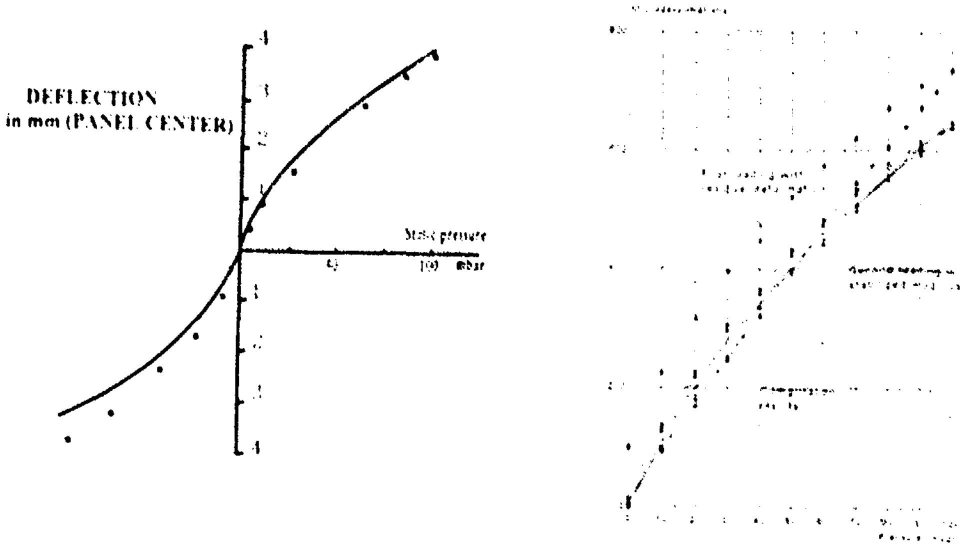

Planche 5

Calcul des effets non linéaire dynamique

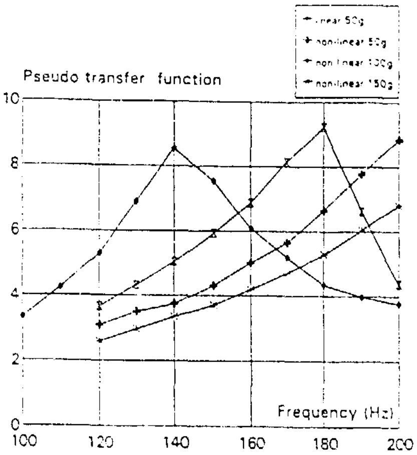

Facteur de surtension
(au centre de la tuile)

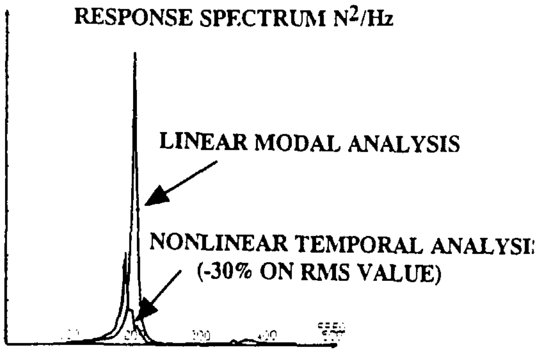

Réaction sur les attaches

Planche 6

Visualisation strioscopique du Mach 0,9

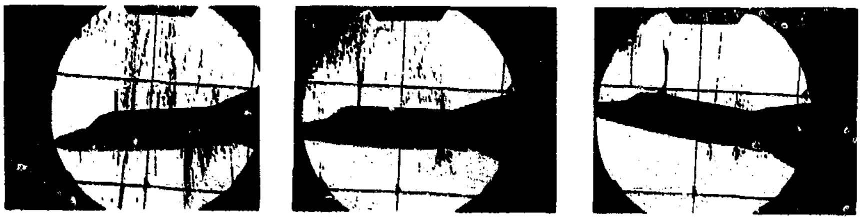

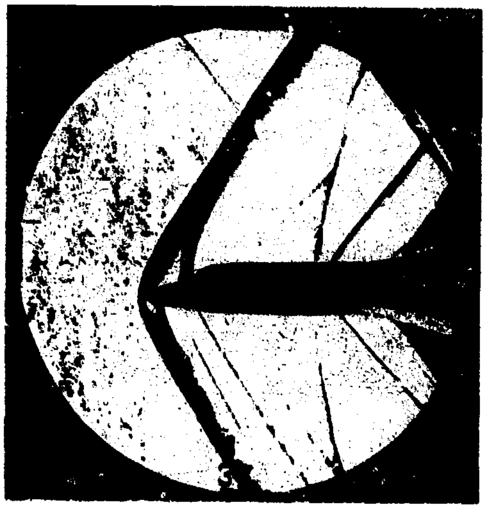

Visualisation strioscopique en supersonique

Planche 7
Installation d'une tuile en paroi de la soufflerie HST du NLR
(Derrière un déflecteur)

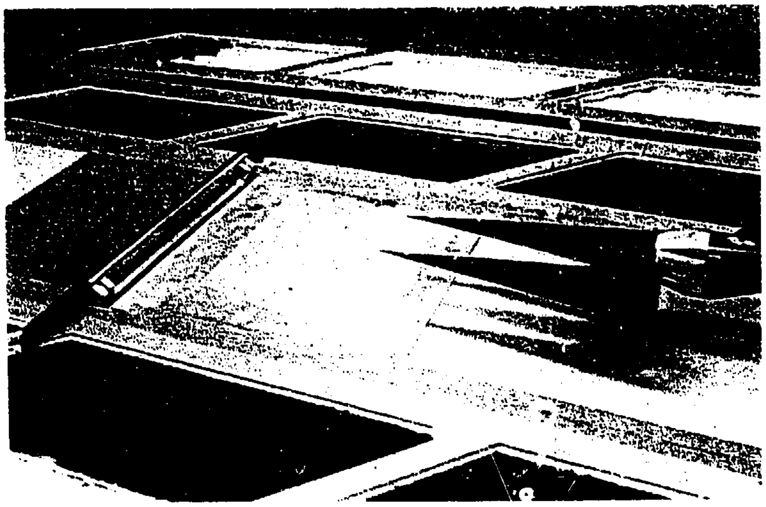

Planche 8
Tube à ondes progressives de l'IABG

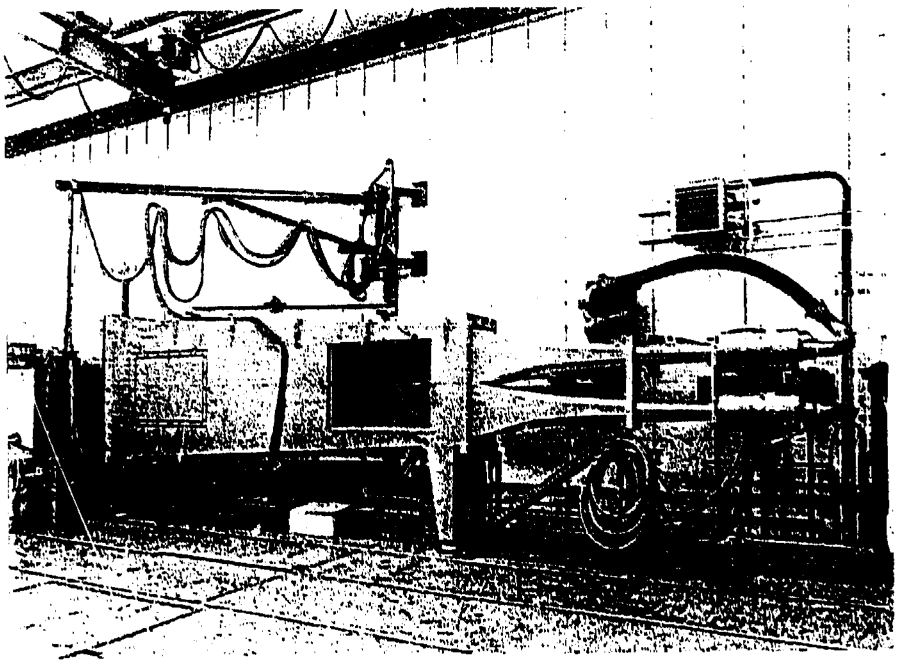

Planche 9
Comparaison des moyens d'essais

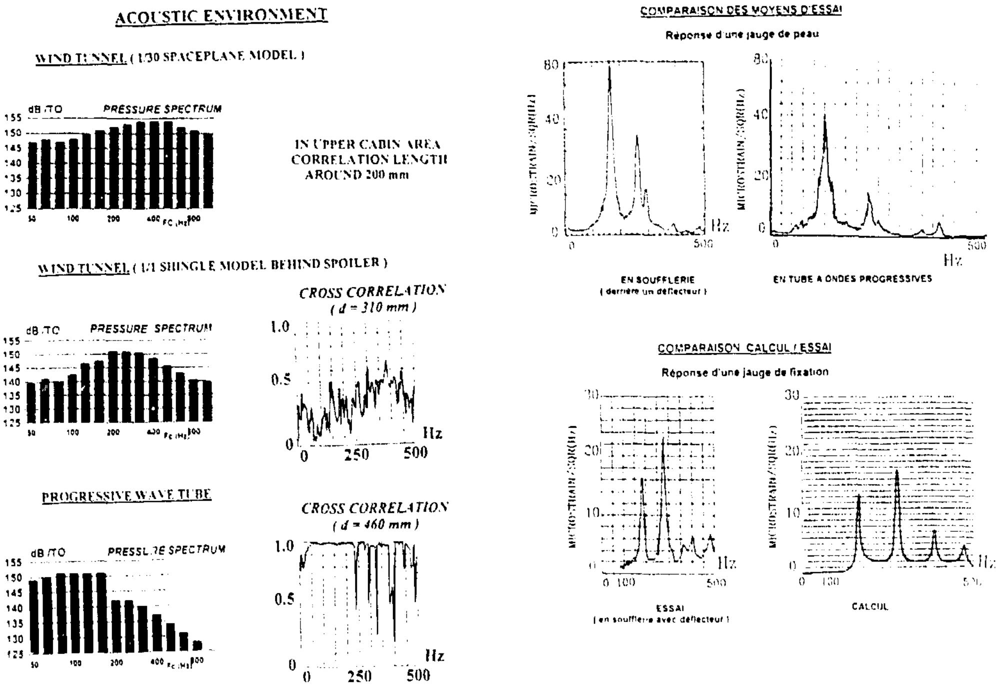

Planche 10
Influence de l'étanchéité

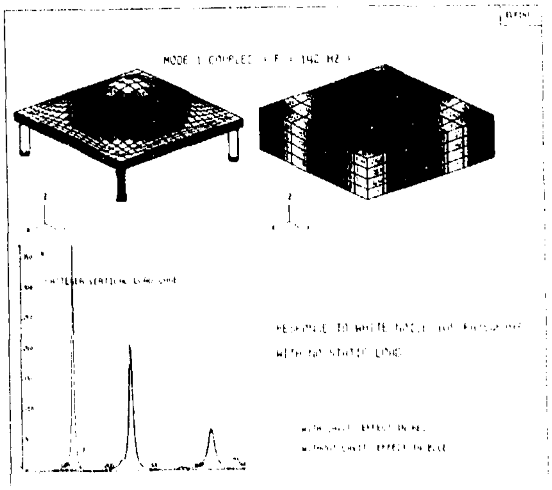

Planche 11

Analyse du Flutter (Tuile dural e = 0,7 mm)

Analyses linéaire classique (domaine fréquence)

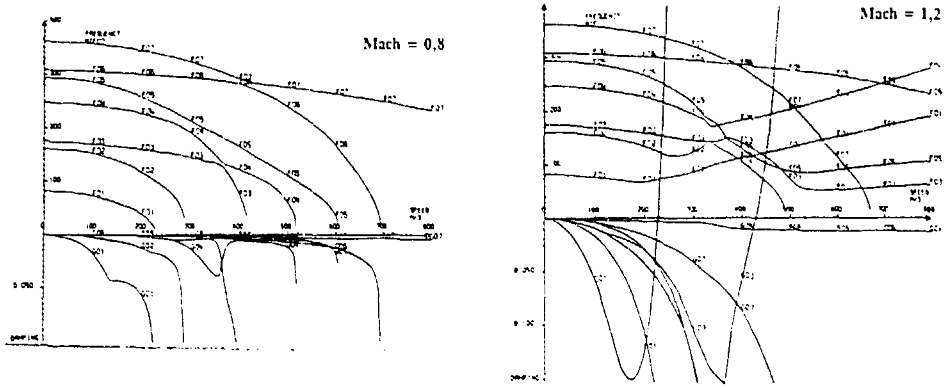

Réponse domaine temps

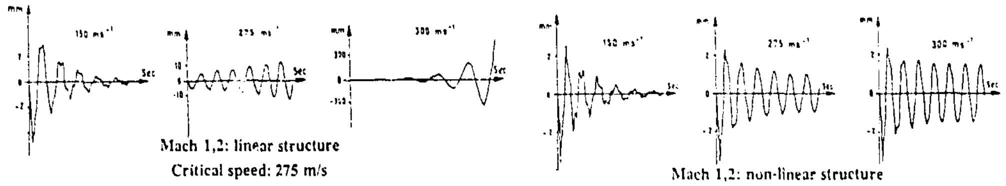

Mach 1,2: linear structure
Critical speed: 275 m/s

Mach 1,2: non-linear structure

Comparaison calcul-essais

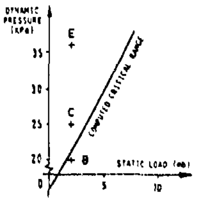

Calculs "linéarisés"
(Influence de la
pression statique)

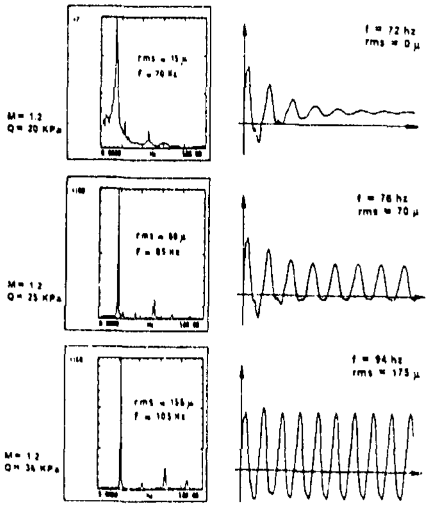

Conf. B

Conf. C

Conf. E

Spectres de
réponses mesurés

Réponse calculée
(domaine temps)

Planche 12
Organisation pour le dimensionnement et la qualification (pour les premiers vols)

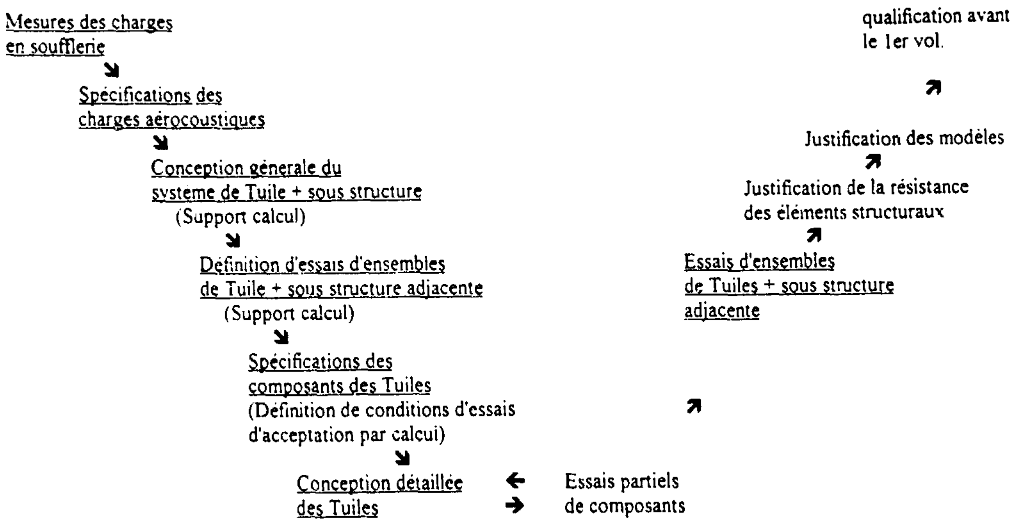

Mesures des charges en soufflerie

↘

Spécifications des charges aérocoustiques

↘

Conception générale du système de Tuile + sous structure (Support calcul)

↘

Définition d'essais d'ensembles de Tuile + sous structure adjacente (Support calcul)

↘

Spécifications des composants des Tuiles (Définition de conditions d'essais d'acceptation par calcul)

↘

Conception détaillée des Tuiles ← → Essais partiels de composants

↗

Essais d'ensembles de Tuiles + sous structure adjacente

↗

Justification de la résistance des éléments structuraux

↗

Justification des modèles

↗

qualification avant le 1er vol.

WEAPONS BAY ACOUSTIC ENVIRONMENT

L. L. Shaw
R. M. Shimovetz
Structural Dynamics Branch
WL/FIBG BLDG 24C
2145 FIFTH ST STE 2
WRIGHT PATTERSON AFB, OH 45433-7006

1. SUMMARY

An aircraft weapons bay exposed to freestream flow experiences an intense aeroacoustic environment in and around the bay. Experience has taught that the intensity of this environment can be severe enough to result in damage to a store, its internal equipment, or the structure of the weapons bay itself. To ensure that stores and sensitive internal equipment can withstand this hazardous environment and successfully complete the mission, they must be qualified to the most severe sound pressure levels anticipated for the mission. If the qualification test levels are too high, the store and its internal equipment will be overdesigned, resulting in unnecessary costs and possible performance penalties. If the qualification levels are below those experienced in flight, the store or its internal equipment may catastrophically fail during performance of the mission. Thus, it is desirable that the expected levels in weapons bays be accurately predicted.

A large number of research efforts have been directed toward understanding flow-induced cavity oscillations. However, the phenomena are still not adequately understood to allow one to predict the fluctuating pressure levels for various configurations and flow conditions. This is especially true at supersonic flow speeds, where only a small amount of data are available. This paper will give a background of flow induced cavity oscillations and discuss predictions, control and suppression, and the future of weapons bay acoustic environments.

2. BACKGROUND

The study of flow induced cavity acoustic environments which relate to aircraft weapon bays date back to the mid 1950s when Roshko (1) and Krishnamurty (2) conducted research in this area. Roshko varied the cavity dimensions systematically while obtaining the time averaged effects in the cavity. He measured the pressure on the walls and floor. A single vortex was seen to exist for the shallow case. For very shallow configurations he noted that the shear layer reattached to the cavity floor. This observation has been repeated many times in more recent studies of very shallow cavities. As missiles became longer and smaller diameter, the need for shallower weapon bays arose. Roshko noted that the impingement of the shear layer on the downstream wall of the cavity was the cause of increased drag which occur with open cavities. Karamcheti, conducting his research at about the same time as Roshko, studied rectangular cavities exposed to free stream Mach number flows of 0.25 to 1.5. He actually obtained sound pressure levels from his tests with levels as high as 160 dB being observed. An important observation made by Karamcheti was that there is a minimum cavity length at which the shear layer will span the opening and not impinge on the downstream wall of the cavity, thus not resulting in acoustic resonance. This is the physical basis of control of the high acoustic environment in cavities. If the shear layer can be made to span the cavity, or reattach at a stable stagnation point, no feedback process is established and hence no resonance.

One of the most referenced historical works in the flow induced cavity acoustic area is that of Rossiter (3). He made measurements of the time average and unsteady pressures on the "roof" (or floor) and behind a series of rectangular cavies set in the roof of a 2 foot by 1.5 foot transonic wind tunnel. Data for cavities with length-to-depth ratios from 1 to 10 were presented for Mach numbers from 0.4 to 1.2. His major conclusions were shallow cavities ($L/D>4$) produce mainly broadband acoustic spectra and deeper cavities ($L/D<4$) produce a periodic tone. The periodic tone was attributed to acoustic resonance in the cavity and excited by a phenomenon similar to that causing edge tones. The amplitude of the periodic tone can be as larger as 0.35 times the free stream dynamic pressure. He also investigated methods to suppress the periodic fluctuations and concluded that they may be suppressed by placing a small spoiler ahead of the cavity. The only explanation given as to why a spoiler is effective is that it thickens the boundary layer. He is most referenced

Presented at a Symposium on 'Impact of Acoustic Loads on Aircraft Structures' held in Lillehammer, Norway, May 1994.

because of his equation to predict the possible resonant frequencies in an open cavity. Even today it is referenced often as the "Rossiter Equation" and gives a very good prediction of the resonant frequencies in a cavity, if the correct phase and convection terms are used. The equation will be presented later in the paper.

Plumbee et al (4) conducted theoretical and experimental investigations of the flow induced cavity acoustic problem. A detailed analytical prediction method was developed based on the radiation impedance of the cavity opening. A table of radiation resistance and reactance was provided to utilize the method. It is an iterative approach and does not readily converge. The method has not been referenced in subsequent publications mainly due to the difficulty in use of it. They also conducted extensive experimental tests on cavities obtaining wind tunnel data for Mach numbers from 0.2 to 5.0. The major conclusions were that the acoustic levels were higher in the rear of the cavity, width has little effect on acoustic levels, and there exist an onset Mach number below which the cavity tones are not excited. Smith and Shaw (5) formulated an empirical acoustic predictions method which was based on an extensive flight test data base. The method predicts the frequency and amplitudes of the first three acoustic modes in the cavity as well as the broadband spectrum level. The prediction method also gives the spatial distribution of the modal energy. It is easy to use and gives a good first order prediction of the flow induced levels.
Heller and Bliss (6) contributed a better understanding of the cavity oscillation phenoneon through their water table visualization test. The moving pressure waves in the cavity were clearly visible in the experiment. A video of the results was made. Analytical work as well as experimental tests were conducted. Small and large scale wind tunnel test were performed for cavities with L/D ratios between 2.3 and 5.1 for a Mach number range of 0.2 to 2.0. The analytical work yielded a theory that predicted only the lowest pressure-mode shape and failed to predict the higher modes. This inadequacy was believed to be caused by the omission of the effect of shear layer thickness in the analytical model. The wind tunnel test results yielded mode shapes, temperature data, consecutive cavity effects and suppression effectiveness. Cavity internal pressure-mode shapes were determined for the first three modes and for the range of $2.3 < L/D < 5.1$. In all cases, definite amplitude minima were observed; however, they were qualitatively displaced in the upstream direction. In all cases, a pressure maximum appeared at the leading-edge bulkhead indicating that this surface acts as a "hard-reflecting wall." In contrast, pressure amplitude maxima were observed a small distance upstream of the trailing-edge bulkhead; this indicates that acoustically the trailing edge is undefined because of the violent flow patterns. In this study, mode shapes were obtained that differ from those observed in Air Force flight tests, however, in the latter experiment, mode shapes were determined on the cavity floor, while in the former experiments, mode shapes were determined within the cavity volume. Thus, dependence of mode shape on the vertical position in the cavity seems to exist; this issue needs clarification.

Experiments on consecutive geometrically identical cavities reveal that they are strongly coupled and resonate in phase. The Mach number dependence of mode levels for consecutive cavities was found to differ from that of single cavities. However, this may be because of the differing length-to-width ratio of the single and the double cavity system. While resonant frequencies are essentially determined by the cavity length, mode levels seem to be affected by the relative cavity width. This problem has not been studied and requires further research.

Of the various ways to affect the oscillation process, introduction of vorticity into the shear layer and the provision of a slanted trailing-edge bulkhead were found to have a stabilizing effect on the external free shear layer. Oscillation amplitudes can be minimized solely by a slanted trailing-edge, over a Mach number range of at least 0.8 to 2.0, for cavities with length-to depth ratios above 4. Cavities with a length-to-depth ratio below 4 require the addition of upstream vortex generators (spoilers), which further reduce resonant amplitudes.

Shaw and Smith (7) presented results of a full scale flight test of an instrumented store in a weapons bay. The aircraft was an F-111 and the store was a BDU-8/B instrumented with 21 microphones. Data were recorded for altitudes of 3,000, 10,000, and 30,000 feet and Mach numbers from 0.75 to 1.3. The results showed that the acoustic levels on the store scale with free stream dynamic pressure. The levels on the store increased toward the rear.

There are significant circumferential variations in the acoustic levels at different longitudinal locations.

Shaw (8) presented results from a flight test for suppression of the cavity internal acoustic levels. Numerous leading edge and trailing edge suppression devices were flight tested. Excellent suppression results were obtained for simple leading edge spoilers and rear bulkhead ramps. Nearly 30 dB suppression was obtained for the best configuration. The list of references of work related to open cavities is very long. Only a small percent of even the major efforts are referenced in this paper. As an example of the large number of reports presenting results related to aircraft cavity flow, in 1982 Betry and Rohrer (9) compiled a survey containing 144 references on this subject. Since then at least another 50-100 have been published. Thus only high relevancy efforts are referenced herein.

Two additional survey papers should be mentioned because of their broad nature. Komerath et al (10) in 1987 presented a survey on the prediction and measurment of flow over cavities. Their paper addressed all aspects of the flow induced cavity environment problems. Then in 1992 Chokani (11) also published a survey paper on flow induced oscillation in cavities. It is not as in depth as Komerath but it has merit since it included a discussion on computational predictions and turbulent modeling.

3. CAVITY DEFINITION

An aircraft weapons bay with its doors open constitutes an open cavity. Since most bombs or missiles are long and slender, most weapon bays are long and shallow relative to their length. The main parameter used to characterize a cavity is its length-to-dept (L/D) ratio. When the L/D ratio is greater than 1 it is considered deep. The justification for this classification is that when L/D>1 the response in the cavity is longitudinal, in the direction of free stream flow, and when L/D <1 the response is in the depthwise direction.

Another fairly recent description of cavities is that of being open or closed. This does not refer to a cavity with or without an opening but how much the shear layer is deflected into the cavity. When the shear layer spans the cavity opening the cavity is considered open, but when the cavity is long enough or shallow enough for the shear layer to reattach to the cavity floor, the cavity is referred to as being closed. For those in between the two, it is called transitional. Figure 1 shows the three types of cavities.

Plentovich et al (11) defines the three regions in terms of L/D ratio as being open for L/D< 6-8, transitional for L/D=7-14, and closed for L/D>9-15. The fairly wide bands are necessary because the shear layer deflection is very sensitive to Mach numbers.

The flow of a fluid over a cavity has been divided into three basic types by Rockwell and Naudascher (12). The three types are fluid dynamic, fluid-resonant, and fluid elastic and are illustrated in Figure 2. Basically the fluid dynamic case does not contain acoustic standing waves in the cavity while the fluid-resonant case does and they tend to control the shear layer. The fluid-elastic case simply is flow over a cavity with at least one of the walls elastic. For practical cases such as an aircraft weapons bay it is very difficult to select any one case to represent the actual phenomenon since features of all three are usually present.

4. DESCRIPTION OF PHENOMENON

The flow induced weapons bay acoustic phenomenon has been described by many authors such as in Reference 2, 3, 5, 6, 12. In some references vortices are observed to be shed at the leading edge of the cavity and others no vortices are observed even though strong acoustic tones are generated in the cavity. Whether or not vortices are formed is not as important as the interaction of the shear layer at the downstream wall. This is where the source of the acoustic energy is located. The basic phenomenon is shown is Figure 3. As the shear layer separates at the leading edge, instabilies are inherent and tend to grow as they travel down stream. At any longitudinal location the shear layer appears to be moving in a transverse direction, thus at the trailing edge it is moving in and out of the cavity periodically impinging on the rear wall. When it is impinging on the rear wall mass is added to the cavity and then as the shear layers move out of the cavity mass is withdrawn from the cavity through entrainment. Also during the impingement process a high amplitude pressure wave is generated which travels forward until it reaches the front wall. At that point it reflects and starts to travel towards the rear wall but also imparts energy into the shear layer. As seen in the figure there are fore and aft travelling waves which establish a standing acoustic which establish a standing acoustic mode. Several orders of standing modes have been measured is cavities as shown by Shaw (8). As the process of trailing edge impingement and forward traveling waves continues, a feedback cycle is established. When the cycle time for the acoustic wave and the convective cycle of the shear layer coincide, a strong resonance occurs in the cavity.

5. EXAMPLES OF ENVIRONMENT

An example of the acoustic environment in the B-1A weapons bay is shown in Figure 4. The amplitudes of the resonant modes are well above the broadband level for the first four modes. The spectrum level of the first mode is seen to be 155 dB which is high enough to cause structural damage in a very short time. The first mode frequency is 18 hertz and the second mode is approximately 45 hertz. These low frequencies can easily coincide with structural resonant frequencies and thus cause structural resonant response and possibly failure. Spectra from the F-111 are shown Figure 5. The acoustic modes do not appear as broad as in Figure 4 because these spectra are 1/3 octave band and each tone includes a wider band of energy. Caution must be used to compare the two data. If the tone is at least ten dB above the broadband level in 1/3 octave band data, one can safely assume that the peak level is close to the spectrum peak of the same data. The second mode peak in Figure 5 is 161 dB but the equivalent spectrum level would be approximately 159 dB. This is an extremely high level and will cause damage. The other spectrum in the figure will be discussed later. Based on the spectra from these two aircraft the need for understanding the phenomenon and controlling the amplitudes is readily evident.

6. PREDICTION

6.1 Frequency

In the design stage of an aircraft it is necessary to be able to predict the environment and loads that the structure and equipment must be designed and qualified for. The environment in the weapons bay includes the frequency of the acoustic modes, amplitudes of the modes, and the broadband level. There have been many methods developed to predict the cavity flow induced acoustic environment but only a few of the more useable and typical examples will be discussed.

Prediction of the resonant acoustic frequencies has been addressed at least an order of magnitude more than the amplitude. The most referenced and utilized method for predicting the frequencies is the so called Rossiter (3) equation. The equation is:

$$f_m = \frac{u_\infty}{L}\,\frac{m-\alpha}{M_\infty/\left(1+\frac{\gamma-1}{2}M_\infty^2\right)^{1/2}+1/K_v} \qquad (1)$$

where α is a phase lag term, γ is the ratio of the specific heats, and K_v is the convection speed of the shear layer. The equation is derived by assuming the complete cycle time is the sum of the downstream convection time and the upstream acoustic propagation time along with a phase lag of α between the two.

Rossiter observed a convection velocity of 0.57 and showed that the phase lag varies from 0.25 for L/D=4 to 0.58 for an L/D of 10. However, all his data agree fairly well with using $\alpha = 0.25$ inspite of the wide variation in actual averaged values of α he presented. Much of the data obtained since his work illustrate the need to use his recommended phase lag values. A comparison of flight and wind tunnel data with the Rossiter equation is shown in Figure 6. The agreement is acceptable but could be improved at the lowest frequency if the different phase lag values offered by Rossiter were used. It should be noted that as the mode number increases the sensitivity of the equations to the phase lag term decreases significantly. But since the second mode is normally the highest level, the phase lag value should not be assumed constant. There have been several attempts to refine both the phase lag and convective term in Rossiter's equation. One attempt by Kaufman et al (13) derived a table of values for the convective term from their data and used the table of values given by Rossiter for the phase term and then compared predicted values with their measured values. Only minor improvement was noted. Others (14, 15) have looked at the acoustic eigenmodes of the cavity assuming that the radiation loss of the opening was very low.

The solution of the two dimensional wave equation is given in Ref. (14) and is

$$\frac{f_{mn}L}{U} = \frac{c}{2U}\sqrt{(m-1)^2+(n-1/2)^2(L/d)^2} \qquad (2)$$

is where the speed of sound in the cavity and the ordered integers (*m, n*) denote the longitudinal (*L*) and the transverse (*d*) mode numbers, respectively. Some of these modes are shown together with the data in Figure 7. Only a few data points agreed with the cavity acoustic mode calculation. In reality, the radiation loss through the open end is very significant unless $L/d << 1$. The net effect of using more appropriate radiation boundary condition is to change the effective depth of the cavity resulting in a shift of the curves.

Considering the numerous research efforts which addressed frequency prediction, the Rossiter equation, with the most accurate phase and convection term available, will result in as accurate prediction of the resonant frequencies as any other method.

6.2 Amplitude

Prediction of the amplitudes of the weapons bay or cavity acoustic environment is much more difficult than predicting the resonant frequencies. One of the earliest theoretical amplitude prediction methods was presented by Plumblee et al (4). The method relies on the calculation of the radiation impedance of the cavity opening and then solving the wave equation with the other five sides of the cavity having infinite impedace. It is an iterative solution which must converge. It is not convenient to utilize and is not that accurate.

Smith and Shaw (5) developed an empirical prediction method for the amplitudes of the resonant frequencies as well as the longitudinal distribution of the energy in the cavity. The method is presented here because of its ease of use and very good first order prediction of the flow induced acoustic environment.

$$f_m = \frac{V}{L}\;\frac{m - 0.25}{\dfrac{M}{\left(1 + \frac{K-1}{2}M^2\right)^{1/2}} + 1.75} \qquad m=1,2,3$$

$$20 \log (P_m/q)_{X/L} = 20 \log (P_m \max/q)$$

$$- 10 \left[1 - |\cos a_m X/L| + (0.33L/D - 0.6)(1-X/L)\right]$$

$$a_1 = 1.5 \text{ rad}$$

$$a_2 = 6.3 \text{ rad}$$

$$a_3 = 10.0 \text{ rad}$$

$$20 \log (P_2 \max/q) = 25 \operatorname{sech}\left[2(M-1)\right] - 3.3\, L/D - 27$$

$$20 \log (P \max/q) = 20 \log (P_2 \max/q) + 1.5\, L/D - 13$$

$$20 \log (P_3 \max/q) = 20 \log (P_2 \max/q) - 13\, M + 9$$

$$20 \log (P_n \max/q) = 20 \log (P_2 \max/q)$$

$$+ \left[3.3\, L/D - 28 + 3(1-L/D)(1-X/L)\right]\left[1.2-0.4M\right]$$

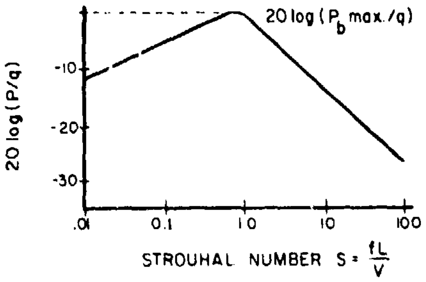

Another semiemperical prediction method was recently developed by Bauer and Dix (16). They utilized the Rossiter frequency equation but proposed a modified convection term. The amplitudes were based on a response coefficient for each mode which was a function of viscous and wave damping. The results of their effort are somewhat lacking because the predictions do not agree well with data and their predicted overall acoustic level is below the level of the resonant modes. This is totally incorrect. Figure 8 is an example of a comparison of their prediction method (CAP code) with data. The disagreement is clearly evident. Until this method is further refined, it is not recommended.

6.3 COMPUTATIONAL

Many efforts have been conducted to predict the flow induced acoustic environment in cavities by numerically solving the time dependant flow equations. One of the earliest is by Borland (17) who solved the two-dimensional Euler equations for time-dependant inviscid compressible flow. His results were encouraging in that the method resulted in harmonic tones in the cavity and the overall sound pressure levels were of the order of magnitude of measured data. A short time later Hankey and Shang (18) solved the unsteady Navier-Stokes equations. Both the predicted frequency and magnitude of the unsteady pressure fluctuations in the cavity were confirmed with the experimental data.

More recent computational work has been performed by Baysal et al (19), Morgenstern et al (20), and Harden and Pope (21), all addressing flows past open cavities. Some of the results were encouraging but others need more refinement. Such assumptions as turbulence model, dissipation, damping, grid size, time step, initial and boundary conditions all require that the codes be iterated with actual wind tunnel data to get them to yield meaningful results. Once a code is producing meaningful results, it can be used as a research tool to conduct parametric sensitivity studies.

7. SUPPRESSION

Literally hundreds of suppression concepts have been tested for their effectiveness in controlling the acoustic environment in open cavities. Tests with small scale wind tunnels up to full size aircraft have been conducted. Water table tests have been effective in evaluating a large number of devices. Rossiter (3) in 1966 concluded that the acoustic environment could be suppressed by placing a small spoiler ahead of the cavity. Heller and Bliss (6) tested a large number of suppression concepts which included both leading edge and trailing edge devices. Figure 9 shows their four most successful concepts and Figure 10 illustrates the typical level of suppression they achieved. Shaw (22) presented full scale F-111 weapon bay acoustic suppression results. The concepts tested were a leading edge sawtooth spoiler, leading edge 45 degree spoilers, and a 45 degree rear bulkhead ramp. An effective suppression for the 45 degree leading edge spoilers is shown in Figure 5 and is noted to be 24 dB for the peak one-third octave bond. The other devices were not as effective as the 45 degree leading edge spoiler. Tipton (23) documented data from the B-1A weapons bay with and without suppressors. The effectiveness of a porous leading edge spoiler is demonstrated in Figure 11. The modal tones are greatly reduced or eliminated and the broadband level is also reduced by 15 dB. However, suppression data were obtained at a wide range of Mach numbers and the effectiveness of the leading edge spoilers was observed to decrease at higher Mach numbers. This trend is shown in Figure 12. It points out the need for a better suppression technique which is effective at all speeds. Shaw et al (24) also documented the small Mach number range which a suppressor is effective in as shown in Figure 13.

8. SUMMARY AND CONCLUSIONS

Aircraft weapon bays can and usually do generate a very high intensity fluctuating pressure (acoustic) environment which results in structural or electronic failure of store carried internally. If the weapons bay and stores are designed to withstand this intense environment, a significant weight penalty is incurred. Passive suppression systems can be designed and optimized to control this environment but they are most effective only over a small Mach number range. Future systems will require that a benign weapons bay acoustic environment be assured at all Mach numbers which the aircraft is capable of flying. A passive suppression system will not be able to provide this. Thus, some type of active control system will be needed to be adaptive over the entire speed range.

9. REFERENCES

1. Roshko, A. "Some Measurements of Flow in a Rectangular Cutout," N.A.C.A. Tech. Note 3488, 1955.

2. Krishnamurty, K., "Acoustic radiation From Two-Dimensional Rectangular Cutouts in Aerodynamic Surfaces," N.A.C.A. Tech. Note 3487, 1955.

3. Rossiter, J.E., "Wind Tunnel Experiments on the Flow Over Rectangular Cavities at Subsonic and Supersonic Speeds," Royal Aircraft Establishment, ARC R.&M. No. 3438, 1966.

4. Plumblee, H.E., Gibson, J.S., and Lassiter, L.W., "A Theoretical And Experimental Investigation of The Acoustic Response of Cavities In An Aerodynamic Flow," WADD -TR- 61- 75, March 1962.

5. Smith, D.L., and Shaw, L.L., "Prediction of The Pressure Oscillation In Cavities exposed to Aerodynamic Flow," AFFDL-TR-75-34, Oct 1975.

6. Heller, H. H., and Bliss, D.B., " Aerodynamically Induced Pressure Oscillations in Cavities-Physical Mechanisms and Suppression Concepts," AFFDL-TR-74-133, Feb 1975.

7. Shaw, L.L., and Smith D.L., "Aeroacoustic Environment of A Store in an Aircraft Weapons Bay," AFFDL-TR-66-18, Mar 1977.

8. Shaw, L.L., "Suppression of Aerodynamically Induced Cavity Oscillations," AFFDL-TR-79-3119, Nov 1979.

9. Betry, M.R., and Rohrer , L.A., "Literature Survey of Aircraft Cavity Flow," AFWAL-TR-83-160-FIMM, May 1982.

10. Komerath, N.M., Ahvja, K.K., and Chambers, F.W., "Prediction and Measurement of Flows Over Cavities -A Survey," AIAA-87-0166, Jan 1987.

11. Plentovich, E.B., Stallings, R.L., Tracy, M.B., "Experimental Cavity Pressure Measurements at Subsonic and Supersonic Speeds," NASA TP-3358, Dec 1993.

12. Rockwell, D. and Naudascher, E., " Review-Self-Sustaining Oscillation of Flow Past Cavities," Journal of Fluids Engineering, Vol 100, pp 152-165, Jun 1978.

13. Kaufman, L.G., Maciulaitus, A., and Clark, R.L., "Mach 0.6 to 3.0 Flows Over Rectangular Cavities," AFWAL-Tr-82-3112, May 1983.

14. Yu, K., Gutmark, E., Smith, R.A., and Schadow, K.C., "Supersonic Jet Excitation Using Cavity-Actuated Forcing," AIAA 94-0185, Jan 1994.

15. Bartel, H.W., McAvoy, J.M., "Cavity Oscillation In Cruise Missile Carrier Aircraft," AFWAL-TR-81-3036, Jun 1981.

16. Bauer, R.C., and Dix, R.E., "Engineering Model of Unsteady Flow In A Cavity," AEDC-TR-91-17, Dec 1991.

17. Borland, C.J., "Numerical Perdition of The Unsteady Flowfield in an Open Cavity," AIAA-77-673, 1977.

18. Hankey, W.L. and Shang, J.S., "Analysis of Pressure Oscillation In An Open Cavity," AIAA Journal Vol 18, No 8 pp 892-898, Aug 1980.

19. Baysal, O., and Yen, G., "Implicit and Explicit Computations of Flows Past Cavities With and Without Yaw," AIAA-90-0049, Jan 1990.

20. Morgenstern, A, and Chokami N., Computation of Hypersonic Flow Over Three Dimensional Cavity," AIAA-94-0631, Jan 1994.

21. Hardin, J.C., and Pope, D.S., "Sound Generation By Flow Over A Two-Dimensional Cavity," AIAA 93-4327, October 1993.

22. Shaw, L. L., "Full Scale Flight Evaluation of Suppressions Concept For Flow-Induced Fluctuating Pressure In Cavities," AIAA-82-0328, January, 1982

23. Tipton, A.G., "Weapon Bay Cavity Noise Environment Data Correlation and Prediction For The B-1 Aircraft," AFWAL-TR-80-3050, June, 1980.

24. Shaw, L.L., Bartel, H., and McAvoy, J., "Prediction and Suppression of the Acoustic Environment in Large Enclosures With a Small Opening Exposed to Aerodynamic Flow" AIAA-82-0121, January, 1982.

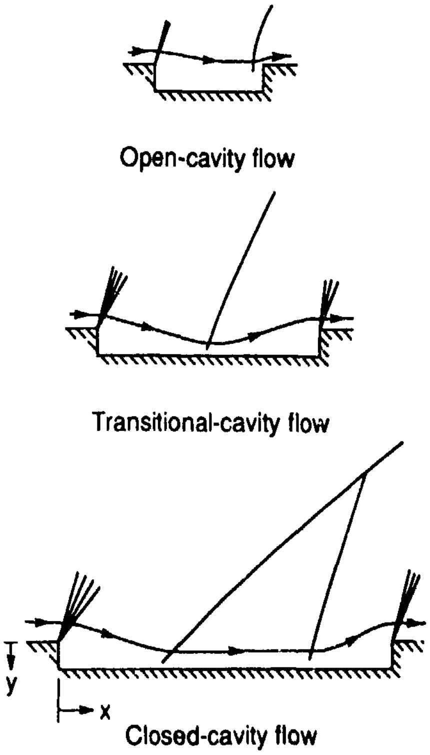
Open-cavity flow
Transitional-cavity flow
Closed-cavity flow
y
x

Fig 1 Three types of cavity flow

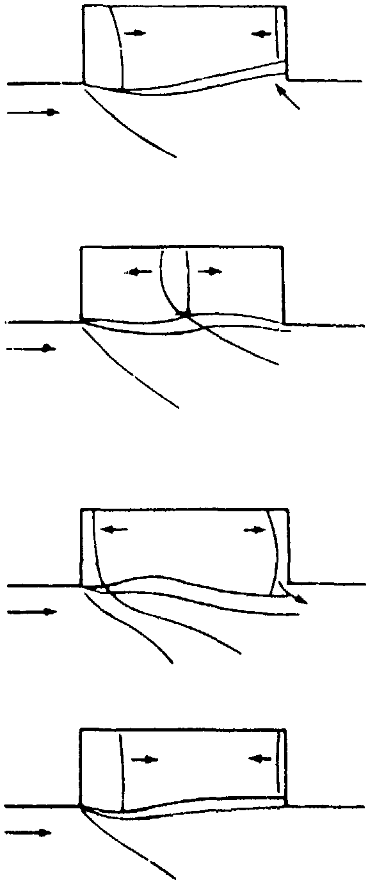

Fig 3 Sketch of basic cavity Phenomenon

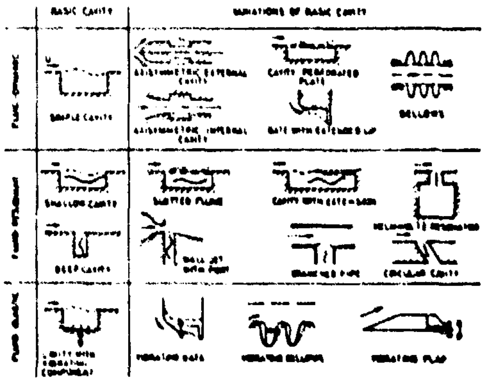
BASIC CAVITY
VARIATIONS OF BASIC CAVITY
SIMPLE CAVITY
BELLOWS
SHALLOW CAVITY
DEEP CAVITY

Fig 2 Classification of cavity flows (Ref 12)

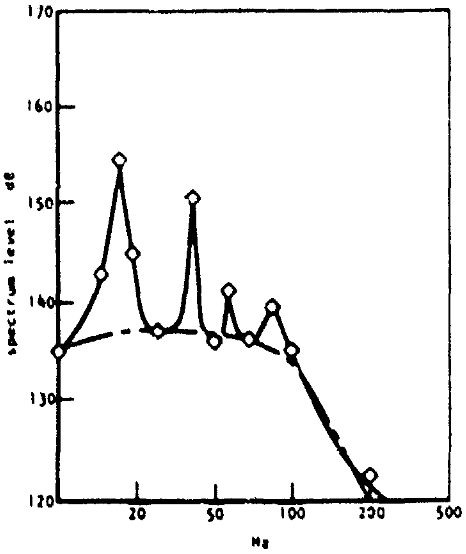

Fig 4 Full scale B-1A weapons bay acoustic levels for Mach number 0.7 at 20,000 feet

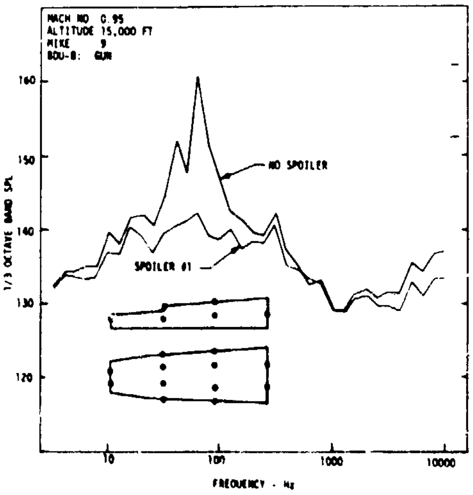

Fig 5 Full scale F-111 weapons bay spectra

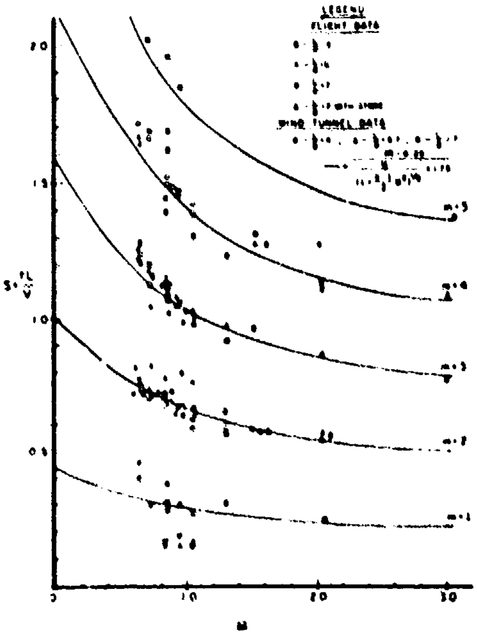

Fig 6 Non-dimensional resonant frequencies as a function of Mach number

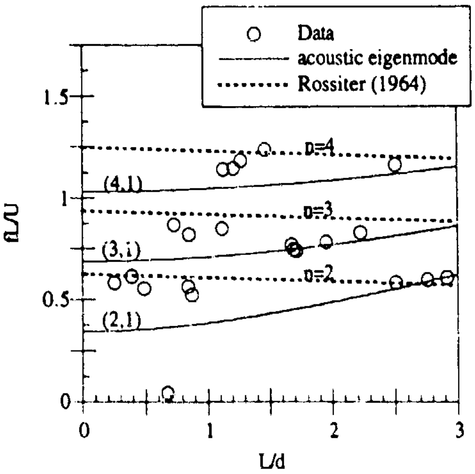

Fig 7 Comparison of cavity acoustic modes and Rossiter's equation (Ref 14)

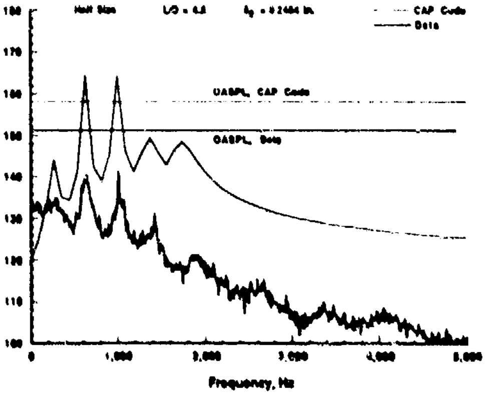

Fig 8 Comparison of Cavity Acoustic Pressure (CAP) code with Mach [illegible] Data (Ref 16)

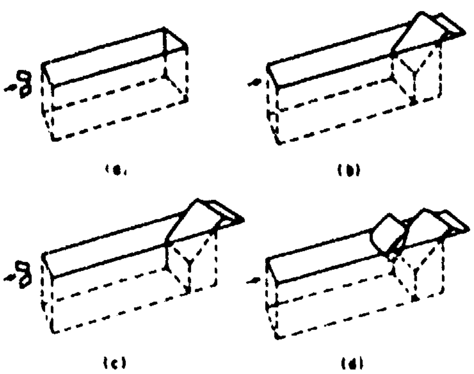

Fig 9 Four most promising suppression concepts (Ref [illegible])

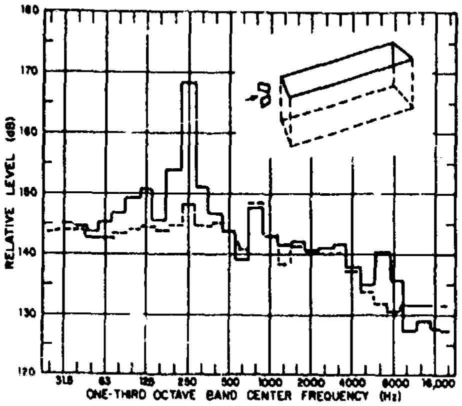

Fig 10 Example suppression of leading edge spoilers (Ref 6)

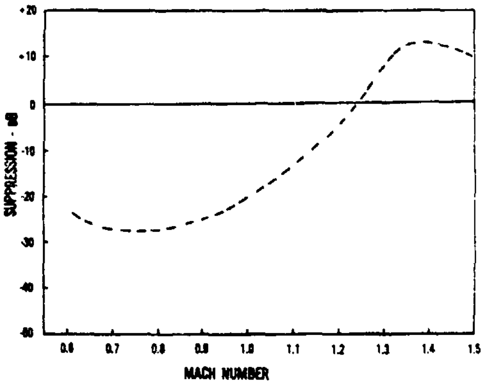

Fig 12 Variation of suppressor effectiveness with Mach number (Ref 23)

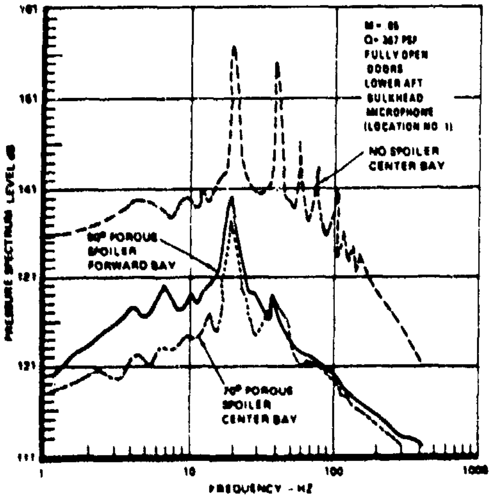

Fig 11 Forward and center bay acoustic levels (Ref 23)

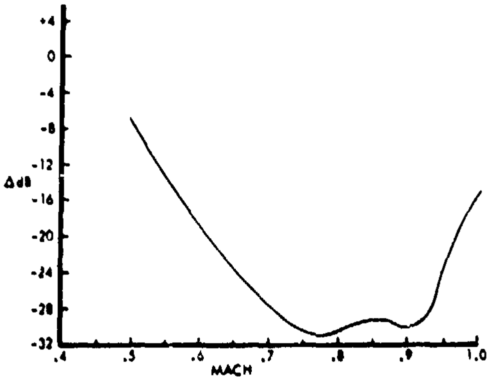

Fig 13 Optimized Suppression of Maximum Oscillation (Ref 24)

IMPACT OF NOISE ENVIRONMENT ON ENGINE NACELLE DESIGN

R. Giuzio
E. Dalle Mura
G. Giuffrè
ALENIA Un'Azienda Finmeccanica s.p.a.
Corso Marche, 41
10146 Torino - Italia

SUMMARY

The present paper describes the general philosophy and the followed methodology in engine nacelle acoustic design, usually resulting in the embodiment of acoustic treatment in intake and exhaust ducts to make the relevant aircraft compliant with noise certification requirements.

General description of conventional acoustic liners, currently in service, and liners of innovative design, in course of research, is also enclosed, giving emphasis to the methodology for the selection of the proper acoustic treatment.

Finally the Alenia software package (ALNOIS), ad hoc developed to cover the complete engine nacelle acoustic design and to support the acoustic panels manufacturing, is briefly described.

1. INTRODUCTION

With the increase of air traffic and the development of more and more powerful engines the impact of aircraft noise emission on community has become a problem of great importance to be considered in the nacelle design.

To control the noise pollution and noise intrusion on community life, especially near airports, noise limits during flight operations have been imposed for the aircraft certification (FAR Part 36 and ICAO Annex 16). In parallel, more restrictive measures and rules have been adopted by some airports where the noise problem had become a national concern.

For certification purposes of commercial aircrafts the emitted noise is quantified in terms of Effective Perceived Noise Level (EPNL), in dB scale, and A-weighted overall sound pressure level (peak dBA). Both account for the sound perception by an observer on ground, at fixed position, from the aircraft appearance to its disappearance during take-off and landing manoeuvres.

dBA accounts for loudness effects and approximates the human hearing characteristics for moderate sound levels. EPNL combines human annoyance to loudness and tonality characteristics of noise, a time averaging effect is also taken into account as the noise increases from the background floor up to a maximum and then decreases to the initial level during the overhead aircraft flyover.

For general purposes most nations with an airport noise problem have developed an own annoyance index which accounts for individual aircraft noise and frequency of operation (noise intrusion). The map, on ground, of iso-level noise curves represents the so called aircraft noise signature that new engine design, nacelle acoustic treatment and proper flight procedures contributed to reduce over the years.

2. PROGRESS IN COMMUNITY NOISE

Aircraft noise certification appeared at the beginning of 1970s (FAA 1969, ICAO 1970) with initial rules applicable to new design only. This favoured the research on the development of quieter engines.

Successively the regulation was extended to new production of older types (FAA 1973, ICAO 1976). This action had both the effect to favour the development of "hushkits", that could report the aircraft to comply with the certification requirements, and to stop the production of those aircrafts, like B707, which could not meet the requirements unless a re-engine activity would be pursued.

Finally in 1978 new limits were introduced (FAR Part 36 Stage 3, ICAO Annex 16 Chapter 3) jointly to the banishment of Chapter 1 (Stage 1) and Chapter 2 (Stage 2) aircrafts. Chapter 1 aircrafts disappeared in 1989, Chapter 2 aircrafts banishment will be completed within 2002.

Hushkits reduced the aircraft noise level from a minimum of 1 EPNdB to a maximum of 4 EPNdB, the main effect was to make "legal" the relevant aircraft but they do not resolved the pollution problem, as a change of 3 EPNdB is virtually imperceptible by the human ear, needing a change of 10 EPNdB to halving or doubling the annoyance.

Of primary importance on the community noise reduction was instead the technological evolution of the engine/nacelle combination.

Pure jet engines, that dominated the commercial fleet in 1950s, were substituted by Low By-Pass Ratio (LBPR, typically 3:1) turbofans, appeared in 1960s, and High By-Pass ratio (HBPR, typically 6:1) turbofans, appeared in 1970s. This evolution led to a progressively reduction of the aircraft emitted noise in spite of a complication of noise source components and nacelle design.

Presented at a Symposium on 'Impact of Acoustic Loads on Aircraft Structures' held in Lillehammer, Norway, May 1994.

The single source (jet mixing noise) domination of pure jet engines has been replaced by a multitude of tonal and broadband noise sources that combine with combustor and jet mixing noise (see Figure 5.1). Fan noise normally results the dominant source at approach conditions and is a significant contributor also at take off conditions.

Future engines generation with Very High By-Pass Ratio (VHBPR, typically 9:1) and Ultra High By-Pass Ratio (UHBPR, typically 12:1+15:1) turbofans are expected to increase the fan noise (because of the larger fan configurations and the probably increase of in flow distortion interacting with fan due to the shorter nacelle) accompanied by a shifting of fan tones towards low frequency (because of the larger fan diameter and the reduced number of revolutions per minute).

Therefore fan noise will be the more important community noise source, while buzz-saw noise (a series of equally spaced tones produced by shock waves originating at supersonic fan tip speed) will probably be a major cause of annoyance in the cabin.

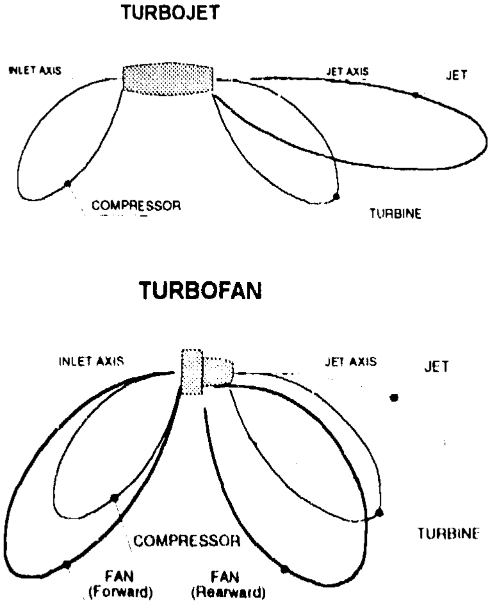

Figure 5.1 - Noise sources directivity of turbojet and turbofan engines

The noise sources of current generation of turbofan engines, being originated inside the engine (jet noise originates outside as a consequence of the mixing process between the exhaust flow of the engine and the atmosphere), have been controlled by the embodiment of acoustic panels in the nacelle air and gas flow ducts (see Figure 5.2), in addition to fan tip speed reduction and rotor stator gaps increasing

The design of nacelle acoustic liners, acting to attenuate the propagating sound and then the far-field radiated noise, required a great effort of research, even if absorbent materials were known from many years.

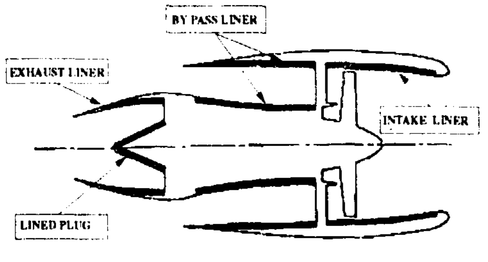

Figure 5.2 - Typical acoustic liner installation in a current HBPR turbofan engine

In fact the severe nacelle environment (e.g. wider range of temperatures, -50°C + +500°C, freeze/thaw action on retained water, combustible-fluid retention, etc.) limited the application of commercially available bulk absorbent materials, that would have matched the low weight requirement, and specific structural solutions needed to be derived.

The embodiment of the acoustic liners led the nacelle to gain a fundamental role on the design of a quieter aircraft. The provided benefits on the community noise were remarkable, as can be seen from Figure 5.3 showing the trend of noise reduction for medium range two engine commercial aircrafts.

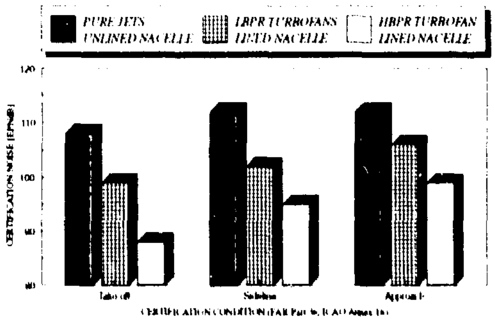

Figure 5.3 - Noise progress related to jet engine evolution and nacelle improvement

The lower surface availability in shorter inlets of advanced turbofans and the low frequency content of the emitted noise will represent a technological challenge for nacelle and engine manufacturers to which is demanded the development of low frequency liners, no neglecting any possible application of active control noise techniques

3. NACELLE ACOUSTIC DESIGN METHODOLOGY

As showed before the emitted acoustic noise has become a very important aircraft performance parameter due to the more stringent community noise regulations

With the advent of turbofan engines and the reduced importance of jet noise the nacelle represents the link between the turbomachinery noise sources and the external ambient to which is demanded the duty to silencer the engine noise.

The nacelle acoustic design requires the availability of an accurate prediction of individual noise sources in order to define the optimum liner which makes the relevant aircraft to comply with certification limits and with more stringent airport rules, for market competitiveness.

The complete loop of analysis is shown in Figure 5.4.

The preliminary prediction of the aircraft noise emission requires the knowledge of engine and aircraft geometric and performance parameters.

Previous experience on similar engine/airframe combination will simplify the design procedure and save costs of project as development tests need to be not performed or may be reduced to a minimum

Engine/airframe of new design will require the availability of noise measurements from engine static tests, for the tailoring of turbomachinery noise prediction methods, and from aircraft prototype flight trials, for the refinement of the airframe noise prediction method and engine installation effects.

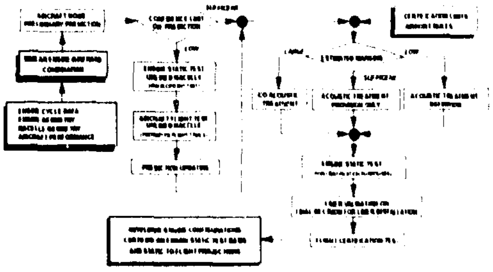

Figure 5.4 - Nacelle acoustic design methodology

The following main steps in the nacelle acoustic design procedure need to be outlined

- the initial aircraft noise prediction accounts of no acoustic treatment in nacelle ducts (hard wall ducts),
- the turbomachinery noise prediction is updated on the basis of flight projection of static noise measurements, collected during preliminary engine static tests using an unlined nacelle,
- the validation of the airframe noise prediction is based on noise measurements during prototype flight trials, also useful for engine installation effects verification,
- the updated aircraft noise prediction is compared with the target noise limits (certification limits and/or airport rules) and the relevant margins are estimated to take a decision on the adoption of acoustic treatment in the nacelle intake and exhaust ducts,
- low margins require the definition of a target attenuation for the intake and exhaust ducts: this target constitutes an input for the acoustic treatment design;
- finally the effectiveness of the defined acoustic treatment is verified during engine static tests and aircraft flight tests for certification purposes.

3.1. Aircraft noise prediction

Aircraft emitted noise calculation consists in the evaluation of the noise perceived by an observer on ground during an aircraft manoeuvre (e.g. Take off, Sideline, Approach, etc.) in terms of EPNL, overall peak dBA or any other local index.

To perform this calculation the following input data are required:

- aircraft manoeuvre characteristics (flight path, flight speed, etc.);
- engine geometry (fan diameter, number of blades, etc.);
- aircraft geometry (wing span, flap area, landing gear wheel diameter, etc.);
- engine parameters (fan rpm, exhaust gases speed, pressures, temperatures, etc.),
- intake and exhaust ducts acoustic treatment insertion loss matrix (if present).

The far field radiated noise is then evaluated, for each time interval of the aircraft manoeuvre evolution, in three steps: first by calculating the contributors of individual noise sources, second by correcting the predicted noise for a several number of effects during propagation, third by summing all the corrected contributors.

For a complete analysis the first step shall consider the following noise sources, though some of them are of less importance on the overall aircraft noise (i.e. compressor broadband noise and tones, turbine noise, combustor noise)

- fan broadband noise (forward and rearward),
- fan buzz-saw noise,
- fan steady flow distortion tones (forward and rearward),
- fan wake interaction tones (forward and rearward),
- compressor broadband noise,
- compressor wake interaction tones,
- combustor noise,
- turbine broadband noise,
- turbine flow distortion tones,
- turbine wake interaction tones,
- jet turbulent mixing noise,
- jet shock associated noise,
- jet wing/flap interaction noise,
- airframe noise

Details on the generation mechanisms of these noise components may be found on papers in references from 1 to 10.

The calculated far field noise is then corrected to take into account for the following propagation effects [11, 12, 13]:

- insertion loss due to the presence of in-duct acoustic treatment (intake and exhaust ducts);
- aircraft structure shielding and reflection effects;
- Doppler effect on noise intensity and frequency;
- convection or flight speed effects;
- refraction and scattering effects related to the speed difference between external flow and exhaust gases flow;
- atmospheric attenuation;
- ground reflection;
- measuring instrument bandwidth filtering simulation.

Finally the noise perceived on ground by the observer is obtained from the summation of all the above corrected components in terms of useful indexes (EPNL, peak dBA, etc.).

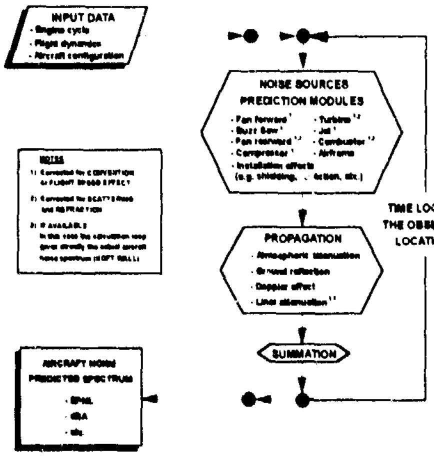
INPUT DATA
- Engine cycle
- Flight dynamics
- Aircraft configuration
NOISE SOURCES PREDICTION MODULES
- Fan forward
- Buzz Saw
- Fan rearward
- Compressor
- Installation effects (e.g. shielding, reflection, etc.)
- Turbine
- Jet
- Combustor
- Airframe
NOTES
PROPAGATION
- Atmospheric attenuation
- Ground reflection
- Doppler effect
- Liner attenuation
TIME LOOP AT THE OBSERVER LOCATIONS
SUMMATION
AIRCRAFT NOISE PREDICTED SPECTRUM
- EPNL
- dBA
- etc.

Figure 5.5 - Aircraft noise prediction flow chart

3.2. Aircraft noise updating

Prediction methods are usually based on the existence of a data base of measured data

When a new engine is developed or when the design modifications of an existing engine are such that substantial differences in noise emission are expected, the usual procedure is to perform dedicated on ground engine static tests on open-air facilities

Static test measurements are largely accurate, giving a repeatability better than 1 dB over a wide range of frequencies, therefore they result a cost-saving feature of the noise certification process

For static test purposes the engine, equipped with a dummy nacelle and an in-flow control device (a screen that reduces the distortion of flow nearly simulating the flight conditions), is suspended to a jig, with minimised reflection effects, on a test arena with no obstacles that may cause acoustic interference.. The ground floor is characterised by low absorption and high thermal reflection. Far field noise measuring microphones have a circular disposition (10° equally spaced from 0° to 180°) and are face-down positioned to eliminate ground reflection interference effects.

A typical lay out of an open-air noise test arena is showed in Figure 5.6.

Small changes in noise levels related to minor power-plant modifications are better quantified during static tests than flight tests, so static tests are largely used both for turbomachinery noise sources prediction methods updating and for noise certification of re-engined aircrafts.

Nevertheless for a new airframe configuration flight tests, other than required for noise certification, are necessary to be performed in order to check the validity of the airframe noise prediction method and engine installation effects.

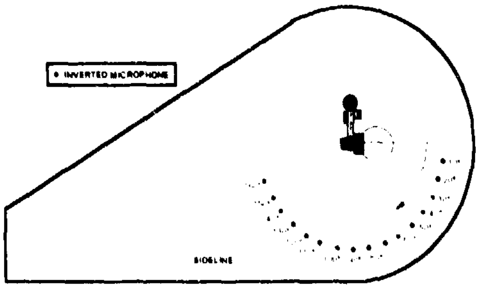
INVERTED MICROPHONE
SIDELINE

Figure 5.6 - Typical test arena lay out for noise measurements during engine static test

4. A/C NOISE REQUIREMENTS

Aircraft noise requirements are to be divided in certification requirements, defined by the international regulation organisms (FAA and ICAO), and local requirements, imposed by airport authorities

FAR and ICAO regulations impose a ceiling on the noise permitted by commercial aircraft by specifying noise limits at the same three critical conditions (take off, sideline and approach) and reference points around the airport

Noise limits are given in terms of EPNdB as function of maximum take off weight and number of engines Heavier long range aircraft are allowed to produce more noise, similarly four engine aircrafts may be noisier at take off

The higher noise allowed for heavier aircrafts is related to the total airport noise problem control In fact long range aircrafts operates quite rarely if compared with the short and medium range ones, so the intrusion factor will be less severe.

The higher noise allowed for multi-engine aircrafts is related to the airworthiness requirement of aircraft take off capability with an engine failure occurring during the most critical take off phase, that is, after there is insufficient runway to abort the take off. For this reason a two engine aircraft has 100% more thrust than the minimum required for take off, with both engines operating, so it climbs extremely quickly. A four engine aircraft has only 33% excess thrust and with all engines operating climbs very slowly. Hence the four engine airplane results comparatively close to the community when it overflies the reference microphone at 6500 m from the brake release; the three engine is somewhat higher and the two engine is even higher (see Figure 5.7).

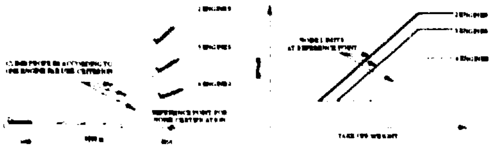

Figure 5.7 - Climb profiles of commercial jet aircrafts and relevant noise limits

For all class of engines a power cut-back operation procedure is allowed at take off to make the aircraft departure more silent.

The two regulations are nominally equivalent, differences are present only in some details, making FAR 36 more stringent.

A summary of certification requirements for Stage 3 aircrafts is given in Figure 5.8.

Local requirements generally raise from the noise pollution problem caused by the air traffic.

In fact in addition to the single event of noise related to the aircraft arrival or departure it is also to be considered the noise intrusion on the community life related to the number of daily/nightly operations. This led airport authorities to define operational restrictions, general limitations and penalties for noisy aircrafts.

The currently more stringent noise control measures for night-time operations are adopted by the Washington National airport. Noise limits are expressed in term of overall A-weighted sound pressure level as follows.

from 22.00 to 06.59	72 dBA for Take off 85 dBA for Approach
from 07.00 to 21.59	no limitations

Nevertheless Washington airport authorities are forced by residents to further reduce the above noise limits according to the following proposal

from 22.00 to 22.59	72 dBA for Take off 85 dBA for Approach
from 23.00 to 05.59	67 dBA for Take off 80 dBA for Approach
from 06.00 to 06.59	72 dBA for Take off 85 dBA for Approach
from 07.00 to 21.59	no limitations

ICAO Annex 16 Chapter 3 - FAR Part 36 Stage 3

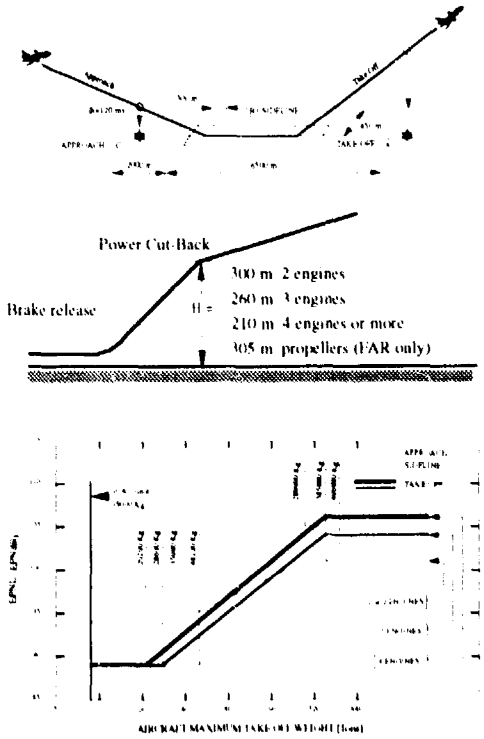

Figure 5.8 - Exemplification of certification requirements for Stage 3 aircrafts

5. LINER DESIGN

The overall procedure for the design of nacelle ducts acoustic treatment is shown in Figure 5.9. It starts from the definition of a required attenuation and continue through the duct-acoustic analysis to quantify the acoustic treatment area needed to match the required attenuation.

The required attenuation is generally based, alternatively, on the three following criteria

- total radiated sound power attenuation (as function of frequency);
- radiated sound power attenuation for specific angular sectors (as function of frequency);
- radiated far field sound pressure level (as function of frequency and angular location).

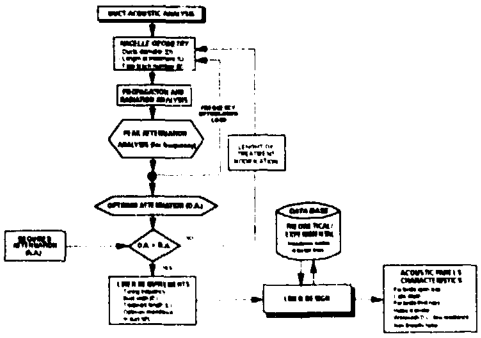

Figure 5.9 - Duct-acoustic analysis and liner design procedure

Next step is to determine which liner is capable to give the required attenuation with minor modification of the nacelle structure. This is accomplished by studying the in-duct sound propagation (e.g. mode theory) [14] and the far field sound radiation (e.g. Green functions) [13, 14].

As far as conventional (locally reacting) liners are concerned, an important reference parameter, for the choice of the right type of liner to be used for the acoustic treatment, is the Optimum Impedance, herein defined as the theoretical impedance (vs. frequency) of duct surface which would give the best results (maximum attenuation); this impedance is only theoretical, because it is impossible to realise an acoustic panel matching the Optimum Impedance over the whole frequency range of interest, however it is an useful reference point for the liner design.

The evaluation of the Optimum Impedance, for a given duct geometry (diameter and length) and internal flow velocity, requires the construction, for each frequency, of a data-base containing the attenuation provided by a set of duct internal surface impedances.

The data base is calculated by applying the mode theory and by restricting the analysis to the hard wall acoustic cut-on modes (modes which propagate with no attenuation for the hard wall duct case). Some assumptions regarding the acoustic energy distribution among ducts modes are necessary. Commonly the equal energy distribution, sometimes factored by a biasing function (more emphasis to well cut-on modes) [15], is considered.

In particular cases, when the acoustic energy is mainly stored in a limited number of acoustic modes (e.g. for the fan tones), it can be useful to define the Optimum Impedance with reference to that group of propagating modes.

A typical plot for the single frequency attenuation data-base is shown in Figure 5.10; the maximum attenuation point, obtained by interpolating the sound power attenuation contours on the impedance plane, corresponds to the Optimum Impedance for the frequency under examination.

An analysis complication is represented by the boundary layer effect on sound propagation. Studies and experiments on this subject [16] showed that the boundary layer has negligible effects on sound propagation along exhaust ducts but remarkable effects on the attenuation characteristics of the least attenuated mode (lowest order mode) in case of inlet flows. This effect results in a reduction of the obtainable attenuation, with a decrease of the Optimum resistance of the single mode [17], for boundary layer thickness to duct radius ratios (δ/R) above 0.025. For large nacelles the above ratio is usually less than the limit and therefore the boundary layer effect can be neglected.

If the Optimum Impedance is not sufficient to furnish the required attenuation it is necessary to modify the nacelle structure, generally by increasing the treated area length, and repeating the optimisation loop of calculation for the modified duct.

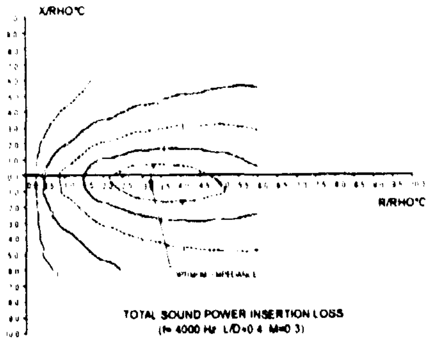

Figure 5.10 - Example of single frequency sound power attenuation contours for Optimum Impedance definition

At the end of the above process the definition of the acoustic treatment is focused on those liners having impedances as near as possible close to the Optimum Impedance especially in those frequency ranges which are considered more critical for aircraft noise certification (e.g. fan blade passing frequency and relevant harmonics).

The liner design procedure is based on the availability of impedance models data-base and is articulated as follows:

- derivation of a set of acoustic liners (in terms of geometric and acoustic characteristics) that match in a quite good manner the Optimum Impedance curve;

- calculation of the far field noise attenuation considering the duct lined with this set of liners;
- definition of the acoustic panel geometry.

6. LINER CHARACTERISTICS

Acoustic liners can be divided in two main groups:

- the locally reacting liners whose acoustic behaviour at each point depends only on the acoustic field characteristics at that point;
- the non locally reacting liners whose acoustic behaviour is related to the complete acoustic field along the panel (e.g. acoustic pressure distribution).

Locally reacting liners represent the current generation of in-service acoustic panels. Their acoustic behaviour is characterised by the complex ratio between the instantaneous values of the acoustic pressure, p(f), and the acoustic particle velocity, u(f); this ratio, called acoustic impedance, Z(f), is a function of sound frequency and is constant for every point of the liner surface exposed to the acoustic field.

The impedance is generally expressed as:

$$Z(f) = \frac{p(f)}{u(f)}$$

Real and complex part of impedance are named resistance, R(f), and reactance, X(f), respectively so that it is common to find the equation:

$$Z(f) = R(f) + iX(f)$$

The impedance property of locally reacting liners allows to perform the in-duct sound propagation analysis, for the evaluation of the acoustic treatment performance, in a closed form solution by using the mode theory.

The fundamental properties of locally reacting liners are summarised in Figure 5.11

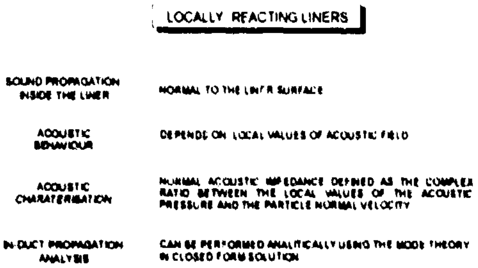

LOCALLY REACTING LINERS

SOUND PROPAGATION INSIDE THE LINER	NORMAL TO THE LINER SURFACE
ACOUSTIC BEHAVIOUR	DEPENDS ON LOCAL VALUES OF ACOUSTIC FIELD
ACOUSTIC CHARATERISATION	NORMAL ACOUSTIC IMPEDANCE DEFINED AS THE COMPLEX RATIO BETWEEN THE LOCAL VALUES OF THE ACOUSTIC PRESSURE AND THE PARTICLE NORMAL VELOCITY
IN-DUCT PROPAGATION ANALYSIS	CAN BE PERFORMED ANALITICALLY USING THE MODE THEORY IN CLOSED FORM SOLUTION

Figure 5.11 - Locally reacting liners properties

Locally reacting liners can be grouped in three different main classes (see Figure 5.12):

- mainly resistive liners;
- resistive/reactive liners;
- linear resistive/reactive liners.

Mainly resistive liners are generally constituted by porous material. They are not used in engine nacelle ducts because of their capacity to retain water, with possible decrease of porosity and acoustic performances due to freeze/thaw cycles, combustible-fluids, which are a fire hazard, etc..

Resistive/reactive liners constitute the simplest and earlier generation of liners for nacelle applications. They have a sandwich structure, single or double layer, whose components are: perforated facing sheet and septum, honeycomb cores and backing sheet.

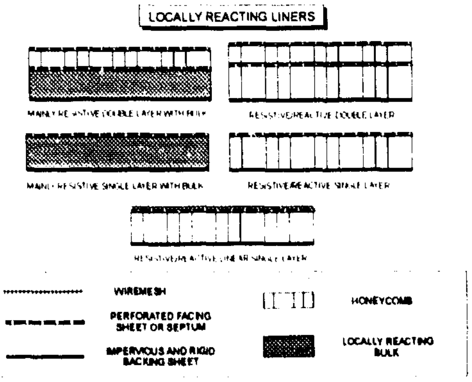
LOCALLY REACTING LINERS
MAINLY RESISTIVE DOUBLE LAYER WITH BULK
RESISTIVE/REACTIVE DOUBLE LAYER
MAINLY RESISTIVE SINGLE LAYER WITH BULK
RESISTIVE/REACTIVE SINGLE LAYER
RESISTIVE/REACTIVE LINEAR SINGLE LAYER
WIREMESH
PERFORATED FACING SHEET OR SEPTUM
IMPERVIOUS AND RIGID BACKING SHEET
HONEYCOMB
LOCALLY REACTING BULK

Figure 5.12 - Typical configurations of locally reacting liners

Liner impedance contributions becomes from:

- the perforated plate (holes diameter, sheet thickness, open area), that gives mainly a resistive contribution,
- the honeycomb core depth, having a reactive contribution only and determining the frequency for maximum attenuation.

A slight contribution to the reactance is also given by the perforate and is called inertance.

Large variations of liners impedance are caused by grazing flow Mach number and sound pressure level of the incident sound field.

Linear resistive/reactive liners have the same structure of the perforated ones but include a metallic wire cloth (wiremesh) on the perforated facing sheet having an high open area.

The wiremesh effect is to increase the resistive contribution of the facing sheet making it nearly constant over the whole frequency range and less sensitive to the grazing flow.

Design parameters are the D.C. flow resistance and the non linearity factor, defined as the ratio between the D.C. flow resistance values at flow velocities of 200 and 20 cm/s.

Also for this type of liners the reactive part of impedance is mainly governed by the honeycomb core depth with similar effects to those of perforated liners.

Non locally reacting liners are currently matter of research. The acoustic response of this class of panels depends on the whole acoustic field acting on the panel surface (acoustic pressure distribution) and it is not possible to identify a single parameter characterizing the liner acoustic behaviour.

The acoustic performances of non locally reacting liners can only be quantified in terms of insertion losses for each duct/panel combination.

The duct propagation analysis in presence of this type of liners shall be performed using a finite element or finite difference technique; no closed form solution is available.

The fundamental properties of non locally reacting liners are summarised in Figure 5.13.

NON LOCALLY REACTING LINERS

SOUND PROPAGATION INSIDE THE LINER	PARALLEL AND NORMAL TO THE LINER SURFACE
ACOUSTIC BEHAVIOUR	DEPENDS ON THE ACOUSTIC PRESSURE DISTRIBUTION OVER THE WHOLE PANEL SURFACE
ACOUSTIC CHARACTERISATION	INSERTION LOSS OF THE COMPLETE PANEL RELATED TO THE WHOLE ACOUSTIC FIELD AND FLOW CONDITION
IN-DUCT PROPAGATION ANALYSIS	ONLY BY MEANS OF NUMERICAL METHODS

Figure 5.13 - Non locally reacting liners properties

Special cases of non locally reacting liners are those that behave as non locally reacting in only one direction (e.g. circumferential).

Figure 5.14 shows some configurations of non locally reacting liners characterised by a non locally reaction along the circumferential direction only.

The acoustic response of such panels depends on the circumferential acoustic pressure pattern in the duct, for each circumferential distribution it is possible to define an equivalent impedance for the duct/panel combination.

Considering that the acoustic modes of the duct are grouped on the basis of circumferential pressure lobe number (mode circumferential order) it is possible to define the acoustic performance of a duct/panel combination using the mode theory (solution in closed form), different impedances are to be considered for each circumferential mode order.

Circumferential non locally reacting liners are currently under investigation by Alenia and others European partners inside a CEC (Committee of European Community) research.

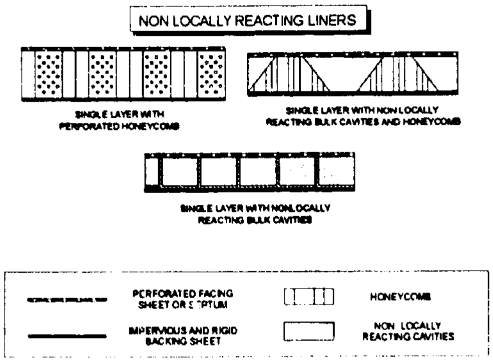
NON LOCALLY REACTING LINERS
SINGLE LAYER WITH PERFORATED HONEYCOMB
SINGLE LAYER WITH NON LOCALLY REACTING BULK CAVITIES AND HONEYCOMB
SINGLE LAYER WITH NON LOCALLY REACTING BULK CAVITIES
PERFORATED FACING SHEET OR SEPTUM
HONEYCOMB
IMPERVIOUS AND RIGID BACKING SHEET
NON LOCALLY REACTING CAVITIES

Figure 5.14 - Typical configurations of circumferential non locally reacting liners currently under investigation inside a CEC research

7. LINER DEVELOPMENT TOOLS

The liner design process requires the availability of impedance models that relate the geometrical and physical characteristics of liner components to the resulting impedance.

Liner impedance models are derived with the effort of test results obtained from a dedicated test program and using special tools.

Locally reacting liners impedance models are determined semi-empirically [18, 19, 20, 21, 22] through the experimental measurement of the acoustic properties of its components.

Tools and test facilities dedicated to these tests are summarised in Figure 5.15.

Facing sheet characteristics, usually measured by means of a Raylometer, are the following:

- perforated sheet D.C. flow resistance,
- wire mesh D.C. flow resistance and non linearity factor,
- bulk material D.C. flow resistance for unit of thickness.

Impedance measurements on liner test sample are performed using an impedance tube, with no grazing flow, and a flow duct facility, in presence of grazing flow and boundary layer.

The flow duct facility [23, 24] consists of two reverberation chambers (upstream and downstream) each other connected by a sort of wind tunnel consisting of an inlet bellmouth, a test set and a diffuser. Flow is generated by blowers, fan or ejectors. Air supply and air exhaust ducts are acoustically treated to reduce unwanted noise in the facility and outside noise intrusion.

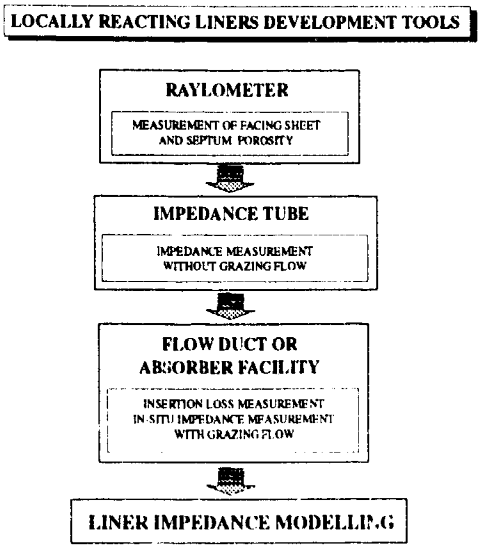
LOCALLY REACTING LINERS DEVELOPMENT TOOLS
RAYLOMETER
MEASUREMENT OF FACING SHEET AND SEPTUM POROSITY
IMPEDANCE TUBE
IMPEDANCE MEASUREMENT WITHOUT GRAZING FLOW
FLOW DUCT OR ABSORBER FACILITY
INSERTION LOSS MEASUREMENT
IN-SITU IMPEDANCE MEASUREMENT WITH GRAZING FLOW
LINER IMPEDANCE MODELLING

Figure 5.15 - Locally reacting liners development tools

This arrangement allows to simulates the sound propagation pattern inside nacelle intake and by-pass ducts: the diffuse sound field at inlet bellmouth permits an equal energy distribution among the acoustic duct modes, while the sound generated inside one of the two reverberation chambers simulates, alternatively, the upstream propagation (nacelle intake duct) and the downstream propagation (nacelle by-pass duct).

Test section is usually rectangular, which approximates the annular geometry of by-pass ducts and allows the manufacturing of flat test samples

The flow duct facility allows the derivation of liner impedance both indirectly, by performing insertion loss measurements (difference between the sound pressure level, for each 1/3 octave band centre frequency, in the receiving room without and with acoustic panels in the test section), and directly through the in-situ measurement technique using miniature microphones

A typical lay out of a flow duct facility is showed in Figure 5.16

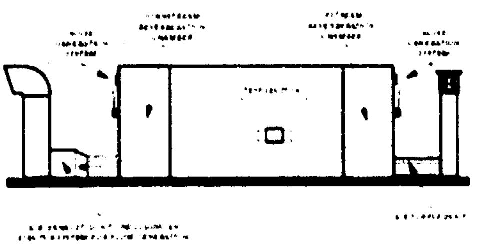

Figure 5.16 Flow duct facility lay out

The theoretical modelling of non locally reacting liners results currently almost complicated.

Facing sheet and septum characteristics, can be still measured by means of a Raylometer.

The flow duct facility can be used to correlate the insertion loss of the complete panel with the incident sound field.

Nevertheless of great importance is the exact simulation of the sound field propagation pattern, as the acoustic behaviour of this class of panels varies with the ducts mode order.

Tools and facilities dedicated to the experimental testing of non locally reacting liners are summarised in Figure 5.17.

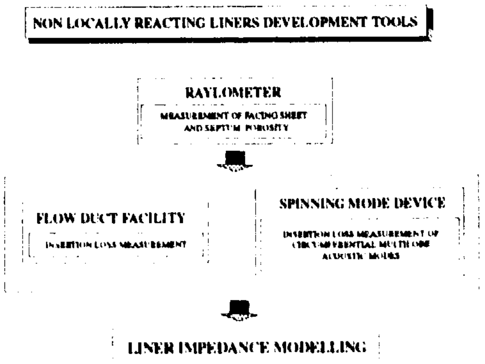
NON LOCALLY REACTING LINERS DEVELOPMENT TOOLS
RAYLOMETER
MEASUREMENT OF FACING SHEET AND SEPTUM POROSITY
FLOW DUCT FACILITY
INSERTION LOSS MEASUREMENT
SPINNING MODE DEVICE
INSERTION LOSS MEASUREMENT OF CIRCUMFERENTIAL MULTILOBE ACOUSTIC MODES
LINER IMPEDANCE MODELLING

Figure 5.17 Non locally reacting liners development tools

For nacelle applications of circumferential non locally reacting liners an useful tool is a specific device allowing the generation and control of spinning multilobe pressure pattern, so simulating the sound propagation characteristics inside the nacelle ducts

Such a device [24, 25] herein called spinning mode device, can substitute the rectangular test section of the flow duct facility or installed in a low noise wind tunnel Major components are

- a spining mode generator unit, moveble from one end to the other for upstream and downstream sound propagation, consisting of a circumferential array of equally spaced sound generators (whose number depends on the maximum spinning mode order to be generated), sound generators run at the same driving frequency but properly phased to reproduce the wanted number of lobes and the spinning nature of the pressure pattern,
- two pressure pattern measuring rakes, provided with a radial and circumferential traverse mechanism,
- a boundary layer control and measuring device,
- the lined portion, alternatively unlined for measurements comparison,
- two end mufflers, to reduce the reflected noise

A device of this type is showed in Figure 5.18.

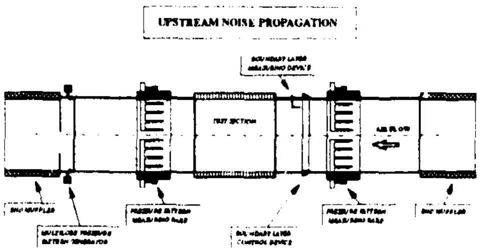
UPSTREAM NOISE PROPAGATION
BOUNDARY LAYER MEASURING DEVICE
TEST SECTION
AIR FLOW
PRESSURE PATTERN MEASURING RAKE
MULTILOBE PRESSURE PATTERN GENERATOR
BOUNDARY LAYER CONTROL DEVICE
PRESSURE PATTERN MEASURING RAKE

Figure 5.18 - Spinning mode device lay out

8. ALENIA SOFTWARE PACKAGE

In order to perform the whole calculation activity for the aircraft noise verification and the nacelle acoustic design Alenia developed a dedicated software package named ALNOIS (ALenia NOise Integrated Software).

The package is mainly constituted by three calculation modules (see Figure 5.19):

i) AIRCRAFT PREDICTION MODULE This module contains a set of sophisticated noise prediction methods and requires the knowledge of a large amount of engine internal geometry and performance parameters. The module can manage the engine static test and flight test data (broadband noise and discrete tones separation, noise sources breakdown, tones origin identification) and gives suggestions for prediction methods updating.

ii) DUCT-ACOUSTIC ANALYSIS MODULE This module is capable to analyse circular and annular ducts by determining the relevant attenuation data-base which is used for the definition of the Optimum Impedance. The in-duct noise propagation analysis is performed using the Mode Theory and considering as propagating the cut on modes of the unlined duct case (hard wall). The sound radiation analysis is performed using the Green functions.

iii) LINER DESIGN MODULE This module can evaluate the impedance characteristics of locally reacting liners of the following type:

- mainly resistive,
- resistive/reactive,
- linear resistive/reactive.

Besides it is used to support the research, development and manufacturing of nacelle acoustic panels in Alenia.

A detail of the ALNOIS modules relevant to the aircraft noise prediction and the duct-acoustic analysis is showed in Figure 5.20.

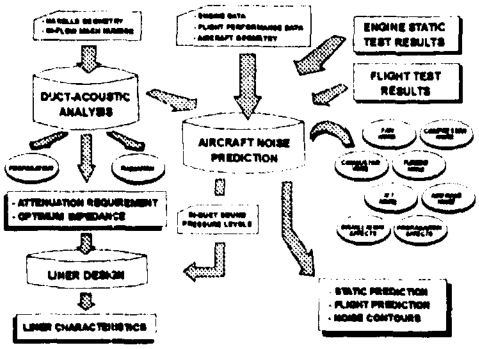
ENGINE DATA
FLIGHT PERFORMANCE DATA
AIRCRAFT GEOMETRY
ENGINE STATIC TEST RESULTS
FLIGHT TEST RESULTS
DUCT-ACOUSTIC ANALYSIS
AIRCRAFT NOISE PREDICTION
- ATTENUATION REQUIREMENT
- OPTIMUM IMPEDANCE
IN-DUCT SOUND PRESSURE LEVELS
LINER DESIGN
LINER CHARACTERISTICS
- STATIC PREDICTION
- FLIGHT PREDICTION
- NOISE CONTOURS

Figure 5.19 - Structure of ALenia NOise Integrated Software (ALNOIS) package

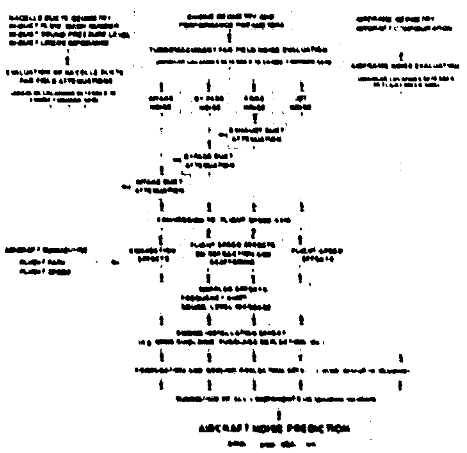
AIRCRAFT NOISE PREDICTION

Figure 5.20 - ALNOIS detail of duct acoustic analysis and aircraft prediction modules

The ALNOIS software architecture in modules gives it a great flexibility and allows the possibility to entry from different points, as function of the input data available or supplied for the nacelle acoustic treatment definition (see Figure 5.21):

- 1st ENTRY aircraft geometry, engine data and aircraft flight performance. In this case the complete loop of calculation is performed starting from the initial aircraft noise prediction and finishing with the definition of the liners characteristics for the nacelle ducts,
- 2nd ENTRY duct attenuation requirement. This option permits to jump directly to the run of the duct-acoustic analysis module avoiding all the calculations related to the aircraft noise prediction,
- 3rd ENTRY impedance requirement. In this case only the liner design module needs to be run.

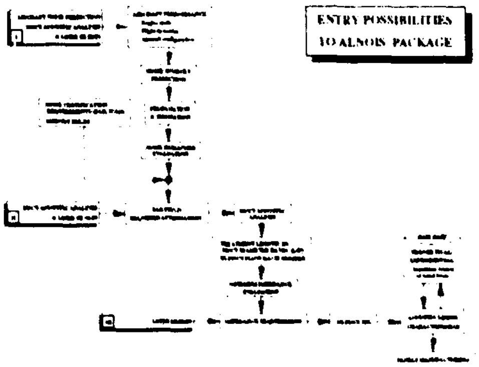

Figure 5.21 Possible entries to ALNOIS software package

9. CONCLUSIONS

The paper presented a general overview on aircraft noise emission problem and relevant requirements for noise certification

Particular emphasis has been given to those aircraft equipped with high by-pass ratio engines that, jointly with a proper nacelle acoustic design, strongly contributed to community noise abatement

General philosophy and methodology to be followed in engine nacelle acoustic treatment design, together with a general overview on conventional (locally reacting) and innovative (non locally reacting) liners, have been described

Finally a short description of Alenia Software Package (ALNOIS) capabilities for engine nacelle acoustic design and liners manufacturing support has been reported

REFERENCES

1 Anonymous, "ESDU Engineering Science Data Noise Sub-series", ESDU International

2 Heidman, M.F., "Interim Prediction Procedure for Fan and Compressor Source Noise", NASA TMX 71763, 1976 and 1979 update

3 Anonymous, "Gas Turbine Jet Exhaust Noise Prediction", SAE ARP 876 C

4 Zorumski, W.E., "Aircraft Noise Prediction Program (ANOPP) Theoretical Manual", NASA TM-83199

5 Waman, W. Bhat and Gallo-Rosso, D., "Effect of Forward Speed on Jet Wing/Flap Interaction Noise", AIAA Paper 75-477, 1975

6 Stone, J.R., "Interim Prediction Method for Jet Noise", NASA TMX-7168, 1974

7 Anonymous, "Gas Turbine Co-Axial Exhaust Flow Noise Prediction", SAE AIR 1905

8 Tam, C.K.W., "Broadband Shock-Associated Noise from Supersonic Jets in Flight", J. of Sound and Vibration, 151, pp 131-147, 1991

9 Tyler, J.M. and Sofrin, T.G., "Axial Flow Compressor Noise Studies", SAE Transaction 70:309, 1962

10 Smith, M.J.T., "Aircraft Noise", Cambridge, UK, Cambridge University Press, 1989

11 Broadbent, E.G., "Noise Shielding for Aircraft", Prog. Aerospace Sci., 17, pp 231-268, 1977

12 Amiet, R.K., "Correction of Fan Noise for Effects of Forward Flight", J. of Sound and Vibration, 89, pp 243-259, 1983

13 Morse, P.M. and Ingard, K.U., "Theoretical Acoustics", Mc Graw-Hill Book Company, 1968

14 Munjal, M.J., "Acoustics of Ducts and Mufflers", John Wiley & Sons, 1976

15 Rice, E.J., "Multimodal Far Field Acoustic Radiation Pattern Using Mode Cutoff Ratio", AIAA Journal, 16, pp 908-911, 1977

16 Eversman, W., "Effect of Boundary Layer on the Transmission and Attenuation of Sound in an Acoustically Treated Circular Duct", J. of Ac. Soc. of America, 49, pp 1372-1380, 1971

17 Rice, E.J., "Spinning Mode Sound Propagation in Ducts with Acoustic Treatment and Sheared Flow", AIAA Paper 75-519, 1975

18 Zorumski, W.E. and Tester, B.J., "Prediction of the Acoustic Impedance of Duct Liners", NASA TMX-73951, 1976

19 Melling, T.H., "The Acoustic Impedance of Perforates at Medium and High Sound Pressure Levels", J. of Sound and Vibration, 29, pp 1-65, 1973

20 Allard, J.F. and Champoux, Y., "New Empirical Equations for Sound Propagation in Rigid Frame Fibrous Materials", J. of Ac. Soc. of America, 91, pp 3346-3353, 1992

21 Armstrong, D.L., "Acoustic Grazing Flow Impedance Using Wave Guide Principles", NASA CR 120848, 1971

22 Hersh, A.S. and Rogers, T., "Fluid Mechanical Model of the Acoustic Impedance of Small Orifices", NASA CR-2682, 1976

23 Zandbergen, T. and Mathews, D.C., "The NLR/NGTE Joint Programme on the Measurement of Attenuation and Impedance in Acoustic Flow Duct Facilities", NLR TR 81012 U, 1981

24 Guzzo, R. and Dalle-Mura, L., "Preliminary Technical Specification for an Aeroacoustic Test Facility", 65NT 8206/93011, Alenia internal document

25 Rademaker, E.R., "Experimental Validation of a Liner-Duct Acoustic Model Including Flow", ASME 90-WA/NCA-2, 1990

IMPACT OF DYNAMIC LOADS ON PROPULSION INTEGRATION

J.M. Seiner
Fluid Mechanics and Acoustics Division
NASA Langley Research Center
Hampton, VA 23681 USA

SUMMARY

Aircraft dynamic loads produced by engine exhaust plumes are examined for a class of military fighter and bomber configurations in model and full scale. The configurations examined are associated with the USAF F-15 and B-1B aircraft, and the US F-18 HARV and ASTOVL programs. The experience gained as a result of these studies is used to formulate a level of understanding concerning this phenomena that could be useful at the preliminary stage of propulsion/airframe design.

1 INTRODUCTION

Prediction of dynamic loads for aircraft is very complex. In order to arrive at a conservative estimate for a particular structure's service life, one must often consider dynamic inputs from several sources that can couple and non-linearly interact with the structure. The most familiar of these dynamic inputs are those associated with turbulent boundary layer fluctuations, turbulent wake flow, flow over cavities, and vorticity shed from the aircraft forebody. One additional source for aircraft dynamic loads is associated with interaction of the structure with acoustic energy produced by the aircraft propulsion exhaust system.

These acoustic load sources, which are the subject of this paper, are generally overlooked in the aircraft design stage because, up to now, they were considered insignificant relative to the other source mechanisms. However, one can equally argue that insufficient information exists to clearly define this phenomenon to enable generation of an appropriate design procedure. The purpose of this paper is not to develop such a design procedure, but to show that dynamic loads induced by noise from the aircraft engines are important.

Over the last several years at NASA, we have been involved in the study of aircraft dynamic plume loads. Our efforts have been entirely devoted to the study of several different fighter and bomber aircraft, ranging from model to full scale. Our earliest studies involved the problem of fatigue failure of the engine nozzle outer divergent flap system on the F-15 fighter (Ref. 1) and the B-1B bomber aircraft (Ref. 2). The study in Ref. 1 also considered the sonic fatigue environment associated with the twin 2D-CD rectangular nozzles of the F-15 S/MTD (Short Take-off and Landing Maneuver Technology Demonstrator) aircraft. Other studies involved the investigation of dynamic vane loads associated with the vectoring flaps of the NASA F-18 HARV (High Alpha Research Vehicle) and dynamic loads on the fuselage and aerodynamic control surfaces associated with the take-off and cruise modes of the joint US/UK supersonic ASTOVL (Advanced Short Take-Off and Vertical Landing) aircraft. This paper attempts to provide a coordinated account of the key results of this research experience, and where possible, describe potential methods for reducing dynamic loads at the integration design stage.

The paper is organized as follows. A brief review is presented of supersonic plume acoustic sources to provide understanding of physical characteristics of the dynamic structure loads. This is followed by a discussion of the fatigue of outer divergent nozzle flaps, vectoring vanes, jet impingement loads, and cruise scrubbing loads. Finally, methods are discussed to enhance component service life through reduction of these loads.

2 SUPERSONIC PLUME ACOUSTIC SOURCES

A comprehensive review of supersonic jet noise source mechanisms is given in Refs. 3 and 4. Here, we will only highlight significant features of these sources to provide better understanding of role they play as potential mechanisms for the sonic fatigue loads. These noise sources are generically related to the divergence of the gradient of the turbulent Reynolds stress tensor. Large differences in sound amplitude occur depending on whether the sources are convected subsonically or supersonically and, in particular, if the turbulence is convected through shock waves in the plume. For purposes here, we shall simply be concerned with the directivity, amplitude, and spectral features of these noise sources.

2a MACH WAVE EMISSION

Of particular significance is turbulence that is convected at speeds supersonic relative to the sound speed of the surrounding air. Under these circumstances, intense noise is radiated into a narrow cone surrounding the jet axis. This noise is denoted, after Phillips (Ref. 5), as "eddy Mach wave emission", and is easily recorded by standard shadowgraph or schlieren methods. The half cone angle, θ, defines the region for Mach wave emission, and is determined from equation 1.

$$\theta = \cos^{-1}(1 / M_c) \qquad (1)$$

where the convective Mach number, M_c, for Kelvin Helmholtz Instability Waves (KHIW), Supersonic Instability Waves (SSIW), and Subsonic Instability Waves (SIW) is given by (see Oertel, Ref. 6),

$$\text{KHIW} \quad M_c = (V_j + c_j) / (c_j + c_a) \qquad (2)$$

$$\text{SISW} \quad M_c = V_j / (c_j + c_a) \qquad (3)$$

$$\text{SIW} \quad M_c = (V_j - c_j) / (c_j + c_a) \qquad (4)$$

where V_j and c_j are respectively the fully expanded jet exit velocity and sound speed. The surrounding air sound speed is represented by c_a. The convective Mach number for the KHIW, SSIW, and SIW can also be computed from solutions of the compressible Rayleigh equation.

Presented at a Symposium on 'Impact of Acoustic Loads on Aircraft Structures' held in Lillehammer, Norway, May 1994

Within the framework of the acoustic analogy approach, Ffowcs Williams and Maidanik (Ref. 8) theoretically predict that acoustic energy emitted by the Mach wave mechanism is proportional to M_c^3. This proportionality arises at supersonic convection speeds when individual quadrupole sources radiate as monopole sources. Under these circumstances, there is no net near field cancellation of sound, and the acoustic source efficiency is maximized. The Mach wave source mechanism produces acoustic energy between 0.1% (cold jets) and 1% (hot jets) of the jet mechanical energy. At angles beyond the Mach wave emission angle, the acoustic source efficiency drops to that associated with subsonically convected quadrupoles, which is in the order of 0.01% of the jet mechanical energy.

The data of Figure 1 illustrates the features discussed above for turbulent generated noise from jets operating fully pressure balanced (i.e. no plume shocks). Here the hot jet far field acoustic data reported earlier by Seiner et. al. (Ref. 9) is extrapolated to a path co-linear with the jet axis with a 2.5 jet diameter displacement. The exit design Mach number and diameter of the nozzle are respectively 2 and 9.144 cm. In this extrapolation, the jet sources are presumed to be located along the jet lip-line and at a distance of 5 jet exit diameters downstream. The acoustic levels along this co-linear path are given in terms of psi-rms for four jet exit total temperatures of 313, 755, 1114, and 1370°K.

Table I. Mach Emission Characteristics of KHIW for Mach 2 Jet.

T_o, °K	M_c	θ	X/D	Y/D
313	1.32	40.7	7.33	2.5
755	1.66	52.8	6.52	2.5
1114	1.80	56.2	6.34	2.5
1370	1.87	57.7	6.26	2.5

The data in Figure 1 clearly demonstrate the importance of the Mach wave emission mechanism. Pressure amplitudes near 0.6 psi-rms are achieved for an unheated (T_o = 313°K) Mach 2 jet and levels at 1.0 psi-rms are reached for extremely hot jets (T_o = 1370°K). For most fighter aircraft configurations this is of no consequence. However, the fuselage tail, horizontal and vertical stabilizer structures of bomber and ASTOVL configurations with supercritical engine nozzle pressure ratios need to be designed to handle these loads. The Y/D = 2.5 distance used in Figure 1 is typical of most bomber aircraft, and to halve these observed levels would require a doubling of the distance from the jet lip-line. Several of the supersonic ASTOVL designs have jet centerline to fuselage distances of one jet diameter. This places much of the aircraft tail in the hydrodynamic pressure field where dynamic load levels exceed 1 psi-rms. Many aircraft operate at military power settings that have jet total temperatures in the range 755 to 1114°K.

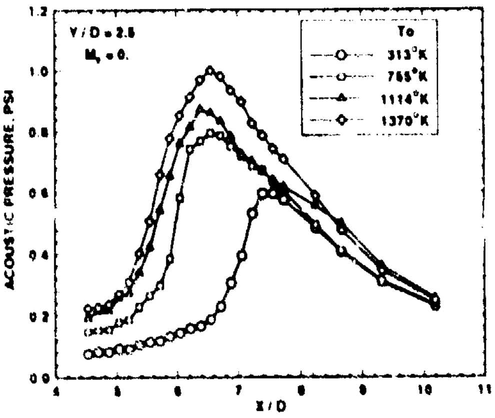

Figure 1 Near Field Acoustic Pressure Along Co-Linear Path to the Jet Axis

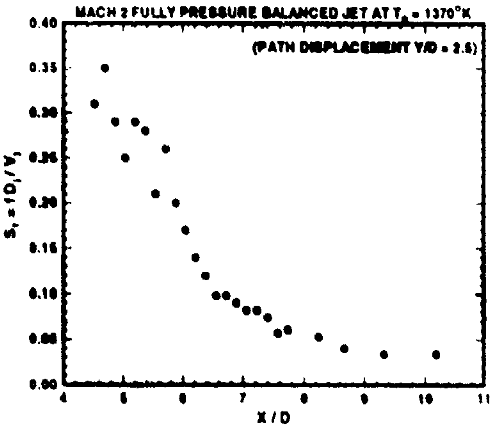

Figure 2 Strouhal frequency of peak acoustic energy along co-linear path to jet axis at Y/D = 2.5

The large increase in acoustic pressure beyond X/D ~ 5 can be attributed to Mach wave emission due to the KHIW. Table I lists the convective Mach number, Mach emission angle, and axial location of peak energy emitted along this ray path as predicted by equations 1 and 2 for the KHIW. Based on the analysis of Ref. 9, for the range of jet exit temperatures in figure 1, the SSIW emit only small amplitude waves and the SIW do not exist. A good comparison is exhibited between the predicted peak energy locations of the KHIW and those peak amplitude locations shown in Figure 1. The sound emitted at locations X/D < 5 is associated with turbulence being convected at subsonic speeds, that is M_c < 1 based on equations 1 through 3. Here the acoustic source radiates acoustic energy as a quadrupole source with much lower acoustic efficiency.

In addition to the dynamic load level, the structural design method requires consideration of the loads spectrum. The data in Figure 2 present the variation of Strouhal frequency, S_t, along the same co-linear path of Figure 1 for the jet exit temperature of 1370°K. The values for S_t are those associated with the peak spectral amplitude of the spectrum at each axial location. The Strouhal frequency is given by $S_t = fD/V_j$, where f, D, and V_j are respectively the frequency, jet exit diameter, and fully expanded jet velocity. Near X/D ~ 7, the value for S_t is 0.08, which would correspond in most full scale applications, to a frequency near 100 Hz. The location, X/D ~ 7, is representative of where maximum load levels are found for all jet temperatures investigated and shown in Figure 1.

2b SHOCK GENERATED NOISE

For those aircraft missions involving supercritical engine nozzle pressure ratios, it is extremely difficult to schedule engine nozzle geometry to achieve fully pressure balanced operation over its mission cycle. Additionally, nozzle geometry has yet to be developed that entirely eliminates internally generated shock waves, like that achieved using a geometry designed by the method of characteristics. Thus all supercritical engine operations always lead to the presence of shock waves in the jet plume. The presence of shock waves in an exhaust plume gives rise to an additional noise source.

When turbulence is convected through a shock wave its interaction increases the fluctuating energy in the vorticity, entropy, and sound modes. For purposes of this paper, it is the sound mode, termed shock noise, that is of interest. Shock noise consists of a broadband spectrum, termed broadband shock noise. This source noise component has an energy peak in the spectrum that is Doppler dependent. When the plume shock cell spacing is near an integer multiple of the wavelength for the most highly amplified fixed frequency wave of the jet shear layer, the shock waves will oscillate at that frequency producing what is termed jet screech. The screech mechanism requires feedback of acoustically generated noise to the nozzle exit to be properly maintained.

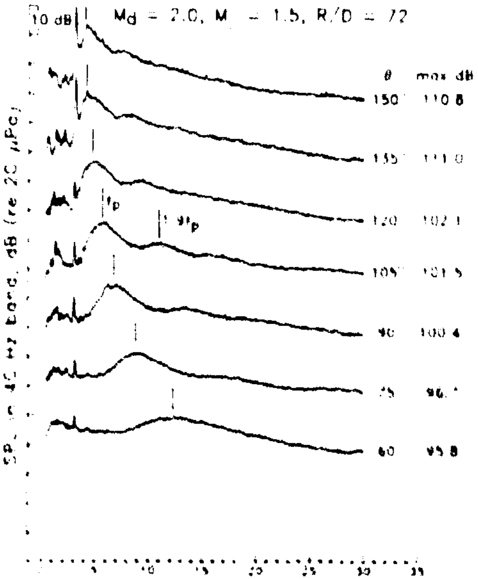

Figure 3 Example shock noise spectrum showing broadband and screech components

Figure 3 provides a typical example of the acoustic far field (R/D = 72) properties of both broadband shock noise and jet screech. This example pertains to the overexpanded operation of an unheated Mach 2 nozzle at a fully expanded jet Mach number of 1.5. The Doppler shift of the frequency, f_p, of the broadband spectral peak amplitude value is clearly observed. The screech frequency, shown as a narrow spike just below f_p at θ = 150°, is not Doppler shifted.

Prediction of the broadband shock noise source for simple jets has been achieved through both the analogy approach (Howe and Ffowcs Williams, Ref. 10) and the compressible Rayleigh model (Tam, Ref.11). The model of Tam has thus far achieved the most success when results are compared to measured data for hot jets in forward flight. Prediction of the amplitude of jet screech still remains a formidable challenge, since one needs to first resolve the initial jet shear layer's receptivity to acoustic forcing by the upstream generated noise produced in the jet screech cycle. The frequency of jet screech can be predicted from Powell's model (Ref. 12), or more appropriately, using the compressible Rayleigh model (Ref. 13).

Simple relations can be used to predict the frequency of jet screech and the frequency at which the broadband shock noise spectrum achieves maximum amplitude, and the energy produced by broadband shock noise. These relations are as follows,

Screech Frequency :

$$S_{ts} = f_s D_j/V_j = V_c D_j(1 - M_f)/(L V_j(1 + M_c - M_f)) \qquad (5)$$

Frequency for Broadband Peak Amplitude :

$$S_{tp} = f_p D_j/V_j = V_c D_j(1 - M_f)/(L V_j(1 - M_c\cos\theta - M_f)) \qquad (6)$$

Broadband Shock Noise Intensity

$$I\ (\text{watts/m}^2) = \varepsilon\beta^4(1 - \beta_d^2/\beta^2)^2 \approx \varepsilon(M_j^2 - M_d^2)^2 \qquad (7)$$

where in the above, D is the jet exit nozzle diameter, M_d is the nozzle design Mach number, M_j is the fully expanded jet Mach number, D_j is the fully expanded jet diameter (Ref 14), V_j is the fully expanded jet velocity, M_c is the convection velocity for the KHIW, V_c the convection velocity determined from $c_j M_c$ using equation 2, M_f the flight Mach number, θ is the emission angle from the jet axis, $\beta = (M_j^2 - 1)^{1/2}$, L is the plume shock spacing, and ε is a shock noise amplitude parameter given in Table II. Plume shock spacing can be computed using numerical simulations to obtain the effect of flight, as shown in Ref. 15, or from the empirical relationship derived from laboratory data for static round jets as given by,

$$L = aD(M_j^2 - 1)^{b} \qquad (8)$$

where the coefficients a, b, and ε are listed in Table II.

Table II Shock Noise Coefficients

M_d	ε	a	b
1.0	0.6	1.16	1.00
1.5	2.0	1.09	1.17
2.0	3.0	0.76	1.59

Equation 7 is only valid for jet plumes that contain weak oblique shocks. However, despite this, equation 7 predicts that sufficient shock noise energy is generated to be competitive with that associated with the eddy Mach wave mechanism. At θ = 60°, Figure 3 shows that both the broadband and jet screech components produce nearly equal sound levels to those generated by the jet noise component

The maximum sound pressure levels listed in Figure 3 show that the shock noise components radiate most of their energy upstream in the direction of the nozzle inlet. In this direction, shock noise totally dominates the jet noise components described in section 2a.

By way of illustration, Figure 4 shows the excess noise generated by screech and broadband shock noise for a series of nozzles. Here the measured sound pressure level, recorded at R/D = 80 and $\theta = 150°$, is plotted against the parameter $\beta = (M_j^2 - 1)^{1/2}$, which is related to the nozzle pressure ratio through M_j. These sound pressure levels are shown to vary significantly above those recorded for shock free nozzles. The solid line represents measured sound pressure levels for shock free jets. Point A represents the Mach 1.5 nozzle design point at $\beta = 1.1$. Point C represents peak shock noise for overexpanded operation of the $M_d = 1.5$ nozzles, and point B the peak shock noise for their corresponding underexpanded operation. The nozzle that appears to have the worst trend for high amplitude shock noise generation is the conical convergent-divergent (C-D) Mach 1.5 nozzle. There appears to be no operational point where shock noise is significantly reduced. Its model nozzle geometry is derived from that used on F-100 engines at cruise power setting for F-15 aircraft. Except for a few operational points near its design Mach number, the convergent nozzle appears to be more satisfactory than the conical C-D.

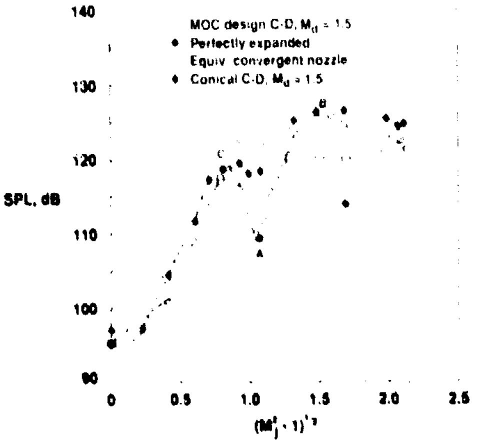

Figure 4 Shock noise amplitude behavior of convergent and convergent divergent nozzles

In the above discussion, we have reviewed from a generic point of view characteristics of both the jet and shock noise source components for supersonic jets. We will now begin to look at several of the aircraft cases that have had component fatigue failures to see what role acoustics has had in contributing to these failures.

3 ENGINE NOZZLE OUTER DIVERGENT FLAPS

Outer divergent flaps are used on all engine nozzles that operate with supercritical pressure ratios and have variable area geometry. They are used to avoid excessive nacelle afterbody drag penalties that would arise from massive flow separation over the engine nozzle cowl if they were removed. Two aircraft that have been plagued by failure of their engine nozzle outer divergent flap system are the F-15, powered by twin Pratt & Whitney F-100 engines, and the B-1B aircraft, powered by four General Electric F-101 engines in two twin nacelles. The F-15, which currently performs its mission without these flaps, experienced fatigue failure of its outer engine nozzle divergent flaps on early production aircraft delivered to the USAF. The B-1B aircraft experienced fatigue failure of the forward hinge mechanism that held the divergent flap in place at the trailing edge of the nozzle lip. However, for the B-1B, it was not possible to remove the divergent flaps, unless one was willing to reduce mission potential.

It is important to note that not all aircraft which use outer divergent flaps have had failures with their system. Notable examples of trouble free operation are provided by the F-14 and F-18 aircraft. These aircraft have wider engine centerline spacings. To understand the problem associated with the F-15 and B-1B, it is necessary to introduce two important phenomena that occur specifically in aircraft with twin engine nacelles, and with engine centerline spacings near 2 jet diameters in the cruise power setting.

The first phenomenon, termed twin supersonic plume resonance (Ref. 14), is associated with phased coupling of the turbulent large scale structure of each engine's exhaust plume. Under these circumstances, acoustic feedback associated with the jet screech cycle is increased producing substantially higher dynamic levels at the inter-nozzle exhaust plane. The second phenomenon is associated with the shedding and bursting of vorticity from aircraft forebody parts. Twin engine nacelles generate a region of low static pressure in the nacelle afterbody inter-nozzle region. This low static pressure provides a driving force for the convection of burst vorticity into the region of the nacelle afterbody. Each of these phenomena can be illustrated using model results.

3a TWIN JET PLUME RESONANCE

Figure 5a shows a phase averaged schlieren record of the twin plume exhaust from a F-15 model empennage. Both nozzles are convergent, and operating unheated at a nozzle pressure ratio of 2.85 (i.e. $M_j = 1.32$). The centerline spacing of each plume is 1.9 nozzle diameters. The schlieren record is created by phased firing of a high frequency spark source at a fixed point in the jet screech cycle. From this photograph, one can easily determine that the entire flow structure from each plume is coupled by large scale helical plume structures. Intense noise is seen to emerge from each plume in a region 4 to 5 shock cells downstream of the nozzle exit. The radiated jet screech component then propagates toward the nozzle afterbody. Based on results of the study conducted in Ref. 14, the amplitude of the waves in the inter nozzle region of the afterbody, is 5 times greater than that associated with operation of a single nozzle. It is this region where most frequent failures occurred on the F-15 and B-1B aircraft.

The reduction of twin plume resonance can easily be accomplished by use of devices that destroy symmetry of the jet screech cycle. Introduction of flow disturbances at the nozzle exit can often be used to destroy the growth of organized structure. In this case, it is important that the introduction of the disturbance be applied to one nozzle. Figure 5b shows the resulting twin jet plume structure when

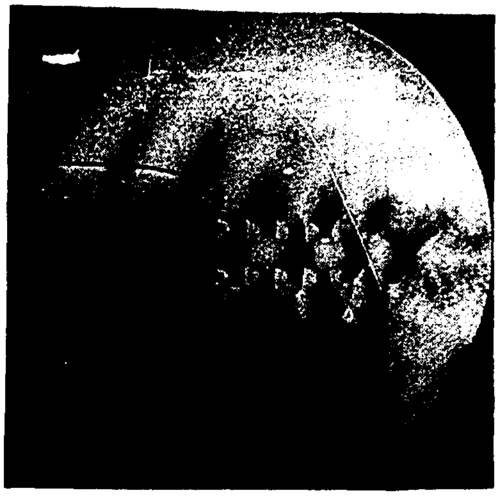

a. phase averaged schlieren of unsuppressed mode

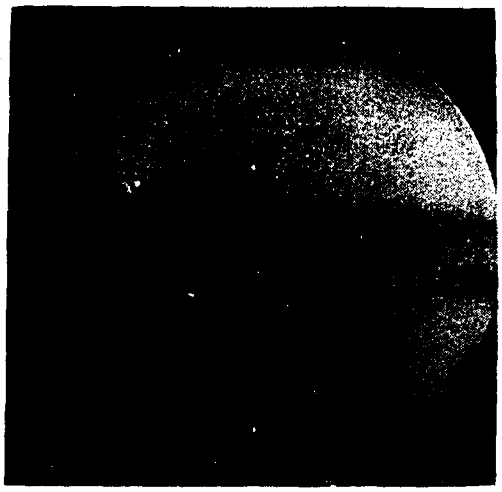

b. phase averaged schlieren of suppressed mode

Figure 5. Illustration of twin jet plume resonance and method for reduction.

a single tab-like device is applied to the upper nozzle. It is clear from this schlieren record that the flow structure of each plume is uncoupled and that the shock cell length of the affected plume is shorter than the undisturbed plume. Under these circumstances, no organized feedback can take place in the jet screech cycle.

Figure 6 shows the resulting reduction of amplitude of the jet screech component in the nacelle afterbody inter-nozzle region when the twin jets are operated unsuppressed and with a tab in one nozzle. The dynamic pressures were obtained over a very wide range of fully expanded jet Mach numbers. Levels approaching 0.4 psi-rms at M_j = 1.3 are observed for the unsuppressed screech mode. This level is well above the 0.16 psi-rms value, where Ref. 16 reported significant sonic fatigue and crack growth problems on the F-15 fuselage, vertical and horizontal stabilizer components. This reference level for fatigue is shown in Figure 6 by the dashed line. Application of the tab to one nozzle reduces the amplitude of screech to less than 0.1 psi-rms. The azimuthal location of the single tab is unimportant.

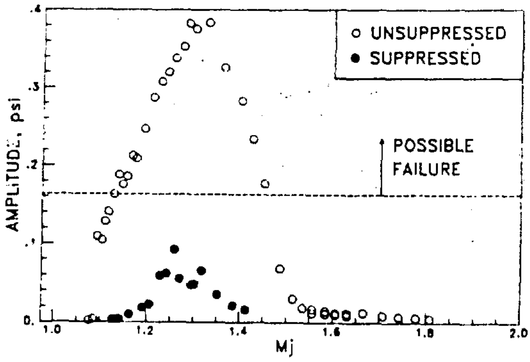

Figure 6. Magnitude of inter-nozzle dynamic pressures in unsuppressed and suppressed modes.

3b SWEPT FOREBODY SEPARATED FLOW

To enable study of the second phenomenon associated with twin engine nacelles, a flow visualization study was conducted on a 1/72 scale full span model of the B-1B aircraft. The right hand twin engine nacelle was constructed with flow through inlets and exhaust nozzles. Flow through this powered nacelle was adjusted to correspond to a jet to free-stream velocity ratio of 2.07. Dye tracers were injected at the aircraft nose and at locations just upstream of the nozzles on the over-the-wing fairing. The sweepback angle of the wing was fixed at 67.5° and photographs of the dye streaks were acquired with aircraft angles of attack of α = 0° and 2°.

Figure 7 shows the flow visualization results. The dye tracer released at the nose of the model aircraft indicates smooth, undisturbed flow to a region near the leading edge of the wing body junction. At this point, a vortex rolls up, bursts mid-chord, and is convected into the inter-nozzle region of the twin engine nacelle afterbody. When the dye tracer is released at points on the over-the-wing fairing the flow is again seen to be swept into the same inter-nozzle region.

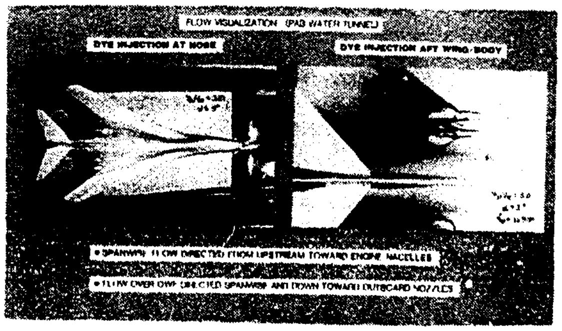
FLOW VISUALIZATION (PAD WATER TUNNEL)
DYE INJECTION AT NOSE
DYE INJECTION AFT WING/BODY
• SPANWISE FLOW DIRECTED FROM UPSTREAM TOWARD ENGINE NACELLES
• FLOW OVER OWF DIRECTED SPANWISE AND DOWN TOWARD OUTBOARD NOZZLES

Figure 7. Flow visualization of 1/72 scale B-1B full span model with flow through inlet and exhaust.

In order to attain an understanding of how each of these phenomena contributed to the dynamic fatigue failure of the engine nozzle outer divergent flaps on the F-15 and B-1B aircraft, we shall have to look at results obtained with full span wind tunnel tests and full scale flight experiments.

3c F-15 FULL SCALE STUDIES

Full scale studies were conducted at the NASA Dryden Flight Research Center using their F-15 research aircraft. This aircraft was still equipped with engine nozzle outer divergent flaps. These flaps, as indicated in Figure 8, were instrumented with static and dynamic pressure sensors, thermocouples, accelerometers and strain gages. The aircraft was flown throughout its entire flight envelope including supersonic dash at altitudes from 1.5 km to 13.7 km and at all engine power settings including one engine at idle. Representative results from this study are shown in figures 9, 10, and 11.

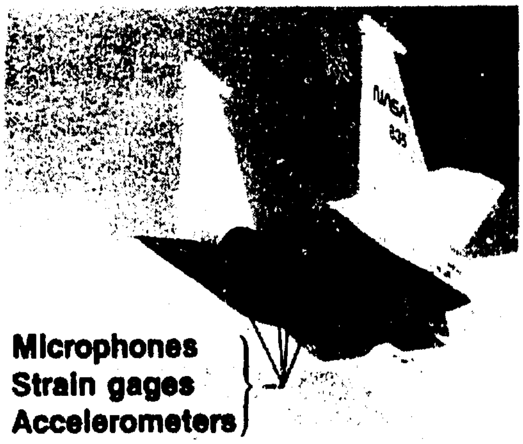

Figure 8. Ames-Dryden F-15 flight test vehicle.

Figure 9 shows the measured dynamic pressure spectrum in psi-rms for the divergent outer D-flap on the left-hand engine. The sensor is mounted in the central section of this flap. The D-flap is one that is located in the inter-nozzle region of the afterbody nacelle, where we expect the highest dynamic loads to be found based on field reports of fatigue failure. Both F-100 engines are operating at military power with an aircraft angle of attack, $\alpha = 0°$, flight Mach number of $M_f = 0.723$, and altitude of 4.72 km. The predicted screech frequency, f_s, for these engine power settings and aircraft speed is 63 Hz., as indicated in Figure 9. This frequency is computed using equation 5. From equation 6, the predicted peak amplitude frequency for broadband shock noise, f_p, is near 70 Hz. As can be seen, there are peaks in the spectrum near these frequencies. The discrete tone at 400 Hz. is aircraft power line frequency. The frequencies between 60 and 90 Hz. contain most of the energy in this loads spectrum.

The magnitude of the spectral components for full scale, however, fall far below the levels recorded in the small model study shown previously in Figure 6. The spectrum peak amplitude level of 0.008 psi-rms lies 20 times below the reference level of Ref. 16 for sonic fatigue failure. It should be noted, however, that amplitude level by itself is not a definitive parameter, for sonic fatigue. One generally needs to consider a structures response to the applied dynamic load. To do this consider for the same flight conditions of Figure 9 the following acceleration and strain spectrum in Figure 10.

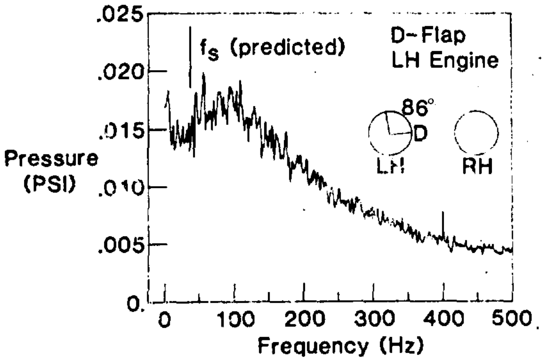

Figure 9. F-15 full scale aircraft outer flap dynamic loads spectrum.

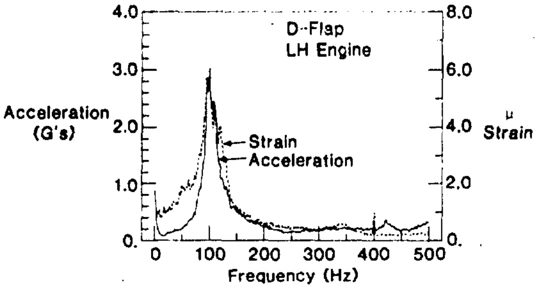

Figure 10. F-15 full scale acceleration and strain spectrum.

Here the accelerometer is located on the D-flap in the same vicinity of the dynamic pressure transducer. The strain gage is located near the trailing edge of the D-flap, where most fatigue failures were reported. Both the acceleration and strain spectrum show a high amplitude narrow band content centered near 100 Hz. In laboratory testing of the titanium outer flap, Pratt & Whitney determined a fundamental flap resonance frequency of 104 Hz. Thus the measured response of the flight hardware lies close to that determined in earlier studies at Pratt & Whitney. We see from these spectra that the excitation loads spectrum lies close to the natural response of the outer divergent structure under flight conditions.

In Figure 11 it is shown, that a good correlation exists between the applied dynamic pressure load and the flap's response to this load.

Based on data similar to that in Figures 9, 10, and 11, for other flight conditions and engine power settings, it is possible to estimate the time to failure of the F-15 aircraft's outer divergent flaps. The number of cycles to failure can be estimated from equation 9 as follows,

$$N\ (\text{cycles}) = (\sigma_u / \sigma)^m = (\sigma_o / E\varepsilon)^m \tag{9}$$

where for a titanium panel, $\sigma_o = 3.3*10^5$ psi, $E = 15.5*10^6$ psi, $m = 5$, and ε is the strain. The data from the flight

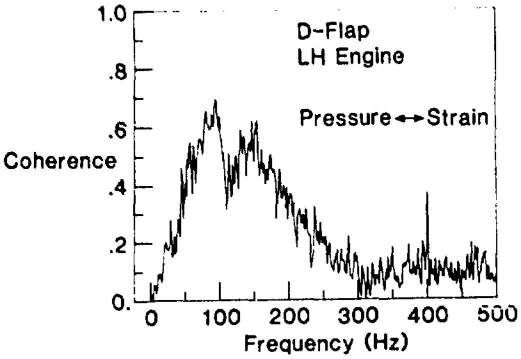

Figure 11. F-15 full scale coherence between applied dynamic load and flap strain field.

study produced the following correlation of strain with aircraft dynamic pressure, Q, as follows,

$$\begin{aligned} \varepsilon \text{ (strain)} &\approx 3.9 * 10^{3} \text{ P (psi)} \\ \text{P (psi)} &\approx 2.6 * 10^{4} \text{ Q (psf)} \end{aligned} \tag{10}$$

Substitution of the correlations in equation 10 into 9 produces the following estimate for time to failure,

$$\text{T (Hrs.)} \approx (f_o N / 3600) = (f_o / 3600)(Q_o / Q) \tag{11}$$

where the reference aircraft dynamic pressure, Q_o, is 21,200 psf and the fundamental flap resonance frequency, f_o, is 104 Hz. The estimated time to failure of the F-15 aircraft engine nozzle outer divergent flaps is plotted in Figure 12 from calculations based on equation 11. Field reports on flap failures usually followed after use of the engine afterburner and often with as little as 15 hours of flight time. Most afterburner applications involve aircraft operation where Q is in the order of 800 psf. From the time to failure curve in Figure 12, we see the prediction for flap failure is in line with field experience.

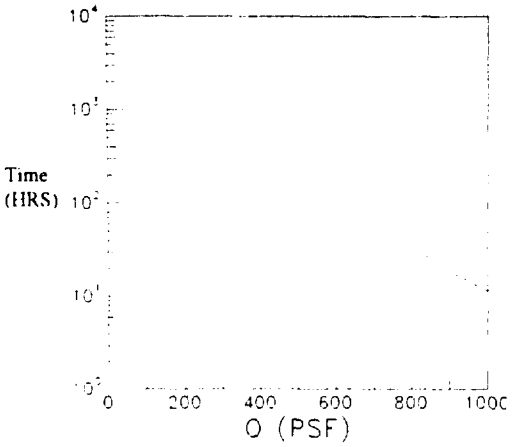

Figure 12. Estimated time to failure of F-15 aircraft engine nozzle outer divergent flaps.

3d F-15 WIND TUNNEL TESTING

A study involving acquisition of dynamic loads data on an 8.33% full span model of the F-15 and F-15 S/MTD was conducted in the NASA Langley 16 Ft. Transonic Wind Tunnel. The full span models are shown in figures 13a and 13b. The objectives of this study were to determine if testing in a wind tunnel would produce similar results to the F-15 flight test program and to determine whether the F-15 S/MTD research airplane with its 2D-CD nozzles would face potential fatigue problems like those that plagued the F-15 airplane.

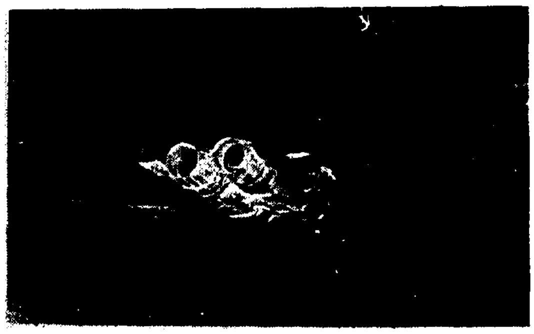

a. 8.33% F-15 model with axisymmetric nozzles.

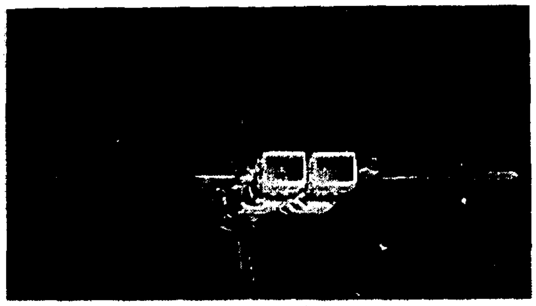

b. 8.33% F-15 S/MTD model with 2D-CD nozzles.

Figure 13. Full span model testing in Langley 16 Ft. tunnel.

Figure 14 presents a summary of the dynamic loads recorded in both wind tunnel and flight tests. These loads are correlated with the aircraft dynamic pressure, Q. All results pertain to operation of both nozzles at a pressure ratio of 3.89. Transducer 72 is positioned at the D-flap location in both the flight and wind tunnel experiments. Transducer 75 is located on the model in the L-flap location of full scale, which corresponds to an outboard location on the left-hand engine 180° from the D-flap sensor.

Both the wind tunnel and flight experiments produce nearly equivalent dynamic load levels at the D-flap location. This gives a good indication that wind tunnel testing can provide adequate representation of the loads environment associated with the afterbody nacelle in twin engine configurations. The full span model results also indicate that outboard flap locations have remarkably lower dynamic load amplitudes. This is consistent with the model scale studies of Ref. 14. In that study, inter-nozzle dynamic pressures were found to be 5 times greater than those recorded at outboard locations.

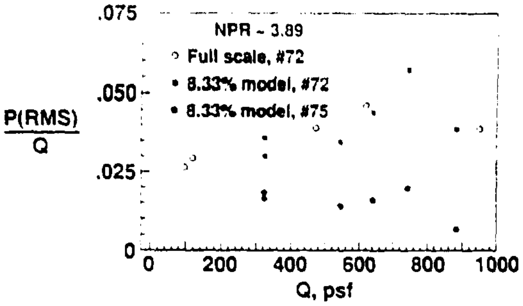

Figure 14. Model and full scale dynamic loads scaling with aircraft dynamic pressure.

In a similar fashion to the data presented in Figure 14, Figure 15 shows results obtained with the F-15 S/MTD model. Here, it can be observed that the dynamic loads on the divergent outer flap and in-board sidewall are considerably lower than those obtained with the F-15 axisymmetric nozzles. This observation has yet to be confirmed from flight test data.

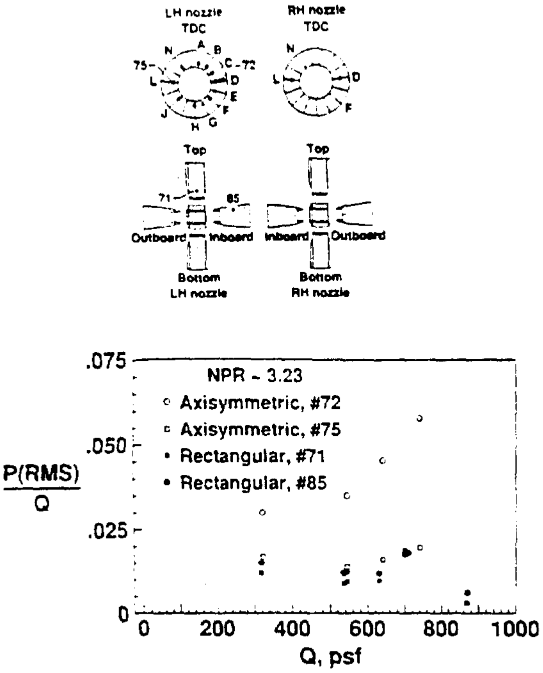

Figure 15. Comparison of dynamic load amplitudes between axisymmetric and 2D-CD nozzles.

3C B-1B FULL AND MODEL SCALE RESULTS

The B-1B research aircraft represents a more complex challenge than the F-15 aircraft. In the B-1B aircraft, both the twin jet plume resonance and separated flow mechanisms compete in different parts of the flight mission to define the dynamic loads spectrum.

Figure 16 shows a typical loads spectrum acquired from the B-1B flight test program. The spectrum is from a sensor located in the inter-nozzle region near the trailing edge of the left-hand engine outer divergent flap. For this flight condition, $M_f = 0.85$, and engine power setting, equation 5 predicts a jet plume screech frequency, f_s, of 31 Hz, and equation 6 a broadband spectral peak amplitude at a frequency $f_p = 70$ Hz. As can be seen, these predicted frequencies agree well with the spectral peaks in the flight spectrum. Wind tunnel tests with a 6% full span model in the Langley 16 Ft. tunnel, shown in Figure 17, provide a different interpretation of the flight test spectrum of Figure 16.

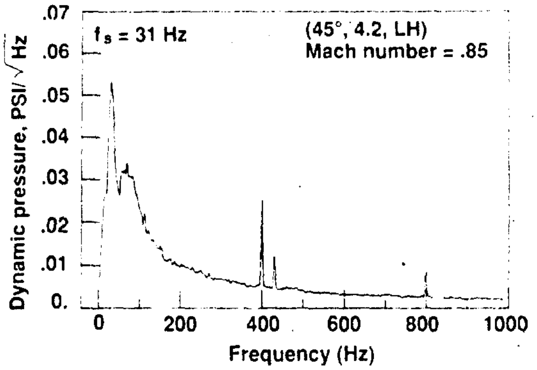

Figure 16. Typical engine outer divergent flap dynamic loads spectrum from B-1B flight test program (from Ref. 2).

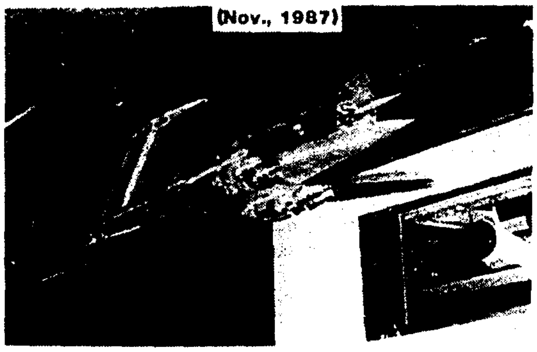

Figure 17. B-1B 6% full span model in 16 ft. tunnel.

To see this, consider the sample dynamic loads spectrum of figure 18, which is derived from the wind tunnel model tests. In this spectrum, contributions from both the separated flow and twin jet plume resonance phenomena are identified. At the relatively low speed of the simulated forward flight Mach number of 0.2, both mechanisms produce well defined spectral peaks at different locations in the spectrum. As the forward flight speed increases, the separated flow mechanism produces a spectral peak amplitude frequency that shifts to higher values due to the increased convection velocity. The opposite trend applies to the twin jet resonance phenomenon, where the spacing of plume shocks is increased due to forward speed effects and screech and broadband shock noise frequencies decrease as is predicted by equations 5 and 6. At a flight Mach number of 0.85, both mechanisms have spectral peak amplitudes near the same value of frequency. In the flight case spectrum, both mechanisms produce spectral peak amplitudes near 30 Hz.

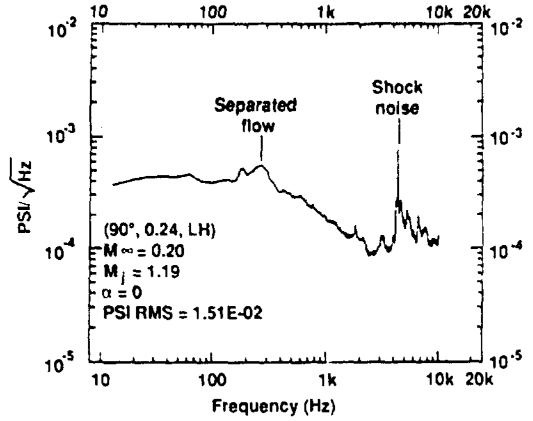

Figure 18. Characteristic spectrum showing competing mechanisms.

To further confirm this observation, Figure 19 shows a plot of the spectral peak amplitudes associated with each phenomenon as a function of the wind tunnel Mach number. The nozzle pressure ratio is held constant with a value of 2.4 for this comparison. Here it is observed that dynamic pressures due to twin jet resonance diminish with wind tunnel Mach number, while those due to separated flow increase. The two mechanisms have equal dynamic pressures at $M_f = 0.5$. The wind tunnel data suggest that the spectral peak amplitude near 30 Hz. in the B-1B flight spectrum at $M_f = 0.85$ is most likely produced by the separated flow phenomenon. This phenomenon is illustrated by the dye streaks of the flow visualization study shown in Figure 7. A similar flow visualization study by Lorincz (Ref. 17), using a full span model F-15, revealed that separated flow from the aircraft forebody was not convected into the engine nacelle afterbody region. It is important, of course, that this issue be resolved, since very different methods would be required to reduce dynamic loads for each mechanism.

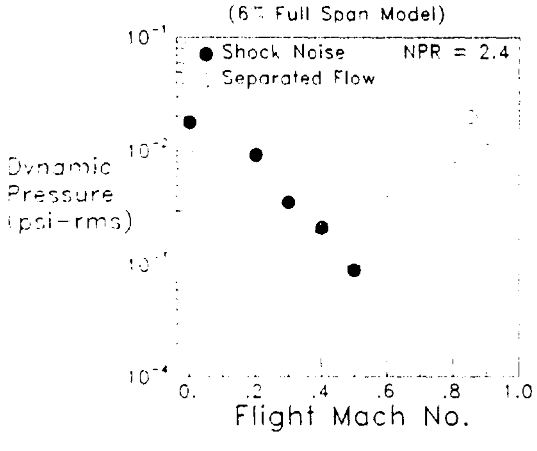

Figure 19. Dependence of flight on peak dynamic pressure amplitudes.

One final point needs to be made regarding the external engine outer divergent flap. This is the question regarding the value of retaining such a device for production aircraft and incurring the expense of costly maintenance, or removing the flaps and incurring a performance penalty which could effect the aircraft mission profile.

In the wind tunnel study, a test was conducted to address this issue. A three component shell balance was placed in the left-hand nacelle. The external flap contour was removed from an additional set of dry powered nozzles, as shown in Figure 20. As shown in Figure 21, a difference of six drag counts is representative of the average difference in nacelle C_d over the Mach number range investigated. The nacelle afterbody drag increases sharply beyond $M_f = 0.85$ even for the nozzles with outer divergent flaps due to massive separation of flow induced by a shock on the nozzle afterbody. The variation of afterbody drag was found to depend only slightly on aircraft angle of attack.

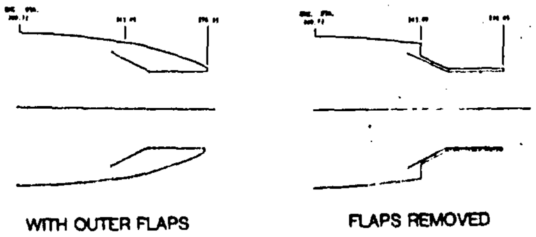

Figure 20. Dry powered nozzles with and without external flaps.

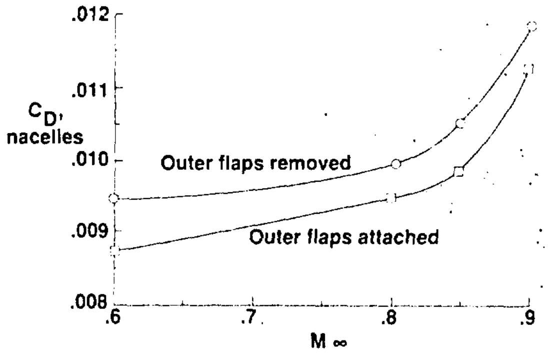

Figure 21. Performance penalty associated with removal of outer flaps on B-1B (Ref. 2).

4. F-18 HARV AEROACOUSTICS

A study was conducted using a 7% scale nozzle afterbody of the NASA F-18 High Alpha Research Vehicle (HARV) to assess the dynamic pressure loads on vectoring vanes deployed into the nozzle engine exhaust to achieve full vector authority. The model, with vectoring vanes, is shown in Figure 22. One additional major concern of this program was related to excessive noise levels recorded in the inter-nozzle region of the HARV aircraft after removal of the divergent nozzle section from each nozzle of the twin F-404 engines. Dynamic pressure levels increased by a factor of 3, which could entirely be attributed to shock noise, for the test were conducted statically. Figure 23 shows a comparison of the measured inter-nozzle sound pressure levels between the baseline convergent-divergent nozzles and the resulting convergent nozzles at the military power setting.

These measured inter-nozzle dynamic pressures fall below the reference criteria of Ref. 16 (i.e. 0.16 psi-rms = 155 dB SPL), but were sufficient to cause fatigue of engine nozzle attachment components. The component failures occurred within one hour of test time. The model scale vane loads were found to be substantially higher, as expected, than those in the inter-nozzle region. This is shown in Figure 24, for an aircraft vector angle of -20°.

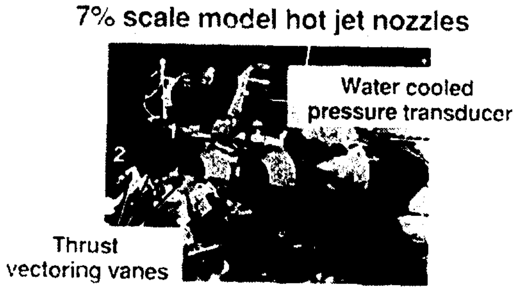
7% scale model hot jet nozzles
Water cooled pressure transducer
1
2
Thrust vectoring vanes

Figure 22. HARV 7% scale model nozzle afterbody.

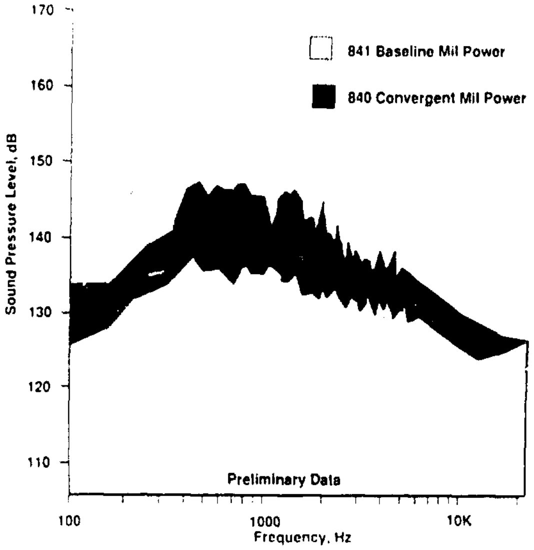

Figure 23. F-18 HARV aircraft inter-nozzle spectra.

Over a very wide range of nozzle pressure ratios, the measured pressure amplitude exceeds 1 psi-rms for those vanes deployed into the exhaust plume. The retracted vanes, at -10°, experienced pressure amplitudes approaching 0.5 psi-rms. This amplitude is substantially higher than those recorded for the B-1B and F-15 aircraft, as indicated on Figure 25, and certainly higher than could be expected from either shock noise or eddy Mach wave sources. Evidently, the flow impingement noise associated with the vectoring vanes substantially increases the dynamic pressure amplitudes on non-vectoring vanes.

The NASA F-18 HARV program proved successful from the perspective that the aircraft met all aerodynamic performance goals and experienced no component failures. The vectoring vanes, which were designed to handle the dynamic loads from the model scale tests, experienced no fatigue over the duration of the test flight program.

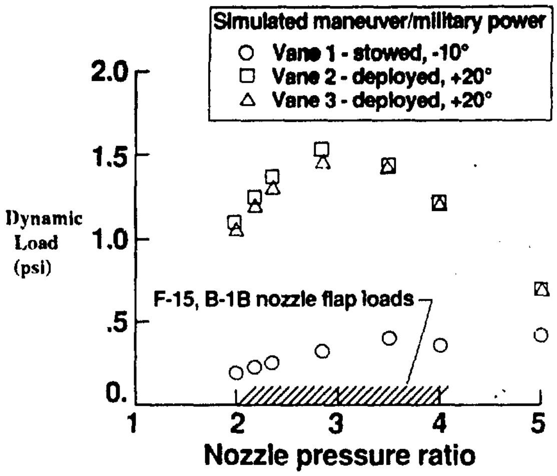

Figure 24. Dynamic pressure loads on thrust vectoring vanes of HARV 7% model.

5. SUPERSONIC ASTOVL

The joint US/UK supersonic ASTOVL program produced aircraft designs that were most challenging from a structural design viewpoint. Its predecessor, the subsonic MCAIR AV-8B, had always recorded high amplitude dynamic loads in both the take-off, hover, and cruise modes of its mission. Figures 25 and 26, from Ref. 18, respectively provide an example of typical measured surface dynamic pressures levels in SPL for both take-off and cruise modes. Levels as high as 153 dB were recorded for take-off and as high as 167 dB for cruise. Component failures were reported in the vicinity of the 167 dB SPL.

The potential upgrade of the AV-8B, to include supersonic dash capabilities in its mission profile, raised concerns that the potentially higher levels expected from both Mach wave radiation and shock noise sources would severely compromise the durability and reliability of numerous aircraft structural components. We shall briefly consider, from model scale studies with supercritical nozzle pressure ratios, the noise environment associated with both the take-off and cruise modes.

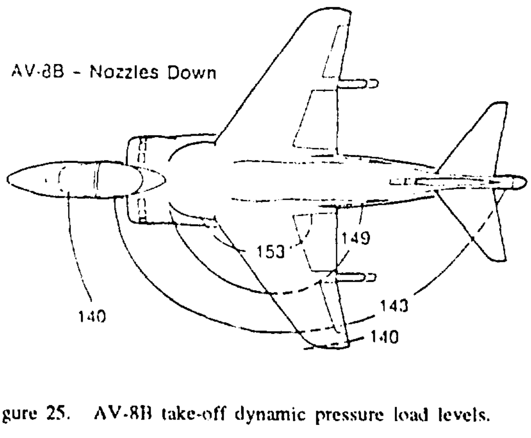

Figure 25. AV-8B take-off dynamic pressure load levels.

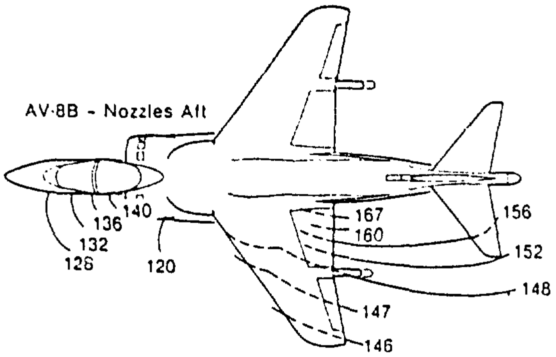

Figure 26. AV-8B cruise dynamic pressure load levels.

5a ASTOVL TAKE-OFF MODE

To achieve stability, the supersonic ASTOVL configurations generally involve a cluster of four engine exhausts in the take-off mode. Two main twin engine exhausts are deflected to the ground plane near the aircraft C_g. Two other twin exhausts, driven off of fan by-pass air, are directed to the ground from the vicinity of the swept wing leading edge. Early studies at NASA (Refs. 19 and 20) and McDonnell Douglas (Refs. 21 and 22) concentrated on the physical mechanics associated with the ground impingement of the twin main engine exhausts. Two concerns existed with regarding dynamic loads. The first was the unknown aerothermal dynamic loads on the fuselage in the vicinity of the twin jet fountain upwash described in Ref 21. The second concern was excessive loads on aerodynamic control surfaces, such as the wings and canards.

Norum's experiments (Ref. 19) show that the impingement loads from the ground impingement of a single rectangular nozzle consists of tones and broadband noise components associated with jet plume interaction on the ground plane and jet shock noise processes. The impingement tone frequencies, f_n, were found to satisfy the loop equation for feedback developed by Neuwerth (Ref. 23), which is,

$$f_n = n/[L^*(c_i + c_a) / c_i^* c_a] \qquad n= 1,2,3... \qquad (12)$$

where L is the distance of the nozzle exit to the ground plane, c_i is the phase velocity of convecting large scale flow instabilities, and c_a is the ambient sound speed. The impingement noise in Norum's experiment was found to achieve maximum amplitude in the range of $3 \leq L/D \leq 10$. Beyond L/D = 10, jet screech and broadband shock noise processes dominated the loads spectrum.

A comprehensive study was conducted in the NASA Lewis 9 X 15 Ft. low speed wind tunnel using a 9.2% powered full span advanced STOVL model (Ref. 24). Figure 27 shows the model mounted in the wind tunnel. The objectives of this study were to assess hot gas ingestion into the inlet and dynamic pressure loads on aerodynamic control surfaces and the fuselage. The model utilized twin splayed rectangular convergent nozzles for the main engine exhaust, as shown in Figure 27. Representative results from this study are shown in Figures 28 and 29.

Figure 28 shows measured dynamic loads spectra associated with a sensor located at a mid-canard on the lower surface.

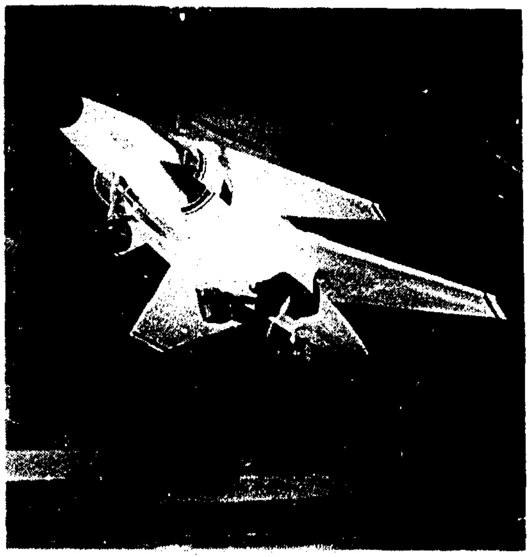

Figure 27. ASTOVL 9.2% model in NASA Lewis 9X15 Wind Tunnel. (from Ref. 24)

The simulation was conducted with a forward wind speed of 11.3 m/sec. and at nozzle pressure ratios of 1.7 and 3.1. The dynamic load level, in OASPL dB, for the three jet total temperatures of 260, 400, and 538°C is shown in the figure for a range of model aircraft heights from 0 to 30.48 cm. The model aircraft height is the distance of the landing gear from the ground plane. The model height is adjusted from 0 to 24 equivalent nozzle diameters. At the lower altitudes, the jet impingement noise, which consists mainly of tones, dominates the overall dynamic loads amplitude. This peak amplitude occurs near 2 equivalent nozzle exit heights, is invariant to jet total temperature but substantially higher in the supersonic mode (i.e. NPR = 3.1). At higher altitudes, the dynamic loads are dominated by jet shock noise, which is dependent on jet total temperature. For subsonic operation, like that of the AV-8B, the maximum dynamic load levels are controlled by the jet impingement process at low aircraft altitudes and both mechanisms at higher altitudes for more typical engine exhaust temperatures. At supercritical pressure ratios, the maximum dynamic load levels are controlled by the shock noise process, particularly at high jet total temperatures. The peak dynamic load level of 155 dB in hover with supercritical nozzle pressure ratio represents a particularly difficult challenge because it involves a control surface.

Similar results, for the sensor located on the mid-wing lower surface, are shown in Figure 29. Here, dynamic load levels are higher for both nozzle subcritical and supercritical operation. The wing sensor is located closer to the nozzle exit plane than the canard sensor. For both nozzle modes of operation and all jet temperatures, the peak dynamic load level is dominated by the jet impingement process, which occurs at the same altitude of 2 equivalent nozzle diameters. The peak dynamic load level is near 160 dB SPL. Ref. 24 reports that levels on components impacted by the jet fountain upwash were near 175 dB in the worst case.

The data reported in Ref. 24 is of real concern because the dynamic load levels are significantly higher than those

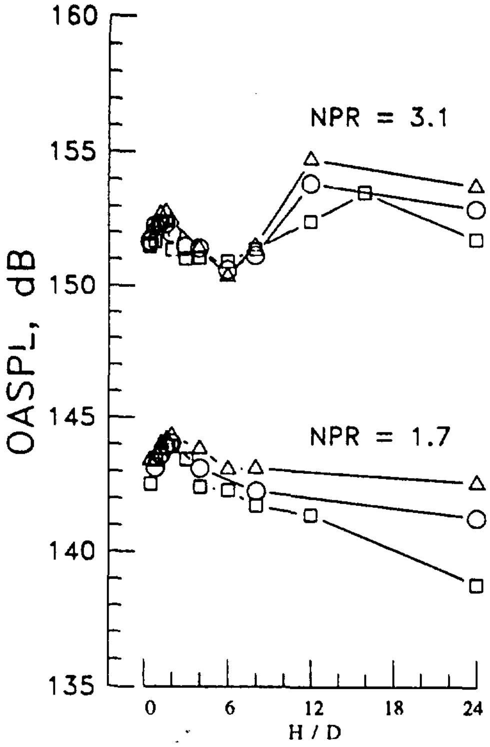

Figure 28. Dynamic pressure loads on Canard.

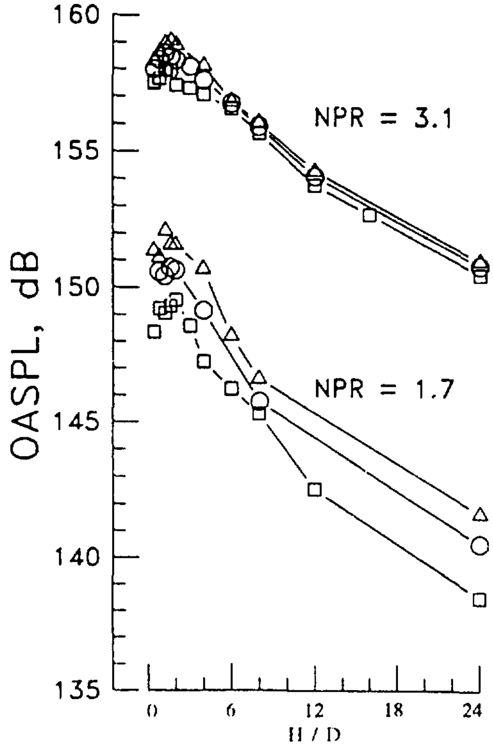

Figure 29. Dynamic loads on wing surface.

discussed for the F-15 and B-1B aircraft. Further methods can be applied to reduce these loads other than the use of rectangular nozzles, like those used in the studies of Refs. 19, 20, and 24. The use of a low speed co-flowing airstream would help considerably to interrupt the feedback path and reduce both the jet impingement and shock noise process.

Numerical simulations of the jet impingement problem have been undertaken in Refs. 24 and 25. The study in Ref. 25 has the long term goal of eventually simulating methods associated with the reduction of the dynamic loads.

5b ASTOVL CRUISE LOADS

In addition to high dynamic load levels in the take-off and hover modes, the cruise mode also represents a very serious aerothermal load problem. In this mode, the supersonic hot jet exhaust is positioned very near the fuselage at the wing trailing edge. Often the nozzle exit centerline to fuselage separation is within one nozzle height for rectangular nozzles. Figure 30 shows a schlieren image obtained with such a configuration. Here, the rectangular nozzle was designed with a 2 to 1 throat aspect and was operated unheated and fully pressure balanced at $M_j = 1.35$. From this photographic record it is easy to observe a Coanda effect, where the nozzle plume can be seen being sucked toward the fuselage side of the plume. This causes premature scrubbing of the jet plume with the wall, which leads to fuselage surfaces exposed to higher aerothermal loads. A corresponding dynamic loads spectrum for the flow conditions of the Figure 30 schlieren record is shown in Figure 31. The wall mounted surface sensor is located spanwise from the jet centerline at X/H = 0.873, where H is the nozzle height and downstream a distance Z/H = 5.183. This location places the wall sensor just upstream of the region where the flow impacts the wall. A screech frequency of 5370 Hz. was calculated using equation 5 and appears to agree well with the measured results. The amplitude of the screech component is very near 174 dB SPL. Based on the results presented in Figure 1, had this jet been heated to representative engine cycle conditions, the dynamic levels would be much higher across the spectrum, particularly at locations downstream of where the jet plume scrubs the wall. The levels in Figure 31 for the unheated

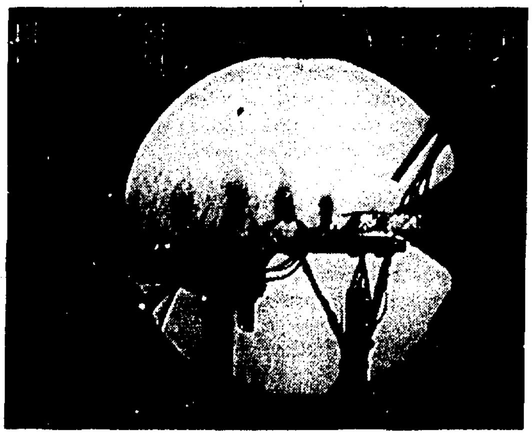

Figure 30. Schlieren image of supersonic jet plume scrubbing in ASTOVL cruise mode.

jet, by themselves, raise serious concerns regarding reliability and durability of many large fuselage components that would be impacted by the plume.

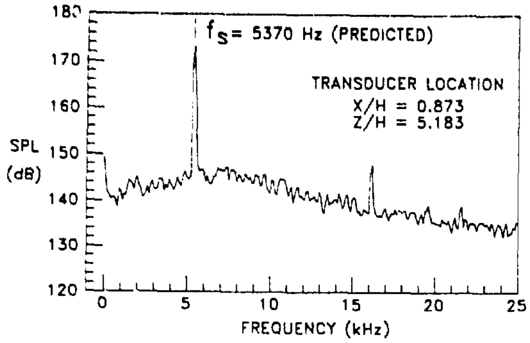

Figure 31. Dynamic loads in cruise mode from model scale ASTOVL studies.

6. DISCUSSION AND CONCLUSIONS

In this paper the sonic fatigue environment has been examined for structural fatigue concerns associated with the engine nozzle outer divergent flaps of the F-15, F-15 S/MTD and B-1B aircraft, thrust vectoring vane loads on the F-18 HARV aircraft, and take-off and cruise dynamic loads for ASTOVL aircraft. A brief review of principle supersonic jet noise sources was conducted to introduce these mechanisms as additional contributors to structural component failure. The principle sources were eddy Mach wave radiation and shock noise, both broadband and screech. In almost all cases examined, the shock noise source played a prominent role in defining the dynamic loads spectrum. But often competing mechanisms were found to dominate in different regions of the aircraft mission profile.

For the engine nozzle outer divergent flaps, twin jet plume resonance (i.e. jet screech) dominated the loads spectrum at low flight Mach numbers for the B-1B, but the convection of forebody separated flow into the twin engine nacelle afterbody dominated the loads spectrum at higher flight Mach numbers. The problem was found configuration dependent, in that the swept forebody vortex never entered the nacelle afterbody of the F-15 aircraft based on flow visualization experiments at model scale. The thrust vectoring vanes of the F-18 HARV experienced the highest dynamic load levels of all configurations examined, amplitudes were found to exceed 1.5 psi-rms with a 20° thrust vector. The non-vectoring vanes were found to be exposed to levels in excess of either shock or eddy Mach wave sources. The most probable cause for this was attributed to impingement noise from the thrust vectoring vanes. The supersonic STOVL configuration was found to be dominated by noise associated with jet impingement, dynamic load levels reached 160 dB SPL on aerodynamic control surfaces. The cruise mode for supersonic STOVL was found to be of severe concern, since practical configurations with small nozzle to fuselage separation would suffer severe scrubbing by the jet plume. Levels as high as 174 dB SPL were observed.

In general, the aeroacoustic scientific community has not yet reached a stage where prediction of the dynamic load levels and particularly the loads spectrum with source coherence is possible with the complex aircraft configurations examined in this paper. It is clear, however, that sonic fatigue of aircraft components occurs quite frequently, and with levels much lower than the 0.16 psi-rms reference level suggested in Ref. 16. This is due partly to the nature of the source mechanism. Jet screech produces frequencies in full scale aircraft, that in many cases, lie near a structural component's resonant frequency. This occurs frequently, because during an aircraft's full mission profile the screech frequency can shift over one decade and become a concern at a point in the mission profile. Often this has been found to occur in cruise, where an aircraft spends most of its time. Jet screech also produces an acoustic wave that has a spatial coherence at least as large as the size of many aircraft components. Thus the excitation of the structure is maximized.

Methods for reducing dynamic loads associated with supersonic jet plume sources are numerous, though often not practical. It would appear, however, that investigations should be conducted involving the use of fan by-pass air, where possible, to diminish the amplitude of jet screech and impingement loads. Porous surfaces are known to work well at reducing the strength of plume shocks, which would substantially reduce both sock noise sources. Mach wave emission can also be substantially reduced through the use of propulsion efficient mixers. The requirement here is to reduce the axial extent of jet plume where turbulent structures convect supersonically relative to the ambient sound speed. Some measure of noise reduction is required for the current applications investigated in this paper. When one considers the advantages of using advanced composite material on aircraft components to reduce aircraft weight, the need for jet source noise reduction is more paramount, since little is known of the fatigue properties of these materials at high levels of dynamic load.

REFERENCES

1. Seiner, J.M., Pontoon, M.K., Pendergraft, O.C., Manning, J.C., and Mason, M.L., "External Nozzle Flap Dynamic Load Measurements On F-15 S/MTD Model", AIAA Paper 90-1910, July, 1990.

2. Seiner, J.M., Manning, J.C., Capone, F.J., and Pendergraft Jr., O.C., "Study of External Dynamic Loads On a 6 Percent B-1B Model", J. Eng. For Gas Turbine and Power, Vol. 114, 1992, pp. 816-828.

3. Seiner, J.M., "Fluid Dynamics and Noise Emission Associated With Supersonic Jets", Studies In Turbulence, edited by Gatski, Sarkar, and Speziale, Springer Verlag, N.Y., ISBN 0-387-97613-2, 1992, pp 297-323.

4. Seiner, J.M., "Advances In High Speed Jet Aeroacoustics", AIAA Paper No. 84-2275, 1984.

5. Phillips, O.M., "On the Generation of Sound by Supersonic Turbulent Shear Layers", J. Fluid Mech., Vol. 9, Pt. 1, 1960, pp. 1-28.

6. Oertel, H., "Coherent Structures Producing Mach Waves Inside and Outside of the Supersonic Jet", in Structure of Complex Turbulent Shear Flow, IUTAM Symposium, Marseille, 1982.

7. Tam, C.K.W., and Hu, F.Q., "On Three Families of Instability Waves of High Speed Jets", J. Fluid Mech., Vol. 201, 1989, pp. 447-483.

8. Ffowcs-Williams, J.E., and Maidanik, G., "The Mach Wave Field Radiated by Supersonic Turbulent Shear Flows", J. Fluid Mech., Vol. 21, Pt. 4, 1965, pp. 641-657.

9. Seiner, J.M., Pontoon, M.K., Jansen, B.J., and Lagen, N.T., "The Effects of Temperature On Supersonic Jet Noise Emission", Proc. of the 14th Aeroacoustics Conference, May 1992 DGLR/AIAA Paper No. 92-02-046.

10. Howe, M.S., and Ffowcs Williams, J.E., "On the Noise Generated by an Imperfectly Expanded Supersonic Jet", Phil. Trans. RoyalSoc. London, Vol., 289, No. 1358, 1978, pp. 271-314.

11. Tam, C.K.W., "Broadband Shock-Associated Noise of Moderately Imperfectly Expanded Supersonic Jets", J. Sound and Vib., Vol. 140, Pt. 1, 1990, pp. 55-71.

12. Powell, A., "On the Mechanism of Choked Jet Noise", Proc. Roy. Soc., Vol. 66, Pt. 12B, 1953, pp. 1039-1056.

13. Tam, C.K.W., Seiner, J.M., and Yu, J.C., "Proposed Relationship Between Broadband Shock-Associated Noise and Screech Tones", J. Sound and Vib., Vol. 110, 1986, pp. 309 -321.

14. Seiner, J.M., Manning, J.C., and Pontoon, M.K.,"Dynamic Pressure Loads Associated With Twin Supersonic Plume Resonance", AIAA J., Vol. 26, No. 8, August 1988, pp 954-960.

15. Seiner, J.M., Dash, S.M., and Wolf, D.E., "Analysis of Turbulent Underexpanded Jets, Part II: Shock Noise Features Using SCIPVIS", AIAA J., Vol. 21, No. 5, 1985, pp. 669-677.

16. Guinn, W.A., Balena, F.J., and Soovere, " Sonic Environment of Aircraft Structure Immersed in a Supersonic and Jet Flow Stream", NASA CR-144996, 1976.

17. Lorinez, D.J., "A Water Tunnel Flow Visualization Study of the F-15", NASA CR-144676, 1978.

18. Mixson, J.S., and Roussos, L.A., "Acoustic Fatigue: Overview of Activities at NASA Langley", NASA TM-89143, 1987.

19 Norum, T.D., "Supersonic Rectangular Jet Impingement Noise Experiments", AIAA J., Vol. 29, No. 7, 1991, pp. 1051-1057.

20. Norum, T.D., "Ground Impingement Noise of Supersonic Jets from Nozzles With various Exit Geometries", AIAA J., Vol. 29, No. 6, 1992, pp. 993-998.

21. Kibens, V., Saripalli, K.R., Wlezien, R.W., and Kegleman, J.T., "Unsteady Features of Jets in in Lift and Cruise Modes for VTOL Aircraft", Proc. Intl. Powered Lift Conf., P203, Paper No. 872359, Santa Clara, CA, 1987, pp. 543-552.

22. Wlezien, R.W., Childs, R.E., Bower, W.W., Pal, A., Howe, M.S., and Kibens, V., "A Parametric Analysis of the Unsteady Pressure Field On the Undersurface of a STOVL Aircraft in Hover", NASA CR-191486, 1993.

23. Neuwerth, G., "Acoustic Feedback of a Subsonic and Supersonic Free Jet Which Impinges on an Obstacle", AGARD CCP 308,1981, pp 13.1-13.7.

24. Johns, A.L., Neiner, G.H., Bencic, T.J., Norum,T.D., Mitchell, L.K., Kegelman, J.T., Flood, J.D., and Amuedo, KC., "Characteristics and Laser Sheet Flow Visualization of a 18-Deg Forward Nozzle Splay Vectored Thrust STOVL Concept", AIAA Paper No. 91-1901, 1991.

25. Glininky, M.M., Seiner, J.M., Jansen, B.J., and Bhat, T.R.S., "Supersonic Gasdispersional Jets and Jet Noise", AIAA Paper 93-4389, 1993.

26. Seiner, J.M., Manning, J.C., and Jansen, B.J., "Supersonic Jet Plume Interaction with a Flat Wall", Proc. Intl. Powered Lift Conf., Paper No. 872361, Santa Clara, CA, 1987, pp. 563-574.

HIGH-TEMPERATURE ACOUSTIC TEST FACILITIES AND METHODS

Jerome Pearson
Chief, Structural Integrity Branch
Wright Laboratory
2130 Eighth Street, Suite 11
Wright-Patterson AFB, Ohio 45433-7552
USA

SUMMARY

The Wright Laboratory is the Air Force center for air vehicles, responsible for developing advanced technology and incorporating it into new flight vehicles and for continuous technological improvement of operational air vehicles. Part of that responsibility is the problem of acoustic fatigue. With the advent of jet aircraft in the 1950s, acoustic fatigue of aircraft structures became a significant problem. In the 1960s the Wright Laboratory constructed the first large acoustic fatigue test facilities in the United States, and the laboratory has been a dominant factor in high-intensity acoustic testing since that time. This paper discusses some of the intense environments encountered by new and planned Air Force flight vehicles, and describes three new acoustic test facilities of the Wright Laboratory designed for testing structures to these dynamic environments. These new test facilities represent the state of the art in high-temperature, high-intensity acoustic testing and random fatigue testing. They will allow the laboratory scientists and engineers to test the new structures and materials required to withstand the severe environments of captive-carry missiles, augmented lift wings and flaps, exhaust structures of stealthy aircraft, and hypersonic vehicle structures well into the twenty-first century.

1. Introduction

The U.S. Air Force recently reorganized its major commands. The Strategic Air, Tactical Air, and Military Airlift Commands have been replaced by the Air Combat and Air Mobility Commands. Similarly, the Systems and Logistics Commands have been merged into the new Materiel Command. This change was combined with a restructuring of the Air Force laboratories, which are now under the new Materiel Command. There are four major development centers under the command, responsible for space and missiles, electronics, air vehicles, and human systems. Each of these centers has its associated laboratory--the Phillips Laboratory for space and missiles, the Rome Laboratory for electronics, the Wright Laboratory for air vehicles, and the Armstrong Laboratory for human systems. The Wright Laboratory is responsible for aeronautical technology, and is an amalgam of the older Air Force laboratories for avionics, electronics, flight dynamics, materials, and propulsion. The Wright Laboratory technologies and programs are direct descendents of the original Aircraft Laboratory of the 1950s.

2. Acoustic Fatigue in Aircraft Structures

The Wright Laboratory has long been a leader in the technologies required for aircraft structures, and one of these driving technology areas is that of the dynamic environments of acoustics and vibration. Until the 1950s, the main emphasis in structural dynamics had been the control of sinusoidal vibration from reciprocating engines and from helicopter rotors. The electrodynamic shakers, vibration measurement equipment, and dynamic response analyses of those days were designed to handle combinations of sinusoidal forces related to blade passage frequencies and piston engine rotation frequencies.

With the advent of long-range jet aircraft flying at nearly the speed of sound, random vibration and acoustic inputs became much more important. The first indications of

Presented at a Symposium on 'Impact of Acoustic Loads on Aircraft Structures' held in Lillehammer, Norway, May 1994.

the severe acoustic environments experienced by jet aircraft were the problems of the KC-135 fuselage fatigue and the B-52 wing structure, which showed cracking failures much sooner than expected. After extensive study and flight measurements, the acoustic environments were shown to be a severe combination of inputs from several sources, including jet noise, boundary layer noise, and disturbed air flow around control surfaces and other protuberances. The general features of jet aircraft combined environments are shown in Figure 1. These acoustic inputs typically reach levels of 150-155 dB, which are much higher than previous aircraft environments. These are very severe acoustic levels, because even 140 dB sound pressure levels can cause acoustic fatigue and cracking of aircraft secondary structures.

To deal with these acoustic environments, Wright Laboratory researchers Bianchi et al. (1962) reviewed the state of the art in acoustic testing, and the laboratory constructed its Sonic Fatigue Facility in the 1960s. Kolb and Rogers (1962) developed plans for the facility, and the final form i described in Kolb and Magrath (1968). This facility is now operated by the Structural Dynamics Branch. A schematic of the branch facilities is shown in Figure 2. The centerpiece of the test facility was the large scale test chamber, a reverberant chamber with a volume of 155,000 cubic feet, or 4390 cubic meters. The acoustic input was originally provided by 36 air sirens, each producing sound from air flowing through slots opened and closed by rotating and static disks. Each siren covered a narrow frequency band, and the combination provided the broadband acoustic output. The sirens have been replaced by electro-pneumatic modulators with broadband random acoustic outputs.

The original sonic fatigue facility included a quarter-scale reverberant chamber whose dimensions are one-fourth of the large chamber, and a small chamber for testing much smaller specimens. The quarter-scale and small chambers are configured as progressive wave tubes, in which the air flow from a compressor has acoustic energy added to it by the air modulator, is expanded through an exponential horn, propagates through a tube of rectangular cross-section, and impinges on the test structure, which comprises one wall of the tube. The acoustic energy is absorbed in a termination section composed of acoustic absorption wedges, and the air is exhausted to the atmosphere. Progressive wave tubes are able to generate more accurate simulations of acoustic inputs impinging on flight structures than reverberant chambers, and are now the most common type of high-intensity acoustic test chambers. The combined environment test chamber also shown in Figure 2 is a new addition, and will be discussed later.

3. Acoustic Environments of Missiles in Captive Carry

In recent years, Air Force front-line fighter aircraft such as the F-15 have been called upon to carry newer, more capable missiles like the Advanced Medium-Range Air-to-Air Missile, or AMRAAM. Because of the speed and maneuverability of the F-15, the missiles are subjected to very severe acoustic environments even before they are launched, when they are in captive carry under the F-15 wings. Wright Laboratory engineers measured the captive-carry AMRAAM environment on F-15s and found it to reach overall sound-pressure levels of 175 dB over frequencies of 30 to 2000 Hz.

To test the missile to realistic levels in existing facilities was very difficult. The simplest solution was to remove the fins and insert the missile into a 12-inch-diameter progressive wave tube driven by 3 Wyle WAS-3000 air modulators. The missile was mounted on its LAU-106 launcher for a realistic mounting condition. Figure 3 shows the schematic of the missile in the tube, and also shows the required test spectrum as a solid line and the achieved third-octave sound pressure levels with x's.

This test represented the highest broadband acoustic levels ever achieved for a missile. As a result of lab testing by the Wright Laboratory and government and contractor flight testing of AMRAAM structures, the missile was successfully modified by the contractor and qualified for flight under the entire flight envelope of the F-15. The AMRAAM will also be the main armament of the new Air Force advanced tactical fighter, the F-22.

4. High-Temperature Acoustic Environments from STOL and Stealth

To achieve short takeoff distances and rapid climb rates, new aircraft have been designed with larger flaps for additional lift. The lift from the aircraft wing and flap is limited by the velocity and volume of air flowing beneath the surface, and this lift can be augmented by flowing additional air from the engine across the lifting surface. This was first applied in the YC-14 and the YC-15 short-takeoff and landing (STOL) aircraft prototypes in the early 1970s, and is now being used in the Air Force C-17 airlifter.

However, augmenting the lift by using engine exhaust gas subjects the wing and flap structure to intense noise and temperature inputs. An example from the YC-14 is shown in Figure 4. In addition to raising the acoustic input from the typical level of 155 dB to about 165 dB, the augmented lift subjects the structures to temperatures of 500-700 F. Many structures can withstand high dynamic forces at normal temperatures, but lose their strength rapidly at higher temperatures. New, high-temperature structures must be designed and tested to this combination environment, or the fatigue lives of these high-lift devices will be limited, increasing the maintenance costs of the aircraft.

To achieve stealthier aircraft, modern designs such as the F-117 fighter and the B-2 bomber use a variety of techniques to reduce their radar and infrared signatures. To reduce the emission of infrared energy from the heat of the engine exhaust toward the ground, these aircraft are designed with multiple engine nozzles that exhaust over the top of the aft structure so that the exhaust gases are cooled before they become visible from beneath the aircraft.

The result of this is that the aircraft aft structures are subjected to high-temperature acoustic environments much like the blown flaps of STOL aircraft. Stealthy aircraft, like STOL aircraft, need materials and structures that can maintain their strength and fatigue resistance at higher temperatures. This translates into requirements for flight testing of the actual environments and for developing laboratory test facilities for high-temperature fatigue testing.

5. Thermo-Acoustic Environments of Hypersonic Vehicle Structures

Hypersonic vehicles will operate at much higher dynamic pressures than conventional vehicles, leading to severe acoustic environments associated with both turbulent boundary layer and high thrust engines. Intense thermal fluxes will be present over large areas of the airframe, increasing the potential for acoustic fatigue damage. Local flow separation and shock impingement will aggravate both the acoustic and the thermal environments.

The initial predictions of the thermo-acoustic environments and heating levels, or Q, for typical hypersonic vehicles range from a Q of 20 Btu per square foot per second on the upper body to a Q of more than 500 on the airframe nozzle. The corresponding acoustic levels range from 150 dB up to an unprecedented 190 dB for the nozzle. There are no existing facilities that can duplicate these dynamic environments, and these acoustic test requirements are the most challenging yet encountered by the Wright Laboratory.

6. The Wright Laboratory Acoustic Test Facilities

The Structural Dynamics Branch of

the Wright Laboratory is responsible for acoustics and vibration of aircraft. To meet the test requirements of these new classes of vehicles--STOL, stealth, and hypersonic--the branch is greatly increasing its capability for high-intensity acoustic testing of flight structures by building three new test chambers. Two of the new chambers incorporate high-flux heating and multiple acoustic drivers into new progressive wave tubes; the third combines shaker fatigue testing with a temperature- and pressure-controlled environmental chamber.

The Random Fatigue Chamber provides the capability to determine the random fatigue characteristics and damage mechanisms of advanced material coupons and structural sub-elements. A schematic of the chamber is shown in Figure 5. The facility consists of an electrodynamic shaker that can produce a random force output of 20,000 pounds RMS, coupled with an environmental chamber capable of operating from -250 F to 2600 F with variable atmospheric pressure and partial pressure gas environments. This chamber is now on-line and is being used to generate stress vs. cycles to failure data and determine the influence of temperature, pressure and gases on materials and coating systems for hypersonic structures.

The Sub-Element Acoustic Chamber provides a progressive wave tube for response and fatigue testing of structures up to 12" by 18" at temperatures up to 2500 F and sound pressure levels up to 180 dB overall. A schematic of the chamber is shown in Figure 6.

The high-intensity acoustic environment is generated by four Wyle WAS-3000 air modulators connected by exponential horns to a one-foot-square progressive wave tube. The low-flux thermal environment is provided by banks of quartz lamps incorporated inside the acoustic chamber. New mounting systems have been designed to allow modified lamps to survive the acoustic environment in order to be as close to the test specimens as possible. This technique eliminates the large, expensive quartz window used in previous high-temperature acoustic test facilities. The quartz lamps can provide input fluxes of up to a Q of about 100 Btu per square foot per second.

Higher heat fluxes can be achieved by using graphite heaters or plasma arc lamps, both of which have been investigated. In addition, propane burners were also investigated, but were abandoned. Graphite heaters have the potential for reaching a Q of 200, and the plasma arc shows promise of reaching up to a Q of 1000.

The Combined Environment Acoustic Chamber is the third new capability being developed. The chamber, shown in Figure 7, was first operated in July, 1993. It provides a high-temperature acoustic progressive wave tube for response and fatigue testing of larger structural components. The chamber is driven by twelve WAS-3000 air modulators supplied by two air compressors.

The chamber is designed to accommodate two test sections. The four-foot section is designed for testing actively cooled structures at temperatures up to 3000 F and sound pressure levels up to 180 dB. The six-foot test section will be added later, and is designed to provide the capability for elevated temperature testing of larger structures at acoustic levels up to 175 dB. Low heat fluxes will be achieved using quartz lamps, and higher fluxes will be achieved with plasma arc heaters.

The development of these new high-temperature acoustic and vibration test chambers will maintain the Wright Laboratory at the forefront of structural dynamics testing of aircraft structures, making the laboratory capable of testing structures for all the critical flight vehicle applications now envisioned. This continues a long history of leadership for the Wright Laboratory in acoustic testing. This leadership is illustrated in Figure 8, which shows a summary of the historical trends in high-intensity acoustic testing.

The sound-pressure-level capabilities of various test organizations is shown over forty years, in psi on the left scale and in dB on the right scale. In this figure, WL indicates the Wright Laboratory, MDAC is McDonnell Aircraft Company, and IABG is the German facility near Munich.

The psi scale shows how intense the noise levels are in the new Wright Laboratory test facilities. The Combined Environment Acoustic Chamber is designed to achieve a noise level of 180 dB, or nearly 3 psi, on the test specimen. If this energy were concentrated into one frequency of, say, 100 Hz, it would correspond to a fluctuating load of 1700 pounds of force over a two-foot-square test panel, reversing from +1700 lbs to -1700 lbs one hundred times per second. Such levels show the intense acoustic environments that must be withstood by modern flight structures.

References

1. Bianchi, R.A., Bradshaw, R.T., Farrell, J.H., and Reed, R.E., 1962, "Survey and Evaluation of Sonic Fatigue Testing Facilities," US Air Force Aeronautical Systems Division Technical Report ASD-TR-61-185.

2. Kolb, A.W. and Rogers, O.R., 1962, "The Aeronautical Systems Division Sonic Fatigue Facility," Shock & Vibration Bulletin Nr 30, Part V, pp. 37-50.

3. Kolb, A.W and Magrath, H.A., 1968, "RTD Sonic Fatigue Facility, Design and Performance Characteristics," Shock & Vibration Bulletin Nr. 37 Supplement, pp. 17-41.

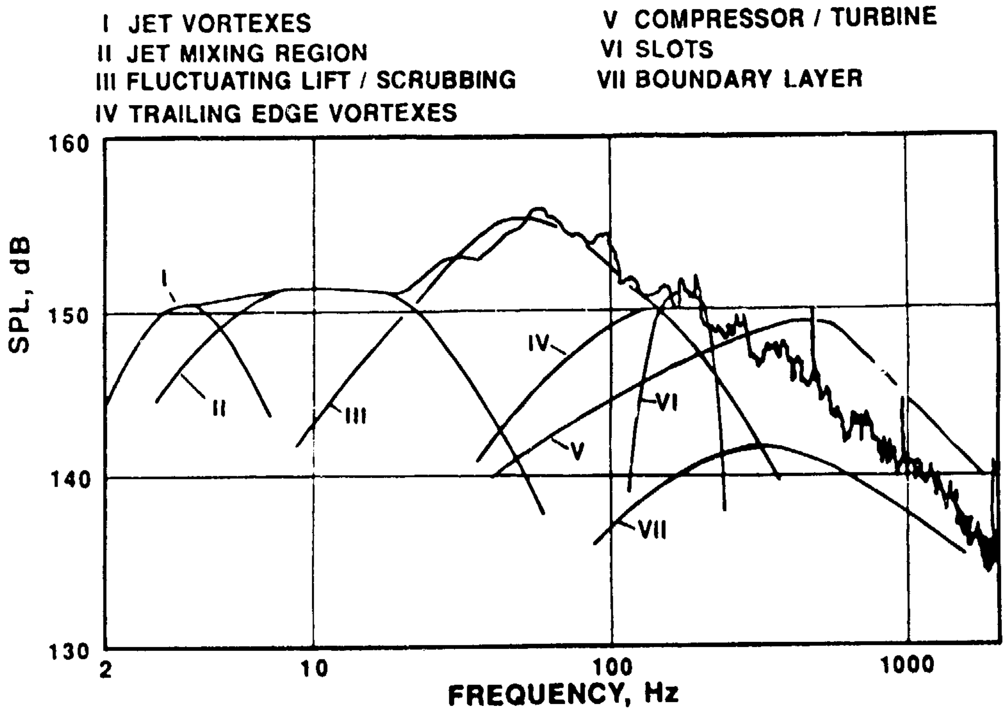

Figure 1. Acoustic Environments Experienced by Jet Aircraft

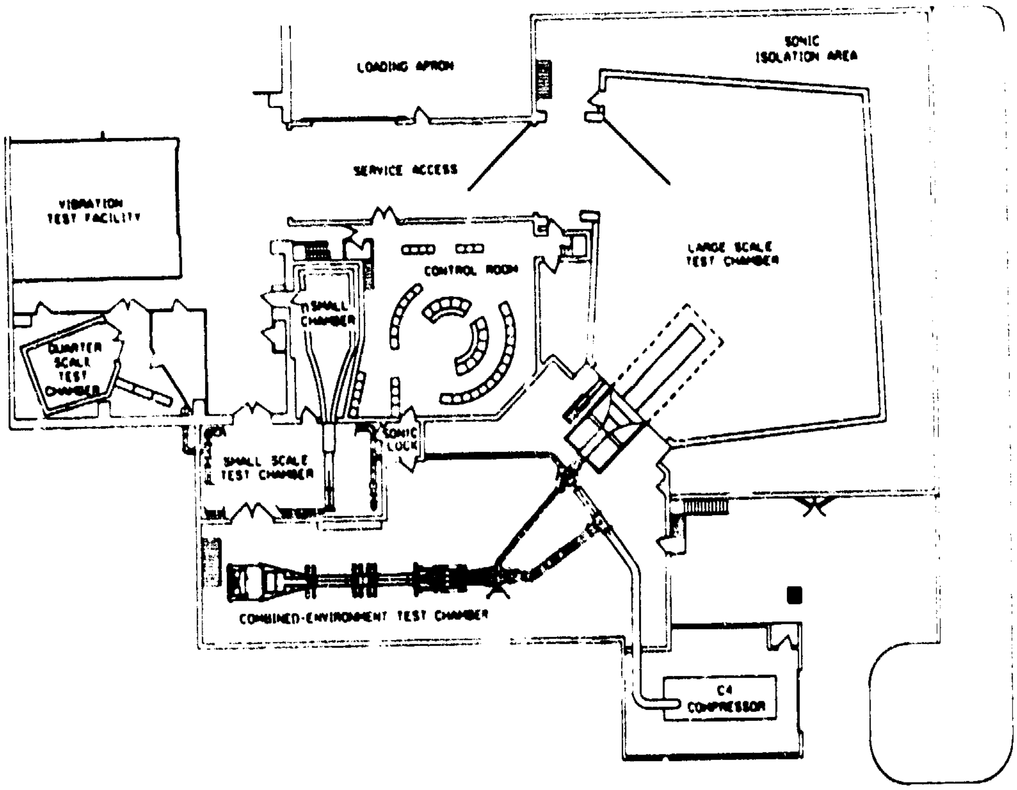
LOADING APRON
SONIC ISOLATION AREA
SERVICE ACCESS
VIBRATION TEST FACILITY
CONTROL ROOM
SMALL CHAMBER
LARGE SCALE TEST CHAMBER
QUARTER SCALE TEST CHAMBER
SMALL SCALE TEST CHAMBER
SONIC LOCK
COMBINED-ENVIRONMENT TEST CHAMBER
C4 COMPRESSOR

Figure 2 The Wright Laboratory Structural Dynamics Facility

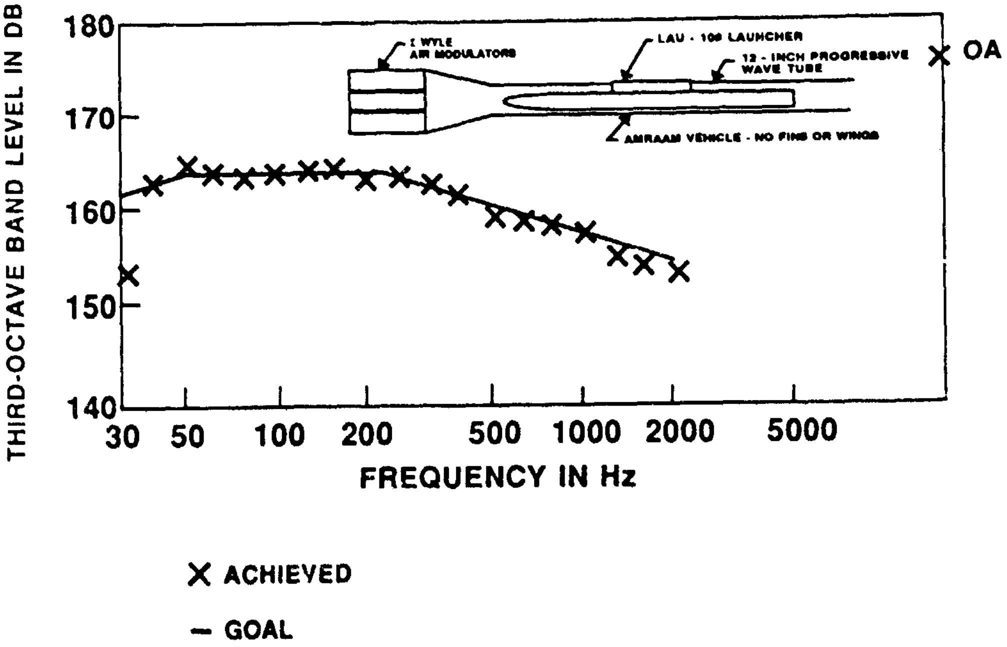

Figure 3. AMRAAM Acoustic Test Spectrum for F-15 Captive Carry

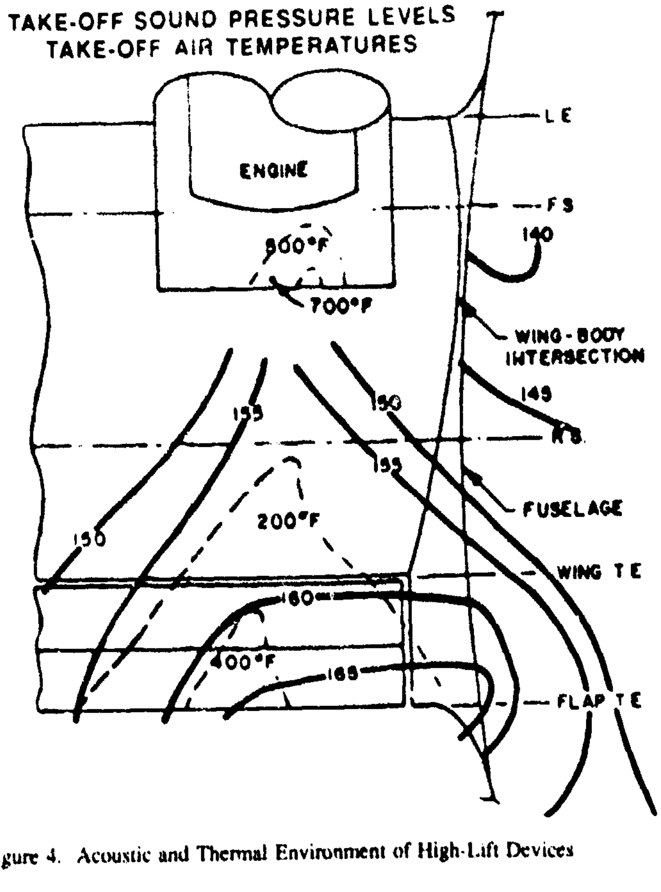
TAKE-OFF SOUND PRESSURE LEVELS
TAKE-OFF AIR TEMPERATURES
ENGINE
LE
FS
140
800°F
700°F
WING-BODY INTERSECTION
145
155
150
RS
155
FUSELAGE
200°F
150
WING TE
160
400°F
165
FLAP TE

Figure 4. Acoustic and Thermal Environment of High-Lift Devices

RANDOM FATIGUE TEST CHAMBER

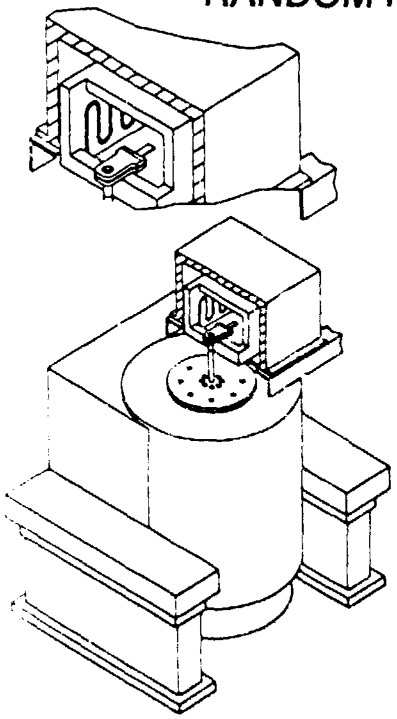

PURPOSE:

Define Basic Fatigue Properties of Advanced Materials at Severe Environments

CAPABILITIES:

- Temperature Range from Cryogenic (-250°F) to High Temp. (2600°F)
- Variable Pressure from Vacuum (0.01 torr) to Atmospheric (1000 torr)
- Partial Pressure Gas Environment: O_2, N_2, He and 3% H_2
- Shaker - 20000 lb_f Random, 24000 lb_f Sine
- Test Specimen - Up to 3" x 7"

Figure 5 Random Fatigue Chamber

HIGH TEMPERATURE ACOUSTIC SUBELEMENT TEST CHAMBER

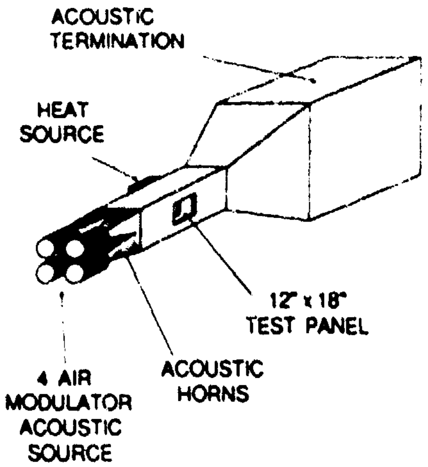
ACOUSTIC TERMINATION
HEAT SOURCE
12" x 18" TEST PANEL
4 AIR MODULATOR ACOUSTIC SOURCE
ACOUSTIC HORNS

PURPOSE

- DESIGN VERIFICATION FOR COMBINED ENVIRONMENT TESTING
- COMBINED ENVIRONMENT TESTING OF SMALL STRUCTURES

CAPABILITIES

- 180 dB SPL
- 50 - 300 Btu/ft^2 sec
- 12" x 18" PANEL, MAX

Figure 6 Sub-Element Acoustic Chamber

COMBINED ENVIRONMENT ACOUSTIC CHAMBER

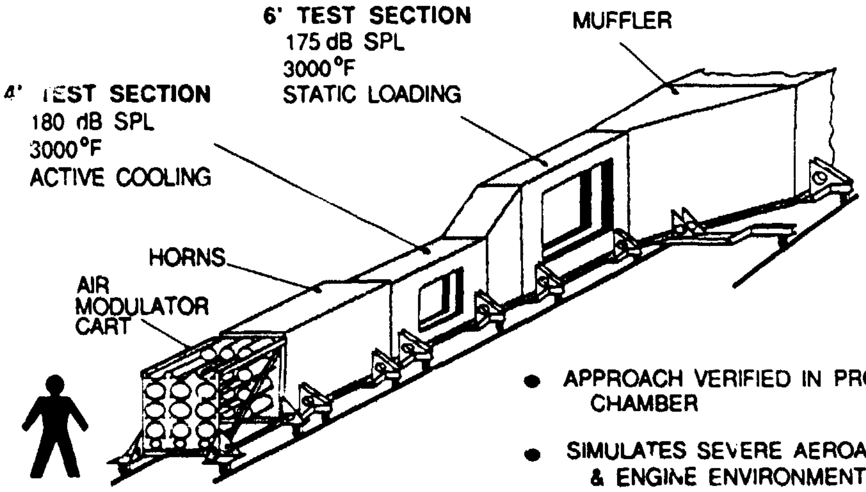
6' TEST SECTION
175 dB SPL
3000°F
STATIC LOADING
MUFFLER
4' TEST SECTION
180 dB SPL
3000°F
ACTIVE COOLING
HORNS
AIR MODULATOR CART

- APPROACH VERIFIED IN PROTOTYPE CHAMBER
- SIMULATES SEVERE AEROACOUSTIC & ENGINE ENVIRONMENTS
- UNIQUE CAPABILITY
- EXPLOITS NEW TECHNOLOGY
- ABILITY TO TEST ACTIVELY COOLED STRUCTURES

ACOUSTIC SOURCE

12 AIR MODULATORS
50 - 1500 Hz
360K WATTS ACOUSTIC POWER

HEATING SOURCES

LOW FLUX - QUARTZ LAMPS
HIGH FLUX - GRAPHITE STRIP HEATERS

Figure 7 Combined Environment Acoustic Chamber

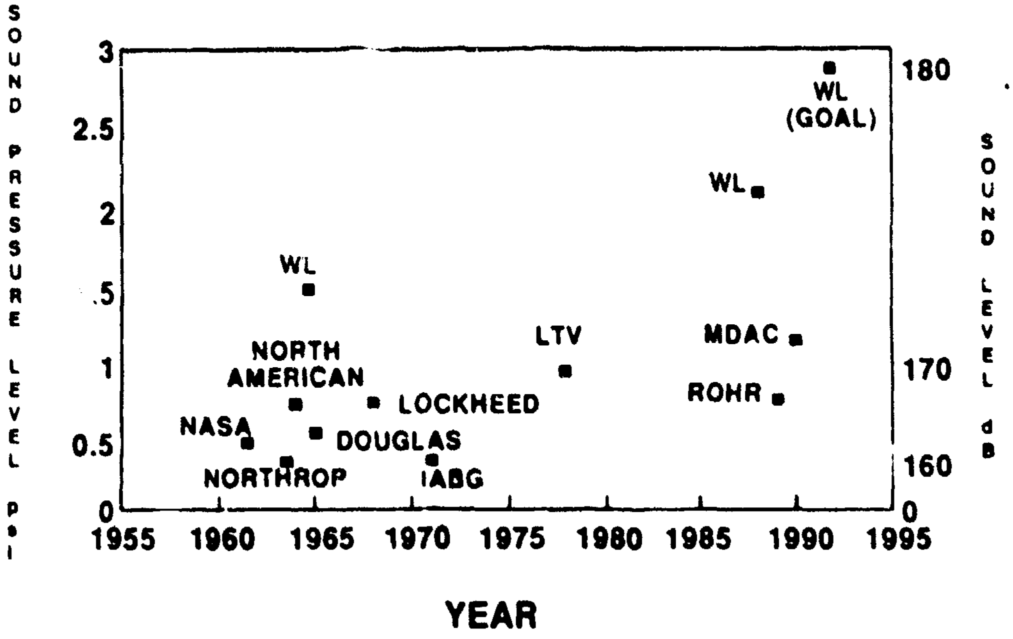

Figure 8. High Intensity Acoustic Testing Capabilities

DESIGN AND OPERATION OF A THERMOACOUSTIC TEST FACILITY

G. Bayerdörfer
L. Freyberg
Industrieanlagen-Betriebsgesellschaft m.b.H.
Einsteinstraße 20
85521 Ottobrunn / GERMANY

1. SUMMARY

Aerothermal environments as encountered during the missions of reusable spacecrafts, hypersonic vehicles, advanced launchers etc. are the major design driver for an advanced Thermal Protection System (TPS) technology. In developing such materials and structures ground testing under simulated operational conditions is of eminent importance.

In order to meet these requirements IABG has designed a thermoacoustic facility which was recently put into operation. The facility is capable to produce surface temperatures up to 1300 °C at sound pressure levels up to 160 dB. The design approach and operational aspects from test work performed so far are described.

2. INTRODUCTION

Apart from analytical methods such as FEM-calculations ground test facilities are an indespensible tool for the development of TPS-hardware (Ref 1,2). Though it is not possible to simulate all the different environments to which TPS-systems may be exposed during their operational life in only one single facility, it is still good practice to combine such loadings which develop strong interactions.

Interaction exists between thermal loading and vibroacoustic response in so far as the stiffness and fatigue characteristics of TPS-materials change with increasing temperatures. Such effects are best investigated by experimental means.

Depending on the mission of the individual vehicle aerothermal environments may be of different nature. A general survey is as follows

AEROTHERMAL CHALLENGES

ASCENT	PROPULSION SYSTEM	
	Radiated Noise	•••
	Radiated Heat	•
	AERODYNAMIC EFFECTS	
	Separated Flows	•••
	Aerodynamic Heating	•
CRUISE	AERODYNAMIC EFFECTS	
	Boundary Layer Noise	••
	Aerodynamic Heating	••
REENTRY	AERODYNAMIC EFFECTS	
	Boundary L./Separated Fl.	••
	Aerodynamic Heating	•••

••• Severe •• remarkable • moderate

3. FACILITY DESIGN

Aerothermal environments are composed of vibroacoustic and thermal loadings of varying severity. In designing a test facility it is essential that a wide range of load combinations becomes available. This can best be achieved if the thermal and acoustic loads are generated independent from each other.

The objective was to use excisting acoustic facilities and combine them with an appropriate heating system. High frequency pressure fluctuations caused by propulsion noise, boundary layers or separated flows can be reproduced to a certain extend by acoustic excitation such as in reverberation chambers or in progressive wave tubes (PWT). These facilities normally operate at room temperature without a capability for elevated temperatures. However, test configurations can be realized which provide very high temperatures in the limited area of the test article.

The selection of an appropriate heating system is a crucial point because of the required compatibility with the acoustic environment. A comparison between the often used quartz lamps and a flame system is given below

	QUARTZ LAMPS	FLAME SYSTEM
CONTROL	GOOD	MODERATE
SURFACE TEMP.	max. 560 °C	> 1300 °C
FATIGUE LIFE	POOR	NO PROBLEMS
OPERATION	EXPENSIVE	CHEAP

Mainly because of the higher surface temperatures and the simpler overall design it was decided to go for the flame system.

Fig. 1 shows an array of nine burners which are mounted on ball pivots to allow individual adjustment. The burners are driven with Methan (CH_4) and Oxygen (O_2) whereby each burner has its separate control valves

Fig. 1 Array of Burners

Presented at a Symposium on 'Impact of Acoustic Loads on Aircraft Structures' held in Lillehammer, Norway, May 1994

Fig. 2 . Flame sensors on top of each row control correct burning, in case of irregularities the relevant valves will shut down the gas supply. Spark plugs for each row allow ignition so that the flame unit can be fully remote controlled.

Fig. 2 Control of Burners

This flame unit can be mounted into a reverberation chamber or installed into a PWT; the relevant data of the resulting facilities are as follows:

	Reverber.Chamber	Progr.Wave T.
SIZE/TEST SECT.	206 m^3	0,8 x 1,2 m^2
OASPL at R.T.	max. 15[illegible] dB	max. 160 dB
FREQUENCY R.	100 Hz-10 kHz	50 Hz - 10 kHz
HEAT FLUX	max.100 W/sec	max.100 W/sec
SURFACE TEMP.	max. 1300 °C	max. 1300 °C

OASPL Overall Sound Pressure Level
RT Room Temperature

No modifications were necessary when installing the flame system into the reverberation chamber. Due to the extensive air flow from the noise generators the temperature increase inside the reverberation chamber is very moderate. As the flame unit is placed in the middle of the chamber the walls are not effected by the heat.

The progressive wave tube, however, had to be substantially modified. Burning a flame system with a heat flux of 100 W/sec inside a PWT is only possible if the basic structure is shielded against this heat input.

Fig. 3 shows the cross section of the thermo acoustic PWT. By insertion of an inner tunnel made of stainless steel the basic structure is protected against the heat. The duct which is formed by these two elements is subdivided into various channels. An air distribution system feeds these channels with predetermined massflows to provide the necessary cooling. The area around the test section which naturally has the highest temperatures is intensively cooled by the highest mass flow whereas the rear side with much lower temperatures obtains only reduced cooling air. The total cooling air is delivered by the same compressor which also feeds the noise generators.

The flame heating system is mounted into a window of the PWT so that the flames impinge directly on the test article which is just opposite. Each burner can be adjusted individually so that the total test section of 0,8 x 1,2 m^2 is uniformally heated.

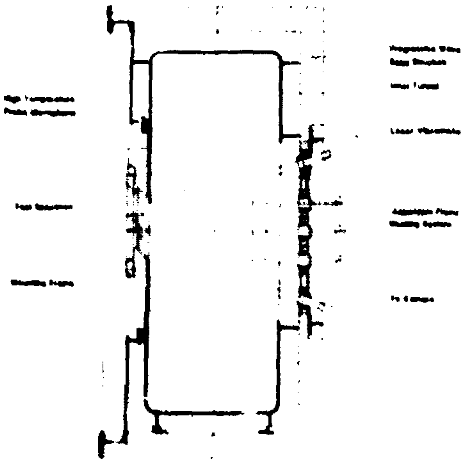

Fig. 3 Thermoacoustic PWT

The instrumentation of the facility consists of

- Reference Microphones (cold zone)
- Probe Microphones (hot zone)
- Thermocouples
- Laser Vibrometer
- TV-Camera

The reference microphones are located upstream of the burners and control the noise output of the generators. The probe microphones can be used in temperature fields up to 700 °C, they allow direct measurements of the fluctuating pressures within the hot zone. For temperatures beyond 700 °C direct sensoring of the dynamic pressures is not possible. In such cases the data from the reference microphones have to be scaled down according to the change of density between cold and hot zones.

Temperature measurements are taken via thermocouples which are directly applied to the exposed surface of the test article. This method is considered more reliable and accurate compared with radiation measurements because the latter are heavily disturbed by the open flames.

As far as the dynamic response of the test article is concerned a laser vibrometer can deliver complete mode patterns even under the extrem conditions of flame heating. Direct strain measurements, however, are not feasable in such a hostile environment.

For the purpose of overall control a TV-camera is employed which checks not only the correct flame burning but also provides information about possible desintegration of the test article during the test.

Mounting of the test specimen into the thermoacoustic PWT needs a dedicated design. The specimen shall be supported as for its intended use and care should be taken to allow for thermal expansion. If necessary the mounting frame can be additionally cooled with water.

4. OPERATIONAL ASPECTS

In order to illustrate the operation of the facilities two different tests which have been recently performed are described.

ARIANE 5 Tank Insulation

The European launcher ARIANE 5 presently in the final development stage is depicted in Fig. 4. The tank marked with an arrow contains Helium and is covered with flexible insulation material to protect it against the heat radiated by the engine of the cryogenic main stage. The insulation is equally exposed to the high noise levels at lift-off and to turbulent flows at transonic speeds. In order to verify that the surface of the tank structure will not be subjected to temperatures above 80 °C as well as to qualify the insulation with respect to the turbulent pressure field a thermoacoustic test was performed.

Fig. 4 ARIANE 5-Launcher

One half of the tank structure partially covered with a sample of the insulation material and the rest covered with ordinary fire resistant carpets was placed inside the reverberation chamber opposite the flame heating system (Fig. 5). Four control microphones were positioned around this test set-up, their locations being well outside the hot zone. In addition a probe microphone was installed for direct measure of the dynamic pressures on the surface of the insulation material inside the hot zone.

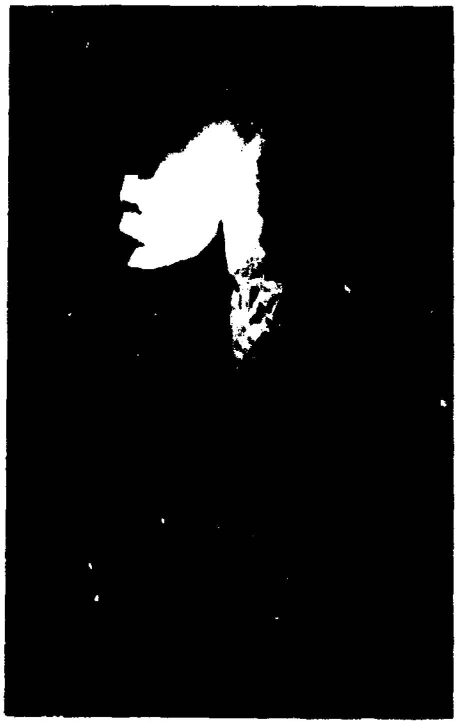

Fig. 5 Thermoacoustic Test
inside Reverberation Chamber

The readings of these microphones are presented in Fig. 6. The upper part contains the spectra as measured under RT. There are certain differences in the frequencies up to 315 Hz and beyond 400 Hz, however, the OASPL-value is the same for the probe microphone and the average out of the four control microphones.

Looking at the lower part it is obvious that the spectra obtained during the flame heating process differ substantially. Whereas the shape of the averaged control microphone spectrum is not very much affected, the probe microphone indicates substantially lower noise levels. Due to the lower density of the hot gas medium the sound pressure levels are considerably reduced leading to an OASPL-value which is 6 dB lower compared with RT.

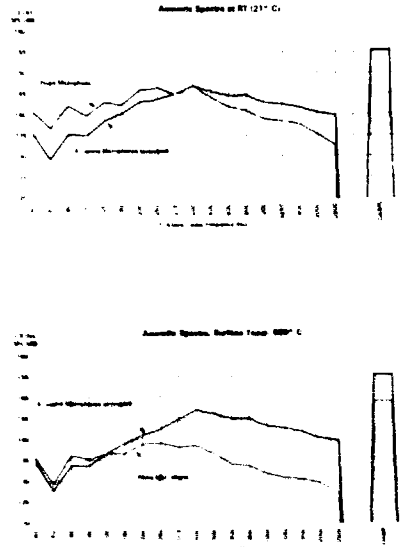

Fig. 6 Acoustic Spectra

The temperature curves as monitored by thermocouples are displayed in Fig. 7. The requirement was to achieve 660 °C on the surface of the insulation material over a period of four minutes. The upper part shows that this requirement was reasonably good fulfilled. The lower part gives the temperature rise of the tank shell (below the insulation). In this case the temperature did not exceed 80 °C as specified.

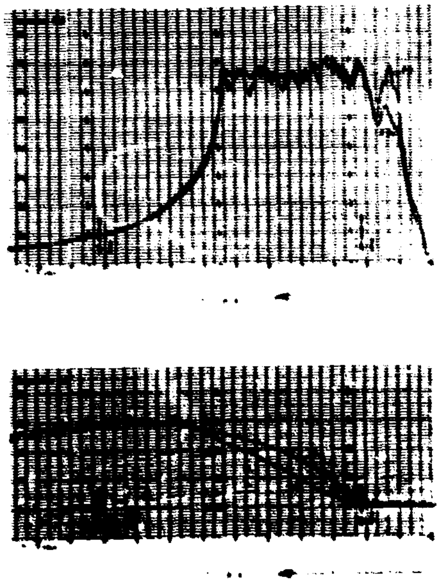

Fig. 7 Temperature Curves

TPS for Advanced Launcher

In the framework of a study sponsored by ESTEC (Ref 3) a multiwall TPS-panel was developed by DASA which was used as a candidate for a thermoacoustic test. The TPS-panel is considered to be taken from a reference vehicle (Fig. 8), the arrow indicating the reference location.

TSTO Reference Vehicle

Fig. 8 Reference Vehicle

Fig. 9 TPS-Panel built into PWT

Critical loadings occur during separation of the two stages with 700 °C surface temperature and sound pressure levels up to 165 dB and during reentry of the upper stage with 1000 °C surface temperature and an OASPL = 140 dB. With the objective to simulate these environments the multiwall panel was installed into the thermoacoustic PWT according to Fig. 9.

Fig. 10 shows the facility with the burners alighted, the test window, however, is still open. In the next step the PWT will be closed and the airflow started. Temperature rise on the panel surface will be observed until the specified values are reached. Finally the noise generators are activated over a predetermined time duration.

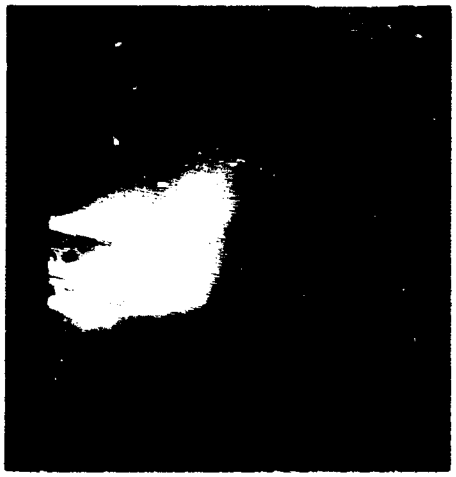

Fig. 10 Burners in PWT being alighted

Acknowledgements

The development of the thermoacoustic facility was sponsored by the Bundesminister für Forschung und Technologie (BMFT) and the Deutsche Agentur für Raumfahrt-Angelegenheiten (DARA) which is highly appreciated.

References:

(1) Rucker C.E., Grandle R.E.
Testing of Space Shuttle Thermal Protection System Panels under simulated Reentry Thermoacoustic Conditions
Seventh Space Simulation Conference
Los Angeles 1973

(2) Bayerdörfer G.
Development of a Thermoacoustic Test Facility
ESA-Conference "Spacecraft Structures and Mechanical Testing", October 1988

(3) Study on Thermal Protection for Advanced Launchers
ESA-ESTEC-Presentation prepared by DASA, ALENIA, ARCS and IABG, February 1994

NONLINEAR DYNAMIC RESPONSE OF AIRCRAFT STRUCTURES TO ACOUSTIC EXCITATION

H.F. Wolfe
WL/FIBG Bldg 24C
2145 Fifth St Ste 2
Wright-Patterson Air Force Base, Ohio 45433-7006, USA
and
R.G. White
Institute of Sound and Vibration Research, University of Southampton
Southampton, SO9 5NH, UK

SUMMARY

Acoustic fatigue failure in aerospace structures has been a concern for many years. New prediction techniques are needed for the new materials and structural concepts of interest and higher sound pressure levels encountered. The objective of this program of work is to improve the fundamental understanding of the nonlinear behavior of beams and plates excited from low to high levels of excitation. Experiments have been conducted utilizing a clamped-clamped (C-C) beam statically tested and shaker driven at increasing levels of excitation. Similarly, C-C-C-C plates were excited by a vibration shaker and in a progressive wave tube. The total strains and the components, bending and axial and the displacements were measured with increasing levels of excitation. Bistable behavior was observed with sinusoidal excitation for both the beams and plates. The measured axial or membrane strains were very low compared to the bending strains for high levels of excitation. The beams randomly excited exhibited a slight frequency shift and peak broadening, which can be attributed to an increased stiffening or hard spring nonlinearity. The plates randomly excited exhibited a greater frequency shift and peak broadening than the beams. The dynamic tests resulted in a nonlinear relationship between the response strains and displacements and the excitation levels. A multimodal model is discussed to estimate the mean square stress response due to high levels of excitation.

INTRODUCTION

Acoustic fatigue problems with military aircraft structures have continued to be expensive to solve. Results of modifications to older aircraft, changes in their usage to accommodate new weapons and equipment, extended usage and lifetimes have all had a significant cost impact. Increased performance capabilities also result in increased acoustic levels. Aircraft designs resulting in direct exhaust gas impingement on structural components have caused increased levels of excitaiton and high termal loads. Flow separation and oscillating shock waves cause very high fluctuating pressure on the structures. Expose to aircraft structures and equipment to these increasing higher noise levels warrants the development of new prediction methods. Methods have been developed over the years to predict and reduce acoustic fatigue, but they have not kept pace with increasing requirements. In addition, future structural configurations with new materials and much higher stiffness-to-weight ratios are evolving. A better understanding of the nonlinear random vibrational response of structures is needed to improve the prediction of acoustic fatigue damage.

The objective of this study was to improve the understanding of the nonlinear behavior of C-C beams and plates exited to high levels of vibration. The prediction of aeroacoustic and thermal loads and fatigue failure are not included. The focus was the development of methods to predict the nonlinear response of simple structures.

Presented at a Symposium on 'Impact of Acoustic Loads on Aircraft Structures' held in Lillehammer, Norway, May 1994.

BACKGROUND

Various design guides for predicting the acoustic fatigue life of metallic and some composite plate-type structures using semi-emperical mathematical expressions and design nomographs have been developed (Ref 1). The predictions are based upon assuming the fundamental mode as the controlling parameter which simplified the analysis. Miner's law and cumulative damage theory and a range of experimental results from various structures were utilized. Design guides were continued, such as those of the Engineering Science Data Unit (ESDU) in London, UK, and updated periodically for use in the government and aerospace industry. Some acousitc fatigue design characteristics for composite materials have been developed using the single-mode assumption, semi-empirical formula established from a statistical analysis of a range of experimental test data (Ref 2). The importance of multi-modal effects was observed in tests involving higher excitation levels (Ref 3). Although the above methods include nonlinear effects up to the limits of the test facilities used, there is a growing interest in higher sound pressure levels and anisotropic materials.

A series of experimental investigations were conducted using beams and plates to understand the nonlinear dynamic behavior. Clamped aluminum alloy and carbon fiber reinforeced plastic (CFRP) beams, pinned beams, and clamped plates were investigated. Linear mode shapes and nonlinear displacement shapes were studied. The response due to random excitation was investigated. For forced vibration studies of beams, electromagnetic coils and annular permanent magnets were used. For the plate studies, a large vibration shaker and acoustic progressive wave tubes (APWT) were used. More details can be found in References 4 and 5.

Both C-C beams exhibited a slight frequency shift and peak broadening. Bistable response (jump phenomena) was obtained with sinusoidal excitation of both types of materials. This occurred when the excitation amplitute was constant and the frequency was swept upward or downward around the fundammental resonant frequancy and when the frequency was constant and the amplitude was increased or decreased. The total strains and the components, bending and axial and the displacements were measured with increasing levels of excitation. The measured axial or membrane strains were very low compared to the bending strains for high levels of excitation. The axial fundamental frequency response was twice that of the bending mode and always positive. Both beams randomly excited exhibited a slight frequency shift and peak broadening, which can be attributed to an increased stiffening or hard spring nonlinearity.

The static strain response of both CFRP beams did not exhibit a nonlinear response as great as the dynamic case with sinusoidal and random excitations.

For high level acoustical excitation of a C-C-C-C plate, the modal frequencies were less pronounced than for low level excitation. Higher modes than the fundamental contributed significantly to the overall induced response. Multimodal effects become more significant at high levels of excitation.

Modal analysis theory is generally based upon linear assumptions where mode shapes are amplitude independent and occur at a single frequency. In the nonlinear case, the displacement shapes and natural frequencies are dependent upon the boundary conditions, the level of the excitation force and the initial conditions.

The study of structural mode shapes has grown considerably over recent years. Development in instruments, computers and testing techniques have resulted in detailed data describing structural response. Nonlinear displacement shapes have been obtained experimentally tor three beam configurations which were sinusoidally excited (Ref 6). Scanning laser vibrometers were utilized to measure the surface velocities which were integrated to yield displacements. Various curve fitting methods were used to smooth the displacement data and provide a mathematical function representing the deflected shapes. The axial strain can be obtained from the elongation obtained from displacement function. The bending strain can be obtained from the second derivative of the function. Three beam cases were analyzed which showed close agreement with strain gauge measurements. Accuracy of the vibrometer method was dependent upon the curve smoothing process used. The linear classical solutions of the equations of motion were not accurate functions to describe the nonlinear displacement shapes. These equations included the summation of sine, cosine, hyperbolic sine and hyperbolic cosine terms. Fourth order polynominals were more accurate for the clamped beam case. A Gaussian function was more accurate for the pinned beam case.

THEORETICAL CONSIDERATIONS

Acoustic fatigue life prediction methods generally include predicting the acoustic loads, estimating the vibrational stress response of the structure and predicting the life from stress versus cycles to failure curves for the material and fastener configuration. As the acoustic load increases, the stress response becomes more nonlinear and very difficult to predict.

The theory of nonlinear random vibration has not reached a state of maturity. Although many methods of solution exist, there can be no general rule about the suitability of any method for a particular nonlinear system (Ref 7). Most theories for the dynamic response of beams and plates for geometric nonlinearities were based upon the Duffing equation or equations of motion with some nonlinear stiffness terms or term. Among the most widely used are the Fokker-Planck equation solutions, perturbation methods, equivalent stochastic linearization, stochastic averaging, cumulant-neglect closure, energy dissipation balancing and the time domain Monte Carlo approach (Ref 8). Two types of excitation are usually considered: deterministic and random excitation. The nonlinear deterministic or sinusoidal cases results in a jump phenomenon. The random excitation case usually results in stochastic chaos.

The identification of mathematical models to represent dynamic systems in general has attracted considerable attention in recent years. Identification of nonlinear systems ranges from methods simply to detect the presence or type of a nonlinear to those which seek to quantify the behavior via some mathematical models.

Benamar, White and Brennouna studied the effect of large amplitudes on the fundamental mode shapes of fully clamped plates. They studied aluminum alloy plates both experimentally and theoretically which resulted in a high degree of geometrical nonlinearity. This was attributed to high in-plane stiffnesses, inducing a higher contribution of the axial strain energy to the total strain energy at large displacement amplitudes. Even higher nonlinearities were obtained with composite plates.

Mei formulated the displacement and stress relationships for C-C plates based upon equivalent linearization methods (Ref 10). By including the in-plane stretching effect in the bending formulation, the nonlinear deflections and stresses were found to be much less than linear theory at the higher levels of excitation. The total strain at the surface is based upon the sum of the bending and axial strain. Small deflection linear bending theory neglects the strain in the mid plane. In cases where the deflections are small in comparison with the thickness of the plate, linear bending theory is usually adequate (Ref 11). For higher load values, the rate of increase of the deflection with increasing load decreases due to the increased resistance by the tensile forces in the midplane of the plate.

It has been useful to study various nonlinear beam and plate theories. Although practical boundary conditions differ from those generally considered in theory, they provide a range of solutions which are useful in estimating the response of practical structures.

A form of the maximum mean square stress in a plate acoustically excited (Ref 1) may be expressed as:

$$\sigma^2 (t) = \frac{\pi}{4\zeta} f_n \, G_x(f_n) \, \sigma_o^2$$

where σ is the static stress, $G_x (f_n)$ is sound power spectral density, f_n is resonant frequency, ζ is damping ratio, and t is time. This equation uses only the first mode response and assumes that the static and dynamic deflected shapes are identical and that the acoustic pressures is in phase over the whole panel. The first, third and fifth vibration modes seemed to be the predominate modes found from the results of the acoustic progressive wave tube test of plates. Assuming the first, third and fifth modes are the major contributing sources of response, an extimate of the total mean square stress may be expressed as:

$$\sigma^2 = A_1 \frac{\pi}{4\zeta_1} f_1 \, G(f_1) \, \sigma_1^2 + A_3 \frac{\pi}{4\zeta_3} f_3 \, G(f_3) \, \sigma_3^2 + A_5 \frac{\pi}{4\zeta_5} f_5 \, G(f_5) \, \sigma_5^2$$

where A is a coefficient and $A_1 + A_3 + A_5 =$ 100%. The static pressure assumption for the first mode is dependent upon the length, width and thickness of the plate. Further approximating the third and fifth modes as one third the length and one fifth the length would produce an estimate of their modal contribution. The critical part is determining the contributions of the higher order vibration modes with the coefficients A_1, A_3 and A_5. These can be estimated from the normalized integration of the strain spectral densities as discussed in the experimental section of this paper.

EXPERIMENTAL INVESTIGATIONS

Base excited shaker testing of clamped plates provides a convenient method of studying the geometric nonlinear response since it provides response transfer functions from well defined forcing functions. Modal coupling and the transfer of energy from one mode to another are important aspects to modeling the forced vibration plate response due to high levels of excitation.

Two types of materials were selected for testing: aluminum alloy 7075-T6 and carbon fiber reinforced plastics (CFRP) Hercules AS4/3501-6 unidirectional prepreg with AS4 fibers in a 3501-6 matrix $(0°/\pm45°/90°)_S$. The unclamped size was 260 x 210 x 1.30 mm for the aluminum plate and 260 x 210 x 1.09 for the CFRP plate. The vibration shaker testing arrangement is shown in Fig 1 with the CFRP plate in the aluminum alloy clamping frame used for both plates. The frame was bolted to the shaker head. The shaker head was rotated to the vertical position to obtain a horizontal excitation force. This method was selected to prevent the mass of the panel from effecting the displacements and the strains measured. Strain gauges were bonded back-to-back to measure total, axial and bending strains as shown in Fig 2. Displacements were measured with a laser scanning vibrometer.

The linear frequencies of the aluminum alloy plate used in the shaker experiments were determined by exciting the plate sinusoidally with an acoustic driver. The modal frequencies found with the aluminum alloy plate were 230 Hz for the first mode, 365 and 485 Hz for the second modes and 618 and 864 Hz for the third modes.

Sine dwell aluminum alloy plate tests were conducted near the fundamental frequencies selected by sweeping slowly from below the fundamental frequency to a point just before the amplitude jumps down to a low level. The jump phenomenum was observed when the fundamental frequency increased from 228.9 to 245.9 Hz as shown in Figs 3 indicating a hardspring nonlinearity.

Random response tests were conducted with a spectrum controller programmed for a flat spectrum shape from 10-1000 Hz. Examples of the excitation spectral densities are shown in Fig 4. This frequency band included combinations of the first through the third modes. The strain responses are shown in Fig 5 for the five strain gauge locations and the displacements at the center of the plate. The highest strain measured was located at the center of the longer side of plate near the clamping frame, strain gauge location 2. The total, axial and bending strains measured for strain gauges locations 2 and 7 are shown in Fig 6. The axial strain was 4.56% of the total strain. The relationship between the total strains at five locations and displacement is shown in Fig 7. This relationship is nonlinear at small displacements. The total strain spectral densities are shown in Fig 8 for location 2. Large strain responses occured around 220, 670 and 900 Hz with peak broadening and shifting to higher frequencies which is indicative of geometrical nonlinearities. The strain spectral densities for total, axial and bending at low levels and high levels of excitation are shown in Figs 9 and 10. The axial or inplane stretching effect occurs at twice the bending resonant frequencies. Over most of the frequency band the bending and total strain spectral densities were about equal except at the high level. The axial strain response was higher than the bending around 460 Hz. This results in a higher total strain response around the axial fundamental mode. The displacement spectral densities are shown in Fig 11, which are similar to the total strain spectral densities except for the relative amplitudes of the higher order modes. One indication of the modal contribution of the strain response can be obtained by integrating mathematically the strain spectral densities and normalizing. An example of this is shown in Fig 12 for the total strain at location 2, where the fundamental mode contributes about 82% of the total frequency response.

The linear modal frequencies of the CFRP plate were also determined by sinusoidally exciting the plate acoustically. The modal frequencies found were 139 Hz for the first mode, 147 and 374 Hz for the second modes and 223 and 865 Hz for the third modes.

Sine dwell CFRP plate tests were conducted similar to the aluminum alloy plate tests. The jump phenomenum was observed when the fundamental frequency increased from 147.5 Hz to 188.7 Hz as shown in Fig 13, which were about 24% lower in frequency than the aluminum plate.

The strain responses are shown in Fig 14 for the random excitation case of the CFRP plate. Very similar overall strain responses to the aluminum case were obtained. The total, axial and bending strains measured for strain locations 2 and 7 are shown in Fig 15. The axial strain was 7.47% of the total strain, almost twice that of the aluminum case. The strain and displacement relationships are shown in Fig 16 which are similar to the aluminum case. The total strain spectral densities are shown in Fig 17. Large strain responses occured around 200, 400 and 900 Hz. The strain spectral densities for total, axial and bending at the low level and high levels of excitation are shown in Figs 18 and 19. The displacement spectral densities are shown in Fig 20, which appear to have more modes than the aluminum case. The integration of the strain spectral densities are shown in Fig 21. The fundamental mode contributes to about 92% of the total frequency response, which was higher than the aluminum case.

Some trends observed in the linear mode shape analysis of the types of plates were noted. The fundamental modal frequency was considerably higher in the aluminum case. This can be attributed to the higher mass density and greater thickness than the CFRP panel. The results of the second, third and fourth modes were unclear, primarily due to the modal coupling. The frequency response was very sensitive to small changes in boundary conditions, temperature, geometry, and material properties.

Some trends observed in the nonlinear mode shape analysis of the two types of plates excited sinusoidally were noted. The range of frequency response was much higher for the CFRP plate than the aluminum plate for the same range of displacements. The CFRP plate exhibited a greater hard spring nonlinearity. Much greater excitation was needed for the CFRP plate which can be attributed to the smaller mass due to a smaller thickness.

Some trends observed in the nonlinear random response of the two types of plates excited were noted. The overall rms strain response levels and displacements were quite similiar with the two plates which have quite different thickness and densities. Major differences were noted in the levels of the axial strains. The aluminum plate were much lower than the CFRP plate. The strain and displacement relationship were quite similar. The spectral content from the strain spectral densities was different. The CFRP plate exhibited more modes and more peak broadening as the excitation level increased than the aluminum plate. This was also the case for the displacement spectral densities. The integrals of the strain spectral densities exhibited less contribution from the first mode for the aluminum case than the CFRP case. The higher modes for the CFRP case were more smeared with no well defined step beyond the fundamental mode.

CONCLUSIONS

1. A comparison between the aluminum alloy plate sinusoidal response around response around the fundamental modal and that of the CFRP plate indicated a greater hard spring nonlinearity in the CFRP plate. The nonlinear displacement shapes extended over a greater frequency range than the CFRP plate.

2. The CFRP plate randomly excited exhibited a greater number of modal response frequencies and more peak broadening than that exhibited by the aluminum alloy plate. The fundamental nonlinear modal response of the CFRP plate contributed more heavily to the overall response spectrum than the aluminum plate.

3. The contribution of higher order modes of plate response is greater as the level of excitation increased. These should be considered in future prediction models.

References

1. Thomson, A.G.R. and Lambert, R.F. "Acoustics fatigue design data", AGARD-AG162-Part I, II, III, and IV, Advisory Group for Aerospace Research and Development, 7 Rue Ancelle 92200 Neuilly Seine France, 1972-1975.

2. Holehouse, I. "Sonic fatigue design guide techniques for advanced composite airplane structures", PhD Thesis University of Southampton, UK, 1984.

3. Galea, S.C.P., "Effects of temperature on acoustically induced strains and damage propagation in CFRP plates", PhD Thesis University of Southampton, UK, 1989.

4. Wolfe, H. F. and White R. G. , "Nonlinear response of a clamped beam and plate to high levels of excitation." DGLC/AIAA 14TH Aeroacoustics conference, Aachen, Germany DGLR/AIAA 92-02-019, 1992,

5. Wolfe, H. F. and White R. G., "Experimental studies of the nonlinear dynamic behavior of clamped-clamped aluminum and carbon fiber reinforced plastic beams at large deflections", 1993 15th AIAA Aeroacoustics conference, Long Beach, CA, AIAA 93-4336.

6. Wolfe, H. F., and White, R. G., "Experimental and analytical studies of nonlinear displacement shape of three straight beams: clamped-clamped aluminum and carbon fiber reinforced plastic beams and a pinned-pinned aluminum beam", Structural Dynamics: Recent Advances, Proceedings of the Fifth International Conference, July 1994 (to be published).

7. Ibrahim, R. A., "Nonlinear random vibration experimental results and research needs", Structural Dynamics: Recent Advances, Proceedings of the Fourth International Conference, July 1991, Elsevier Applied Science, London and NY ISBN 1-85-2660-670-2, pp 58-83.

8. Vaicaitis, R., "Recent advances of time domain approach for nonlinear response and sonic fatigue", Structural Dynamics: Recent Advances, Proceedings of the Fourth International Conference, July 1991, Elsevier Applied Science, London and NY ISBN I-85-2660-670-2, pp 84-104.

9. Benamar, R., White, R. G., Bennouna, M. M. K., "The effects of large vibration amplitudes on the fundamental mode shape of a fully clamped, symmetrically laminated; rectangular plate", Structural Dynamics: Recent Advances, Proceedings of the Fourth International Conference, July 1991, Elsevier Applied Science, London and NY ISBN I-85-2660-670-2, pp 749-760.

10. Mei, C., and Wentz, K. R., "Analytical and experimental nonlinear response of rectangular panels to acoustic excitation", AIAA/ASME/ASCE/AHE 23rd Structure, Structural Dynamics and Materials Conference, New Orleans, LA, 1982, pp 514-520.

11. Timoshenko, S. and Woinowsky-Krieger, S., Theory of Plates and Shells, McGraw-Hill Book Company, 1959, pp 396-428.

Fig 3 Acceleration vs Strain and Displacement, Sine Dwell Aluminum Plate

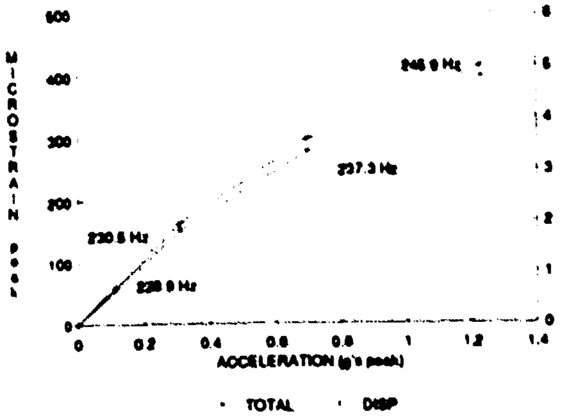

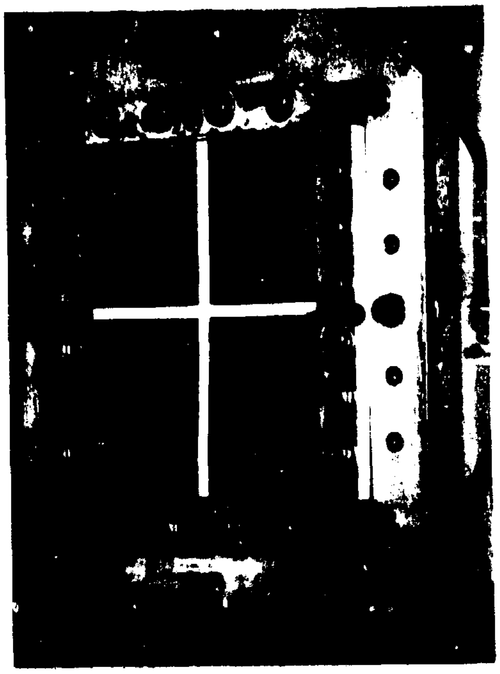

Fig 1 Vibration Shaker Test Plate Installation

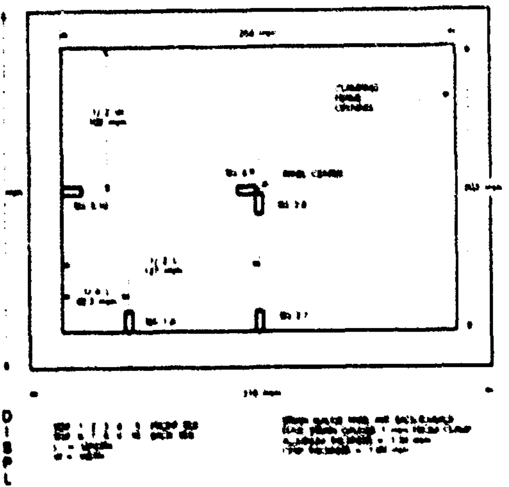

Fig 2 Strain Gauge Locations, Shaker Tests

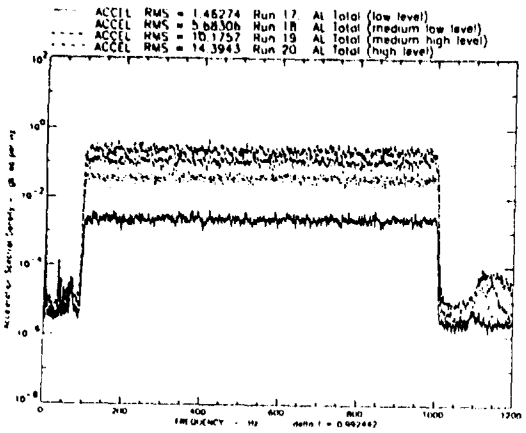

Fig 4 Acceleration Spectral Density

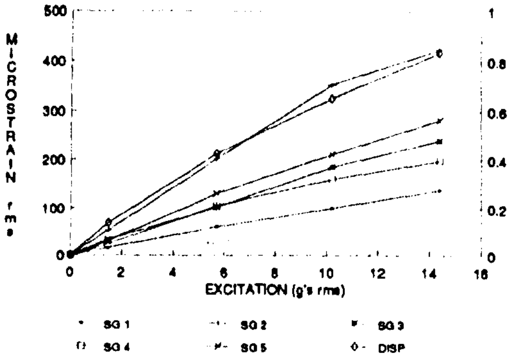

Fig 5 Excitation vs Strain and Displacement, Random, Aluminum Plate

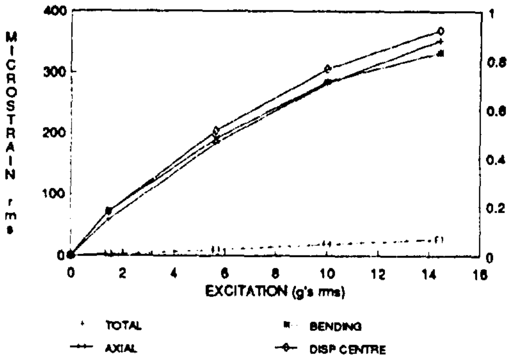

Fig 6 Total, Axial, Bending Strains, SG 2, Random, Aluminum Plate

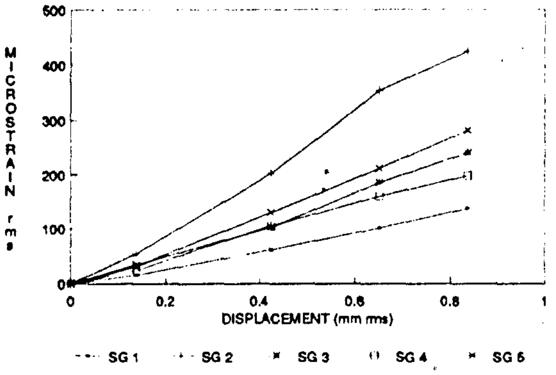

Fig 7 Displacement vs Strain, Random, Aluminum Plate

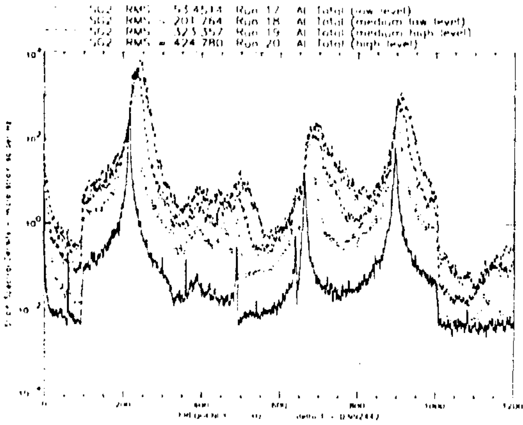

Fig 8 Strain Spectral Densities, SG 2, Random, Aluminum Plate

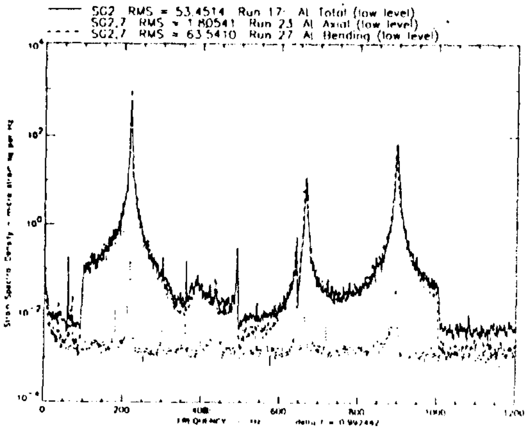

Fig 9 Strain Spectral Densities, SG 2, Total, Axial, Bending, Low Level, Random, Aluminum Plate

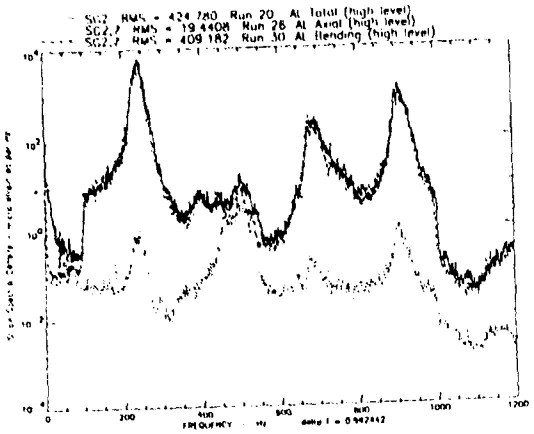

Fig 10 Strain Spectral Densities, SG 2, Total, Axial, Bending, High Level, Random, Aluminum Plate

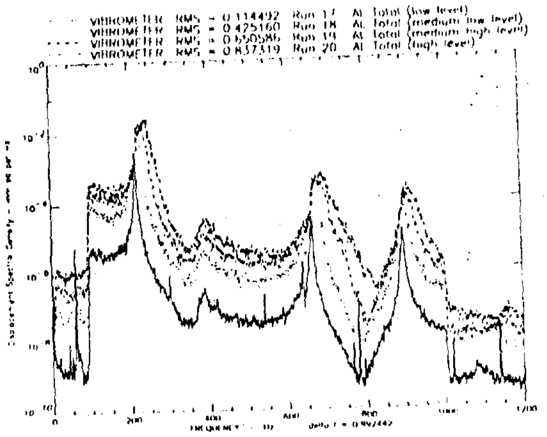

Fig 11 Displacement Spectral Densities, Random, Aluminum Plate

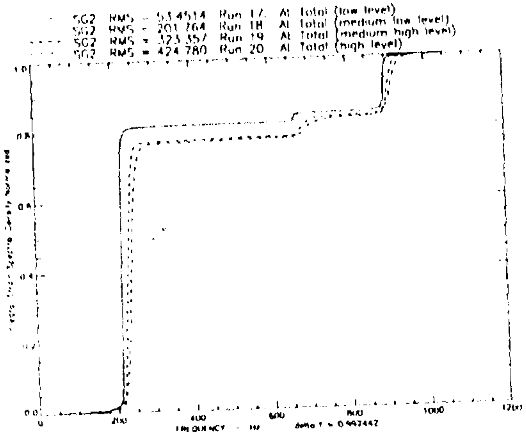

Fig 12 Integral Strain Spectral Density, SG 2, Random, Aluminum Plate

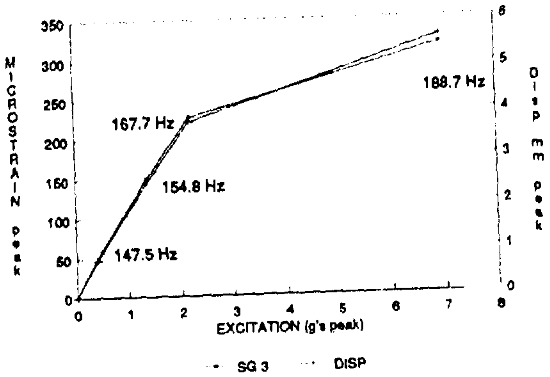

Fig 13 Acceleration vs Strain and Displacement, Sine Dwell, CFRP Plate

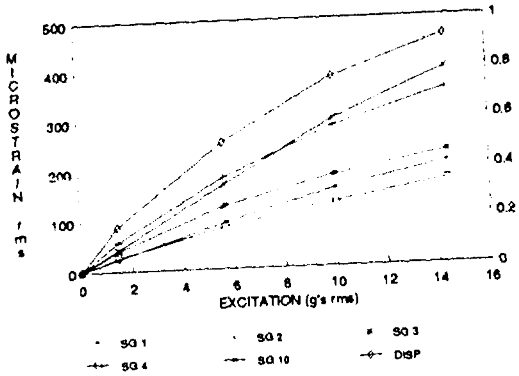

Fig 14 Excitation vs Strain and Displacement, Random, CFRP Plate

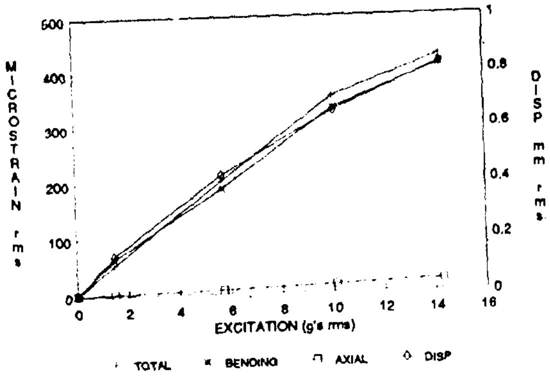

Fig 15 Total, Axial, Bending Strain, SG 2, Random, CFRP Plate

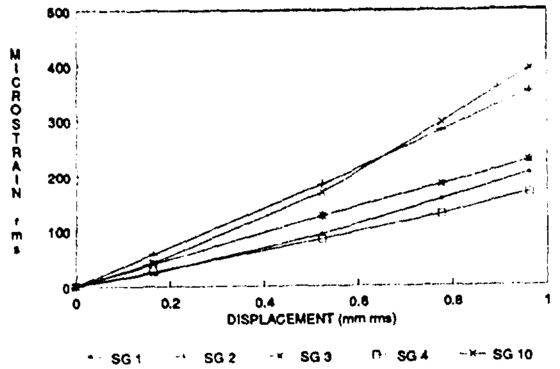

Fig 16 Displacement vs Strain, Random, CFRP Plate

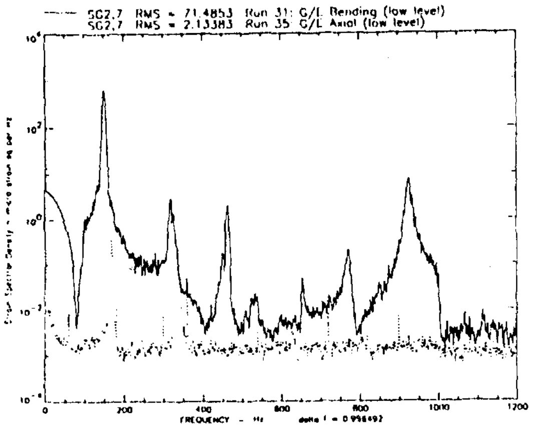

Fig 18 Strain Spectral Densities, Bending, Axial, Low Level, Random, CFRP Plate

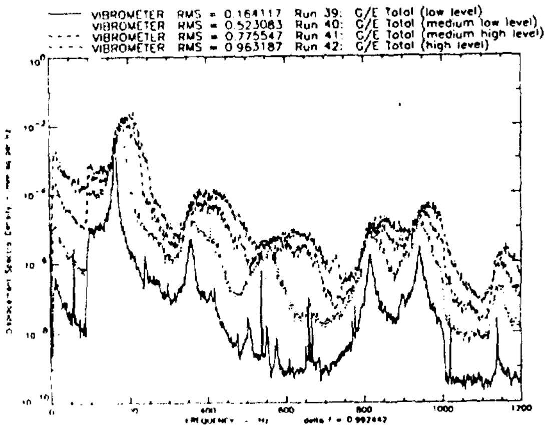

Fig 20 Displacement Spectral Densities, Random, CFRP Plate

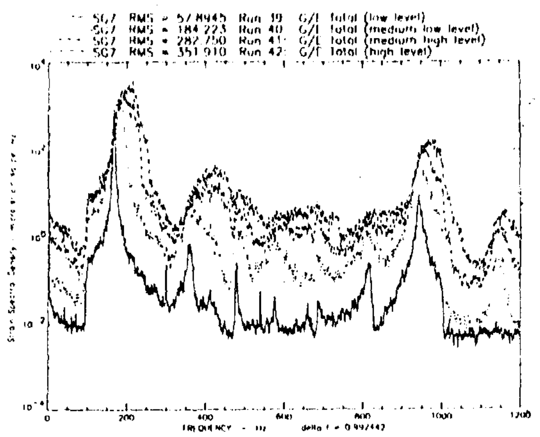

Fig 17 Strain Spectral Densities, SG 7, Random, CFRP Plate

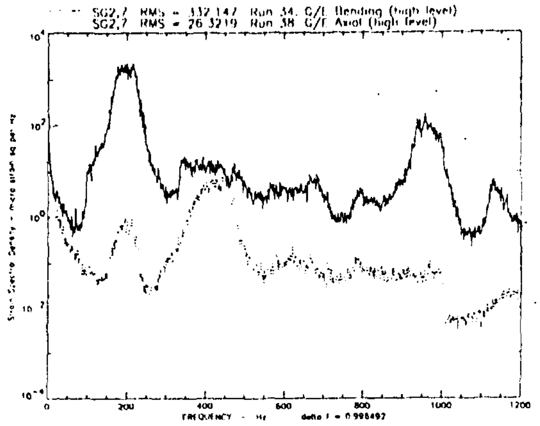

Fig 19 Strain Spectral Densities, Bending, Axial, High Level, Random, CFRP Plate

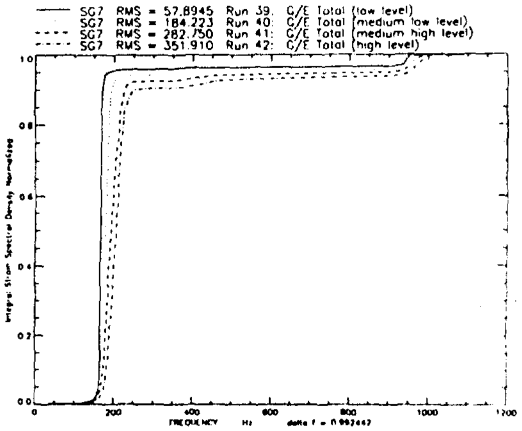

Fig 21 Integral Strain Spectral Density, SG 7, Random, CFRP Plate

ACOUSTICS OF SPACE STRUCTURES

P.Santini[1], F.Morganti[2], R.Giovannucci[1]

Work sponsored by Alenia Spazio and by the Italian Ministero per la Università e per
la ricerca scientifica e Tecnologica and by the Università di Roma " La Sapienza"

Abstract

The problem of the response of a panel belonging to a space structure or to a launcher is considered. By using modal approach in the frequency domain, the structure is described through a finite element model, and the acoustic field through Green's function. The presence of the air is considered, and it leads to the addition to the mass matrix and to the damping matrix of the relevant terms. The transfer function is then applied to the case of random inputs, for which an analytical expression is provided. Some numerical examples show the effect of the additional terms on the spectral distribution and on the relevant RMS value.

List of symbols

λ_a: acoustic wavelength
λ_b: transversal bending wavelength
ω: frequency dummy variable
Ω^2: diagonal matrix of the squared eigenvalues
$q(\omega)$: generalized coordinates vector
Q: eigenvector matrix
$M_a(\omega)$: equivalent air mass
$C_a(\omega)$: radiation damping
$H(\omega)$: complex frequency response
$S_{\ddot{u}}(\omega)$: acceleration PSD
$S_L(\omega)$: PSD of the generalized acoustic input
$S_P(\omega)$: PSD of the far field acoustic input
$J^2(\omega)$: cross-joint acceptance matrix
ρ: air density
$\sigma(x_m, x_n, \omega)$: reverberant field correlation matrix
c: speed of sound
$\hat{\psi}$: Fourier Transform of ψ
ψ^*: complex conjugate of ψ
S_0: radiating surface

1 - Introduction

Modern trend of space and launchers structures shows an increasing evolution towards lightweight, large area surfaces. This circumstance, associated with the broadband frequency environment of space structures, makes it necessary to:

(i) control the random vibrations level produced by the acoustic environment on the structural units installed on the outer parts (e.g., external panels and/or large flexible appendages, such as, f.i., antennas on a satellite);

(ii) predict with sufficient accuracy the dynamic behaviour of such structures under the action of diffuse sound fields;

Two basic approaches are generally used in this area, depending on the frequency domain to be considered. For high frequencies, the so called SEA (Statististical Energy Approach) is used [1], which provides global information on the quantities of interest (frequencies bandwidth averages) and is valid for high modal density only. This method is generally not sufficiently accurate for medium/low frequencies. At low frequencies the structure can be accurately represented through its normal-modes, and the in-vacuum response is calculated via the classical modal approach. The fluid, on the other hand, can be modelled by using BEM (Boundary Elements Method) techniques, mainly in presence of complex structures and acoustical cavities. For extended flat configurations the model can be simplified as Green's function, analytically known and available for the case under concern.

The structural model must take into account the need for an accurate modal basis up to 2000 Hz, and it must be suitable for Green's function determination. Special attention must be (and was) paid to the size of the elements and to the boundary conditions in order to obtain sufficiently representative modes at high frequencies too. The response of the structure is thus calculated considering a random pressure field with correlation given by coherence functions valid in a reverberant environment.

As said, the effect of the air is simulated through Green's function in free space for the calculation of the radiated sound field (Helmholtz Equation). This simulation has provided results which are in good agreement with similar results taken from the current literature, [2], [3].

---

[1] Dipartimento Aerospaziale, Università di Roma
[2] Alenia Spazio SpA, Roma

Presented at a Symposium on 'Impact of Acoustic Loads on Aircraft Structures' held in Lillehammer, Norway, May 1994.

The reasons for the choices as described above are essentially of a practical kind; they are aimed to obtaining an efficient method, minimizing computing time, and taking advantage from FEM models already used during the development of the design phase.

2 - Modal superposition approach

Using the modal superposition approach, as well known, the equation of dynamic equilibrium for a discretized system with N degrees of freedom reads:

$$M\ddot{x} + C\dot{x} + Rx = F(t) \qquad (1)$$

with x = state vector, and M, C, R = mass, damping and stiff matrices respectively. By introducing the modal matrix Q and the vector of modal amplitudes $q(t)$, and taking Fourier 's transform of (1), we have the equation of the structure in the frequency domain:

$$[-\omega^2 I + j\omega C + \Omega^2]\overline{q}(\omega) = Q^T\overline{F}(\omega) \qquad (2)$$

In order to take into account the presence of air, the acoustic field is expressed as the sum of two terms: the first is the pressure that would exist if the structure were replaced by a rigid body (field pressure p_T); the second term is the pressure irradiated by the vibrating flexible structure in the absence of an external acoustic source (radiated pressure p_R) [4], [5]. So we can write:

$$Q^T\overline{F}(\omega) = -Q^T\overline{p}_T(\omega) + Q^T\overline{p}_R(\omega) \qquad (3)$$

3 - Relevant acoustic principles

Starting from Helmholtz' equation [5], [6]:

$$\nabla^2\overline{p} + k^2\overline{p} = 0 \qquad (4)$$

(where $k = \frac{\omega}{c}$ wave number), and using Green's function between points R and R_0:

$$g(|R - R_0|) = -\frac{e^{jk|R-R_0|}}{4\pi|R - R_0|} \qquad (5)$$

one obtains Helmholtz' integral equation:

$$p(R) = -\int_{S_0}(p\frac{\partial g}{\partial \xi} + \rho\ddot{w}g)dS_0 \qquad (6)$$

For some special configurations of the source the component associated with the surface integral disappears, and an explicit expression for the pressure field in terms of a given surface acceleration is obtained as:

$$p(R) = -\rho\int_{S_0} g|R - R_0|\ddot{w}(R_0)dS_0 \qquad (7)$$

For an infinite flat surface this can be written:

$$p(R) = 2\rho\int_{S_0}\ddot{w}(R_0)\frac{e^{jk|R-R_0|}}{4\pi|R - R_0|}dS_0 \qquad (8)$$

The above expression gives a good estimate also for vibrating surfaces sufficiently wide as compared with acoustic wavelengths, (except, of course, near the edges).

4 - Complex frequency response

The complex frequency response is calculated considering the presence of the air as simulated by an equivalent additional mass and by an equivalent damping to be added to mechanical structural damping [4].

For a discretized flat structure in the frequency domain the radiated pressure at a specific point x_m reads:

$$p_R(x_m, \omega) = 2\rho\omega^2\sum_{n=1}^{N}\lambda_n\delta_n\frac{e^{jkr_{mn}}}{4\pi r_{mn}}A_n \qquad (9)$$

where $\delta_n = \sum_{s=1}^{N} Q_{ns} q_s(\omega)$, A_n is the element surroundig P_n and the integral appearing in Eq.(8) has been replaced by the corresponding summation with weights λ_n, and the summation is extended over all the points P_n into which the system has been discretized.

Insertion of the above expression into the equation of motion (2) yields:

$$[-\omega^2(I + M_a(\omega)) + j\omega(C + C_a(\omega)) + \Omega^2]\bar{q} = Q_T f \tag{10}$$

where:

$$M_a(\omega) = 2\rho Q_T G_R Q$$

$$C_a(\omega) = -2\rho Q_T G_I Q$$

$$(G_R)_{m,n} = A_m A_n \frac{\cos kr_{mn}}{4\pi r_{mn}}$$

$$(G_I)_{m,n} = A_m A_n \frac{\sin kr_{mn}}{4\pi r_{mn}}$$

and A_m and A_n are the surface elements relevant to the points x_m and x_n respectively.

As is seen, and as said above, the effect of the air is that of an added mass (M_A) and of an added damping (C_a).

The frequency response (or, better, the transfer function of the structure) is therefore:

$$H(\omega) = \omega^2[-\omega^2(I+M_a(\omega))-2j\omega(C+C_a(\omega))+\Omega^2]^{-1} \tag{11}$$

It should be noticed that the matrices $M_a(\omega)$,$C_a(\omega)$ are not diagonal, as can be seen from the above definition. However, off-diagonal terms are generally very small, and they have been neglected.

5 - Random inputs

Random acoustic inputs (stationary ergodic) induce stochastic vibrations in the structure. Such inputs include loads arising from jet and rocket propulsion events, buffeting, etc., present mainly at take off. The response of the structure is therefore essentially of a statistical nature: f.i., for the acceleration PSD (Power Spectral Density) we have:

$$S_{\ddot{w}}(\omega) = QH(\omega)S_L(\omega)H^*(\omega)Q_T \tag{12}$$

and for the acceleration RMS:

$$a_{RMS} = \sqrt{\frac{1}{2\pi}\int_{-\infty}^{+\infty} S_{\ddot{w}}(\omega)d\omega} \tag{13}$$

In the foregoing equations, S_L is the PSD of the generalized input, given by:

$$\begin{aligned} S_L(\omega) &= Q_T \lim_{T\to\infty} \frac{\pi}{T} p(\omega)p^*(\omega)Q \\ &= S_P(\omega)Q_T\sigma(x_m, x_n, \omega)Q \\ &= S_P(\omega)J^2(\omega) \end{aligned} \tag{14}$$

Here S_P denotes the PSD in the far field of the input pressure; σ stands for the coherence matrix of the excitation (it measures the correlation between the input pressure, as measured at the various points of the field); $J^2(\omega)$ is the cross-joint acceptance, i.e., the part of the energy that each of the modes can extract from the acoustic field.

Many publications [2], [9], confirm that the firing of a missile has a reverberant acoustic behaviour in the whole frequency domain, so that we considered it as a diffuse pressure field, typical of reverberant rooms where [7], [8]:

$$\sigma(x_m, x_n, \omega) = \frac{\sin kr_{mn}}{kr_{mn}} \tag{15}$$

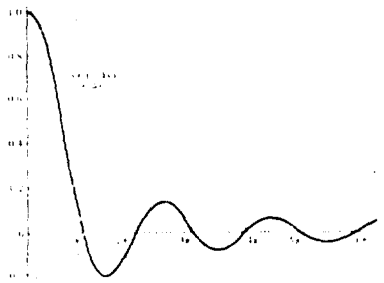

Fig.1 Reverberant field correlation

As an example, Fig. 2 provides a typical acoustic spectrum for the firing of Ariane 4. The spectral density of the input is shown in Tab.1.

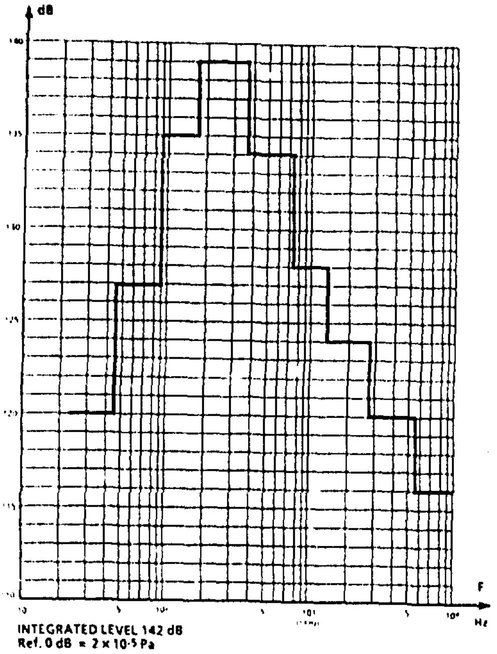

Fig.2 Acoustic spectrum at firing for Ariane 4 (from Arianespace, 1983)

Central frequency of octave (Hz)	Acoustic levels dB (Ref press 2x10-5 Pa)	Spectral density (Pa²/Hz)
31.5	121.5	25.4
63	131	179.2
125	135.8	172.0
250	139.6	206.4
500	142.5	201.2
1000	137.8	34.1
2000	132.5	5.0

Tab.1 Acoustic input data for Ariane 4 (from Arianespace, 1983)

6 - Illustrative examples

Illustrative tests were worked out for a rectangular honeycomb aluminum plate with flexural support and torsional restraint. The data are reported in Tab.2.

Honeycomb type	3/16 5052 007
Skin thickness	0.2 10^{-3} m
Honeycomb height	25 10^{-3}m
Panel lenght	2 m
Panel width	2 m

Tab.2 Data for illustrative example

The finite element model consists of 1200 elements (CQUAD4, CHEXA8), 882 grids, consistent mass option, all D.O.F. retained and the modes up to 1000 Hz were computed; this limit was chosen as the region where the intensity of the acoustic field is most intense, so as to reduce computing time as much as possible.

The mesh was chosen in such a way as to be consistent with the following requirements:

(i) to have representative modes up to 1000 Hz;

(ii) to have sufficiently small elements, so as to obtain high correlation values for the acoustic input.

(iii) in order to validate the 3-D finite element approach, a simplified analytical model was used, i.e., a simply supported rectangular plate including shear deformation and rotary inertia effects. Tab. 3 provides the relevant comparisons up to 800 Hz.

(iv) out-of-plate modes, associate with the finite rigidity of the structure normal to its plane, have no special interest for the work under concern, on account of their very high frequency.

Analitical model	Numerical model
34.3	34.4
85.4	85.5
85.4	85.5
135.9	135.6
169.3	169.9
169.3	169.9
219.0	220.6
219.0	220.6
284.5	285.5
284.5	285.5
300.7	302.1
333.0	333.1
333.0	333.1
412.8	411.8
412.8	411.8
428.6	429.9
428.6	429.9
475.7	475.1
475.7	475.1
522.4	519.3
555.3	519.3
555.3	561.1
599.3	597.4
599.3	597.4
644.0	647.5
644.0	647.5
659.9	659.4
659.9	659.4
719.0	712.2
719.0	712.2
793.8	792.6
793.8	792.6

Tab.3 Comparisons of the eigenfrequences of the analytical and numerical model

This has given rise to the following limitation:

(v) $\frac{\lambda_a}{2} < grid < \frac{\lambda_b}{2}$

Structural damping is assumed constant, and equal to .02.

Several configurations were analyzed in order to evaluate the influence of the surrounding air, of the mass and stiffness distribution, and of the variation of the acoustic input.

Fig.4 describes the variation of the first six diagonal elements of the matrix $M_a(\omega)$; Fig.5 shows the analogous values for the matrix $C_a(\omega)$. Fig.6 illustrates some quantities for other cases.

Fig.3 illustrates the grid used in the analysis. The following results are relevant to the points 111, 221, 325, shown in the same figure.

The effect of the air is obtained through comparison of Fig.7 vs. Fig.8, both providing spectral variation vs. frequency. We see that, at least for the case under concern, the change is for a factor of several unities (5 or more).

The same diagrams are shown in Figs.9, 10 for a panel having the same stiffness, but with a double structural mass. We see that the effect of the air is smaller, as it is natural.

Several other cases were worked out, that cannot be reported here for sake of brevity. From a thorough examination of the relevant results some general remarks can be made.

The presence of air caused reduction in the eigenfrequencies of the structure up to 15%; this is due to an increase of the mass matrix of the order of 10-30% and to an additional damping almost equal to the structural one.

The air mass participanting in the motion is little influenced by stiffness, whereas it decreasing with increasing structural mass, and with increasing frequency. Also radiation damping is strongly affected by the structural mass; it becomes particularly active at medium/high frequencies.

From a response viewpoint, consideration of the presence of air reduces acceleration peaks in PSD diagrams, so they are moved towards lower frequencies. On account of the different feature of the modal shapes, the response at the various points is different: this can be used for equipments positioning.

Finally, variations in stiffness allows modifications in structural frequencies, with a possible movement of PSD peaks to regions where input is less severe.

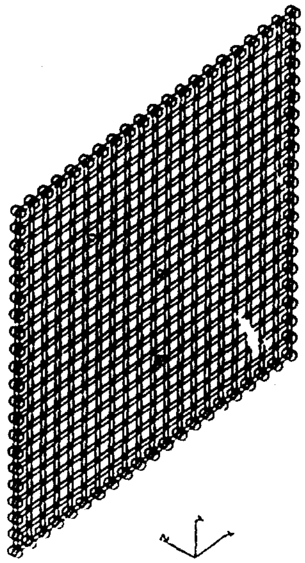

Fig.3 Grid used in the analysis

7 - Conclusions

(i) The behaviour of very light structures for space applications can be analyzed with good accuracy with the method presented in this paper.

(ii) Obtained results show the importance of the presence of air; neglecting it may lead to an overestimation of the response.

(iii) Numerical simulations have provided results in good agreement with the experimental results.

(iv) Limitations of the method arise from:

  (a) at very low frequencies the size of the panel is of the order of magnitude of the acoustic load, and the panel cannot be considered as 'baffled';

  (b) at high frequencies local deformations arise that cannot be described by finite element techniques;

  (c) for the acoustic modeling a highly fine mesh is necessary.

References

[1] R. H. Lyon, "Statistical Analysis of Power Injection and Response in Structures and Rooms", Jour. Acoust. Soc. Amer., 45(3), 545 (1969).

[2] D. C. G. Eaton, "The Use of Reverberant Room Acoustic for Spacecraft Structures and their Payloads", ESA SP 321 (Oct. 1991).

[3] J. Fowler, "Effect of Air Mass on Model Test", ESA SP 290.

[4] Lord Rayleigh, "The Theory of Sound", MacMillan 1896.

[5] M. C. Junger, D. Feit, "Sound, Structure and their Interaction", MIT Press 1986.

[6] F. Fahy, "Sound and Structural Vibration", Accademy Press 1985.

[7] A. Pierce, "Acoustics, an Introduction to its Phisical Principles and Applications", Mc Graw Hill 1981

[8] D. Lubman, "Spatial Averaging in a Diffuse Sound Field", Jour. Acoust. Soc. Amer., 46(3), 532 (1969).

[9] C. Clerc, "Acoustic Prediction on Satellite", ESA SP 321 (Oct. 1991).

[10] F. Morganti, "A Prediction Method to Evaluate the Acoustic Response of Spacecraft External Panels", IAF 91-288 1991.

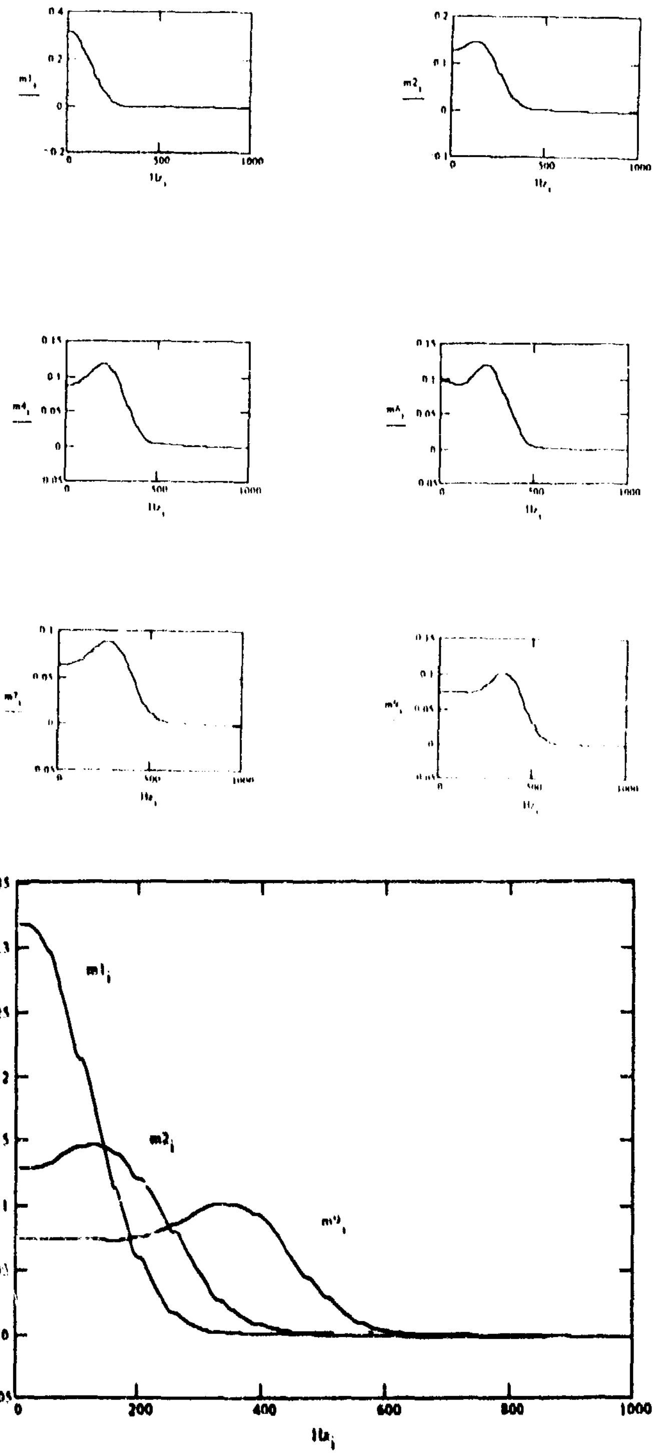

Fig.4 Non dimensional diagonal elements for the matrix M_a

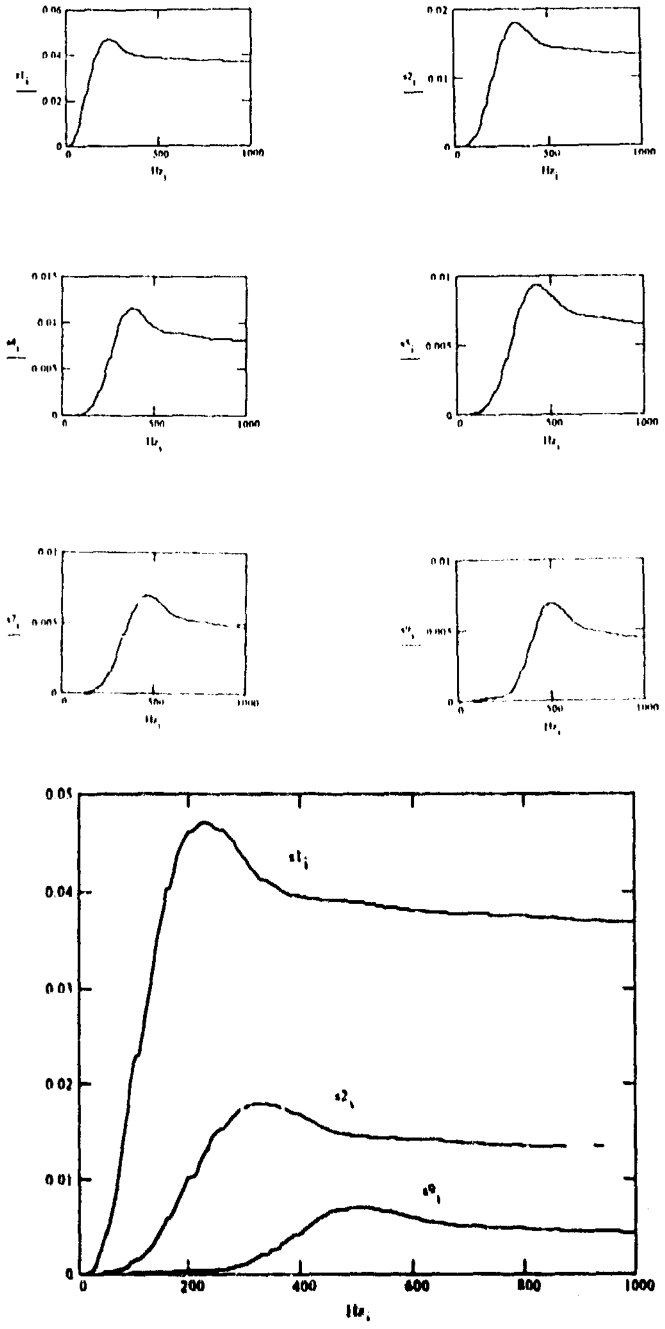

Fig.5 Non dimensional diagonal elements for the matrix C_a

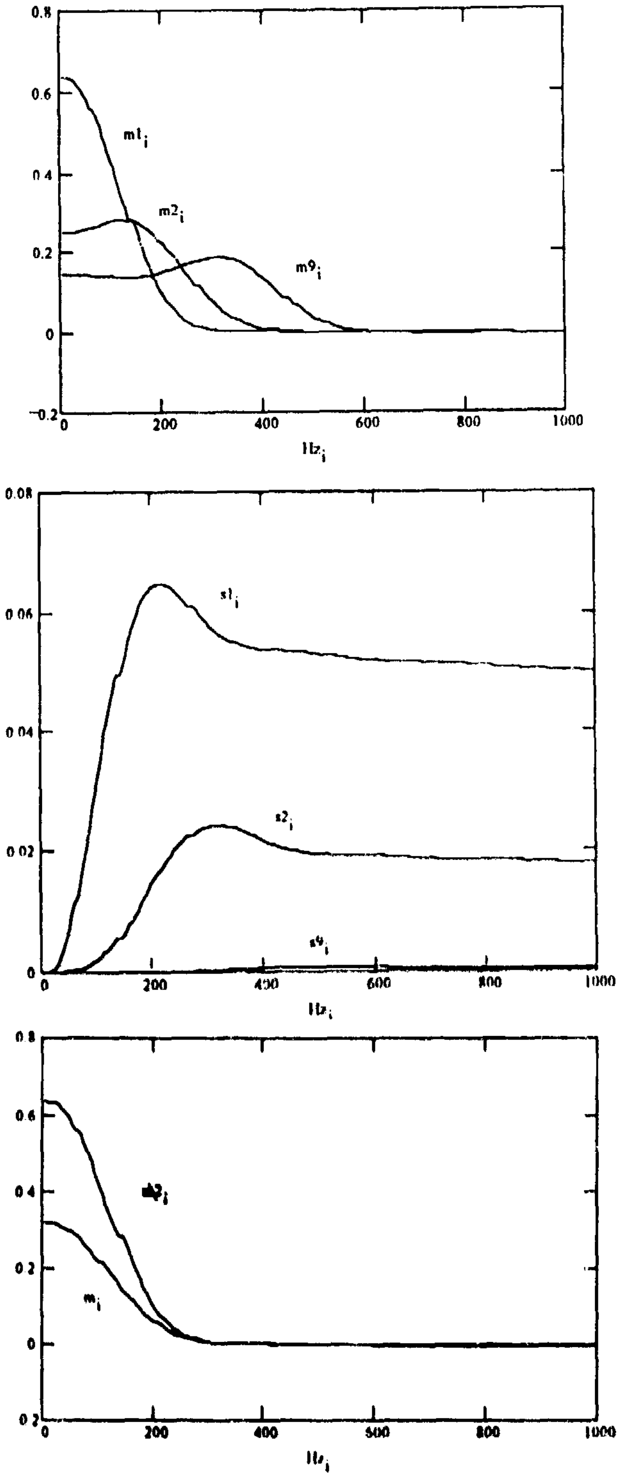

Fig.6 Effects of weight on mass and damping

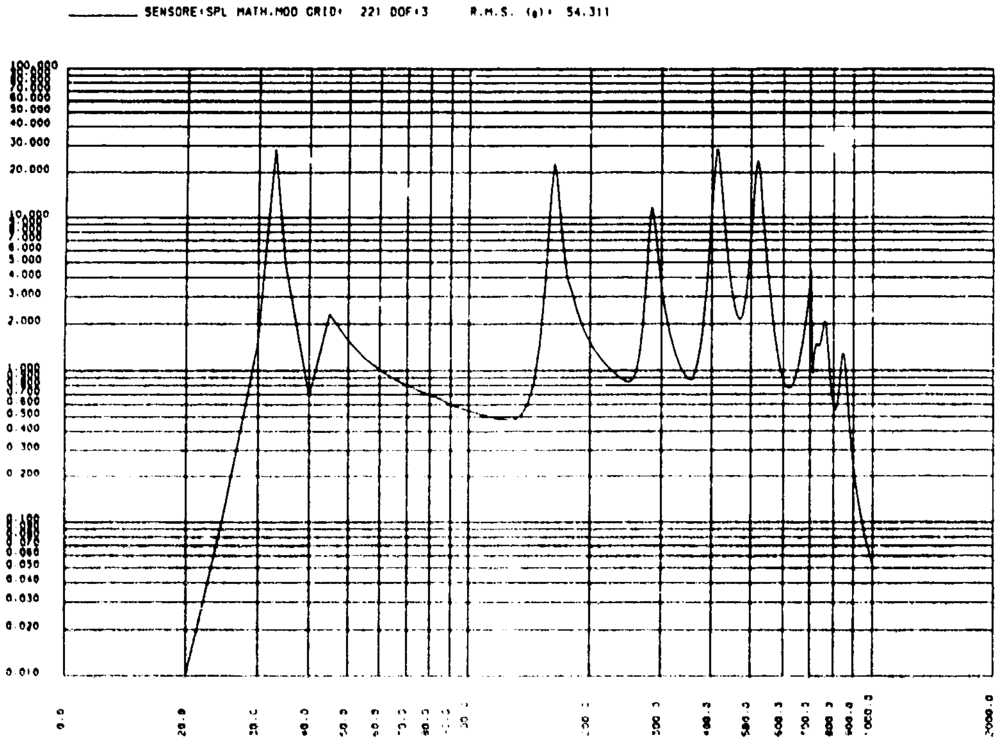

Fig.7 PSD for 3D plate without surrounding air

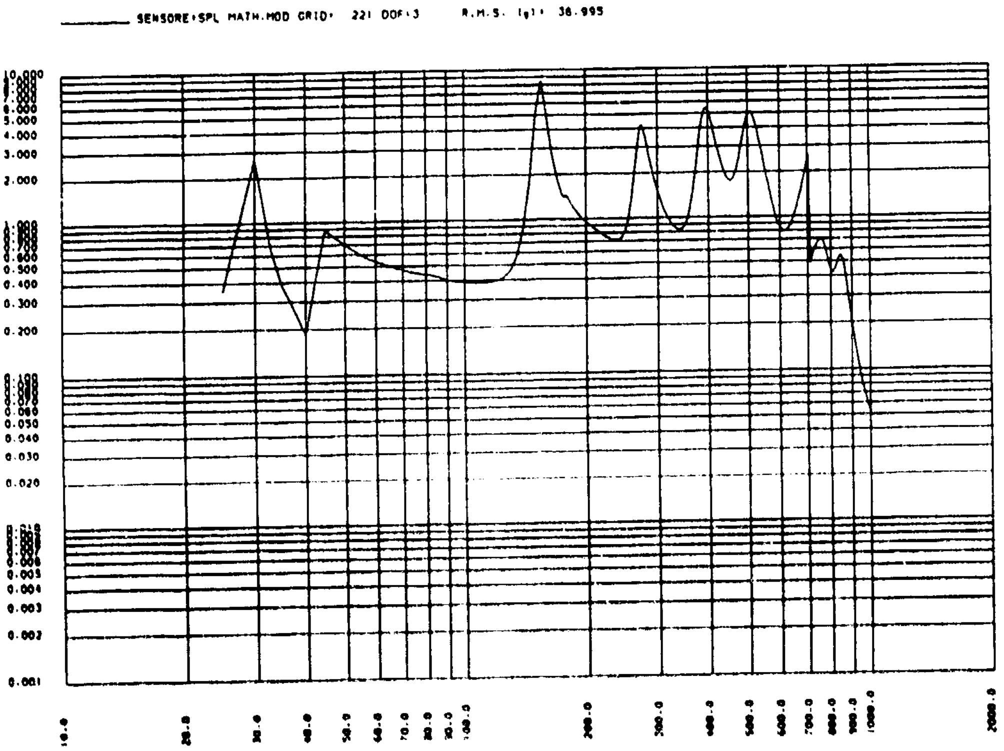

Fig.8 PSD for 3D plate with surrounding air

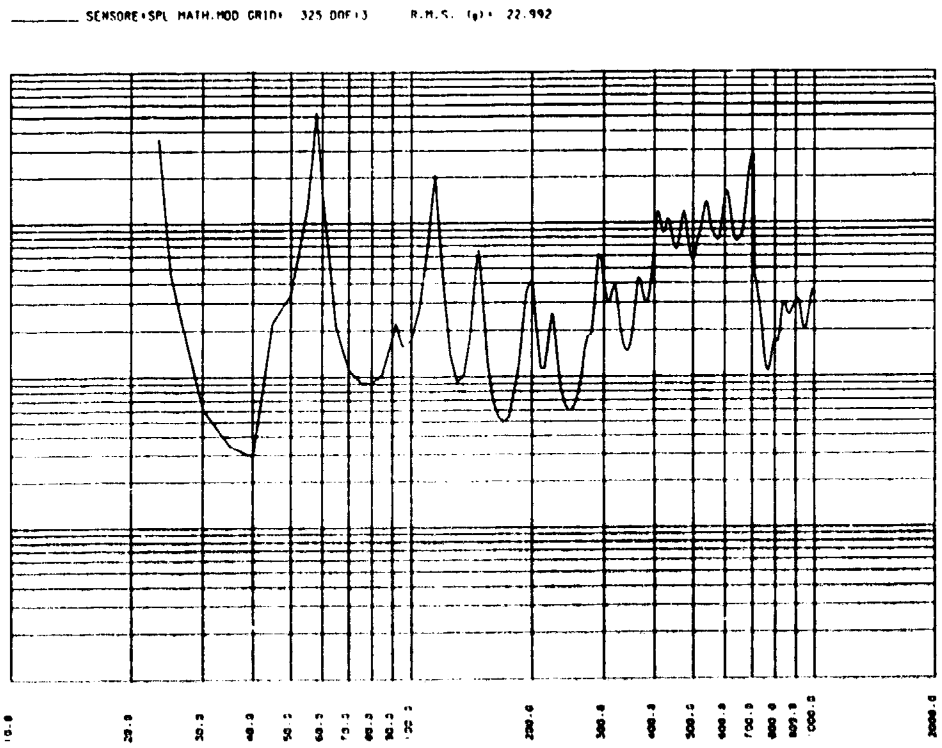

Fig.9 PSD for 3D plate without surrounding air (twice mass)

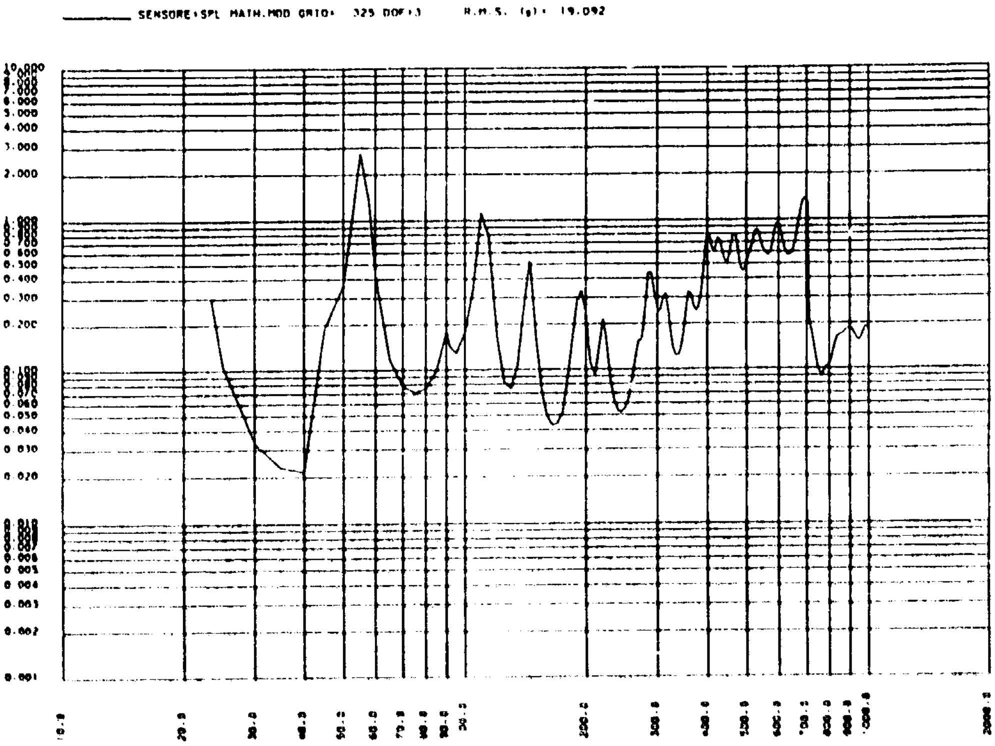

Fig.10 PSD for 3D plate with surrounding air (twice mass)

PREDICTION OF FLUCTUATING PRESSURE AND POWER SPECTRA IN ATTACHED AND SEPARATED COMPRESSIBLE FLOW

A. L. Laganelli

Science Applications International Corporation
Ft. Washington, PA, USA
and
K. R. Wentz
H. F. Wolfe
Rohr Incorporated MS 107X
850 Lagoon Drive
CHULA VISTA
California 91912-0878
UNITED STATES

SUMMARY

A brief review is presented of work by the authors to provide an engineering prediction technique for power intensity (rms fluctuating pressure) and power spectral density (PSD) for attached and separated compressible flow. The review process also considers recent shock/turbulent boundary layer interaction work conducted at the University of Texas at Mach 5. It is shown that prediction techniques are hampered as the result of the requirement to know parameters of flow interactions a priori; in particular, the choice of characteristic length and velocity scales. A technique is presented, based on the Houbolt spectra assumption, that appears to provide engineering solutions to the design resolution of complex flow problems. The method is based on a first moment type of PSD $[f.\phi(f)/(\hat{P}_{OA})^2]$ that has a fixed value for attached and separated flows. Moreover, when applying the concept with the Houbolt spectra, an excellent comparison is shown to PSD data for shock/turbulent boundary layer interactions.

List of Symbols

F_c	transformation function, Eq. (7)
f,ω	frequency
h	enthalpy
K	parameter, Eq. (2)
k'	parameter, Eqs. (2) and (4)
L_i	intermittent region length
M	Mach number
P_w	local boundary-layer static pressure
$\tilde{P},\hat{P}$	rms fluctuating pressure
q	dynamic pressure, $(\gamma/2)PM^2$
r	turbulent recovery factor, 0.896
u,v	velocity in stream and normal directions
V	characteristic velocity
x,y	coordinate distance in stream and spanwise direction respectively
α	shock generator angle
β_o	inviscid oblique shock
β_s	separation line angle
γ	ratio of specific heats, 1.4 for air
Γ	intermittency
δ^*	boundary-layer displacement thickness
λ	compression ramp swept angle
ζ	parameter defined in Eq. (15)
ξ	correction to swept shock, Eq. (9)
ϕ	shock angle based on swept shock/boundary-layer interaction, Eq. (9)
$\phi(\omega),\phi(f)$	power spectral density

Subscripts

aw	adiabatic wall
c	compressible conditions or swept corner angle
e	evaluated at edge of boundary layer
i	incompressible conditions
s	reference to calculated inviscid shock position
w	wall
1	approach flow upstream of interaction
2	shock/boundary-layer interaction region, peak, plateau
∞	freestream conditions

Superscript

*	reference temperature condition

Presented at a Symposium on 'Impact of Acoustic Loads on Aircraft Structures' held in Lillehammer, Norway, May 1994

INTRODUCTION

The ability to predict fluctuating pressure and power spectra in supersonic/hypersonic turbulent boundary layer flow has relied on ad-hoc techniques developed from a database generated on planar, two-dimensional, or axisymmetric shapes. Experiments have led the way to investigate the phenomena due to restrictive assumptions and limitations in analysis. The algorithms developed to date are generally for attached turbulent boundary layer flow where a reasonable database exists for supersonic/hypersonic flow conditions. Moreover, the configurations from which this database has been generated consist of rigid structures (strategic/tactical weapon systems) which are capable to reacting to high pressure and the low and high resonant frequencies associated with these loads. However, future space transportation will require configurations that feature control surfaces as well as ramps and inlets required for an airbreathing propulsion system where the engine is an integral part of the airframe. These structures will require large areas of flat panels which are generally less efficient to pressure loads and low resonant frequencies due to reduced stiffness. Furthermore these lifting body configurations will feature complex 3D flow associated with the control surfaces as well as a multitude of shock/boundary layer interactions as well as shock-on-shock problems that can have a significant impact on the dynamic and strength characteristics of the vehicles structure. Finally, the mission profile for these types of systems will be more demanding than that experienced by modern fighter aircraft or ballistic and maneuvering weapon systems from which the current database and prediction techniques were developed. Figure 1 shows a typical hypersonic configuration featuring 3D non-circular cross-sections with ramps, control surfaces, and regions where shock/boundary and shock-on-shock interactions can occur.

The objective of this paper is to provide a brief review of work developed by the authors to predict the unsteady flow behavior of fluctuating pressure associated with attached and separated turbulent flow conditions. The review will also focus on work generated in the past several years on flow interactions (separated flow). Three excellent reviews of the subject matter are provided by Laganelli and Wolfe (Ref. 1), Dolling (Ref. 2), and Laganelli et al (Ref. 3). In Reference 1, both attached and separated flow results are discussed. Fluctuating pressure and power spectra are described for zero pressure gradient flow on smooth and rough surfaces, while the non-attached flow results were developed using approach flow conditions that were subsequently augmented using oblique shock relations. Reference 2 provides a tutorial and update on fluctuating loads in shock wave/turbulent boundary layer interactions. This excellent review focused on the experimental work which has been limited to the supersonic flow regime ($M_\infty \leq 5$). Fluctuating wall pressure interaction experiments (Ref. 4) were conducted at $M > 5$ but have not been published (to our knowledge). The data reported in Reference 2 consist of interactions generated by unswept or swept compression ramps, forward facing steps, flares, sharp and blunt fins, cylinders, and by impinging shocks. Moreover, the experimental results were primarily obtained at Mach 3 (series of experiments at the University of Princeton) and Mach 5 (series of experiments generated at the University of Texas). The emphasis of this work was concerned with the quantification of the effects of the dynamic and unsteady separation of the interaction, in particular the intermittent regions where the separation shock foot translates. In order to accommodate this research, strong shock generating angles were required that are not practical for hypersonic efficient aerodynamic structures.

As noted in Figure 1, interactions can occur along the intersections of control surfaces (horizontal/vertical stabilizers, strake/body), inlets (corner flow), and shock impingement (bow shock on cowl lip, stabilizers, or inlet) on various surfaces. Moreover, the flow leading into the inlet along the ramp can be both viscid and inviscid i.e. variable Mach number. No fluctuating database exists for these type of interactions thereby requiring the designer to use engineering judgement or heuristic techniques that are often very conservative and can result in significant weight penalties. This is further emphasized in the combustor region which can have a dramatic impact on the structure and subsequent weight penalties. Problems associated with the latter conditions are discussed in References 5 and 6.

Laganelli et al (Ref. 3) attempted to address the above interaction regions where no database exists. A type of Reynolds analogy was introduced where $\dot{q}_w \; \alpha \; \tau_w$ and coupled with the acoustic relationship $\hat{P}$

$\alpha\ \tau_w$ such that $\dot{q}_w \ \alpha\ \tau_w \ \alpha\ \hat{P}$. In this manner a significant database could be drawn upon involving heat transfer in shock wave/turbulent boundary layer interactions. For this situation, augmentation factors were approximated between peak rms pressure and peak heating using the $M \leq 5$ 2D/3D database and subsequently applied to the more extensive heat transfer database for $M > 5$.

It is further noted that experiments were conducted by Laganelli et al (Ref. 7) and Laganelli (Ref. 8) on a cone/slice/flap configuration and bi-cone/slice/flap configuration, respectively at Mach numbers of 4, 8, and 10. Angle of attack and flap angles were varied during the test in order to provide flow separation. The number of acoustic gages were limited (approximately six in the slice/flap region) that would make it difficult to capture peak rms pressure levels. However, careful CFD studies indicated that the 3D nature of the flow provided significant pressure relief as well as the fact that the sonic line in the boundary layer was very close to the surface. If separation did occur, it would have been in the region very close to the slice/flap intersection which could not accommodate instrumentation. Finally, while Reference 2 provides for an excellent review of fluctuating loads associated with shock/turbulent boundary layer interactions, Settles and Dolling (Ref. 9) describe the regions associated with swept shock/boundary-layer interactions.

DISCUSSION

The prediction methodology for aeroacoustic noise generated in attached and shock/boundary layer turbulent flow can be found in the recent work of Laganelli and Wolfe (Ref. 1). The attached flow techniques resulted from the earlier works of Laganelli et al (Ref. 7) while the shock/boundary layer interaction techniques were first presented in Reference 10. For continuity of the present paper, some of these results will be presented herein. The basis of the analysis is the relationship between the rms pressure and power spectra as provided by Houbolt (Ref. 7). This gives a discussion of the Houbolt algorithm and Ref. 11 provides extensive details which are germane to the present paper.

For attached flow, the PSD can be generalized as a function of the spectrum as

$$\phi(\omega) = \frac{\phi(0)}{1 + K^2\omega^2} \qquad (1)$$

where K represents an attenuation in the PSD profile to be compliant with the flow medium. K is dependent upon the properties of the flow, namely

$$K = k'l/V \qquad (2)$$

with k' to be defined. Using the definition of rms pressure $(\hat{P})^2 = \int_o^\omega \phi(\omega)\, d\omega$ together with Eq. (1), there results

$$\left[\frac{\hat{P}}{q}\right]^2 = \frac{\phi(0)\pi/2}{k'(l/V)q^2} \qquad (3)$$

where normalization was made with the dynamic pressure $[q = P(\gamma/2)M^2]$ based on boundary-layer edge conditions. Equations (1) and (3) can then be written as

$$\frac{\phi(\omega)V}{q^2 l} = \frac{(\hat{P}/q)^2 k'(2/\pi)}{1 + [k'(l/V)\omega]^2} \qquad (4)$$

which is recognized as the familiar format for representing PSD in the literature. The characteristic length is generally chosen as the boundary-layer displacement thickness, while the characteristic velocity as the boundary-layer edge value. The term k' appeared to have physical interpretation representing compressibility and heat transfer of the fluid medium (Ref. 7). This was a consequence of the magnitude of the PSD as $\omega \to 10^4$ Hz ($f \to 2000$ Hz, i.e., $\omega = 2\pi f$). It was shown that $k' \sim k'(F_c) \sim F_c^A$ and represents a method of tailoring the spectra profile in terms of peak values and roll-off with frequency. The exponent $A = A(n,m)$ where n and m represent the velocity power law exponent and viscous power law exponent, respectively. The parameter F_c is defined below. If one considers the low frequency ($\omega \to 0$) regime, Eq. (4) becomes

$$\frac{\phi(\omega \rightarrow 0)V}{q^2 l} \rightarrow \left[\frac{\hat{P}}{q}\right]^2 k' \, \frac{2}{\pi} \qquad (5)$$

Solutions are obtained using correlations developed for the overall rms pressure for attached (References 1, 11, and 12) and separated flows (References 1, 2, 3, and 13).

rms Pressure Predictions

The overall rms pressure for attached flows is given as

$$(\hat{P}/q) = 0.006/F_c \qquad (6)$$

where F_c represents the heat transfer and compressibility of the medium and is expressed as

$$F_c = C_{f_i}/C_{f_c} = h^*/h_e = \tfrac{1}{2}\frac{h_w}{h_e}\left[\frac{1}{2} + r\frac{\gamma-1}{2}M_e^2\right] + 0.22r\,\frac{\gamma-1}{2}\,M_e^2 \qquad (7)$$

and for adiabatic flow reduces to

$$(\hat{P}/q)_{aw} = 0.006/[1+0.13M_e^2] \qquad (8)$$

It is to be noted that arguments have been made on the incompressible (F_c = unity) value of $(\hat{P}/q)_i \rightarrow 0.006$ due to gage size limitations.

Solutions for rms pressure in unattached flow have not reached the level as those in attached flows inasmuch as the low and high frequency contributions due to the interactions provides for a significant variation in power intensity. Figure 2 shows typical results of a compression ramp interaction (Ref. 14) and a fin-generated shock/turbulent boundary layer interaction (Ref. 15). It is noted that the 2D compression corner and the 3D fin-generated interaction, while providing similar characteristics of peaks and plateau levels, are inherently different which resulted from the same approach flow. Tran (Ref. 15) compared compression corner and fin-generated interactions and noted that the rms pressure peaks for the latter where approximately one-half the levels experienced for the former for a similar approach flow and similar shock strength. The interactions showed a strong dependence on the intermittent characteristics that included the inviscid pressure rise, peak rms pressure rise, pressure gradient, and spatial extent of large amplitude disturbances. This earlier work has been corroborated and/or expanded upon in a series of experiments performed at Mach 5 (Ref. 2).

Laganelli and Wolfe (Ref. 1 and 10) attempted an engineering correlation of the compression corner and fin-generated interactions for the intermittent and plateau regions of the interaction. The objective was to use known characteristics of the flow, inparticular the inviscid pressure rise generated by the 2D or 3D geometry and approach flow conditions. A modified inviscid oblique shock angle was introduced that allowed for the 2D/3D interactions to coalesce in the intermittent region and is given as

$$\phi = \alpha + \xi \sin^{-1}(1/M) \qquad (9)$$

where

$$\xi = \text{unity}@\text{2D interactions}(\phi = \beta_0) \qquad (10)$$

$$\tfrac{1}{2} < \xi < 1@\text{3D interactions}$$

for β_0 the inviscid oblique shock angle and is defined as

$$\beta_0 \simeq \alpha + \sin^{-1}(1/M_1) \qquad (11)$$

where α is the shock generator angle. Figure 3 shows this result with the Mach 3 and 5 database (as well as the earlier work at Mach 2 (Ref. 16)) using $\xi \approx 0.6$ for the 3D interactions. The inviscid oblique pressure rise is expressed as

$$(P_{w_i}/P_{w_1})_{\phi,MAX} = \frac{2\gamma M_1^2 \sin^2\phi - (\gamma-1)}{\gamma+1} \qquad (12)$$

and the approach flow (noted by subscript 1) rms pressure is defined by Eq. (6). Attempts to coalesce the data with Mach number using the similarity parameter M Sin ϕ showed variant results. It should be noted that the Mach 5 compression ramp data were obtained with one ramp angle (28°).

While the data shown in Figure 3 did not collapse, comparable shock generating angles (α = 20°) for Mach 3 and 5 show the normalized peak rms pressure to decrease with increasing Mach number. Moreover, if the abscissa is normalized by M^2, the data would tend to coalesce which would imply that the normalized peak rms pressure would scale with the sin ϕ, the modified inviscid shock angle. This result is shown in Figure 4. While Eq. (12) suggests that peak rms pressure levels would increase with Mach number in separated flow regions as opposed to asymptotic levels experienced in attached flow, the Mach 3 and Mach 5 data tended to coalesce in individual bands, and as noted above, showed a tendency to decrease with Mach number (comparable shock angles of 20°).

Dolling (Ref. 2) also provided for potential correlations of the peak rms pressure in the intermittent region as developed in the works of References 13 and 17. In the former the overall variance in peak rms pressure in terms of upstream and downstream pressure fields was shown to be approximated as

$$(\hat{P})^2 / (\Delta P)_s^2 \approx \Gamma/(1-\Gamma) \qquad (13)$$

where $(\Delta P)_s$ is the pressure rise across the separation shock and Γ is the intermittency. The maximum rms value of the pressure occurs at $\Gamma \approx 0.5$. Figure 5 shows this interesting result for a number of shock/boundary layer interacting geometries. However, as noted by Dolling, the difficulty of using Eq. (13) as a prediction technique is that $(\Delta P)_s$ is usually not known a priori. In the work of Reference 17, the peak rms pressure was normalized with free stream pressure and shown as a function of sweep angle (β_s) of the interaction. Figure 6 shows this result. From an engineering prediction point of view, this potential correlation has very attractive features. However, when the data of Reference 14 (unswept compression ramp) was applied to the correlation, a considerable scatter was experienced as λ_c (ramp leading edge angle to the approach flow) approached zero. When the swept corner data of Tran (Ref. 15) was applied (24° ramp angle), it appears that a family of curves may be generated with different ramp angles that could be subsequently developed into an engineering prediction technique.

The above has essentially addressed rms pressure predictions for peak conditions associated with the intermittent region. Correlations have been presented by Laganelli and Wolfe (References 1 and 10) for the plateau region. Readers interested in these results are referred to in the above references.

Power Spectra Predictions

Prediction techniques for the power spectra in attached subsonic, supersonic, and hypersonic flows have been presented by Laganelli et al (References 1, 7, 8, 10, and 11). The focus in this paper will be for prediction techniques associated with separation flows (shock/turbulent boundary layer interactions). The very early work in this area was conducted by Robertson (Ref. 18) and Coe et al (Ref. 16) which was influenced by Space Shuttle requirements. The work was conducted at Mach numbers < 3. It is further noted that these authors conducted a series of transonic flow experiments (References 19 through 22) on cylinders with varying frontal shapes and reported rms pressure levels commensurate with compression ramp levels.

Relative to power spectra predictions in separated flow regions, Robertson (Ref. 18) used a modified form of the Lowson (Ref. 23) technique by modifying exponents to fit the limited database available at the time. He also choose normalization parameters of the approach flow as was the practice of attached flow investigators i.e. freestream dynamic pressure and velocity and boundary layer thickness. Coe et al (Ref. 16) represented their data in similar coordinates for the power spectra and dimensionless frequency (Strouhal number), but did not attempt any correlations. Rechtien (Ref. 24) re-examined the data of Reference 16 while also conducting experiments at Mach 2. Several characteristic distances were examined to coalesce the data. It was determined that distance measured behind the shock (to the shock generator) provided the most appropriate length parameter for frequency scaling.

More recently Laganelli and Wolfe (Ref. 1) attempted predictions based on approach flow and augmenting the spectra with oblique shock relations. Their focus was in the frequency regime < 2000 Hz where Eq. (5) could be used. The reason for this limitation was the inability to obtain the rapid roll-off of the spectra in interaction flows using the Houbolt form of power spectra, Eq. (4) for example, since characteristic lengths and velocities are not adequately known. However, the authors did provide for a reasonable engineering solution for the peak (intermittent) and plateau levels for frequencies < 2000 Hz. Dolling et al (see Ref. 2) also recognized the difficulty in selecting a characteristic length of the various flow interactions studied at the University of Texas on a number of shock generating geometries. Of particular interest was the work of Reference 13 that considered flow interactions with cylinders (both unswept and swept) which identified the intermittent region length (L_I) as a firm characteristic length. However, he cautions on the use of the freestream velocity when non-dimensionalizing the frequency. Moreover, it was further noted that use of the intermittent region length is not practical since it is not known a priori. On the other hand, the Mach 5 results from Reference 13 showed that $L_I/D \simeq 0.8$ for separation sweepback less than 30°, and between 30° and 60°, L_I/D increases linearly with about 1.15D (here D is the cylinder decimeter). Finally, Dolling et al have chosen to represent the power spectra in a non-dimensional format as $f.\phi(f)/(\hat{P})^2$ as a function of dimensional frequency or non-dimensional frequency (Strouhal), as well as other graphical representation of the spectra, which will be further discussed below.

First Moment Representation of the Power Spectra

As a result of the difficulty of determining the characteristic lengths and velocities of flow interactions (separated flow), other techniques have been sought that may provide engineering level solutions. These techniques are more germane to interacting flows for strategic and tactical (aircraft and missile) weapon systems where shock generating angles, shock strength, and complex geometries render choices of characteristic lengths and velocities as virtually impossible, even with the most sophisticated CFD techniques.

With consideration to the Houbolt form of the power spectra, namely Eq. (4), we can write

$$\phi(f)/(\hat{P}_{OA})^2 = \zeta/[1+(\pi/2)^2\zeta^2 f^2] \qquad (14)$$

where

$$\zeta = 4\ k'\ell/V \qquad (15)$$

Figure 7 shows the results of Eq. (14) with ζ as a parameter. Data from several sources are also provided. It is noted that increasing values of ζ tend toward the flow regimes where interactions occur (i.e. short time) while decreasing values of ζ occur for flow with long residence time for vorticity as experienced in attached flows. Moreover, the roll-off that is shown for the attached flow cases occur at low frequencies ($\omega\delta^*/U_e < 0.2$) and do not contribute significantly to the energy intensity i.e. the rms pressure thus rending the use of the Houbolt spectra as a potential engineering tool for attached and separated flows. It should be noted that a number of experiments from various subsonic, transonic, supersonic, and hypersonic facilities follow the trend shown in Figure 7 for both attached and separated flows. However, one is still left with the dilemma of knowing the value of ζ (i.e., characteristic lengths and velocities).

Another interesting aspect of the Houbolt spectra is when the PSD is normalized in a first moment type representation as suggested by Black (Ref. 25) as well as Houbolt and employed in the attached flow supersonic/hypersonic experiments of Laganelli and Howe (Ref. 11). With consideration to the definition of the rms pressure i.e. $\hat{p}^2 = \int_0^\infty \phi(\omega)d\omega = \int_0^{\omega_1}\phi(\omega)d\omega + \int_{\omega_1}^\infty \phi(\omega)d\omega$, the second integral is a higher order term for frequency >20KHz. If one considers a change in variable dz = dω/ω then $\hat{p}^2 = \int_0^{z} \omega\ \phi\ (\omega)\ dz$ which suggests

$$\frac{f\ \phi\ (f)}{(\hat{P}_{OA})^2} = \text{function}\ \left[\frac{f\ell}{V}\right] \qquad (16)$$

Several characteristic velocities and lengths were suggested by Black and Houbolt for attached flow conditions. However when Eq. (14) is structured into the first moment format a very interesting characteristic of the spectra evolves i.e.

$$f.\phi(f)/(\hat{P}_{OA})^2=f.\zeta/[1+(\pi/2)^2\zeta^2f^2] \tag{17}$$

where the left side of Eq. (17) has a peak value for all values ζ. This implies that the first moment has a unique value for all flow conditions attached and separated, when using the Houbolt spectra. This phenomena is shown in Figure 8. Also shown are incompressible and compressible data for attached flow conditions as well as peak values from a number of experiments from shock/turbulent boundary layer interaction experiments that include ramps (with swept corners), cylinders (swept/unswept), and fin-generated interactions. The attached flow data show a trend to the expression given by Eq. (17) while the unattached flow provide for peak conditions at the predicted value of $f.\phi(f)/(\hat{P}_{OA})^2=0.318$. Moreover the shape of the interaction flow conditions is different than that of the attached flow conditions (see insert from Ref. 13 for the various shock generating geometries). Again one has the dilemma of knowing the frequency where the peak first moment occurs that requires a knowledge of the characteristic lengths and velocities.

RESULTS

If one is given a PSD distribution for any flow condition, the subsequent overall rms pressure $(\hat{P}_{OA})$ can be obtained by the usual integration process. A value of the peak PSD, $\phi(f_p)$, can be selected as well as a peak frequency, f_p. Using Eq. (14) for the condition $(\pi/2)^2 \zeta^2 f^2 << 1$, where peak conditions occur by the Houbolt spectra, together with the condition that

$$f_p.\phi(f_p)/(\hat{P}_{OA})^2=0.318 \tag{18}$$

an iterative process can be established for the correct selected values of f_p and $\phi(f_p)$. Equation (14) can then be expressed as

$$\phi(f)=\phi(f_p)/[1+\left(\frac{\pi}{2}\right)^2\frac{\phi^2(f_p)}{(\hat{P}_{OA})^4}f^2] \tag{19}$$

Figure 9 shows the result of the engineering prediction technique of Eq. (19). Both attached and shock/turbulent boundary layer interactions are shown to provide a good fit to the data for a compression ramp as well as a fin-generated shock. Similar results have been obtained for subsonic, supersonic, and hypersonic attached flows as well as other shock/turbulent boundary layer interaction flows.

The above represents a technique that can be used for engineering prediction of the power spectra of arbitrary flow conditions. The key is in the selection of $\phi(f_p)$. Correlations are available for the overall rms pressure as discussed within. The two conditions combined together with Eq. (18) provides for a definition of the peak frequency. The technique does not require knowledge of the characteristic lengths or velocities. The methodology is a fall-out of the Houbolt spectral distribution which was developed from attached flow characteristics.

ACKNOWLEDGEMENTS

The authors wish to acknowledge the sponsorship of this work under U. S. Air Force Contract F33615-87-C-3227 entitled, "Thermo-Vibro-Acoustic Loads and Fatigue of Hypersonic Flight Vehicle Structures" which was monitored by Wright Patterson Air Force Base - WL/FIBG.

REFERENCES

[1] Laganelli, A. L. and Wolfe, H. F. "Prediction of Fluctuating Pressure in Attached and Separated Turbulent Boundary-Layer Flow" J. of Aircraft, Vol. 30, No. 6, NOV/DEC, 1993, PP. 962-970.

[2] Dolling, D. S. "Fluctuating Loads in Shock Wave/Turbulent Boundary Layer Interactions - Tutorial and Upgrade," AIAA Paper 93-0284, Reno, NV, Jan. 1993.

[3] Laganelli, A. L., Wolfe, H.F., and Wentz, K. R., "Prediction of Fluctuating Pressure in Attached and Separated Compressible Flow," AIAA Paper 93-0286, Reno, NV., Jan. 1993.

[4] Holden, M. S., "Studies of the Mean and Unsteady Structure of Turbulent Boundary Layer Separation in Hypersonic Flow" AIAA Paper 91-1778, 22nd Fluid Dyn./Plasma Conf., Honolulu, June 1991.

[5] Pozefsky, P., Blevins, R. D., and Laganelli, A. L., "Thermo-Vibro-Acoustic Loads for Fatigue of Hypersonic Flight Vehicle Structures - Phase I Report" AFWAL-TR-89-3014, Feb. 1989.

[6] Parrott, T. L., "Unsteady Loads Measurements in a Scramjet Engine Model via Recessed Transducers", AIAA Paper 93-0287, 31st Aerospace Sciences Meeting, Reno, NV., Jan. 1993.

[7] Laganelli, A. L., Martellucci, A. and Shaw, L., "Wall Pressure Fluctuations in Attached Boundary Layer Flow," AIAA J., V. 21, N. 4 April 1983.

[8] Laganelli, A. L., "Prediction of the Pressure Fluctuations on Maneuvering Reentry Weapons", AFWAL-TR-83-3133, February 1984.

[9] Settles, G. S., and Dolling, D. S., "Swept Shock/Boundary-Layer Interactions-Tutorial and Update", AIAA Paper 90-0375, AIAA 28th Aerospace Science Meeting, Reno, NV, Jan. 1990.

[10] Laganelli, A. L. and Wolfe, H., "Prediction of Fluctuating Pressure in Attached and Separated Turbulent Boundary Layer Flow", AIAA Paper 89-1064, San Antonio, TX, April 1989.

[11] Laganelli, A. L. and Howe, J. R., "Prediction of Pressure Fluctuations Associated with Maneuvering Re-Entry Weapons", AFFDL-TR-77-59, Vol. I, July 1977.

[12] Laganelli, A. L., Christoph, G. H., Fiore, A. W., "Experimental and Analytical Acoustic Technique to Measure Wall Shear", AIAA Paper 84-0103, Jan. 1984.

[13] Gonsalez, J. and Dolling, D. S., "Effects of Interaction Sweepback on the Dynamics of Shock-Induced Turbulent Separation", AIAA Paper 93-0776, 31st Aero. Sci. Meeting, Reno, NV, Jan. 1993.

[14] Dolling, D. S. and Or, C. T., "Unsteadiness of the Shock Wave Structure in Attached and Separated Compression Ramp Flowfields", Experiments in Fluids, Vol. 3, 1985, pp. 24-32.

[15] Tran, T. T., "An Experimental Investigation of Unsteadiness in Swept Shock Wave/Turbulent Boundary Layer Interactions," PhD Thesis, Princeton University, ME Department, March 1987.

[16] Coe, C. F., Chyu, W. J., and Dods, J. B., "Pressure Fluctuations Underlying Attached and Separated Supersonic Turbulent Boundary Layers and Shock Waves," AIAA Paper 73-996, Oct. 1973.

[17] Schmisseur, J. D., and Dolling, D. S., "Unsteady Separations in Sharp Fin-Induced Shock Wave/Turbulent Boundary Layer Interaction at Mach 5", AIAA paper 92-0748, Reno, NV, Jan. 1992.

[18] Robertson, J. E., "Predictions of In-Flight Fluctuating Pressure Environments Including Protuberance Induced Flow", Wyle Lab Rep #WR-71-10, Mar. 1971.

[19] Robertson, J. E., "Steady and Fluctuating Pressures on Cone-Cylinder Missile Configurations at Transonic Speeds" AEDC-TR-65-269, Feb. 1966, AD477938.

[20] Coe, C. F. and Kaskey, A. J., "The Effects on Nose Bluntness on Pressure Fluctuations Measured on 15° and 20° Cone-Cylinders at Transonic Speeds" NASA TMX-779, Jan. 1963.

[21] Coe, C. F., "The Effects of Some Variations in Launch-Vehicle Nose Shape on Steady and Fluctuating Pressures at Transonic Speeds" NASA TMX-646, Mar. 1962.

[22] Coe, C. F., "Steady and Fluctuating Pressure at Transonic Speeds on Two Space-Vehicle Payload Shapes" NASA TMS-503, Mar. 1962.

[23] Lowson, M. V., "Prediction of Boundary Layer Pressure Fluctuations", AFFDL-TR-67-167, April 1968.

[24] Rechtien, R. D., "A Study of the Fluctuating Pressure Field in Regions of Induced Flow Separation at Supersonic Speeds" U. of Missouri, UMR Research Report, May 1970.

[25] Black, T. J. "An Analytical Study of the Measured Wall Pressure Field Under Supersonic Turbulent Boundary Layers" NASA CR-888, April 1968.

[26] Muck, K. C., Dussauge, J. P., and Bogdonoff, S. W., "Structure of the Wall Pressure Fluctuations in a Shock-Induced Separated Turbulent Flow", AIAA Paper 85-0179, Jan. 1985.

[27] Tan, D. K., Tran, T. T., and Bogdonoff, S. M., "Wall Pressure Fluctuations in a 3-D Shock-Wave/Turbulent Boundary Layer Interaction", AIAA J., V.25,N. 1 Jan. 1987.

[28] Erengil, M. E., and Dolling, d. S., "Effects of Sweepback on the Dynamics of Unsteady Separation in Mach 5 Compression Ramp Interactions", AIAA Paper 92-0430, Reno, NV, Jan. 1992.

[29] Bull, M. K., "Wall-Pressure Fluctuations Associated with Subsonic Turbulent Boundary Layer Flow", J. Fl. Mech., Vol. 28, Part 4, 1967.

[30] Chaump, L. E., Martellucci, A., and Monfort, A., "Aeroacoustic Loads Associated with High Beta Vehicles", AFFDL-TR-72-138, May 1973.

[31] Raman, K. R., "Surface Pressure Fluctuation in Hypersonic Turbulent Boundary Layers", NASA CR2386, Feb. 1974.

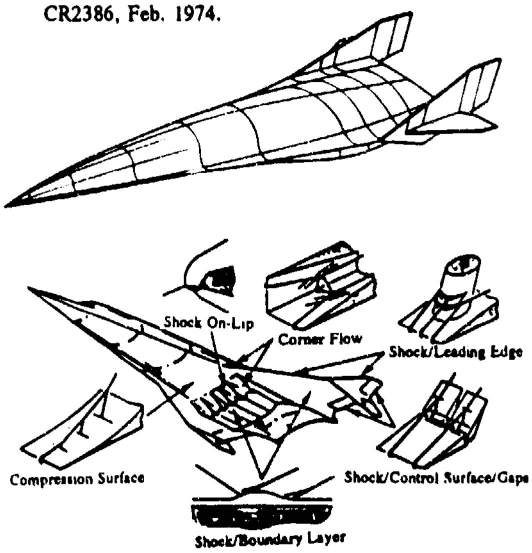

Figure 1. Space transportation system with flow interactions

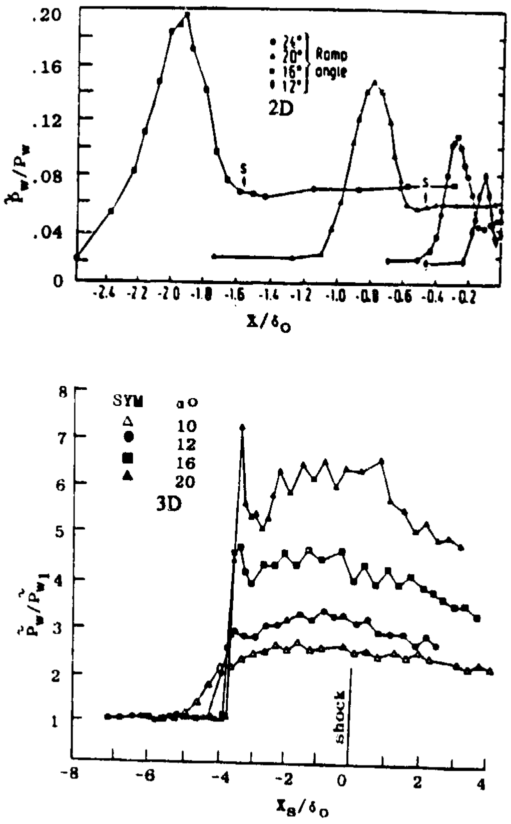

Figure 2. Normalized rms pressure distribution with 2D (Ref. 14) and 3D (Ref. 15) shock strength

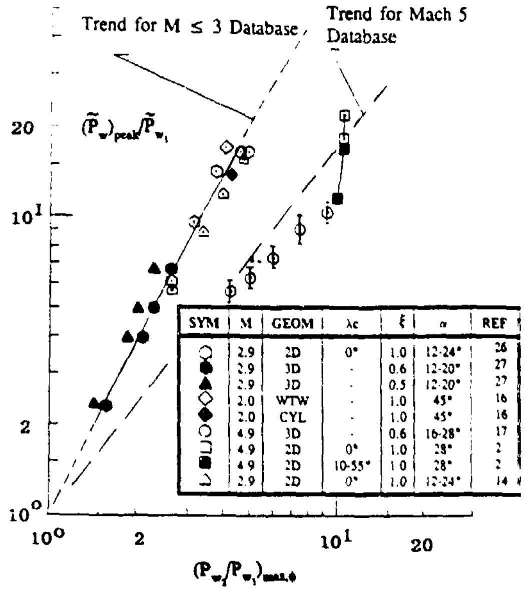

SYM	M	GEOM	λc	ξ	α	REF
○	2.9	2D	0°	1.0	12-24°	26
●	2.9	3D	-	0.6	12-20°	27
▲	2.9	3D	-	0.5	12-20°	27
◇	2.0	WTW	-	1.0	45°	16
◆	2.0	CYL	-	1.0	45°	16
○	4.9	3D	-	0.6	16-28°	17
□	4.9	2D	0°	1.0	28°	2
■	4.9	2D	10-55°	1.0	28°	2
△	2.9	2D	0°	1.0	12-24°	14

Figure 3. Correlation of peak rms pressure with modified oblique shock relationship (Ref. 1)

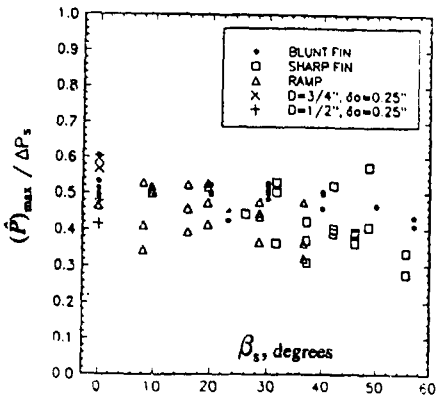

Figure 5. Normalized peak rms pressure with pressure rise across separation shock (Ref. 13)

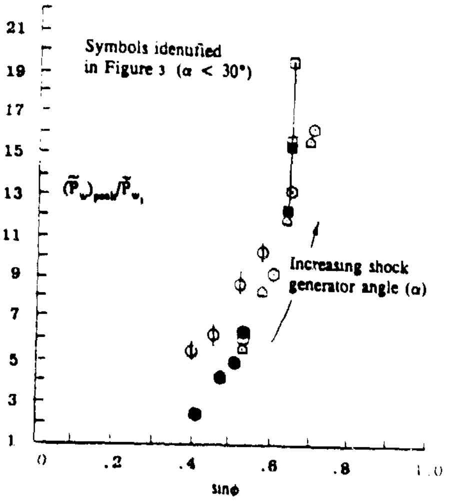

Figure 4. Correlation of peak rms pressure with modified inviscid shock angle (Ref. 1)

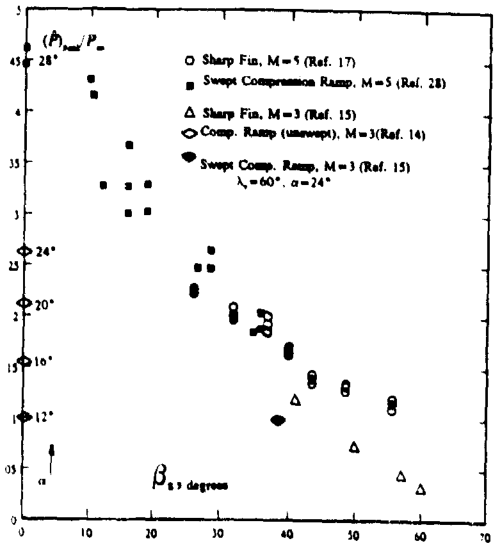

Figure 6. Normalized peak rms pressure with sweep angle for 2D and 3D interactions

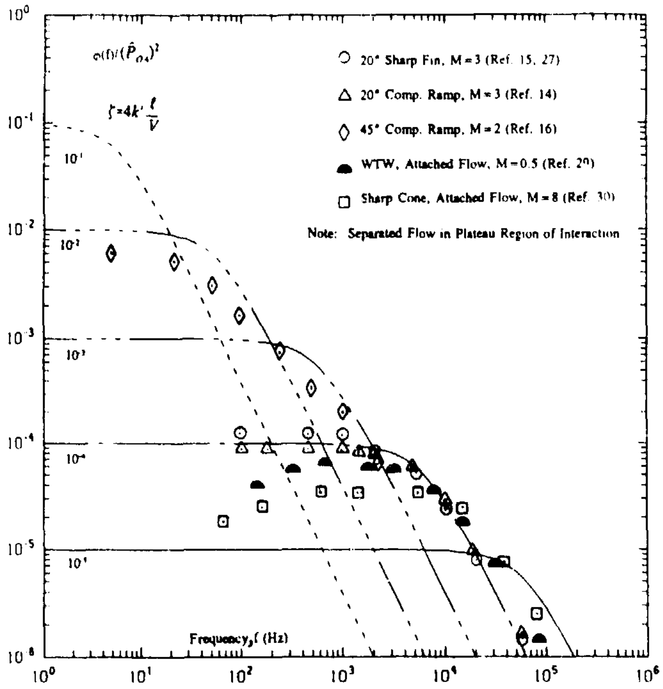

Figure 7. Normalized PSD for attached and separated flow conditions

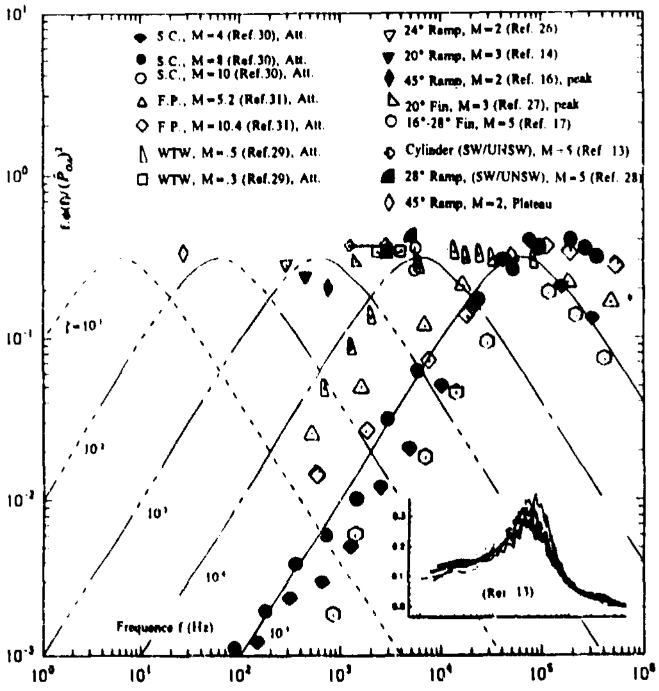

Figure 8. First moment of PSD for attached and separated flow conditions

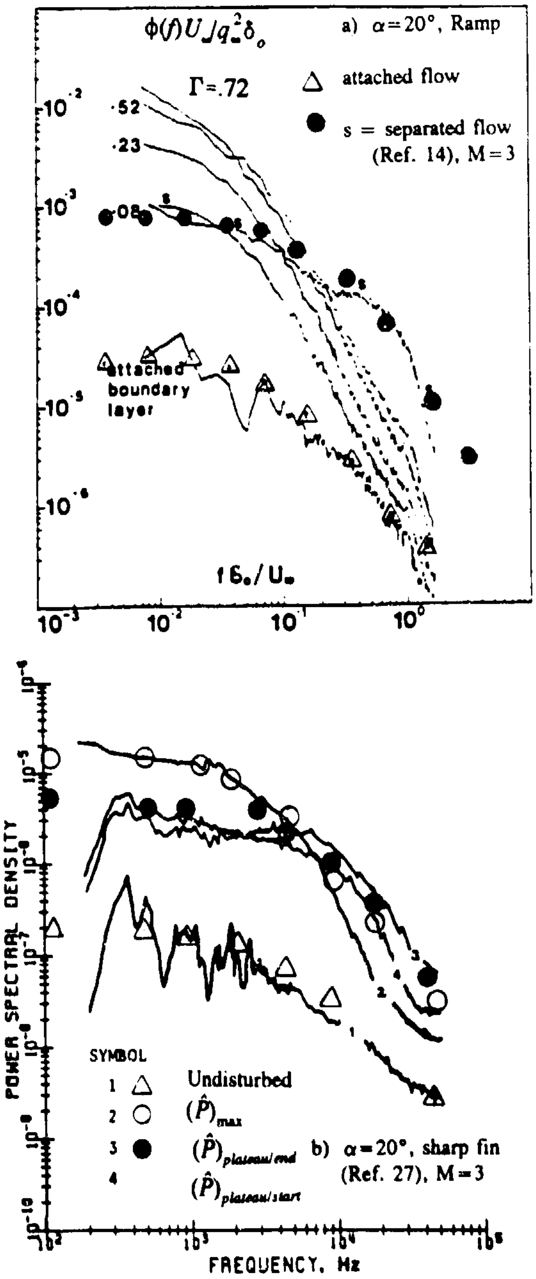

Figure 9. Comparison of the PSD prediction technique to 2D(a) and 3D(b) interactions

Modelling Structurally Damaging Twin-Jet Screech

Mary Kae Lockwood
Steven H. Walker

Wright Laboratory
WL/FIMA Bldg. 450
2645 Fifth St. Ste 7
Wright Patterson AFB. OH 45433-7913

Alan B. Cain

McDonnell Douglas Corporation

1. SUMMARY

Closely spaced twin jet aircraft have been known to be susceptible to aftend structural damage due to the high sound pressure levels resulting from twin jet screech. An initial engineering workstation tool to predict the occurrence of screech, ultimately allowing the design of configurations which will not result in screech, is presented here. The model has been developed in a modular fashion to facilitate upgrades. The implementation takes advantage of a graphical interface, yielding predictions of screech amplitude versus frequency within a few seconds once the initial flowfield is defined. The four physically based modules in the code, for the instability waves, shock-vortex interaction, acoustic feedback and receptivity, are based on analytical, computational and experimental research. Preliminary results for 2-D jets illustrate the effects freestream Mach number and shear layer growth rate have on the screech amplitudes and frequency.

2. INTRODUCTION

Currently USAF F-15 aircraft are flying without external nozzle flaps, due to the continuous structural fatigue experienced by the flaps and the cost of replacing them. Although the aft region of the aircraft is known to experience high aerodynamic loads due to massive unsteady flow separation; there is evidence that severe acoustic loads contribute to the observed structural damage. These acoustic loads are attributed to a phenomenon known as jet screech. Screech is essentially a resonance feedback loop in the jet flowfield that can set up between the nozzle lip and the jet shock cells. It is most severe for medium spaced twin jet aircraft and can occur during subsonic flight with a non-perfectly expanded supersonic jet. Screech has been measured at levels of 160 dB; high enough to exceed the fatigue failure limit for metallic aircraft structures.[1]

Other medium spaced twin-jet aircraft, such as the B-1, the Tornado and the EFA have the potential to be adversely affected by nozzle screech. For these aircraft, removing the external nozzle flaps may not be an acceptable solution. For example, removal of the nozzle external flaps on the B-1B would increase the nozzle drag by as much as 32 counts over the Mach number range of .55 to .85.[2] This increase in drag results in a 602 nm decrease in range, which is unacceptable for a strategic bomber.

A methodology to predict the occurrence of aerodynamically induced jet screech, ultimately allowing the design of configurations which will not result in screech, is required. Until now models of the screech feedback loop have focused on the prediction of the screech frequency only. Thus the amplitude of screech, indicating the extent of possible damage to the aircraft, has not been previously predicted. The model described here has been developed to predict the amplitude as well as the frequency of screech. The method is an analytical model based on results from analytical, computational and experimental research. It is designed to run in a few seconds on an engineering workstation such that it can be used by a nozzle design engineer. The model incorporates a Computational Fluid Dynamics, CFD, input interface and a graphical analysis capability.[3] A description of the workstation model as well as an example of the screech prediction results for a given nozzle flowfield will be presented in this paper.

3. PHYSICS OF SCREECH

A screech resonance feedback loop can set up at subsonic flight Mach numbers with an imperfectly expanded supersonic jet or jets as illustrated in Figure 1. Instability waves inherently present in the shear layer of the jet plume increase in amplitude while traveling downstream by extracting energy from the mean flow. These instability waves then interact with each of the shock cells in the jet. Acoustic waves are produced at each shock cell, which can propagate upstream toward the nozzle trailing edge. The spectrum of acoustic waves at the nozzle lip is therefore dependent on

Presented at a Symposium on 'Impact of Acoustic Loads on Aircraft Structures' held in Lillehammer, Norway, May 1994.

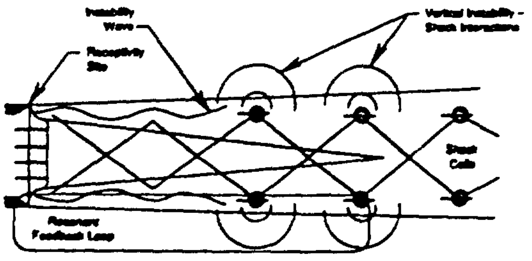

Figure 1: Screech feedback loop.

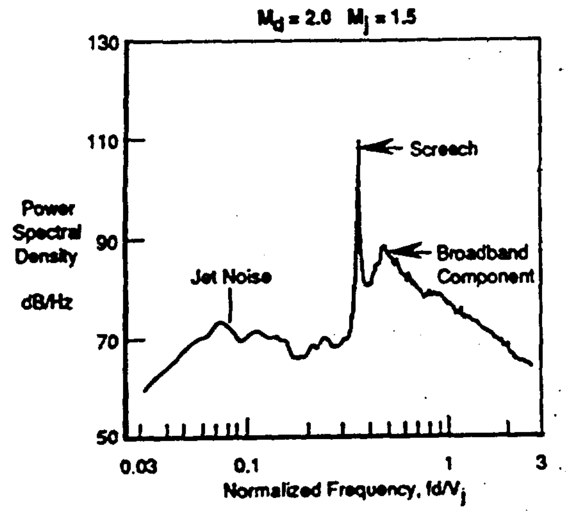

Figure 2: Power spectral densities for jet mixing noise, broadband shock associated noise and screech

the amplitude, frequency and phase of the acoustic waves produced at each of the jet shock cells and the summation of these waves at the nozzle lip. The energy from the acoustic waves is transferred in part to instability waves at the nozzle lip through the process known as receptivity. Depending on the amplitude of the newly excited waves, resonance may be produced.

Screech as implied above, is driven by inviscidely dominated instability waves made possible by the inflection point in the shear layer between the jet and the freestream. In other words, it is driven by a Kelvin Helmholtz type instability of the shear layer. The instability of the shear layer also results in the production of turbulence which is responsible for the other two types of noise associated with a jet, jet mixing noise and broadband shock associated noise. Jet mixing noise, present in both subsonic and supersonic jets, results from the turbulent mixing of the jet with the freestream. Broadband shock associated noise, present in supersonic jets, is generated by the interaction of turbulence with the jet shock cells. Screech is distinguished from the broadband shock noise by the fact that the acoustic waves produced in the interaction between a particular instability wave and the shock cell ultimately act to increase the instability wave amplitude at the nozzle lip, thus setting up the resonance loop. Figure 2 illustrates typical sound pressure levels for jet mixing noise, broadband shock associated noise and screech. Note that screech is characterized by the single frequency spike having significantly greater amplitude than either the mixing noise or the broadband shock associated noise. Due to the different mechanism and substantially higher amplitudes of screech as compared to broadband noise, broadband formulas cannot be used to predict screech amplitude.

The time averaged picture of a jet in screech mode will exhibit the typical diamond shock patterns of imperfectly expanded jets. However viewed in time, a jet in screech is characterized by a dramatic unsteady motion. The motion driven by the instability mode, is dependent on the shape of the nozzle exit area, the fully expanded jet Mach number and the nozzle pressure ratio. For example, single axisymmetric jets and low aspect ratio rectangular jets exhibit helical and/or toroidal motions depending on the fully expanded Mach number and nozzle pressure ratio of the jet. Historically, the mode types have been designated A1, A2, B, C and D as illustrated in Figure 3 from Norum[4]. For an axisymmetric jet, the toroidal spacial structure is characterized by shorter wavelength and thus higher frequencies and would be represented by the 'A' labels in Figure 3. The helical spacial structure is characterized by longer wavelength, lower frequency, waves. In Figure 3 this spacial mode would be represented by the 'B' type mode. In general the helical mode results in the highest screech amplitudes. In a similar manner, single 2-D jets and high aspect ratio rectangular jets exhibit a flapping motion, driven by the antisymmetric mode, and can also exhibit a symmetric mode. Generally the flapping mode is dominant for the 2-D jet at typical operating conditions.

The amplitude of screech for twin jets has been shown to be considerably greater than that for single jets. An example of this is shown in Figure 4 from Walker[5], where the twin jet dB level for design Mach 1.4 axisymmetric jets slightly underexpanded is over 10dB greater than that for a single jet. The distance between the twin jets has a significant impact on the magnitude of jet screech. The most extensive jet coupling and thus the greatest sound pressure levels have

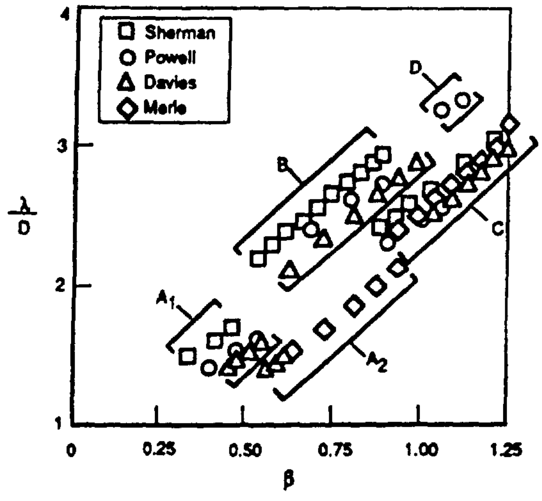

Figure 3: Screech modes for an axisymmetric sonic nozzle

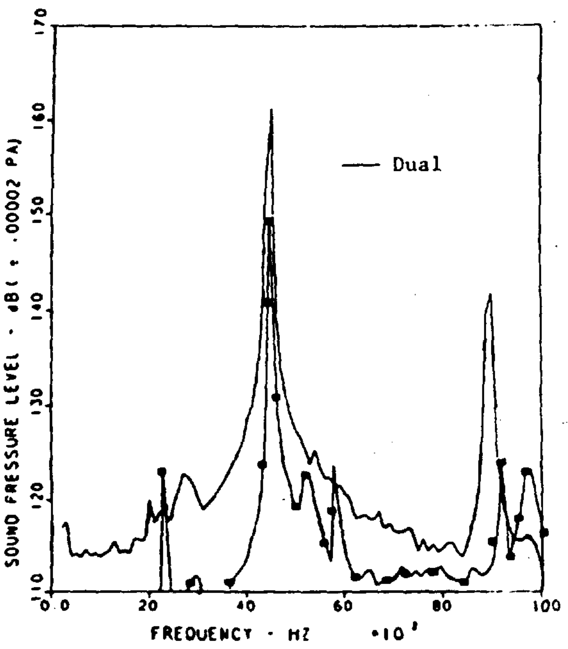

Figure 4: Single vs twin jet sound pressure levels.

been measured for moderately spaced jets, approximately two jet diameters apart.[6] Jets closer or farther apart do not exhibit the extensive coupling and thus don't produce amplitudes much greater than those of a single jet. The screech amplitude resulting from the twin jet coupling is believed to contribute to the structural damage of the nozzle external flaps on the F-15.

As noted above, jet exit cross sectional geometry, fully expanded jet Mach number, nozzle pressure ratio and twin jet separation distance can have a significant impact on the amplitude of screech. Other physical factors that have an influence include jet temperature, freestream Mach number and shear layer growth rate. In addition, modeling assumptions, regarding whether the instability wave phase speed is assumed to be constant or allowed to vary, have proven important. The effects of freestream Mach number and shear layer growth rate will be discussed in this paper.

Although it is possible to analyze a plume flowfield for screech prediction using the full unsteady Navier Stokes equations on a computational grid[7], it is currently impractical as a design tool. To resolve the acoustic pressures, which is necessary for the prediction of screech, the density of the computational grid required is several times greater than that required for a more commonly run CFD solution, run for the prediction of aerodynamic forces. Specifically, the ratio of the acoustic pressure to mean pressure at a 100dB SPL is only 10^{-5}. If the computational grid is not fine enough, the discretization, or truncation errors due to the grid will overshadow the physical acoustic pressure level. This high grid density requirement results in run times and memory allocations which are prohibitive for use as a design tool. Even Cray run times for solutions on simplified configurations require on the order of CPU days.[7] Thus a simplified model which represents the physics of the screech mechanism is required for design purposes.

4. WORKSTATION ANALYSIS TOOL

The screech model is an analytical model based on the results from analytical, computational and experimental research. The screech prediction code, as illustrated in Figure 5, is designed to run within a few seconds on an engineering workstation once the flowfield has been defined. The input to the code is a CFD solution of the jet-on aircraft aft end. Using information from the CFD solution as described further below, the code proceeds through the four modules of the code, each representing one component of the screech mechanism. The modules complete the calculation of the instability waves, the shock-vortex interaction, the acoustic feedback, and the receptivity. The code's primary output are the screech frequency and amplitude. The code has been written in a modular structure to allow each module to be easily upgraded as research in each component of the mechanism progresses. The modularity also facilitates sensitivity studies to determine the impact of one module on the predictions.

The entire code is run within a graphical interface provid-

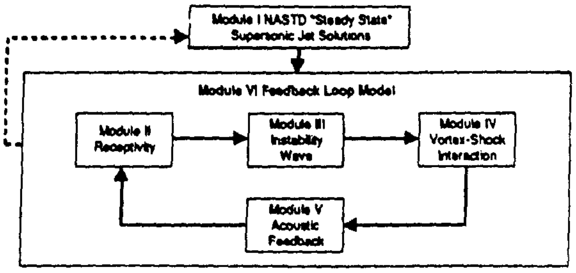
Module I NASTD "Steady State" Supersonic Jet Solutions
Module VI Feedback Loop Model
Module II Receptivity
Module III Instability Wave
Module IV Vortex-Shock Interaction
Module V Acoustic Feedback

Figure 5: Screech prediction tool flowchart.

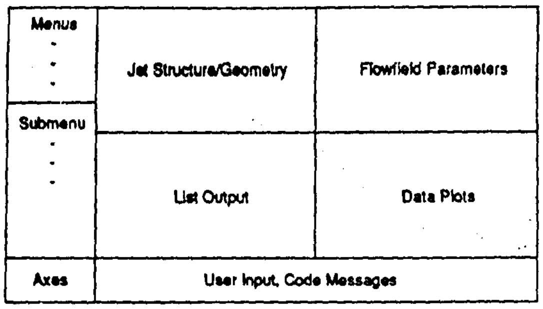

Figure 6: Screech prediction tool screen layout.

ing visual information relating the input CFD flowfield to the output amplitude vs. frequency plots, as well as allowing a user less familiar with the screech process to run the code. An illustration of the screen display is shown in Figure 6. A CFD flowfield cut can be entered as shown on the top left corner of the screen. From the menu, various information about the CFD solution is entered. For example, using the **jet** command, the jet exit Mach number, pressure and temperature are specified as well as the shear layer thickness at the nozzle lip and the shear layer growth rate. Using the **cut** command, the jet shock cell spacing and shock pressure jumps are specified. After the flowfield is defined, the **frequency** command is used. As an easy reference point, the **Tam** option is chosen which estimates the screech tone frequency using a formula from Tam, Seiner and Yu[8]. The **spread** command is used to generate a list of analysis frequencies about and including the estimated frequency. Once the analysis frequencies have been defined the **iterate** command is selected from the menu. For each frequency, the workstation tool progresses through the four modules to determine whether or not the particular frequency instability wave is amplified. The resulting output of the code, viewed by choosing the **plot** command, yields an xy plot of amplitude vs frequency in one of the windows selected on the screen, as shown in Figure 6. If desired all four window sections can be used to plot data comparing various runs of the code. Each of the modules are described in further detail below and some results for a sample aft end flowfield are given.

4.1 Instability Module

As noted in the introduction, previous models of screech have focussed on predicting the frequency of screech only. The method employed here predicts frequency and also tracks the growth rate and amplitude of the instability wave. In addition, a constant phase speed is not assumed in this work, which can turn out to have a significant effect depending on the particular jet flowfield conditions.

It is important to recognize that as a disturbance of fixed physical frequency convects downstream in the jet, the local shear layer thickness increases. This change in the flowfield characteristics results in a change in the disturbance propagation, i.e. phase speed and growth rate of the instability wave. Since the disturbance propagation is modeled locally at successive downstream locations, it is necessary to compute a wide range of solutions just to model the propagation of one physical instability frequency. Using dimensional analysis, it is possible to define a locally scaled dimensionless frequency range, scaled by shear layer thickness and shock cell spacing, that characterizes all important physical disturbances. In all, approximately 200 scaled frequencies must be analyzed to give a reasonable characterization of a stability mode for a given jet. However, once the stability mode is characterized, the phase speed and growth of any instability wave as it convects downstream is known for the given jet.

The code used to predict the disturbance propagation is the spectral based version of the LInearized Stability Analysis code, LISA, developed by Flow Dynamics Corporation under the guidance of Dr. Thorwald Herbert. The code uses a parallel linearized compressible flow equation, analogous to the incompressible parallel flow Orr-Sommerfeld formulation. To complete a scaled frequency sweep, with the spectral version of the LISA code, approximately 8 hours on an Indigo Silicon Graphics workstation are required. Since this is a prohibitive amount of time, if the workstation tool is to be used for design, a neural network has been developed to represent the results of the LISA code for a class of jets, for example either 2-D or axisymmetric. In the present work, the network has been completed for 2-D jets. The neural network has been developed by McDonnell Douglas and is based on the ideas in three articles written by Caudill[9,10,11]. It includes five parameters in addition to the scaled frequency. They are freestream Mach number, nozzle pressure ratio or fully expanded jet Mach number, wake amplitude, the ratio of jet to freestream temperature and dimensionless shear layer thickness. To train the network five to eight data points are required for each parameter, and 41 of the 201 scaled frequencies run in LISA are selected to accurately define the effect of scaled frequency for one set of parameters. In fact, this results in $8^5 \times 41$ LISA data points to develop the neural network for one class of jets. This turns out to be a non-trivial application of the neural network, since the limit of data that a network can currently handle is close to this number. The neural network allows the calculation of instability wave amplification for an entire sweep of physical frequencies, represented by scaled frequencies in the network, in less than a second on a workstation, instead of the hours that would be required if the linear stability analysis itself were performed.

4.2 Shock-Vortex Interaction Module

Previous models of the shock-vortex interaction have approximated the jet shock structure as having equally spaced shock cells from the nozzle exit to an infinite distance downstream. Since the jet shock cell pattern dissipates with distance downstream, cell spacing is not constant in an actual jet. In fact, the dissipation suggests that only the first several shock cells would result in a significant shock-vortex interaction. Figure 7 from Rice and Taghavi[12] illustrate the acoustic sources from a convergent rectangular nozzle with a fully expanded Mach number of 1.44. As shown, the largest interactions and therefore noise sources are produced just downstream of the 3rd and 4th shock cells. Therefore it seems desirable to model the shock-vortex interaction locally at the strongest upstream-most shock cells. Modeling the shock-vortex interaction separately at each shock cell appears to be an attractive alternative to earlier approaches. As a first approximation, the shear layer in this module can be represented as a zero thickness vortex sheet since the shear layer is thin relative to the wavelength of the relevant disturbances. Note however that the prediction of the instability wave growth rate and propagation speed from the Instability Wave Module is based on a finite thickness shear layer. Thus the results from the finite thickness shear layer in the Instability Wave Module are used to define the amplitude and phase of the instability mode in the vortex sheet of the Shock-Vortex Interaction Module. Finally, the jet is assumed to be slightly imperfectly expanded such that shock cell pressure jumps can be modeled linearly. With these assumptions it is possible to model the shock-vortex interaction in closed form. The resulting solution yields the

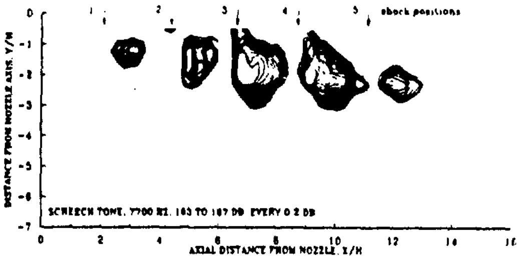

Figure 7: Acoustic sources. Numbers indicate shock cell locations.

acoustic wave amplitude and phase, for the given instability wave frequency, at each shock cell location.

An experimental study to further understand the shock vortex interaction is currently on-going as part of this program.[13] The experimental set-up consists of a Mach 1.35 rectangular nozzle exhausting into an anechoic chamber. An array of microphones immediately outside the jet shear layer will record nearfield measurements and a single microphone positioned on a circular arc will record farfield measurements. In addition, the miniature microphone probe technique of Rice and Taghavi[12] will be used to accurately locate the shock-vortex interaction noise sources. To determine the frequency and amplitude of the instability waves, hot-wire measurements will be taken in the subsonic portion of the shear layer. By comparing these measurements for a screeching and non-screeching jet, the instability frequency responsible for screech can be identified. Using a technique developed by Thomas and Chu[14,15], and taking hot-wire measurements upstream and downstream of the previously determined noise source locations, the local spectral dynamics of the shear layer can be evaluated. By correlating the spectral dynamics to the near-field acoustic measurements, the mechanism of shock-vortex interaction will be further understood, and results can be used to motivate refinements of the shock-vortex interaction module in the prediction tool.

4.3 Acoustic Feedback

Knowing the amplitude, phase and wavelength of the acoustic waves generated at a given shock cell location, as well as the distance from the shock cell to the nozzle lip, either a cylindrical or spherical decay process can be selected to determine the amplitude of the waves at the nozzle lip. The phase at the nozzle lip can be determined using the distance from the shock cell and the velocity of propagation of the wave, which is estimated by the speed of sound in the freestream minus the freestream velocity along a straight path between the source and the lip. Thus from the phase and amplitude of the acoustic waves from each of the shock cells, a summation of the acoustic waves can be determined at the nozzle lip.

4.4 Receptivity

Receptivity describes how external disturbances generate instability waves in a flowfield. In the screech phenomena, the receptivity describes how energy is transferred from the acoustic pressure waves to the vortical instability waves of the same frequency. In screech, the acoustic wave scattered from the nozzle lip acts to excite the instability wave in the jet shear layer. Thus, the receptivity defines the amplitude and phase of the amplified instability waves. Receptivity is a complex process and can be influenced by nozzle geometry, material type and the aftbody flowfield. The current model utilizes a vortex sheet formulation, assumes 2-D flow in the vicinity of the trailing edge and assumes a sharp nozzle trailing edge.

5. RESULTS

A 2-D planar Mach 1.35 nozzle with a 12″ exit height has been used in the following examples. The effects of freestream Mach number and shear layer growth rate are presented.

Figure 8 shows the net gain for one pass through the screech loop versus frequency for a hot jet where the plume to freestream temperature ratio is five. In this case, the freestream Mach number is .4, the shear layer growth rate is .05 and the fully expanded Mach number is 1.5. Note that the value of amplitude in these figures is the sum of the amplitudes from each of the shock cells with reinforcement and cancellation accounted for. Note that the jet shows no screech loop gain, since the resulting amplitudes are all less than the original amplitude, i.e. $A/A_0 < 1$. Figure 9, 10 and 11 show the jet at the same conditions, but with increasing freestream Mach numbers of .7, .85, and .95, respectively. Note that the feedback amplitude increases with freestream Mach number and that in each of the higher Mach number cases there is a screech loop gain at two or more frequencies. Also, the number of frequencies at which a loop gain does occur increases dramatically with increasing freestream Mach number. The mechanism by which this occurs is as follows. The basic screech process generally results in a screech wavelength on the order of the jet shock cell spacing. For reference purposes, the instability mode can be considered to propagate at roughly the freestream speed of sound. The acoustic waves propagate upstream at the speed of sound minus the freestream speed. Thus as the freestream speed approaches the freestream speed of sound, the propagation speed of the upstream propagating acoustic waves is a small fraction of the downstream propagating vortical instability wave. As a consequence of these disparate speeds, the slow traveling acoustic waves will group in substantial numbers relative to the downstream propagating wave. Thus with a small change in frequency, large acoustic wave phase variations occur at the nozzle lip. This tightly clusters the acoustic interference pattern, from differing downstream shock cells, resulting in an increased number of frequency peaks at the higher freestream Mach number. This observed behavior has significant implications for aircraft aftend structures.

Figures 12 through 15 in comparison to Figures 8 through 11 show the effect of doubling the shear layer growth rate for hot jets, with a jet to freestream ratio of 5.0, at Mach numbers .4, .7, .85 and .95, respectively. Note that the faster shear layer growth rate results in decreased feedback amplitudes. In fact for this jet the higher shear layer growth rate results in no feedback loop gain. Again, the trend of an increased number of peaks with increasing Mach number is evident in Figures 12 through 15.

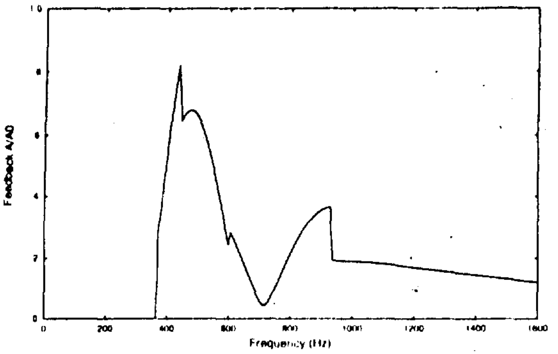

Figure 8: M_∞ = .4, Shear layer growth rate = .05.

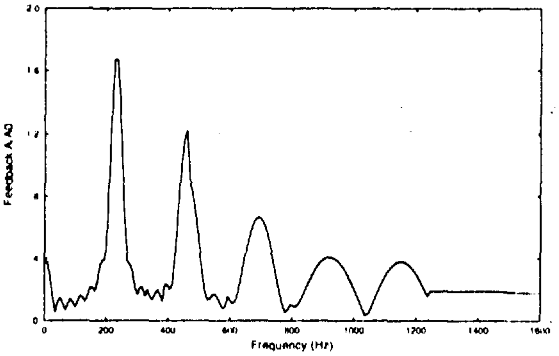

Figure 9: M_∞ = .7, Shear layer growth rate = .05.

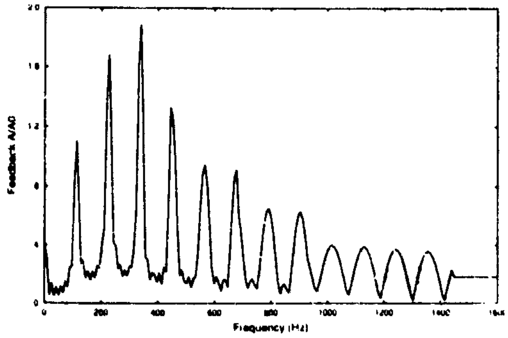

Figure 10: M_∞ = .85, Shear layer growth rate = .05.

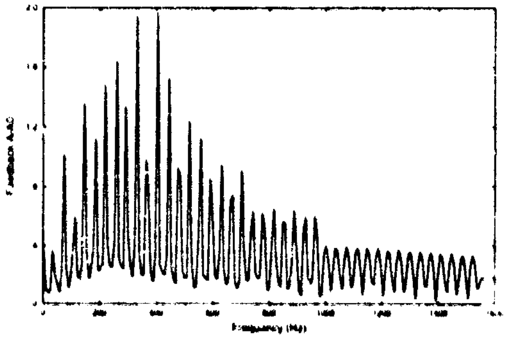

Figure 11: M_∞ = .95, Shear layer growth rate = .05.

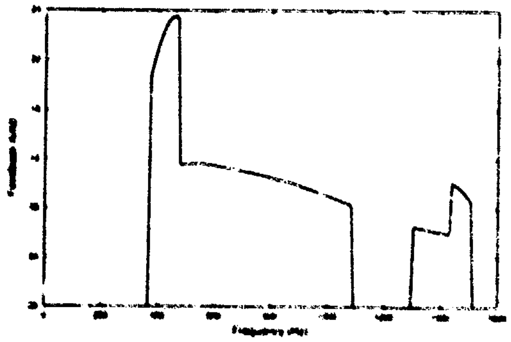

Figure 12: M_∞ = 1, Shear layer growth rate = .1

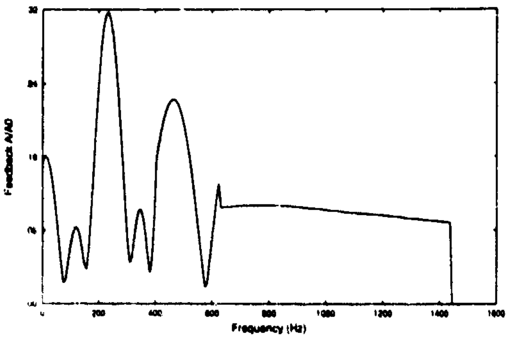

Figure 13: M_∞ = .7, Shear layer growth rate = .1.

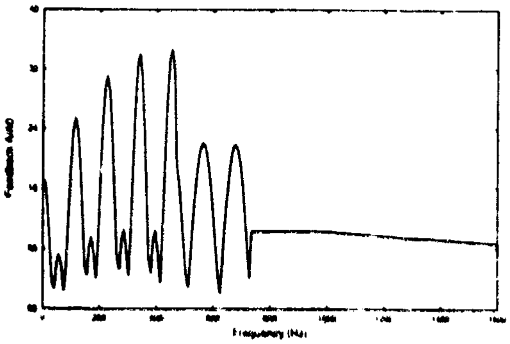

Figure 14: M_∞ = .85, Shear layer growth rate = .1.

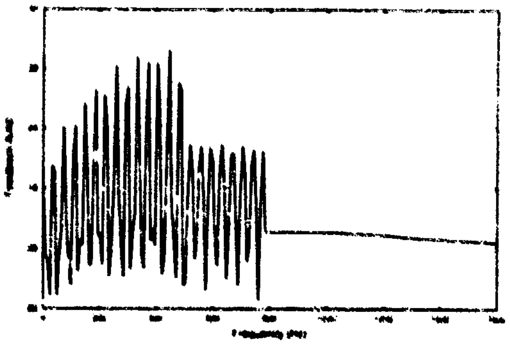

Figure 15: M_∞ = .95, Shear layer growth rate = .1

6. CONCLUSIONS

An engineering design tool to predict screech frequency and amplitude has been developed. The current code, developed in a modular fashion to model the instability waves, shock-vortex interaction, acoustic feedback and receptivity, runs in a few seconds on a workstation. The code takes advantage of a graphical interface. Within this interface, the CFD solution of the jet to be analyzed can be displayed, the screech prediction code can be run using the appropriate menu selections, and the variation of predicted screech amplitude gain versus frequency can be plotted.

Preliminary results from a single 2-D jet illustrate the effects of freestream Mach number and shear layer growth rate on both the screech amplitude and frequency. Increasing freestream Mach number has been shown to dramatically increase the number of frequencies at which a feedback loop amplitude gain occurs. And, the amplitude of the peaks is seen to increase with increasing Mach number. Increasing the shear layer growth rate has been shown to significantly decrease the amplitude of the screech peaks at all frequencies for each freestream Mach number.

7. ACKNOWLEDGEMENTS

In writing this paper, the authors benefitted from prior contributions and discussions with W.W. Bower, R.H. Bush, J.A. Johnson and W.W. Romer from McDonnell Douglas and E.J. Kerschen from The University of Arizona.

8. REFERENCES

1. Seiner, J.M., Manning, J.C. and Ponton, M.K., "Model and Full Scale Study of Twin Supersonic Plume Resonance," AIAA-87-0244, 1987.

2. Berndt, D.E. and Butler, L.P., "Drag Estimate of B-1B Engine Nozzles with Outer Nozzle Flaps Removed," Rockwell International Technical Report, TFD-87-1118, 1987.

3. Cain, A.B., Bower, W.W. and Romer, W.W., "Fluid Mechanics of Screech, A Workstation Analysis Tool, Phase I," WL-TR-94-3054, November, 1993.

4. Norum, T.D., "Screech Suppression in Supersonic Jets," AIAA Journal, Vol. 21, No. 2, 1983.

5. Walker, S.H., "Twin Jet Screech Suppression Concepts Tested for 4.7% Axisymmetric and Two-Dimensional Nozzle Configurations," AIAA-90-2150, 1990.

6. Wlezien, R.W., "Nozzle Geometry Effects on Supersonic Jet Interactions," AIAA Journal, 27, 1989.

7. Cain, A.B., "Computation of Supersonic Jet Screech," Proceedings of ASME Forum on Aero and Hydro Acoustics, Washington, D.C., June 21-24, 1993.

8. Tam, C.K.W., Seiner, J.M. and Yu, J.C., "Proposed Relationship Between Broadband Shock Associated Noise and Screech Tones," J. Sound and Vibration, 110, 1986.

9. Caudill, M., "Neural Networks Primer, Part I," AI Expert Journal, December, 1987.

10. Caudill, M., "Neural Networks Primer, Part II," AI Expert Journal, February, 1988.

11. Caudill, M., "Neural Networks Primer, Part III," AI Expert Journal, June, 1988.

12. Rice, E.J. and Taghavi, R., "Screech Noise Source Structure of a Supersonic Rectangular Jet," 30th Aerospace Sciences Meeting, AIAA-92-0503, 1992.

13. Walker, S.H., "Experimental Investigation of a Screech Feedback Loop," Research Proposal, University of Notre Dame, 1994.

14. Thomas, F.O. and Chu, H.C., "Experimental Investigation of the Nonlinear Spectral Dynamics of Planar Jet Transition," Phys. Fluids A, Vol. 3, No. 6, 1991.

15. Thomas, F.O., "An Investigation of the Vorticity Wave/Shock Wave Interaction in a Supersonic Jet Under Screech Conditions," Unofficial Research Proposal to Air Force, 1992.

APPLICATION OF THE PSD TECHNIQUE TO ACOUSTIC FATIGUE STRESS CALCULATIONS IN COMPLEX SUBSTRUCTURES.

H. Climent
J. Casalengua
Structural Dynamics Department
CONSTRUCCIONES AERONÁUTICAS S.A.
Getafe, 28906 Madrid, Spain

SUMMARY

A method for stress calculation using the Power Spectral Density (PSD) technique for acoustic fatigue evaluation is presented.

The sound pressure levels (SPL) are converted to acoustic pressures PSD and applied to a finite element model representation of the substructure. This technique can cover: complex geometries in substructures, detailed effect of reinforcements and the contribution of several normal modes, improving the previous procedure based on ESDU data sheets that accounts for simple geometries and only contribution of the first mode is considered.

The method is used to predict stresses at substructures subjected to severe acoustic environment.

Comparison with acoustic fatigue test results show good correlation between experimental data and theoretical analyses in terms of stresses and accelerations providing an encouraging basis for further work in this direction.

1 INTRODUCTION

Since aeronautical structures are getting lighter, more complex and aircraft performances enhance, acoustic fatigue arises as a problem in areas subjected to severe acoustic environment, even becoming critical for substructures design, especially for large panels with small thickness.

The complete problem can be split into:

- Determination of Input Spectra (i.e. Sound Pressure Levels (SPL), Overall Sound Pressure Levels (OSPL), etc).
- Determination of Structural Response (i.e. rms stresses, accelerations, internal actions and number of positive crossings)
- Fatigue Life Evaluation.

The solution of the first part still relies basically on flight and ground test data. During a project development and design phases, when no flight test data are available, input spectra estimates are obtained based on empirical procedures, past experience and read-across from other aircrafts, with similar aircraft mission and performances.

The solution of the last part has the additional difficulty of the low amount of available data concerning the new materials often used for these substructures.

This paper is focused on the intermediate part: the structural response. Subsequent sections summarise the theoretical development and application of a Power Spectral Density (PSD) technique to obtain rms structural responses ($\overline{A}$) and the number of positive crossings (N0) for further acoustic fatigue life evaluations.

Although the idea of using the statistical characteristics of structural response to random input loading can be already found in the 50's [1], it has been necessary to wait for finite element methodology to mature and computer capabilities to explode before applying it to actual aircraft structures. Even with today's standards the computer resources needed to perform these kind of calculations are still high.

The input spectrum is assumed to be known. SPL are then converted to acoustic pressures PSD and applied to a finite element model representation of the substructure. The effect of complex geometries and the contribution of several normal modes is considered, improving empirical approaches that take only into account the contribution of the first normal mode in simple geometries (i.e. ESDU data sheets).

Validation of the procedure includes sensitivity analysis to the relevant parameters from the fatigue stress prediction standpoint: structure boundary conditions, frequency cut-off, damping values etc. To tune all this parameters, an exhaustive validation program has been envisaged, covering:

- Application to simple cases and comparison with results obtained from alternative procedures.
- Application to a specimen tested under laboratory conditions.
- On ground test of actual aircraft.
- In flight test of actual aircraft.

Presented at a Symposium on 'Impact of Acoustic Loads on Aircraft Structures' held in Lillehammer, Norway, May 1994.

The validation task is still in progress and only information concerning the first three steps is available and presented within this paper. Good correlation has been obtained with the simple cases reproduced with alternative procedures. With the specimen tested under laboratory conditions, stresses and accelerations were predicted and compared with test results showing in general good correlation (within method limitation). Description of this application constitutes the bulky part of the paper. A limited amount of information regarding ground test is also presented. The paper ends with a discussion on the scope and limitations of the method.

2 ADVANTAGES OF THE FEM + PSD METHOD

The standard empirical approach [6] to obtain stresses for fatigue evaluation has limitations that restricts its use to only some cases.

Previous limitations overcome when using PSD technique to obtain acoustic fatigue stresses instead of method of [6] are summarized in table 1.

Nevertheless, suitability of the method should be shown by means of an exhaustive validation procedure.

Conditions:	Method from [6]	FEM + PSD Method
Substructure:	Simple geometries	Complex geometries
Boundary conditions:	All edges fixed	Any boundary condition
Modes contributing:	Only the fundamental mode	All desired modes
Input excitation:	Plane wave. Constant acoustic pressure over the frequency range close to the fundamental frequency	Any amplitude and phase Variable acoustic pressure in any frequency range
Output response:	Only r.m.s. stresses at rivet line N0 = fundamental mode frequency	r.m.s. stresses, accelerations and internal actions at any point of the substructure N0 includes contributions of several modes

Table 1: ADVANTAGES OF FEM + PSD METHOD

3 BASIC ASSUMPTIONS

1. Linear behaviour of the structure (small displacement amplitudes).
2. Fluid pressure is the force causing stresses on the structure and leads to an isotropic force field, then only displacements normal to the fluid-structure interface surface contribute to the work done by external forces and thus only d.o.f. normal to the surface have been considered in computing the normal modes.
3. The characteristic length of the pressure oscilations variation is assumed to be high when compared with the problem characteristic length given by overall structure dimensions, thus leading to a time dependant plane wave acting on the structure.
4. Inviscid fluid is considered through the analysis, thus not accounting for oblique fluid-structure interaction.
5. The coupling effects may be neglected if the fluid cavity is large enough. The present analyses do not include any cavity effects because of the engine exhaust vecinity, thus no fluid-structure coupling analysis is necessary.
6. The spectral distribution is assumed continuous with small rate of change of level with frequency.
7. Simulated structures should have small curvature.
8. All dB values in this paper are referred to a reference pressure of $20 \mu Pa$.

4 FINITE ELEMENT AND PSD APPROACH

The approach includes the following steps:

- Modelling of the substructure.
- Setting up the input excitation.
- Response evaluation.
- Parametric variations.

The substructure is modelled using conventional F.E. modelling techniques. Although due to geometrical characteristics of structures potentially subjected to acoustic fatigue problems, the elements used are basically plate elements that can withstand pressures acting in the normal direction of their surface, any other elements needed to adequately simulate the stiffness characteristics of the structure are also used.

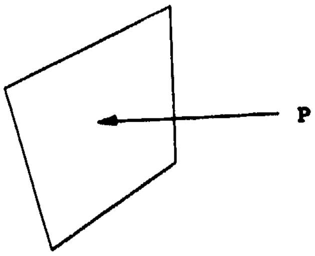

Figure 1: Plate Element and Pressure

The random acoustic loading is simulated by means of fluctuating pressures acting on one side. Advanced Finite Element Codes have embodied suitable modules to deal with random analyses [2] that take into account the advantages of the Power Spectral Density (PSD) formulation. The underlying theory is well known [3] being the main conclusion the relationship between the power spectral density of the response ($S_j(\omega)$) and the power spectral density of the source ($S_a(\omega)$) that allows the statistical properties of system response to random excitation to be evaluated via the techniques of frequency response: (quoted from [2])

$$S_j(\omega) = |H_{ja}(\omega)|^2 \times S_a(\omega) \qquad (1)$$

where $H_{ja}(\omega)$ is the frequency response of any physical variable u_j, due to an excitation source, Q_a that verifies the transfer function theorem:

$$u_j(\omega) = H_{ja}(\omega) \times Q_a(\omega) \qquad (2)$$

where $u_j(\omega)$ and $Q_a(\omega)$ are the Fourier transforms of u_j and Q_a.

Once response PSD is known, the rms value ($\overline{A}$) is computed as the squared root of the PSD area:

$$\overline{A} = \sqrt{\frac{1}{2\pi}\int_0^\infty S_j(\omega)d\omega} \qquad (3)$$

And the expected value of the number of zero crossings with positive slope per unit time ($N0$) as:

$$N0 = \sqrt{\frac{\int_0^\infty \left(\frac{\omega}{2\pi}\right)^2 S_j(\omega)d\omega}{\int_0^\infty S_j(\omega)d\omega}} \qquad (4)$$

The input spectrum is assumed to be known (based on test data or read-across) in third octave band. Besides this is the most common way this spectrum is provided, hypothesis 6 is automatically satisfied and makes the method less sensitive to substructure imperfections (either in the model or in the specimen itself due to manufacturing tolerances)

4.1 Sound Pressure Level Spectrum Conversion into spectral density of acoustic pressure

Starting from the available sound pressure level spectrum in third octave band, the spectral density is obtained in three steps:

1. Relation between the sound pressure level $(SPL)_{Hz}$ at a particular frequency and the level in third octave band $(SPL)_{\Delta f\frac{1}{3}}$ centered at that frequency f_c.

   From [4]:

   $$(SPL)_{Hz} = (SPL)_{\Delta f\frac{1}{3}} - 10\log_{10}\Delta f \qquad (5)$$

   $$\Delta f = f_2 - f_1 = 2^{\frac{1}{6}} f_c - \frac{f_c}{2^{\frac{1}{6}}} = 0.235633 f_c \qquad (6)$$

   $$(SPL)_{Hz} = (SPL)_{\Delta f\frac{1}{3}} - 10\log_{10} f_c + 6.3533 \qquad (7)$$

2. Relation between sound pressure level and r.m.s. fluctuating pressure p_{rms}.

   From [5]:

   $$(SPL)_{Hz} = 20(\log_{10} p_{rms} + 4.69897) \qquad (8)$$

   When p is in Pa and $p_{ref} = 20\mu Pa$

   From equation 8 the relation between p in Pa and $(SPL)_{Hz}$ in dB (referred to $20\mu Pa$) can be extracted:

   $$p_{rms} = 10^{\left[\frac{(SPL)_{Hz}}{20} - 4.69897\right]} \qquad (9)$$

3. Relation between the spectral density of acoustic pressure $PSD(f)$ and the root mean square fluctuating pressure.

   When unit bandwith is used, the squared root mean square fluctuating pressure is numerically equal to the spectral density of acoustic pressure at frequency f in Pa^2/Hz $[(N/m^2)^2/Hz]$ units.

$$PSD(f) = [p_{rms}]^2 \qquad (10)$$

   Therefore:

$$PSD(f) = [10^{\frac{(SPL)_{Hz}}{20} - 4.69897}]^2 \qquad (11)$$

   in Pa^2/Hz $[(N/m^2)^2/Hz]$

   NOTE: when mm units are used instead of m the expression becames:

$$PSD(f) = [10^{\frac{(SPL)_{Hz}}{20} + 1.30103}]^2 \qquad (12)$$

   in $(MPa)^2/Hz$ $[(N/mm^2)^2/Hz]$

4.2 Sensitivity to relevant parameters:

- Mesh size. Starting with coarse meshes, results convergence to mesh size should be checked using successively finer meshes. As a general rule, a minimum of 4 elements in each mode shape wave of the highest frequency mode of interest should be used.
- Reinforcements modeling. Most of the time, the "complexity" of the structure is not due to its overall dimensions but to its reinforcements, beads, feeding channels etc. As large stress gradients are anticipated close to substructure's edges, careful attention should be given to that modeling.
- Cut-off frequency. It determines the amount of normal modes contributing to the response. The modal frequency response limit should be selected once the truncation error has proved to be negligible. Usually, the response PSD shows a decreasing pattern with frequency that allows cut-off frequencies in the 500 Hz to 1000 Hz range.
- Frequency integration interval. Should be small enough to allow frequency resolution between adjacent response peaks. A typical value is 1.5 Hz.
- Boundary Conditions. The only real boundary condition easy to reproduce in a finite element model is free-free. Actual substructures boundary conditions are seldom free-free being a combination of clamped, fixed or simply supported. Attachments flexibility provides additional uncertainties to boundary conditions making necessary to perform sensitivity analysis of this parameter.

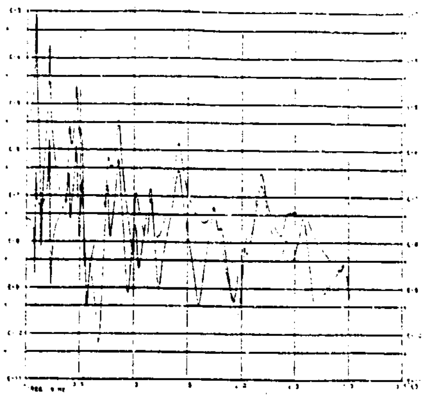

Figure 2: Typical PSD response [0-3000 Hz.]

- Damping. Being a very difficult subject, not only to predict but even to measure on test, it is far beyond the scope of the present paper to perform an exhaustive discussion concerning damping. Contributions to damping of the substructure are: structural damping, air damping, damping due to sound radiation, damping due to air pumping at structural joints, etc. The reader can find in [1] some basic principles. More specific items can be addressed in [7]. Either structural or modal damping may be used. Nevertheless, in the absence of actual modal damping measurements or better estimates, a constant structural damping value of g=0.01 can been used for isolated specimens (as those tested in laboratory facilities) and g=0.034 (as recomended by [6]) for airplane built-in substructures. Figure 3 shows a typical evolution of a response with the amount of structural damping using the present method which matches with a similar curve from [6]. A response value of 1 has been selected to normalise the curves at g=0.034.

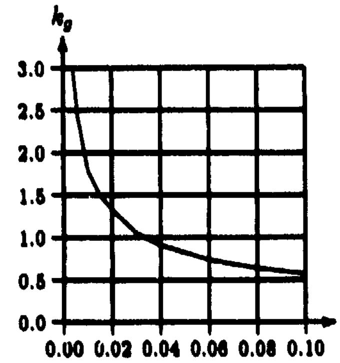

Figure 3: Damping ratio correction factor

5 PRELIMINARY VALIDATION (COMPARISON WITH ALTERNATIVE METHODS)

Preliminary validation was achieved by comparison of results obtained with the present method and those obtained using [6] applied to three different cases: a flat plate, a slightly curved plate and a series of panels with increasing curvature. Aluminum material with Young's modulus E = 70000 Mpa, mass density $\rho = 2710 Kg/m^3$ and a constant exciting spectrum of 120 dB were used. Analyses conditions were those of method [6] validity: contribution of a single mode (fundamental) and all edges fixed. Damping value used was $g = 0.03$.

Table 2 shows the comparison of results obtained with [6] method and with method presented herein. Results provide fundamental mode frequency and rms stresses at the rivet line. Dimensions of plates are expressed as: *Straight edge length* (a) × *Curved edge length* (b) × *Thickness* (t).

Good agreement has been obtained for flat and slightly curved panel, providing the present method stresses about +6% higher in the flat plate case and +2% higher for the slightly curved panel. Series of increasingly curved panels show that higher differences arise as curvature of the panel increases.

Due to the limitations imposed by the conditions of those analyses, an additional validation was envisaged, based on comparison with an acoustic fatigue laboratory test of an actual aircraft substructure.

6 VALIDATION WITH LABORATORY TEST RESULTS

6.1 Test Specimen

A test was conducted in a reverberation chamber to study the response characteristics to various acoustic excitations.

Figure 4 shows the test specimen location on aircraft engines area, isolated test specimen planform and longitudinal cross-section where feeding channels and bead shapes may be seen.

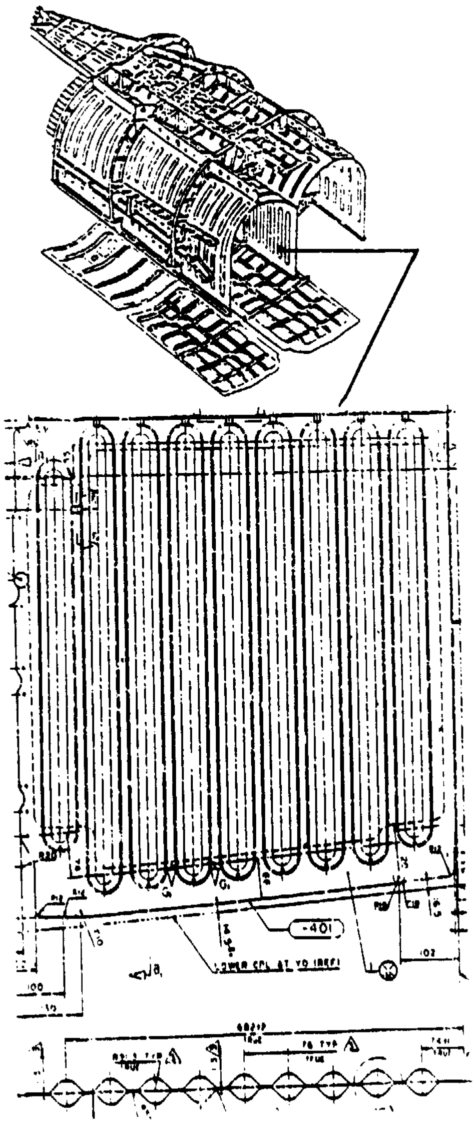

Figure 4: Test Specimen

Plate	Dimensions $a \times b \times t$ (m)	Curvature 1/R (m^{-1})	RESULTS			
			[6] Method		Present Method	
			Freq. (Hz)	Stresses (MPa)	Freq. (Hz)	Stresses (MPa)
Flat	0.6 × 0.4 × 0.002	0.000	82.6	22.0	83.7	23.80
Curved	0.36 × 0.3 × 0.0012	1.111	415.	2.10	442.	2.14
Incrs. Curv.	0.48 × 0.4 × 0.002	0.000	93.8	19.0	94.1	21.75
		0.125	128.8	11.0	129.2	13.72
		0.250	197.5	6.0	197.8	5.35
		0.625	350.0	2.1	350.3	3.85
		1.250	401.3	1.0	405.6	0.53

Table 2: COMPARISON OF [6] METHOD RESULTS WITH PRESENT METHOD

Test article was mounted in test frames to simulate the stiffness of the adjacent structure, the assembly was soft suspended in the reverbaration chamber and then subjected to acoustic excitation.

The test specimen is a part of the keel beam separating the two engine tunnels between two fuselage frames, built as a single piece by superplastic forming/diffusion bonding (SPF/DB) of titanium alloy. Initially, two flat panels are placed into a mould and feeding channels are used to inflate the beads at high temperature when titanium plasticity is achieved. Thus, feeding channels significantly contribute to the upper edge stiffness. Specimen dimensions are aproximately 700 by 800 mm.

6.2 Specimen Finite Element Model

The Finite Element Model representing the specimen consists of 2647 nodes and 2897 elements and may be seen in figure 5. Plate elements are used to model flat areas and beads and beam elements to simulate the feeding channels. The specimen mass is distributed all along the model by inclusion of actual titanium density.

Boundary conditions are imposed to the F.E. model simulating the actual built up of the panel in the aircraft: clamped conditions on upper keel beam upper edge and simply-supported conditions on the other three edges. Such conditions have been also reproduced in the test specimen.

Trials with simplified models have shown that the keel beam cannot be modeled either as a flat or as a rectangular panel or as a corrugated plate with open-ended beads. Feeding channels and bead ends also influence the keel beam stiffness features. Therefore these characteristics must be simulated in the model.

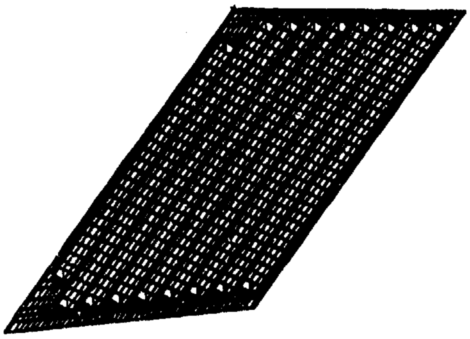

Figure 5: Specimen F.E. Model

TEST SPECIMEN FEM SUMMARY	
NODES	No. ELEM.
2647	2897

Table 3: Test Specimen FEM Summary

6.3 External Forces

Exciting forces are usually given as one third octave band spectra and sometimes as octave band spectra. In both cases the sound pressure levels are converted into acoustic pressures PSD and applied to the finite element model representation of the specimen. Figure 6 shows the actual test spectrum.

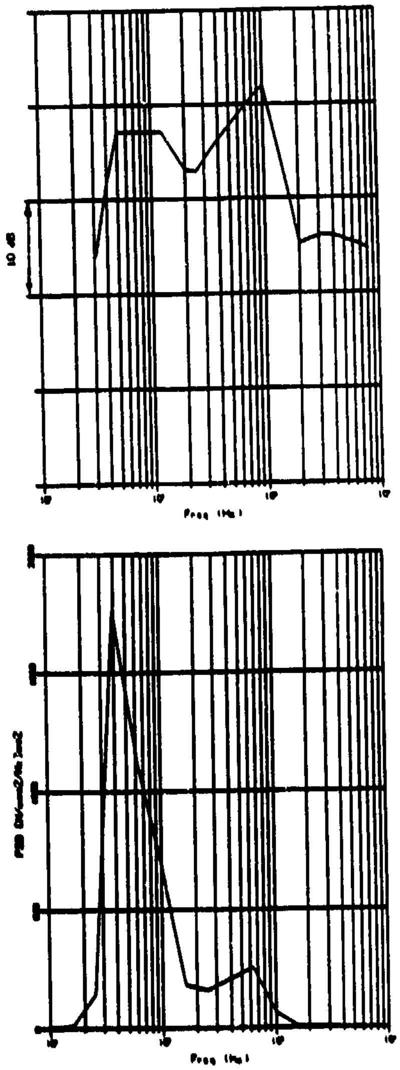

Figure 6: 1/3 Octave Band and PSD Test Spectrum

6.4 RESULTS

6.4.1 *Normal modes and frequencies:*

The modified Householder method was used to obtain the normal modes. A previous static (Guyan) reduction to the normal to the plate degrees of freedom was performed in order to reduce the CPU time.

Figure 7 shows the first two theoretical normal mode shapes.

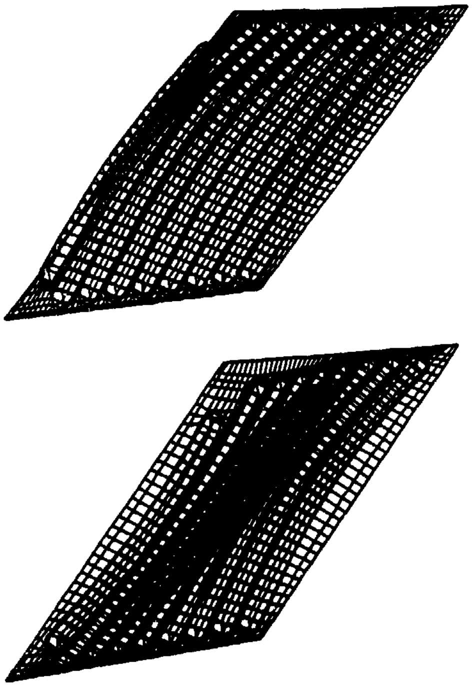

Figure 7: Keel Beam Normal Modes 1 and 2

MODE (NO.)	THEORETICAL ANALYSIS FREQ. (Hz)	TEST MEASURED FREQ. (Hz)
1	162	170
2	194	190
		215
3	250	245
		270
4	314	315
5	383	370
6	443	440
7	485	470

Table 4: Keel Beam Natural Frequencies

The natural frequencies measured on test have been obtained by processing accelerometers and strain gauges response and considering natural frequencies where response peaks occur. Digital samples with a sampling frequency of 5 kHz were used to obtain root mean square values and power spectral density distributions. Table 4 shows the natural frequencies predicted in the analysis and the frequencies measured in test.

Predicted frequencies are close to those measured during test. Only test response peaks at 215 and 270 Hz have not been obtained in the theoretical analysis. Nevertheless, these peak responses in the test are low when compared with the most important contributing modes of 170, 190 and 315 Hz frequencies.

6.4.2 *Stresses and Accelerations*

In order to have correlation between prediction and test results as well as stress and acceleration distributions over the model, rms stresses have been obtained at different locations (see figure below):

- Clamped edge (FEM)
- Elements adjacent to clamped edge (FEM) (edge distance:4.3 mm)
- Elements on vertical center strip (FEM)
- 7 Accelerometers (Test) ▲
- 5 Strain gauges (Test) ▮
- 4 Rosettes (Test) ●

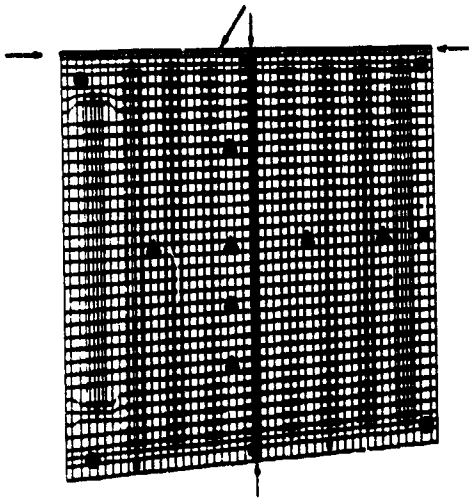

Theoretical Stresses in vertical direction $(\sigma_y)_{rms}$ on external plate surface on the selected locations of the model are shown on the following plots:

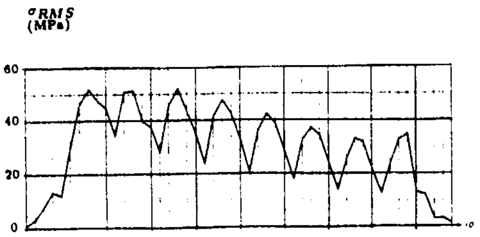

Figure 9: Theoretical stress output at clamped edge

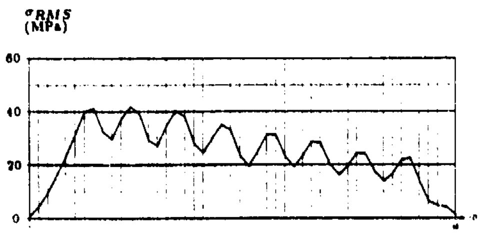

Figure 10: Theoretical stress output at elements adjacent to clamped edge

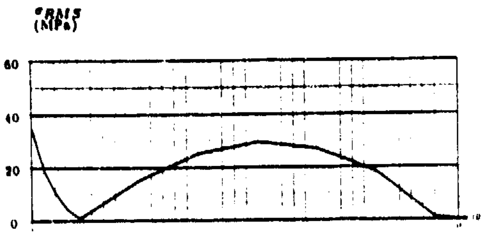

Figure 11: Theoretical stress output at central line elements

Predicted stresses and accelerations are in good agreement with those obtained in acoustic test, as may be seen in figure 12 where least squares fit method is used to obtain the regression line and linear correlation coefficient ρ.

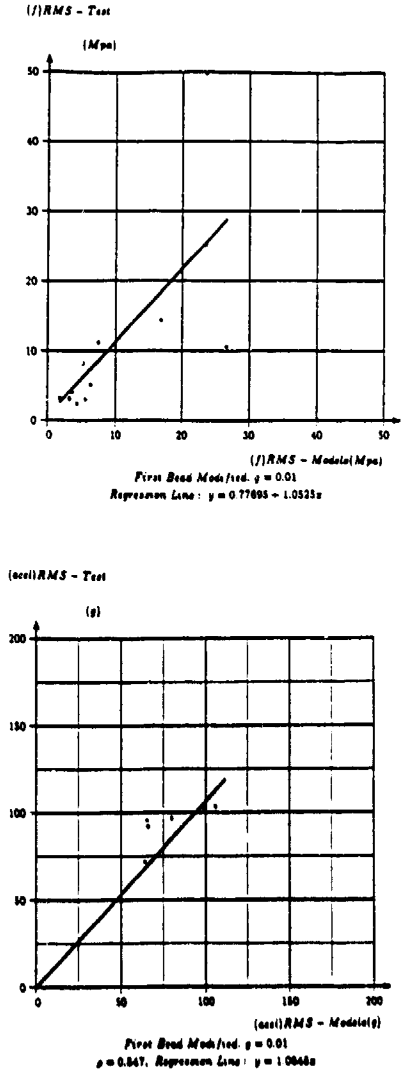

Figure 12: Predicted vs Test Stress and Acceleration Correlation

Regression line coefficient value close to 1 -as obtained- indicates a good global correlation, nevertheless the plots show some particular points -specially in the stresses comparison- with large discrepancies. The explanation may be in the high stress gradient near the specimen edges and specially in the neighbourhood of the clamped line, in which small differences in position could give large differences in stresses. The exact strain gauge and accelerometer locations cannot be known without some level of uncertainty. In addition, the actual damping value is also unknown. The scatter is lower in the case of the accelerations (the accelerometers are located relatively far from the specimen edges).

6.4.3 *Crack location and growth*

Visual inspections to detect possible damages and their development were performed during the keel beam acoustic fatigue test. A crack of 210 mm was detected after 9 hr test time close to upper keel edge. Figure 13 shows the location where crack appeared (superimposed to F.E.M. plot) and also approximate development of damage occured during test.

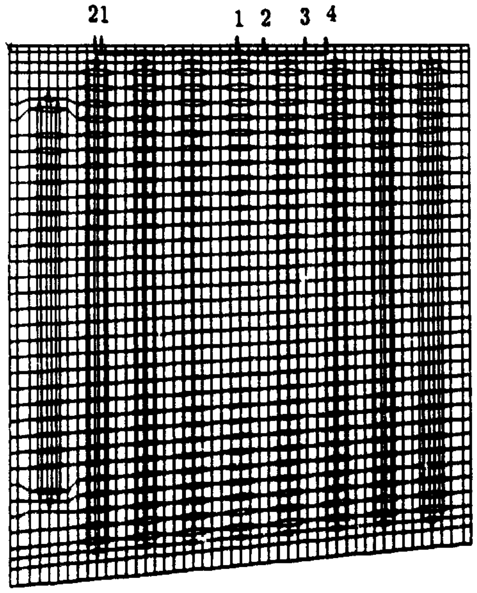

Development of damage until the end of test was:

(1 - 1) cracklength 210 mm after 9 hrs
(2 - 2) cracklength 255 mm after 10 hrs
(2 - 3) cracklength 325 mm after 11.5 hrs
(2 - 4) cracklength 335 mm after 13.5 hrs
(2 - 4) cracklength 335 mm after 15.0 hrs (no growth)

Figure 13: Keel Damage

Stress output (fig 9) shows that location where the highest predicted stresses occur is in accordance with crack starting location. Rapid initial crack growth is also explained due to the fact that stress levels are significantly equal over the line where crack started to run. The region of similar high stress levels corresponds roughly with the crack length. The crack stopped in the final hours of the test, in the position in which the theoretical model predicts a decrease of stresses. It should be pointed out that the presence of the crack can have an influence (local change of boundary conditions and stiffness) leading to local stress redistribution that has not been covered by the analysis.

7 APPLICATION TO ACTUAL AIRCRAFT SUBSTRUCTURES TESTED ON-GROUND

7.1 Substructures and models

Two structural components being part of the same keel beam as the laboratory specimen have been used. Each one is also built as single piece by superplastic forming / diffusion bonding of titanium alloy. Thus feeding channels and beads contribute to stiffness. The substructures have been modelled using similar criteria than in the laboratory specimen. Next figures and table show FEM's summaries.

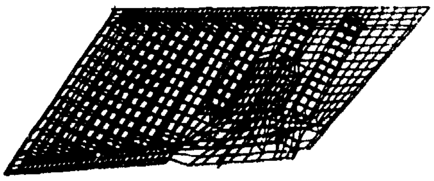

Figure 14: Aft keel beam model

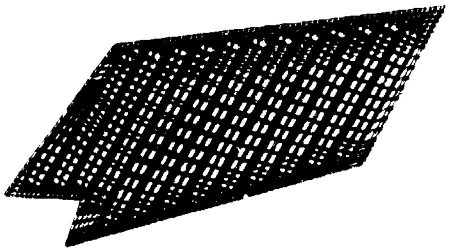

Figure 15: Mid-aft keel beam model

KEEL BEAM MODELS			
MODEL	DIMENSIONS (m)	NODES	No. ELEM.
AFT	0.900 × 0.381	1585	1808
MID-AFT	0.948 × 0.500	2256	2479

Table 5: Keel beam FEM's Summary

7.2 On-ground test

Engine ground test were performed with limited amount of instrumentation (one microphone and one accelerometer on the center of each keel beam) to measure the acoustic excitation and the vibration response on the keel beams.

In those tests some of the assumptions of validity of the method are satisfied (linearity, small curvature of the structure etc) while others are not fully satisfied (plane wave, acoustic coupling...). As those hypothesis correspond to the worst case scenario, results from theoretical predictions will be -in general- conservative. Nevertheless, test can be used to derive correction factors if enough repeatibility and correlation between different runs is provided.

27 different runs were performed covering left, right or both engines running, different engine settings from idle to maximum dry and bay doors open and closed conditions. Measured microphone acoustic excitation expressed in one third octave band for each run was subsequently used as input to the analytical simulations. Accelerometer signals were postprocesed to obtain PSD's and rms values. Peaks on PSD plots occur at frequencies that can be identified either as normal mode frequencies of the substructures or frequencies associated with engine r.p.m.'s.

Figures 16 and 17 show the comparison between simulated and measured acceleration rms values for the 27 on ground engine runs and the two substructures: aft keel beam and mid-aft keel beam. A regression line has been also superimposed on each plot.

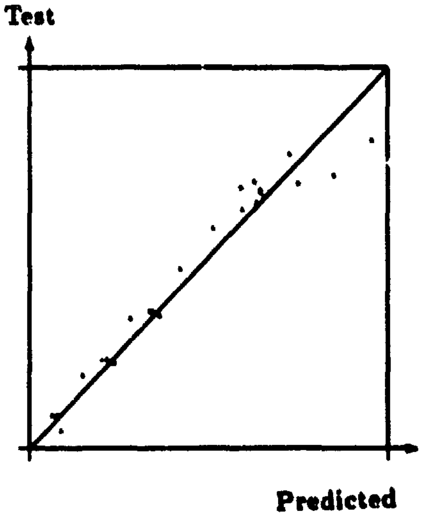

Figure 16: Aft keel beam Comparison

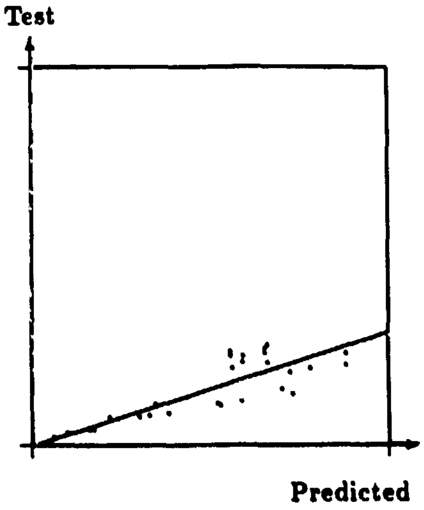

Figure 17: Mid-aft keel beam Comparison

As can be seen, there is a factor of roughly 3 between the slopes of the two regression lines. Nevertheless the correlations obtained are excelent in the case of the aft keel beam ($\rho = 0.980$) and fairly good in the mid-aft keel beam ($\rho = 0.823$).

On-ground measured values are conservative because ground, wall and roof reflections on test facilities will not occur in flight. The corrections used to match theoretical predictions with on ground test results are considered to be applicable to in-flight conditions.

More on ground test measurements will be performed and a complete survey of flight test is envisaged that will show the validity, applicability and limitations of the FEM + PSD method presented.

8 CONCLUDING REMARKS

A FEM + PSD method to compute acoustic fatigue stresses has been presented. The method uses already existing modules embodied in commercial finite element codes to evaluate system resposes to random excitation, and overcomes the limitations of the previous empirical methods, allowing to consider complex geometries, different boundary conditions, contributions of several normal modes and to compute output responses in any position of the modelled structure.

Despite its limitations, the method is considered to:

- Adequately compute relative responses within the same substructure, that can be used to select test instrumentation and predict possible crack positions.

- Predict absolute response values when the hypothesis of validity are satisfied. As those hypothesis use to correspond to a worst case scenario (i.e. plane wave), if some are not verified, results of the method will be a conservative estimate. A single factor that match test comparisons can then be used to correct the theoretical predictions.

The method presented has predicted adequately stresses and accelerations in a complex substructure tested to a severe acoustic environment in laboratory facilities. The likely location of the crack and some assessment concerning the crack length could have also been made prior to the test. This information can be either used directly for fatigue life evaluation or can help to define the most suitable position of an acoustic fatigue test instrumentation.

Only limited information concerning on-ground test of actual aircraft substructures is available at the present moment. In these cases, not all the hypothesis of validity of the method are totally fulfilled. Nevertheless good repeatibility and correlation has been found between measured and predicted accelerations. More extensive on-ground test are envisaged and the conclusions obtained on-ground for a particular substructure using this method are expected to be fully applicable to in-flight conditions, just modifying the input (excitation) spectrum. In-flight test are also envisaged.

On the other hand, the method should be used with caution when some of the assumptions are not fully aplicable. A typical case is application to largely curve panels in which this method should be corrected to take into account non-planar waves, possible cavity effects, reflections and in-plane stress effects.

The method requires very fine-mesh models, and when application of the method is made to structures built up in an airframe, a sensitivity analysis has to be performed to check the effect of changes in boundary conditions, damping values, number of modes, etc. Therefore the modelling effort and the massive CPU consumptions needed to apply this method to actual structures limit the scope of application to only those substructures which design is likely to be dominated by acoustic fatigue considerations. Although no general rule can be derived, at CASA typical values of exciting OASPL close or above 145 dB are used to switch from routine task (empirical approach) to the PSD technique.

Finally, it was beyond the scope of the study presented herein to perform the fatigue life evaluation itself or more detailed analyses including the change of local boundary conditions of the model due to the effective presence of the crack. Despite the limitations described and the scatter observed in some few particular points between predicted and measured stresses, the results obtained provide an encouraging basis for further work with this approach.

9 REFERENCES

1. Harris, C.M. and Crede, C.E. (Editors), Shock and Vibration Handbook. McGraw-Hill, New York 1961.
2. Gockel, M.A. (Editor), MSC/NASTRAN Handbook for Dynamic Analysis, The MacNeal-Schwendler Corporation. 1983.
3. Newland, D.E., An introduction to Random Vibrations and Spectral Analysis. Longman, London 1983.
4. Harris, C.M. (Editor), Handbook of Noise Control. McGraw-Hill, New York 1957.
5. The relation between sound pressure level and r.m.s. fluctuating pressure. Engineering Sciences Data Item Number 66018. September 1978.
6. The estimation of r.m.s. stress in stiffened skin panels subjected to random acoustic loading. Engineering Sciences Data Item Number 72005. July 1984.
7. Torvik, P.J. (Editor), Damping Applications for Vibration Control. Presented at The Winter Annual Meeting of the American Society of Mechanical Engineers, Chicago, November 16-21, 1980.

ACOUSTIC FATIGUE TESTING ON DIFFERENT MATERIALS AND SKIN-STRINGER ELEMENTS.

Klaus König

Deutsche Aerospace Airbus GmbH
Hünefeldstr. 1-5, 28183 Bremen, Germany

Summary

Within a comparative study, 29 different coupons covering 8 different designs and 6 different materials were fatigued by an excitation of 30 g^2/Hz on a shaker. The selected designs and materials represent realistic alternatives of an aircraft surface structure.

The investigation led to the following conclusions:

- Besides classical aluminium, CFRP is the best material with regard to sonic fatigue.
- Al/Li, ARALL and Al layer materials showed shorter life times than the classical Al.
- The most striking improvement in design for the dimensions selected here was achieved with separate doublers between skin and stringer.
- The modal damping found was most often smaller than the 1.7% of the critical as known from ESDU for Al
- Pure CFRP without rivets showed the smallest damping: 0.6 - 0.9%

Introduction

"Acoustic fatigue" means fatigue of aircraft surface structures due to acoustic loading from different noise sources.
The phenomenon is well known. Regulations exist (e.g. MIL-A-87221, MIL-A-8893, JAR (FAR) 25.571 d).
Design recommendations and some methods of strength demonstration are given, for example, in the ESDU data sheets.

But nevertheless there are still some open questions. They concern amongst others, the influence of some design parameters, the characteristics of new materials and the safety criterion itself.

Furthermore, it should be mentioned that acoustic fatigue is high cycle fatigue (up to 10 E11 cycles) at a very low level of strain. For strength demonstration, acoustic fatigue is usually studied independently of other static or low cycle fatigue loadings with all the consequences.

In the following, the results of a comparative study will be given. 29 different coupon types were tested on a shaker. This covered 6 different materials and 8 different designs. For details s. ref. (1).

2. Test Specimens

The coupon design was as shown in Fig. 2.1 and Tab. 2-1.
Some coupons had separate or integrated doublers between skin and stringer and some had a second stringer angle to allow symmetry.
For the CFRP materials the outer fibre of the skin was perpendicular to the stringer (90, 45, 0, 0, -45, 90/sym).
A survey is given in Tab. 2-2 together with the weight which varied between 0.5 and 1.4 times a reference value.
One of the coupons (1-I) had a layer of sealing material on its skin to improve the damping.
Three of the coupons were manufactured and tested in a separate campaign one year after the others.

3. Test Method

First, it must be stated that the test method is only a substitution of realistic acoustic fatigue conditions.
Firstly, the footpoint excitation on the shaker is not a pressure excitation on the aircraft. But theoretical studies (s. ref. 2) showed that the vibration behaviour of the coupons is not so different if they are excited by footpoint acceleration or by pressure on skin.
Secondly all shaker tests are accelerated tests. Accelerated from realistic life times of the aircraft of some 1000 hours to shaker times of some minutes. This is reached by an increase of the excitation level with all its consequences.

To cover scatter, 3 specimens of each coupon type were clamped at the same time on the shaker.
Excitation was a vertical white noise acceleration.
At least the strain was measured by two strain gauges on each specimen. The one on the skin, the other on the stringer as shown in Fig. 2-1.

In a first step a 1 g^2/Hz broadband excitation between

Presented at a Symposium on 'Impact of Acoustic Loads on Aircraft Structures' held in Lillehammer, Norway, May 1994.

100 and 1000 Hz was applied to find the resonance peaks or eigenfrequencies as shown in Fig. 3-1. Then the frequency of maximum strain belonging to the "symmetrical" bending mode of the skin was selected and a $20g^2/Hz$ small band excitation was applied. The bandwidth now covered 90-110% of the selected eigenfrequency. This intermediate test was performed to check the influence of the loading level on the eigenfrequency and to allow a last correction of the frequency centering.
After that the final test with $30g^2/Hz$ and 90-110% bandwidth was performed.

The spectrum of strain as measured at the beginning of this test is also shown in Fig. 3-1.

During the test the change of the eigenfrequency is watched and plotted over the time as shown in Fig. 3-2. This picture gives a typical result. Three periods can be clearly distinguished. First a short period of steeper frequency decay, second a longer period of slow decay and finally a steep decay just before the fracture becomes visible.
These 3 periods can most probably be allocated to a phase of initial settling of the coupon, to the real fatigue phase and to the time after an initial fracture.
From figures such as Fig. 3-2 it is possible to derive the finally wanted result - the life time up to fatigue. A classical definition says that it is reached if the frequency is reduced by 2%. But it may be difficult to read an exact value of life time if the gradient of frequency decay is small and the scatter of test results large. A further test result of interest is the modal damping of the vibration which results from the spectrum of strain by a classical single mode analysis since only the response is used.

4. Accuracy of Test Results

Test results may be influenced by:

- excitation method
- excitation level
- test and measurement equipment
- environmental conditions
- data processing
- data analysis methods

Test results given without any information on the order of magnitude of the influences of these parameters are of limited value.

To get some information, some pretests and some computations were performed.
Fig. 4-1 shows the shape of the two first vibration modes of a clamped asymmetric coupon as computed.
Fig. 4-2 gives the strain distribution on the skin as measured and computed for a low level excitation.
The maximal strain was measured over the stringer edges and a bit higher on the shorter side of the skin. Therefore the strain gauges for the final tests were placed at this side just outside of the stringer. The measured values agree with the computation with a fully connected stringer. But during the final tests the strain gauges on the skin very often already failed at $20g^2/Hz$ and for coupon 1-I, as shown in Fig. 4-2, the fracture appeared in the rivet line. This would fit better to the computation with a connection between skin and stringer just by the rivet as shown in Fig. 4-2. So effects of redistribution of strain due to the increase of the excitation level or simple stress concentration effects may have some influence. This question needs deeper investigations by computions and tests.
Fig. 4-3 gives some more details of the influence of the excitation level. Strain increases with the increase of the excitation but a stronger influence on the frequency and the modal damping is also visible.

Fig. 4-4 gives some information on the influence of the bandwidth of excitation and the scatter of the test results. The strain decreases with the increase of the bandwidth as the modal damping does while the frequencies show a smaller but opposite tendency.

The scatter measured from 10 samples each is different. It reached about ± 0.5% of the frequency; ± 3 % of the strain and ± 15% of the modal damping.
It is remarkable that 10 different tests sometimes showed the same scatter as 10 different analyses of the tape data of one single test.

Different equipment and bandwidth of analyses used also show their influence. It is negligible for the frequencies but clearly visible for the damping and the strain.

Finally it must be mentioned that a smaller number of the composite specimens showed some deviations in the behaviour. Fig. 4-5 gives two examples. They are found in the strain spectra of the stringer strain gauges at lower excitation levels.
Consequences of these deviations on the final test results could not be detected.

5. Test Results

5.1 Eigenfrequencies

Table 5.1.-1 compares the first symmetric eigenfrequencies of the coupons. They vary between 0.9 and 2.5 times a reference value. This indicates that all the advanced materials and the more expensive designs result in more stiff and less heavy structures.
The influence of the design can be separated as shown in Table 5.1-2. It reaches factors between 1 and 1.5.

5.2 Modal Damping

Theoretically, the magnitude of vibration response is proportional to the square root of the modal damping. Therefore the knowledge of reliable damping values is fundamental for all theoretical studies of acoustic fatigue.
First, it must be mentioned that the increase of damping with the increase of the excitation level (s. Fig. 4-2) most probably results from the larger airdamping due to the larger vibration amplitudes at larger excitations.
Due to the large scatter of the measured values details of the measurement and final conclusions are given in Fig. 5.2-1 and 5.2-2.
These final damping values vary between 0.6 and 2.1% of the critical.

The classical aluminium design reaches values between 1.2 and 1.7 which is in generally smaller than the value of 1.7 as used in the ESDU data sheets. Whether 1.7 is reached at the flying aircraft due to pressure loading at a much smaller excitation level is a question which remains.

The "damping" material applied on coupon 1-I gave only a poor efficiency though it increased the measured damping from 1.5 to 2.1, that means by about 30%. Aluminium/lithium, ARALL and aluminium layers gave about the same values as the classical aluminium while the CFRP materials showed clearly reduced values.

It is also obvious that the symmetric designs produced smaller values than the asymmetric ones.

5.3 Strain

Strain values are not discussed here since it was not clear that the strain gauges were really placed at the critical locations. For some information, see ref. 1.

5.4 Reached Life Times

Fig. 5.4-1 shows the smoothed and normalised time histories of the measured eigenfrequencies from which the reached life times were determined.
First of all one can see very large differences. Some coupons failed after 1.4 minutes (7-I and 6-IV), others lasted for more than 27 hours (one specimen of 8-IV).
The scatter between the different specimens of one coupon is also sometimes rather large and that especially for the CFRP coupons. The specimens of the best coupon (9-IV) showed delamination after 42, 1348 and more than 1609 min, but without major frequency decays.
Fig. 5.4-2 gives the locations of the final fracture found after the tests.

One can distinguish between:

- failure of bonding, if there are no rivets (coupon 6-IV)
- failure of the relatively weak aluminium stringers if they are used together with the stronger CFRP skins (IV and V). Fracture at the clamping for asymmetric and at the stringer radius for symmetric coupons
- fibre delaminations in the triangle between skin and stringer (coupon 8-IV)
- fracture in the skin over the doubler edge if there is a separate doubler, and at the shorter skin side if the coupon is asymmetric
- fracture in the milling edge if the doubler is chemically milled (coupon 7-I)
- fracture in the rivet line of the skin if there is no doubler

In general the failure location is nearly independent of material.
Numbers of the life time in minutes reached by the different coupon (averaged over the three specimens) are given in Table 5.4-3.

Three different failure criteria were selected.

The first:
2% frequency decrease from the starting frequency (at $30 g^2/Hz$)).

The second:
2% frequency decrease from the settling frequency while the settling frequency itself was chosen in the middle of the largest concave curvature (s. Fig. 3-2) of the smoothed curves of frequency over time.

The third:
At the point of initial fracture which was defined in the middle of the largest convex curvature (s.Fig.3-2) of the smoothed curves.

It is remarkable that sometimes all the three criteria give about the same life time while in some other cases only the second and the third criterion result in equal values. But also three completely different results can be found.
It seems that these effects are not so much dependent on the material but on the type of design:

coupons without doubler (type 1 and 4) show three different values
- asymmetric coupons with doubler (type 2 and 3) show three equal values
- symmetric coupons with doubler (type 5 and 7) show more or less two different values.

The question therefore arises which criterion is the most adequate for acoustic fatigue strength demonstrations. Some further considerations concerning this topic are also given in ref. 2.
Obviously it can not be criterion 3 because there would be no reserve left for other loading conditions which are checked independently of acoustic fatigue, as already mentioned.
On the other hand, criterion 1 will perhaps give results depending too much on the chosen excitation level and could be too strong which would result in unnecessarily heavy aircraft.

A final conclusion cannot be given today. More and deeper investigations are necessary. They have to check whether the independent safety analysis for low and high cycle fatigue is really reasonable or unavoidable and whether the vibration behaviour of the coupons is really representative of the vibration behaviour of the realistic aircraft surface structure.

Nevertheless, Table 5.4-3 gives a good survey over the measured test results. But comparisons between these different results and evaluations should be based more on the following.

The values of the measured life time T_a as given in Table 5.4-3 are valid for an equal footpoint acceleration. Tests with an equal pressure load on the skin of all coupons could not be performed. But on the assumption that the pressure load is proportional to the acceleration multiplied by the mass of the skin and the additional assumption that fatigue exponents as given in the S-N curves of ESDU 72015 Fig. 4 for aluminium with countersunk butt holes (χ = 4.83) and in ESDU 84027 Fig. 2 for CFRP (χ = 8.49) are valid, one could try to transfer the measured life times for equal acceleration T_a to life times for equal pressure T_c by

$$T_c = T_a \cdot (m/m_{ref})^{\chi}$$

The results are given in Table 5.4-4 as ratios of $T_c/T_{c\,ref}$.
They look rather different in comparison with the directly measured life times, but should allow an evaluation closer to the reality of the aircraft with its pressure loading.

It is evident that the best coupon is more than 13 times better than the reference coupon, while the worst one reached a life time of less than 0.1 times the reference life time. That is a large range. Furthermore, it is obvious that CFRP is the only material better than the classical aluminium if it is not combined with aluminium stringers. Pure bonding of CFRP without rivets is rather dangerous with respect to acoustic fatigue (s. 6-IV).
Aluminium/lithium, ARALL and aluminium layers are not as good as the classical aluminium.

The different efficiency of the different coupons is remarkable if one compares the different failure criteria.
The last table 5.4-5 allows a clearer survey over the influence of the design on life time. Different ratios of life time $T_a \ldots / T_b \ldots$ are given. Though there is obviously some influence of the materials and of the failure criterion one can say that for the dimensions and conditions of this study:

- the addition of a separate doubler will give the largest increase of life time
  - -- but the influence is larger on asymmetric than on symmetric coupons
- in general integrated doubler are not so effective, they could even reduce the life time
  - -- chemically milled "doubler" produce the strongest reduction
- the addition of a second stringer angle also increases the life time
  - -- but for coupons with separate doublers the influence is rather small or even negative.

6. Conclusions

- Fatigue results from shaker tests are not equal to the fatigue from pressure loadings, but can be made comparable.
- Strain distribution, frequency and damping may depend on the level of loading.
- The amount of scatter is relatively large.
- Test and analysis equipment has some influence.
- Nevertheless the comparison of the test results showed clear tendencies.
- All the new materials allow lighter structures with higher eigenfrequencies.
- Most of the damping values found were smaller than the values given in ESDU.
- CFRP materials have lower damping than aluminium.
- Symmetrical coupons produce smaller damping values than asymmetrical ones.
- The classical aluminium is still a good material only surpassed by CFRP.
  CFRP may be several times better while aluminium/lithium, ARALL and even aluminium layers are slightly worse in comparison with the classical aluminium.
- Much improvement is also possible by the design. Most effective are separate doublers while chemically milled "doublers" reduce the life time strongly.
- The application of a damping material gave only poor improvements.
- Bonding without rivets gave the worst results.
- Symmetric coupons gave no larger improvement compared with asymmetric ones.
- Stress concentration effects most probably contri-

bute to the results.

- Deeper investigations for the definition of qualified failure or safety criteria are necessary.
- New qualified test methods are desired, especially for the measurement of strain without touching the specimens.

References

1. Koenig, K.: "Vergleichende Untersuchung zur Ermüdung verschiedener Materialien und Bauweisen unter Belastung durch Schall"
ZFW 15 (1991) p 373-378

2. Koenig, K.: "Limits of Representative Acoustic Fatigue Predictions"
ICAF 93, Stockholm 7-11.6.93

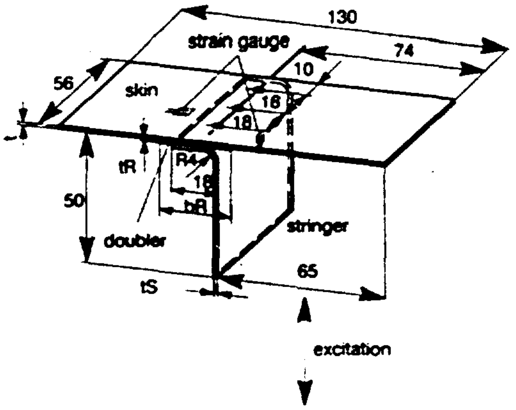

Fig. 2-1 DESIGN OF COUPON

No		I			II		III	IV		V	VI
	material of skin	Al 3.1364T3		+ sealing material	Al/Li 8090		ARALL	CFRP CFRP stringer	 Al stringer	[illegible] (CFRP/GFRP)	Al layers
	type of design	t=1.2 mm	t=1.4 mm	t=1.4 mm	t=1.2 mm	t=1.4 mm	t=1.1 mm	t=1.5 mm	t=1.5 mm	t=1.46 mm	t=3 x 0.4 mm
1	Al (CFRP)		1 ref 46.4 gr	1.2		0.9		0.7	0.8	0.8	1.0
2	Al	1.0	1.0		0.9		0.9				1.0
3	Al								0.9	0.9	
4	Al (CFRP)		1.4			1.3		0.9	1.2	1.2	1.3
5	Al	1.4			1.3		1.3				1.4
6	CFRP							0.9			
7	Al	1.4							1.3	1.3	
8	CFRP							0.5			

Table 2-2 COMPARISON OF THE WEIGHT RATIOS OF THE COUPONS

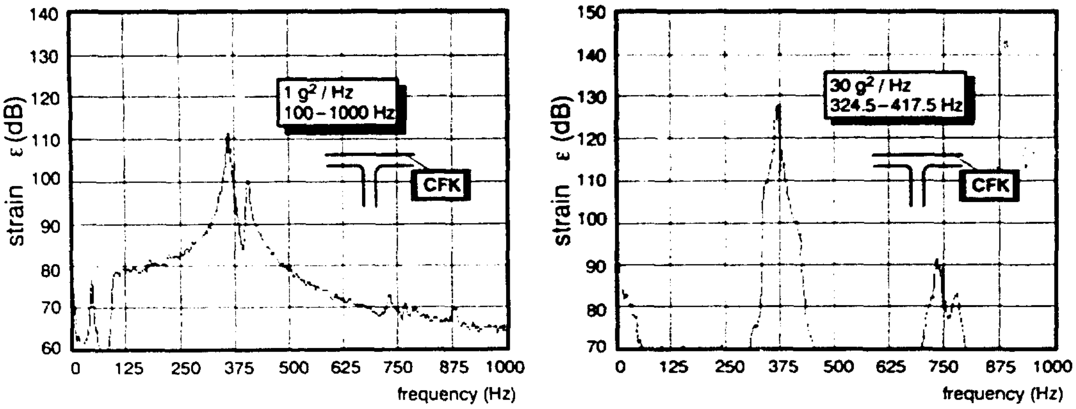

Fig. 3-1 AUTOSPECTRUM OF STRAIN IN SKIN
(coupon 8-IV; two different bandwidths of excitation; Δf=2.5 Hz)

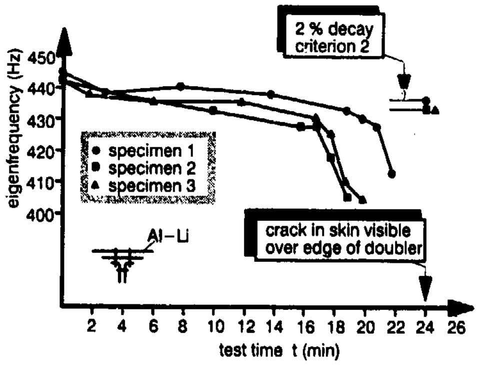

Fig. 3–2 DECAY OF EIGENFREQUENCY
coupon 5–II

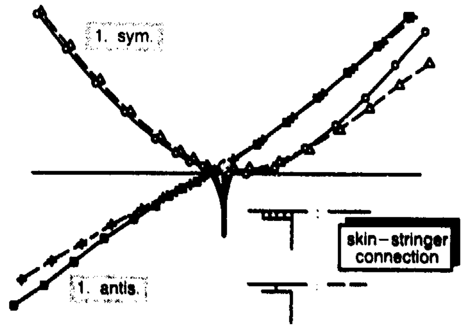

Fig. 4–1 TYPICAL MODE SHAPES OF COUPON 1–I
influence of rivet modeling

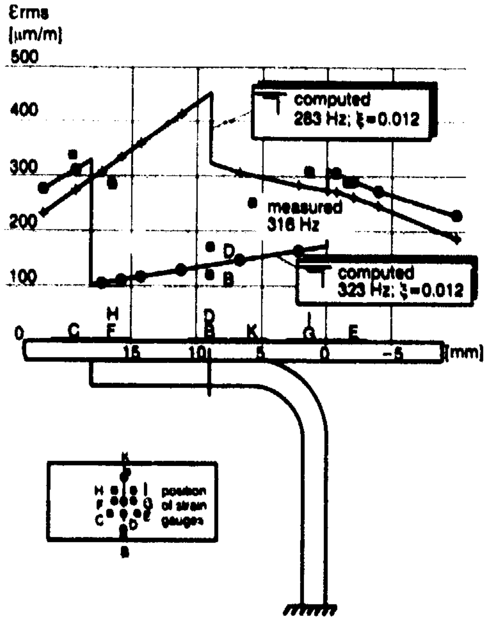

Fig. 4–2 STRAIN DISTRIBUTION IN SKIN (coupon 1–I, 1g²/Hz; 100–1000 Hz)

type of design	tR [mm]	bR [mm]	tS [mm]
1	0	0	1.8
2	0.6	28	1.8
3	0.625	28	1.8
4	0	0	2 x 1.6
5	0.6	46	2 x 1.6
6	0.625	54	2 x 1.5
7–I	0.6	46	2 x 1.6
7–...	0.625	46	2 x 1.6
8	0	0	1.5

Tab. 2–1

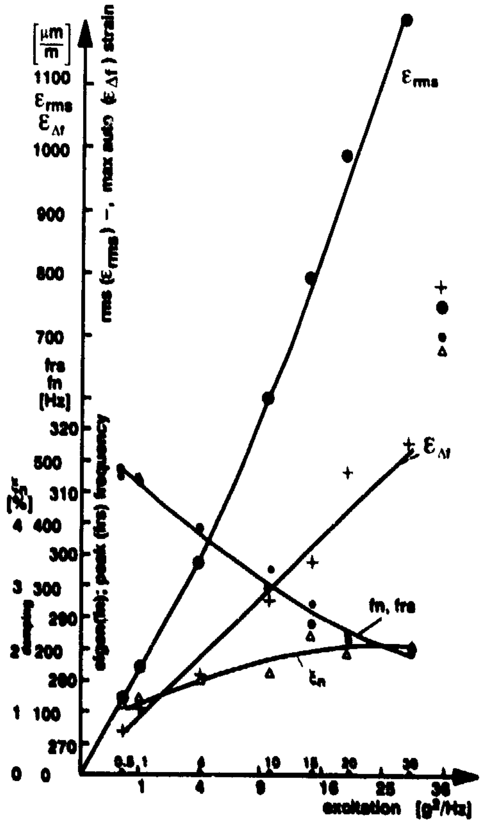

Fig. 4–3 INFLUENCE OF EXCITATION LEVEL ON TEST RESULTS (VP 4.1; skin; $f_a - f_e = 100$ Hz)

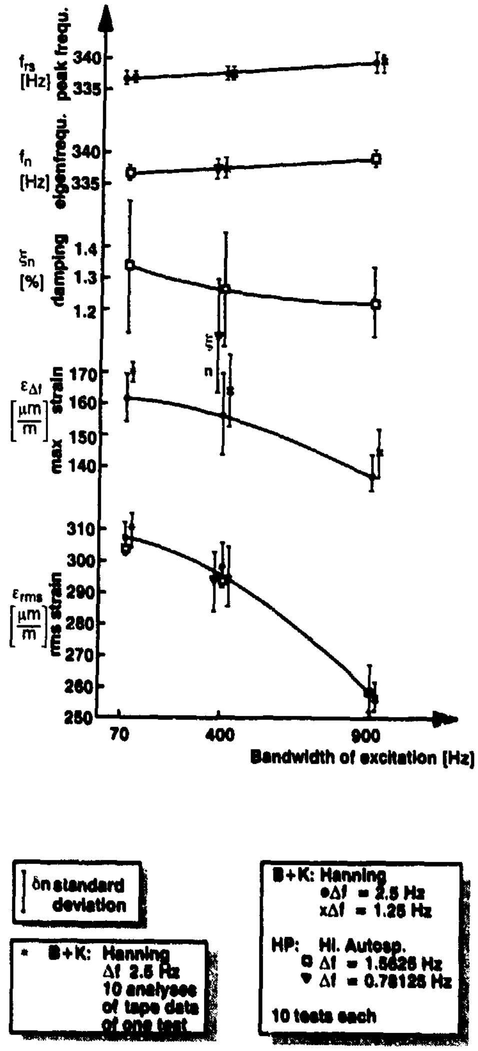

Fig. 4-4 SCATTER AND INFLUENCE OF DIFFERENT TEST CONDITIONS ON TEST RESULTS (VP2 1.6mm; 1g²/Hz; skin; averages of 10)

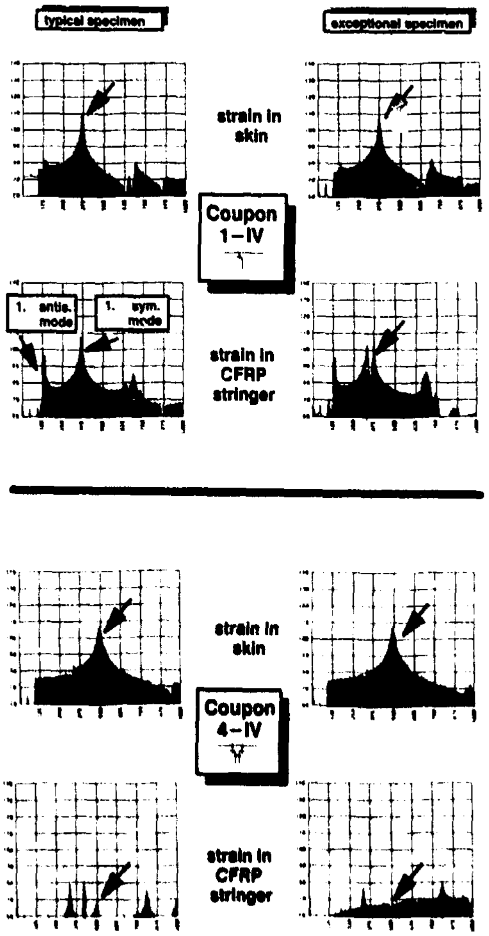

Fig. 4-5 DEVIATIONS OF THE BEHAVIOUR OF SOME SPECIMENS 1 g²/Hz; 100 - 1000 Hz

No		I			II		III	IV		V	VI
	material of skin	Al 3.1364T3		+ sealing material	Al/Li 8090		ARALL	CFRP CFRP stringer	CFRP Al stringer	Minisandw. (CFRP/GFRP)	Al layers
	type of design	t=1.2 mm	t=1.4 mm	t=1.4 mm	t=1.2 mm	t=1.4 mm	t=1.1 mm	t=1.5 mm	t=1.5 mm	t=1.45 mm	t=3 x 0.4 mm
1	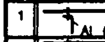 Al (CFRP)		1 ref 287 Hz	0.9		1.1		1.2	1.4	1.4	1.1
2	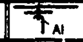 Al	1.1	1.3		1.2		1.2				1.3
3	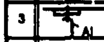 Al								1.6	1.4	
4	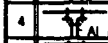 Al (CFRP)		1.2			1.3		1.6	1.7	1.6	1.2
5	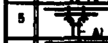 Al	1.4			1.5		1.5				1.7
6	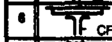 CFRP							2.6			
7	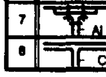 Al	1.5							2.1	1.9	
8	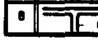 CFRP							1.3			

Table 5.1–1 COMPARISON OF EIGENFREQUENCY RATIOS $(f_n.../f_n ref)$ first symmetric mode, measured at $30g^2/Hz$

deeq. numb. of ratio	studied influence			material									averaged ratio
	type of design (I)					II		III	IV		V	VI	
				1.2 mm	1.4 mm	1.2 mm	1.4 mm	1.1 mm	1.5 mm	1.5 mm	1.45 mm	3 x 0.4 mm	
2/1	influence of added doubler	asym	sep.		1.25							1.24	1.2
3/1			inte. CFRP							1.12	1.08		1.1
5/4		sym.	sep.									1.35	1.4
7/4			inte. CFRP							1.23	1.18		1.2
7/5	doubl. integr. (sym)			1.02									1.0
4/1	influence of added 2. angle	without doubl.			1.23		1.19		1.31	1.20	1.18	1.17	1.2
5/2		with dbl	sep.	1.28		1.27		1.29				1.28	1.3
7/3			inte. CFRP							1.31	1.29		1.3
7(b)/1	add. doubl. + 2. angle									1.47	1.39	(1.58)	1.5

Table 5.1–2 INFLUENCE OF DESIGN ON EIGENFREQUENCY RATIOS

No		I			II		III	IV		V	VI
	material of skin	Al 3.1364T3		+ sealing material	Al/Li 8090		ARALL	CFRP CFRP stringer	CFRP Al stringer	Minisandw. (CFRP/GFRP)	Al layers
	type of design	t=1.2 mm	t=1.4 mm	t=1.4 mm	t=1.2 mm	t=1.4 mm	t=1.1 mm	t=1.5 mm	t=1.5 mm	t=1.45 mm	t=3 x 0.4 mm
1	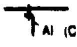 Al (CFRP)		1.1 2.2 1.9	3.0 2.8 3.5		1.3 – 1.3		0.9 1.2 1.0	1.6 – 1.3	1.2 0.9 1.2	1.5 – –
2	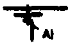 Al	1.4 – 2.0	– – –		1.4 – 1.2		1.7 – 1.2				1.2 – 1.1
3	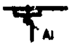 Al								1.0 – 1.0	1.2 – 1.3	
4	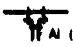 Al (CFRP)		1.2 1.1 1.1			1.3 – 1.2		1.3 1.1 1.0	1.2 – 1.2	1.2 1.3 1.2	1.6 – 1.1
5	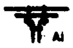 Al	1.2 – 1.1			1.1 – 1.6		1.9 – 1.7				1.1 – 1.2
6	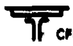 CFRP							0.7 – 0.5			
7	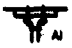 Al	1.0 – 1.2							1.1 – 1.1	2.3 – 1.3	
8	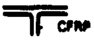 CFRP							1.1 0.8 0.7			

Table 5.2–1 DAMPING VALUES OF DIFFERENT SPECIMENS MEASURED ON SKIN AT 20g/Hz [% of critical]

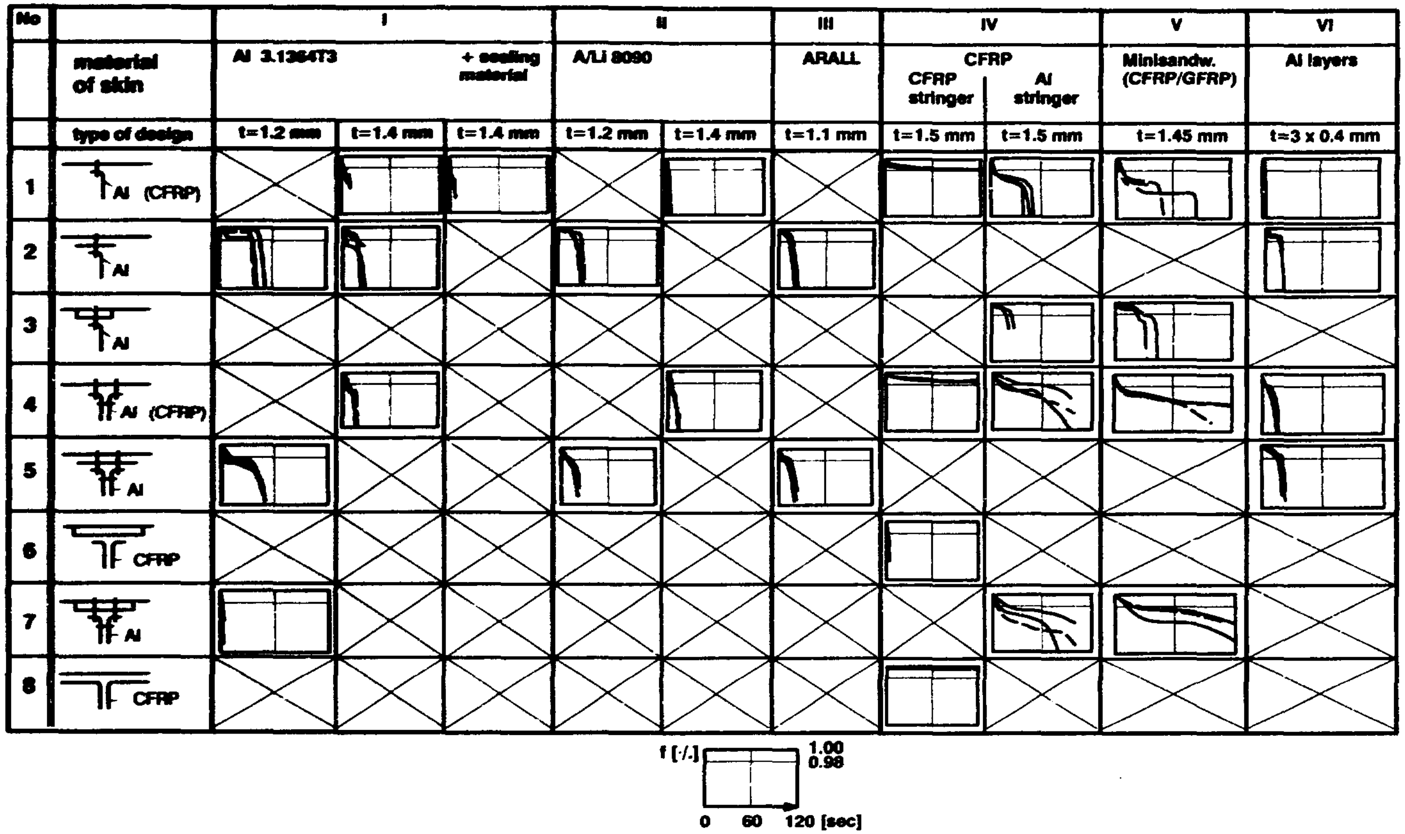

No		I			II		III	IV		V	VI
	material of skin	Al 3.1364T3		+ sealing material	A/Li 8090		ARALL	CFRP CFRP stringer	 Al stringer	Minisandw. (CFRP/GFRP)	Al layers
	type of design	t=1.2 mm	t=1.4 mm	t=1.4 mm	t=1.2 mm	t=1.4 mm	t=1.1 mm	t=1.5 mm	t=1.5 mm	t=1.45 mm	t=3 x 0.4 mm
1	Al (CFRP)	X			X		X				
2	Al			X		X		X	X	X	
3	Al	X	X	X	X	X	X	X			X
4	Al (CFRP)	X		X	X		X				
5	Al		X	X		X		X	X	X	
6	CFRP	X	X	X	X	X	X		X	X	X
7	Al		X	X	X	X	X	X			X
8	CFRP	X	X	X	X	X	X		X	X	X

Table 5.4–1 FREQUENCY OVER TIME; CURVES SMOOTHED AND NORMALIZED

No		I			II		III	IV		V	VI
	material of skin	Al 3.1364T3		+ sealing material	Al/Li 8090		ARALL	CFRP CFRP stringer	Al stringer	Minisandw. (CFRP/GFRP)	Al layers
	type of design	t=1.2 mm	t=1.4 mm	t=1.4 mm	t=1.2 mm	t=1.4 mm	t=1.1 mm	t=1.5 mm	t=1.5 mm	t=1.45 mm	t=3 x 0.4 mm
1	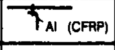 Al (CFRP)		1.4 1.6 1.7	2.1 2.1 3.1 –		1.3 1.3 1.3 1.5		1.2 1.2 1.0 1.1	1.4 1.4 1.5 1.4	1.3 1.3 1.1 1.2	1.4 1.5 1.5 1.7
2	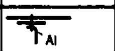 Al	1.7 1.7 1.7 1.3	1.6 1.6 1.1		1.4 1.4 1.3 1.6		1.3 1.3 1.5 1.2				1.3 1.4 1.2 1.4
3	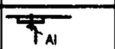 Al								1.2 1.2 1.0 1.1	1.1 1.1 1.3 1.2	
4	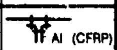 Al (CFRP)		1.3 1.2 1.1 1.2			1.0 1.2 1.3 1.3		1.3 1.2 1.1 1.4	1.1 1.2 1.2 1.2	1.2 1.2 1.2 1.4	1.4 1.4 1.4 1.6
5	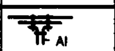 Al	1.2 1.2 1.2 1.3			1.2 1.2 1.4 1.0		1.1 1.2 1.8 1.1				1.2 1.2 1.2 1.1
6	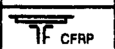 CFRP							0.6 0.6 0.6 0.4			
7	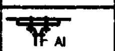 Al	1.3 1.1 1.1 0.8							1.1 1.1 1.1 1.1	1.2 1.2 1.8 1.3	
8	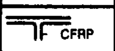 CFRP							1.0 0.9 0.9			

skin
30 g^2/Hz
stringer
30 g^2/Hz
chosen
value
skin
20 g^2/Hz
stringer
20 g^2/Hz

Table 5.2−2 AVERAGED DAMPING VALUES [% of critical]

No		I			II		III	IV		V	VI
	material of skin	Al 3.1364T3		+ sealing material	Al/Li 8090		ARALL	CFRP CFRP stringer	Al stringer	Minisandw. (CFRP/GFRP)	Al layers
	type of design	t=1.2 mm	t=1.4 mm	t=1.4 mm	t=1.2 mm	t=1.4 mm	t=1.1 mm	t=1.5 mm	t=1.5 mm	t=1.45 mm	t=3 x 0.4 mm
1	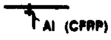 Al (CFRP)		skin in rivet l.	skin in rivet l.		skin in rivet l.		del. in str. rad. + skin	stringer clamping	stringer clamping	skin in rivet line
2	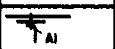 Al	skin over doubler e. short side	skin over doubler e. sh. side		skin over dbl. e. sh. s. + string.		skin over dbl. edge both sides				skin over dbl. e. l. s. + string. cl.
3	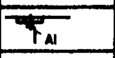 Al								stringer clamping	stringer clamping	
4	Al (CFRP)		skin in rivet line			skin in rivet l.		del. in stringer radius	stringer radius	stringer radius	skin in rivet l.
5	Al	skin over dbl. edge b. sides			skin over doubler e.		skin over doubl. e.				skin over doubler e.
6	CFRP							bonding			
7	Al	doubler corner b. sides							stringer radius	stringer radius	
8	CFRP							delamin. in radius			

Table 5.4−2 DAMAGE LOCATION

No		I			II		III	IV		V	VI
	material of skin	Al 3.1364T3		+ sealing material	Al/Li 8090		ARALL	CFRP CFRP stringer	Al stringer	Minisandw. (CFRP/GFRP)	Al layers
	type of design	t=1.2 mm	t=1.4 mm	t=1.4 mm	t=1.2 mm	t=1.4 mm	t=1.1 mm	t=1.5 mm	t=1.5 mm	t=1.45 mm	t=3 x 0.4 mm
1	Al (CFRP)		3.8 6.8 12.8	1.2 5.7 8.3		2.9 3.1 10.1		276.7 >387.3 >480	3.6 n 30.4 n 43.2 n	2.8 n 58.0 n 66.5 n	2.9 3.0 3.0
2	Al	40.2 40.7 40.0	19.0 22.2 24.9		22.5 24.3 n 26.9		19.1 15.6 16.9				15.3 16.0 16.0
3	Al								21.2 n 21.8 n 21.5 n	26.3 n 26.6 n 32.5 n	
4	Al (CFRP)		4.7 9.5 15.3			4.5 6.1 12.9		348.3 344.0 >374.6	17.3 n 76.0 n 76.0 n	5.5 n 56.0 n 106.7 n	3.7 11.1 10.1
5	Al	5.6 39.8 39.8			12.2 16.9 16.0		8.8 16.8 16.6				17.0 19.1 18.3
6	CFRP							1.4 n 1.4 n 1.4 n			
7	Al	1.4 1.4 1.4							9.8 n 77.7 n 76.5 n	14.0 n 109.9 n 114.0 n	
8	CFRP							>1019 > >			

n: fracture not in skin

Table 5.4−3 MEASURED LIFE TIMES T_K DEPENDING ON FAILURE CRITERION
- 2 % decrease from starting frequency
- 2 % decrease from settling frequency
- initial fracture (averages [min])

No		I			II		III	IV		V	VI
	material of skin	Al 3.1364T3		+ sealing material	Al/Li 8090		ARALL	CFRP CFRP* stringer	Al stringer	Minisandw. (CFRP/GFRP)	Al layers
	type of design	t=1.2 mm	t=1.4 mm	t=1.4 mm	t=1.2 mm	t=1.4 mm	t=1.1 mm	t=1.5 mm	t=1.5 mm	t=1.45 mm	t=3 x 0.4 mm
1	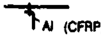 Al (CFRP)		1 1 ref. 1	1.0 2.1 1.6		0.5 0.2 0.6		3.5 >2.1 >1.8	0.2 0.6 0.6	0.1 1.1 0.9	0.6 0.2 0.2
2	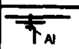 Al	5.1 2.2 1.5	4.2 2.5 2.0		1.9 0.9 0.7		1.2 0.5 0.4				3.0 1.3 0.9
3	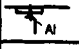 Al								1.0 0.4 0.3	1.1 0.5 0.4	
4	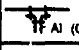 Al (CFRP)		1.2 1.1 1.2			0.8 0.4 0.7		3.2 1.9 1.4	0.8 1.5 1.1	0.2 1.0 1.4	0.7 0.9 0.6
5	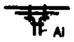 Al	0.7 2.2 1.5			1.0 0.6 0.5		0.8 0.6 0.4				3.3 1.6 1.1
6	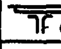 CFRP							0.0 0.0 0.0			
7	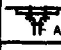 Al	0.2 0.1 0.1							0.5 1.6 1.1	0.6 1.9 1.5	
8	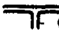 CFRP							>13.0 > >			
m/m ref		0.86	1.0	1.28	0.79	0.93	0.78	0.70	0.70	0.69	0.94

$$\frac{\left(T_C = T_K \cdot \left(\frac{m}{m_{ref}}\right)^x\right)}{T_{C\,ref}}$$

x = 4.83 (*x = 8.49)
m: mass of skin only
TK: as measured s. Tab. 5.4-3

Table 5.4-4 COMPARISON OF HARMONISED LIFE TIME RATIOS
- 2 % decrease from starting frequency
- 2 % decrease from settling frequency
- initial fracture

design numbers of ratio	studied influence			material									averaged ratio
	type of design (I)			I		II		III	IV		V	VI	
				1.2 mm	1.4 mm	1.2 mm	1.4 mm	1.1 mm	1.5 mm	1.5 mm	1.45 mm	3 x 0.4 mm	
2/1	In-fluence of added doubler	asym.	sep.		4.2 2.5 2.0							5.3 5.3 5.3	4.8 3.9 3.6
3/1			inte. CFRP							5.0 0.7 0.5	9.0 0.5 0.5		7.0 0.6 0.5
5/4		sym.	sep.									4.6 1.7 1.8	4.6 1.7 1.8
7/4			inte. CFRP							0.6 1.0 1.0	2.5 1.8 1.1		1.5 1.4 1.0
7/5	doubl. integr. (sym)			0.3 0.1 0.1									0.3 0.1 0.1
4/1	influence of added 2. angle	without doubl.			1.2 1.1 1.2		1.6 1.6 1.3		0.9 0.9 0.8	4.0 2.5 1.8	2.0 0.9 1.6	1.3 3.7 3.7	2.0 1.8 1.7
5/2		with dbl	sep.	0.1 1.0 1.0		0.5 0.7 0.7		0.6 1.0 0.9				1.1 1.2 1.1	0.6 1.0 0.9
7/3			inte. CFRP							0.5 3.8 3.6	0.5 3.8 3.8		0.5 3.7 3.6
7(5)/1	add. doubl. + 2. angle									2.7 2.6 1.8	6.0 1.7 1.7	5.5 (8.4) 5.1	4.5 3.6 3.3

Table 5.4-5 INFLUENCE OF DESIGN ON LIFE TIME RATIOS ($T_K \ldots / T_K \ldots$)
- 2 % decrease from starting frequency
- 2 % decrease from settling frequency
- initial fracture

ACOUSTIC FATIGUE CHARACTERISTICS OF ADVANCED MATERIALS AND STRUCTURES

J. H. Jacobs
McDonnell Douglas Aerospace - East
McDonnell Douglas Corporation
P.O. Box 516 , St. Louis, Missouri 63166-0516
United States

M.A. Ferman
Parks College of Saint Louis University
Aerospace Engineering Department
Cahokia, Illinois 62206
United States

SUMMARY

A summary of McDonnell Douglas Aerospace's (MDA) capability for treating acoustic loading on modern fighter aircraft structure is given. A brief overview of techniques that were developed since the mid-70's are presented. In the mid 1970's, the introduction of composites and new metallic structure fabrication concepts such as Super Plastic Formed/Diffusion Bonding (SPF/DB) suddenly required new analysis procedures. In addition, the 1980's brought the additional complications of structures exposed to high thermal and acoustic environments on such vehicles as the AV-8B Harrier II and National Aerospace Plane (NASP). Methods developed to handle these new material forms, intense noise, and thermal loads are discussed. The influences of nonlinear structural responses on fatigue life due to combined load environments is also discussed. Additional developments in thermal-acoustic testing capability are also discussed.

1 INTRODUCTION

While acoustic loading was always present in some form since aircraft first flew, the advent of the jet engine drastically changed the level of intensity possible. Also, with this increased power, the ability to fly faster produced new levels of aerodynamic noise. In the mid 70's, the introduction of composite materials, new metallic alloys and new manufacturing techniques , such as Super Plastic Formed/Diffusion Bonding (SPF/DB) were developed to promote increased performance and weight savings. These new materials were required to meet even more stringent noise, temperature, and fatigue requirements on the aircraft. Both highly maneuverable aircraft such as the F-15 Eagle and Vertical/Short Take off and Landing (VSTOL) aircraft such as the AV-8B Harrier II posed many new challenges including separated flow, hot plumes, hot ducts and complex exit nozzles. These designs produced extremely complex problems of high temperature vibro-acoustic applications, considered to be unique to these aircraft. This situation quickly dictated the need for new methods and new test techniques to treat strength, fatigue and dynamic design requirements.

Of particular interest was the acoustic fatigue problem since it is the aggregation of all of these disciplines. The designer was now faced with a two fold problem of understanding the material degradation behavior itself as well as developing structural response prediction methods for components which may include thermal, mechanical and nonlinear influences. The challenge for these new material forms, manufacturing techniques and structural applications, was to develop an applicable acoustic fatigue design methodology. A brief summary of the work since the mid-70's including today's developing capability at MDA is outlined.

2 ANALYTICAL DEVELOPMENT

Acoustic fatigue methods utilized at MDA over the past 20 years are summarized in Figure 1. Many viable techniques were developed by industry and academia in this time period and this list is not intended to be comprehensive but rather a look at the techniques employed in practice on MDA's aircraft structures. The pre-1975 approaches are shown for reference, at which time the usual method consisted of either standard handbook idealized approaches for panel structures or simple analytical calculations considering only basic modal characteristics. Testing was used extensively to augment these results.

Early in the 1975-1988 period the Sonic Fatigue Design Guide For Military Aircraft (Ref. 1) was released. This document combined both theoretical and empirical results to form useful equations for the analysis of many modern aircraft structural components. Isotropic bi-stiffened structural response equations were adopted for use in the design of typical fuselage structural components under nominal acoustic loading conditions. These semi-empirical equations include the effect of chem milling, rivet type, hole type, and static pressures. While these techniques were considered robust for the specific structural configuration of a bi-stiffened isotropic panel, the emergence of composite structures in this time frame required a considerably different approach. Here a sharp departure was made from prior approaches. Since very limited test data existed for co-cured or post-cured stiffened composite structures, MDA began to characterize these new materials extensively in order to establish the influences of pre-load, temperature, manufacturing technique , and thermal mechanical coupling on fatigue life. Analytical developments were concentrated on equivalent single

Export Authority 22CFR 125.4(b)(13)

Presented at a Symposium on 'Impact of Acoustic Loads on Aircraft Structures' held in Lillehammer, Norway, May 1994.

degree of freedom equations for simple composite panel material systems. These methods coupled with experimental validation yielded gross approximations to structural response and fatigue life of complex composite structures and provided the necessary foundation for future developments. During this time period as well, more detailed effects on composite structural behavior became available in linear, nonlinear and thermal effects. (Refs. 2,3) Throughout this entire time period, NASTRAN was used as the major workhorse for analyzing detailed composite structures where panel level equations were not adequate. Other multi-purpose finite element codes such as ABAQUS, ANSYS, NISA, and MARC were also evaluated but did not prove as robust.

During this same time period, methods to analyze SPF/DB metallic parts were also addressed. To analyze panel-type structures a local-global analysis procedure was utilized. Overall panel response was treated by using an equivalent "smeared stiffness" approach to predict global level strains. Local panel response was then performed at the stiffener level to address the added high frequency and stress concentration effects.

By 1988, linear elastic response of isotropic and composite panel type structures was fairly well understood. The primary emphasis in this period was the development of techniques which could incorporate combined loading conditions and nonlinear structural response behavior in order to predict more accurate fatigue lives. In addition, during this time frame the NASP program was developing very complicated built-up structural concepts which had to survive temperatures near 2000°F and acoustic loads exceeding 180 dB. These combined load environments induced the added complication of nonlinear structural response behavior. To address this behavior a nonlinear response code for bi-stiffened composite panels was created (Ref. 4). This investigation showed that random response for a classical nonlinear duffing oscillator system does not exhibit the same response characteristics as sinusoidal excitation (Figure 2). This method explained the apparent widening of the band for random response cases. To extend this research, in 1990 MDA in conjunction with NASA Langley Research Center Structural Acoustics Branch co-developed a finite element based nonlinear response code which was capable of analyzing built-up multi-material composite structures under thermal and acoustic loads. This research was based on the work of Mei and Locke discussed in References 5 and 6. The new code was entitled "Thermal Acoustic Response and Fatigue of Pre Buckled and Post Buckled Structures" (TAPS). The code was also developed to include an extensive material database and automated flight profile fatigue life prediction system (Ref. 7). Results are described later in this paper. Recently NASA Langley Research Center has incorporated the same nonlinear structural response formulation into NASTRAN V67.

Future work in the acoustic fatigue of aircraft structures is directed towards the linking of codes such as TAPS which addresses panel level response and fatigue to NASTRAN which can address larger scale aircraft structural response issues. This is part of a much larger effort to establish a global-local optimization procedure for aircraft structures exposed to static, dynamic, thermal, and aerodynamic loads.

3 TESTING CAPABILITY

Testing capability to characterize advanced materials for acoustic fatigue has steadily advanced, with the current capability depicted in Figure 3. The baseline progressive wave chamber has a test section roughly 72" x 36" x 7". The structural test section size can range from 72" x 36" to 12" x 12". A strong box-like enclosure can be mounted to the panel backside for pressure tests and or temperature tests. Noise levels of up to 171 dB broad band and up to 174 dB narrow band can be produced using grazing incidence excitation.

The progressive wave chamber was upgraded in 1990 to handle higher temperature and noise requirements of new advanced aircraft programs by the addition of quartz lamp bank assemblies across the test section. These then provide a heat flux on the noise side of the panel. The three section quartz lamp band assembly can obtain a local panel temperature up to 1200°F over a 36" x 30" region. Numerous panels and substructures have been tested in this facility to validate analytical predictions and evaluate durability or aircraft components (Refs. 8,9).

The high temperature electrodynamic shaker has been used to characterize random fatigue of advanced materials systems up to 2000 F such as Carbon-Carbon, Titanium Metal Matrix composites (TMC), Carbon-Epoxy, Ceramic Matrix Composites (CMC), and many others (Ref. 10). The system uses four quartz lamps and a reflector plate to obtain uniform thermal profiles on the coupon specimens. A non-contacting laser vibrometer is used to measure response at high temperatures when strain gages prove ineffective. The random strain to failure data generated in this facility is an integral part for full scale acoustic fatigue life predictions.

4 DESIGN APPROACHES

The level of complexity of an acoustic fatigue analysis for an aircraft part is dependent on its structural type, loading conditions, material information availability and design specifications. Figure 4 summarizes the general design procedure used to evaluate structures for acoustic fatigue life. As mentioned earlier, typical bi-stiffened isotropic structure is analyzed for response with a series of specialized semi-empirical computer programs. If a structure in question can be treated as a composite or built up panel, the TAPS code is used for response analyses

When a structural part becomes very complex, such as a contoured inlet duct, more elaborate approaches such as NASTRAN are implemented. All of these methods produce a series of random strain values from acoustic excitation which are analyzed through a sonic fatigue material database for ultimate fatigue life. When analyses are performed at the panel level, the option to evaluate the structure for a given flight profile loading spectrum is also available. Depending on the application, testing in the acoustic chamber or on the electrodynamic shaker can be used for validation of fatigue predictions or qualification testing. All of these approaches assume the existence of some sort of dynamic strain to failure material information. This information must be generated in the form of random strain to failure curves in order for any acoustic or combined load fatigue lives to be predicted. These design approaches have been proven over the past 25 years to be cost effective and applicable to the design of fighter aircraft structures for the F-15, AV-8B, F/A-18, NASP, T-45, YF-23 and other advanced flight vehicles (Fig. 5).

5 RESULTS AND EXAMPLES

To demonstrate in the simplest manner the importance of using the correct analysis method for acoustic fatigue, consider Figure 6. Here results from an isotropic 10"x 20"x0.063" 7075-T6 Aluminum panel tested in MDA's progressive wave chamber are shown. The panel was clamped on all sides rigidly with a bolted connection. Test results are shown along with the analytical predictions for a variety of computational schemes. The simple one degree of freedom linear theory (Ref. 11) and semi empirical 9 bay equation (Ref. 1) predict responses well above the experimental data at the high dB levels. Using the nonlinear response formulation in the TAPS code, much improved results are obtained at the higher dB levels. These results indicate the importance that the designer must realize in using the correct structural representation and response equations. Sometimes linear theory can severely penalize the structural weight because of over designing the part to meet unrealistic strain levels. While this conclusion seems quite obvious, quite frequently these simple design rules are ignored in the literature and in practice.

To illustrate the added complication of a stiffened composite structure, consider Figure 7. Here a three bay Graphite/Epoxy panel tested at MDA in 1990 is shown. In this case, the standard bi-stiffened isotropic panel equations were obviously not applicable while the TAPS code was. Simple single degree freedom linear theory is shown for comparison. The first strain gage position on the edge of the panel responds very linearly somewhat between a fully clamped condition and a clamped simple support condition. This result is expected but the interesting point in this case is linear single degree of freedom theory for a completely clamped panel significantly under-predicts the strain response. The second strain position behaves much more non-linearly than the first. It is evident that the response again falls between a fully clamped panel and a panel which is clamped-simple supported but in a nonlinear fashion. The linear theory significantly over-predicts the response at high dB levels. This example again illustrates the need to have a robust response prediction tool for composite structures where design book guidelines may not apply. The last design example, Figure 8, is in the calculation of the fatigue life of a TMC panel used in the NASP program. The first line indicates the baseline fatigue life of the panel was analyzed using linear single-degree-of-freedom theory and sinusoidaly generated low frequency fatigue data. Obviously for acoustic fatigue analyses, random fatigue data is required. This lowers the fatigue life by 85% for this example, as is shown in the second line. Using sinusoidal fatigue data in conjunction with nonlinear response theory, an overall lifetime improvement of 51% is realized and is shown in the third line. Hence, using nonlinear response theory in conjunction with incorrect material properties can results in very non-conservative designs. When the correct random fatigue data is used with nonlinear response theory, the fatigue life is now 47% lower that the baseline scenario in line one. Hence, comparing lines two and four of this figure, a factor of 3 improvement in fatigue life is realized between a linear/sinusoidal analysis and a nonlinear/random analysis. The latter design procedure will hence reduce structural weight since fatigue life has been improved. This example does not include the effects such as thermal and mechanical pre-load, but rather illustrates the point that acoustic fatigue life predictions must be performed with a firm knowledge of the structural system and material characteristics.

6 CONCLUDING REMARKS

MDA's methods both experimental and analytical have advanced significantly since the mid-70's. This technology was spurred by the advent of composite material properties, new structural configurations and higher noise levels which posed a new challenge to the designer. Today's analysis techniques range from simple panel codes for isotropic structures to fully involved finite element models for complicated composite structures. In either case, it has been shown that the correct linear or nonlinear structural response formulation is imperative in obtaining reliable results. With adequate knowledge of the random excitation material characteristics of a new structural system early in the design cycle, much more accurate life predictions can be made. More research is needed to further understand the effects of composite material fabrication and bonding techniques on acoustic fatigue life as well as the global local optimization of acoustic fatigue prone structures. Considering these issues early in the design, rather than employing fixes at a later design cycle phase, will result in lighter more durable aircraft structures with extended service life.

REFERENCES

1) Rudder,F.F., and Plumblee, H.E., "Sonic Fatigue Guide for Military Aircraft", AFFDL-TR-74-112, May 1975

2) Jacobsen, M. "Advanced Composite Joints; Design and Acoustic Fatigue Characteristics", AFFDL-TR-71-126, April 1972

3) Holehouse. I., "Sonic Fatigue Design Techniques for Advanced Composite Aircraft Structures", AFFDL-TR-80-3019, April 1980

4) Ferman, M.A., Jacobs, J.H. "A New Technique and Application for Nonlinear Acoustic Fatigue of Stiffened Composite Panels", 1989 ASME Winter Annual Meeting, December 1989

5) Mei, C. "Response of Nonlinear Structural Panels Subjected to High Intensity Noise", AFWAL-TR-80-3018, March 1980

6) Locke J., Mei C., "A Finite Element Formulation for the Large Deflection Random Response of Thermally Buckled Plates", AIAA-89-1100, AIAA 12th Aeroacoustics Conference, April 1989

7) Jacobs, J.H. "Linear and Nonlinear Acoustic Fatigue Methods for Aircraft Structures", 2nd Annual Advanced Materials and Structures Technology Workshop, MDC Internal Conference, October 1993

8) Jacobs, J.H., Ferman, M.A., "Thermal Vibro-Acoustic Response and Fatigue of Advanced Composite Materials" Work in Progress, Fourth International Conference on Recent Advances in Structural Dynamics, South Hampton, England, July 1991

9) Jacobs, J.H., Gruensfelder, C., Hedgecock, C.E., "Thermal-Acoustic Fatigue of Ceramic Matrix Composite Materials", AIAA-93-1317-CP, AIAA 34th Structural Dynamics and Materials Conference, April 1993

10) Jacobs, J.H., Kirk, E.M.,"High Temperature Random Fatigue of Carbon-Carbon", 15th Annual Conference on Composites, Materials and Structures. January 1991

11) Miles, J. W., "On Structural Fatigue Under Random Loading, "Journal of Aeronautical Sciences, Vol. 21, November 1954

Time Period	Acoustic Fatigue Techniques Applied
Pre-1975	• Panel Analysis Using Semi-Empirical Equations or Simple Model Differential Evaluations • Limited Use of Finite Element Theory • Heavy Use of Experimental Results
1975 - 1988	• Sonic Fatigue Guide Semi-Empirical Equations Used for Bi-Stiffened Isotropic Structures • Composite Parts Analytical With Single DOF Equations • Jacobsen's Methods Extended • Heavy Experimental Characterization of Composite Materials • Combined Load Effects Considered in Fatigue • Techniques Applied to Aircraft Projects • Finite Element Codes Used for Large Scale Analyses
1988 - Present	• Nonlinear Response Effects Developed Into Multi-Mode Equations (NRAP Code) • TAPS Code Developed to Handle Combined Load Conditions, Thermal Loads, Composites, Fatigue Database, Flight Profiles • Techniques Implemented on NASP and Other Aircraft Programs • NASTRAN Used Heavily for Large Structure Analysis
Future	Multi-Disciplined Optimization of Strength and Acoustic Fatigue Research Using NASTRAN TAPS, and Other Analysis Codes

GP34-0097-1-V

Figure 1. McDonnell Douglas Aerospace Acoustic Fatigue Methods Development

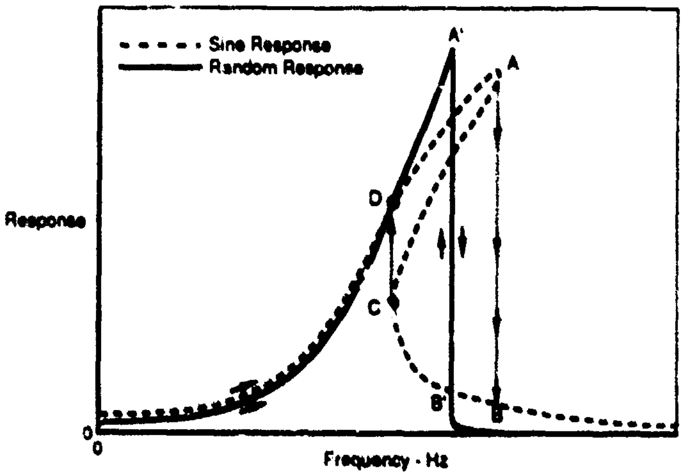

GP34-0097-4-V

Figure 2. Sine and Random Nonlinear Response Functions

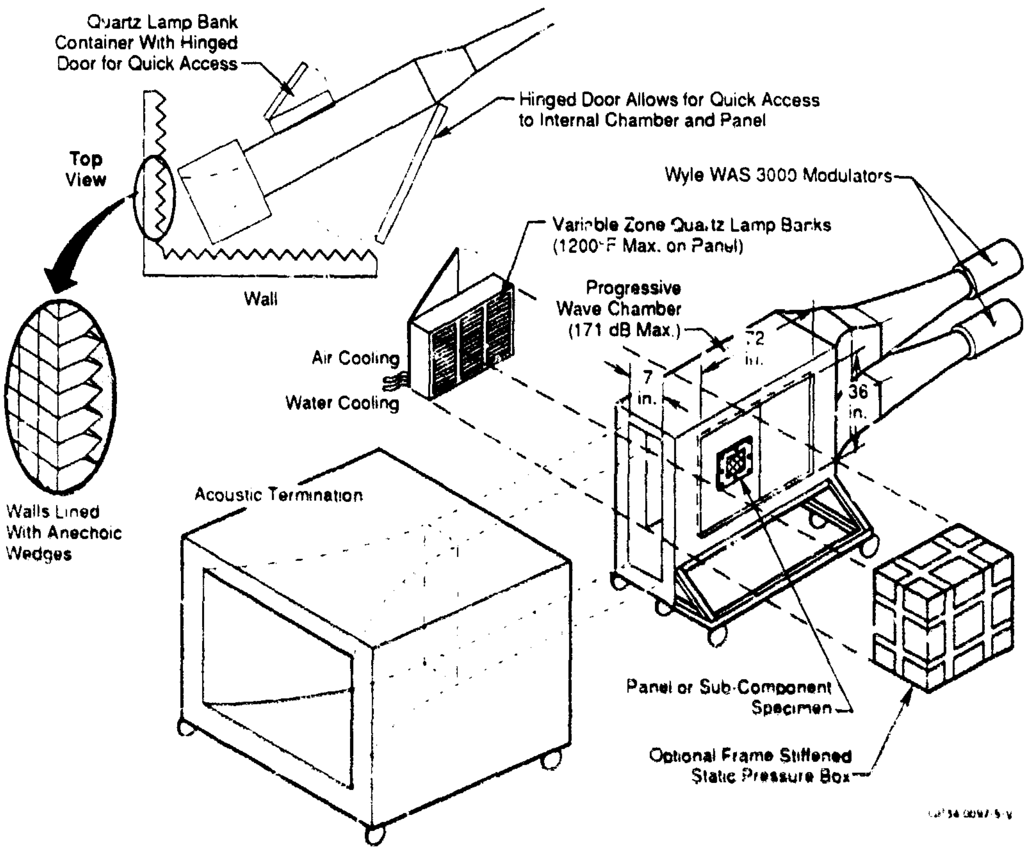
Quartz Lamp Bank Container With Hinged Door for Quick Access
Hinged Door Allows for Quick Access to Internal Chamber and Panel
Top View
Wall
Walls Lined With Anechoic Wedges
Wyle WAS 3000 Modulators
Variable Zone Quartz Lamp Banks (1200°F Max. on Panel)
Progressive Wave Chamber (171 dB Max.)
72 in.
7 in.
36 in.
Air Cooling
Water Cooling
Acoustic Termination
Panel or Sub-Component Specimen
Optional Frame Stiffened Static Pressure Box

Figure 3A. Thermal/Acoustic Test Facility
Facility Is Capable of 171 dB Acoustic Loading With Simultaneous Cross Flow

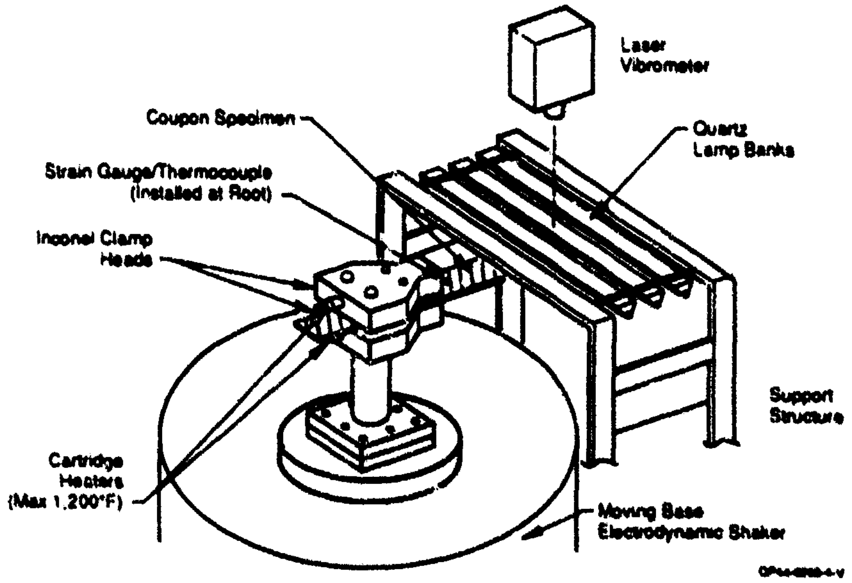
Laser Vibrometer
Coupon Specimen
Quartz Lamp Banks
Strain Gauge/Thermocouple (Installed at Root)
Inconel Clamp Heads
Support Structure
Cartridge Heaters (Max 1,200°F)
Moving Base Electrodynamic Shaker

Figure 3b. General Setup of High Temperature Beam Fatigue Test Facility

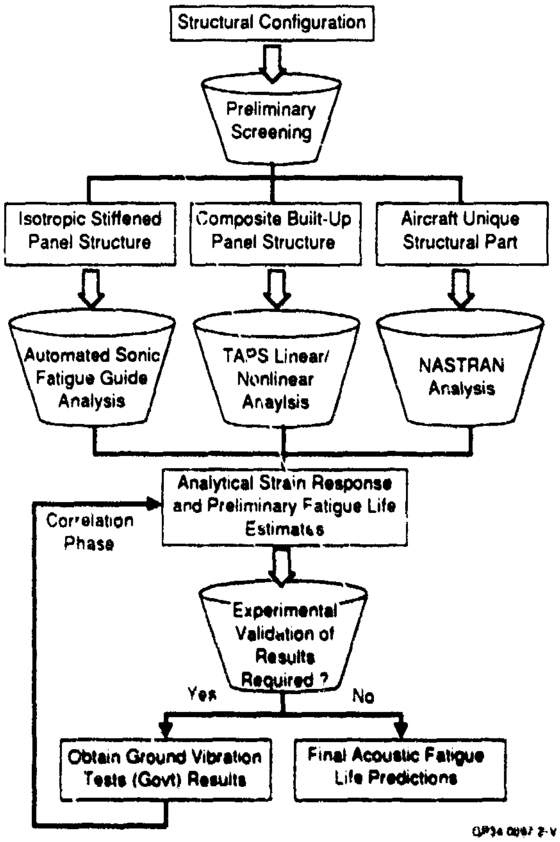
Structural Configuration
Preliminary Screening
Isotropic Stiffened Panel Structure
Composite Built-Up Panel Structure
Aircraft Unique Structural Part
Automated Sonic Fatigue Guide Analysis
TAPS Linear/ Nonlinear Anaylsis
NASTRAN Analysis
Analytical Strain Response and Preliminary Fatigue Life Estimates
Correlation Phase
Experimental Validation of Results Required ?
Yes
No
Obtain Ground Vibration Tests (Govt) Results
Final Acoustic Fatigue Life Predictions

GP34 0067 2-V

Figure 4. Acoustic Fatigue Design Approach

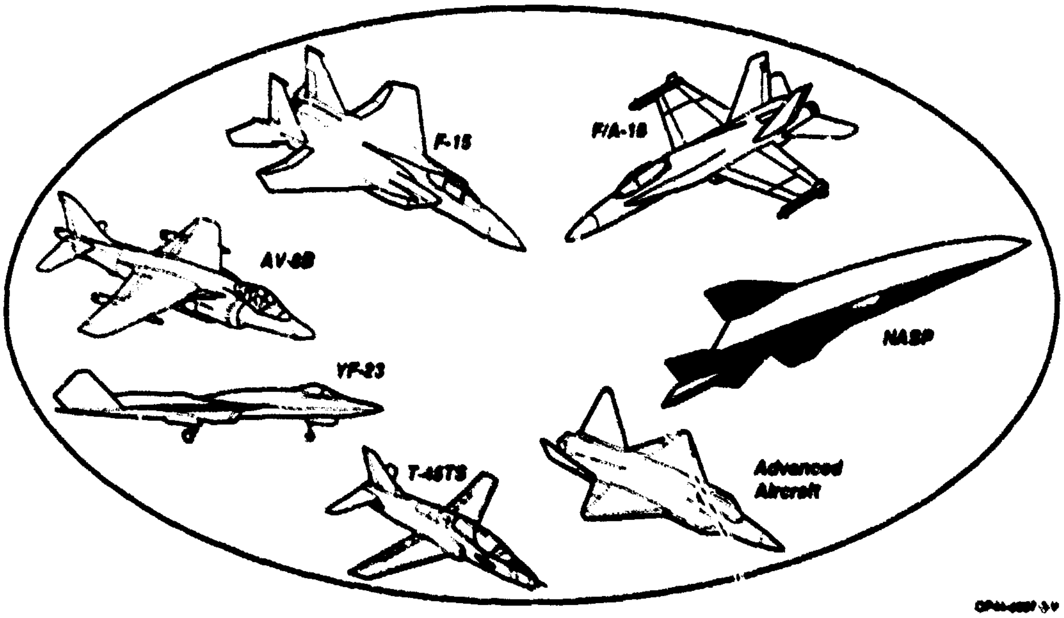
F-15
F/A-18
AV-8B
NASP
YF-23
T-45TS
Advanced Aircraft

GP94-0007-3-V

Figure 5. McDonnell Douglas Aerospace Vehicles Where Acoustic Fatigue Procedures Have Been Successfully Employed

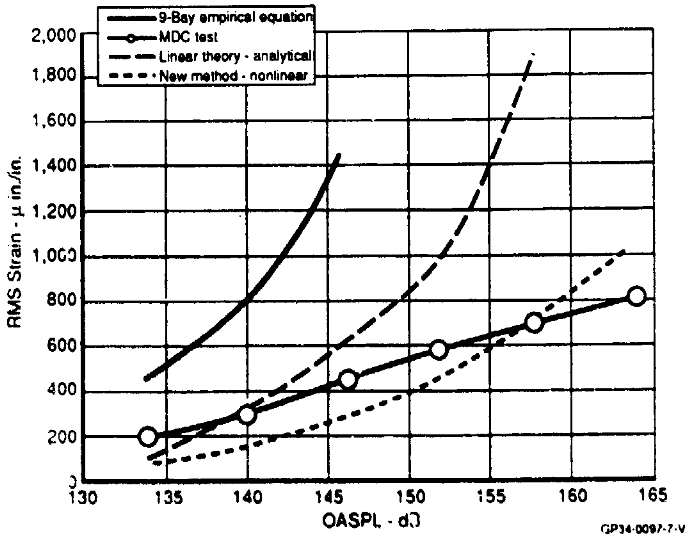

Figure 6. Strain Response Under Acoustic Excitation of Clamped Aluminum Panel
10 in. x 20 in. x 0.063 in. 7075-T6 Panel, Narrow
Band Random Excitation

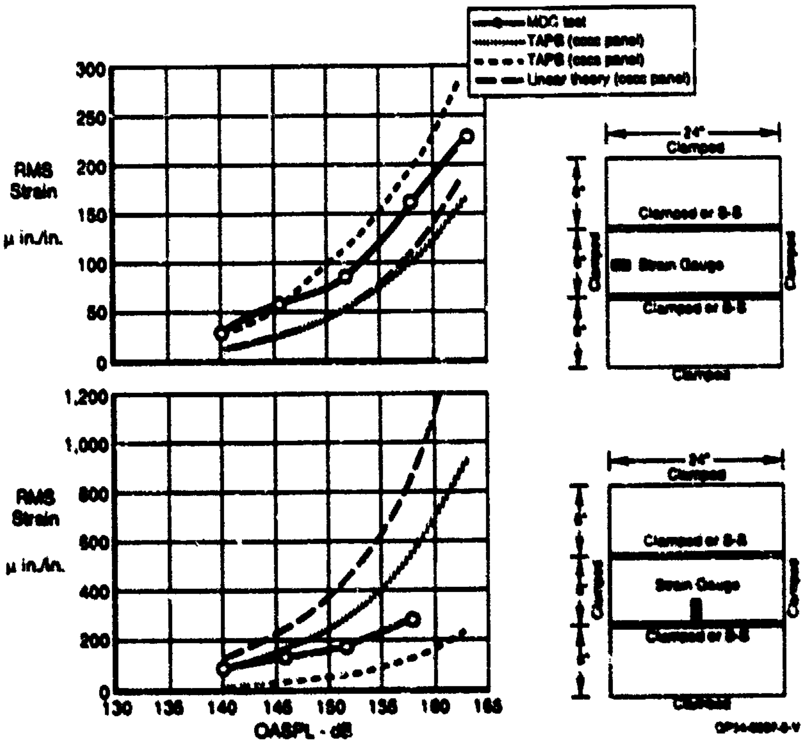

Figure 7. Strain Response Under Acoustic Excitation of Clamped 3-Bay G/E Panel

Case	Analysis Method	Dynamic Strain (μin./in.)	Fatigue Data Used	Cycles to Failure	Cycles to Failure / Case ① Cycles to Failure
1	Linear	1,939	Sine	7.85 E6	1.0
2	Linear	1,939	Random	1.22 E6	0.155
3	Nonlinear	1,602	Sine	1.19 E7	1.51
4	Nonlinear	1,602	Random	4.19 E6	0.533

GP34-0097-9-V

Figure 8. Combined Loads Fatigue Evaluation
TMC Panel Used in NASP Program (OASPL = 180 dB)

ACOUSTIC FATIGUE OF CARBON FIBRE STRUCTURES

G. Müller
M. Grünewald

Daimler-Benz AG F1 M/E
Forschung 4, Technik
Postfach 800465
81663 Munich
GERMANY

1. SUMMARY

Based on the acoustic fatigue endurance curve of CFRP-probes (Carbon Fibre Reinforced Plastic) obtained within the BRITE EURAM PROGRAMME "ACOUFAT" further investigations have been carried out with respect to

- nonlinearities in the measurements for the calibration of the different transducers
- effects of residual strength for the coupons
- effects of moisture and temperature in the material due to storage and testing in humid environment

The sum of these effects leads for one choosen coupon type to a reduction of the allowable strain in the range of high cycles by a factor ~ 4 compared to the value obtained originally for the coupon using the 2 % failure criterion and tested at room temperature. The modifications are considered step by step and the resulting curve is given in this paper.

2. INTRODUCTION

The application of advanced materials as CFRP tends to increase in the construction of airplanes due to their high strength at low specific weight. Large efforts are made by the aircraft manufacturers in order to qualify their structures, to avoid maintenance problems for those parts exposed to large noise levels and to define weight optimised design solutions against acoustic fatigue.

For the investigation of the acoustic fatigue parameters ε_{rms}/N during the BRITE EURAM PROGRAMME "ACOUFAT" [1] in 1992 tests were carried out with eight different types of CFRP coupons.

This programme defined as a pilot phase was aimed to understand about the CFRP fatigue behaviour and to derive appropriate test and analysis procedures.

Because of the limitations within the EC programme further investigations were performed to gain better confidence in the results and to increase the knowledge about the influences of moisture and temperature in the material. Another important issue is the definition of the failure criteria including possible reductions of the residual strength for CFRP material under acoustic loads.

This paper discusses further investigations based on the fatigue results of the coupon type No 7 from "ACOUFAT" excited by simulated acoustic loads using a dynamic shaker.

The calibration procedure of the measuring devices has been improved by considering the linearity of the response versus the input load.

For the compensation of the residual strength reduction the failure criterion is redefined.

Additionally for this coupon type the influence of the storage and testing in humid environment on the ε_{rms}/N - curve is investigated by read across from the results of other specimens.

Considering all influences a recalculated lifetime curve is given taking into account safety margins.

Based on these considerations further investigations are needed for the verification of the measurement and analysis procedures as well as the definition of the failure criterion for deriving the ε_{rms}/N - curves.

3. TEST SPECIMEN

The considered coupon (type 7) consists of a skin with 8 plies (1mm) which was reinforced by a cocured landing (5 plies). A L-Stringer was bolted with Hi-Lok with a sealing material implemented between stringer and skin. The dimensions (in mm) and lay up directions are given in *Fig 1*.

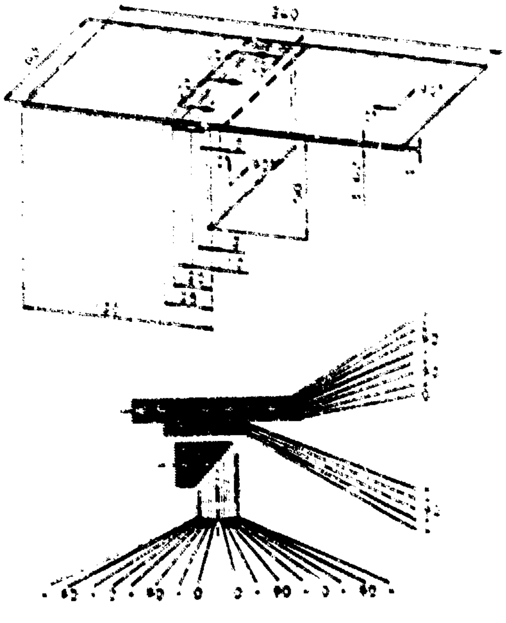

Fig.1 : Dimensions of the "ACOUFAT" coupon type 7

Presented at a Symposium on 'Impact of Acoustic Loads on Aircraft Structures' held in Lillehammer, Norway, May 1994.

4. TEST PROCEDURE

Three specimens were tested simultaniously fixed by a clamping device which was mounted on the excitation table of the shaker (*Fig 2*). On this device an accelerometer was installed for reference and shaker control as well. The random vibration load was produced by a dynamic shaker SA30-V560/ Unholtz-Dickie controlled by a random signal generator . For the tests at high and low temperature and within humid environment a climate chamber was used. The data were digitized after amplification and analysed with a PC. The measurement intervals were at the beginning 5 seconds and increased with the test time up to 10 minutes. The test facility is shown schematically in *Fig.3*.

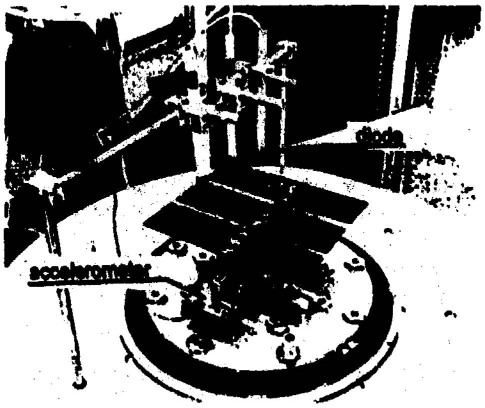

Fig. 2: Coupons mounted on the excitation table

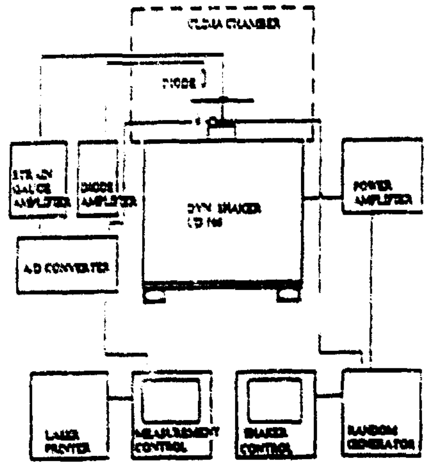

Fig 3 Test facility

The endurance tests were performed for four load levels to obtain several ε_{rms}/ N points for establishing the lifetime curve. The frequency bandwidth was chosen in order to excite only the first symmetrical eigenmode of the three specimens. The maximum bandwidth was about 70 Hz depending on the shaker performance.

Preliminary tests to obtain the strain distribution on the skin surface, resonance tests to determine the frequency of the lowest symmetric bending mode and its damping coefficient for low excitation levels were performed. Additionally linearity checks under static loading have been made as described in the ESDU 93027 [2].

Foil strain gauges were bonded at the surface for measuring the strain in the outer laminate at the locations of the maximum strain. Since the strain gauges operate only properly for a limited time an optical diode was used to measure the deflection of the skin additionally. Its signal is proportinal to the maximum strain. The diode was calibrated by the strain gauge. The measurement area of the strain gauges was 1.2 x 1.5 mm. The diode was combined with an optical fiber to enable measurements in the climate chamber.

5. ANALYSIS

The measurements of strain, deflection and excitation load started generally before the ramping phase of the shaker to obtain the frequency of the specimens and the damping values for the structure unaffected by fatigue at the very beginning of the test. At that time the load level was 20 dB below the steady state excitation level. For example 0.4 g^2/Hz was the start level at the ramping phase for the 40 g^2/Hz excitation level. The modal eigenfrequency and damping value was determined using a SDOF (single degree of freedom) curve fit to the transfer function from strain to input load for strain gauges and to the response displacement to input displacement for the diode. Examples for the transfer function (magnitude and phase), the rms strain spectrum and the rms input spectrum are given in *Fig. 4*.

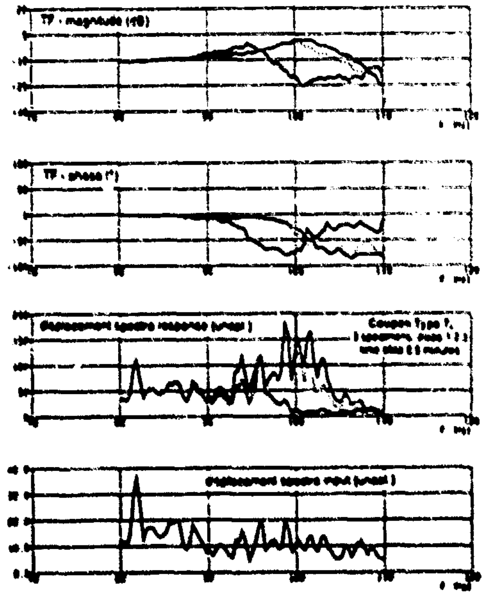

Fig 4: Examples of the measured input load, responding strains and the transfer functions

6. CALIBRATION OF THE OPTICAL DIODE

Due to the early failure of the strain gauge, in general during the ramping phase of the shaker at high level excitations, the diode had to be calibrated using the first measuring sequencies. A calibration example is given in *Fig. 5*. For calibration the rms values of the half power bandwidth (3dB-values) were used being independent from the excitation bandwidth, which has been changed in some cases due to the limited shaker power.

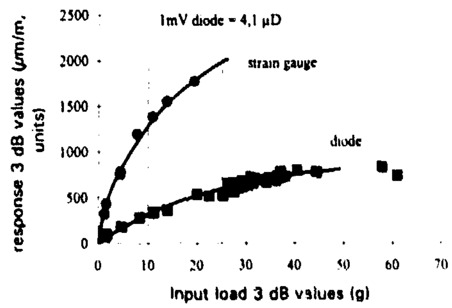

Fig. 5: Example of the calibration of the diode using strain gauge results (3dB-values)

7. DETERMINATION OF THE LIFE TIME CYCLES N

For the endurance data the strain level was determined at the time, when the input load reached the steady state level. For the definition of the failure point for the structure a 2 % drop of the frequency of the lowest bending mode was used (*Fig. 6*). For the corresponding time the number of cycles N_1 was determined. The settling phase included the structural settling as well as the landing separation. It was not considered here as a structural failure. The fundamental frequency f_0 (100%) was deterermined at the time when the slope of the frequency curve reduced and remained constant for some time interval.

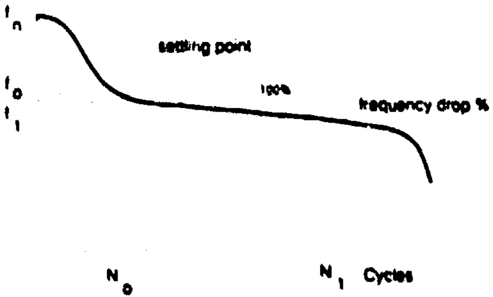

Fig. 6 Definition of the failure criterion

8. CALCULATED ε_{rms} / N CURVE

The derived ε_{rms}/N curve is given for the considered coupon type 7 in *Fig 7* for room temperature. The straight line was fitted to the endurance data in a least squares sense from 10^3 up to 10^8 cycles, which exceeds the measurements by about a factor of 10 for each margin.

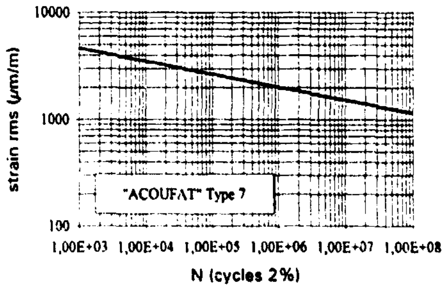

Fig. 7: Calculated ε_{rms}/N curve of coupon type 7 (L - Stringer with landing)

9. EFFECTS DUE TO THE NONLINEARITY OF THE TESTS

As shown in *Fig.5* the strain did not increase linearily with the input load because of the increased damping of the bending mode at large vibration levels caused by the airpumping. This effect was investigated in order to verify the relative calibration of the diode versus the strain data. In the curves given in *Fig.5* the calibration factor for the input load 10 g where the strain gauge values were still significant was 4.1 µstrains / mV diode, the factor at 25 g would be 3.5 µstrains, which would lead to a lower ε_{rms}- value by factor 1.17. These different factors refering to the input load could be caused by the different measurement locations as well as by the different transducer behaviour under random loading with increasing level. In order to improve the calibration procedure the measured 3dB-values of strain ε_{3dB} with their half power bandwidth Δf and the corresponding input load g_{3dB} were used for consideration of the nonlinearity due to different damping ratios and its influence on the measured strain (*Fig 8*).

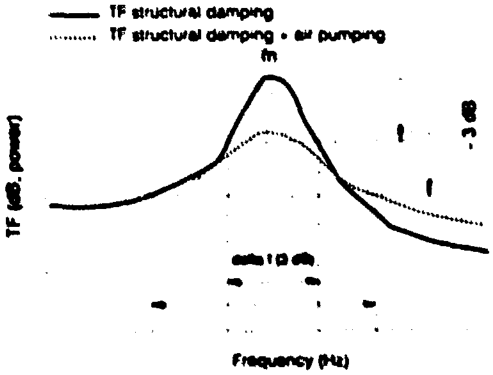

Fig. 8: Transfer function strain to input acceleration

Using the formula [2.1] of ESDU 72005 [3] and incorporating the input load as acceleration density acting on a cantilever probe with one end fixed (Fig.9) the strain can be estimated by

$$\varepsilon_{rms} = \left(\frac{9}{16} \frac{l^2}{t} \frac{\lambda_i^2}{\delta} G_b(f) \sqrt{\frac{\rho^3}{3E^3}} \right)^{\frac{1}{2}}$$

with

$G_b(f)$	spectral density of input acceleration at frequency f
δ	damping ratio
λ_i	fixing coefficient for the first bending mode
ρ	mass density
l	free length of the cantilever
t	thickness
E	Young's modulus

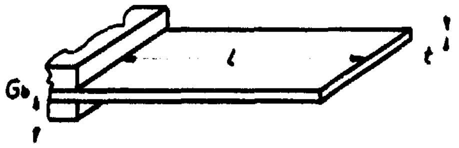

Fig. 9: Model cantilever beam acceleration excited

Leaving for one coupon excited by one load the dimensions and material properties constant the damping due to the nonlinear air pumping effect changes the resulting strain generally by

$$\varepsilon_{rms} \sim \varepsilon_{3dB} \sim \sqrt{\frac{1}{\delta}}$$

With the measured damping δ_M and the corresponding eigenfrequency f_n the half power bandwidth Δf is

$$\Delta f = 2\delta_M \cdot f_n$$

and the 3 dB-value of the input load is

$$g_{3dB} = \sqrt{G_b \cdot \Delta f}$$

Assuming the measured damping ratio at very low input loads to be representative for the structural damping, the measured strain and the measured input load for the constant damping ratio δ_{ref} value can be recalculated resulting in new pairs of data values.
The corrected strain value $\varepsilon_{3dB(ref)}$ is then

$$\varepsilon_{3dB(ref)} = \varepsilon_{3dB(M)} \left(\frac{\delta_M}{\delta_{ref}} \right)^{\frac{1}{2}}$$

and the corresponding input load level

$$g_{3dB(ref)} = g_{3dB(M)} \left(\frac{\delta_{ref}}{\delta_M} \right)^{\frac{1}{2}}$$

The corrected values are shown in Fig.10 indicating that the response of the coupons was linearly related to the input load.

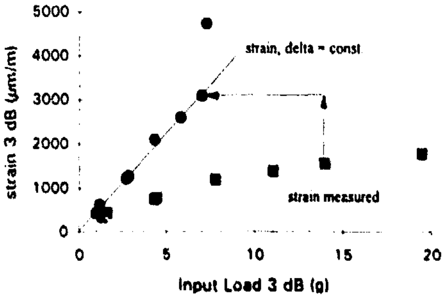

Fig. 10: Strain versus input load (3 dB values) at constant damping

This procedure can be used also for deriving overall values, where only the correction of the strain is required, because the bandwidth of the input load is constant. An example is given in *Fig. 11*.

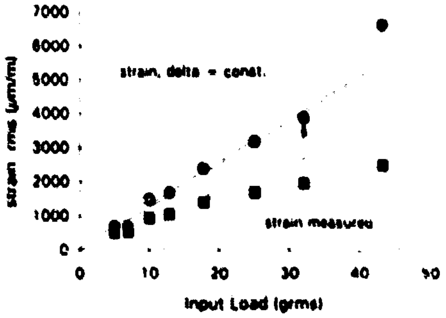

Fig. 11: Strain versus input load (over all values) at constant damping

Using the above given procedure for a recalculation the modified strain and diode values depended to a large degree linearly from the input load and could be used for the calibration of the measurement devices (*Fig 12*). The recalculated ε_{rms} / N curve for coupon type 7 resulted in lower allowable strain or less numbers of cycles as original (*Fig 13*).

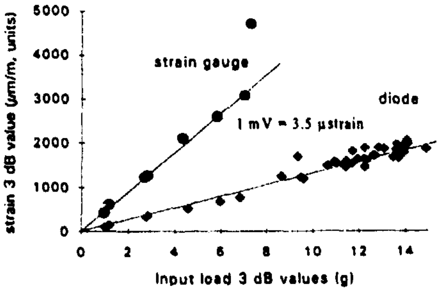

Fig. 12: Calibration of the diode using the 3dB-values (δ = constant)

The allowable strain is reduced in the range of large cycles up to factor 1.7 for this coupon type.

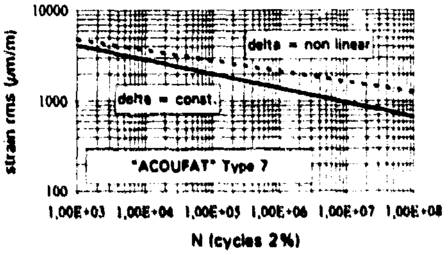

Fig. 13: ε_{rms}/N curve of coupon type 7 with and without linear calibration

10. EFFECTS OF ACOUSTIC FATIGUE FOR THE RESIDUAL STRENGTH

Further tests were performed for the verification of the influence of acoustic fatigue on the reduction of the residual strength. Cantilever probes of similar material as used for the "ACOUFAT" coupons were excited until the frequency dropped between ~ 0.5% to ~ 4% for different samples. The results of the succeeding compression tests are shown in *Fig 14*. Residual strength tests of several coupon types [1] resulted generally (*Fig 15*) in the same behaviour, though the decrease of the break stress of bolted skin structures seems to be larger for the cantilever probes.

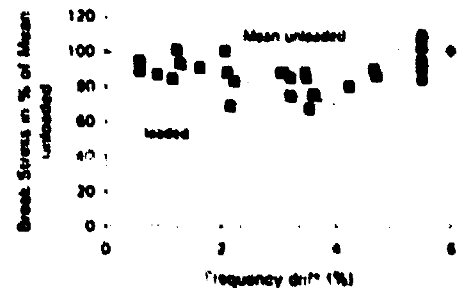

Fig. 14: Residual strength (compression) results for cantilever probes

The tendency of the "ACOUFAT" results based only on few tests is confirmed by the data above and the conclusion from these results is to include the decrease of the residual strength in the life time estimates by redefining the failure criterion as given below.

Provided the few measurements obtained for the bolted coupon types are significant for the residual strength a statistically-based material property, the B-basis value [4] was calculated and used for the evaluation of the compression test results.

The B-basis value gives dependent on the measured values and number of measurements a lower tolerance bound above which 90 percent of the population will be with 95% certainty.

It is calculated by

$$B = \bar{X} - k_B S$$

where

$\bar{X}$ = the sample mean based on n measurements
S = the sample standard deviation
k_B = one side tolerance limit factor

The results are shown in *Fig 15* below.

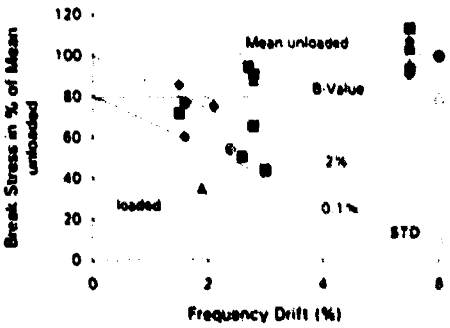

Fig. 15: Results of compression tests of loaded and unloaded (type 7 coupons)

Assuming that 95% of the residual strength values have to be located above the B-bases value, at the example above the failure criterterion arrives at a frequency drop of about 0.1% instead of 2% as used. This effect leads to a reduction of the allowable strain by a factor 1.6.

11. EFFECTS OF MOISTURE AND TEMPERATURE

With similar CFRP material as coupon type 7 stored in humid environment (70°C/ 85 % humidity, 10 weeks), endurance tests were performed for 70°C/ 70% humidity. The results show a reduction of the allowable strain by a factor 1.7 in the high cycle range which is used for the coupon considered here.

The moisture after storage of the used material was about 0.6 weight percent and refering to the material spezification about one third less than the "ACOUFAT" material would have been assimilated in the same storage environment at the same time.

The reduction in life time is due to the moisture and the temperature as well. Therefore further tests for the verification of the influence of the moisture are planned with wet material under room temperature conditions.

12. TOTAL REDUCTION FOR THE ε_{rms}/N - CURVE

The ε_{rms}/N curve for the worst case is given hypothetically below. Correcting for the effect of damping, incorporating the revised failure criterion from the residual strength tests and adding the influence of storage and test in high humidity and high temperature the overall reduction of the allowable strain is about a factor 4 compared to the ε_{rms}/N curve at room temperature with the 2% failure criterion from "ACOUFAT". These curves are given in *Fig.16* with the ε_{rms}/N curves puplished in ESDU 84027 [5] Fig.3 (riveted specimens). The obtained results show a large decrease of the original ε_{rms}/N curve due to the described effects. The effect of moisture and temperature could be given by read across only.

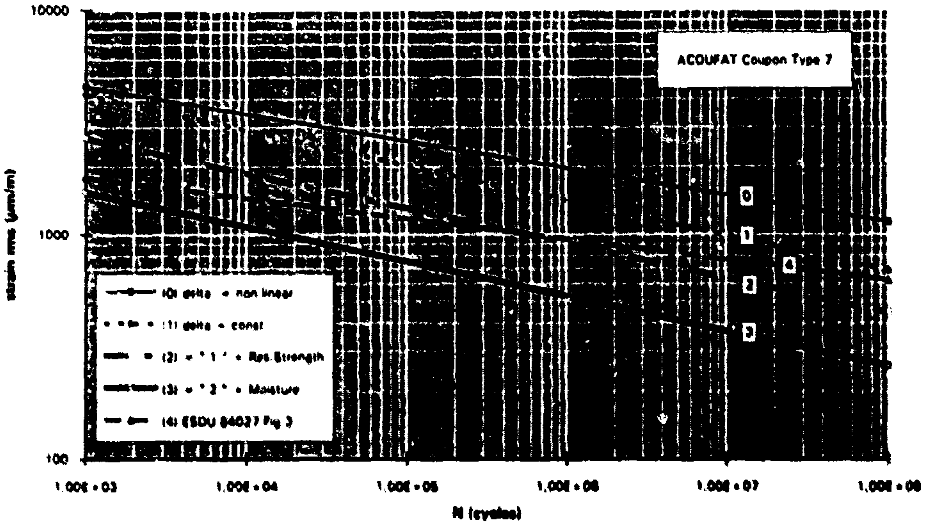

Fig 16 ε_{rms}/N curve for coupon type 7 "ACOUFAT" determined with constant damping, covering the influence of residual strength and moisture / temperature.
Additional with ESDU 82027 Fig 3 (CFRP) for comparison.

13. CONCLUSIONS

The performed investigations have shown, that

- the shaker tests indicate a nonlinear increase of the strain rates with the input load due to the nonlinear damping mainly.
  This effect can be taken into account for the calibration of the transducers.

- acoustic fatigue leads to a reduction of the residual strength. So far the strength has been measured for compressional loads only.

- compound structures (bolted skin/stringers) indicate compared with cantilever probes a greater reduction of the residual strength.

- in order to take into account the reduction of the residual strength, the applied failure criteria have to be changed.

- the storage and testing of the specimens in high humidity and high temperature leads to a reduction of the allowable strain (read across).

Further investigations should be carried out for the verification of the obtained results using probes of identical material and joints.

ACKNOWLEDGEMENTS

Part of this work has been carried out within the Brite/Euram programme ACOUFAT for which the financial contribution of the European Community and the cooperation of the ACOUFAT partners are gratefully acknowledged.

The financial support from Deutsche Aerospace AG allowing to carry on this kind of research work is very much appreciated.

REFERENCES

[1] ACOUFAT: FINAL TECHNICAL REPORT
DOCUMENT AERO 0025-1079/Rept 6/1

[2] ESDU 93027, Methods of tesing for endurance of structural elements using simulated acoustic loading
ENGINEERING SCIENCE DATA UNIT, LONDON

[3] ESDU 72005, The estimation of r.m.s: stress in stiffened skin panels subjected to random acoustic loading
ENGINEERING SCIENCE DATA UNIT, LONDON

[4] MIL - HDBK - 17 - 1D, Chapter 8. ANALYSIS AND PRESENTATION OF DATA

[5] ESDU 84027, Endurance of fibre-reinforced composite, laminated structural elements subjected to simulated random acoustic loading.
ENGINEERING SCIENCE DATA UNIT, LONDON

BRITE-EURAM PROGRAMME : ACOUFAT
ACOUSTIC FATIGUE AND RELATED DAMAGE TOLERANCE OF ADVANCED COMPOSITE AND METALLIC STRUCTURES

D. Tougard
Coordinator of the ACOUFAT programme
DASSAULT AVIATION - Structures Division
78 Quai Marcel Dassault
Cedex 300
F - 92552 Saint Cloud Cedex

1 SUMMARY

The Brite/Euram programme ACOUFAT is concerned with "Acoustic fatigue and related damage tolerance of advanced composite and metallic structures". Three main fields of the ACOUFAT results are discussed :

1 : The use of a "frequency degradation" criterion, usually applied to classical metallic materials and early Carbon Fiber Reinforced Plastic (CFRP) materials, is not considered suitable, as the only parameter, for determination of CFRP specimen "failure" in acoustic fatigue. It is suggested that a suitable criterion should be based, in further work, upon the degradation of the mechanical properties of the specimens.

2 : On the basis of Wind-Tunnel (WT) calibration tests, a semi-empirical model of the spatio-temporal characteristics of the aero-acoustic loads exerted on a flat panel by the turbulent field created by a flap has been developed and utilized as "Load Data Input" for Finite Element (FE) calculations. The WT tests have been reasonably well represented : the development of this semi-empirical model is an encouraging initial success. The results from the initial modelling suggest that this can be extended to the modelling of the acoustic loads in Progressive Wave Tubes (PWT).

3 : The excitation of structures by aero-acoustic loads may not be simulated fully in PWT, by simply modifying and correctly shaping the spectral content. The effect of the spatial distribution of the loading is clearly different in both cases and the tested specimen endurance may be significantly different. It is clear that a theoretical approach based on a correct prediction of the responses to both types of environment is required.

2 INTRODUCTION and OBJECTIVES

2-1 : Definition and General Objectives

The term "Acoustic Fatigue" implies the structural fatigue caused by the predominantly resonant response of structural components to radiated sound fields (fluctuating pressures). Acoustic / aerodynamic excitation aspects are coupled with structural dynamic behaviour and endurance aspects.

The fundamental objectives of the ACOUFAT programme were :

- to enhance the knowledge and the understanding of the acoustic fatigue strength data of selected advanced composite and metallic materials,
- to develop the analytical / computational and experimental methodologies applied (for dimensioning and certification) to predict the fatigue life of modern civil aircraft structures subjected to acoustic excitations.

The safety and the efficiency of aircraft operations can be then improved and the maintenance costs of future aeronautical structures reduced.

2-2 : Fields of study

To improve the prediction of the acoustic fatigue life of structures, the following three main areas are studied :

- the loads applied to the structures (dynamic characteristics of the acoustic excitation),
- the structural dynamic response evaluation which provides stresses S_{rms} and frequencies
- the acoustic fatigue strength data for the materials and the selected designs (rivets, ...).

Stress levels + Frequencies + Acoustic fatigue strength data → Fatigue life prediction

For each area, technical objectives have been defined with experimental tasks (calibration) and theoretical tasks (prediction).

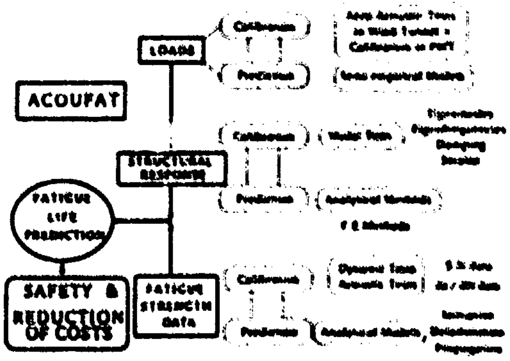
ACOUFAT
LOADS
Calibration
Prediction
Aero Acoustic Tests in Wind Tunnel + Calibration in PWT
Semi empirical Models
STRUCTURAL RESPONSE
Calibration
Modal Tests
Eigenmodes
Eigenfrequencies
Damping
Stresses
Prediction
Analytical Methods
F E Methods
FATIGUE LIFE PREDICTION
SAFETY & REDUCTION OF COSTS
FATIGUE STRENGTH DATA
Calibration
Dynamic Tests
Acoustic Tests
S N data
da / dN data
Prediction
Analytical Models
Initiation
Delamination
Propagation

Presented at a Symposium on 'Impact of Acoustic Loads on Aircraft Structures' held in Lillehammer, Norway, May 1994.

2-2-1 : The Acoustic Loads Evaluation :

At present, the aero-acoustic loads data is limited and is described mainly in the time domain. To simulate the response of structures accurately, the space distribution of the acoustic field is required. Consequently, the results of acoustic tests which are performed using Reverberant Chambers or Progressive Wave Tubes , may not, structurally, be representative of the effect of the real aircraft flight environment.

Work performed : On the basis of Wind-Tunnel calibration tests, a semi-empirical model of the spatio-temporal characteristics of the aero-acoustic loads on a flat panel by the turbulent field created by a flap (simple configuration of a typical turbulence) has been developed and utilized as "Load Data Input" for Finite Element (FE) calculations. Furthermore, with the same panel, investigations were conducted in the PWT to try and match the strain spectral densities obtained in the WT. These significant parts of the ACOUFAT results are detailed in sections 4 and 5.

2-2-2 : **The Structural Dynamic Response Evaluation** (Srms stresses and frequencies) :

At the present, the main available computational methods for the calculation of the structural response are FE dynamic analysis taking into account the aero-elastic or the acoustic coupling with the fluid.

Work performed : Several computer codes were available for this study. Their ability to deal with the problem have been recognized by comparison with each other and with test results. Non linear dynamic behaviour, which is apparent in structures at higher acoustic loads, can also be simulated.

These assessments improve predictive capability, define the analysis assumptions and provide rules of use. They are the necessary support to the testing activity planned in this program.

2-2-3 : **The Acoustic Fatigue Strength Data** for the selected materials and the associated designs (riveted, bonded, etc...). For advanced metallic and composite materials, the standard acoustic fatigue strength data such as S-N endurance curves and da/dN or dA/dN curves, crack or damage growth rate data, are limited at the present.

Work performed : Standard S-N endurance curves have been developed for 5 selected advanced materials (2 CFRP + GLARE + Aluminium-lithium + SPF-DB Titanium) with different specimen designs representative of aeronautical structures (≈ 600 coupons tested by shaker excitation + 6 large panels in PWT). The commonly used methodology for this type of test has been critically analysed. This significant part of ACOUFAT is detailed in section 3, but limited to the CFRP materials.

On the basis of these tests, analytical work concerning the damage initiation and the damage propagation / accumulation has been also performed for CFRP materials.

2-2-4 : Furthermore, the synthesis of this Pilot Phase study has enabled major recommendations, related to the qualification methodology (testing strategy and calculating strategy) applied to aircraft areas subjected to acoustic loadings.

3 RANDOM VIBRATION ENDURANCE INVESTIGATIONS FOR CFRP - MATERIALS

3-1 : Presentation

The endurance data produced is detailed in other papers and published by the ACOUFAT partners involved in this activity. This section is focused only on the main results and recommendations related to the Carbon Fiber Reinforced Plastic (CFRP) materials.

Two of the main purposes of the testing activity were :

* to elaborate the standard endurance data of typical designs from CFRP materials with simple coupons tested by random excitation on shaker,

* to assess this standard endurance data by comparison to large panel tests to verify if accurate life prediction of aircraft panel / stringer constructions subjected to acoustic loading, can be made using simple coupon tests.

3-2 : Coupon Tests by Shaker Excitation

From the standard engineering publications (e.g. ESDU Acoustic Fatigue Volumes), only very limited information is available for CFRP. Nevertheless these ESDU data were considered as the reference for defining test procedures and for comparison of the results.

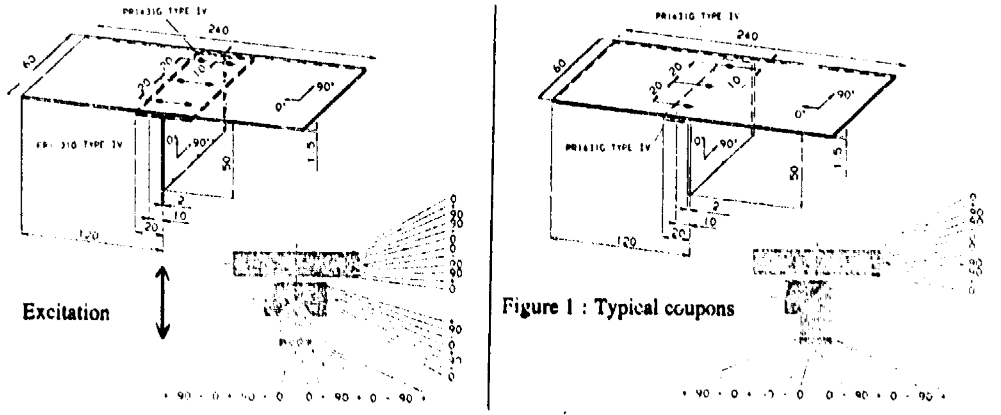

Figure 1 : Typical coupons

3-2-1 : Tests definition :

Selected CFRP - materials : T800/924 and HTA/6376 (- 50°C, RT, 80°C, 120°C)

Typical coupons designs : L- and T- shaped stringer/skin coupons, with riveted stringer, skin with/without cocured landing or skin with taper, and skin with/without initial damage.

Excitation : unimodal vibration using a narrow band random load spectrum, centred around the specimen 1st bending mode frequency determined from a sine sweep, to assure that the bandwidth of excitation always covers the response spectrum.

Either the loading level in terms of specimen-strain (or deflection) was kept constant or the specimens were tested at a constant g^2/Hz - level. Since the required strain levels exceeded shaker limits, tip mass was added to the free ends of specimens.

Failure criterion (1st reference) : 2% drop in the settled natural coupon frequency. Nevertheless, number of tests were continued until visible damage was detected.

3-2-2 : Specimen damage & NDT investigation :

Some CFRP specimens have been tested either until complete failure or only until fulfillment of the 2% criterion, for high and low excitation levels. NDT inspections revealed similar damage in all specimens :

1. For the HTA/6376 specimens with a step landing, separation of the landing edges across the coupon width (separation length ≈ 10 to 20 mm on each side).
2. Development of sub-surface delaminations around rivet holes.
3. Development of delaminated surface strips from the rivet holes, growing in a direction to ward the specimen ends (outer ply direction).
4. Possible development of sub-surface delaminations at the edges of the coupons, near tapered regions (edge effect).
5. Most of the surface delaminations occurred on the outer skin side.

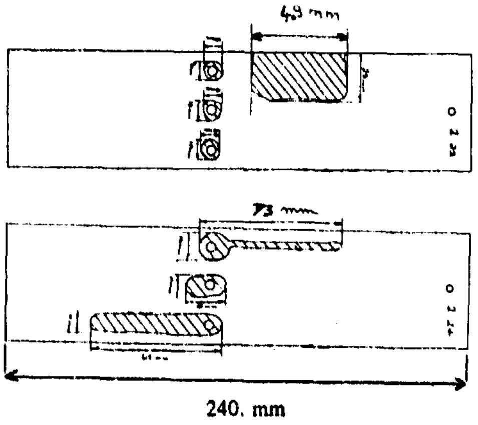

Figure 2 : Typical delamination areas, with CFRP T800/924 coupons

6. Consequence of the damage extension, is observed a rapid decrease in bending stiffness, particularly at high excitation levels.

Discussion :

- Coupons with initial damage have been tested. But, from these tests it was impossible to produce meaningful dA/dN data for continuous delamination growth, as it was originally planned.
- The delaminations around the bolt region are considered to be of a type that is likely to occur in panel attachment regions. Delaminations at the free edges (4.) of the coupons are obviously failures that would not occur in panels. These edge delaminations can affect the coupon stiffness and, unfortunately, any frequency drop criterion.

3-2-3 : Specimen settling characteristics :

Generally, the metallic coupons do not exhibit a significant "settling phase". From the CFRP coupons tests, several types of settling characteristics were observed.

- The HTA/6376 coupons with a step landing showed a fast drop in coupon frequency due to the separation of the cocured step landing from the skin :

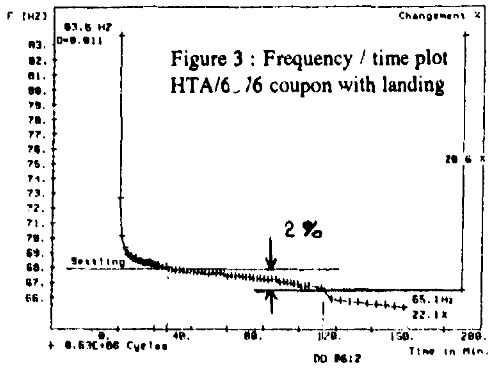

Figure 3 : Frequency / time plot HTA/6376 coupon with landing

- The predamaged HTA/6376 coupons demonstrated a significant settling phase which consisted of a sharp reduction in frequency followed by a more gradual decrease until the onset of linearity :

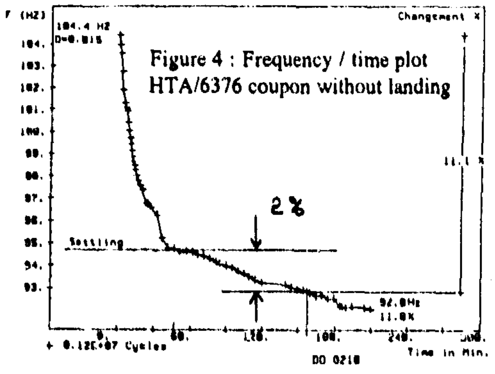

Figure 4 : Frequency / time plot HTA/6376 coupon without landing

- The T800/924 coupons with smooth taper in the bolted region, had a reduced settling phase with a gradual change in frequency before the onset of linearity :

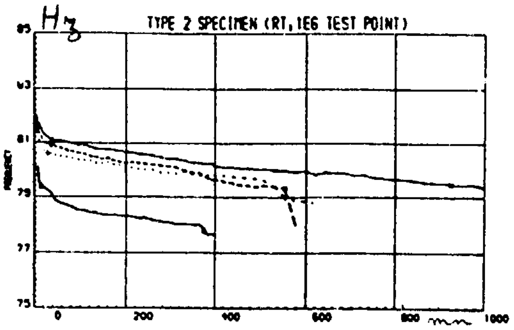

Figure 5 : Typical frequency vs time plot
T800 / 924 coupons, with smooth landing

Discussion :

- In some cases, it is difficult to determine where the actual settled point occurred (major problem when applying any frequency drop criterion).
- The phase of settling is influenced by several effects and may be attributable to micro-cracking of the CFRP material, clamping arrangement, joint interfaces or propagation of delaminations within the specimen. For coupons with cocured step landing, the settling phase is obscured by the effect of the separation of the landing from the skin. Further investigations are required to establish the mechanisms which contribute to the CFRP specimen settling.

3-2-4 : Specimen strain distribution :

The strain distribution on the skin is complex (see figures 6 and 7) but it must be correctly determined to define the reference Srms in the S-N curves. The reference location was, by convention, the expected maximum strain value location which can be different from the failure position.

Discussion :

- When determining the reference strain by static calibration, the two levels upwards and downwards must be averaged.
- Due to the effect of stacking sequence, a slight rocking motion of the specimen may occur and cause a strain gradient across the specimen (see figure below).
- The strain distribution in the thickness should be taken into account for each ply (through thickness ϵ_{ii} and ϵ_{ij} , classically evaluated e.g. for static bending tests).
- Where the strain gradient is high, the measured value can be dependent on the gauge size (integration length).
- The strain distribution can be modified during the fatigue test by damages, e.g. delamination of the landing.
- There can be a significant difference in the level of measured strains during the strain- and load-monitored tests (the ϵ_{rms} increase with time).

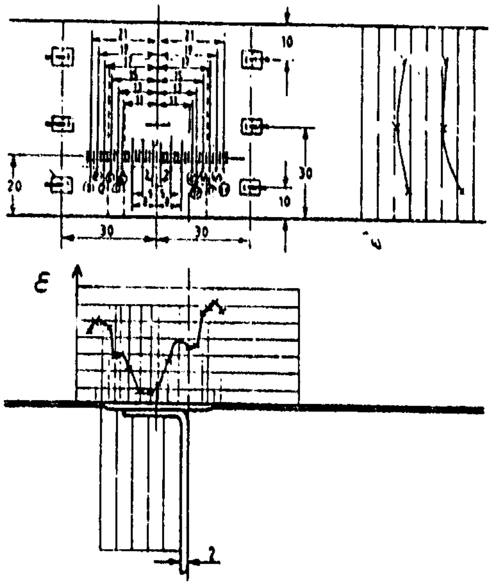

Figure 6 : Measured strain distribution for L-shaped HTA / 6376 coupon with landing

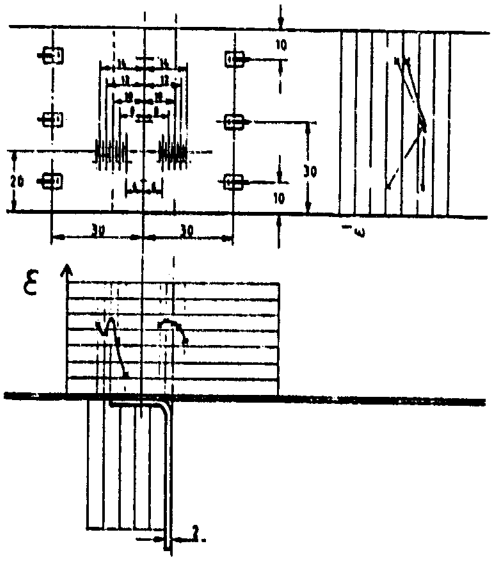

Figure 7 : Measured strain distribution for L-shaped HTA / 6376 coupon without landing

3-2-5 :Endurance data :

The S-N curves have been established on the basis of the 2% reduction frequency criterion. To decrease the number of tests, these S-N curves were assumed to be straight regression lines (as presented in the ESDU).

Testing performed on the CFRP materials, demonstrated that the endurance marginally decreased with increasing temperature.

The endurance of the predamaged coupons was similar to the undamaged type.

Discussion :

- The main difficulties encountered to value the "Srms" strains and the "N" number of cycles have been discussed § 3-2-4 and § 3-2-3.
- At 2% drop in settled frequency, all coupons revealed various regions of delamination .
- Nevertheless some specimens (tested up to failure) demonstrated that there is considerable fatigue life in the CFRP specimens after the 2% criterion (this is also the case for the tested GLARE specimens and the Aluminium-Lithium specimens).
- Consequently, the use of a "frequency degradation" criterion, as the only parameter, was not considered suitable for determination of specimen "failures". It is suggested that a suitable criterion should be based upon the degradation of the mechanical properties which can be determined by by residual strength tests of the specimens.

3-2-6 : Residual strength tests :

Additionally residual strength tests were carried out by applying compression loads to the skin. Even after severe acoustic loading, these tests (only HTA/6376) demonstrated that the remaining static strength is :

- greater than 80% of the initial strength if the load direction is along the stringer axis
- about 70% of the initial strength if the load direction is perpendicular to the stringer, at 2% frequency drop, despite that there was no evident visible failure in some cases.

Discussion : These tests were a first attempt to evaluate the degradation of the mechanical properties. Further investigations are required.

3-3 : Endurance Tests of CFRP Panels in PWT

The design of shaker coupons is dictated by the assumption that panel behaviour can be adequately represented by the dynamic behaviour of a thin strip. To validate the coupon test-results and the coupon testing procedure, one T800/924 panel and one HTA/6376 panel have been fatigue loaded in PWT.

For the 2 panels, the main damage areas were located in the skin, above the rib-stringer intersection. This type of damage was explained (and quantified with the support of F.E. calculations) by the effect of the out-of-plane loads induced by the suspended mass of the stringers which had no direct connections to the ribs. In these areas, the strains ϵ_{ii} are lower than those in the middle of the long side bay which is the classical critical location in a panel.

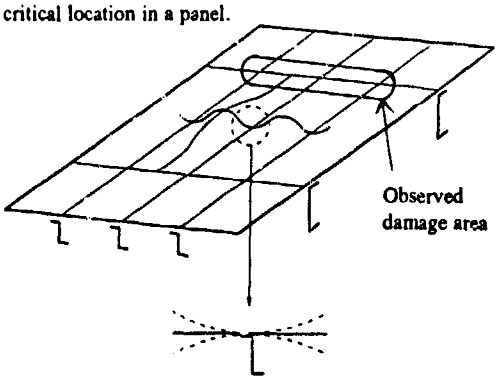

Figure 8 : Classical critical location in a stiffened panel and observed damage area for the CFRP panels.

Discussion :

- No coupon tests were representative of this type of damage (the coupons were designed to study the in-plane bending effect, not the out-of-plane loads effects). Consequently no endurance comparison could be evaluated between panels and coupons.
- These results outlined, while using new materials or new designs, the absolute necessity of maintaining large panel tests in PWT for identification of the possible failure modes and of the damage-developments with a multi-mode dynamic response and multi-axial stresses.
- To reduce the test-duration (for financial aspects), the test-excitation load level is generally increased from that of the aircraft. In fact, the damping-levels and the non-linear membrane effects increase with increased load input levels. This can modify significantly the strain-distribution and the strain-ratio between different areas of the panel. The aircraft endurance limit cannot be then simply deduced and non-linear dynamic F.E. calculations must be performed to evaluate it correctly.

3-4 : Recommendations for Random Vibration Endurance Tests

(i) : Further work is required to investigate the reasons for the "settling phase" observed in CFRP materials.

(ii) : A suitable criterion is required for all types of specimens tested, possibly based on residual strength characteristics of the specimen. In the meantime, current data should be fully documented for use (i.e. with initial frequency, strain, input load and damping, plus damage-analysis).

(iii) : An assessment of coupon failures compared to complex structural failures is required in order to validate the usage of current coupon designs and endurance data.

(iv) : Non-linear aspects must be evaluated when testing with enhanced acoustic load levels.

4 AERO - ACOUSTIC LOADS STUDY : Experimental and Analytical Results

4-1 : Presentation

Acoustic fatigue failures have occured in structures lying close to, or in the path of, the jet efflux (acoustic excitation with a large correlation length). Similar failures have occured in other regions of pressure fluctuation such as within the intake duct of fan engines, close to propeller tips and in regions of separated flow near control surfaces, such as elevators, flaps, rudders, or near items such as spoilers which are used on some aircraft during manoeuvres (acoustic excitation with a reduced correlation length). But, at present, aero-acoustic loads data are very poor. There is no general data base and the available data concern mainly the time fluctuation, rather than the space distribution which, nevertheless, is strictly essential to calculate the structural response.

The objectives of the ACOUFAT programme in this field of study were :

- to develop a semi-empirical model of aero-acoustic loads, in areas of separated flows, with space distribution and time fluctuation, on the basis of informations collected from the open literature, and of the pressure measurements obtained by tests in Wind-Tunnel (WT),
- and to validate the use of this model as "Load Data Input" of Finite Element (FE) calculations to simulate the dynamic response of a test-box, representative of aircraft structures.

4-2 : Experimental Study of the Acoustic Loads in Areas of Separated Flows (Wind - Tunnel Tests)

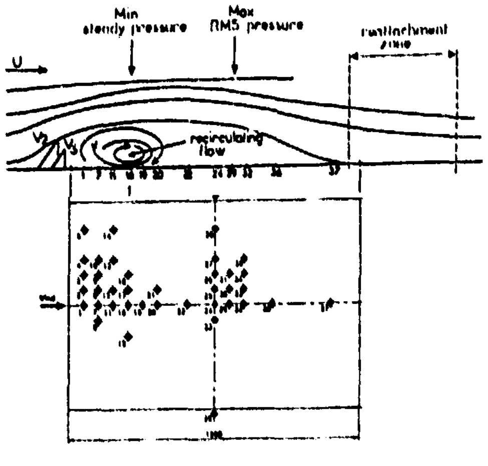

Figure 9 : Location of pressure measurements

Separated flows were generated by placing a test set-up into the S1 - Modane ONERA Wind Tunnel. When operated at transonic speeds, a turbulent pressure field is developed behind an elevated spoiler. This configuration was chosen to simulate actual flight conditions, where separated flows occur behind control surfaces such as spoilers, flaps, speed brakes, etc... (simple configuration of a typical turbulence).

In a *1st step*, a measuring plate containing 40 pressure sensors (Figure 9) was installed behind the spoiler. The fluctuating pressure field in the area of the recirculating bubble behind the flap was evaluated for different flap sizes and Mach numbers.

Each individual sensor signal was evaluated in terms of pressure spectral density and selected pairs of microphones were analyzed with respect to their coherence. Typical results are shown in Figure 10 for the pressure spectral density. The plots indicate high intensities in the frequency range around 100 Hz with a rapid decay towards the higher frequencies. The maximum intensity and the corresponding frequencies depend on the test configuration which is given by Mach-number, size of spoiler and location of pressure transducers. However, all spectra exhibit a continuous energy distribution due to the randomly fluctuating pressures.

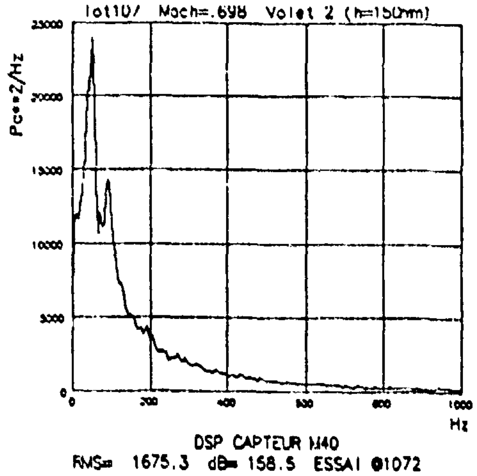

Figure 10 : Wind-Tunnel tests : Typical Pressure Spectral Densities (Pa²/Hz) vs Frequency (Hz)

Coherence functions have been produced between selected pairs of microphones and typical plots are shown in Figure 11 (real and imaginary parts of the coherence functions). They indicate that the spatial coherence is generally very low. This implies that the microstructure of the turbulence field contains a high number of uncorrelated eddies.

The basic experimental data recorded in the frame of those WT tests, are the reference data for elaborating a mathematical model of the statistical characteritics of the excitations.

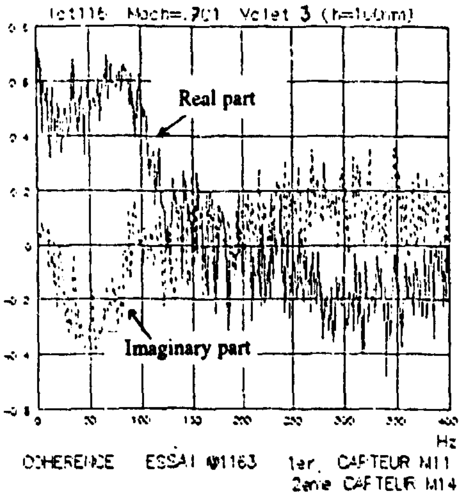

Figure 11 : Wind-Tunnel tests : Typical Correlation Factors (selected pair of microphones) vs Frequency

4-3 : Experimental Study of the Associated Structural Response

In a ***2nd step***, a calibration test box (i. e. a stiffened aluminium panel, representative of aeronautical structures) was mounted in the WT, in place of the measuring plate containing pressure sensors, downstream the previous deflector.

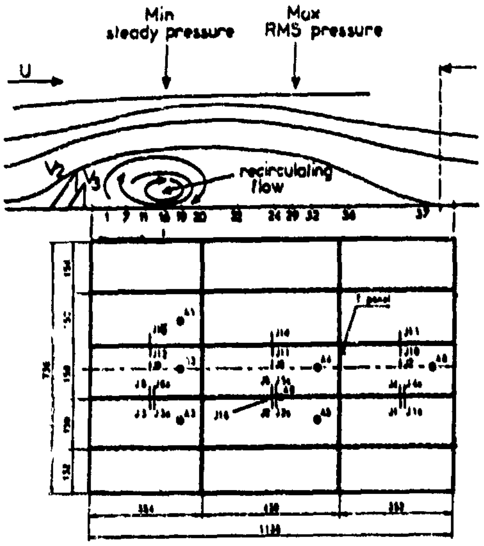

Figure 12 : Location of strain gauges on test box

The structural response of the test box was identified by 16 active strain gauges on the panel, for the aerodynamic configurations studied in the first step (different flap sizes and Mach numbers of § 4-2).

4-4 : Analytical Model of the Aero-Acoustic Loads in Areas of Separated Flows

The aim of the present analytical work was to develop a semi-empirical model to calculate the spectra of the spatial and temporal correlations of the acoustic pressure associated with fatigue loads, for comparison with experiments of panel tests in WT (and additionally in PWT). The modelled Cross - Spectra law can be then used as load input for FE calculations.

In both cases, WT and PWT, a statistical independence is invoked to split the space-time spectra into factors corresponding to temporal spectra and spatial spectra in each dimension e.g. longitudinal and traverse. The simplest case is the test in PWT which, under the restriction of linear sound, lead to similar spectra in all space-time dimensions (see section 5). The case of test in WT leads to progressive complications : a modified Gaussian correlation of phase shifts leads to spectra which are still stationary, but involve Hermite polynomials, besides Gaussian functions ; the positioning of the observer close to a flap of finite span leads to non-stationary spatial spectra, involving error functions as well. All together is obtained an hierarchy of spectra, the simplest of which depend on the rms phase shift and correlation scales (time and lengths) and excitation parameters (frequency and wave numbers). Multiple scattering involves the double reflection coefficient and non stationary correlations introduce geometric parameters into the exact and asymptotic evaluation of spectral integrals, which generalize the Gaussian type.

The final equation used to determine the normalized Cross - Spectra law, input as load data in FE calculations, is presented Figure 13.

This model involves 8 semi-empirical parameters (underlined twice). On the basis of the transducer-responses obtained during the WT tests, the values of the 8 parameters were defined in such a way that the computed Cross - Spectra could be thought to be identical to the measured one.

As Figure 14 shows, the meantrend of the real and imaginary parts is acceptable. The peaks which appear in the experimental data cannot be modelled. However, the imaginary part seems not to stick to reality as good as the real part does.

Along the bandwidth [0-2000 Hz], the Cross - Spectra value tends to decrease and that's what was noticed during the experiment as the Figure 14 shows.

$$\gamma_{\hat{x}\hat{y}}(x_1-x_2, y_1-y_2, w) = \frac{e^{i(\underline{K_0}x+\underline{k_0}y)}\sum_{n,m=1}^{\infty}\underline{D}^{n+m-2}\, e^{-\underline{a}}\left\{2\sqrt{\pi}\,\delta(\underline{\Omega})+\sum_{j=1}^{\infty}\left[\frac{\underline{b}\,E(x)\,E(y)}{V_j}\right]^{j} e^{-\underline{\Omega}^2/4j}\sum_{p=0}^{j}\frac{(8j)^{-p}}{p!\,(j-p)!}\,H_{2p}\left(\frac{\Omega}{2j^{1/2}}\right)\right\}}{\sum_{n,m=1}^{\infty}\underline{D}^{n+m-2}\, e^{-\underline{a}}\left\{2\sqrt{\pi}\,\delta(\underline{\Omega})+\sum_{j=1}^{\infty}\frac{\underline{b}^{j}}{V_j}\, e^{-\underline{\Omega}^2/4j}\sum_{p=0}^{j}\frac{(8j)^{-p}}{p!\,(j-p)!}\,H_{2p}\left(\frac{\Omega}{2\sqrt{j}}\right)\right\}}$$

Choice of parameters of model

- double reflection coefficient: D
- excitation frequency: $\omega_0 = 2\pi \times 100$ Hz.
- transverse excitation wavenumber: $K_0 = 0.05$.
- longitudinal excitation wavenumber: $K_0 = 1.11\ m^{-1}$.
- longitudinal correlation scale: $L = 25$ cm.
- root mean square phase shift: $\sigma = 2$. Taking $r = \Delta K.\xi$
- transversal correlation scale: $\ell = 50$ cm.
- correlation time: $T = 0.003$ s is of the order $2\pi L/c = 0.005\ s^{-1}$

$$\begin{cases} E(x) = \left(1-\dfrac{2x^2}{\underline{L}^2}\right) e^{-\frac{x^2}{\underline{L}^2}} \\ E(y) = \left(1-\dfrac{2y^2}{\underline{l}^2}\right) e^{-\frac{y^2}{\underline{l}^2}} \\ \Omega = (w-\underline{w_0})\,\underline{T} \end{cases} \qquad a = \frac{1}{2}\,\underline{\sigma}^2(n+m) \qquad b = \frac{1}{2}\,\underline{\sigma}^2\left[n+m-(n-m)^2\right]$$

$$H_{2p}\left(\frac{\Omega}{2\sqrt{j}}\right) = 2\left(\frac{\Omega}{2\sqrt{j}}H_{2p-1}-(2p-1)H_{2p-2}\right) \qquad H_0 = 1,\quad H_1 = 2x\ \ldots$$

Hermite Polynomials.

Figure 13 : Semi - empirical model of the normalized Cross - Spectral densities of the fluctuating pressures, downstream the spoiler (Wind Tunnel tests).

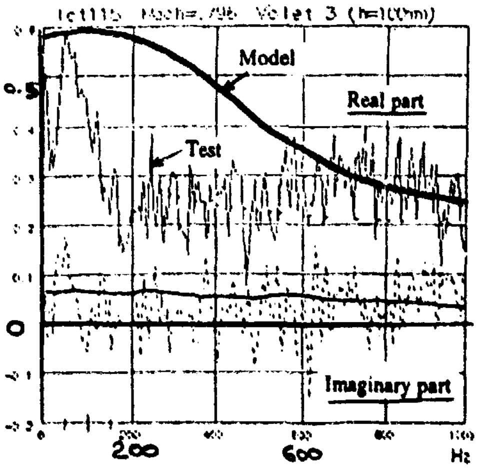

Figure 14 : Comparison Test/Model of the normalized Cross-Spectral densities of fluctuating pressures in WT

4-5 : Similation of the Structural Response by FE Calculations : Computational Strategy

The test panel was modelized : the FE model displayed consists in 7400 nodes and 38400 degrees of freedom. This FE model was statically and dynamically adjusted by experiment.

To predict the dynamic random response of this structure with the Finite Element Program ELFINI, was followed a computational strategy in which computations are carried out in two stages :

1st stage : Computational grid

The excited surface of the structure is divided into a number of subareas or elements (the computational grid is a coarse mesh in comparison the structural FE mesh). To each element of the grid is associated a Pressure Spectra Density definition. The PSD of pressure are assumed to be uniform over each grid element and perfect spatial correlation is assumed between any two points lying within the same element (in-phase condition). The correlations between grid elements are defined by the Cross - Spectra. The pressure and the Cross - Spectra density definitions can be defined by measured data or by an analytical model. The complete power spectral matrix of auto- and cross-spectra for this multiple-pressure input system is then established, on the basis of the measured (or predicted) auto- and cross- spectra.

2nd stage : Projection on the FE model

The pressure load (the Power Spectral Density and the Cross - Spectra) of each grid element is projected into basic loads on the FE model of the structure.

The PSD of stresses and accelerations at given points are then carried out, from selected elements of the FE model, with the above projected pressure and the associated power spectral matrix, as load input.

4-6 : Evaluation of the Analytical Model as Load Data Input for FE Calculations

To evaluate the analytical model, the previous computational strategy was applied twice, to simulate the structural response of the panel :

1st simulation : with the experimental Pressure Spectral Density (WT test measuremenus) and with the experimental Cross-Spectra (WT test measurements).

The computational strategy of § 4-5 was applied with the measured pressure field as input on the grid.

The damping levels were determined from an analysis of data which respected the proportions of the different

modes for a same gauge, the ratio of a same mode for different gauges.
The results (PSD) of the strain-gauge J5 (see location on Figure 12), representative of the panel behaviour, are shown on Figure 15b. The calculated PSD diagrams (Figure 15b) are in good correspondance with the measured PSD diagrams (Figure 15a).

2nd simulation : with the experimental Pressure Spectral Density (WT test measurements) and with the analytical Cross-Spectra (analytical model).
The analytical model was input as Cross - Spectra law on the computational grid of the acoustic loads.
The results (PSD) are shown on Figure 15c for strain-gauge J5 : they are very close to the results obtained with the WT data (Figure 15b). Despite that there is only partial agreement on correlation spectra, one could be surprised at the better agreement on panel response calculations. A possible explanation is that the model and measurements agree in the range of frequencies where are located the main resonances of the panel.

From the panel response, we can infer that the analytical model of pressure field is of good accuracy and allows the behaviour of the panel to be predicted inside the WT.

4-7 : Conclusion

A semi-empirical model of the acoustic loads, downstream a spoiler, has been developed from the WT experimental data. This model was used as the analytical loads input to FE calculations, to simulate the test-box response. Based on initial success of this work, the following is suggested :
- to refine this type of model and extend it to other types of acoustic sources encountered by aircraft in real service,
- to develop this model for the classical test facilities, in particular for the PWT's which should remain the standard test facility for reason of cost and availability.

5 TESTING of STRUCTURAL ELEMENTS in WT and in PWT's

5-1 : Presentation

Testing of large scale structures to aero-acoustical loads is impractical and potentially very expensive. However, there is a need to validate the integrity and endurance of structural elements subject to a variety of acoustic loads. One option available to aircraft manufacturers is to perform tests on structural elements where the acoustic environment is simulated in a Progressive Wave Tube (PWT) facility i.e. a duct capable of generating a controlled unsteady pressure field. To determine the acoustic fatigue life of aircraft structures, which are a function of ground and in-flight conditions and the associated aircraft in use, a method of read across between the PWT and aircraft responses is required.

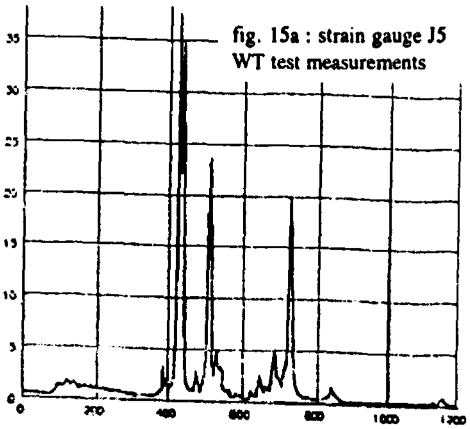

fig. 15a : strain gauge J5 WT test measurements

FE computations :
fig. 15b : Load input = Pressure test measurements

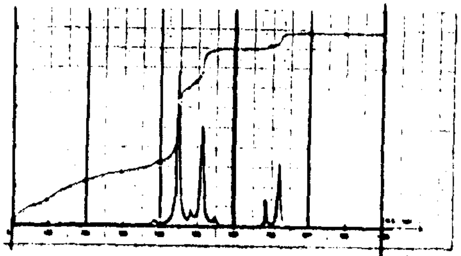

fig. 15c : Load input = Analytical model

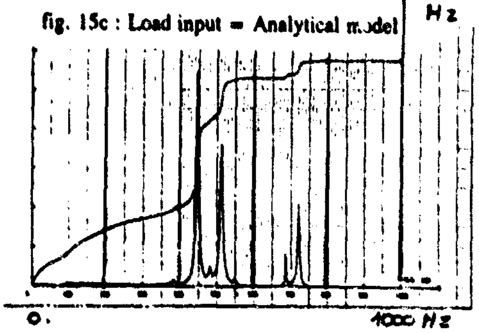

Figure 15 : Wind-Tunnel tests : PSD of the reponse of the strain gauge J5 : Comparisons between :
fig. 15a : J5 test results (measurements),
fig. 15b : FE computations with pressure measurements as load input,
fig. 15c : FE computations with the analytical model as load input.

5-2 : Study of the Acoustic Loads and of the Associated Structural Response

For this purpose, a stiffened aluminium panel (the one used for the aero-acoustic loads study - see section 4) was used to study its structural response under different types of acoustic loads.

1st test-phase : In the first phase, the test panel was mounted into the Wind Tunnel (WT) and excited by a turbulent pressure field which was generated by an upstream spoiler. This configuration was described in the previous section 4, related to the aero-acoustic loads study (see Figure 12).
The structural response of the panel was investigated by 16 strain-gauges. Pressure field spectra for one of the test configurations (flap size, Mach number) were used as reference levels for the following PWT tests.

2nd test-phase : After the WT tests, the panel was mounted into a first PWT ("PWT1"). Investigations were performed to establish response of the panel at the reference levels and, if necessary, to modify the applied acoustic spectra in the PWT to match the strain spectral densities measured on the panel in the WT.

3rd test-phase : Finally the test-panel was subjected to a similar test campaign in a second PWT ("PWT2"). The test data were reduced to the same standard so that all three test facilities could be compared in terms of their exciting pressure fields and their induced structural responses.

5-3 : Loading Actions in WT and PWT's

5-3-1 : The pressure spectra obtained in the WT under separate flow conditions are characterized by high intensities at frequencies below 200 Hz, with a strong decay towards the higher frequencies. Even with this decay, a continuous energy distribution due to the randomly fluctuating pressures is present for all the test-configurations (see Figure 10). The spatial coherence of the pressure field is generally very low depending on the local flow conditions which contains a high number of uncorrelated eddies (see Figure 11).

5-3-2 : Compared with the smooth curves of the energy distribution in the WT, the pressure spectra, measured in the two PWT's, exhibit pronounced peaks which are due to internal acoustic resonances (standing waves specific of the duct geometry and rigidity) (see Figure 16). Furthermore the correlation factors of the acoustic pressure are very high : the total pressure field is almost in phase in the PWT's (see Figure 17).

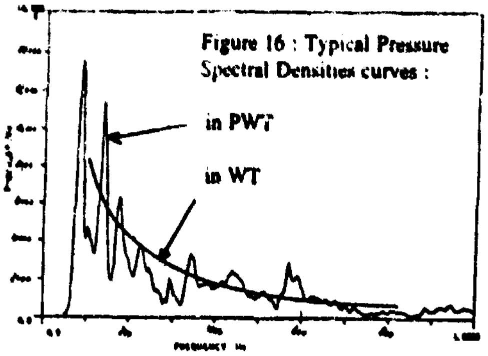
Figure 16 : Typical Pressure Spectral Densities curves :

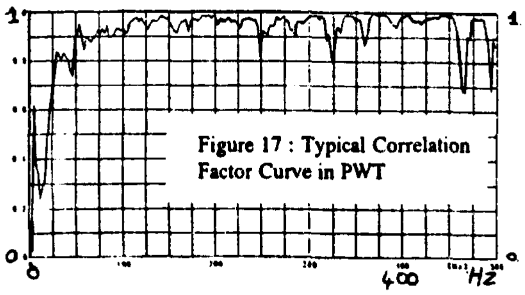
Figure 17 : Typical Correlation Factor Curve in PWT

5-4 : Structural Response Characteristics (Main Results) :

One main objective was to compare the structural response of the test-panel under WT- and PWT-excitation and to define, if necessary, a testing strategy to get the same structural response in both cases. The comparison was performed on the Power Spectral Densities of the strain-signals, in WT and in the 2 PWT's. The comparison has been focused on 2 (of 15) representative strain gauges : S10, S11 (see Fig. 18).

5-4-1 : The test-panel has a multi-modal vibration response, where the dominant modes occur in the frequency range 400-800 Hz. It is apparent for S10 that only 2 of the dominant modes, at 515 & 545 Hz can be significantly excited in the PWT's, in comparison to the 4 being excited in the WT at 440, 475, 515 & 560 Hz. On S10, the high spectral peak at 475 Hz (in the WT) could not be excited in the PWT (see Fig. 18).
For S11, only 2 of the dominant modes, at 520 & 720 Hz can be significantly excited in the PWT's, in comparison to the 4 being excited in the WT at 385, 425, 520 & 720 Hz. However, in this case, the highest spectral peak was excited (see Fig. 18).
Other strain gauges also show similar characteristics.

5-4-2 : Narrow band excitation : To match WT excitations at strain gauges number 10 & 11, there is a requirement to excite panel modes at 440, 475 Hz for gauge 10 and modes at 385, 425 Hz for gauge 11. For this purpose, narrowband excitation was restricted to between 400 and 592 Hz center frequencies. However, this resulted in forced vibrations of the panel, together with excessive response at resonant conditions. Consequently, it was not possible to define a testing strategy to obtain the same structural response in the PWT's as in the WT.

5-4-3 : FE calculations support : From a survey of the Finite Element analysis work it is apparent that the symmetric modes of the panel are being excited in the PWT, whereas both symmetric and anti-symmetric modes were excited in the WT.
More generally, the study of the influence of the correlation factors on the dynamic response was simulated by FE calculations. It confirms that, when

Figure 18 : Dynamic response of the test - box in WT and in PWT's

PSD of strain gauges 10 and 11 (see location figure 11) (micro dl / l) ** 2 / Hz :

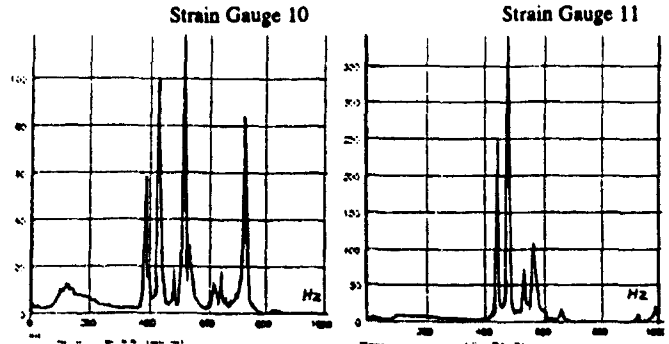

Figure 18a : measurements in the Wind - Tunnel

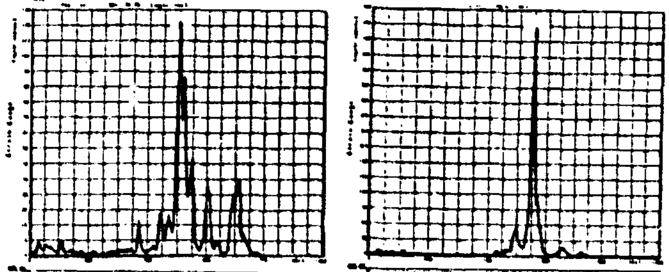

Figure 18b : measurements in the Progressive Wave Tube n° 1

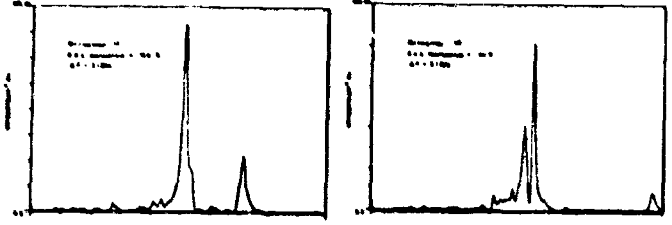

Figure 18c : measurements in the Progressive Wave Tube n° 2

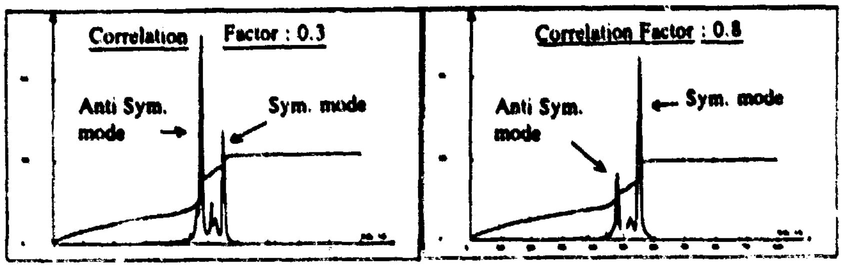

Figure 19 : Finite Element simulation of the influence of the correlation factor on the structural response : Comparison of the PSD response of strain gauge 1, for two correlation levels : 0.3 and 0.8

the correlation level increases from low value (0.1) to higher values (1.), the symmetrical panel modes dominate whereas the anti-symmetrical modes reduce (see Figure 19).

5-5 : Conclusions :

5-5-1 : Even with a simple structural and aerodynamic configuration, the phenomena involved are already rather complicated. Several fundamental mechanisms appear to be simultaneously responsible for the fluctuation pattern on the panel. Representing the statistical characteristics of the pressure fluctuations (in WT and PWT) with a mathematical model requires extraction and modelling of these fundamental mechanisms from the available experimental data.

5-5-2 : Comparing the characteristics of excitation in the PWT's with those in the WT, some significant differences are observed. Whereas the pressure spectral density in the WT is continuously distributed with high intensities at low frequencies, the PWT's exhibit very peaky spectral densities, due to internal acoustic resonances. Furthermore the coherence of the fluctuating pressures is very much higher in the case of the PWT's compared with the region of separated flows in the WT.

Owing to differences in structure acoustic coupling between the progressive wave field of the PWT and separated field in the WT, different modes will be excited and hence spectral levels are different. Consequently the endurance of the tested specimen may be significantly different.

Narrow band excitation has been used to try and excite modes which would otherwise be excited in the WT : this has resulted in forced vibration of the panel and excessive forcing at resonnance. In consequence, it was not possible to define a testing strategy to obtain the same structural response in the PWT's as in the WT.

The knowledge of this difficulty is considered as one of the main ACOUFAT results.

5-5-3 : This work will provide a valuable basis for the clearance of structures to acoustic environments in PWT, especially when it is respected that the aero-acoustic clearance of large scale structures is both impractical and expensive.

6 CONCLUSION

Three main aspects of the ACOUFAT programme have been investigated and discussed.

6-1 : Standard Random Vibration Endurance Data for CFRP Materials

The use of the "frequency degradation" criterion which is commonly applied as standard endurance limit of classical metallic materials, has been evaluated for CFRP materials. This "frequency degradation" criterion, as the only parameter, was not considered suitable for determination of specimen "failures". Further work is required to investigate the reasons for the "settling phase" observed in CFRP materials. It was thought that a suitable criterion should be based upon the degradation of the mechanical properties which can be determined by residual strength tests of the specimens.

Furthermore, an assessment of coupon failures compared to complex structural failures is required in order to validate the usage of current coupon designs and endurance data.

6-2 : Aero-Acoustic Loads Study (in WT)

On the basis of Wind-Tunnel calibration tests, a semi-empirical model of the spatio-temporal characteristics of the aero-acoustic loads exerted on a flat panel by the turbulent field created by a flap (simple configuration of a typical turbulence) has been developed and utilized as "Load Data Input" for Finite Element calculations. The WT tests have been reasonably well represented : the development of this semi-empirical model of the spatio-temporal characteristics of the aero-acoustic loads is encouraging with this initial success. The results from the initial modelling suggests that this can be extended to modelling the PWT loads.

6-3 : Testing of Structural Elements in WT and in PWT's

By the ACOUFAT study, it became clear that, even for a simple aerodynamic configuration, the excition of structures by aero-acoustic loads may not be simulated fully in PWT, by simply modifying and correctly shaping the spectral content. The effect of the spatial distribution of the loading is clearly different in both cases and the tested specimen endurance may be significantly different. It is clear that a theoretical approach based on a correct prediction of the responses to both types of environment is required. If this could be achieved, then it may be possible to design acoustic tests in the PWT (perhaps by applying narrowband acoustic excitation with additional mechanical excitation) that would excite structures to the same level and spatial stress / strain distribution even in individual modes of the structure.

6-4 : Since the ultimate aim is to dimension and to qualify structures subjected to acoustic loads, FE calculation coupled to load input models would be the preferred solution to establish a valid comparison of the structural behaviour in real flight conditions and in PWT or other ground-test environment (i.e. different coupling fluid / structure). For this purpose, the FE calculation is the only available valid tool.

6-5 : The results of this ACOUFAT programme have convinced all the partners of the necessity to cooperate, to achieve and extend on the fundamental work related to the above areas.

Acknowledgements : The financial support provided by the European Community and the cooperation of the ACOUFAT partners are appreciated and acknowledged.

List of the ACOUFAT partners :

Dassault Aviation (coordinator).
British AErospace Defence Limited.
DASA (MBB).
    Eurocopter Deutschland GmbH
    DASA Airbus.
Dornier Luftfahrt GmbH.
Fokker Aircraft B.V.
Industrieanlagen - Betriebsgesellschaft mbH (IABG).
Institute of Sound and Vibration Research (ISVR).
Instituto Superior Tecnico (IST - LISBOA).
Katholieke Universiteit Leuven (KUL).
Nationaal Lucht - en Ruimtevaart Laboratorium (NLR)
Office National d'Etudes et de Recherches
    Aérospatiales (ONERA).
PER UDSEN Co., Aircraft Industry A / S.
SAAB - SCANIA AB.
Société Anonyme Belge de Constructions
    Aéronautiques (SABCA).

ACOUSTIC FATIGUE BEHAVIOUR OF GLARE COMPOSITES

P.T. Elangovan[1], H. Ottens[2] and G. Bayerdorfer[3]
[1] Fokker Aircraft, Schiphol,NE; [2] NLR, Marknesse,NE; [3] IABG, Ottobrunn,GE
IABG/Abt TFA
Einsteinstrasse 20
85521 Ottobrunn
GERMANY

Summary

The Glare laminates being new type fibre metal laminates with promising fatigue behaviour are evaluated for their acoustic fatigue properties. In the investigation, the endurance data are developed by using shaker test specimens. Since the Glare laminates make use of lay-ups and metal bonding, the influence of the laminate lay-up configuration and temperature on the acoustic fatigue strength is investigated from the shaker test results. Four types of shaker specimens are used in this investigation: plain cantilever, riveted skin-stringer, bonded skin-stringer and rib-mode vibration specimens. Two stiffened Glare skin panels are tested in the Progressive Wave Tube (PWT) at IABG. The panel testing indicates the importance also of the secondary structure in the acoustic environment, although the Glare skin itself does not show any damage.

INTRODUCTION

To meet the stringent safety and damage tolerance regulations for the aerospace vehicles, there has been considerable research to develop new materials which have high fatigue and damage tolerance properties. Using the light weight and high strength fibre reinforced plastics, the composites are designed to reduce the structural weight of aerospace vehicles considerably. The composites are shown to be weak in impact-damage tolerance; this is not a serious problem for metallic materials since they are usually formable and undergo a large plastic deformation before failure. Combination of the high strength fibre reinforced plastics with metallic layers is a good receipt to bolster the static as well as fatigue strength of the material. Since there is a high amount of experience in metal bonding technology, bonding the metallic and fibre reinforced pre-preg layers does not pose a problem any longer. Thus a class of new materials is born. Aramide Reinforced ALuminium Laminate (ARALL) is the first aluminium laminate to appear in the market, followed by GLass Aluminium REinforced (GLARE) laminates. The Glare laminates are more suitable for bi-axial applications, where formability is essential. The Glass fibres have higher plastic strain limit than the aramide fibres in ARALL. The Glare laminates are proposed for use in fuselage construction.

The acoustic fatigue behaviour of conventional aluminium alloys is widely investigated by means of tests and analyses [1-4]. The aluminium is assumed to be isotropic for all practical purposes, and the frequency derivations of stiffened or unstiffened plates are analytically performed [5]. The Carbon Fibre Reinforced Composites (CFRC) attracted a lot of attention due to its high specific static strength. The investigation of CFRC as a viable aircraft material is also extended to their acoustic fatigue strength [6,7]. The fibre metal laminates are of recent origin although the concept itself is old. The investigation into the acoustic fatigue behaviour of fibre metal laminates is interesting. Here, the attention is focused on one type of fibre metal laminates, namely GLARE.

A Glare laminate is built-up of a number of aluminium and uni-directional Glass Reinforced Plastic (GRP) layers, as shown in fig.1. The GRP layer is lighter and stronger than aluminium layer. However, due to the presence of the low modulus epoxy matrix material, the average elasticity modulus is lower than that of aluminium. This aspect is important for the stiffness related problems such as buckling or structural response due to dynamic or acoustic loading. This is all the more reason to investigate into the acoustic fatigue behaviour of Glare laminates if they are to be applied to structural parts prone to acoustic fatigue. Since the fibre metal laminates use a large proportion of matrix material, the material damping behaviour of the Arall laminates is investigated [8]. The investigation showed that the material damping is improved, but its value compared to the total amount of structural damping is still negligible. The general fatigue behaviour of fibre metal laminates is showed to be superior to the aluminium alloys [9]. The acoustic fatigue behaviour is not investigated for these laminates until now, and a first attempt is made here to investigate into the acoustic fatigue behaviour of Glare laminates mainly by means of tests.

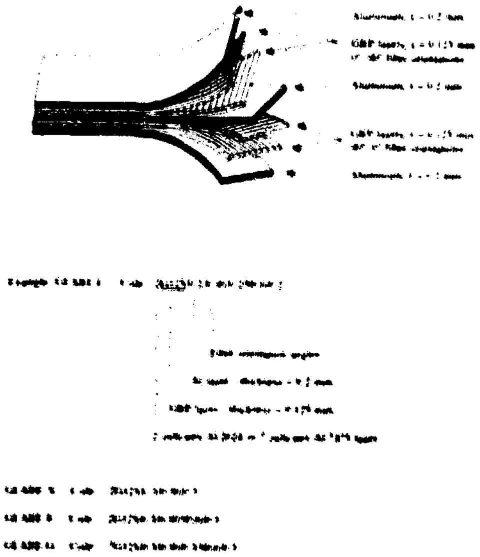

Fig. 1 Glare Laminate Lay-up and Code Details

In the frame work of the European collaborative BRITE/EURAM program, an acoustic loading and fatigue evaluation project [10] is launched in September, 1990 for a duration of two years. The project with an acronym 'ACOUFAT' is dealing with 'Acoustic Fatigue and related damage tolerance of advanced composite and metallic structures'. A part of the project is to determine the acoustic fatigue strength data of Glare laminates and thereby to evaluate the implication to Glare panel design. To generate fatigue strength data of Glare laminates, a series of shaker tests is

Presented at a Symposium on 'Impact of Acoustic Loads on Aircraft Structures' held in Lillehammer, Norway, May 1994.

performed at NLR [11] and at Fokker [12] on Glare coupons. To evaluate the design implication to Glare panel, two typical panels are designed by Fokker and tested at the PWT test facility of IABG in Munich [13]. This paper deals with the results obtained by the above mentioned tests and their consequence to the future design in Glare laminates.

SHAKER TESTS

Due to the presence of matrix material in the GRP, the elasticity modulus is lower than that of the aluminium. At the same time, the matrix material can contribute to the material damping. The temperature influence on the Glare material is interesting to evaluate since the matrix material and the bonding strength can be easily affected by the temperature fluctuations. Three operating temperatures, -50°C, RT and 80°C, are chosen for the tests. Another interesting aspect to Glare material testing is to evaluate the influence of the laminate lay-up. A stiffened Glare skin panel being subjected to acoustic loading responds to vibration modes which cause relatively higher bending stresses at the attachment locations of the skin with the stringer or the frame. Typical coupon configurations are chosen to represent the joint design and also the vibrations modes under acoustic loadings. The panel vibration mode at the attachment causes bending stresses in the skin. The skin-mode vibration tests establish the fatigue strength of skin at the stringer or frame joints. But, the secondary parts attached to the skin can also be vulnerable to fatigue damage. The rib-mode vibration tests establish the fatigue strength of the secondary parts, which are stringers and ribs (or frames) in the stiffened panels.

Summarizing, the coupons are tested with the following variations:

1. Three laminate lay-ups are tested.
2. The coupons are tested at three temperatures, -55°C, RT and 80°C.
3. Two typical vibration modes, one in skin-mode vibration and another in rib-mode vibration, are tested.
4. The coupons are tested with bonded or riveted stiffeners

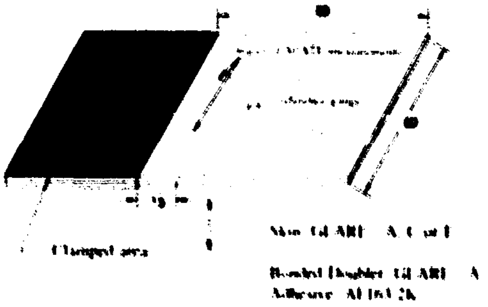
80
80
15
Clamped area
Skin: GLARE - A, C or E
Bonded Doubler: GLARE - A
Adhesive: AF163-2K

Fig. 2 Plain specimen

Glare coupon specimens

The details of the laminate lay-ups and the code of Glare-C are given in fig.1 for illustration. From the code, one is able to determine the lay-up details. The codes of other glare laminates used in the tests are also presented in fig.1. Glare laminates, GLARE-A, C and E, are used for skin elements and Glare-G is used only for the stringers. The four types of Glare specimens are shown in figs. 2 to 5.

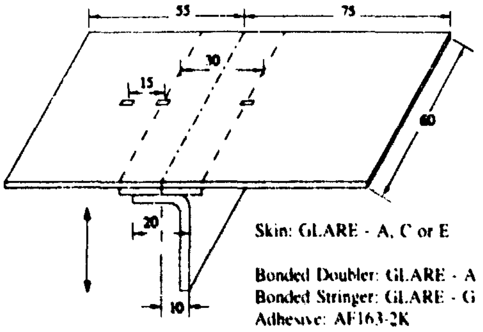
55
75
30
15
60
20
10
Skin: GLARE - A, C or E
Bonded Doubler: GLARE - A
Bonded Stringer: GLARE - G
Adhesive: AF163-2K

Fig. 3 Bonded-stringer specimen

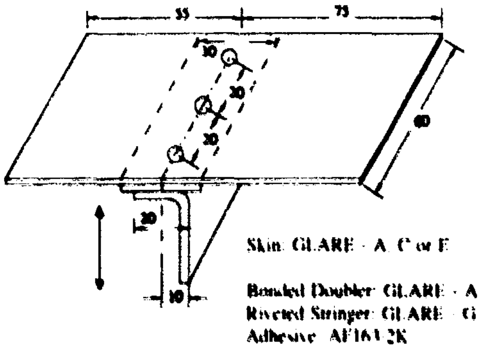
55
75
30
30
20
60
20
10
Skin: GLARE - A, C or E
Bonded Doubler: GLARE - A
Riveted Stringer: GLARE - G
Adhesive: AF163-2K

Fig. 4 Riveted-stringer specimen

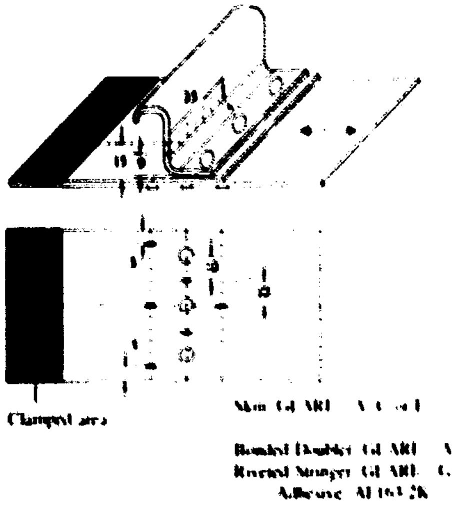
35
15
20
Clamped area
Skin: GLARE - A, C or E
Bonded Doubler: GLARE - A
Riveted Stringer: GLARE - G
Adhesive: AF163-2K

Fig. 5 Rib-mode vibration specimen

Plain specimens (fig. 2): with this specimen type, the fatigue strength of a skin in the presence of a discontinuity in the thickness is tested. These tests are used to evaluate the influence of laminate lay-ups and temperature. Three types of skin lay-ups are tested, each type in three temperature levels. Bonded skin-stringer specimens (fig.3) are tested to find the influence on the fatigue strength of the bonded skin-stringer attachments, and similarly riveted skin-stringer specimen (fig.4) for the fatigue strength of a riveted skin-stringer attachment. Rib-mode vibration specimens (fig.5) are tested to determine the influence on the joint fatigue strength when the secondary element, which is stringer in this case, is in resonance.

Test procedure

The acoustic fatigue tests are performed on an electromagnetic shaker. Three specimens are clamped simultaneously in a fixture mounted on the shaker. The specimens are loaded by a narrow band frequency centred around the average fundamental frequencies of the specimens (f_a) as shown in fig.6. The bandwidth is so chosen that the specimens continue to resonate even if there is a frequency drop in one or more of the specimens.

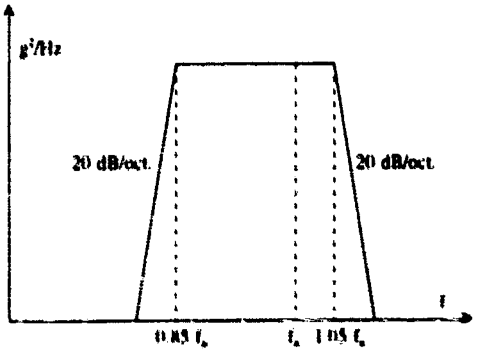

Fig. 6 Shaker narrow-band loading

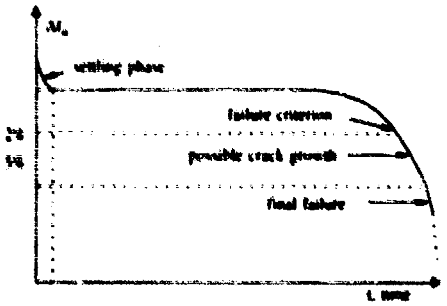

Fig. 7 Failure criterion for shaker specimens

The testing is carried out in two phases, pre-test phase and actual test phase. The pre-test phase is intended to explore the dynamic behaviour of each specimen type, the proper positioning of strain gauges to locate the maximum strain and the calibration of measuring devices. SPATE (stress pattern analysis by the thermo-elasticity method) is used at NLR to determine the stress distribution during the pre-test level. In the actual test phase, the nature frequencies of the specimens are continually measured at NLR by monitoring the Hall generator which generates current induced from a fluctuating magnetic field.

First an allowance is made for the drop in frequency due to the initial settlement. After that, a 2% drop in frequency during the test is defined as the failure criterion for the specimens (fig.7). The frequency can drop due to stiffness reduction following a crack, delamination between layers, change in support condition due to rivet failure, de-bonding of stiffener and skin or matrix cracking. If no visual damage is found, the test is continued sometimes by adjusting the frequency range around the then resonant frequency. Mostly, after 2% frequency drop, the deterioration is quick and the damage growth life is not high (fig.8). The failure condition of each specimen is studied and recorded.

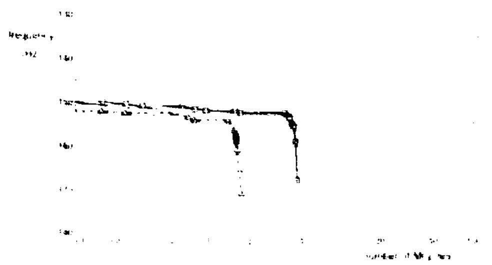

Fig. 8 Frequency measurements for Glare specimens

For the high and low temperature tests, an isolator box is placed over the specimens which are mounted on the shaker. The temperature condition within the box is realized by blowing in either liquid nitrogen or hot air.

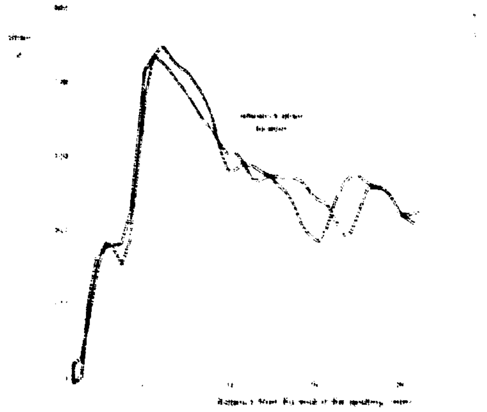

Fig. 9 Strain distribution - SPATE measurements (see fig.2 for locations)

The strain gauge locations on the specimens are shown in figs. 2-5. In the NLR tests, the reference gauge readings are used to calculate the maximum stress level by using the transfer function established earlier in the pilot tests. The calculated maximum rms-strain levels are used in the endurance plots. In the Fokker tests, the strain gauges are placed at the maximum stress locations and the gauge readings are directly used in the test evaluation.

Specimen test results

Typical curves of the SPATE measurements are shown in fig.8 for the Glare-A laminate plain specimens. The results of the fatigue tests are presented in figs.10-15

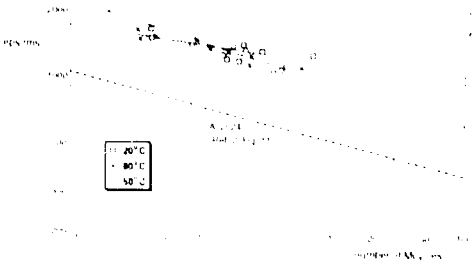

Fig. 10 Edurance plots: temperature influence - plain specimen Glare-A

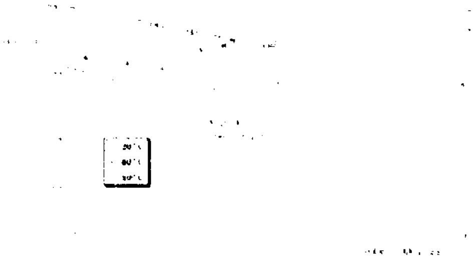

Fig. 11 Endurance plots: temperature influence - plain specimen Glare-C

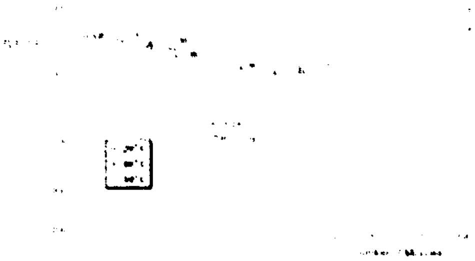

Fig. 12 Endurance plots: temperature influence plain specimen Glare-E

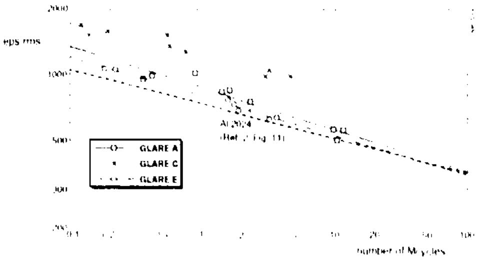

Fig. 13 Endurance plots: influence of lay-up configuration - plain specimens

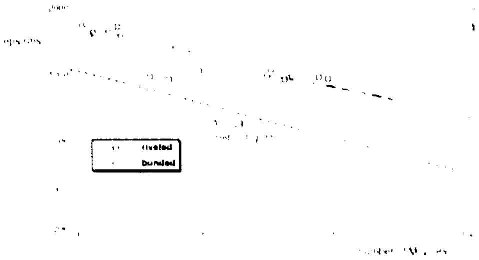

Fig. 14 Endurance plots: comparison of riveted and bonded-stringer specimens

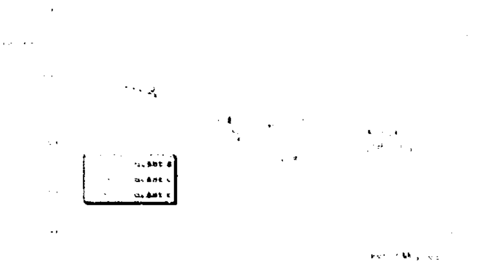

Fig. 15 Endurance plots: rib-mode vibration specimens

Plain specimen results: the influence of the three temperature variations and the laminate lay-ups is investigated by the plain specimen tests. There is hardly any influence of temperature observed for the fatigue behaviour of Glare-A and Glare-E. For Glare-C, deterioration of the fatigue properties is observed both at high (+80°C) and low (-50°C) temperature, see figs.10-12. At room temperature, the fatigue behaviour of Glare-C is better than that of Glare-A or Glare-E (fig.13). The damping ratios of Glare-A,C and E are 0.171%, 0.169% and 0.152% respectively.

Riveted and bonded stringer-skin specimens: Here too, the fatigue behaviour of Glare C is better than that of Glare-A or of Glare-E. The fatigue lives of the bonded skin-stringer specimens are better than those of the riveted skin-stringer specimens (fig.14).

Rib-mode vibrations specimens: The tests are conducted with the same shaker input level for all three specimen types. The fatigue behaviour of Glare-A is better than that of Glare-C and E (fig.15). The damping ratio of Glare-A and E is higher than that of Glare-C. From the material point of view, Glare-C and E are of the same metal-GRP composition except for the differences in the laminate lay-up. From the tests of these specimens, it is seen that Glare-E specimens have the lower maximum stress for the same shaker input, higher damping ratio and higher fatigue life than those of Glare-C specimens.

PWT TESTS

PWT Specimens

Within the framework of the BRITE/EURAM collaborative program, two Glare panels are designed and manufactured at Fokker and tested at the IABG acoustic facility. The panel details are shown in fig.16. The panel design is typical of a wing skin, stiffened with stringers and ribs. The stringers get free passage through the ribs, by means of castellation. The joint at the intersection between a stringer and a rib is an important part of design. Except for the top skin, the panel design is identical for the both specimens.

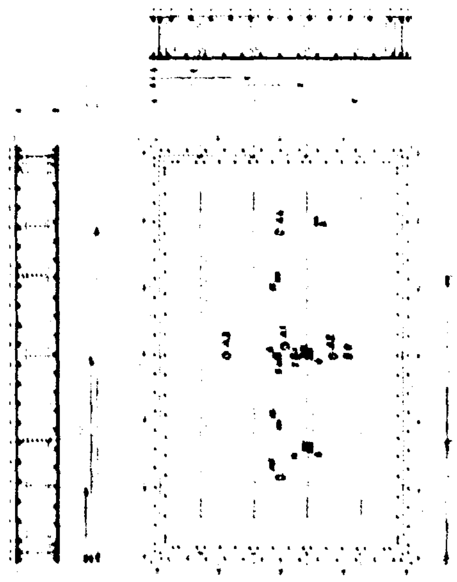

Fig. 16 PWT test-panel design details

Each test panel is built as a top panel of a box. The (top) panel skin is of either Glare A or Glare E. Hornet doublers are made of Glare A, and they are also bonded to the skin, so that the skin is thickened at the locations where the stringers or ribs are attached. The aluminium stringers are bonded on to the skin doubler, and the ribs are riveted to the skin. The design details of the side walls and the bottom skin are not relevant to the present investigation. However, the side walls and the bottom thick skin panel are designed not to interfere with the acoustic fatigue behaviour of the test panel. The dynamic behaviour of the box, including the test panel is analyzed by means of finite element calculations. The calculations are carried out by Dassault as a collaborative task within the framework of the Brite/Euram program. The calculations show how thick the bottom skin must be in order to avoid any interference with the top test panel.

PWT tests and results

The panels are tested in two phases, the first for modal test and the second for acoustic fatigue test. The modal response of the two test panels is first evaluated by exciting the panels by a loudspeaker at sound pressure level of 104 dB. The natural frequencies, mode shapes and damping factors are determined from the measurements of five accelerometers which are mounted on the panel. The typical plot of vibration mode is given in fig.17. The damping of the individual natural modes is obtained from the decay oscillations as well as from the frequency response curves (3 dB method). The values of loss factor η are 0.0158-0.0255 for the Glare A panel and 0.005 - 0.0123 for the Glare E.

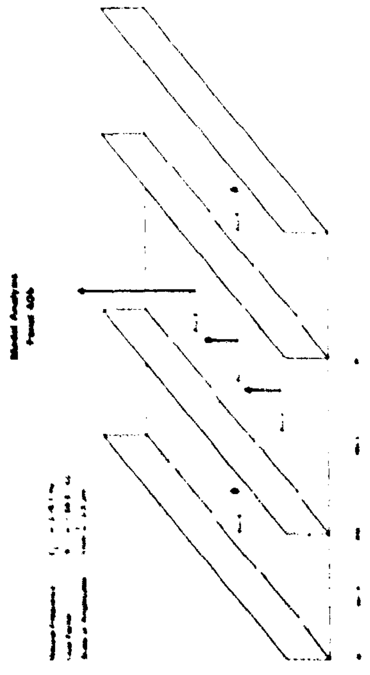

Fig. 17 Modal Analysis Test - Glare-A panel

Acoustic fatigue tests are performed in the PWT, and the panels are excited by the acoustic spectra, whose excitation band width is predefined from the results of the modal tests. The linearity check is first carried out by increasing SPLs and measuring strain gauge rms-strain values. Both panels show the same non-linearities which are characterized by a digressive ratio in the case of SG1 (strain gauge no.1 in fig.18) and progressive ratio in the case of SG11 (and SG12), as shown in fig.19. The non-linearities are attributed to the presence of membrane stresses, preventing the skin from vibrating in large amplitudes. From the regular fatigue tests in run 1-6, a number of PSD-plots are made. The plots indicate that with increasing acoustic loading, the higher order modes become more pronounced when compared with the amplitudes of the fundamental mode. The total number of modes is slightly reduced for higher SPLs. Two such typical plots are given in fig.20 and 21.

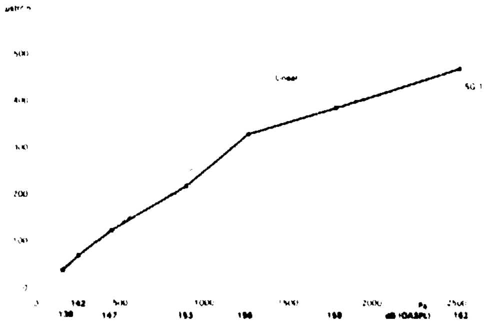

Fig. 18 Linearity Check with strain gauge-1 (SG1) readings

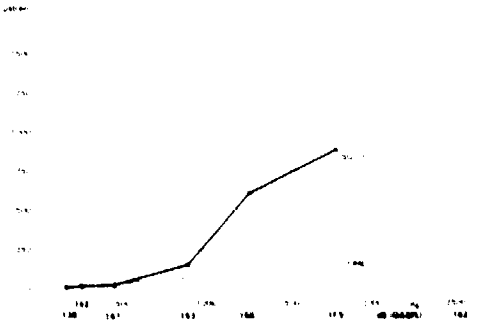

Fig. 19 Linearity Check with strain gauge-11 (SG11) readings

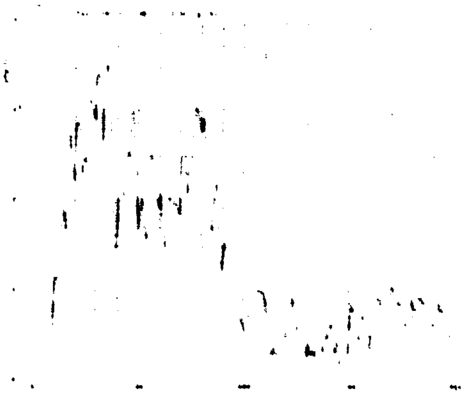

Fig. 20 PSD plot at an OASPL of 124 dB/terz input

In the first set of tests, the strain gauges at the rib flange attached to the skin show very high stresses, and the test was interrupted prematurely by noticing the failure of the rib flanges. The damage location and details are shown in fig 22. This is a typical rib failure, which is seen in the past for such ribs with aluminium panels [14]. However, no damage is noticed in the Glare skin, and so also in the stringers. The geometrical details of the rib are shown in fig.23. The panels are repaired by strengthening the rib-castellations close to the skin. An additional back-up L-profiles are used with the ribs as shown in fig.24. After the repairs, the second set of acoustic fatigue tests began at an OASPL of 159 dB for four hours and at 162dB for the last one hour. Cracks are seen again at the rib-skin flange corners during the tests and they do not grow critically even after the 162 dB OASPL tests. The corners of the rib-skin flange are rather damaged at a number of locations. The Glare skins remain intact throughout the tests. The damage details are shown in fig.25.

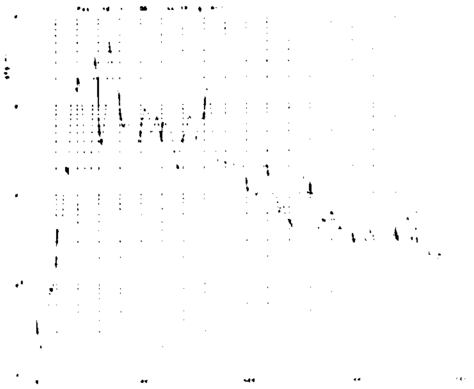

Fig. 21 PSD plot at an OASPL of 148 dB/terz input

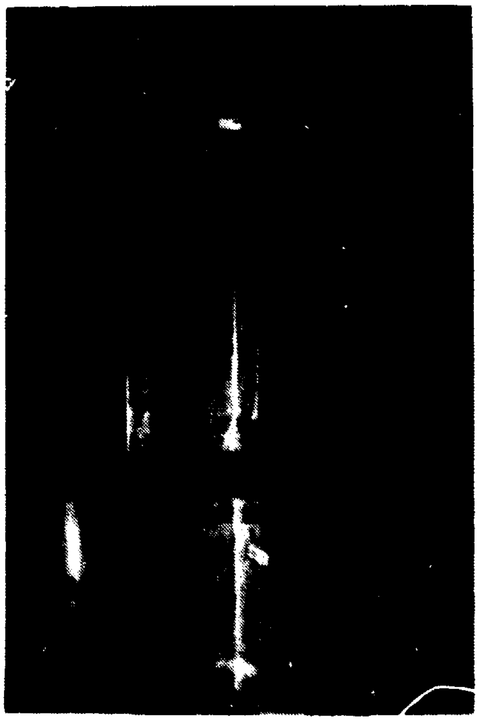

Fig. 22 First set of acoustic fatigue tests in PWT - castellation damage and separation from skin

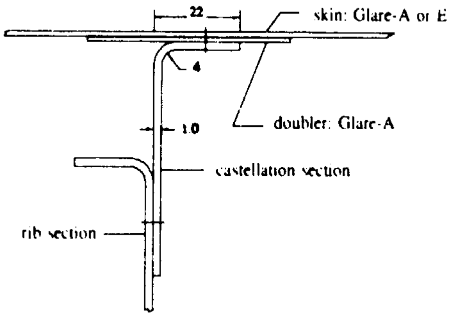

Fig. 23 Rib-castellation details in the initial design

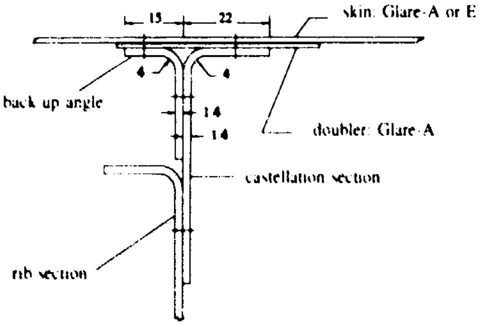

Fig. 24 Rib-castellation details after repairs

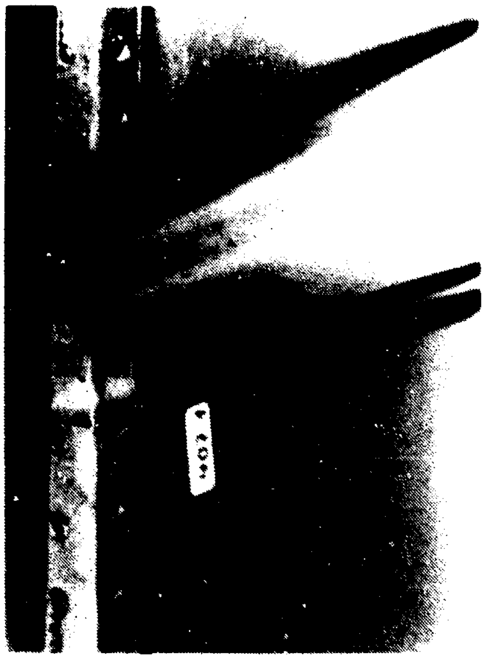

Fig. 25a Second set of acoustic fatigue tests in PWT - cracks at the castellation connection with the stringers

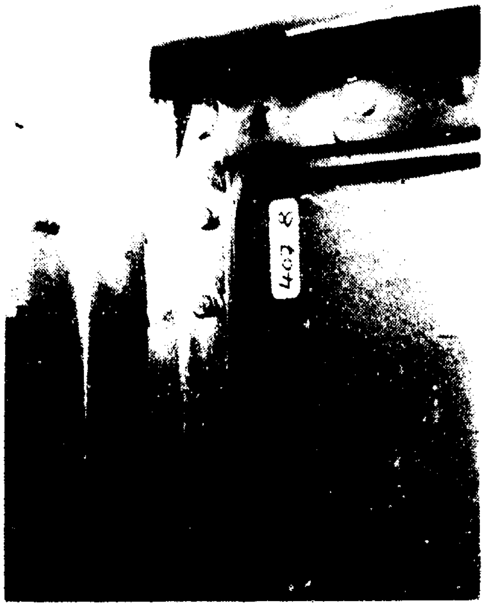

Fig. 25b Second set of acoustic fatigue tests in PWT - damage at the castellation connection with the stringers

DISCUSSION AND CONCLUSIONS

The shaker tests are limited in numbers, and a detailed statistical analysis is not performed on the results. In the shaker test, the effect of laminate lay-up is investigated. During the rib-mode vibration tests, question arose whether the tests were to be carried out with the same input level of g^2_{rms}/Hz or the same strain level for both specimens under comparison. For instance, for the same g^2_{rms}/Hz input level, Glare E samples show lower strain than Glare C samples, and Glare E samples have higher fatigue lives than Glare C samples. If the test is carried out at the same strain in both samples, but with different g^2_{rms}/Hz input levels, Glare C samples have higher fatigue lives than Glare-E samples. This show how difficult it is to make an objective comparison between the results of others. The damping property and the stress levels are both important, and evaluation shall not be easy if damping behaviour is not known. In comparison with Aluminium specimens, Glare samples are seen to be better. The above statement is subject to the assumption that damping is the same in both material and samples.

The acoustic fatigue strength of Glare-A and E laminates is not affected by the temperature fluctuations at the aircraft normal operation. However, the temperature influence on Glare-C is found to be detrimental to the fatigue strength. The bonded joint is more desirable than the riveted as far as the acoustic fatigue is concerned. The lay-up configuration of the Glare laminates does not play any decisive role to improve the fatigue lives.

The panel tests show that both the primary and secondary parts are design critical for acoustic loading. The tests show that Glare panels can withstand high acoustic loads, if support structures are properly designed. The rib design seems to be the most critical for a wing-like structure subjected to acoustic loads.

Acknowledgements

The research work is carried out under the auspices of Brite/Euram program, and the partial financial support provided by the program is appreciated. The calculation support given by Dassault engineers through the B/E program is also gratefully acknowledged.

References

1. Schijve, J. and de Rijk P., "Enige Orienterende Geluidsvermoeiingsproeven op een triltafel", NLR TR 730581,1973.

2. ESDU item no. 72015, "Endurance of Aluminium Alloy Structural Elements Subjected to Simulated Acoustic Loading",1972

3. Bayerdorfer, G., "Experimental Investigation to establish Acoustic Fatigue Design Charts", Journal of Sound and Vibration,17,1,1971,pp 55-62.

4. Clarkson, B.L., "Estimates of the Response of Box Type Structures to Acoustic Loading", AGARD Symposium on Acoustic Fatigue, 1972.

5. Rudder Jr., F.F., "Study of Effects of Design Details on Structural Response to Acoustic Excitation", NASA CR-1959, 1972.

6 Wolf, N.D. and Jacobson, M.J., "Design and Sonic Fatigue Characteristics of Composite Material Components", AGARD Symposium on Acoustic Fatigue, 1972

7 Holhouse, I., "Sonic Fatigue Design Techniques for Advanced Composite Aircraft Structures", Technical Report AFFDL-TR-80-3019, Wright-Patterson Air Force Base, Ohio, 1979

8 Schijve, J., "Development of Fibre-Metal Laminates, ARALL and GLARE, New Fatigue Resistant Materials", Delft University of Technology report LR-715,1993

9 Waleson, J.E.A. "De Acoustische Eigenschappen van Arall-Materiaal", Master's thesis at the Technical University of Delft, 1987

10 Tougard, D., "Acoustic Fatigue and Related Damage Tolerance of Advanced Composite and Metallic Structures", Technical Annex, Brite/Euram, Project AERO 0025/1079, 1990

11 Ottens, H.H. and Bongers J.A.M., "Acoustic Fatigue Tests on Glare Coupon Specimens", NLR CR 92023L, 1993

11. Elangovan, P.T., "Acoustic Fatigue Test Result Summary of Glare Coupons in Rib-mode Vibration", Fokker Report SP-147, 1993.

12. Bayerdorfer, G., "Acoustic Noise Tests on two Glare-panels", IABG Report B-TA 3139, 1993.

THERMO-ACOUSTIC FATIGUE DESIGN FOR HYPERSONIC VEHICLE SKIN PANELS

Kenneth R. Wentz
Acoustics and Sonic Fatigue Section
Wright Laboratory
Wright-Patterson AFB, Ohio 45433

Robert D. Blevins
Ian Holehouse
Rohr Incorporated MS 107X
850 Lagoon Drive
CHULA VISTA
California 91912-0878
UNITED STATES

SUMMARY

Thermo-vibro-acoustic analysis and test of skin panels for airbreathing hypersonic vehicles is made for a generic vehicle and trajectory. Aerothermal analysis shows that impingement of the bow shock wave on the vehicle and engine noise produce high fluctuating pressures and local heat fluxes. Maximum temperatures will exceed 2700 F (1480 C) at the top of the ascent trajectory and engine sound levels will exceed 170 dB at takeoff. As a result, loads due to engine acoustics and shock impingement dominate the design of many transatmospheric vehicle skin panels.

1. INTRODUCTION

Thermal, acoustic, engine, material and performance issues are interdependent in the design of airbreathing hypersonic vehicles. This paper identifies a generic Blended Wing Body (BWB) vehicle [1,2] Aeroacoustic loads and engine-induced loads on the skin are then determined. Thermal, static, and dynamic responses are found using finite element methods. Tests are made on subelements and material coupons to assess the thermal capability and fatigue strength under these loads.

The mission objectives of the hypersonic vehicle are to 1) reach orbit with a single stage vehicle and, 2) maintain hypersonic cruise using primarily airbreathing engines. To support combustion using the oxygen from the atmosphere, ascent trajectories fall between a lower static pressure limit of 200 lb/ft^2 (10000 Pa) and a maximum dynamic pressure of 2600 lb/ft^2 and the orbital velocity limit of Mach 25 as shown in Fig. 1.

Hypersonic flight in the atmosphere causes aerothermal heating of the vehicle skin. This aerothermal heating is considerably more severe for airbreathing vehicles than rockets, such as the space shuttle, which carries oxygen internally and reaches hypersonic speed above the earth's atmosphere.[3] Two ascent trajectories were analyzed: 1000 q and 2600 q, where q is the dynamic pressure of the incoming air in pounds per square foot that the vehicle maintains during ascent. Both ascent trajectories are plotted in Fig. 1. Time to orbit is 15 minutes, and the acceleration of the vehicle is assumed to be a constant 0.93 g, where g is the acceleration due to gravity at the earth's surface.

For a given vehicle Mach number, the dynamic pressure q is higher in the dense air of lower altitudes. For the same Mach number, the 2600 q ascent trajectory is at lower altitudes and in denser air than the 1000 q ascent. During both ascents, aerothermal heat fluxes will cause high skin temperatures. To reduce the heat flux and slow down the rate of skin panel temperature rise, the vehicle must gain altitude into less dense air as speed increases. This is shown by the isothermal skin trajectory lines in Fig. 1. Descent from orbit is made with the airbreathing engines shut down at 200 q in a trajectory similar to the descent trajectory of the space shuttle (Fig. 1).

2. DESCRIPTION OF VEHICLE

Optimized airbreathing transatmospheric vehicle design concepts are driven by the single-stage-to-orbit objective and the need to carry large

Presented at a Symposium on 'Impact of Acoustic Loads on Aircraft Structures' held in Lillehammer, Norway, May 1994

volumes of cryogenic liquid hydrogen fuel. The Blended Wing Body (BWB) hypersonic transatmospheric vehicle design (Fig. 2) was selected for generic analysis. To increase internal fuel capacity (about 60% of gross take-off weight is fuel), recent transatmospheric vehicle designs are evolving toward somewhat stockier lines than those of the BWB of Fig. 2. However the BWB twin tail and lower midbody engine configuration remains the baseline for most studies.

The Blended Wing Body vehicle has an overall length of approximately 100 feet (30 m), and has a 150,000 lb (68000 kg) gross weight. Location of the engine is important. The BWB hypersonic vehicle has airbreathing scramjet engines placed at midbody. This allows the vehicle forebody to act as a compression surface for the inlet and the aft body to be an expansion nozzle for the exhaust. The disadvantage of midbody engine placement is that the aftbody vehicle skin is exposed directly to engine acoustic radiation.

The high temperatures of hypersonic vehicle skin panels require unconventional materials. Conventional high temperature aluminum alloys such as 2219 Al have upper working temperatures of 350 F (175 C) but may be used to 500 F (260 C) for limited periods of time with some degradation of properties. High temperature titanium alloys such as Ti-6Al-2Sn-4Zr-2Mo have a nominal maximum temperature limit of 1000 F (540 C), but recent test suggest that they may be used to 1200 F(650 C) if exposure duration is limited to forestall phase changes. Nickel and iron based superalloys are limited by oxidation and creep beyond 1800 F (980 C).

Silicon and carbon ceramics are capable of temperatures in excess of 2000 F (1090 C). In homogenous solid form, these ceramics are too brittle and damage-sensitive for use as primary structure. Composites with carbon or silicon fibers in a ductile matrix have the toughness and maximum temperatures capability to allow their use for primary structure. Three ceramic composites were considered for vehicle skin panels: TMC, Si-C SiC/SiC and carbon-carbon. Titanium-metal-matrix-composites (TMC) have silicon carbide ceramic fibers in a ductile titanium matrix, Si-C composites have silicon carbide fibers in a carbon matrix, SiC/SiC is a composite of silicon carbide fibers in a silicon carbide matrix, and carbon-carbon has carbon fibers in a carbon matrix.

Carbon and silicon carbide fiber composites are generally limited by the temperature capability of the matrix rather than the strength of the fiber. Oxidation, the spontaneous combination of atmospheric oxygen with a carbon matrix to form gaseous CO2, is a common high temperature failure mode of carbon matrix composites. Silicon carbide glass coatings, applied at high temperature by gaseous diffusion or by direct surface compaction of powder, have been developed to inhibit the penetration of atmospheric oxygen into carbon-carbon. Powdered oxidation inhibitors can be added to the carbon matrix to retard oxidation if the coating becomes damaged. Metallic composites also suffer from oxidation at high temperature if coatings are not applied. Current generation titanium matrix alloys, such as 15V-3Cr Ti, are degraded by oxidation and creep above 1000 F (540 C). Titanium matrix alloys such as 15Mo-3Mb-3Al Ti are being developed to improve oxidation and creep properties of TMC.

Skin panels representative of the BWB hypersonic vehicle (Fig. 2) were designed and fabricated as part of a study of aero-thermal-acoustic fatigue of hypersonic vehicles.[3] Carbon-carbon was chosen for the forebody and the ramp skin panels because of thermal and weight considerations. The lower forebody panel is shown in Fig. 3. The carbon-carbon laminate consists primarily of 0°/90° plies of carbon-carbon fabric sandwiched between two outer plies of fabric oriented at 45°. The 45° fabric plies were included to increase buckling allowables.

The blade stiffeners taper off into thickened side rails (Fig. 3) to avoid the unacceptable interlaminar stress that would result if the blades were tied directly into the side rails. The blade-type stiffener is chosen because it avoids the re-entrant corners of Z-, T-, and hat-stiffeners which cannot be coated with silicon carbide glass to inhibit oxidation. A layer of alumina insulation between the panel and the substructure minimises heat transfer into the cryogenic hydrogen tank.

The upper fuselage midbody and aftbody skin are single-faced corrugated panels formed from advanced titanium matrix composite (TMC) as shown in Fig. 4. Typically the panels are 4 feet by 4 feet (1.2 by 1.2 m) with 32 corrugated stiffeners per panel. The panels are attached to underlying titanium ring frames and longerons. TMC was chosen for midbody and aftbody skin panels because it has the stiffness required to resist local panel buckling (the failure mode for much of the midbody) while withstanding the midbody skin temperatures.

The wings and vertical stabilizers are also fabricated from advanced titanium metal matrix composite with corrugation-stiffened single skins which are separated by I-section spars. The corrugations are on 1.7 inch (4.3 cm) centers and are 2.5 inches (6.35 cm) in height. All webs and flanges are 0.015 inch (0.38 mm) thick – the minimum gage for TMC. Figure 4 shows a prototype of a TMC wing panel section. The silicon carbide fibers in TMC are formed by vaporization of silicon carbide on a graphite filament. The fibers are then coated with a carbon-rich layer. The skin sheet in Fig. 4 is a laminate of seven lamina (layers) of alternating 0°/90° fibers. The TMC hat-stiffener sheet is diffusion bonded to the skin.

The nozzle structural concept is an actively cooled panel shown in Fig. 5. Active cooling is achieved using liquid hydrogen which is passed through channels milled into the face sheets before entering the engine. The actively cooled panel core is titanium. The face sheets are advanced titanium matrix composites. The panels are 48 inches (1.2 m) square. The panels are supported by advanced titanium matrix composite frames, which are in turn attached to the underlying structures. The actively cooled honeycomb sandwich was selected in consideration of the extreme temperatures and heat fluxes from the engine exhaust – conditions which make passively cooled structures untenable in the nozzle region. However, ongoing evaluations indicate a possible chemical incompatibility between titanium and liquid hydrogen. Thus, use of materials other than titanium may be required for actively cooled panels.

3. AEROTHERMO ANALYSIS

Aerothermal heating and aeroacoustic pressure fluctuations are produced in the boundary layer (Ref. 4) and amplified by shock wave impingement (Refs. 5, 6), shown in Fig. 6. Nozzle loads were determined by a separate analysis of the burning gases Typical peak heat flux on the nozzle was computed to be 250 $BTU/ft^2 \cdot sec$ (2.83 MW/m^2) at the combustor exit, with an average value of 180 $BTU/ft^2 \cdot sec$ (2.0 MW/m^2). This nozzle heat flux is ten times greater than the heat flux associated with attached turbulent boundary layer on the remainder of the vehicle. The nozzle heat flux would lead to temperatures in excess of 3000 F (1650 C) on nozzle skin panels if active cooling were not provided.

The Laganelli and Wolfe (Ref. 5) correlation predicts that the rms fluctuating skin pressure at shock impingement is 166 dB, with a peak local heat flux of 92.5 $BTU/ft^2 \cdot sec$ (1.05 MW/m^2) at Mach 20 in the 1000 q ascent trajectory. These loads increase by a factor of two for the 2600 q ascent. In the absence of shock impingement the heat flux for the 1000 q ascent is 20 $BTU/ft^2 \cdot sec$ (0.22 MW/m^2) and the fluctuating pressure is only 140 dB (Fig. 9). Thus location of shock impingement is critical to the design of hypersonic vehicle skin panels.

Transient thermal analysis of the carbon-carbon skin panels was made to determine skin panel temperatures during ascent to orbit. The panels receive thermal energy from aerodynamic heating of their surface and reradiate this thermal energy into space. An alumina insulation blanket is placed between the panel and the substructure to limit convective heat transfer into the substructure. Temperature rise of the forebody panel due to aerodynamic heating of the attached boundary layer during ascent is maximum at the center of the skin bay. The minimum temperature rise occurs adjacent to the substructure attachments. For the 1000 q ascent, the calculated peak temperature is 2670 F (1460 C) for the forebody and 2510 F (1375 C) for the ramp. See Fig. 7. For the 2600 q case, the corresponding peak temperatures of 3250 F (1790 C) and 3010 F (1650 C), are above the 3000 F (1650 C) maximum-use temperature for carbon-carbon. If the flow relaminarizes, maximum temperatures are reduced by 1200 F (650 C) to a maximum of 2050 F (1140 C), which is within the temperature range of carbon-carbon. Thus, analysis of laminar/turbulent transition and heat flux is critical in the design of the forebody and ramp panels.

4. ENGINE ACOUSTIC LOADS

The Blended Wing Body (BWB) hypersonic vehicle has rocket engine thruster modules mounted in twin rows across the tail as shown in Fig. 2. The thrusters are used to reach speeds Mach 2 to 3, at which point the scramjet becomes efficient. The noisiest portion of the flight occurs during takeoff when the rocket engines and the scramjet engine are both operating. Sound levels on the lower half of the vehicle are higher than on the upper half of the vehicle owing to reflections from the runway, as well as direct acoustic radiation from the lower midbody mounted scramjet.

The NASA and Von Gierke (Refs 7 and 8) methods were used to predict overall sound power radiated by the rocket and scram jet engines. THe NASA technique give an overall acoustic power of 194 dB relative to 10^{-12} watts. The engine sound spectrum is relatively flat between 500 and 5000 Hz as the high frequency noise from the rocket thrusters combines with the lower frequency noise from the scramjet.

A directivity index was used to determine off-axis sound levels (Ref. 9). Reflection from the ground was taken into account to estimate overall sound levels on the vehicle skin during takeoff as shown in Fig. 12. Direct radiation from the engines results in overall Sound Pressure Levels in the 170 to 180 dB range (relative to 20 micro Pascal) on skin panels in the inlet and exhaust regions. These levels are comparable to the highest level measured in turbojet engines. As shown in Table 1, engine loads are considerably higher than the attached turbulent boundary layer loads, and they are comparable to loads due to shock impingement.

5. SKIN PANEL STRUCTURAL ANALYSIS

Static and dynamic structural analyses of the forebody, ramp, and actively cooled panels were made using the MSC/NASTRAN finite element code. For the forebody and ramp panels, the quadralateral plate element was used with carbon-carbon material properties determined from test. Mean loads were incorporated in the analysis. Mean (i.e., static) loads on the panels are of three types: (1) thermal loads associated with aerodynamic heating of the panel surface, (2) aerodynamic pressure loads applied directly to the skin, and (3) vehicle carry-through loads imposed at the panel boundaries by vehicle deformation and maneuvers. Thermally induced loads are generally highest when vehicle temperature is greatest, which occurs when the vehicle is at the top of the ascent trajectory (Fig. 11).

Dynamic analysis of the forebody and ramp panels was made by first calculating the mode shapes and natural frequencies of the panels, and then determining the dynamic response to fluctuating surface pressures in each mode (Ref. 10). For the forebody panel, the effect of the carry-through loads imposed by the fasteners was incorporated using a nonlinear solution. Modal analysis shows that the panel modes are generally have either modes where adjacent panel bays deflect inphase, and modes where adjacent bays deflect out of phase, causing the intermediate stiffener to rotate as shown in Fig. 9. The lowest frequency mode of the forebody panel was at 524 Hz, with in-phase motion of adjacent bays. The ramp panel, which has wider stiffener spacing and thinner skin gage than the forebody panel, has an out-of-phase mode at 258 Hz.

The forebody and ramp panels respond to engine noise and aeroacoustic loads. Aeroacoustic analysis shows that the maximum aeroacoustic fluctuating pressures due to boundary layer turbulence on the forebody panel fall in the 130 to 145 dB range, a factor of 3 to 6 smaller than the engine Sound Pressure Levels of 155 to 160 dB. The engine noise at the ramp panel is estimated at 160 to 170 dB. Shock waves emanating from the inlet can impinge on the ramp to generate fluctuating pressures that equal or exceed the engine noise on the ramp panel. Both the engine noise and the shock impingement loads exceed attached turbulent boundary layer loads on the ramp panel.

For the forebody panel, the maximum cyclic stress is 4000 psi (27.6 MPa) rms and is within the 6000 psi (41.4 MPa) rms random vibration fatigue allowable for carbon-carbon. The calculated maximum ramp panel stress of 16,080 psi (111 MPa) rms is over two-and-half times the carbon-carbon allowable. As a result, either the skin gage of the proposed ramp panel must be increased, or stiffener spacing must be decreased to avoid in-service failure due to engine noise.

6. COUPON AND PANEL TESTS

Facilities which can simultaneously apply aerothmal heat flux and aeroacoustic pressure fluctuations on panels have been developed at Rohr Industries to validate designs and materials. High temperature shaker testing of material is routinely done to 1800 F (980 C) to establish high cycle fatigue allowables of material coupons and joint subelements under random loading. A heated acoustic progressive wave tube has been constructed at Rohr Industries which uses quarts lamps to achieve 1800 F (980 C) over a 33 by 23 inch (0.83 by 0.58 m) test section with 168 dB overall Sound Pressure Level. The facility, shown in Fig. 10, was designed for testing the panels shown in Figs. 3, 4, and 5.

A total of 104 shaker test specimens and 7 thermo-acoustic test panels have been designed and fabricated. THe shaker specimens include titanium, titanium-aluminide, carbon-carbon, SiC-SiC, and titanium Metal Matrix (TMC) materials. The panels are TMC, carbon-carbon, and titanium. At this time approximately 70% of the shaker material coupons specimen tests have been completed. Joint sub-element shaker testing and panel acoustic testing will be continued over the next few months.

Tests at temperatures to 1800 F (980 C) with carbon-carbon specimens showed two unusual phenomena. First, the stiffness (modulus) of the material increases with temperature, apparently due to a tightening of the carbon matrix with temperature. Second, carbon-carbon is process and damage sensitive - a sensitivity which can lead to premature oxidation failure if the coating is breached. Some specimens failed prematurely at the point of strain gage apparently because of local damage of the adhesive to the coating which led oxygen to penetrate the matrix. This type of failure has occured both on uninhibited and inhibited matrix carbon-carbon. Random fatigue data for inhibited carbon-carbon at 1800 F (980 C) is shown in Figure 11.

The metallic TMC and titanium alloys generally gave more reliable results than carbon-carbon, but at lower temperatures. Tests on Ti 6-2-4-2 at 1100 F (590 C) gave good fatigue strength. TMC utilizing beta 21S titanium matrix exhibited good fatigue strength up to 1500 F (815 C). Figure 12 shows random fatigue results for Ti 6-2-4-2 at 1150 F (620 C) and TMC at 1500 F (815 C). However, it should be noted that these results are only for high cycle fully-reversed fatigue. Creep deformation of titanium alloys and titanium matrix composites can be limiting above 1100 F (590 C).

As the subelements and the panel tests are completed, the results will be compared with and incorporated in the analysis to determine the accuracy of the analysis and acceptability of proposed materials for hypersonic application. Design methods will be validated.

7. CONCLUSIONS

An analytical study was made and test are in progress of vibroacoustic fatigue of hypersonic flight vehicle skin panels. A single-stage-to-orbit mission and Blended Wing Body vehicle were developed which are representative of present transatmospheric vehicle design studies. The external flow field and boundary layer heating were determined by parabolised Navier-Stokes flow analysis. Engine acoustic loads were developed. Detailed thermal, static, and dynamic analyses have been made of the forebody, ramp, and nozzle panels.

The study shows that engine acoustic loads and shock-impingement loads will govern the design of many skin panels. The conclusions of the study are as follows:

1. Overall aeroacoustic Sound Pressure Levels on the skin are highest on components in line-of-sight of the engine inlet and engine exhaust and where shock wave impinge on the vehicle skin The maximum engine acoustic Sound Pressure Levels range between 170 and 180 dB overall. At hypersonic speeds, shock waves bend aft from the bow and from the inlet, and cause maximum shock-boundary layer interaction fluctuating surface pressures are between 160 and 170 dB and will be accompanied by local heat fluxes as high as 50 $BTU/ft^2 \cdot sec$ (0.6 MW/m^2).

2. Finite element analysis of the 0.15 inch (3.8 mm) thick carbon-carbon forebody skin panel shows that the maximum skin temperature is 2667 F (1460 C) at the end of a 1000 q ascent and 3220 F (1770 C) for a 2600 q ascent. These results are based on turbulent boundary layer heating. If a laminar boundary layer exists, the temperatures can be 1200 F (650 C) lower.

3. Finite element analysis has been conducted on ramp and fore body panels indicates that panels which act as heat shield will be design critical for thermal-acoustic loading.

4. Test are underway on material coupons and panels fabricated of carbon-carbon, TMC, titanium aluminide, SiC-SiC and high temperature titanium alloys. Shaker testing of titanium, titanium aluminide, carbon-carbon and TMC have been completed. Joint subelement tests and panel acoustic tests will be completed in the next few months. Ti 6-2-4-2 and Beta 21S TMC have good fatigue strengths to 1150 F(620 C) and 1500 F (815 C), respectively. Carbon carbon possesses adequate fatigue strength at 1800 F (980 C) but suffers from a sensitivity to coating damage either due to handling damage or process flaws which can lead to a rapid premature failure.

Acknowledgements

This paper reports work sponsored by the Flight Dynamics Laboratory, Wright-Patterson Air Force Base, and performed by a team from Rohr Industries, San Diego, California, McDonnell Douglas, St. Louis, Missouri, and Science Applications International, Ft. Washington, Pennsylvania.

References

1. Report of the Defense Science Board Task Force on the National Aerospace Plane (NASP), AD-A201-124, Department of Defense, Washington D.C., September, 1988.

2. Blevins, R.D., Holehouse, I., and K.R. Wentz, "Thermo-Vibro-Acoustic Loads and Fatigue of Hypersonic Flight Vehicle Structure," *AIAA Journal of Aircraft* 30, 971-978 (1993).

3. Tauber, M.E., G.P. Menees, and H.G. Adelman, "Aerodynamics of Transatmospheric Vehicles," *Journal of Aircraft*, Vol. 24, Sept. 1987, pp. 594-602.

4. Laganelli, A.L., A. Martellucci, and L.L. Shaw, "Wall Pressure Fluctuations in Attached Boundary Layer Flow," *AIAA Journal*, Vol. 21, 1983, pp. 495-502 (also AFFDL-TR-77-59).

5. Laganelli, A.L. and H. Wolfe, "Prediction of Fluctuating Pressure in Attached and Separated Turbulent Boundary Layer Flow," *AIAA Journal of Aircraft* 30, 962-970 (1993).

6. Zorumski, W.E., "Fluctuating Pressure Loads under High Speed Boundary Layers," NASA Technical Memorandum 100517, October 1987.

7. Eldred, K.M. "Acoustic Loads Generated by the Propulsion System", NASA SP-8072, June 1971.

8. Von Gierke, H.E., "Aircraft Noise Sources," Chapter 33 in Handbook of Noise Control, C.M. Harris (ed.), McGraw-Hill, 1957.

9. McInerny, S., "Rocket Noise - A Review," AIAA Paper 90-3981, AIAA 13th Aeroacoustics Conference, Tallahassee, October 1990.

10. Blevins, R.D., "An Approximate Method for Sonic Fatigue Analysis of Plate and Shell Structures", Journal of Sound and Vibration, Vol. 129, 51-71 (1989).

Table 1 Typical maximum aeroacoustic loads at Mach 10 for q = 2600 ascent

Loading	Overall SPL, dB*	Heat flux, BTU/ft²-s
Attached turbulent boundary layer	145	22
Shock impingement on boundary layer	167	49
Engine exhaust on nozzle at takeoff thrust	176	100

*Re 20 μPa

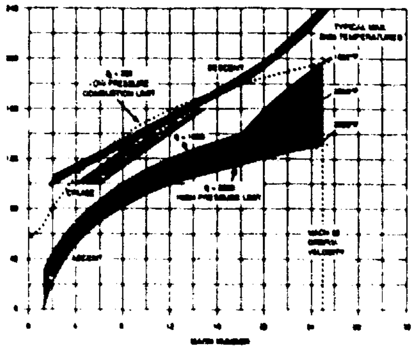

Fig. 1 Transatmospheric vehicle flight trajectories. The air breathing combustion flight envelope is bounded by a total pressure of q_t = 200 lb/ft² (10,000 Pa) and a dynamic pressure of q = 2600 lb/ft² (150,000 Pa).[1]

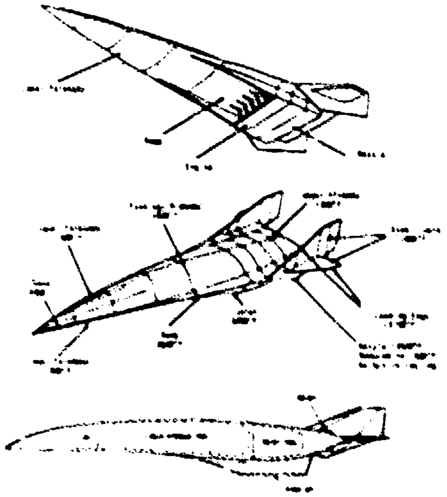

Fig. 2 Blended wing body transatmospheric vehicle design concept.[1]

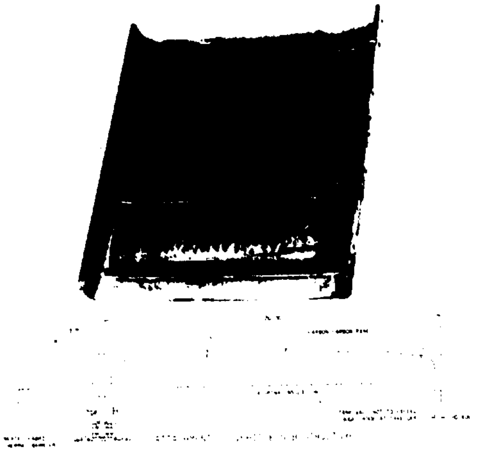

Fig. 3 Carbon-carbon lower forebody panel.

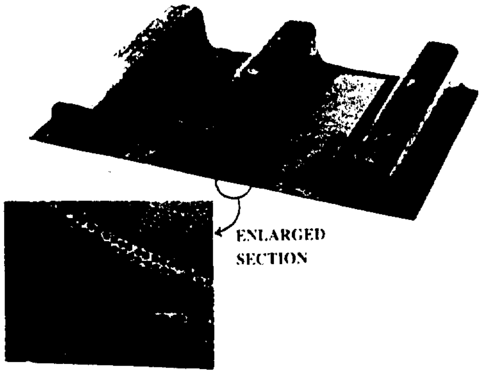
ENLARGED
SECTION

Fig. 4 Titanimum metal matrix prototype wing skin panel. The silcon carbide fibers in the 15V-3Cr titanium matrix are 0.006 in. (0.15 mm) in diameter.

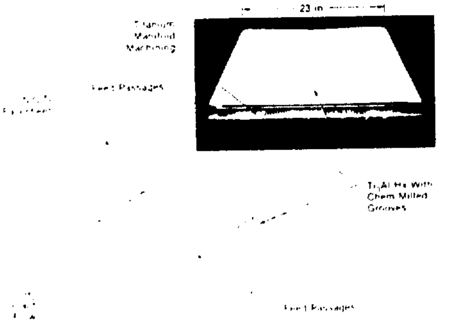
23 in
Titanium
Manifold
Machining
Fuel Passages
Ti3Al+Nb With
Chem Milled
Grooves
Fuel Passages

Fig. 5 Actively cooled nozzle panel section.[2]

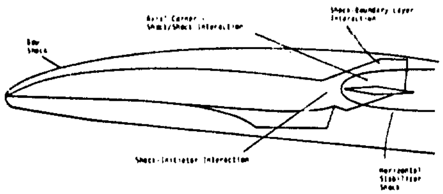
Bow
Shock
Axial Corner -
Shock/Shock Interaction
Shock-Boundary Layer
Interaction
Shock-Initiator Interaction
Horizontal
Stabilizer
Shock

Fig. 6 Shock waves impinging upon vehicle skin panels.[5]

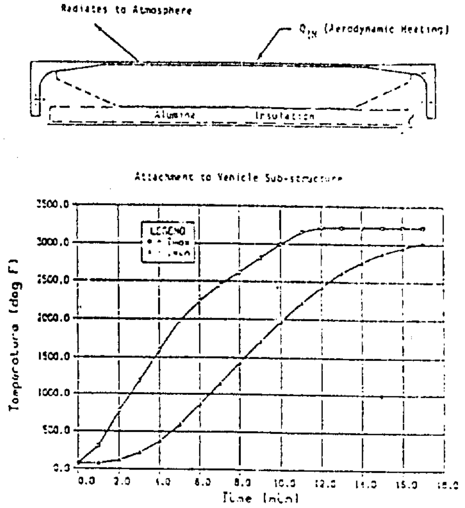

Figure 7 Forebody panel temperature rise for 1000 q ascent.

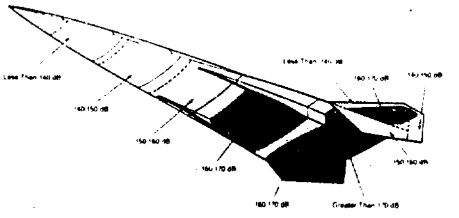
Less Than 140 dB
140-150 dB
150-160 dB
160-170 dB
160-170 dB
Less Than 140 dB
160-170 dB
140-150 dB
150-160 dB
Greater Than 170 dB

Figure 8 Overall Sound Pressure Levels relative to 20 micro Pa due to engine noise at takeoff.

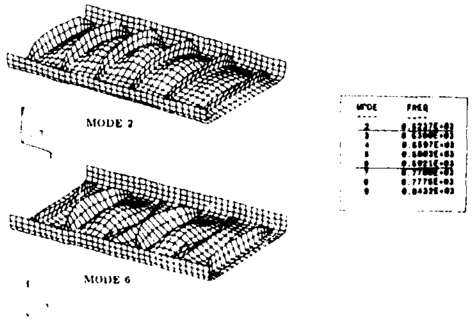
MODE 2
MODE 6
MODE
FREQ

Figure 9 Forebody panel in-phase and out-of-phase vibration modes.

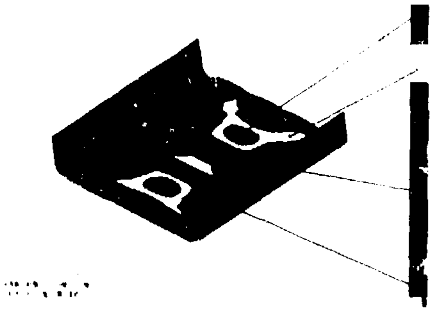

Figure 10 Ramp panel carbon-carbon sonic fatigue rms stress field.

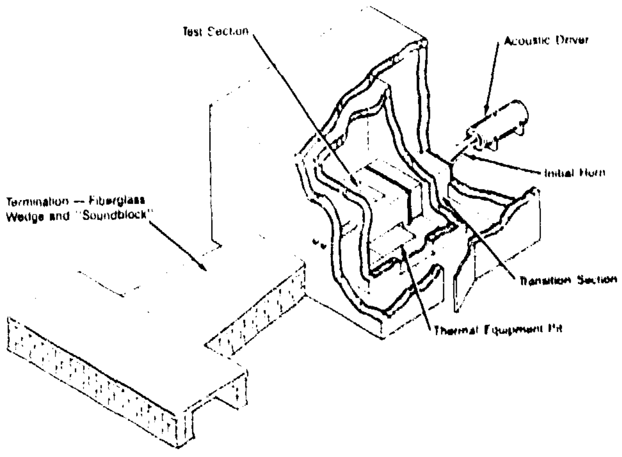
Test Section
Acoustic Driver
Initial Horn
Termination — Fiberglass Wedge and "Soundblock"
Transition Section
Thermal Equipment Pit

Figure 11 Thermal Acoustic Progressive wave tube.

Figure 12 Random fatigue shaker test data for carbon-carbon coupons at 1800 F (980 C).

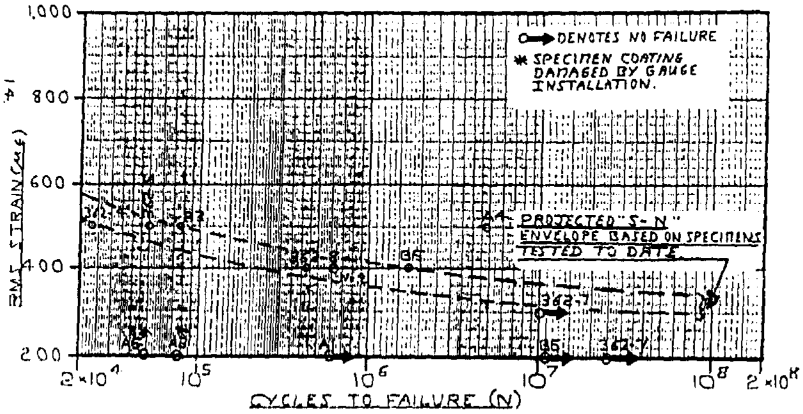

Figure 13 Random fatigue data for titanium Beta 21S metal matrix composite coupons.

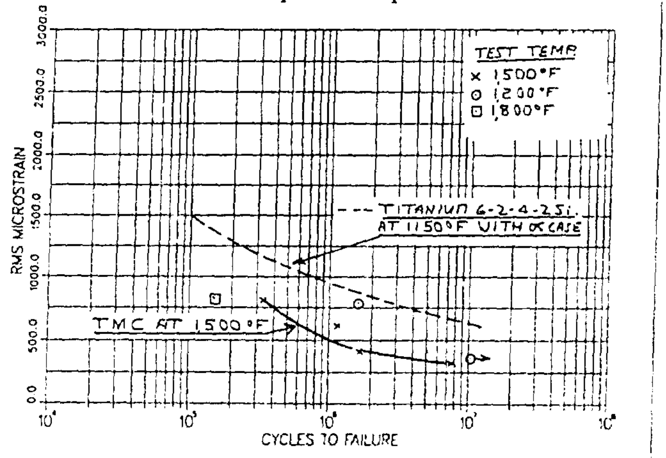

APPLICATION OF SUPERPLASTICALLY FORMED AND DIFFUSION BONDED STRUCTURES IN HIGH INTENSITY NOISE ENVIRONMENTS

R. J. Cummins
J. P. C. Wong
British Aerospace Airbus Limited
NTC, PO Box 77
Bristol BS99 7AR, UK

SUMMARY

Two specimens, representing an aircraft control surface and an access door, have been tested under high intensity acoustic excitation. The access door was also subjected to an elevated temperature environment of 150°C during this test. These specimens were manufactured as multi-cell box configurations by superplastic forming and diffusion bonding (SPFDB) to a similar structural weight as existing aircraft components produced by alternative means of construction. The influence of the spandrel-shaped void, formed at the skin/stringer intersection, is considered on the acoustic fatigue performance.

1. INTRODUCTION

Superplastic behaviour of certain metals occurs when the material is of fine grain size and at elevated temperature; in an inert atmosphere it can be subjected to extensive elongation without pronounced localised thinning. For the process of diffusion bonding the mating surfaces are brought into intimate contact at elevated temperature and atomic diffusion across the interface produces the bond. For titanium, diffusion is aided by the fact that the oxide film, which in the case of other metals inhibits diffusion, is absorbed within the metal at high temperature. As both superplastic forming and diffusion bonding occur at the same temperature in titanium (925°C to 950°C) the combination of the two processes is often exploited.

Using the SPFDB process components such as control surfaces, doors and fairing panels can be formed in a single operation using prepared blanks. The structure is usually designed as a multi-cell box using a four-sheet blank. The inner sheets are joined by welding in order to form the internal stiffening construction, see Figure 1.

One result of this type of construction is that a small spandrel-shaped void is formed in the skin/stiffener interface, as shown in Figure 2. This void provides an inherent stress concentration and a probable location for crack initiation when the structure responds to acoustic excitation. Random vibration endurance tests have been performed on T-shaped coupon specimens extracted from multi-cell SPFDB titanium boxes. The test results confirmed the expected crack location, see Figure 3, which could initiate from either the outer or inner skin surface into the void. However the overall resistance to acoustic fatigue for this feature has to be compared against other forms of construction, with their inherent design features, based on components designed to a similar weight. This paper describes the test experience and summarises some general design considerations on the application of SPFDB titanium structures.

Presented at a Symposium on 'Impact of Acoustic Loads on Aircraft Structures' held in Lillehammer, Norway, May 1994.

2. SUPERPLASTIC FORMED AND DIFFUSION BONDED (SPFDB) TEST COMPONENTS

As the SPFDB process requires an expensive tool for forming, a relatively large one-off research specimen concentrating on the skin/stiffener feature would have been expensive, so use was made of available aircraft development tooling. This has the advantage that the specimen was fully representative of an aircraft component although containing more complex features than required from a general research basis. In addition, information was available for both components from acoustic tests on similar geometry components using different constructional methods.

2.1 Aircraft Control Surface (Spoiler)

This was a multi-cell wedge shaped box structure having 27 internal ribs and a single longitudinal spar formed from the two central core sheets of the blank. The stiffeners were terminated short of the panel trailing edge to allow gas flow between cells during the forming process. This was achieved by the welding pattern applied to the inner two sheets of the SPF-DB blank which also produced a flared effect at the stiffener run-out.

The overall dimensions are shown in Figure 4. As with most aircraft control surfaces the component was hinged and attached along one edge, to allow for control movement, by 3 fittings with hinge lugs. The central hinge fitting was bolted into a recessed area, see Figure 4. These fittings provided a suitable means for mounting the component for test.

2.2 Aircraft Access Door Panel

This multi-cell box structure was manufactured from a four-sheet blank having single curvature with three longitudinal stiffeners and two frames formed from the four central core sheets. The inner skin was cut away over the cells leaving a continuous cap-strip over the stiffeners and frames, see Figure 5. Attachment to adjacent structure was by a single row of fasteners around the peripheral door flange. For test the specimen was mounted in a fully representative door surround structure and was attached by fasteners on all four edges so that the skin/stiffener modes were the major responses which were excited.

3. EXCITATION ENVIRONMENT

The applicable environment for the control surface panel, based on the actual aircraft location, would be a maximum overall sound pressure level (OASPL) of 142 dB broad band noise loading with relatively low temperature (< 100°C) exposure. However, as it was typical of a four-sheet multi-cell box construction which could be used in a high noise environment, it was decided to test using a broad band excitation of about 160 dB OASPL, see Figure 6. This was with the aim of provoking failures at the skin/stiffener intersection due to the stress concentration caused by the spandrel-shaped void.

The access door panel was tested at a representative elevated temperature of 150°C using a higher noise level of 165 dB OASPL of broad band excitation but with some high level tones present, see Figure 6. The intention of this test was to perform a direct comparison in the same environment with another access door employing the current aircraft construction. This was a light alloy fabricated framework of traditional skin/stiffener construction with a titanium sheet skin and all attachments with solid rivets.

The original panel was tested first followed by the SPFDB version at the same siren location. Both specimens were exposed to 40 hours of acoustic excitation with the outer skin at grazing incidence in the PWT working section. The thermal environment was supplied by a bank of quartz-tungsten electric heaters which were arranged to apply the heat to the inside of the specimens due to the difficulty of operating the heaters within the PWT working section. The specimens were allowed to reach a stable temperature of 150°C (300°F) before commencing the acoustic loading.

All specimens were excited at grazing incidence in a progressive wave tube (PWT). For the access door panels the PWT used a Stentor Noise Generator as the noise source whereas the tests on the control surface panels employed LTV-EPT200 generators.

4. TEST PERFORMANCE

4.1 Control Surface Panel

After the preliminary resonance tests to identify structural response modes the panel was subjected to the fatigue endurance test. The first damages were detected after 24 hours of testing and although associated with the skin/stiffener junction the initiation was from the end of the internal stiffener close to the panel trailing edge. Damage was initiated at several similar locations where the stiffeners were terminated and no damage initiated from the spandrel-shaped void in the skin/stiffener intersection. As for many cases of acoustic fatigue damage the initiation was due to a detail design feature. Endurance testing on the panel was continued until 30 hours where the damages had propagated to the extent shown in Figure 7.

Non-destructive examination confirmed that there were no internal cracks along the skin/stiffener junction, damage had initiated near the panel trailing edge in the stiffener termination feature. Some subsequent propagation of the cracks was then along the skin/stiffener junction as shown in Figure 7.

The panel was attached at the three hinge fitting locations along one edge with the other edges free to represent the actual boundary conditions. The structures response test demonstrated that the control surface panel was able to respond more readily to the overall modes occurring in the lower frequency range as well as being excited by the skin/stiffener panel modes occurring in a higher frequency range, see Figure 8.

The deflections at the component trailing-edge would give rise to high stress concentrations at the stiffener terminations.

In a comparable aircraft installation the control surface panel was manufactured from carbon-fibre. The two components were of similar weight but had a major design difference in that the central hinge attachment on the SPFDB design required only 6 fasteners, making use of the material strength of titanium. The carbon-fibre component used 31 fasteners to spread the loading which greatly increased the number of potential damage initiation locations. However there were no suitable acoustic endurance test data to provide a comparison between carbon-fibre and SPFDB.

4.2 Access Door Panel

In the aircraft situation this panel was subjected to a combined high noise and high thermal environment.

The SPFDB access door survived the test with no detectable damage after visual, ultrasonic flaw and x-ray inspection. The titanium skinned aluminium alloy specimen sustained damage at three locations, as shown in Figure 9, which had resulted in extensive propagation by the end of 40 hours endurance. In addition a number of the countersunk fastener heads were found to be damaged. Damages to the central stiffener area and cracking in the cleat at the lower edge of the forward stiffener are shown in Figure 9.

4.3 Discussion

In general the SPFDB titanium structures provide better resistance to accidental and debris damage than carbon-fibre composite structures and better repairability. For example carbon-fibre composite flaps situated behind landing gears may be subjected to a stone damage on the skins which would then be readily propagated under the acoustic excitation. However, like all constructions subjected to high noise environment the detail design is of the prime importance as this is usually where the damage occurs. The spandrel shaped void itself, which is formed at the skin/stiffener interface in SPFDB structures manufactured by the 4-sheet technique, appears to be no more of a problem than those introduced by other means of fastening, in similar weight structures. In the final comparison, if all structures can withstand the noise loading and meet the weight requirement, it is the cost of manufacture which will dictate the chosen method.

5. CONCLUSIONS

The SPFDB access door demonstrated a clear advantage in performance compared to the fabricated structure based on a similar component weight. As the purpose of the test was to compare the two construction methods the SPFDB panel was not tested to failure.

Neither of the tests on the SPFDB components provoked a failure involving the spandrel-shaped void feature of the skin/stiffener intersection.

From this available test evidence the main design advantages for using SPFDB construction in a high noise environment are:

i) the ability to withstand a higher temperature environment than standard carbon or glass-fibre composite and aluminium structures.

ii) superior acoustic fatigue resistance to aluminium alloy fabricated structure when designed for the same weight.

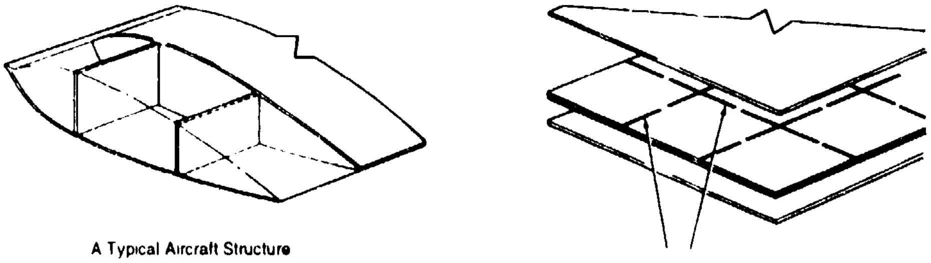

A Typical Aircraft Structure

Four Sheet SPF/DB
The Core Sheets' are joined at the locations where internal stiffeners are required

BLANK PREPARATION

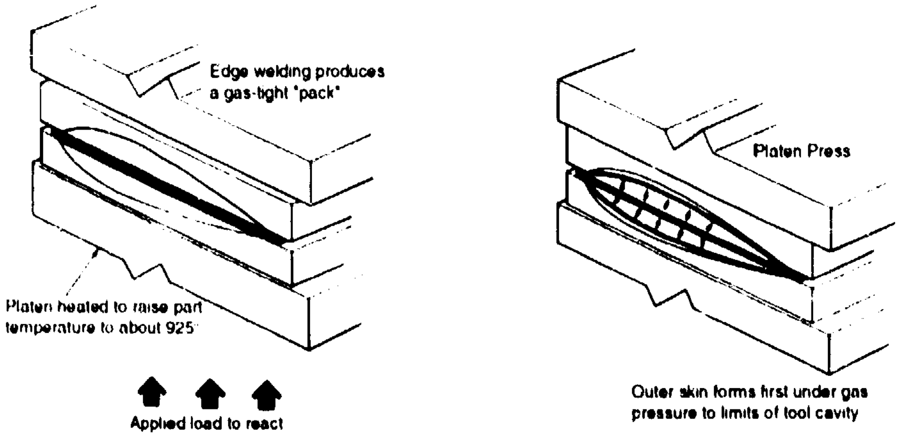

Edge welding produces a gas-tight 'pack'

Platen Press

Platen heated to raise part temperature to about 925

Applied load to react to gas pressure

Outer skin forms first under gas pressure to limits of tool cavity

SKIN FORMING

FIGURE 1 (a) SPFDB FORMING FOR MULTI-CELL CONSTRUCTION

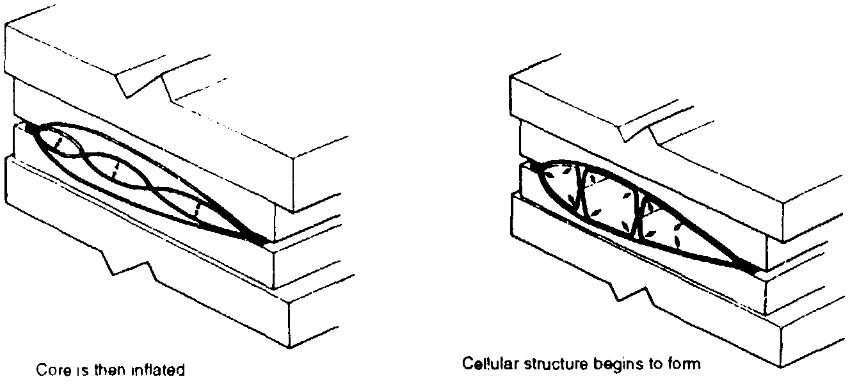

Core is then inflated

Cellular structure begins to form

WEB FORMING

FIGURE 1 (b) SPFDB FORMING FOR MULTI-CELL CONSTRUCTION

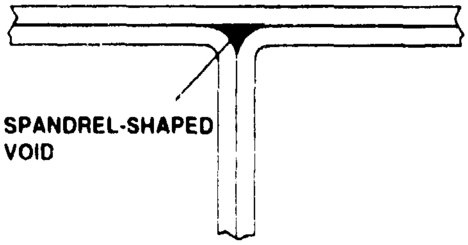
SPANDREL-SHAPED
VOID

FIGURE 2 DETAIL OF SKIN/STIFFENER INTERFACE

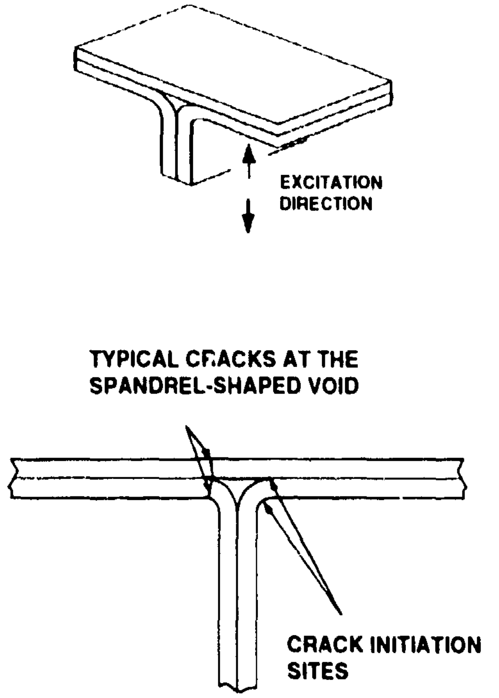
EXCITATION
DIRECTION
TYPICAL CRACKS AT THE
SPANDREL-SHAPED VOID
CRACK INITIATION
SITES

FIGURE 3 TYPICAL DAMAGE LOCATIONS FOR COUPON SPECIMENS

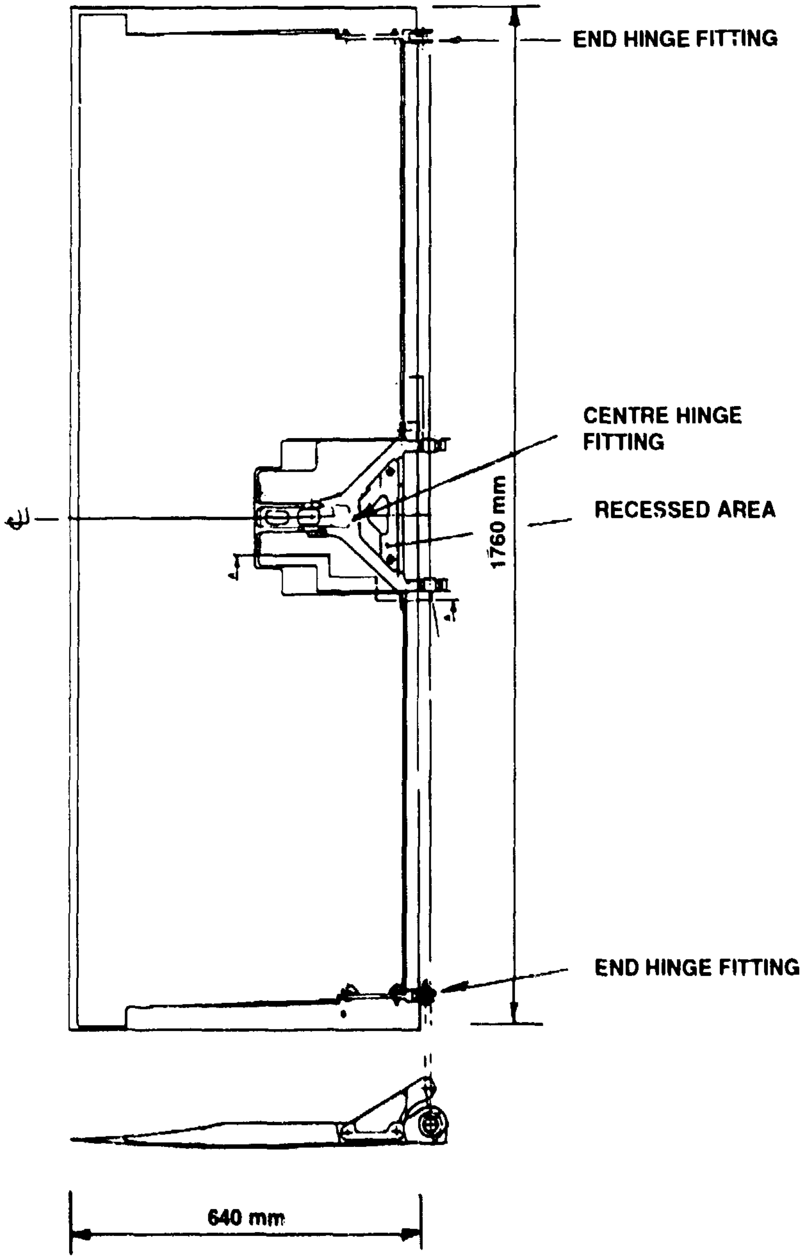
END HINGE FITTING
CENTRE HINGE FITTING
RECESSED AREA
1760 mm
END HINGE FITTING
640 mm

FIGURE 4 GENERAL ARRANGEMENT OF THE SPFDB TITANIUM SPOILER (BOTTOM SURFACE SHOWN)

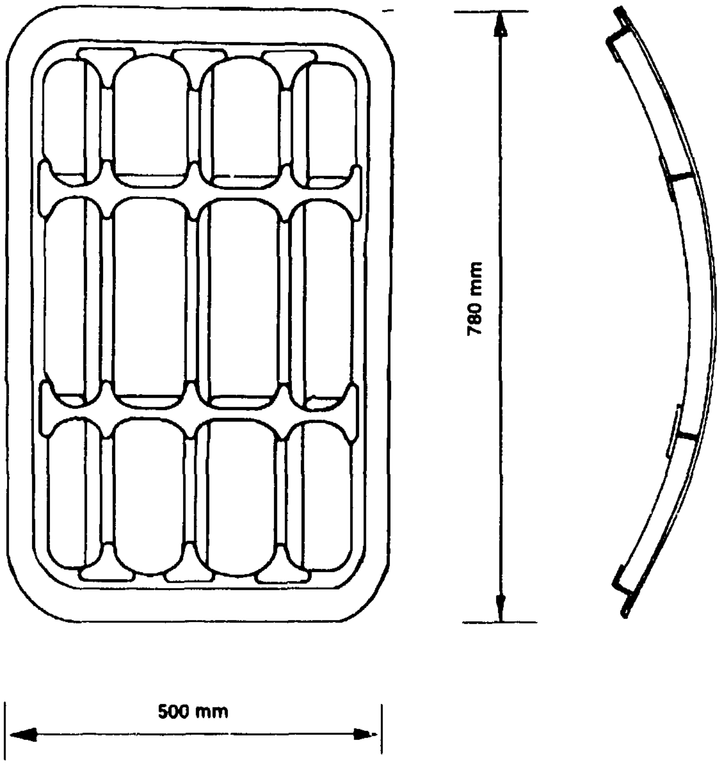

FIGURE 5 GENERAL ARRANGEMENT OF THE ACCESS DOOR PANEL (ORIGINAL ALUMINIUM DOOR PANEL SHOWN)

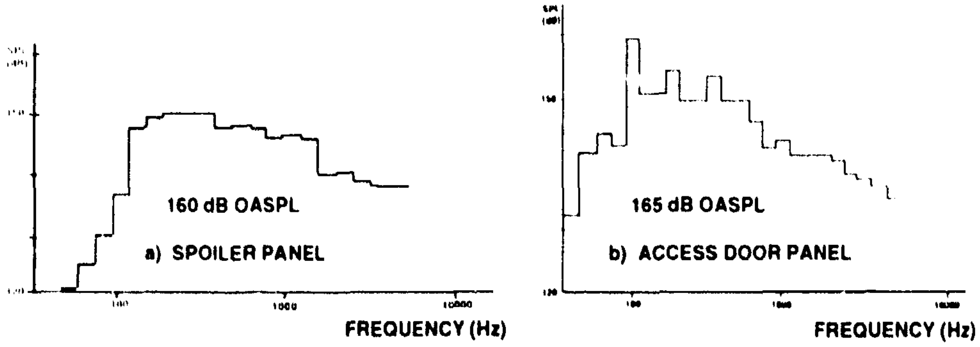

160 dB OASPL

a) SPOILER PANEL

165 dB OASPL

b) ACCESS DOOR PANEL

FIGURE 6 ACOUSTIC EXCITATION : 1/3 OCTAVE BAND SPECTRUM

A) CRACK LOCATION ON THE SPECIMEN PANEL

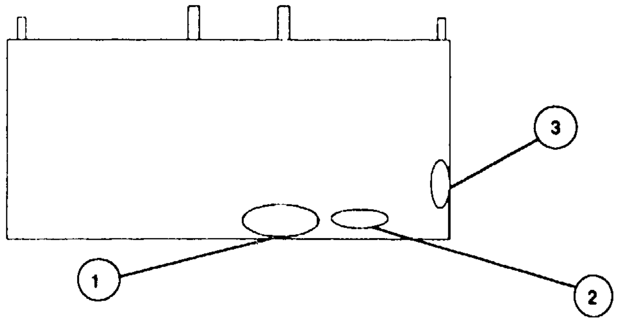

a) CRACK LOCATIONS

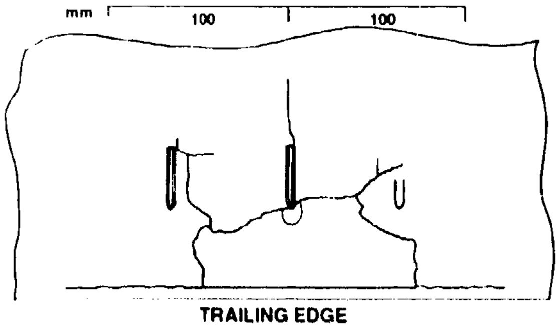
mm
100
100
TRAILING EDGE

b) LOCATION 1

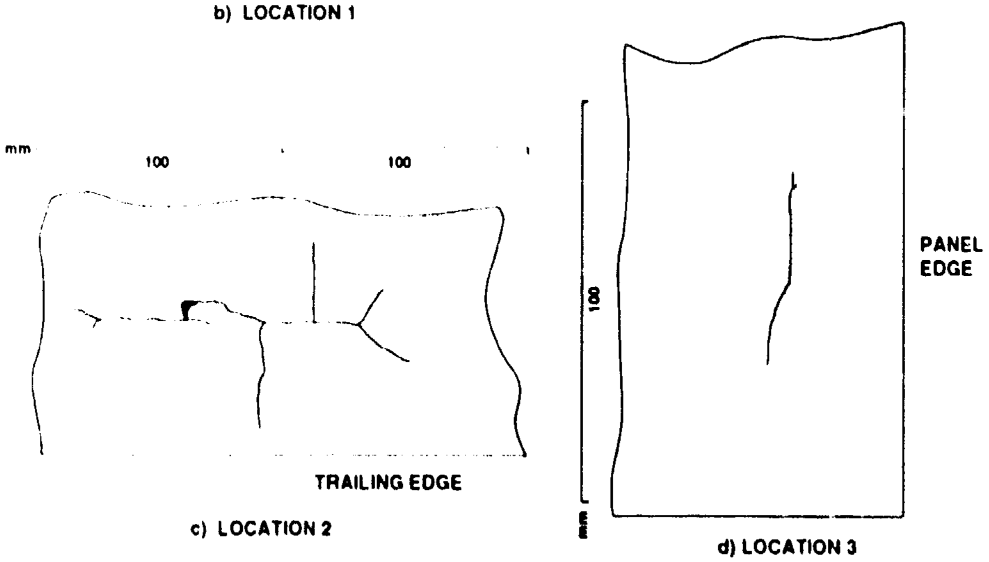
mm
100
100
TRAILING EDGE
100
mm
PANEL
EDGE

c) LOCATION 2

d) LOCATION 3

FIGURE 7 DAMAGE LOCATIONS FOR SPOILER PANEL

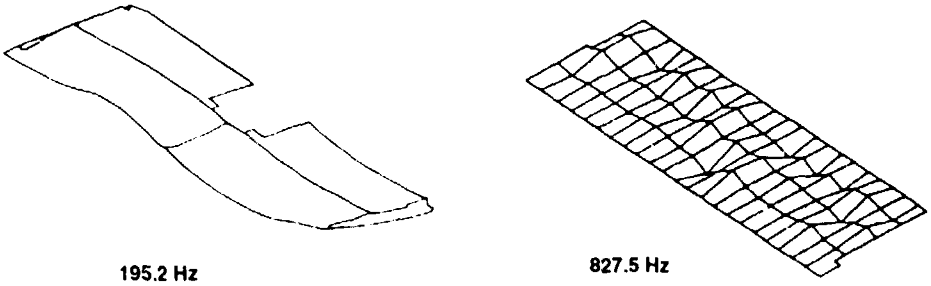

a) TYPICAL SPOILER RESPONSE MODE IN LOWER FREQUENCY RANGE

b) TYPICAL SPOILER RESPONSE MODE IN HIGHER FREQUENCY RANGE

FIGURE 8

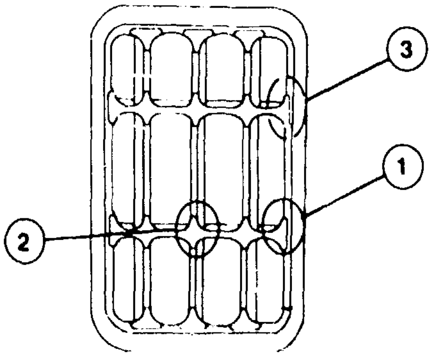

a) LOCATIONS OF ACOUSTIC FATIGUE DAMAGE

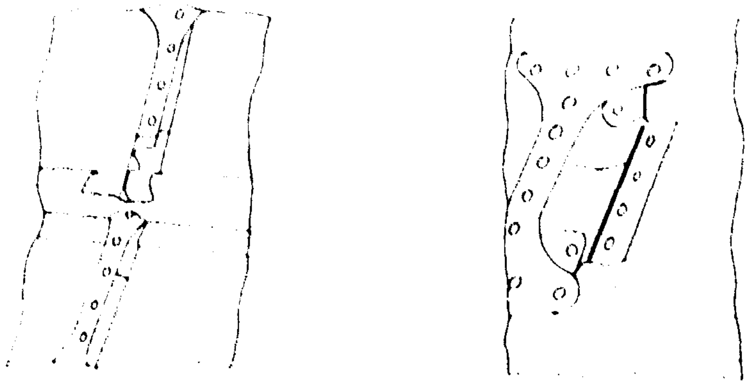

b) LOCATION 2

c) LOCATIONS 1 AND 3

FIGURE 9 DAMAGE LOCATIONS FOR THE FABRICATED ALUMINIUM ACCESS DOOR PANEL

AN OVERALL APPROACH OF COCKPIT NOISE VERIFICATION IN A MILITARY AIRCRAFT

R. Giuzio
ALENIA Un'Azienda Finmeccanica s.p.a.
Corso Marche, 41
10146 Torino - Italia

M. Norese
AERMACCHI s.p.a.
Via Paolo Foresio
21040 Venegono Superiore (VA) - Italia

SUMMARY

The present paper describes the applicable concepts for cockpit noise verification in a military aircrafts.

A design-to-noise procedure is outlined and the overall requirements for medical, intelligibility and operational aspects are deeply discussed, including the proposition of an adequate index to quantify the quality of noise at pilot's ear.

Guidelines for cockpit noise control, to be applied during the design phase of the project, are given together with the expected benefits.

Advanced noise control measures and noise measuring techniques are also dealt with and a specific case of cockpit noise verification is described.

1. INTRODUCTION

Cockpit noise environment in a military aircraft has recently become of great concern for flight members service operability, mainly for the risk of hearing handicap that noise exposure can cause. Therefore more attention is required by design engineers for the delivery to the customer of a final product which meets the requirements of recent military standards and air force regulations aimed to eliminate hearing handicap noise hazard and to provide good quality of communication. Finally a comfortable noise environment is still to be pursued.

Airframe weight reduction resulting from structural optimisation design and usual procedure to save weight for noise control measures, in favour of customer requirements of additional fuel, weapon loads or avionics equipment, has changed during years the helmet role from impact protection to noise protection.

Unfortunately structural optimisation results in an increase of cockpit noise in the low frequency range, where standard helmets offer poor attenuation, due to leakage past the earcup seals, and acoustic modes of cavity are likely to be coupled with structural resonances.

A proper design-to-noise approach is then to be followed, starting from the preliminary design phase of the aircraft, to reduce the overall noise sound pressure level (OASPL) inside the cockpit and to improve the quality of noise, related to subjective human perception of noise, at pilot's ear.

This target may be reached through a careful use of technical solutions for noise and vibration control in order to optimise costs and benefits of the project.

2. COCKPIT NOISE IMPACTS

Cockpit noise impacts on flight members may be summarised in the three following aspects:

- MEDICAL, related to noise induced hearing impairment,
- INTELLIGIBILITY, related to quality of communication,
- OPERATIONAL, related to individual comfort.

2.1. Medical aspects

Daily noise exposure to a combination of sound pressure level, duration and frequency content may cause risk of hearing loss (i.e. Permanent Threshold Shift, PTS) which is usually preceded by a reversible effect called "Temporary Threshold Shift" (TTS).

The TTS, usually below 20 dB, appears in the audiometric test performed on subjects after the exposure to high noise levels and disappears if the audiometric test is repeated after some hours of out-of-noise exposure.

Figure 20-1 shows typical pure tone audiograms assuming 0 dB as the audible threshold for a 1000 Hz pure tone having a sound pressure of 20 μPa. Normal hearing audiogram corresponds to threshold shifts of ≤ 5 dB.

Usually the effects on ear damage related to frequency and level of noise are taken into account by the overall A-weighted sound pressure level in dBA, representing the summation of all frequencies contribution, but giving less sensitivity to low frequency noise (below 500 Hz) that is of less concern for hearing conservation purposes. dBA approximates the human hearing characteristics for moderate sound levels.

Presented at a Symposium on 'Impact of Acoustic Loads on Aircraft Structures' held in Lillehammer, Norway, May 1994

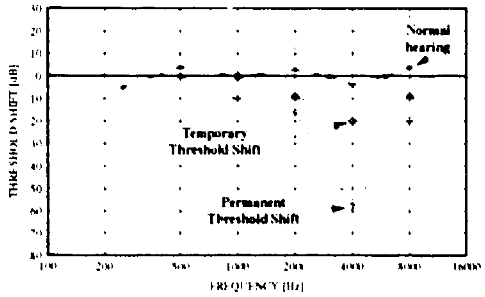

Figure 20.1 - Typical pure tone audiograms

2.2. Intelligibility aspects

Ambient noise may degrade communication causing speech interference and limiting pilot performance as more attention needs to be given to speech understanding.

Speech intelligibility is mainly reduced when communication occurs in presence of high noise levels in the octave bands centred on the preferred frequencies 500, 1000, 2000 and 4000 Hz. The arithmetic average of noise sound pressure levels in dB at these four preferred frequencies is called Preferred Speech Interference Level (PSIL).

A practical approximation considers noise levels in dBA equal to noise levels in PSIL plus 4 dB (e.g. 76 PSIL equals 80 dBA).

Speech interference is sometimes also quantified by the old index SIL (Speech Interference Level), which is the arithmetic average of noise sound pressure levels in dB in the three octave bands 600 to 1200 Hz, 1200 to 2400 Hz and 2400 to 4800 Hz; approximately SIL equals PSIL minus 3 dB.

PSIL and SIL criteria are commonly used for face-to-face communication in presence of noise.

When communication systems are used the intelligibility assessment of communication in presence of noise is performed through the Articulation Index (AI) design criterion and the Modified Rhyme Test (MRT) verification criterion.

2.3. Operational aspects

Strictly related to subjective evaluations depending upon a lot of concurrent factors, noise may be cause of discomfort, nausea, loss of attention, work load increase, etc.

The human response to noise depends on noise characteristics (e.g. level, spectral distribution, impulsiveness, tonality, fluctuation, etc.), psychological aspects and physiological conditions. In addition annoyance may be reduced in case of acquired familiarity with noise.

At present time, due to the lack of collected or published data, it is very difficult to exactly quantify this effect of noise on a military aircraft pilot.

Studies attempting to correlate objective measurements with subject response are currently in course in the automotive industry. Nevertheless the derived indexes (mainly the Composite Rating of Preference, CRP, and its modifications, 2nd ATA International Conference on Vehicle Comfort - October 14-16, 1992) result of poor application for military aircraft noise quality description.

In the present work the Tone Corrected Perceived Noise Level (PNLT), defined in FAR Part 36 and ICAO Annex 16 for commercial aircraft noise emission regulation and certification purposes and reflecting the human annoyance to sound at different frequencies and levels, has been found to provide sufficient correlation with pilot noise quality reporting.

This could be related to the specific nature of jet aircrafts cockpit noise, where characteristics of impulsiveness or rapid fluctuations are not present, and to the typical spectrum shape at pilot's ear, where low frequencies are dominant.

3. THE DESIGN-TO-NOISE APPROACH

A realistic cockpit design-to-noise approach is summarised in the flow chart of Figure 20.2, where the following phases are outlined:

- requirements definition,
- prediction, theoretical or based on similar aircraft measured data,
- engineering design recommendations for cockpit noise control, saving space for additional noise control measures, if required by measurements,
- on-board measurements, during ground and flight operations,
- requirements verification,
- noise insulation optimisation, if necessary,
- final assessment.

The first phase is undoubtedly the most important one for design engineers in optimising costs and benefits of the project.

The applicable standards and the verification procedure of requirements shall be clearly agreed between manufacturer and customer during the contractual phase. In fact, being the requirements of the applicable standards usually derived for civilian workers, their application to military aircraft flight members is highly conditioned by the standard equipment noise attenuation characteristics.

The lower attenuations addressed to cover a large percentage of wearers (mean values minus one or two standard deviations) may led, for a jet fighter aircraft, to an unrealistic noise environment at pilot's ear that can have impacts both on the hearing damage risk and on the quality of noise.

The design-to-noise approach will be deeply discussed in the following Chapters.

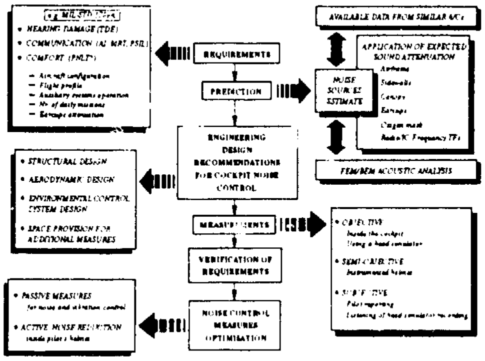
e.g. MIL-STD-1789A
• HEARING DAMAGE (TDE)
• COMMUNICATION (AI, MRT, PSIL)
• COMFORT (PNLT)
– Aircraft configuration
– Flight profile
– Auxiliary systems operation
– Nr. of daily missions
– Earcups attenuation
REQUIREMENTS
PREDICTION
AVAILABLE DATA FROM SIMILAR A/Cs
NOISE SOURCES ESTIMATE
APPLICATION OF EXPECTED SOUND ATTENUATION
Airframe
Sidewalls
Canopy
Earcups
Oxygen mask
Radio/IC Frequency TFs
FEM/BEM ACOUSTIC ANALYSIS
ENGINEERING DESIGN RECOMMENDATIONS FOR COCKPIT NOISE CONTROL
• STRUCTURAL DESIGN
• AERODYNAMIC DESIGN
• ENVIRONMENTAL CONTROL SYSTEM DESIGN
• SPACE PROVISION FOR ADDITIONAL MEASURES
MEASUREMENTS
• OBJECTIVE
Inside the cockpit
Using a head simulator
• SEMI-OBJECTIVE
Instrumented helmet
• SUBJECTIVE
Pilot reporting
Listening of head simulator recording
VERIFICATION OF REQUIREMENTS
NOISE CONTROL MEASURES OPTIMISATION
• PASSIVE MEASURES
for noise and vibration control
• ACTIVE NOISE REDUCTION
inside pilot's helmet

Figure 20.2 - Cockpit noise design and verification

4. COCKPIT NOISE REQUIREMENTS

Requirements concerning cockpit noise design and verification may be found in Mil-Std-1789A "Sound Pressure Levels in Aircrafts", superseding Mil-S-008806.

Requirements are confined to the maximum allowable sound pressure level for hearing conservation and satisfactory communication. Nothing is said about pilot comfort criteria.

A summary of cockpit noise requirements for a fighter aircraft is reported in Table 20.1.

COCKPIT NOISE REQUIREMENTS *Based on MIL-STD-1789A*				
HEARING DAMAGE	COMMUNICATIONS			COMFORT
	AI	SIL	PSIL	
CONTINUOUS NOISE 8 hours daily noise exposure TDE ≤ 1 based on aircraft usage mission profiles, flight member standard equipment	Design criterion	Verification criterion Test in noise field simulating the actual environment	Based on distance compromising voice intelligibility of communication	Subjective evaluation depending on noise characteristics level spectral distribution fluctuation impulsiveness tonality
IMPULSIVE NOISE SPL ≤ 140 dB peak if time between peaks ≤ 1 second Different level and duration for repeated impulses	Calculation method ANSI S3.5	Verification procedure ANSI S3.2	Verification by analysis	psychological aspects physiological conditions familiarity with noise
WHOLE BODY NOISE SPL ≤ 145 dB or 150 dBA whichever is less in any octave band from 1 to 40000 Hz	TS Ratio ≥ 0.5 R ≥ 0.1	TS Ratio ≥ 75% R ≥ 75%		Suggested value PNLT ≤ 100 dB

Table 20.1 - Summary of cockpit noise requirements

4.1. Hearing damage

Mil-Std-1789A defines the allowable A-weighted sound pressure levels and exposure times at the ear canal of crew and passengers of United States Air Force (USAF) aircrafts to prevent hearing damage, keep effective performance and avoid damage or unwanted responses of the whole human body.

4.1.1. CONTINUOUS BROADBAND NOISE

Daily exposures to continuous noise shall not exceed 84 dBA, in the frequency range 25÷20000 Hz, for 8 hours.

For different noise levels, L, the limiting daily duration (LDD) of exposure is to be determined from the equation:

$$LDD\ (hours) = 2^{\frac{96-L}{4}}$$

which is based on the assumption that an increase of the overall level of 4 dBA halves the allowable exposure time.

No limit of exposure is stated for noise levels below 78 dBA, whilst levels higher than 115 dBA are never allowed.

In case of daily exposure to noise fields differing in level and duration the Total Daily Exposure (TDE) shall be calculated by adding the fractions

$$\frac{\text{Observed Daily Duration}}{\text{Limiting Daily Duration}} = \frac{ODD}{LDD}$$

for all the exposures in any one workday.

TDE shall not exceed unity (1).

For flight members the TDE criterion shall be based on aircraft usage and mission profiles at flight conditions during which noise levels are effectively constant with all the required auxiliary systems (e.g. environmental control system, defrosting system, etc.) in operation. Calculations shall include noise produced by the In-Flight Refuelling Probe (IFRP) and external stores, where applicable.

The allowable daily missions, for the same pilot, will be 1/TDE.

4.1.2. IMPULSIVE NOISE

Impulsive noise, if time between peaks is 1 second or less (e.g. gunfire), shall not exceed 140 dB peak sound pressure level and shall be treated as a continuous broadband noise.

Separate criteria for repeated impulses with and without reflection are given as function of level and duration.

4.1.3. WHOLE BODY NOISE EXPOSURE

In order to prevent adverse effects of high levels of sound on the whole body a limit of 145 dB or 150 dBA, whichever is less, is specified for any octave band in the frequency range 1÷40000 Hz.

4.2. Communication

Three criteria are specified for the assessment of communication intelligibility in the presence of noise in a military aircraft.

4.2.1. ARTICULATION INDEX

The Articulation Index (AI) is a design criterion useful for predicting and resolving potential communication systems intelligibility problems quite early in the design process.

For a two seat fighter aircraft the AI criterion, applying to pilot/copilot and communication equipment, may be:

– UHF/VHF radio communication	AI ≥ 0.5
– Interphone communication	AI ≥ 0.3

Table 20.II reports the speech intelligibility associated to the AI value

ARTICULATION INDEX	SPEECH INTELLIGIBILITY
from 0.0 to 0.3	Unsatisfactory or marginally satisfactory
from 0.3 to 0.5	General acceptable
from 0.5 to 0.7	Good
from 0.7 to 1.0	Very good to excellent

Table 20.II - Quality of speech intelligibility

The AI shall be calculated in accordance with the third octave band calculation method reported in ANSI S3.5 and using predicted or measured noise spectra. A visual explanation of the calculation procedure is given in Figure 20.3

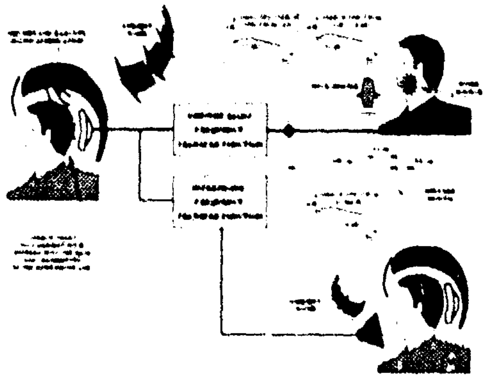

Figure 20.3 - Articulation Index calculation procedure

AI verification procedure for ground-to-air radio communication shall consider the following:

- talker mouth distance from the microphone, in order to exactly quantify the speech spectrum to be used (ANSI S3.5 reports an idealised speech spectrum at 1 m from the talker mouth);
- frequency transfer function of the communication system at different volume controls;
- ambient noise;
- headset sound attenuation.

AI verification procedure for air-to-ground and air-to-air radio communication and interphone communication shall also take into account for the oxygen mask transmission loss.

4.2.2. MODIFIED RHYME TEST

The Modified Rhyme Test (MRT) is a verification criterion for the worst case noise conditions.

The MRT is based on the understanding percentage of monosyllabic english words by operational personnel, routinely used by talkers and listeners, in a noise field that simulates the actual aircraft noise at the flight member's position. Scores less than 70% are considered unacceptable. Table 20.III shows a comparison between AI and MRT criteria.

A description of the MRT testing is contained in AFAMRL-TR-80-25, reporting on a facility located at USAF medical centre (Ohio), called VOCRES (VOice Communication Research Evaluation System).

A method for measuring the intelligibility of speech over communication systems is given in ANSI S3.2

COMMUNICATION REQUIREMENTS	SCORE	
	MRT	AI
Exceptionally high intelligibility, separate syllables understood	97%	0.7
Normally acceptable intelligibility, about 98% of sentences correctly heard, single digits understood	91%	0.5
Minimally acceptable intelligibility, limited standardised phrases understood, about 90% sentences correctly heard	75%	0.3

Table 20.III - Comparison between AI and MRT

4.2.3. SPEECH INTERFERENCE LEVEL

This criterion shall be applied in case of face-to-face communications to mission areas or phases in which they are critical or desirable.

Requirements are given in terms of SIL (alias PSIL) based on distance, level of communicating voice and criticality of communication. Verification must be done by analysis.

Confusion results between SIL and PSIL, as they are defined just in the opposite manner. The effects of different levels of noise on voice communication are shown in Figure 20.4

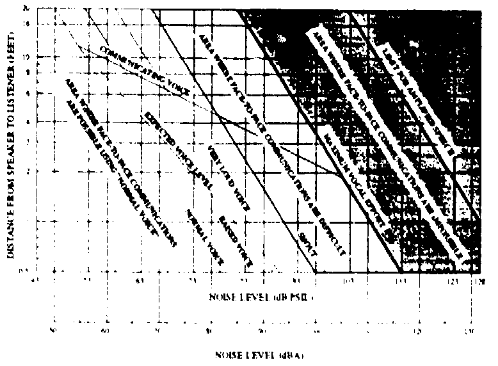

Figure 20.4 - Effectiveness of voice communication

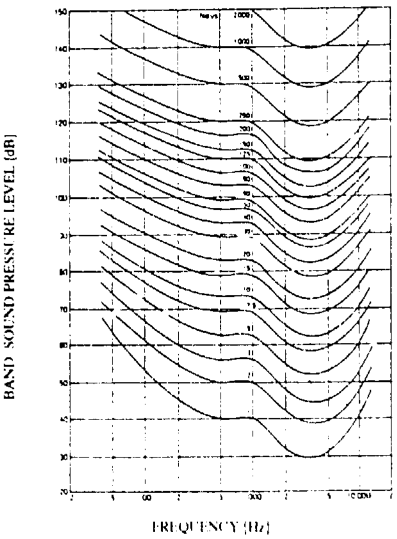

Figure 20.5 - Human response to sound loudness accounting for annoyance

4.3. Comfort

The subjective noise perception, in a military aircraft cockpit noise verification procedure, shall be considered as much as medical and communication impacts

Noise characteristics at pilot's ear may result unsatisfactory even if no hearing damage risk and good communication have been verified

The most annoying noise characteristics, despite an acceptable overall level, are tonality, sharpness and spectral distribution Helmet and earcups role on this matter, as already said before, is of fundamental importance

A suggested verification tool could be the PNLT index that, like dBA, is a weighted sound pressure level (based on the Noy curves) and combines human annoyance to loudness, also accounting for tonality characteristic of noise

Figure 20.5 shows how the human annoyance response curve changes as function of noise level The Perceived Noise Level (PNL) scale indicates that a change of 10 PNdB halves or doubles the annoyance

A simple mathematical transposition was developed that integrates the Noy values over an analysed 1/3 octave band spectrum to give a single-number annoyance value in perceived noise decibels (PNdB)

A special "penalty" for discrete tone (which varies with the frequency and the difference in level between the tone band and the adjacent frequency bands) is added to the PNL to account for the tone sensing characteristic of the human hearing system The final result of the computation is the tone corrected perceived noise level (PNLT)

Based on the Alenia/Aermacchi experience described in Chapter 9, the PNLT values scale reported in Table 20.IV is suggested for the evaluation of noise quality at pilot's ear

PNLT [dB]	NOISE QUALITY
below 90	Excellent
from 90 to 95	Very good
from 95 to 100	Good
from 100 to 105	General acceptable
from 105 to 110	Marginally satisfactory
above 110	Unsatisfactory

Table 20.IV - Possible scale for noise quality quantification

5. COCKPIT NOISE PREDICTIONS

Current state-of-the-art does not allow to perform an effective and accurate prediction of cockpit noise

When data from similar aircrafts are available the problem is rather simplified unless variations are foreseen in the auxiliary system arrangement or strong modifications of cockpit volume are necessary (e.g. transformation of a single seat fighter aircraft into a two seater)

Calculation methods to predict external noise exciting the cockpit surrounding structure are only available for a limited number of sources (i.e. turbulent boundary layer noise, jet noise, external store noise, cavity noise), resulting the aerodynamic contribution the principal one at high dynamic pressure

The quote part of external noise that is transmitted inside the cockpit through air paths is regulated by structure transmission loss and is a cockpit noise component of medium importance

Structure-borne noise is instead the major component but it is very difficult to be predicted in level.

FEM/BEM (Finite Element Model/Boundary Element Model) techniques represent a numerical tool for an acceptable acoustic design of the project. These techniques are currently used as a "what-if" methodology, that means that the model is used to evaluate trial modifications of the project until an acceptable noise and vibration reduction is achieved.

Even if large models are used the FEM/BEM qualitative assessment may be considered of sufficient confidence for the low frequency range (up to 200 Hz) but the predicted noise levels are still questionable. The advantage is the possibility to improve the acoustic design of the project ignoring the exact quantification of the exciting sources.

6. DESIGN RECOMMENDATIONS

Main attention for cockpit noise control shall be put in the structural, aerodynamic and environmental control system design.

Aerodynamic and environmental control system design recommendations are usually based on experience.

Structural design recommendations may be a result of FEM/BEM analysis. Nevertheless the mathematical modelling of the structure results to be available when the aircraft design has been fully developed, therefore noise and vibration problems which require major redesign actions are encountered when modifications are difficult to be introduced, unless delays in the design cycle and costs increase are accepted.

6.1. Structural design recommendations

The structural design shall consider both transmitted noise attenuation and source noise reduction The following guidelines may be stated

6.1.1. AIR-BORNE NOISE CONTROL

Cockpit surrounding structure shall match the right compromise of high mass and low stiffness to offer an acceptable barrier (transmission loss) to air-borne transmitted noise from outside For the current standard of airframe structures this component of cockpit noise is not of primary importance so the initial design may exclude peculiar solutions against air-borne noise Noise barriers can be quickly integrated into the thermal insulation treatment if required by prototype tests

Cockpit surrounding structure shall be as much as possible insulated from compartments or bays where specific noise sources are located (e g environmental control system bay, gun bay, etc) or high noise levels are expected to be reached (e g landing gear bay, weapon bay, IFRP bay for retractable installations).

Canopy transmission loss shall be comparable with fuselage sidewalls one. Plexiglas or polycarbonate canopies shall have a medium thickness not lower than 8 mm (better 12 mm) with higher values for large surfaces. Bullet-resisting solutions will offer both higher protection from outside noise and higher damping for canopy vibrations radiated noise. Cockpit noise penalties are to be expected when the ejection seat system requires canopy transparency with high brittleness characteristics.

Windscreen and canopy shall incorporate additional seals to the pressurisation one if high velocity air penetration in the coupling slots is expected to occur.

6.1.2. STRUCTURE-BORNE NOISE CONTROL

Structure-borne noise shall be controlled by avoiding the use of large panels and attempting to increase as much as possible, compatibly with weight restrictions, the frequency of the fundamental vibration modes, both of single panels and of assembled structure.

High frequency vibrations are unlikely to be coupled with cockpit volume acoustic modes and may be better controlled using sound absorbing and viscoelastic damping materials.

Viscoelastic damping materials acts to dissipate the vibrational energy in the structure that radiates as sound. Damping suppresses mainly resonant motion, out of resonance forced vibrations are slightly attenuated by the parallel effect of stiffness and mass increasing.

Viscoelastic selection shall account for frequency, temperature and thickness of the panel to be attenuated Constrained-layer damping systems shall be preferred to free-layer ones as more energy is dissipated by shear deformation of the damping layer. In the free-layer system energy is dissipated as a result of extension and compression of the damping layer.

Free-layer damping systems are attached directly to the structure surface with a bonding agent, constrained layer damping systems are bonded on a constraining layer so to form a sandwich when attached to the structure.

Large panels, like floor and bulkheads, shall have high characteristics of stiffness and damping to reduce sound radiation Sandwich solutions, consisting of two sheet of metal and a viscoelastic inner layer, are to be preferred for panels which are expected to be a significant noise source

Structural damping characteristics of components in composite materials may be increased by placing a SYNCORE ply in between the two skin

No physical connections shall be allowed between cockpit floor or bulkheads and ducts or pipes with high velocity internal flow.

Avionics bay doors shall be cured in order to maximise sealing and to avoid backlash and hammering of the locking levers.

6.2. Aerodynamic design recommendations

The aerodynamic design shall be addressed to minimise potential noise sources and to keep them as weak as possible.

Alignment of avionics bay doors, windscreen and canopy with airframe structure shall be cured to avoid both vortex shedding and air penetration.

Engine air intake shall be preferable located far away from the cockpit. The diverter profile for a subsonic aircraft shall avoid large flow accelerations that can generate shock waves and flow separation with great mechanical excitation of the cockpit surrounding structure. Mass air flow spillage and related vortex generation, usually occurring in flight for engine intake of fixed geometry, shall not impinge the fuselage otherwise an adequate shield plate shall be introduced.

Fixed non retractable IFRP installations require a proper aerodynamic design of the root fairing to avoid local sonic flow, shock waves and flow separation; nevertheless overall cockpit noise increments of 2+3 dB may be found.

The aerodynamic design of excrescences, antennae and avionics system fairings located near the cockpit shall follow the same criteria detailed for the IFRP fairing.

6.3. Environmental control system design recommendations

The air distribution line of the environmental control system requires proper design recommendations to avoid that an optimised mass air flow, based on environmental control requirements, results in a too high flow velocity for low noise levels.

The air velocity in the system should preferably not exceed 15 m/s and should be kept to be the same as far as possible

Bifurcations shall be foreseen before duct restrictions and air flow accelerations.

Flow balance orifices or elements producing a discrete disturbance shall be located at least 8 diameters upstream of the outlet.

Number of elements producing discrete disturbance in the distribution system should be kept to a minimum.

Plenum chambers to reduce propagating noise shall be considered; the interior surfaces shall be covered with sound absorbing material properly protected to avoid air flow abrasion.

Outlets air velocity shall be kept to a minimum. Jet related noise is not significant but noise resulting from the interaction between flow and guide vanes or grilles shall be controlled by the application of sound absorbing material.

If the pressure ratio of flow regulating valves exceeds 1.75 (internal flow almost supersonic) the exit flow velocity shall be progressively reduced by placing a porous septum of sintered metallic material (retimet) just downward the valve.

Sound tonalities that are expected to propagate in the air distribution line shall be attenuated by sound absorbing material inside ducts. Radiated sound from ducts shall be controlled using vibration damped solutions.

Ram-air inlet ducts shall be positioned far away from the cockpit and if long ducts are imposed by space restrictions intake NACA type shall be preferred to the SCOOP type, that can excite the inlet duct like an organ pipe.

6.4. Space provision for additional measures

Space provision for future modifications of the project that may be required by flight measurements shall be foreseen in the initial design to avoid possible rejections of the modification embodiment on cost-effective considerations basis.

This mainly applies to the environmental control system if plenum chambers have not been considered in the initial design or when an increase of air distribution ducts diameter will be required to introduce sound absorbing material.

Moreover the introduction of viscoelastic damping materials and sound absorbing materials on some fuselage panels may result impossible in retrofit if not considered in advance.

7. COCKPIT NOISE MEASUREMENTS

This is a very delicate point as measurements should be as more objective as possible.

Mil-Std-1789A suggests that measurements shall be taken at pilot's ear position with pilot absent, if possible. This is obviously impossible for a single seat fighter aircraft and only theoretically possible for a two seater; in fact, due to the small volume of the cockpit, the absence of one pilot can modify the acoustics of cavity

Microphones, tape recorders and analysers shall conform to the requirements of ANSI S1.2, S1.4, S1.6, S1.10, S1.11, S6.1

All tape recorded data shall be analysed in third octave band and a correction shall be made for the frequency response of the measurement and analysis system

Instrumented helmets should be used only for qualitative or semi-objective purposes as they can furnish variable measurements from flight to flight as function of test pilot use in tightening his helmet.

The use of a head simulator, when possible, will be the best solution in terms of objectivity of measurements.

8. ADVANCED NOISE CONTROL MEASURES

The demanding performance required from a modern combat aircraft results in little mass or volume available for passive noise attenuation.

The cockpit noise is typically on the order of 110+120 dB OASPL, with highest levels in the 250 and 500 octave bands.

The attenuation provided by the helmet is generally poor at low frequencies so the result is an unpleasant working environment for the pilot and a degradation of communication quality.

Speech intelligibility can be impaired by the noise picked up by the talker's microphone (reproduced in the listener's earphone) and by the noise reaching the ear directly through the helmet.

Noise cancelling microphones help to reduce noise in the first case; in the second case an Active Noise Reduction (ANR) system can be used at low frequency to complement the passive earphone noise attenuation at high frequency.

The objective of the ANR system is to create a quieter environment at the ear and clearer communication capability. This goal is achieved by cancelling the acoustic noise with an out-of-phase noise.

By using miniature microphones mounted inside special earcups of the headset, the system monitors the acoustic environment at the pilot's ear and compares it with the communication signal. The difference between the two signals is used to generate the out-of-phase noise.

Some ANR systems are close to qualification for use in modern military combat aircraft; with a light weight they by-pass all the low frequency cockpit noise problems that are difficult to be controlled using passive measures.

9. A SPECIFIC CASE

Recent experiences on a high subsonic two seat fighter aircraft, derived from the single seat version, allowed to collect data both for noise sources identification and cockpit noise verification.

Moreover the use of passive noise control measures, identified as cost-effective with relation to the current development state of the project, enabled to quantify the produced benefits on medical, intelligibility and operational aspects.

Two contributions were found to be dominant in the noise spectrum at rear pilot's ear and responsible of possible impacts on flight members for medical, intelligibility and comfort aspects at high performance flight conditions. The first contribution was the structure-borne noise originating by boundary layer turbulence, mass air flow spillage from engine intake impinging the fuselage (close to the rear pilot station), flow acceleration on the diverter profile and IFRP (fixed non retractable installation) root fairing effects; the second one was a pure tone introduced by the defrosting system, rather annoying at forward position only for moderate flight speed.

Figure 20.6 reports a schematic view of the aircraft and the noise sources location.

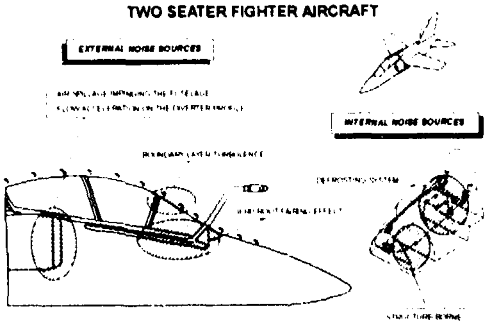
TWO SEATER FIGHTER AIRCRAFT
EXTERNAL NOISE SOURCES
AIR SPILLAGE IMPINGING THE FUSELAGE
FLOW ACCELERATION ON THE DIVERTER PROFILE
INTERNAL NOISE SOURCES
BOUNDARY LAYER TURBULENCE
DEFROSTING SYSTEM
IFRP ROOT FAIRING EFFECT
STRUCTURE-BORNE

Figure 20.6 - Two seater fighter aircraft schematic view and noise sources location

Cockpit noise measurements were collected using conventional instrumentation. In addition, in order to subjectively evaluate and objectively quantify noise and intelligibility at pilot's ear, an artificial head measuring technique was successfully adopted using the HMS II.3 HEAD ACOUSTIC SYSTEM. This is a head and torso simulator having human average characteristics (geometry and impedance) in particular with respect to the ear characteristics (see Figure 20.7).

Designed for experimental tests in the field of telecommunications, HMS II.3 is equipped with artificial mouth, ear simulators with B&K 4165 microphones (phase matched), preamplifiers, equalizers (to keep compatibility with conventional measuring systems), battery package (2 hours autonomy), digital recorder (remote control and high dynamics: 110 dB), play-back unit with electrostatic headphones.

The frequency transfer functions of aircraft system communications (UHF/VHF Radio and IC), useful for Articulation Index calculations, were measured with the HMS II.3 system; similarly the head and torso simulator was used in flight for the binaural recording of noise and communication signals at rear pilot's ear and to perform Modified Rhyme Tests (to evaluate interphone and ground-to-air radio communication quality using the play-back system). Helmet attenuation was verified and adjusted before each flight test to reproduce a medium earcups force previously identified to be wearing comfortable.

An ANR experimental kit was also installed inside the standard helmet and evaluated in laboratory tests and in-flight using the HMS II.3 system. In spite of some problems of ANR system tuning, a good attenuation was measured at low frequency making the noise environment more comfortable. The numerical result was confirmed by the subjective impressions after the listening of recorded data.

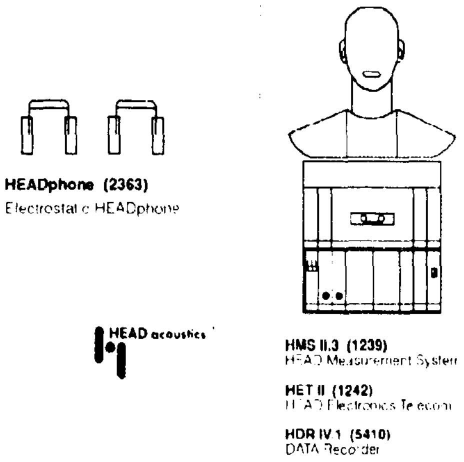

Figure 20.7 - Head Acoustic HMS II.3 System

9.1. Cockpit noise insulation kit

Due to the advanced development state of the project, largely qualified during ground and flight tests on the single seat version, no heavy modifications of the structure with possible impacts on engine performance were justified on cost-effective considerations basis.

Therefore structure-borne noise was controlled using passive measures and improving the IFRP root fairing design. Finally more attention was placed during aircraft assembling to minimise windscreen and canopy misalignment.

The lay up of the noise insulation kit (about 16 Kg) is schematically showed in Figure 20.8, while Figure 20.9 reports the modification of the IFRP root fairing which allowed a cockpit noise reduction of 2÷3 dB OASPL, depending on the flight speed.

To contain the structure radiated sound, constrained-layer viscoelastic damping materials where largely applied over the cockpit surrounding structure, with the exception of very stiff bulkheads.

Thermal insulation blankets on sidewalls, floor and rear bulkhead, already having good sound absorption characteristics, were modified by introducing a noise barrier polymeric sheet.

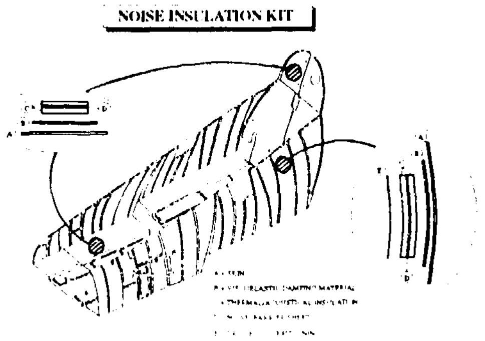

Figure 20.8 - Noise insulation kit lay up

Interior cockpit linings were drilled varying holes diameter and pitch as function of lining distance from the structure. The tuned frequency was kept as lower as possible (about 500 Hz). This modification contributed to reduce cockpit reverberation up to 2 dB OASPL, as measured during full power engine runs at rear position.

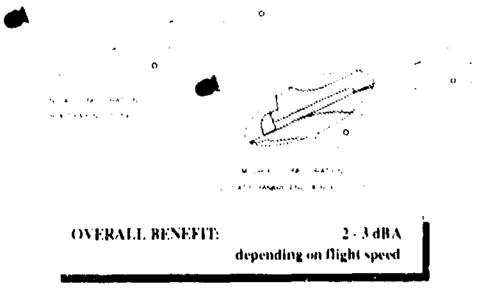

Figure 20.9 - IFRP root fairing modification and relevant benefit

The pure tone at a frequency of 500 Hz introduced by the defrosting system (DEMIST), particularly strong at front position and low flight speed, was completely cancelled by means of a slight modification of the main air distribution duct.

The modification (see Figure 20.10) was articulated as follows:

- duct diameter increasing, to keep the same section areas and flow velocities so to preserve the original mass air flow distribution,
- sound absorbing material insertion for tone attenuation, a proper surface protection was studied to avoid air flow abrasion.

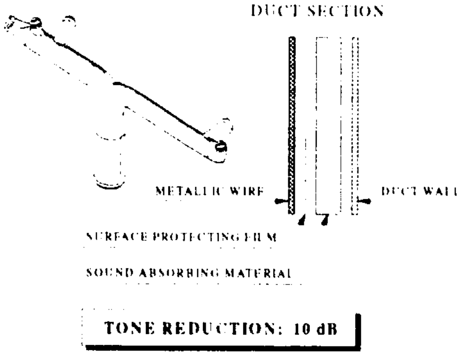

Figure 20.10 - Modification to reduce defrosting system tone

9.2. Overall benefits

Figure 20.11 reports the noise insulation kit benefits in terms of typical noise spectrum modification and dBA OASPL reduction at rear pilot's ear. Measurements were taken with the HMS II 3 system

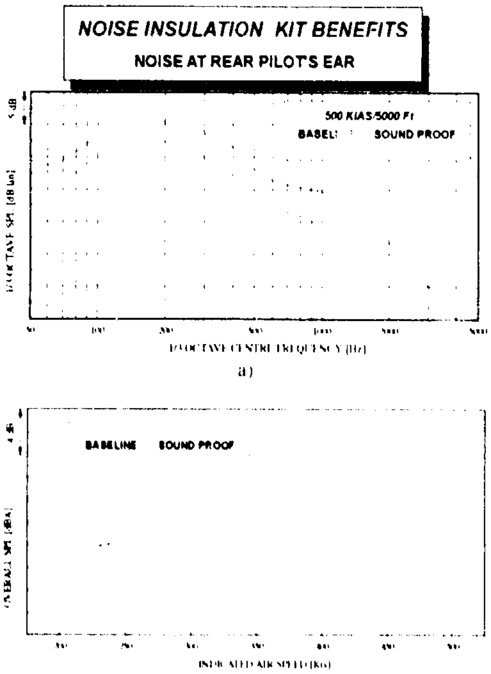

a)

b)

Figure 20.11 - Noise insulation kit benefits at rear pilot's ear: a) typical spectrum shape modification b) dBA OASPL reduction

9.3. Hearing damage verification

The noise insulation kit impact on the allowable number of daily missions, with no risk of hearing handicap, is showed in Figure 20.12 for the rear cockpit position and typical aircraft mission profiles.

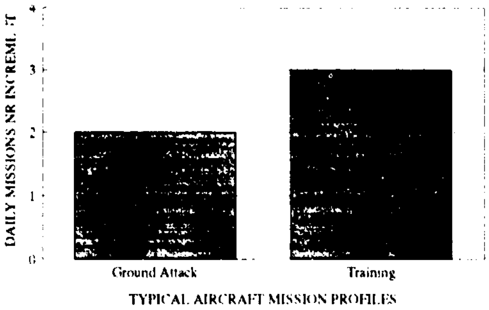

Figure 20.12 - Noise insulation kit benefits in terms of daily missions number increment (rear cockpit)

9.4. Communication intelligibility verification

9.4.1. ARTICULATION INDEX

Articulation Index were calculated for the UHF/VHF radio communication system and IC system on the basis of measured data. A synthesis of results is showed in Figure 20.13 for the rear cockpit and a range of communication systems volume control

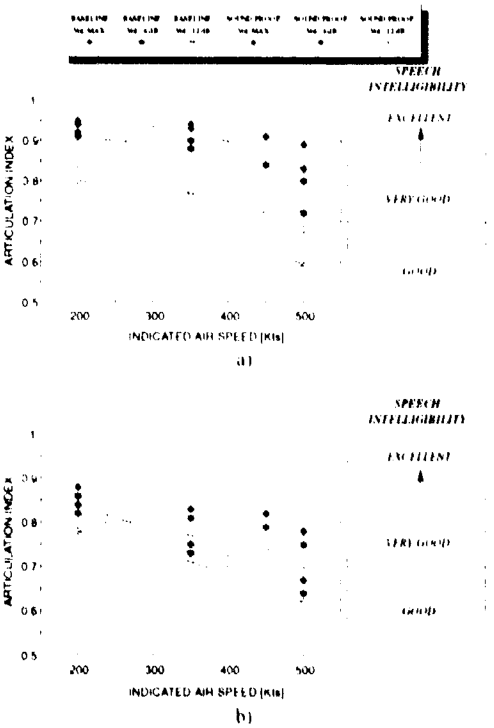

a)

b)

Figure 20.13 - Noise insulation kit effects on AI vs. indicated air speed (rear cockpit), a) UHF VHF radio communication, b) interphone communication

9.4.2. MODIFIED RHYME TEST

Intelligibility tests, according to ANSI S3.2 method, were in-flight carried out, for the sound proof configuration, using the HMS II.3 play-back system.

A preliminary phase for listeners skill to talker's pronunciation was necessary, being required the understanding of monosyllabic english words by subjects of no english mother tongue.

During flight at stabilised flight speed, corresponding to the worst noise environment, two different lists of 50 words were pronounced by the pilot (front cockpit), using the IC system, and by a ground operator, using the UHF radio communication system. Volume controls were selected to -12 dB. All words were recorded by the HMS II.3 data recorder and were successively listened, using the play-back system, by a limited sample of 5 subjects having available, for each listened word, a list of six words within which to select the right one. The MRT scores, corrected for chance, showed good correlation with the calculated AI values at same conditions.

9.5. Pilot comfort verification

In spite of a proved compliance to hearing damage risk and communication requirements, pilot reportings on noise quality were only favourable up to flight speeds quite close to the boundary.

This led to found a possible index, to correlate the objective measurements with the pilot subjective perception of noise, and a relevant scale of values, for a comfortable noise environment quantification.

Best correlation were found using the PNLT index; the calculated values and the suggested noise quality scale are reported in Paragraph 9.6.

9.6. Active Noise Reduction system evaluation

An experimental ANR kit was in-flight investigated after laboratory tests. Measurements were taken with the HMS II.3 system. Some tuning problems at a frequency of 800 Hz were identified despite a more promising specification requirement.

Nevertheless a good attenuation was measured at low frequency, making the noise environment more comfortable.

The impacts on hearing damage and communication intelligibility were instead not as expected because of the noise levels increment in the 1/3 octave band centred on 800 Hz.

Figure 20.14 reports the ANR benefits in terms of typical noise spectrum modification and dBA OASPL reduction at rear pilot's ear, both considering the experimental kit flight test measurements and the defined specification requirements for the active noise control system.

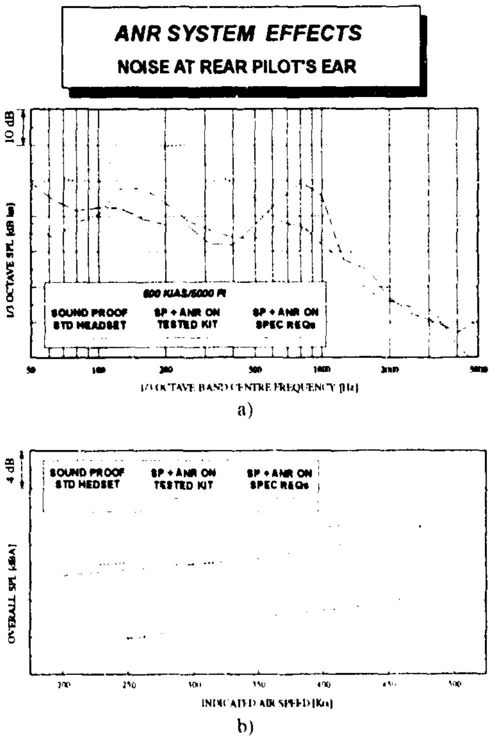

a)

b)

Figure 20.14 - ANR benefits at rear pilot's ear a) typical spectrum shape modification, b) dBA OASPL reduction

Similar impacts on the allowable number of typical daily missions, articulation index and pilot comfort are reported on Figures 20.15, 20.16 and 20.17, respectively.

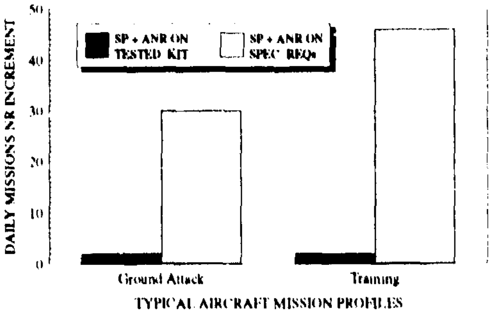

Figure 20.15 - ANR benefits in terms of daily missions number increment (rear cockpit)

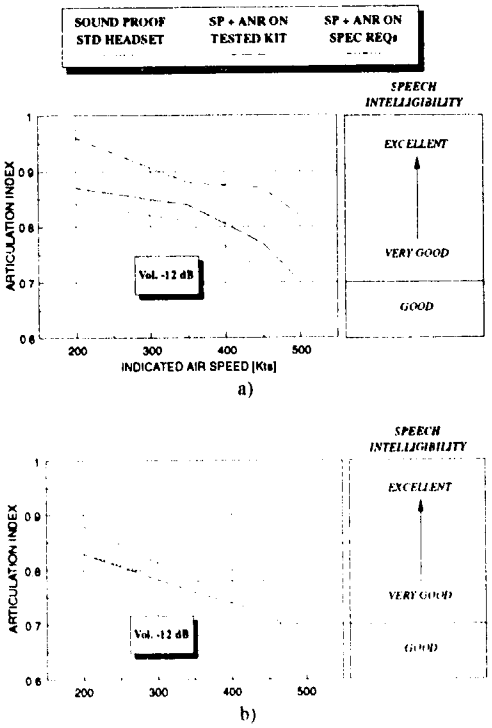

a)

b)

Figure 20.16 - ANR effects on AI vs. indicated air speed (rear cockpit). a) UHF/VHF radio communication, b) interphone communication

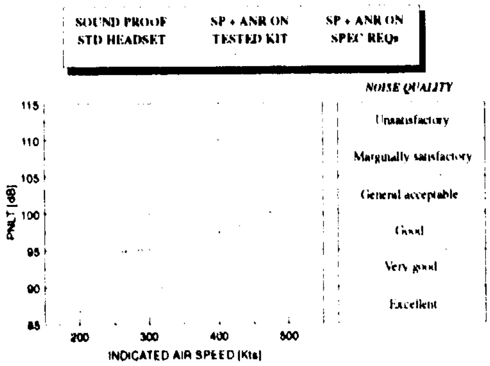

Figure 20.17 - ANR benefits on noise quality

10. CONCLUSIONS

The applicable concepts for cockpit noise verification in a military aircraft have been described giving emphasis to the applicable requirements for medical, intelligibility and operational impacts on flight members.

Structure-borne noise has been identified to be the dominant source and the most annoying component, as poor attenuation at low frequency is to be expected from pilot's standard headset. Design recommendations to contain the cockpit noise problem have been given and an adequate index to quantify the noise quality has been proposed.

Passive control measures can alleviate the overall level at pilot's ear and improve the allowable number of daily missions with no risk of hearing handicap. Some benefits on communication intelligibility and noise quality are also produced.

Active Noise Reduction system appears to be the more promising tool for low frequency noise control. The relevant benefits in terms of allowable number of daily missions, communication intelligibility and quality of noise are remarkable.

Noise Transmission and Reduction in Turboprop Aircraft

Douglas G. MacMartin, Gordon L. Basso
Institute for Aerospace Research
National Research Council of Canada
Montreal Rd., Bldg U-66A
Ottawa, Ontario, Canada
K1A 0R6

Barry Leigh
Structures R&D
deHavilland Inc.
Garrat Blvd., MS N18-06
Downsview, Ontario, Canada
M3K IY5

Abstract

There is considerable interest in reducing the cabin noise environment in turbo-prop aircraft. Various approaches have been considered at deHavilland Inc., including passive tuned-vibration absorbers, speaker-based noise cancellation, and structural vibration control of the fuselage. These approaches will be discussed briefly. In addition to controlling the noise, a method of predicting the internal noise is required both to evaluate potential noise reduction approaches, and to validate analytical design models. Instead of costly flight tests, or carrying out a ground simulation of the propeller pressure field, a much simpler reciprocal technique can be used. A capacitive scanner is used to measure the fuselage vibration response on a deHavilland Dash-8 fuselage, due to an internal noise source. The approach is validated by comparing this reciprocal noise transmission measurement with the direct measurement. The fuselage noise transmission information is then combined with computer predictions of the propeller pressure field data to predict the internal noise at two points.

1 Introduction

Numerous researchers, and many aircraft manufacturing companies have investigated approaches for reducing the noise within the cabin of commercial turbo-prop aircraft (see, for example [1-7].) The methods considered include structural modifications [1], passive damping [2, 3], and active noise [4, 6], or vibration control [5, 7]. DeHavilland Inc. (DHI) has tested tuned vibration absorbers (TVA's) and active noise cancellation systems, and is involved in investigating an active vibro-acoustic system. Prior to flight testing, these and other approaches must be evaluated both on models, and in preliminary ground testing. It is therefore necessary to characterize the aircraft cabin noise properties. The research program at DHI therefore involves two aspects, one on noise reduction techniques, and the other on modelling, model validation, and noise evaluation.

Externally generated cabin noise sources include boundary layer flow noise, acoustic excitation of the fuselage from the propeller, and structure-borne noise due to engine vibration and flow distortion over the wing [8]. For the deHavilland Dash-8 aircraft shown in Figure 1, the proximity of the propeller disc to the fuselage results in the narrowband acoustic excitation of the fuselage being the dominant source of noise.

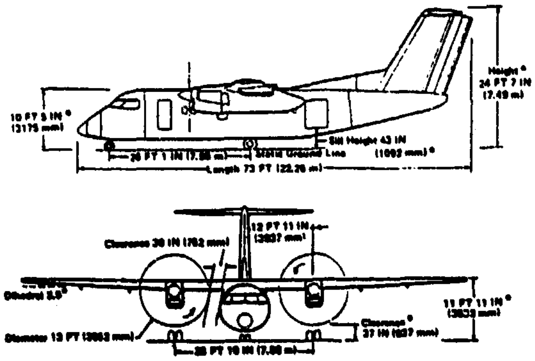

Figure 1: DeHavilland Dash-8 aircraft.

There are several options available for noise reduction. The structure can be modified by stiffening frames, or thickening skin, however, this yields substantial weight penalty for a given noise reduction. Passive acoustic or structural damping is not useful because the response is primarily forced, rather than resonant. Narrowband damping approaches using tuned vibration absorbers have yielded reductions of 10 dB [2], but the improvement is limited by the difficulty of keeping them tuned in a varying environment. The simplest active technique is synchrophasing, which should certainly be used. Flight tests of active control of the internal sound field have yielded 10 dB reductions [4, 6], however, many microphones and speakers are required to obtain this performance. An alternative active approach is to reduce the acoustic transmission of the fuselage using active structural control [5, 7].

Both for model-based design, and for evaluation, these techniques require a method for determining the cabin noise caused by the propellers. Flight tests are ultimately required, but in the early development stages of a potential noise reduction technique, they are undesirable because they are expensive. A ground simulation of the propeller noise field incident on the fuselage surface is possible [9], however this technique requires a complex two-dimensional array of many loudspeakers with mutual phases and gains correctly adjusted to reproduce the correct pressure distribution. This approach is limited in applicability, because the simulation will always be imperfect, and may also be quite expensive. Computer modelling of the propeller noise field, structural dynamics, and acoustic field can be used to predict the interior noise, however, these models must still be validated by experiment at some point in the design process.

An alternative approach to experimentally determining

Presented at AGARD 78th Meeting of the Structures and Materials Panel, Specialist's Meeting on Impact of Acoustic Loads on Aircraft Structures, Lillehammer, Norway, May 1994

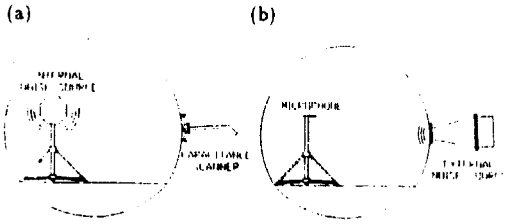

Figure 2: Schematic of reciprocal (a) and direct (b) measurement arrangement.

the cabin noise is to use a reciprocal technique. This approach is much simpler to implement than the direct simulation of the propeller noise field. For a linear, passive system, the response at one point due to a source at a second point is the same as the response at the second point due to a source at the first [10, 11]. Hence, rather than measuring the noise transmission from an external pressure source to a point in the interior of the aircraft, one can measure the surface vibration of the fuselage due to a point noise source inside the aircraft. This information can be combined with computer predictions of the propeller pressure, to predict cabin sound levels. One advantage of such a technique is that once the noise transmission data have been obtained, the internal noise can be predicted for any pressure distribution, corresponding to different engine rpm or flight conditions.

A reciprocal approach for examining structure-borne sound transmission into aircraft has been suggested by Vér [12, 13], who gives an experimental validation comparing the direct and reciprocal transfer functions between a point force and internal sound pressure. Mason and Fahy [14–16] developed a reciprocal approach for measuring transmission from external sound pressure to internal noise. The approach subdivides the surface area into small scan elements, and uses a capacitive measurement of the surface vibration on each element. The technique was validated on a box, with excellent agreement obtained between direct and reciprocal measurements. The reciprocal technique was then used for noise evaluation on scale models of aircraft-like structures [15].

This paper gives a summary of the noise reduction techniques considered at DHI, and then describes the collaborative research involving the National Research Council of Canada (NRC) and deHavilland Inc. on reciprocal noise transmission measurements. This research extends the work of previous authors by developing, validating, and demonstrating a reciprocal approach for measuring sound transmission through the fuselage on a full-scale aircraft. As in Mason and Fahy's work, a monopole sound source is located inside the fuselage, and a non-contacting capacitive probe is used to measure the external surface vibration. The arrangement is shown schematically in Figure 2. To verify reciprocity, the direct transfer function is also measured, using a horn designed to insonify a single element of the fuselage surface. Excellent agreement has been obtained between direct and reciprocal measurements.

The aircraft surface is scanned, and the data obtained is combined with propeller pressure field information to predict the interior noise at two locations. The prediction agrees well with measured flight test data. Finally, the total number of scan elements used is gradually reduced, to determine the minimum number required to obtain a useful prediction.

2 Noise Reduction Techniques

deHavilland Inc. has been a pioneer in the production of regional aircraft with low exterior noise [17]. For a number of years, it has been recognized at deHavilland Inc. that cabin noise levels in turbo-prop regional aircraft must be reduced until they approach those of turbofan powered airliners. Various passive and active methods of cabin noise reduction have been investigated.

The most obvious approach is to first apply control to the relative speeds of rotation of the propellers. This strategy, known as synchronizing, minimizes the annoyance of modulation, or "beating", of the propellers. It is then recognized that the sound fields of the individual propellers can be made to interfere destructively by controlling the relative phase angle of the propellers. This strategy, known as synchrophasing is clearly just a refinement of propeller synchronizing and both are almost always used. The propeller manufacturer designs and builds an effective control unit which the airframe manufacturer then integrates into the aircraft. Noise reductions of several dB(A) are possible, with minimal associated weight penalty and cost.

Typically, the optimization of the angle has been based on flight test data. Microphone information can be taken with the propellers running at different speeds, in order to separate out the effects of each propeller. A second test with the propeller speeds switched yields model information for both propellers at both speeds. Optimization of the relative angle is then straightforward. Only a small change in the optimal phase angle is observed depending on whether the cost function is the peak sound pressure level, or the mean-square level. This is illustrated in Figure 3, where the variation in peak noise, and in total acoustic power are shown as a function of the relative phase angle between the propellers, for a Dash-8 Series 100 aircraft.

The transmission of propeller noise into the cabin is a function of the design of the fuselage shell structure (frames, stringers, skins, etc.) and of both the structural design and attachments of the interior (bins, sidewall panels, etc.). Rigorous optimization techniques [18] and Taguchi (or Design of Experiments) techniques [19] can be used to design fuselage and interior structures with lower noise transmission properties. This strategy will be followed in future DHI designs. Often significant cabin noise reductions can be achieved only at the expense of some increase in weight. The cost is minimal if this strategy forms part of the initial design process.

Substantial effort has been invested in developing passive tuned vibration absorber (TVA) systems for both the Dash-8 Series 100 and Series 300 aircraft. These systems have been flight tested, and are currently available in production aircraft. Noise reductions of several dB(A) are obtained for a total weight penalty of tens of kilograms, along with the cost of the associated hardware.

The TVA is a one degree of freedom spring-mass-damper system with a resonance at one unwanted frequency, usually either the blade passage frequency (BPF) or 2×BPF at cruise engine rpm. Normally, TVA's are mounted on fuselage frames. In the vicinity of the resonant frequency

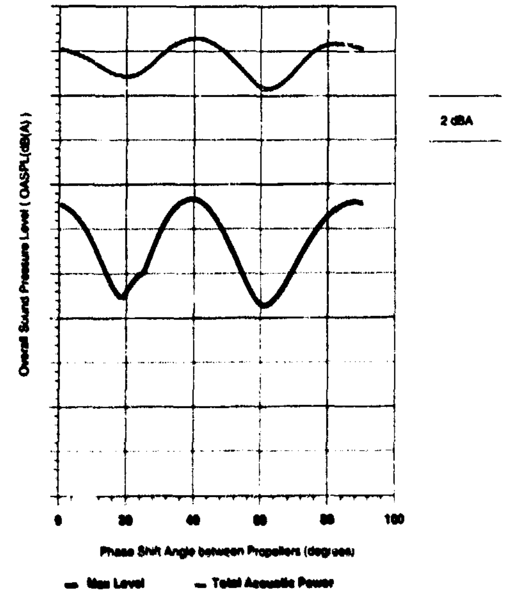

Figure 3: Variation in noise with synchrophase angle.

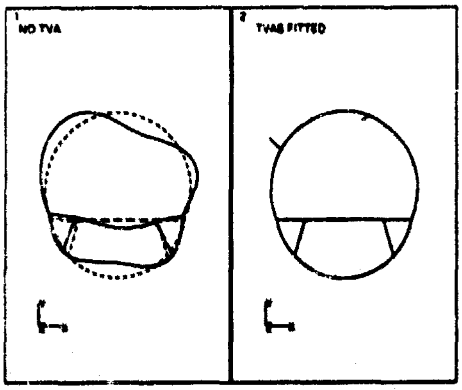

Figure 4: Improvement in deflection shape with TVA's.

the TVA provides a high impedance to vibration at its mounting point. Since the internal acoustic field is forced by the fuselage vibration, reducing these levels also tends to reduce cabin noise. Typical before and after vibration levels achieved on a Dash 8 Series 100 analytical model are illustrated in Figure 4.

In choosing the damping of the TVA, there is a design trade-off between low damping to give better performance at the resonance frequency, and high damping to increase the bandwidth of the dissipation. For this application, a relatively broad bandwidth must be chosen, due to changes in the engine rpm between cruise, climb, and descent, and variability in the system dynamics due to environmental and pressurization effects. This unfortunately translates into poorer performance for each TVA. In practice, the spring element is either metallic, resulting in low damping, or an elastomer selected for low sensitivity to temperature effects, giving moderate to high damping.

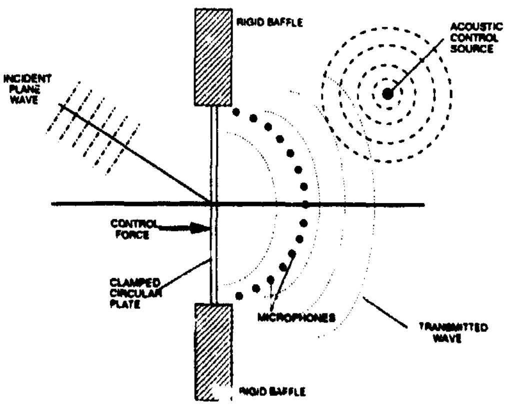

Figure 5: Active noise/vibration control systems.

The locations of the TVA's were chosen based on an intensive optimization that used a purely measurement-based model obtained during flight tests. This motivates the noise transmission studies discussed in the following sections of this paper, since in this case, project costs could probably have been reduced if a verified dynamic vibro-acoustic model were available for design purposes. Turn around time between designs could also be reduced. Finally, cost-benefit trade studies between the number (and thus the weight) of TVA's and cabin noise reduction could have been conducted.

One of the disadvantages of this passive approach, aside from the obvious weight penalty of placing masses in the fuselage, is that of either keeping the TVA's tuned in a varying environment, or accepting the performance reduction associated with increasing the TVA bandwidth. Moreover, the TVA is really only effective over the required range of operating speeds of the propeller, including takeoff, climb and cruise.

In order to reduce the noise level further, various active noise reduction schemes can be considered. One approach is to place a large number of speakers and microphones within the passenger compartment, and use an active noise cancellation (ANC) system to minimize the mean-square sound pressure level at the microphone locations. This setup is illustrated schematically in Figure 5. The engine rpm can be used as an input, so that extremely narrow-band controllers can be implemented, with correspondingly good performance. Similar systems have been flight tested on other aircraft [4,6], with noise reductions of approximately 10 dB. Flight tests conducted with NCT England on the Dash-8 aircraft have achieved generally similar results. The overall installation can be expected to weigh 50 kilograms or less, for a cost of between $10K and $100K.

While this approach has been successfully flight tested, there are still a few disadvantages in addition to weight and cost. It is difficult to integrate a large number of bulky speakers into the passenger compartment. There is a tradeoff between reduced speaker enclosure volume and efficiency. The reliability and maintainance cost of the system remain to be quantified. Finally, flight tests have shown that the system tends to increase cabin vibration levels, which are already high in a turbo-prop aircraft. This is to be expected since cabin accelerations are not typically included in the cost function of an ANC system.

An alternative active approach that is currently being investigated by DHI and NRC is to use structural actuators to control the fuselage vibration [7]. The active vibro-acoustic system is also shown in Figure 5, where a control force is used to reduce the structural vibration that creates the sound. This approach has the advantage that few actuators are needed, since the vibration need only be controlled where the propeller disturbance is highest. This immediately translates into a weight saving. Further advantages can be realized if feedback of structural motion is used rather than of the internal sound field. Similar noise reductions can be achieved, but with a simpler, less intrusive system. Because the transfer functions involved are simpler, robustness is improved, and simple control laws can be used. Simulations with a simple analytical model indicate that a noise reduction of 10 dBA can be achieved with a relatively small number of piezoelectric actuators bonded to fuselage frames [7]. Optimization of actuator and sensor numbers and locations will be determined based on a measurement model.

As with the other noise reduction techniques, design times and therefore cost can be reduced with a detailed analytical model. Such a model can only be used reliably for design if it is validated by measured data at some point in the design process. Therefore, it is necessary to consider simple approaches to obtaining measured data for model validation. The reciprocity technique described herein can also be used for evaluation of noise reduction techniques in ground testing.

3 Reciprocity Theory

Reciprocity was first shown to hold for vibrating systems by Lord Rayleigh [10] in 1873, and it holds for any linear, passive system [11], including vibro-acoustic systems. The aircraft fuselage will have some non-linear damping mechanisms, but the effect of these on the reciprocity relationship is small. The fundamental principle is that the transfer function from a source at one point to a response at another is the same as the transfer function with source and response interchanged. This property holds as long as the product of the input and output variables at each location is proportional to the power flow into the system. This property of systems is used extensively, because it is frequently simpler to measure the reciprocal transfer function than the direct transfer function of interest.

To conduct interior noise measurements due to the propeller pressure field, the external surface of the aircraft fuselage is first subdivided into a number of scan areas, as illustrated in Figure 6. The size of the scan area required is based on the minimum vibration wavelength to be considered, and on the fuselage structural dynamic properties. The subset of scan elements on which the external propeller pressure field is highest is considered, as indicated in the Figure. The noise transmission of the fuselage from each of these scan elements to each internal point desired is measured. The total internal noise is obtained by combining this information with the computer predicted propeller pressure field on each scan element, and summing over the propeller's acoustic "footprint".

The direct noise transmission transfer function on the aircraft fuselage is that from an external pressure field p_e applied to a single scan element to the pressure p_i at an

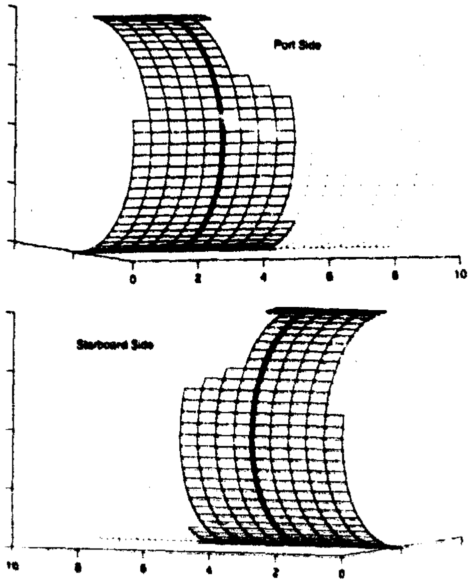

Figure 6: Fuselage scan elements for which noise transmission is measured. The area under the wing-box shroud is left blank. Elements shown dotted were not scanned. The propeller plane is marked with a solid line.

internal point (shown in Figure 2b). The transfer function p_i/p_e is the response that is required to predict internal noise. The *reciprocal* measurement is from an internal acoustic volume velocity source of strength Q_i to the vibrational volume velocity Q_e on the surface (shown in Figure 2a). This transfer function Q_e/Q_i is used instead of the direct measurement, because it is easier to measure the response of a single surface element than it is to apply acoustic loads to only that element. For a single element, reciprocity gives that these two transfer functions are equal:

$$\frac{Q_e}{Q_i} = \frac{p_i}{p_e} \qquad (1)$$

where both quantities are functions of frequency. Reciprocity holds because both $Q_e p_e$ and $Q_i p_i$ represent the power input to the vibro-acoustic system, due to the sources p_e and Q_i respectively.

Given the external pressure distribution, then the internal sound field can be computed as the sum over the N scan elements of the footprint,

$$p_i = \sum_{n=1}^{N} \left(\frac{Q_e}{Q_i} \right)_n (p_e)_n \qquad (2)$$

This form of the reciprocity relationship is clearly presented in [11, 16].

Once the transfer functions Q_e/Q_i have been measured, p_i can be predicted for any external field, i.e. any flight regime. The measurements can be made on operational aircraft without modification, and because the sensor is non-contacting, it does not itself change the response that is observed. However, the source Q_i must be located at each internal point for which p_i is desired, and the fuselage scanned. The number of scan elements required to get an accurate prediction may be large. However, if only the approximate difference in noise level between two cases is needed, then an adequate prediction of p_i could be obtained by measuring Q_e over a much smaller number of elements.

The reciprocal method can also be used to evaluate structure-borne noise. The internal sound pressure due to an externally applied point force is p_i/f_e. By reciprocity, this transfer function satisfies

$$\frac{p_i}{f_e} = \frac{v_e}{Q_i} \tag{3}$$

where v_e/Q_i is the response from the internal volume velocity source to a point velocity measurement taken using an accelerometer located at the point of force application. This result could be used to evaluate the contribution to the interior noise due to engine imbalance and wing vibration loads being transmitted into the internal acoustic field through the wing-box.

4 Experiment Equipment

The full-scale demonstration of the reciprocal approach for noise transmission measurements involves a monopole noise source located inside the aircraft, and a capacitive scanner to measure the external fuselage vibration. This measures the transfer function Q_e/Q_i in Equation (1) or (2). The approach was validated by comparing this transfer function for one element to the directly measured transfer function, p_i/p_e in Equation (1). The direct measurement required a horn designed to insonify a single element of the aircraft fuselage. The arrangement of the sensors and sources in the two approaches is shown in Figure 2. The equipment is described in detail below.

4.1 Aircraft Fuselage

The experimental aircraft is a deHavilland Dash 8 Series 100 fuselage without wings and empennage. The interior is 'green'; there is no trim or seats, although the internal insulation is present. As a result, there is less acoustic and structural damping than would be present in an actual aircraft. The aircraft was supported during the tests by an overhead crane attached to the fore and aft edges of the wing box on either side of the fuselage. The aircraft was prevented from swinging by foam-lined support stands that allowed scanning of the underside of the aircraft. This system provides a reproducible method of supporting the aircraft that is representative of the true flight conditions.

The external surface of the fuselage between the fore and aft ends of the passenger compartment was marked off into scan elements 21.5 inches axially by 5 inches circumferentially. The dimensions were selected so that the element boundaries are defined by the fuselage frames and stringers. The frames and stringers dominate the structural dynamics of the modes that couple with the internal and external acoustic field, and therefore, details of the skin vibration in between frames are irrelevant. The scan elements are labelled A through Q axially, and 01 through 64 circumferentially.

4.2 Monopole Sound Source

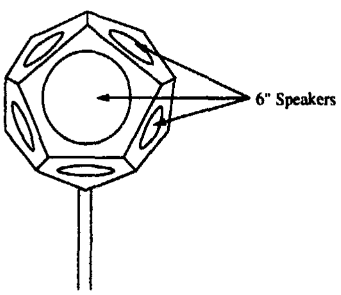

Figure 7: Schematic of dodecahedron noise source used for reciprocal measurements.

The internal sound source is a dodecahedron, shown schematically in Figure 7, with twelve 100 Watt speakers each centred on a pentagon of sides 6 inches. Based on the enclosed volume, the equivalent spherical radius is 7.5 inches, which is small compared to the wavelengths of interest. Calibration tests indicated that this configuration operates as a uniform monopole source between 50 and 500 Hz, except at distances on the order of the equivalent radius or smaller.

The sound source was calibrated in an anechoic chamber using a reciprocal approach. The transfer function from the drive current I_d applied to the dodecahedron source, to the voltage response E_a of an auxiliary speaker was measured. Next, the dodecahedron was replaced by a microphone, and the sound pressure P_d at that location due to the drive current I_a applied to the auxiliary loudspeaker was measured. Reciprocity gives that $E_a/Q_d = P_d/I_a$, since both $E_a I_a$ and $Q_d P_d$ represent power flow into the acoustic system. The calibration curve for the dodecahedron sound source is therefore given by

$$\frac{Q_d}{I_d} = \left(\frac{E_a}{I_d}\right)\left(\frac{I_a}{P_d}\right) \tag{4}$$

4.3 Capacitance Probe

Vibrational volume velocity of the external surface is measured with a hand-held capacitance probe, shown in Figure 8. The probe has a concave surface to match the fuselage curvature, and dimensions equal to a single scan element. The area-averaging effect of the probe is desirable, since only those features of the vibration that transmit sound effectively below 300 Hz are of interest.

The change in capacitance caused by fuselage motion is measured by the circuit in Figure 9. The 1000V polarizing voltage between the probe and aircraft is used to improve sensitivity. This does not pose a hazard to the operator, due to the high impedance of the circuit. The capacitance plate is shielded to reduce noise, and the aircraft is grounded.

The probe has four feet with built-in LVDT sensors and springs to give a measure of the pressure being applied. This information is displayed on a set of LED's so that the operator can maintain a constant holding pressure, and therefore constant offset. The resolution is 0.002 inches, corresponding to a measurement error of ±0.13 dB. The radius of curvature of the Dash 8 fuselage changes at approximately the floor level, and the position of each foot can be adjusted to maintain the correct offset while taking data in this region.

The probe was calibrated using a stiff lightweight plate with the same curvature, and with its first bending mode above the frequencies of interest. The calibration plate

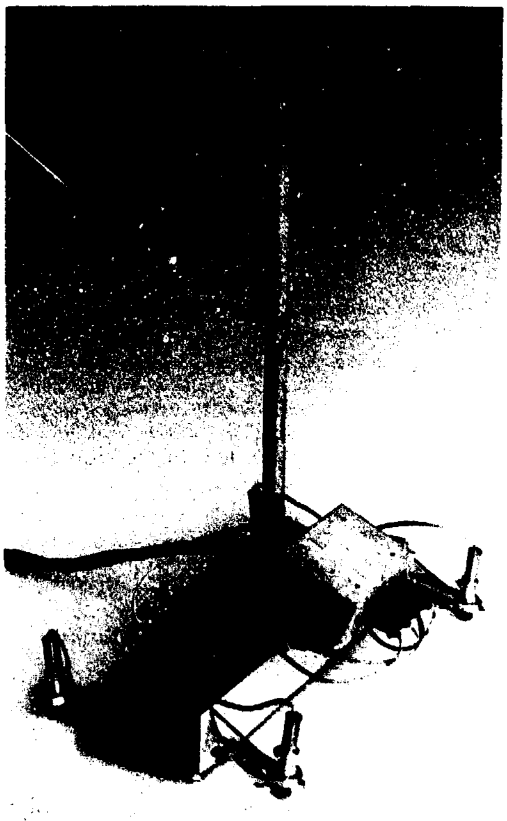

Figure 8: Non-contacting capacitance probe for surface velocity measurements.

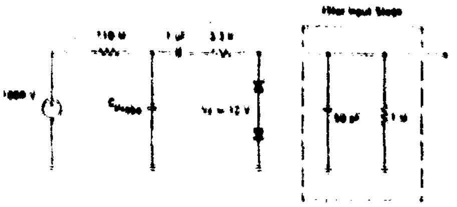

Figure 9: Capacitance probe circuit

was mounted on a shaker, and the output of the probe compared with the output of accelerometers mounted on the plate. At an offset of 0.25 inches, the probe output is approximately 10^4 V/(m/s), with an increase in sensitivity as the offset is decreased. Fringe effects are the order of the offset distance [20], and can therefore be ignored.

4.4 External Sound Source

To validate the reciprocal approach, the fuselage noise transmission properties of one element were measured directly, using a horn designed to insonify a single element of the aircraft fuselage, shown schematically in Figure 10. The inside walls of the horn are lined with foam, to eliminate acoustic resonances and improve the spatial and frequency uniformity of the sound pressure at the mouth of the horn. A probe with a microphone was used to obtain the average value of the pressure field impinging on the aircraft.

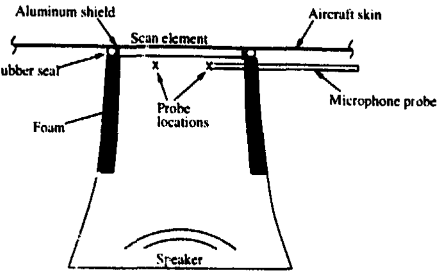

Figure 10: Schematic of external sound source used for reciprocity verification.

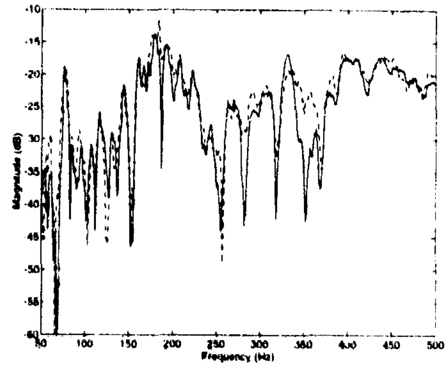

Figure 11: Magnitude of direct (solid) and reciprocal (dashed) measurements of the response from a point force to internal noise.

Particular care in the design of the horn must be paid to the quality of the seal between the horn and the aircraft. The seal used included both an aluminum shroud that did not quite touch the structure, and a flexible rubber hose. The rubber contacts the structure, but does not alter the dynamics substantially due to its high compliance. Even with a good seal, other elements receive substantial noise, due to both leakage from the seal, and radiation from the sides of the horn. The results of a scan of the noise on nearby elements indicated that the total force applied to the structure over all other elements is roughly one third of that applied to the desired element. Thus, it is likely that the extraneous excitation from the horn is the primary source of discrepancy between the direct and reciprocal measurements.

5 Reciprocity Verification

Several experiments were performed on the Dash 8 fuselage to verify that the system obeyed reciprocity, and that the equipment used provided the desired behaviour and did not itself alter the transfer functions being measured. A typical comparison of the direct and reciprocal transfer functions in Equation (4) is given in Figure 11. These data were obtained using a shaker and load cell to force the external surface at a single point, and an accelerometer to measure the surface motion. The reciprocal transfer function used the dodecahedron internal noise source. The point reciprocity test verifies that the vibro-acoustic system is indeed reciprocal, and also verifies the operation of the internal noise source.

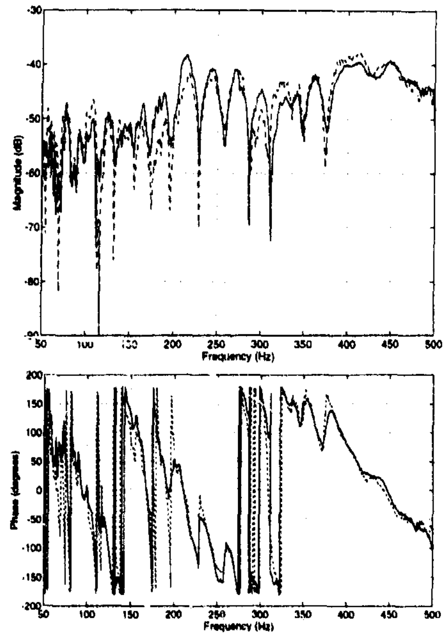

Figure 12: Element reciprocity verification, near location. Direct transfer function (solid) and reciprocal (dashed). Both magnitude and phase are shown.

Results comparing the transfer function between external pressure excited by the horn and internal pressure, and between internal volume velocity generated by the dodecahedron source and the external surface vibration measured by the capacitance probe are shown in Figure 12. The magnitude and phase is shown for an interior location close to the excitation point. Excellent agreement is obtained. Note that while it is only the magnitude of the final prediction p_i that is important, the phases of the transfer functions that are used to make this estimate are critical in order to correctly perform the sum in Equation (2). Furthermore, the good phase agreement provides additional verification of the accuracy of reciprocity.

6 Scan Results

6.1 Procedure

Two dodecahedron noise sources were located in the fuselage interior; one near the peak of the port propeller pressure field, and a second on the starboard side of the aircraft approximately one propeller diameter aft. Both interior points were at the head height of a seated passenger. The capacitance probe was then used to measure the transfer function from the internal volume velocity generated by each dodecahedron to the fuselage volume velocity on 480 of the external scan elements.

Only these elements on which the applied propeller pressure field was within approximately 15 dB of the peak pressure were scanned. The propeller pressure information used was obtained from the propeller manufacturer, and is based on a free field model evaluated at the surface of the aircraft fuselage. As a result, the predicted pressures will be conservative, since the model does not take into account either the reflected field nor any other installation effects. This footprint information is shown superimposed on a "map" of the scan elements, in Figure 13. The centre of the distribution is higher on the aircraft on the port side (where the propeller tips are downsweeping) than on the starboard side. The peak pressure is also higher on the port side. The spatial drop off of the pressure from the peak is far more rapid at higher harmonics, and hence it is the distribution at the blade passage frequency that determines which elements need to be scanned.

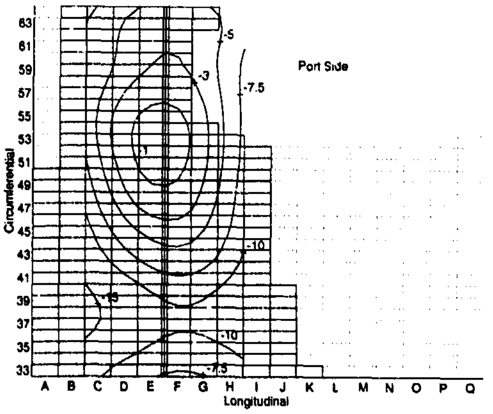

Figure 13: Propeller pressure field magnitude, dB with respect to peak, on port side of aircraft, 1×BPF. The area under the wing-box shroud is left blank. Elements shown dotted were not scanned.

A few elements could not be scanned due to surface protrusions either in that element, or in adjacent elements on which the scanner feet lie. This problem could be alleviated if the offset was determined and maintained based on the actual offset of the plate, rather than on the offset of the feet.

The aircraft cross-section in Figure 2 is drawn to scale; it is important to note that the radius of curvature of the aircraft is not constant. The offset of the scanner had to be individually adjusted for three rows of elements near the floor on either side, where the radius of curvature is only 20", as compared with 53" above this, and 62" below.

6.2 Internal Noise Predictions

The information collected for each scan element can be combined with the propeller pressure field information to predict the internal noise at the dodecahedron noise source locations. Once the scanned data are available, any number of pressure cases can be considered. The response was computed for both the blade passage frequency and the next harmonic for two engine speeds.

Elements for which no data were available due to the wing shroud were ignored; it is assumed that there is little transmission through the extra skin layer. Elements for which no data were available due to a problem in scanning the element were reconstructed based on the average over existing neighbouring elements.

For each case, the internal noise that would have resulted had the disturbance frequency differed by a few percent was computed. The scanned data were used at different frequencies in addition to that desired, however, the ef-

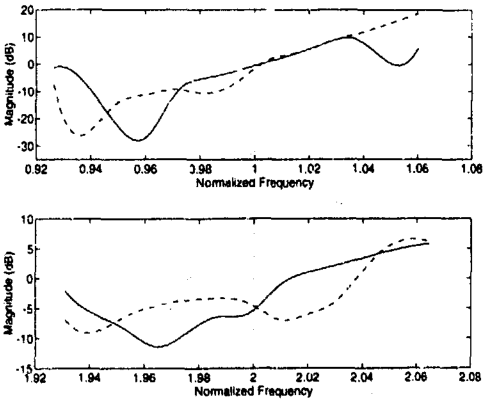

Figure 14: Normalized internal noise prediction at location 1 (solid) and location 2 (dashed). At 1×BPF (upper) and 2×BPF (lower). The frequency of interest is shown by the dotted line.

	BPF		2×BPF	
	near	far	near	far
lower rpm	2.1	−4.9	2.7	−15
higher rpm	0.0	2.1	−2.3	−3.0

Table 1: Average predicted internal noise levels for different engine rpm, at 1 and 2×BPF, and at a near internal point and a far one. dB(A) with respect to the 1×BPF response at the near location for the higher rpm.

fects of the frequency variation on the loading distribution were not accounted for. The reasons for including additional scanned data are twofold. First, errors in the data at a single frequency would produce poor predictions at that frequency. This is particularly important near 60 Hz, where electrical noise affects the results. Second, the variation in internal noise over nearby frequencies is indicative of the variation that could be expected between aircraft or between different operating conditions. Modal frequencies are likely to vary by several percent, and therefore, the variation in the response of a single aircraft over a similar frequency range is representative of the variation in response that may be observed between aircraft. Hence, the average response over neighbouring frequencies is a better prediction of the internal noise than the prediction at only the desired frequency.

Figure 14 shows the internal noise predicted for the higher of the two engine rpm cases considered, for a range of frequencies about the blade passage frequency (BPF) and 2×BPF. The magnitude is normalized by the average response at the first location. The prediction varies by as much as 10 dB from the average values, which are shown in Table 1. The average levels were computed with a triangular weighting on the nearby frequency points, and are consistent with those measured for these harmonics on actual aircraft in flight. The specific entries in this table are not as important as the observed trends. On average, the noise at the near location was 4.2 dBA higher than that at the far location. The response at the blade passage frequency was 2.7 dBA higher than that at the next harmonic. And the response at higher engine rpm was on average 0.9 dBA higher than at the lower speed.

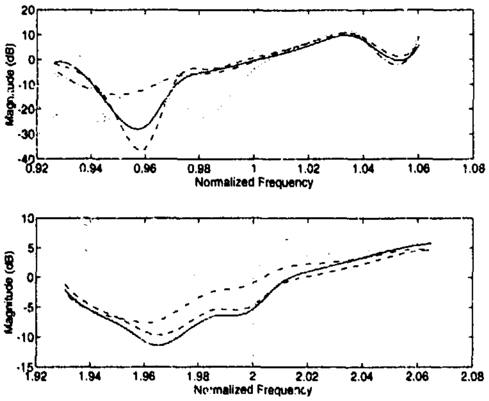

Figure 15: Normalized internal noise prediction using fewer elements. Using all information (solid), only those elements with at least 15 dB below the peak pressure on them (dashed), only elements with 10 dB (dash-dot) and only those with 7.5 dB (dotted). Data is for location 1, at 1×BPF (upper) and 2×BPF (lower).

			Predicted Noise (dB)			
dB level	# elements		1×BPF		2×BPF	
kept	BPF	2×BPF	near	far	near	far
All	450	450	0.0	0.0	0.0	0.0
−15	377	306	1.0	0.2	−0.1	1.9
−10	292	186	0.7	0.6	1.9	5.6
−7.5	202	125	−0.5	1.9	4.2	6.9
−5	95	53	−1.9	1.8	7.1	5.7

Table 2: Change in predicted noise using fewer elements.

Of particular interest is the number of elements that must be scanned to develop an adequate noise prediction. The effort involved could be greatly reduced if fewer elements were required. The noise prediction in Figure 14 used all of the transmission and pressure information available on the aircraft, for a total of 450 elements. For one of the propeller pressure cases, Figure 15 shows the same prediction using only those elements on which the pressure field was highest. Curves are shown for the cases in which those elements that received less than 15 dB below the peak pressure were dropped, less than 10 dB, and less than 7.5 dB. The number of elements used, and the change in the average noise predicted for these cases are shown in Table 2. In general, the reduction in elements kept to the 15 dB level does not substantially alter the prediction. Some degradation occurs at the 10 dB level, and with a further reduction in elements, the prediction quality suffers further. This table implies that fewer elements than the total used herein could be scanned, while still providing an adequate prediction. Furthermore, even with the least number of elements considered, the trends in the data are still noticeable. Thus to establish how much reduction has been obtained by a particular noise reduction scheme, a small number of elements may be adequate.

7 Conclusions

Various approaches to cabin noise reduction have been considered at deHavilland Inc. All of the approaches have drawbacks, however, a vibro-acoustic approach involving structural actuators holds promise.

A reciprocal technique was used to measure the noise transmission characteristics of an aircraft fuselage. This approach can be used for validating computer models, or for evaluating noise reduction methods. The fuselage was divided into a number of scan elements, and the transfer function between interior noise and the response on each element was combined with a specified external propeller pressure field to predict the interior noise at specified locations. The approach uses a monopole noise source inside the aircraft, and a capacitance probe to measure the fuselage surface response. The approach was validated by comparing the direct transfer function for one element with the reciprocal measurement. Excellent agreement between these measurements was obtained.

The total time taken to perform the scan could be reduced by reducing the number of elements used. A reasonable prediction of internal noise is obtained if only those external elements on which the propeller pressure field is within 10 dB of the peak are measured. Further improvements could be made with a lighter scanner to reduce operator strain, or an automated system for moving the scanner. A low bandwidth active control of the offset distance would also reduce the requirements on the operator, and improve accuracy. The data also indicate that the probe used herein provided unnecessary circumferential resolution, however, a larger probe would have been unwieldy. Additional noise sources, or an automated approach to moving those used, would be useful in obtaining noise predictions throughout the cabin.

Acknowledgements

The reciprocity work was a collaborative research and development project with NRC and deHavilland Inc. Dr. Frank Slingerland at NRC played an instrumental role in developing this technique. The assistance of Luc Hurtubise, Michael Baranowski, and numerous others at NRC is greatly appreciated. Work on noise reduction at DHI involved Ralph Garcea, Ray Wong, and many others.

References

[1] Bhat, R. B., Sobieszczanski, J., and Mixson, J. S., "Reduction of Aircraft Cabin Noise by Fuselage Structural Optimization," in *Noisexpo*, 1977, pp. 40-45.

[2] Waterman, E. H., Kaptein, D., and Sarin, S. L., "Fokker's Activities in Cabin Noise Control for Propellor Aircraft," SAE Paper 830736, 1983.

[3] Halvorsen, W. G. and Emborg, U., "Interior Noise Control of the Saab 340 Aircraft," SAE Paper 891080, April 1989. General Aviation Aircraft Meeting and Exposition.

[4] Elliot, S. J., Nelson, P. A., Stothers, I. M., and Boucher, C. C., "In-Flight Experiments on the Active Control of Propeller-Induced Cabin Noise," *J. of Sound and Vibration*, Vol. 140, No. 2, 1990, pp. 219-238.

[5] Fuller, C. R., Snyder, S. D., Hansen, C. H., and Silcox, R. J., "Active Control of Interior Noise in Model Aircraft Fuselages using Piezoceramic Actuators," *AIAA Journal*, Vol. 30, No. 11, Nov. 1992, pp. 2613-2617.

[6] Borchers, I. U., Renger, K., Paillard, J., Billoud, G., Koers, P., and Doppenberg, E., "Selected Flight Test Data and Control System Results of the CEC BRITE/EURAM ASANCA Study." in *Inter-Noise*, (Leuven, Belgium), August 1993, pp. 59-64.

[7] MacMartin, D. G., "Piezoelectric Control of Aircraft Cabin Noise," in *Third International Congress on Air- and Structure-Borne Noise*, (Montreal, Canada), June 1994.

[8] Mixson, J. S. and Powell, C. A., "Review of Recent Research on Interior Noise of Propeller Aircraft," in *AIAA/NASA 9th Aeroacoustics Conference*, (Williamsburg, VA), Oct. 1984. (AIAA Paper 84-2349).

[9] Hackstein, H. J., Borchers, I. U., Renger, K., and Vogt, K., "The Dornier 328 Acoustic Test Cell (ATC) for Interior Noise Tests and Selected Test Results," in *DGLR/AIAA 14th Aeroacoustics Conference*, May 1992. (DGLR/AIAA-92-02-164).

[10] Rayleigh, J. W., "Some General Theorems Relating to Vibrations," in *Proc. of the London Mathematical Society*, Vol. 4, 1873. See also, *Theory of Sound*, Vol. I, pp. 104-110, Dover Publications, 1945.

[11] ten Wolde, T., "On the Validity and Application of Reciprocity in Acoustical, Mechano-Acoustical and other Dynamical Systems," *Acustica*, Vol. 28, 1973, pp. 23-32.

[12] Vér, I. L., "Some Uses of Reciprocity in Acoustic Measurements and Diagnosis," in *Inter-Noise*, (Munich), Sept. 1985, pp. 1311-1314.

[13] Beranek, L. L. and Vér, I. L., *Noise and Vibration Control Engineering. Principles and Applications*, Wiley, New York, 1992.

[14] Mason, J. M. and Fahy, F. J., "Development of a Reciprocity Technique for the Prediction of Propellor Noise Transmission through Aircraft Fuselages," *Noise Control Engineering Journal*, Vol. 34, No. 2, March-April 1990, pp. 43-52.

[15] Mason, J. M., *A Reciprocity Technique for the Characterisation of Sound Transmission into Aircraft Fuselages*, Ph.D. thesis, University of Southampton, July 1990.

[16] Fahy, F. J., "The Reciprocity Principle and Applications in Vibro-Acoustics," in *Proceedings of the 2nd International Congress on Recent Developments in Air- and Structure-borne Sound and Vibration*, (Auburn University), March 1992, pp. 611-618.

[17] Cicci, F. and Toplis, A. F., "Noise Level Measurements on a Quiet Short Haul Turboprop Transport," in *Business Aircraft Meeting*, (Wichita, KS), SAE, April 1976. Paper 760455.

[18] Brama, T., "The Structural Optimization System OPTSYS - Current Status and Applications," in *Integrated Design Analysis and Optimisation of Aircraft Structures*, (Bath, U.K.), AGARD, May 1991. AGARD-R-784.

[19] Ealey, A. L., *Quality by Design - Taguchi Methods and the U.S. Industry*, ASI Press, Dearborn, MI, 1988.

[20] Seely, S. and Poularikas, A. D., *Electromagnetics: Classical and Modern Theory and Applications*, Marcel Dekker Inc., New York, 1979.

Advanced Statistical Energy Analysis

K. H. Heron
Defence Research Agency
Farnborough, Hampshire GU14 6TD
U.K.

1 SUMMARY

A hign-frequency theory (advanced statistical energy analysis (ASEA)) is developed which takes account of the mechanism of tunnelling and uses a ray theory approach to track the power flowing around a plate or a beam network and then uses statistical energy analysis (SEA) to take care of any residual power. ASEA divides the energy of each sub-system into energy that is freely available for transfer to other sub-systems and energy that is fixed within the sub-system. The theory allows for coupling between sub-systems that are physically separate and can be interpreted as a series of mathematical models, the first of which is identical to standard SEA and subsequent higher order models are convergent on an accurate prediction. Using a structural assembly of six rods as an example, ASEA is shown to converge onto the exact results whilst SEA is shown to overpredict by up to 60 dB.

2 INTRODUCTION

Statistical energy analysis (SEA) has been successfully applied to many noise and vibration problems. In particular SEA has become very useful as a framework for interpreting a vibro-acoustic data base. SEA often leads to a better understanding of the problem and SEA can point the way to practical solutions. However when used as a purely predictive theory, without the recourse to measured data, SEA has not been universally successful. Nevertheless in some cases it has been very successful, for example when used to model the interaction between the noise in a room and its vibrating walls, but when applied to complex structural assemblies SEA predictions have often exhibited errors. These errors have been thought due to the fact that plates and beams are usually strongly coupled and one of the assumptions within standard SEA theory (see, for example Lyon[1]) is that all couplings are weak. However, Keane and Price[2] conclude that this assumption should be replaced by the necessity that no individual mode within a given sub-system should dominate the overall response of that sub-system, and this requirement can be met *either* by assuming weak coupling *or* by assuming the presence of many interacting modes. Furthermore, if SEA theory is developed using the wave approach rather than the modal approach this weak coupling assumption does not appear to be required (see, for example Heron[3]).

In this paper we postulate that the errors that sometimes occur when predictive SEA is applied to complex structural assemblies are mainly due to an as yet un-modelled power transport mechanism. This 'tunnelling' mechanism conceptually occurs when direct coupling exists between two SEA sub-systems that are physically separated from each other by other SEA sub-systems. This mechanism of indirect coupling must not be confused with the power transport mechanism by which plate in-plane motion can couple physically separate bending motions; this latter phenomenon is fully modelled by existing SEA theory provided the in-plane sub-systems are included in the model.

A very simple form of tunnelling is associated with the non-resonant acoustic transmission through a plate and is already included in existing SEA theory (see, for example, Price & Crocker[4]; Leppington *et. al.*[5]). However this special case is mainly a function of the change in the dimension between the plate and the adjacent rooms and is not the concern of this paper.

Standard predictive SEA assumes zero coupling between the end plates of, for example, an in-plane assembly of three in-line plates. In this paper we develop a theory that allows for all sub-systems to be coupled to each other. Unlike for the simpler case of non-resonant acoustic transmission through a plate, we would intuitively expect this new theory to produce coupling loss factors that are not only a function of the power transmission coefficients across the various intervening line junctions, but are also dependent on the geometry and damping of the intervening plates.

In the following sections this theory is developed both for beam and plate networks and for want of a better name we will subsequent refer to this theory as advanced SEA or simply ASEA . Fundamentally it uses a ray theory approach to track the power flowing around the network and then uses standard SEA to take care of any residual power.

3 FREE AND FIXED ENERGY

Now all deterministic theories (modal, analytic, FEM, etc.) use field variables such as displacement and pressure and they must therefore include phase in the model, and the very essence of a high frequency model is the simplification associated with ignoring these phase

Presented at a Symposium on 'Impact of Acoustic Loads on Aircraft Structures' held in Lillehammer, Norway, May 1994.

effects. It is not just the need for computational efficiency which drives us to this assumption but as Hodges & Woodhouse[6] point out as we move to higher frequencies any deterministic approach becomes increasingly sensitive to the details of the physical structure under investigation, to such an extent that the results will be influenced by the deviations from the ideal design which inevitably occur in construction and such deviations are unknown. Thus all such deterministic approaches are rejected in this paper without further consideration; power accounting and the use of the sub-system energies as the field variables are the mainstays of SEA, and ASEA will be developed using the same philosophy.

The tunnelling phenomenon that we are attempting to model is associated with the transport of power, from sub-system 1 to sub-system 3 via an intervening sub-system 2 without at the same time inducing any increase in the 'free energy' of the intervening sub-system, and we must now consider what we mean by free energy.

With free energy we mean that part of the total sub-system energy that is available for transport to other sub-systems. In standard SEA all sub-system energy is free energy. Conversely the fixed energy of a sub-system is that part of the total sub-system energy that is not available for transport to other sub-systems. This postulate that the total energy of a SEA sub-system can be partitioned into a free and a fixed part is fundamental to ASEA theory.

Returning to the three in-line plate assembly example, we can now consider the following power flow mechanism. Free power associated with the free energy of sub-system 1 strikes the line junction between plate 1 and plate 2, this causes some power to transmit into plate 2 and as this power transports across plate 2 it will decrease in magnitude due to the damping mechanisms of plate 2. It is this loss of power that is self evidently not available for further transport duties and must be accounted for by a fixed energy field within plate 2. Finally some part of this transported power will strike the line junction between plates 2 and 3 where it will cause power injection into plate 3, and at this level of complexity such power will feed into the free energy field of plate 3.

4 SEA BASICS

Firstly we will find that it is helpful to rewrite the standard SEA matrix equation in a more convenient form for subsequent extension to ASEA such that

$$Ae = P - Me \qquad (1)$$

where e is a column vector of SEA modal energies, P is a column vector of input powers, M is a diagonal matrix of modal overlap factors, and A is a matrix of coupling loss factors. That is

$$M_{ii} = \omega\, n_i \eta_i \qquad (2)$$

where ω is the frequency, n_i is the modal density of sub-system i and η_i is the energy loss factor for sub-system i; furthermore for a three sub-system model A is given by

$$\omega \begin{bmatrix} n_1\eta_{12} + n_1\eta_{13} & -n_2\eta_{21} & -n_3\eta_{31} \\ -n_1\eta_{12} & n_2\eta_{21} + n_2\eta_{23} & -n_3\eta_{32} \\ -n_1\eta_{13} & -n_2\eta_{23} & n_3\eta_{31} + n_3\eta_{32} \end{bmatrix} \qquad (3)$$

where η_{ij} is the usual SEA coupling loss factor.

Of course the more usual SEA matrix equation can be recovered by combining the A and the M matrices in (1). The reason for the above formulation will become apparent as we develop ASEA theory, but for now it is worth noting that each of the three terms in (1) now have a clear physical meaning; the left hand side term incorporates all the power transport and coupling effects and the two right hand side terms model all the power sources and all the power sinks respectively.

Furthermore, if all the equations in (1) are added together we have, by power balance, that the sum of all the right hand side terms is zero, and this is true for all possible P and thus for all possible e. Hence each individual column of A must always sum to zero, which is of course a trivial deduction from SEA. Indeed, assuming SEA reciprocity, A is a symmetric matrix and thus each individual row of A must also sum to zero. However, it is important to note that this row sum rule is a consequence of power balance *and* SEA reciprocity whereas the column sum rule is solely a consequence of the much more fundamental requirement of power balance.

5 ASEA BASICS

In developing ASEA theory we will, as described above, split the total energy field within each sub-system into two parts, a free energy field with a modal energy of e, and a fixed energy field with an 'equivalent' modal energy of d. The term 'modal energy' is used because of its historic link with classical SEA theory, however the reader might find it easier to think of the modal energy as a measure of the energy density of a sub-system with which it is closely related for sub-systems made up of simple beams, plates or rooms.

Using the column vectors e and d as the field variables, ASEA can be encapsulated by the following two matrix equations

$$\begin{array}{ccccc} Ae & = & P & - & Me \\ \begin{array}{c}\textit{free power}\\ \textit{to free}\\ \textit{power}\\ \textit{transfer}\end{array} & & \begin{array}{c}\textit{free power}\\ \textit{input}\\ \\ \\ \end{array} & & \begin{array}{c}\textit{free power}\\ \textit{lost}\\ \\ \\ \end{array}\end{array} \tag{4}$$

$$\begin{array}{ccccc} Be & = & Q & - & Md \\ \begin{array}{c}\textit{free power}\\ \textit{to fixed}\\ \textit{power}\\ \textit{transfer}\end{array} & & \begin{array}{c}\textit{fixed power}\\ \textit{input}\\ \\ \\ \end{array} & & \begin{array}{c}\textit{fixed power}\\ \textit{lost}\\ \\ \\ \end{array}\end{array} \tag{5}$$

and in order to better understand these equations we have attached a physical description to each of the terms. The above equations form the basis for ASEA theory and this paper is mainly concerned with the calculation procedure for the A and the B matrices.

It may be thought that the somewhat arbitrary use of M in the second equation involves an assumption but this is not so since we have yet to specify the precise definition of B and Q, and the requirement to conform with equation (5) creates those definitions.

Once A, B, P and Q are known the responses can be calculated from $e + d$, using exactly the same procedures that we currently use when calculating SEA responses from e. It should be noted that the A matrix of ASEA theory is not the same as the A matrix of standard SEA theory.

From equations (4) and (5), $e + d$ is given by

$$e + d = M^{-1}(Q + R) \tag{6}$$

where

$$R = (M - B)(M + A)^{-1}P \tag{7}$$

Now for the classical excitation of 'rain on the roof' Q is zero, and with this simplification equation (6) can be rewritten as

$$(M + A)(M - B)^{-1}M(e + d) = P \tag{8}$$

and this equation can be considered to be the 'equivalent' standard SEA matrix equation such that if

$$A_{sea}e_{sea} = P \tag{9}$$

then

$$A_{sea} = (M + A)(M - B)^{-1}M \tag{10}$$

and

$$e_{sea} = e + d \tag{11}$$

Finally by applying the same power balancing argument of Section 4 we can easily deduce the important property that each individual column of $A + B$ must always sum to zero.

6 ASEA AND BEAM NETWORKS

In a beam network each beam will consists of four sub-systems associated with its two bending wavetypes, its compressional wavetype and its torsional wavetype. In this Section, for clarity of presentation, we will only consider a network of rods with each rod having only one wavetype. Provided we allow for this one wavetype to be conceptually of any type, for example by not assuming that the group velocity is equal to the phase velocity, then the extension to a beam network is straightforward.

Consider now the free energy field of rod j, represented by its modal energy e_j. Then the total free energy of this rod, E_j, is given by

$$E_j = n_j e_j \tag{12}$$

and the energy density of this free energy is E_j divided by L_j, where L_j is the length of rod j. Now by assuming that this energy field is made up of equal amounts of incoherent power, P_j, flowing both from left to right and from right to left along the rod (equivalent to the random incidence assumption in two- and three-dimensional sub-systems) we have

$$\frac{E_j}{L_j} = \frac{2P_j}{c_{gj}} \tag{13}$$

where c_{gj} is the group velocity of rod j.

Furthermore since for all one dimensional sub-systems

$$n_j = \frac{L_j}{\pi c_{gj}} \qquad (14)$$

we can combine equation (12) and equation (13) to obtain the standard SEA result that

$$P_j = \frac{e_j}{2\pi} \qquad (15)$$

Thus for unit modal energy the power available at each end of rod j, P_{aj} say, for potential transportation to the other rods, is simply $1/2\pi$.

We can now proceed with the calculation of the elements of the matrices A and B. Initially all these are set to zero and the calculation is based on using the elements of these matrices as accumulators. We start by taking a particular end of a particular rod and ultimately repeat the calculation for both ends of every rod.

The power available per unit modal energy P_{aj} at this particular end of rod j will conceptually be all transferred from rod j, and thus P_{aj} must now be added to element (j, j) of matrix A; add rather than subtract because the transfer terms have been conventionally placed on the left hand side of equation (4) and equation (5).

Now we take this available power, P_{aj} say, and multiply it by the appropriate transmission or reflection coefficient. This is then the power at the connected end of a particular receiving rod, rod i say, and this power is now ready for transportation across this rod; rod i can be the same rod as rod j to take care of the reflected wave and indeed the following calculations must be performed for all rods connected to the chosen end of rod j including rod j itself. This start power, P_{si} say, is thusgiven by

$$P_{si} = \tau_{ij} P_{aj} \qquad (16)$$

where τ_{ij} is the power transmission coefficient for power flowing from rod j to rod i.

It is worth keeping in mind at this point the standard SEA theory which would proceed in the following manner

$$\omega n_j \eta_{ji} = P_{si} = \tau_{ij} P_{aj} = \frac{\tau_{ij}}{2\pi} \qquad (17)$$

and thus

$$\eta_{ji} = \frac{\tau_{ij}}{2\pi\omega n_j} \qquad (18)$$

Returning to ASEA theory, power will flow across rod i and will decay as it does so with the exponential factor

$$\exp\left(-\frac{\omega \eta_i L_i}{c_{gi}}\right) = \exp(-\pi M_i) \qquad (19)$$

where M_i is the modal overlap factor of rod i. Thus

$$P_{ei} = \exp(-\pi M_i) P_{si} \qquad (20)$$

where P_{ei} is the power striking the far end of rod i. The power lost during this crossing, P_{li} say, is given by

$$P_{li} = P_{si} - P_{ei} \qquad (21)$$

This lost power must now be subtracted from element (i, j) of matrix B; matrix B rather than matrix A since this power is self evidently unavailable for further transport duties. On the other hand P_{ei} is available for further transport duties, and indeed we can continue the calculation from equation (16) using P_{ei} rather than P_{aj}. Of course within this cycle of the calculation we can only modify column j of either matrix A or matrix B since all of the initial available power comes from rod j. This whole process can be stopped at any stage and having stopped any remaining power, P_{si} say, must then be subtracted from element (i, j) of matrix A. This latter step is essential to maintain power balance and conceptually uses a standard SEA approach to sweep up and account for the residual power P_{si}; it also ensures that all the columns of $A + B$ sum to zero as required by power balance.

7 ASEA AND PLATE NETWORKS

The above theory can be extended to plate networks although its actual implementation could well turn out to be computationally expensive, as compared to standard SEA . However, ASEA plate theory will hopefully guarantee an accurate prediction and the fact that it may not become a practical tool because of the computational load should not deter us from its development. Its use as a tool for the validation of more approximate theories is very important since currently no accurate high frequency theory exists for general structural assemblies.

Whereas with rods we calculated the A and the B matrices by starting with a particular end of a particular rod and with beams we would start with a particular end of a particular beam and with a particular wavetype, with plates we must start with a particular edge of a particular plate and not only with a particular wavetype but also with a particular incidence angle at the chosen edge. In standard SEA the eventual integral over all angles of incidence is carried out implicitly within the model such that the formula for an SEA plate to plate coupling loss factor is a function of the random incidence transmission coefficient as given below in equation (27). In ASEA we can only perform the integral over all possible angles of incidence, 180 degrees, at the end of the A and B calculation; although by converting this integral into a suitably weighted sum we can easily incorporate it into the calculation procedure. Unfortunately line junction transmission coefficients tend to vary a lot with angle of incidence due mainly to the complex interaction effects of the various wavetypes and it is often necessary to perform these calculations over many angles of incidence: typically at every integer degree.

For a random diffuse energy field in sub-system j of a plate the intensity, I_j say, is given by

$$I_j = \frac{e_j k_j}{4\pi} \tag{22}$$

where k_j and e_j are the wavenumber and modal energy respectively of the wavetype associated with sub-system j. The power per unit modal energy striking an edge of length L at a grazing angle of incidence ϕ_j is thus

$$P_{aj} = \frac{L k_j \sin(\phi_j)}{4\pi} \tag{23}$$

and as before this must now be added to element (j , j) of matrix A.

We set

$$P_{si} = \tau_{ij}(\phi_j) P_{aj} \tag{24}$$

however τ_{ij} is now a function of ϕ_j and the transmitted wave angle has to be calculated using trace wavenumber matching such that

$$k_i \cos(\phi_i) = k_j \cos(\phi_j) \tag{25}$$

Again at this point it is worth keeping in mind the standard SEA theory which for plates proceeds as follows

$$\omega n_j \eta_{ji} = \pi^{-1} \int_0^{\pi} P_{si} \, d\phi_j \tag{26}$$

and thus

$$\eta_{ji} = \frac{L k_j \boldsymbol{\tau}_{ij}}{2\pi^2 \omega n_j} \tag{27}$$

where the random incidence transmission coefficient given by

$$\boldsymbol{\tau}_{ij} = \int_0^{\pi/2} \tau_{ij}(\phi_j) \sin(\phi_j) \, d\phi_j \tag{28}$$

Returning to ASEA theory, geometric calculations must now be made in order to track the wave as it is transported across sub-system i. This can result in more than one edge of the plate supporting sub-system i being illuminated and furthermore an illuminated edge need not be illuminated along its entire length; both of these effects must be calculated.

The damping factor, equivalent to the factor $e^{-\kappa M}$ of equation (19), is also more complicated here. Different parts of the wave will travel different distances, however for polygon shaped plates a damping factor averaged over all possible path lengths between two edges can be used and this is given by

$$\frac{e^{-b\kappa} - e^{-a\kappa}}{a\kappa - b\kappa} = D \tag{29}$$

where

$$\kappa = \frac{\omega \eta_i}{c_{gi}} = \frac{2\pi M_i}{A_i k_i} \tag{30}$$

and where a and b are the maximum and minimum path lengths.

Finally

$$P_{ei} = D P_{si} \tag{31}$$

and

$$P_{li} = P_{si} - P_{ei} \tag{32}$$

and P_{li} is subtracted from element (i , j) of matrix B as before.

8 COMPARISON WITH ANALYTICAL RESULTS

ASEA produces a different result dependent on the number of transfers of power across a sub-system that we are modelling. This number which is also one less than the number of junctions crossed we will call the ASEA level number, and with a level number of zero ASEA always produces results identical to standard SEA since both *B* and *d* are then zero. Advanced SEA can thus be thought of as a series of approximations,

$$\mathrm{ASEA}_0(\equiv \mathrm{SEA}),\ \mathrm{ASEA}_1,\ \ldots \qquad (33)$$

with the expectation that this series converges on the required result.

It is important to understand why we have this clear expectation that if the series (33) converges at all it must converge onto the 'correct' result; correct in the sense of giving the best high frequency result possible.

Consider the calculation procedure for ASEA with a very large level number; the level number chosen to be so large as to cause the *A* matrix to be effectively zero. Then the ASEA calculation procedure is nothing more than ray tracing with all phase related effects ignored, or in other words simple power flow analysis. But unless we wish to encroach on the low frequency deterministic domain, any high frequency theory must at least make the assumption, explicitly or implicitly, that all phase effects be ignored. Now with this assumption, and this assumption alone, we can deduce ASEA for an infinite level number. (Self evidently this would also be true for a simple power flow analysis, the subtle difference is that ASEA hopefully converges much faster due to the different treatment of the 'remainder' terms, which are ignored in a simple power flow analysis but are injected into a SEA procedure whose results are added to the truncated power flow analysis during an ASEA calculation.) Thus we fully expect that, if ASEA converges at all, and if an accurate high frequency theory exists at all, ASEA will converge onto the best theoretical result possible.

To show this convergence for a particular case we have chosen a very simple assembly consisting of six different rods all in a line. In principle an assembly of plates could equally well have been chosen, however exact results are extremely difficult to compute for plate assemblies at high frequencies and thus we have chosen an assembly of rods. The inline configuration has been deliberately chosen to highlight the errors in a simple SEA calculation and the subsequent correction of these errors by ASEA. The inability of SEA to predict such a contrived configuration is understandable and does not detract from the usefulness of SEA when applied to more realistic structures, but it should be considered as a warning that the accuracy of SEA is structure dependent.

The coupling between the rods is such that conceptually the whole structure could be made from a single piece of material with the far ends of the chain left unsupported or free. The rod material is such that its longitudinal phase, or group, velocity is 5000 m s^{-1}. The six rods are of lengths 23 , 28 , 25 , 24 , 29 and 21 m and their cross-sectional areas are such that their mass per unit lengths are 1 , 10 , 3 , 7 , 8 and 2 kg m^{-1} respectively. An energy damping value of 2% was chosen for the SEA modelling, and viscous damping with an equivalent critical damping ratio of 0.01 chosen for the exact model. The structure was always driven with a unit force on the first rod.

The exact results were calculated by Keane[7,8] and form a full deterministic analysis for point excitation, they are based on calculating the power flow across the assumed point connections between the rods for a given unit point force excitation on the drive rod. These response data were then numerically averaged over all excitation positions on the drive rod, rod 1, and over all frequencies within the chosen frequency bandwidth of 50 Hz.

Figures 1, 2, 3 and 4 show the results for the averaged response on the four rods furthest from the drive rod; the results for rods 1 and 2 are not shown because SEA and all levels of ASEA lie very close to the exact results for these rods. All the displayed responses have been normalised to unit mean square response velocity at the drive point on rod 1.

As can be seen SEA, or equivalently ASEA_0, is not an adequate model at the higher frequencies; at 10 kHz SEA over predicts the response of Rod 6 by over 60 dB. On the other hand, as expected, ASEA always predicts accurately provided we are willing to calculate to a high enough level number. For a chain of rods driven at one end the rule of convergence appears to be that the ASEA level number should be at least the rod number minus two. This is not so surprising a result since such a level number ensures a direct coupling exist in the ASEA model between the drive rod and the response rod. The convergence of ASEA is not necessarily monotonic with level number as can be seen in Figure 4 where ASEA_3 gives a slightly better result than ASEA_4.

9 CONCLUSIONS

A high frequency theory (ASEA) has been presented which takes account of the mechanism of tunnelling. This mechanism which requires the introduction of coupling between SEA sub-systems that are physically separate is modelled by creating a new set of basic ASEA equations and dividing the energy of a sub-system into energy that is freely available for transfer to other sub-systems and energy that is fixed within the sub-system.

These equations are presented and an attempt has been made to give their component parts physical meaning. The calculation procedure is presented for modelling either a general beam network or a general plate network. ASEA is interpreted as a series of mathematical models, the first of which is identical to standard SEA and subsequent higher order models are convergent on the desired result.

Using a structural assembly of six rods as an example, ASEA is shown to converge onto the exact results whilst SEA is shown to overpredict by up to 60 dB.

10 REFERENCES

1 Lyon, R.H. "Statistical energy analysis of dynamic systems: theory and application", Cambridge: MIT Press, 1984

2 Keane, A.J. and Price, W.G., J. Sound Vib., **117**, 1987, pp363-386

3 Heron, K.H., "The development of a wave approach to statistical energy analysis", in Proc. Inter-noise, Gothenburg, Sweden, 1990

4 Price, A.J. and Crocker, M.J., J. acoust. Soc. Am., **473**, 1970, pp683-693

5 Leppington, F.G., Heron, K.H., Broadbent, E.G. and Mead, S.M.,Proc. R. Soc. Lond., **A412**, 1987, pp309-337

6 Hodges, C.H. and Woodhouse, J., Rep. Prog. Phys., **49**, 1986, pp107-170

7 Keane, A.J.,Proc. R. Soc. Lond., **A436**, 1992, pp537-568

8 Keane, A.J.,private communication

© British Crown Copyright 1994 / DRA

Published with the permission of the Controller
of Her Britannic Majesty's Stationery Office

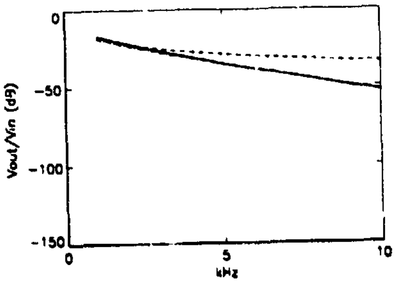

Figure 1 Response of rod 3

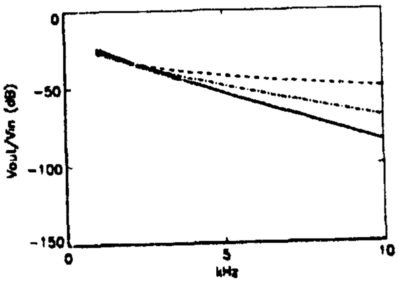

Figure 2 Response of rod 4

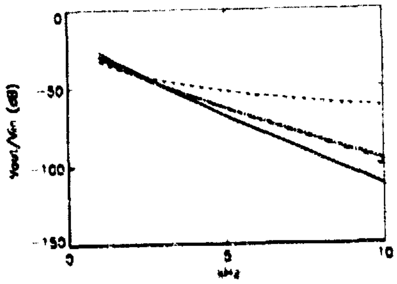

Figure 3 Response of rod 5

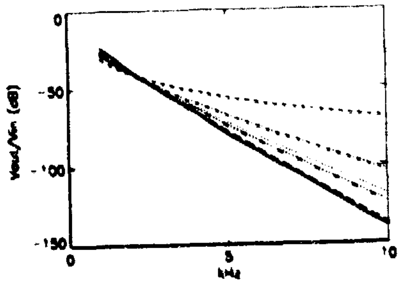

Figure 4 Response of rod 6

where —— is the exact result,
- - - - is the ASEA$_0$ (= SEA) prediction,
-·-·-· is the ASEA$_1$ prediction,
--·--· is the ASEA$_2$ prediction,
······· is the ASEA$_3$ prediction
and ·— — — is the ASEA$_4$ prediction.

IDENTIFICATION AND ANALYSIS OF AIR- AND STRUCTURE-BORNE NOISE AND VIBRATION PATHS

Herman Van der Auweraer
Katrien Wyckaert
Peter van der Linden
Dirk Otte
LMS International
Interleuvenlaan 68
B-3001 Heverlee
BELGIUM

1. SUMMARY

In order to investigate the contribution of individual sources and source transmission paths, a method referred to as "Transfer Path Analysis" has been developed. Its formulation to address structure-borne noise problems is outlined in detail and illustrated with an example from the car industry. Current research in this context is briefly reviewed, including the case of reciprocity techniques and the air-borne noise problem.

2. PREFACE

The optimisation with respect to interior noise is currently a topic of great concern for the automotive industry. An essential element in this process is to obtain a correct understanding of the various noise sources which are present, and of the ways in which these sources are propagated to the critical receiver locations.

Whereas the physical nature of the important noise generating sources are in general well-known and inherent to the vehicle operation (power train noise and vibration or wheel/road interaction in cars, propeller or fan noise, turbulent layer noise in aircraft, ...), the correct quantification of these source strengths, and the quantification of the partial contribution of each of these sources to the overall noise level are in general not available.

To address this problem, a methodology, referred to as Transfer Path Analysis, has been developed and investigated, which aims precisely at the establishment of both types of data: individual source strengths and a partial noise contribution analysis [1,2]. So far, the method has been applied primarily to the analysis of structure-borne noise problems, where vibrating source substructures are connected to the main vibro-acoustic system by means of mounts. Each of the mounts (actually each direction at each mount location) then defines a transmission path. Typical examples are engine vibrations transferred through engine or power train mounts, and car road vibrations transmitted through suspension mounts. A schematic representation of the structure-borne sound paths of engine, wheels, steering system and exhaust of a passenger car is shown in figure 1.

Hereto, in-operation (on the road, in flight) measured vibration and pressure response data are combined with laboratory measurements of frequency response functions. From these data, the operational forces at each of the mounts are estimated and the partial pressure (or vibration), caused by each of the transmission paths is calculated as a function of frequency. The complexity of this analysis is to a large extent dominated by the dimension of the vibro-acoustic operational response. The actual procedures, both for the single source and the multivariate noise problem, are discussed in more detail in the sections below.

The results obtained by such a transmission path analysis are typically used in troubleshooting and prototype refinement, to identify critical mounts and dominant sources and to investigate the influence of the vibro-acoustic system characteristics on the perceived noise [2,3].

Current research focuses on validating the accuracy of this approach for the solution of industrial problems, and on extending it to other problem areas.

One of the most important accuracy elements is the correct identification of the operating forces into the mounts, which requires critical matrix inversion procedures [4,5,14].

The extensions include the use of reciprocity techniques to measure the vibro-acoustic FRFs [6,7,8], the quantification of air-borne source contributions [9], the transfer of structure-borne sound through connected substructures [12, 13], and the physical interpretation of the transmission path phenomena [10, 11].

Also, the applicability of the methodology to derive the optimal configuration of an active noise control system using vibration reduction at the mount locations is a topic of research [5].

Presented at a Symposium on 'Impact of Acoustic Loads on Aircraft Structures' held in Lillehammer, Norway, May 1994

3. SINGLE SOURCE TRANSMISSION PATH ANALYSIS

When considering *nrpath* different possible transmission paths over which energy coming from a single reference source, can be transmitted into the car body, the total operational pressure p at a given target location in the cavity can be written as a summed contribution of the "partial" pressures p_i, related to each given transmission path i. The determination of these partial pressures is based upon the combination of an estimate of the operational force f_i in the given transmission path, together with the mechanic-acoustical transfer function between the target pressure response and a force applied at the body side of the considered transmission path P/F_i.

$$p = \sum_{i=1}^{nrpath} p_i \qquad (1)$$

or

$$p = \sum_{i=1}^{nrpath} f_i \left(P/F_i \right) \qquad (2)$$

In practice, the noise transfer functions are measured after disassembling the source from the car body.

It is difficult to obtain direct measurements of the operating forces. The complex dynamic stiffness technique is one methodology to obtain these operational forces. They are calculated based upon the following relation:

$$f_i = K\left(x_{body,i} - x_{source,i}\right) \qquad (3)$$

with K the measured complex dynamic stiffness of the mounting elements (obtained in 3 directions) as a function of frequency; $\left(x_{body,i} - x_{source,i}\right)$ the relative operational displacement over the mount. This methodology is quite straightforward but does require the (tedious) characterisation of the mounting elements in special test set-ups.

An alternative technique is based upon the measurement of the impedance matrix, containing FRFs between accelerations measured at the body side of all paths and forces, applied at all paths. By inverting this matrix, and multiplying it with the vector of the corresponding body side operational accelerations, estimates of the operational forces are obtained.

$$\begin{Bmatrix} f_1 \\ \cdot \\ f_n \end{Bmatrix} = \begin{bmatrix} \dfrac{\ddot{X}_1}{F_1} & \dfrac{\ddot{X}_2}{F_2} & \cdot \\ \cdot & \cdot & \cdot \\ \dfrac{\ddot{X}_m}{F_1} & \cdot & \cdot \end{bmatrix}^{-1} \begin{Bmatrix} \ddot{x}_1 \\ \cdot \\ \ddot{x}_m \end{Bmatrix} \qquad (4)$$

It is sufficient to take into account a number of responses equal to the number of forces that has to be estimated $(n = m)$, but by taking into account more responses $(m > n)$, the set of equations is over-determined, and better force estimates will be obtained in a least squares sense. The inversion is based upon singular value decomposition algorithms, which allow to artificially increase the conditioning of the inversion [5].

4. MULTIPLE REFERENCE TRANSMISSION PATH ANALYSIS

For a multi-source problem as for instance a road noise problem, the previous approach is not valid. Therefore the transmission path analysis is preceded by a principal component decomposition in which the multi-reference problem is split up into several orthogonal single reference problems. Each of these individual problems are then tackled with the previous single reference approach. The total contribution of a single transmission path to the overall noise level is then calculated as the RMS summation of each of the individual principal component contributions [2].

Practically spoken, during the road tests, a set of reference accelerometers is chosen that serve as phase references for all other measurement locations. Cross-powers are calculated between all measured accelerations and this reference set of accelerometers. The reference signals are in general partially correlated to each other, and by a principal component decomposition of this reference set, an uncorrelated orthogonal reference vector set is obtained, to which all other responses at the "slave" measurement locations are related, represented by a set of single reference cross-powers. Let x_i denote the reference signals and z_i the other measurement locations, then:

$$\left[S_{xx}\right] = \left[U\right]\left[S_{x'x'}\right]\left[U\right]^H \qquad (5)$$

$$\left[S_{zx'}\right] = \left[S_{zx}\right]\left[U\right] \qquad (6)$$

$\left[S_{xx}\right]$ being the reference autopower matrix, $\left[S_{x'x'}\right]$ the (diagonal) autopower matrix of the principal components, and $\left[S_{zx}\right]$ and $\left[S_{zx'}\right]$ the cross-power matrices with references, or principal components, respectively. This is schematically shown in figure 2.

A clear phase relationship exists between all response locations and each principal component. These single reference cross-powers can be weighted with the autopower of the principal component, resulting in so called "virtual" spectra. With these spectra, specified at all response locations of interest, a single reference transmission path analysis can be carried out for each principal component. Combining all the results in an RMS way results in an estimate of the overall pressure.

Let *nrpca* be the number of significant principal components, then for each principal component j, one can write:

$$p_j = \sum_{i=1}^{nrpath} \left(p/F_i \right) \cdot f_{ij} \qquad (7)$$

whereas for each transmission path i :

$$p^2_i = \sum_{j=1}^{nrpca} \left(p/F_i \right)^2 \cdot f^2_{ij} \qquad (8)$$

This is indicated in figure 3. Assessing the influence of one transmission path, an RMS summation must be carried out for the partial pressure results in one transmission path, over all principal components.

5. USE OF MECHANICAL-ACOUSTIC RECIPROCITY

It can be interesting to use an alternative approach for the measurements of mechanical-acoustic transfer functions: reciprocal measurements.

The response of structures and sound fields can be reciprocal. This basically means that the same relations between input and output quantities are measured when the excitation energy is brought into the system at the output side. In literature, several applications of reciprocal measurements on a wide range of constructions, from production machinery to aircraft, have been reported [1,7]. For mechanical-acoustic transfer function measurements on car bodies, truck cabins, etc., the following relation is used:

$$\frac{p_k}{f_v}\Big|_{Q_k=0} = \frac{-\ddot{x}^*_v}{\dot{Q}^*_k}\Big|_{f_v=0} \qquad (9)$$

Q_k being the volume velocity at microphone location k $\left(m^3/s \right)$ and * the reciprocal quantity.

The system is excited by an acoustic source in the cabin and the responses are measured as accelerations at the mountings. The practical advantage of this approach is that the accelerometers at the mountings for the operational measurements can again be used for the transfer function measurements. Another advantage is that a large number of transfer functions can be measured simultaneously to several mountings in all directions.

A basic requirement for reciprocity is linearity. The sound field in the cavity is usually found to be linear in the range of sound pressures during operation and transfer function measurements. Yet, the linearity of the structure (cabin, body or chassis) is less evident, and non-linear stiffness effects and friction damping can cause deviations.

This can be critical since linearisation around normal working conditions will not take place. The velocity amplitudes in the cavity and in the structure will differ even more from normal operation during reciprocal FRF measurement than during the classical direct measurement.

Fortunately it is found in measurements that the linearity of direct and reciprocal FRF measurement is acceptable in general. Figure 4 shows typical direct FRF measurements on a car body/cavity system over a 30 dB excitation range. The deviation of the peak values remains less than 3 dB between 30 and 500 Hz. For the measurements performed with acoustical (reciprocal) excitation, the linearity is even better, as can be seen in figure 5. Further investigation has confirmed that the linearity deviations are mainly of a structural nature.

The next important requirement concerns the conditions given in equation (9). In a direct measurement, the volume velocity at the receiving microphones should approximate zero. This condition is easily met by all modern condenser microphones. The second condition that the force at the mountings should approximate zero is equally necessary for reciprocal and direct measurements. This condition has more serious consequences. It means that the mountings should be de-coupled during the measurements, and, as a result, a cumbersome dismounting of the drive-line and wheel suspensions is necessary.

In practice, it is in some cases possible to measure with attached mountings. The mountings must then be relatively compliant, like rubber bushing and elastic couplings. If the mounting remains coupled, the following condition should be met:

$$K < \frac{\omega^2}{H_{max}} \quad \left(N/m \right) \qquad (10)$$

A typical example of a comparison between direct and reciprocal measurements in a car is given in figure 6. It shows agreements better than 3 dB between 40 and 400 Hz. The differences below 50 Hz seem to be related to the limited linearity. The agreement becomes better when the direct measurement at very low force is used.

The differences at higher frequencies are more related to the accuracy of direct force measurements.

6. AIR-BORNE SOURCE QUANTIFICATION

When considering the relevance of the procedure discussed above to study structure-borne noise transmission paths, it is currently being investigated how the method can be applied or adapted to quantify acoustic sources and air-borne transmission paths.

The required data are now the acoustic source strengths, characterised by their volume velocities, in normal operation, and the acoustic frequency response functions relating local volume velocities at the source location to the sound pressures at the target receiving microphones.

$$p = \sum_{i=1}^{nrpath} p_i = \sum_{i=1}^{nrpath} \left[\frac{P}{Q_i}\right] q_i \qquad (11)$$

In principle, the latter FRF data can be obtained by replacing the sources with loudspeakers. However, in many cases, such as the one where the acoustic source is spatially distributed, and due to a complex radiation surface (e.g. an engine block or exhaust, or a tyre), this is impractical to do.

A far more versatile and practical method of measurement is again based on the application of reciprocity. Hereto, a sound source is placed at the targeted receiver location (e.g. the position of the head of a passenger in the vehicle, or an exterior microphone used to quantify the radiated noise), and sound pressures can be measured in a fine grid around the radiating surfaces (tyres, engines, exhaust, ...).

As far as the source strengths are considered, it is usually virtually impossible to measure them directly in operation, and current investigations [9] are performed on how local pressures measured near the sources can be used in combination with reciprocal FRF measurements. The re-combination of source strengths and FRFs into partial pressure responses can then be done in a vectorial way at lower frequencies or power-only (third octave for example) way at higher frequencies. A schematic overview of the measurement of the transmission path FRFs for a truck engine towards an exterior ISO microphone is given in figure 7.

The corresponding derivation of source strengths from near field acoustic pressure measurements and reciprocal FRFs is given in figure 8. Results measured on engine mock-ups are discussed in [9].

7. IMPEDANCE MODELLING

The methods discussed above all have in common that the actual vibro-acoustic system under study is characterised by FRFs. In the higher frequency ranges where the acoustic phenomena are of relevance, this is most probably the only way to proceed, at least for the structural behaviour, for high modal density in this frequency range renders the identification of a valid experimental modal analysis model nearly impossible.

Nevertheless, the explanation why a certain transmission path is important in a specific frequency region would in principle require the correlation of the operational data with a modal system model. To overcome this problem, alternative methods, directly based on the decomposition of FRF measurements in their principal components ("principal field shapes") have been investigated and proven to yield useful results in practical cases [10,11].

The same issue of not having a valid modal model in the frequency range of interest also arises when design modifications are to be evaluated to reduce the contribution of a specific transmission path by modifying the vibro-acoustic transfer characteristics.

To overcome this problem, design optimisation methods for structural modification and substructure coupling are investigated, which make use of FRF data only [12,13].

This is essential when e.g. the transmission of vibrations between stiffly connected substructures is to be evaluated. An example of such an application in the area of space microgravity experiment set-ups is shown in figure 9.

8. CASE STUDY

8.1 Test Case

The structural transmission of road vibrations to noise inside a car have been investigated in the context of the development of an active road noise control system by vibration control at the suspension car body connections [5]. Several methods to determine the operational forces were investigated.

8.2 Road Measurements

Stationary condition road tests included body and suspension side acceleration measurements at all considered transmission paths, together with pressure measurements at 4 locations in the cavity. Additional acceleration measurements were performed on the car body. In total 30 transmission paths are considered from the suspension into the car body 10 connection points (rear axle, rear shock absorber, 2 front suspension connection locations, front shock absorber), this in 3 directions. Six reference acceleration positions were chosen based upon multiple coherence analysis. Cross-power averaging with respect to these reference accelerations was done, based upon some 300 averages.

The set of 6 reference accelerometers is decomposed into its 6 principal or orthogonal components, and the measurements at all measurement locations are decomposed in this orthogonal base. This cross-power matrix decomposition then results into 6 sets of single reference ("virtual") cross-powers, which are scaled with the corresponding principal component autopower. These are the virtual spectra, which can be used as simple single reference (complex) spectra in all measurement locations. Figure 10 shows the summed virtual spectra over all measurement points for each of the principal components. This indicates that about 4 independent phenomena are important in this road noise analysis. For further calculations all 6 principal components are taken into account.

8.3 In-Laboratory Measurements

After disassembling the suspension from the car body, the acoustical frequency response functions at the 4 driver and passenger ear locations are measured, by using hammer impact excitation at all possible transmission paths. At the same time, the impedance matrix is measured, where acceleration measurements are performed at all transmission paths, and at some 30 additional body side measurement locations. This results in an extensive database of about 2000 FRFs, representing a fully measured matrix.

The mounting elements being disassembled from the suspension and the car body, have been tested in a separate measurement set-up. The complex dynamic stiffness of all mounts was determined in 3 directions, this based upon sinusoidal excitation with the necessary static preload.

8.4 Operational Force Estimates

In order to determine the operational forces, the complex dynamic stiffness methodology is used and compared to the impedance matrix inversion approach. In the complex dynamic stiffness methodology, for each mount and each direction the dynamic mount stiffness is (complex) multiplied with the differential virtual spectra over that particular mount, and this is repeated for each of the 6 principal components. RMS summation of the obtained forces over all principal components yields an estimate of the total operating force in that particular mount location, which gives an indication for actuator requirements. Figure 11 gives for instance for the rear mount the complex dynamic stiffness together with an estimate of the operating force spectrum (square root of power spectral density).

With the impedance matrix inversion approach, an over-determination strategy is used. The matrix measured is of dimension 69x30: 30 forces are to be estimated, and 69 response locations are considered. For each of the 6 principal components, operational acceleration virtual spectra at the above mentioned 69 body side measurement locations are available. This represents an over-determined set of equations that is solved by a pseudo inversion algorithm based upon singular value decomposition. Figure 12 shows the condition number of the 69x30 FRF matrix as a function of frequency. This reveals that in this particular case the condition does not pose any problem for the inversion, this in contrast with other applications published elsewhere [4]. In this case, the measurements are characterised by high damping and high modal coupling, and do not seem to pose any problems in terms of conditioning. In order to assess the importance of the over-determination in the set of equations, also a 30x30 inversion is carried out, with only responses taken into account at all locations where the forces are to be estimated.

Figure 13 shows a comparison of the three strategies for the first principal component for one particular mount location in the front suspension. This particular mount is very stiff compared to other mounts in the front suspension. Clearly the 69x30 inversion gives similar amplitude results as compared to the 30x30 inversion, and to the complex dynamic stiffness method. Phase estimates are much less matching. Figure 14 shows the same type of results for a mount with a much lower complex dynamic stiffness. This figure shows that for a mount with lower stiffness the results of the inversion methodology are deviating from the results of the complex dynamic stiffness. But it is also clear that the over-determined inversion gives results that are closer to the complex dynamic stiffness results than the non-over-determined inversion. The reason why the low level forces, estimated with the inversion method are higher than the low level forces estimated with the complex dynamic stiffness method is still under investigation. It is clear that bias errors dominate the problem, most probably due to bias errors introduced in the impedance matrix. There exists an indication this is due to the quality of the FRF measurements, based upon hammer impact excitation. The direction of impact is not always easy to control, certainly not in a practical set-up on a car. This introduces important "virtual" cross-coupling in the matrix at a given response location.

Even though for the highest forces both methods give reasonable correspondence in the estimates, the operational forces obtained by the complex stiffness method are used for further calculations.

8.5 Transmission Path Analysis Results

The calculations for the transmission path analysis are based upon the forces estimated with the complex dynamic stiffness method, and upon the measured mechanic-acoustical transfer functions. The operational force spectra for each principal component are combined with the corresponding mechanic-acoustical transfer functions, resulting in estimates of the partial pressure, allocated to each of the given transmission paths, for each principal component.

By RMS summation over all 6 principal components of the partial pressures obtained in each of the transmission paths considered, amplitude estimates can be obtained for the total partial pressure, that can be attributed to a specific transmission path. By then combining all partial pressures over all transmission paths, an estimate of the total operational pressure can be obtained. This estimate can then be compared to the total measured operational pressure.

Figure 15 shows the transmission path analysis results at the drivers ear for a typical transmission path in the rear suspension. The upper curves give the calculated total as well as measured total operational pressure (measurement results of two different runs). It is clear that very good approximations are obtained of the total operational pressure with the analysis method. The lower curves represent the contribution of a specific mount in the rear suspension to the total pressure in the cavity, in 3 directions. This particular path is for instance dominant for the noise in the frequency bands up to 150 Hz, with clear booming effects. Figure 16 then shows results for another transmission path in the rear suspension, of which the effect on the interior noise level is negligible as compared to the previous.

As such a quantification of the noise contributions of all the different paths to the total operational pressure can be made. This quantification allows to rank the different paths in terms of their importance for the interior noise problem. This ranking can be used for the selection of the number and the location of needed actuators, in order to come to an as effective as possible noise reduction in the car interior.

9. CONCLUSION

A methodology to analyse noise and vibration problems in terms of individual source and transmission path contributions was presented. Its applicability has been proven so far in several automotive applications, with coherent as well as multivariate noise sources.

The scope of applications not only covers the original engine and road noise problems, where vibrations transmitted through isolated mounts are causing the noise. Possible applications are also situated in air-borne noise problems with distributed sources along radiating surfaces (e.g. tyre noise, air-borne engine noise, aircraft turbulent layer noise), as well as in applications where stiffly connected substructures are transmitting vibrations from one to the other (e.g. machinery in a production environment, precision instrumentation set-ups, as in space microgravity experiments, etc.).

10. ACKNOWLEDGEMENTS

This work was partially sponsored by the European Commission, in the framework of the BRITE EURAM programs (ANRAVA, BE 5931, DIANA, BE 4436, and PIANO, BE 5414), for which we hereby want to express our gratitude.

11. REFERENCES

[1] *Multipath Sound Transfer from Resiliently Mounted Shipboard Machinery*, PhD Dissertation, J. Verhey, 1986

[2] *Development and Integration of an Advanced Unified Approach to Structure Borne Noise Analysis*, D. De Vis, W. Hendricx, P.J.G. van der Linden, Second International Conference on Vehicle Comfort, ATA, 1992

[3] *Suspension Analysis in View of Road Noise Optimisation*, W. Hendricx, D. Vandenbroeck, Proc. of the 1993 Noise and Vibration Conference, SAE P-264, Traverse City, p. 647-652

[4] *On the Ill Conditioned Nature of Indirect Force Measurement Techniques*, J.M. Starkey, G.L. Merrill, Analytical and Experimental Modal Analysis, vol 4 nr 3, 1989

[5] *Transmission Path Analysis in View of Active Cancellation of Road Induced Noise in Vehicles*, K. Wyckaert, W. Hendricx, accepted for publication at Third International Congress on Air- and Structure-Borne Sound and Vibration, Montreal, June 13-15, 1994.

[6] *Using Mechanical-Acoustical Reciprocity for Diagnosis of Structure-Borne Sound in Vehicles*, P.J.G. van der Linden, J.K. Fun, Proc. 1993 Noise and Vibration Conference, SAE-paper 931340, Traverse City, May 10-13, 1993, pp. 625-630.

[7] *The Reciprocity Principle and Applications in Vibro-Acoustics*, F.J. Fahy, Proc. of the Second International Congress on Recent Developments in Air- and Structure-Borne Sound and Vibration, Auburn, March 4-6, 1992, pp. 611-618.

[8] *Experimental Procedures for Quantifying Sound Paths to the Interior of Road Vehicles*, J.W. Verheij, Proc. of the Second International Conference on Vehicle Comfort, Bologna, October 14-16, 1992, pp. 483-491.

[9] *Diagnosis of Pass-By Noise of Road Vehicles*, P.J.G. van der Linden, D. Otte, Proc. Fourth International ATA Conference, Florence, March 16-18, 1994, pp. 1268-1276.

[10] *Vibro-Acoustic Analysis of Trimmed Aircraft through Modal and Principal Field Modelling*, H. Van der Auweraer, D. Otte, F. Augusztinovicz, Proc. Fifteenth AIAA Aeroacoustics Conference, Long Beach, October 25-27, 1993, AIAA paper 93-4380.

[11] *Noise and Vibration Analysis in Propeller Aircraft by Advanced Experimental Modelling Techniques*, H. Van der Auweraer, D. Otte, Proc. Second International Congress on Recent Developments in Air- and Structure-Borne Sound and Vibration, Auburn, March 4-6, 1992, pp. 129-136.

[12] *Prediction of the Dynamics of Structural Assemblies Using Measured FRF Data: Some Improved Data Enhancement Techniques*, D. Otte, J. Leuridan, H. Grangier, R. Aquilina, Proc. Ninth International Modal Analysis Conference, Florence, 1991, pp. 909-918.

[13] *System Dynamics Simulation Based on Structural Modification Analysis Using Response Techniques*, T.C. Lim, G.C. Steyer, Proc. Tenth International Modal Analysis Conference, 1992, pp. 1153-1158.

[14] *Indirect Force Identification Based upon Impedance Matrix Inversion: A study on Statistical and Deterministic Accuracy*, P. Mas, K. Wyckaert, accepted for publication at Nineteenth ISMA Conference, Leuven, September 12-14, 1994.

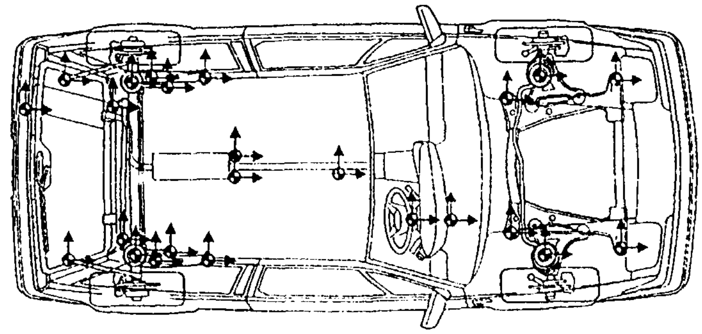

Figure 1 Structure-borne sound paths in a car

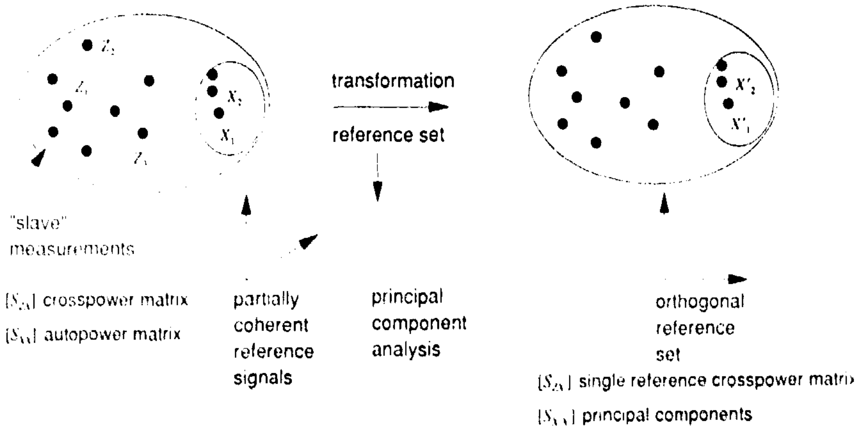
Z₂
Z₁
Z₃
X₂
X₁
transformation
reference set
X'₂
X'₁
"slave" measurements
[S_ZX] crosspower matrix
[S_XX] autopower matrix
partially coherent reference signals
principal component analysis
orthogonal reference set
[S_ZX'] single reference crosspower matrix
[S_X'X'] principal components

Figure 2 Decomposition of multi-reference problem into set of single reference problems

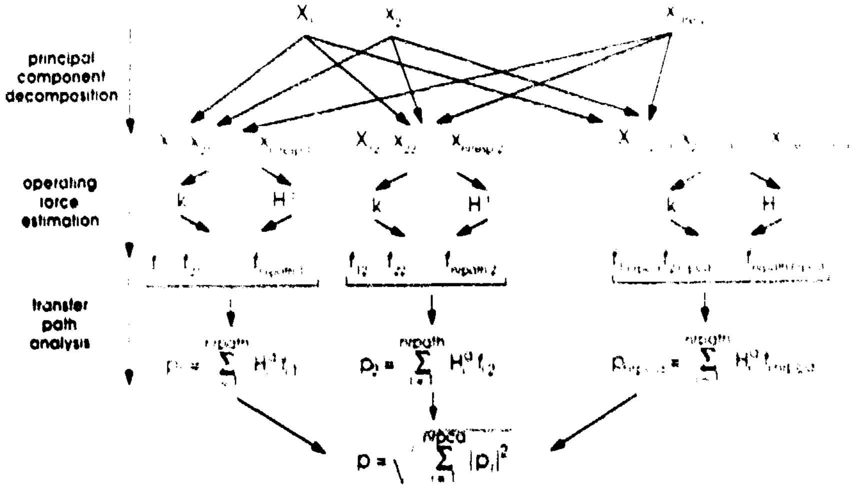
X₁
X₂
X_nref
principal component decomposition
operating force estimation
transfer path analysis
K
H⁻¹
f₁₂
f₂₂
f_npath 2
npath
npca
p = √(Σ |pᵢ|²)

Figure 3 Schematic presentation of multireference transmission path analysis

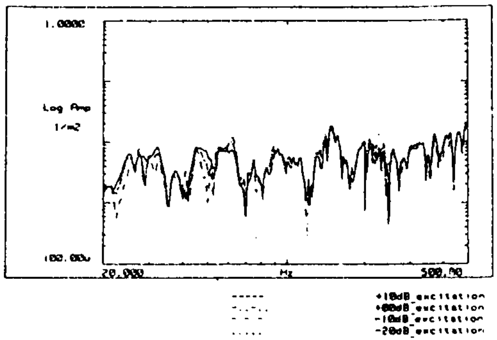

Figure 4 FRF linearity with direct (structural) excitation

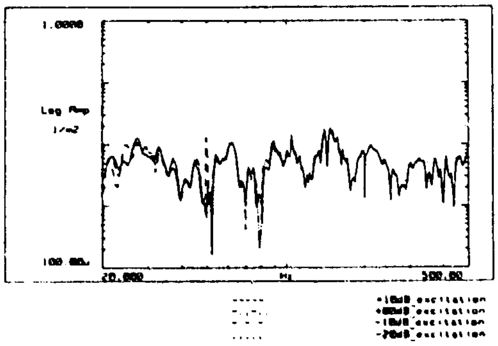

Figure 5 FRF linearity with reciprocal excitation

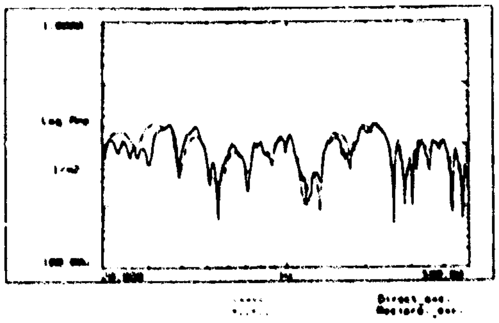

Figure 6 Comparison of direct and reciprocal measurements

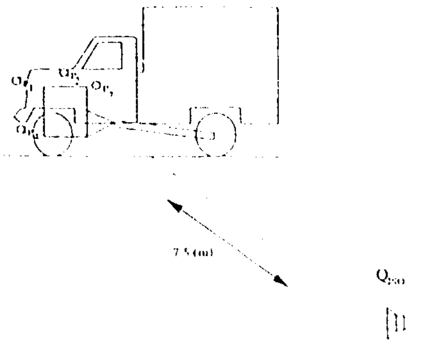

Figure 7 Reciprocal FRF measurement to ISO microphone

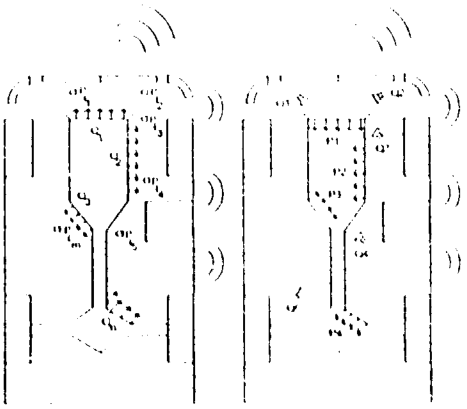

Figure 8 Source characterisation

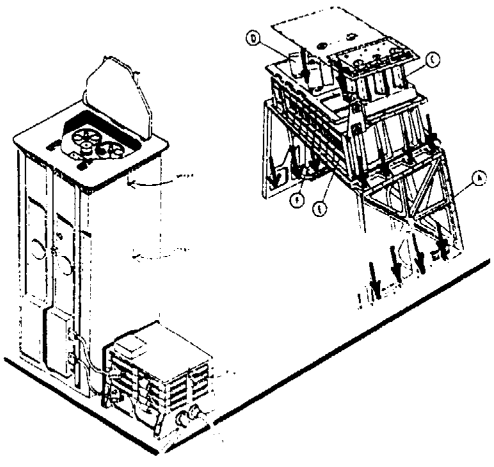

Figure 9 Equipment/base substructures in a space microgravity experiment set-up

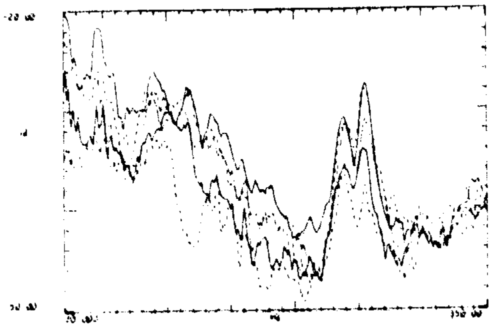

Figure 10 Decomposition in 6 principal components (6 mechanical references) : summed virtual spectra of accelerations measured during the road tests for each principal component

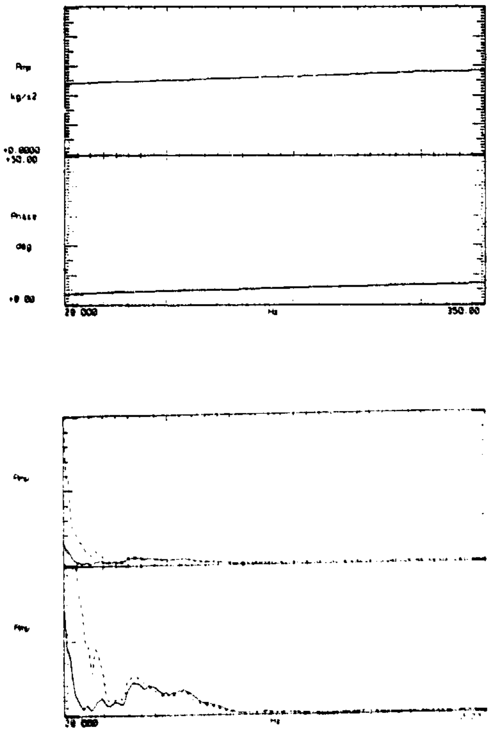

Figure 11 Rear suspension mount : measured complex dynamic stiffness and estimated operational force spectral density (at constant speed)

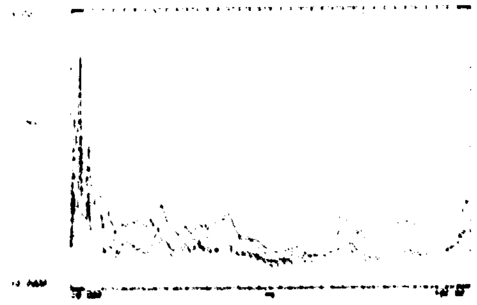

Figure 12 Condition number of 69x30 impedance matrix (full line); effect on condition number by omitting one singular value at the time (consecutiv lines)

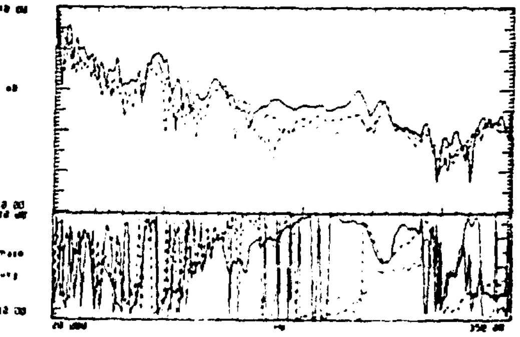

Figure 13 Estimate of operational force (first principal component) at a path characterised by a high dynamic stiffness : comparison of complex dynamic stiffness method (dotted line) with impedance matrix inversion method (69x30 (dashed line); 30x30 (full line))

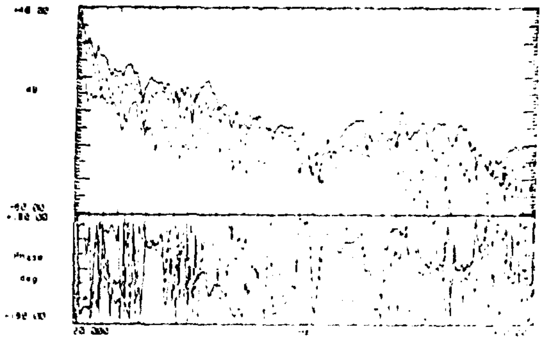

Figure 14 Estimate of operational force (first principal component) at a path characterised by a low dynamic stiffness : comparison of complex dynamic stiffness method (dotted line) with impedance matrix inversion method (69x30 (dashed line); 30x30 (full line)

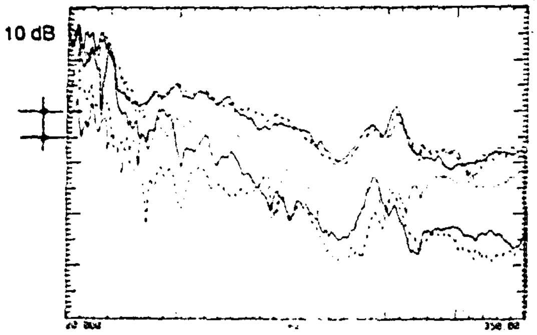

Figure 15 Transmission path analysis results : total measured and calculated operational pressure at drivers seat; partial contribution of important transmission path in rear suspension (full: x-direction, dashed: y, dotted: z)

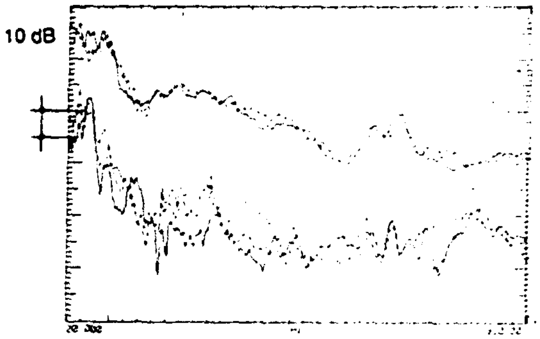

Figure 16 Transmission path analysis results : total measured and calculated operational pressure at drivers seat; partial contribution of less important transmission path in rear suspension (full: x-direction, dashed: y, dotted: z)

Spectrogram Diagnosis of Aircraft Disasters

Mr. F.W. Slingerland
Chief, Structures & Materials Lab.
IAR/NRC of Canada
Montreal Road
Ottawa, Ontario K1A 0R6
CANADA

Abstract

Impulsive forces applied to an aircraft fuselage generate radial vibration waves in the structure analogous to those in a classical thin shell. It has been found that these waves are detected by the cockpit area microphone, and that spectrogram analysis of the microphone recording can provide information on the nature, origin and strength of the source, whether an explosion or a sudden decompression.

INTRODUCTION

In-flight accidents of aircraft are often difficult to diagnose. The breakup of an aircraft at high altitude creates a widely dispersed wreckage trail, and dispersal of such a trail in deep ocean can further limit the amount of significant debris which can be recovered. For example, undersea debris search is still continuing at the site of the Air India disaster which occurred in 1985. However the aircraft's flight recorders are relatively easy to recover, using their radio or sonar transponders. This paper describes a new method of analyzing the cockpit area microphone (CAM) record from the cockpit voice recorder (CVR) which yields the following information:

- The cause of the disaster is clearly distinguished as either a structural failure or an explosive detonation ("bomb").
- The causal event is located along the fuselage to an accuracy of 1 to 2 metres.
- The event is also located as occurring in the passenger or cargo space.
- Information is available from the analysis which, with further experience, should yield the size of the explosive charge and the size of any fuselage perforation.

All this information is derived from a spectrogram of the impulsive sound of the event, heard by the CAM. It is found that this sound is in fact a transduced version of the radial vibrations of the fuselage. The spectrogram presentation - a "3-D" graph of signal strength vs both time and frequency, somewhat like a contour map, reveals the successive passages of these dispersive vibration waves past the CAM. Pattern analysis of the waves provides the information mentioned above.

TYPICAL CAM RECORDINGS

The time traces of four events "heard" by the CAM are shown in Figs. 1 and 2. The voltage scales and time origins are arbitrary. Only one can be identified at present, because of continuing litigation surrounding the events. All have a certain family

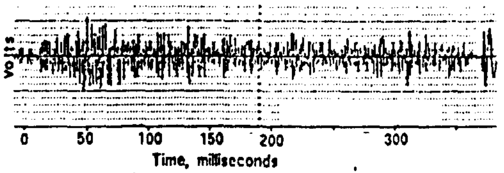

FIG. 1a: Voltage - Time record of event 1

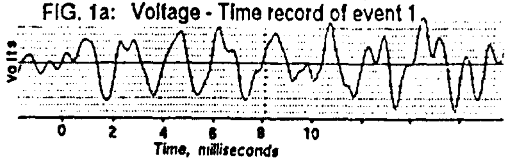

FIG. 1b: Expanded record, start of event 1

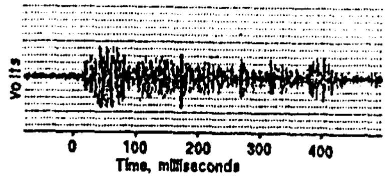

FIG. 1c: Voltage - Time record of event 2

Presented at a Symposium on 'Impact of Acoustic Loads on Aircraft Structures' held in Lillehammer, Norway, May 1994.

resemblance. Each begins with a few cycles of almost pure sinusoid at a frequency between 450 and 700 Hz, depending on aircraft type and flight altitude. (It was these sinusoids which led the writer to realize that these were vibration signatures; not airborne sound signals). The records then show a sudden transition to much more complex waveforms, which then die away in about 400 ms unless shortened by power or signal loss. Event 1 ends with a damped sinusoid typical of signal disconnect from the CVR - probably by in-flight breakup. Event 4 terminates very quickly - probably because of disruption of power supply to the CAM and/or CVR. Event 3 is a succession of several distinct impulsive events.

The signal-to-noise voltage ratios of the signatures vary between 7,5:1 and 12:1. However the voltage histories are strongly influenced by the CAM/CVR automatic gain control (AGC) which has about 35 ms. response time on signal increase and about 70 ms. on decrease.Past attempts to interpret these records have been hampered by failure to recognize AGC action, and by the assumption that the microphone was detecting airborne rather than structure-borne sound. The latter merits some explanation. The CAM is attached to the fuselage just above the pilots' heads. If that part of the fuselage vibrates, it radiates sound like a loudspeaker, and this is heard by the microphone. Also the microphone itself may be shaken by the vibration, and this movement creates alternating pressures on its diaphragm which are also heard. The microphone is in fact a very sensitive detector, able to pick up vibrations from a hand-slap on the fuselage which is otherwise scarcely audible. Indeed, there have been cases of perforating bomb explosions aft of the wing, and of multiple tire bursts, which were not heard by the aircrew. When one considers the tortuous path that must be taken by an explosive blast/sound wave from, say, the aft cargo to the cockpit, this is hardly surprising. The final proof of the vibratory source of the microphone signal is that it travels from the source at observed speeds between three and eight times the speed of sound in air, and these speeds have been experimentally confirmed by test explosions on board (unoccupied!) aircraft. Fuselage vibrations are thus the first messengers of a remote event.

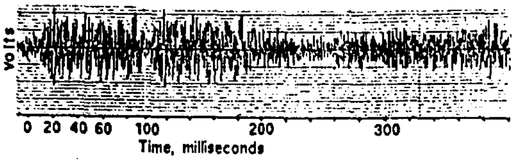

FIG. 2a: Voltage - Time record of event 3

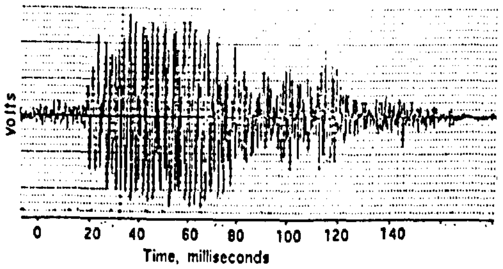

FIG. 2b: Voltage - Time record of event 4

FUSELAGE VIBRATION MODES AND THEIR PROPAGATION

Classical cylindrical shell theory provides a useful qualitative understanding of the various modes of radial vibration which may be excited by a localized zone of under - or overpressure. They are characterized by integral numbers, n, of sine waves around the circumference and sine waves of any wavelength along the length. The lower modes, having n = 0, 2, and 3 are the most commonly observed, since they couple best to a distributed pressure zone. Figure 3 shows typical group velocities of the n = 2, 3, 4 modes, based on typical aircraft dimensions. The n = 0 or ring mode is a special case, in that it propagates at only one frequency, by coupling with axial vibration waves. Its group velocity is well above that of the other low-n modes, and it is the probable source of the initial sinusoids in the CAM recordings. The effect of the floor is to raise frequencies, and to divide each mode into a symmetric and an asymmetric version, with slightly different propagation speeds at any frequency. The two ring modes differ in their phase relation between outward and inward motion above and below the floor, and it appears that the anti-phase variant is the one usually excited.

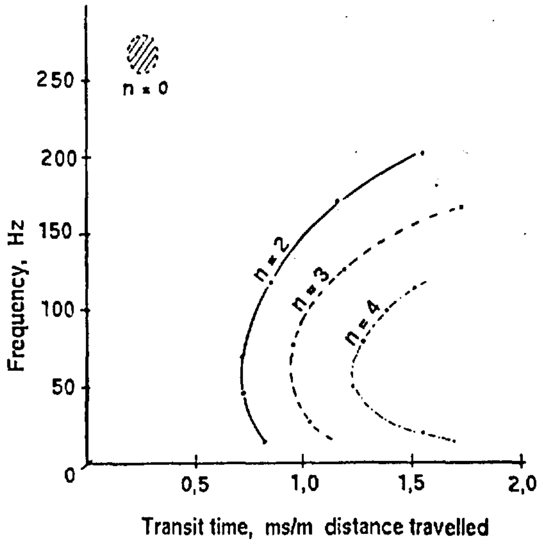

FIG. 3: Transit times of various modes

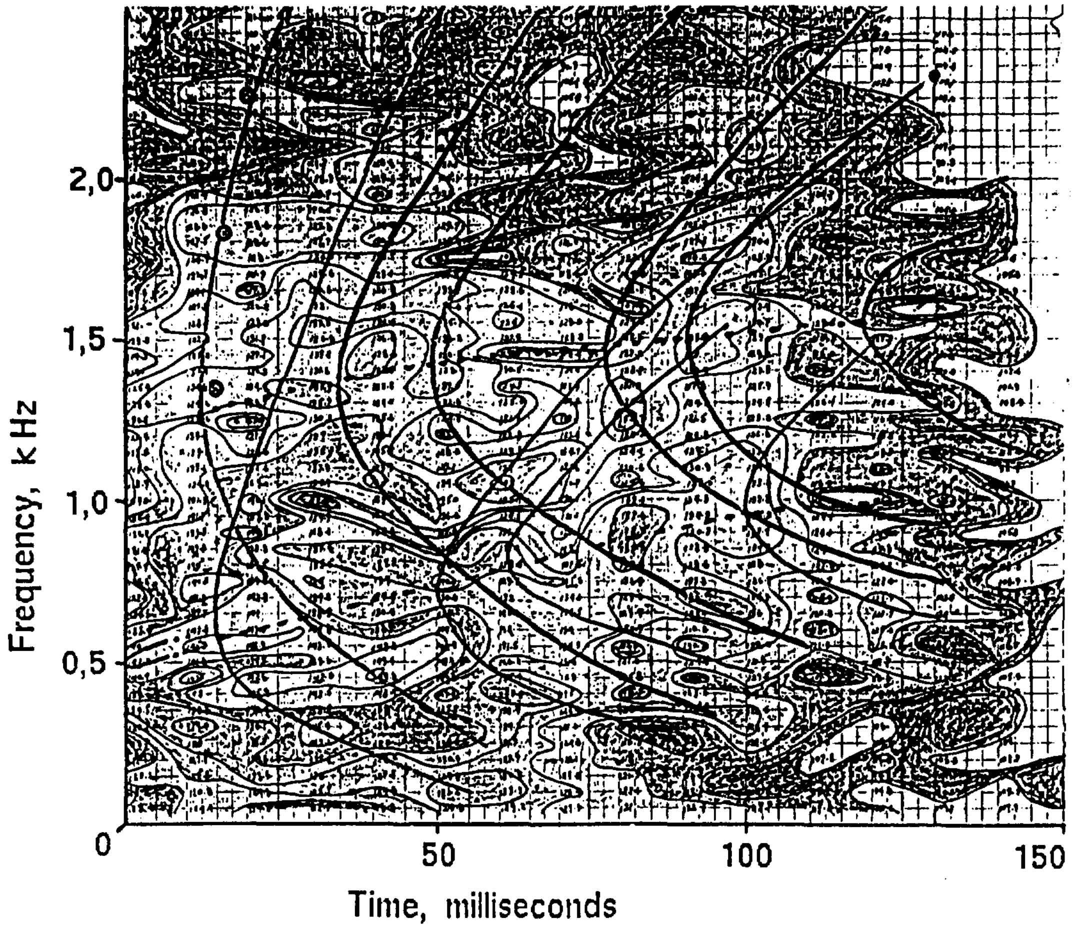

FIG. 4: Spectrogram of Event 4

The spectrogram of event 4, an explosion event, is shown in Figure 4* (a coloured version is on page 26-6). At first it appears to bear no resemblance to the theory of Figure 3, but in fact a series of major and minor peaks can be discerned, about six per wave, which define the successive passages of the waves of two "n" modes past the CAM. The wave contours after the earliest one represent repeated reflection from the ends of the aircraft, and their curvature gradually increases as the slow-travelling components fall increasingly behind the fastest components.

The spectrogram can be formed in various ways, but the most successful to date has been to perform a Fourier transform on successive 20-ms. Hanning-windowed time samples, overlapped 10 ms. Production of the spectrogram from these repeated spectra was done manually for those shown; it has now been mechanized a minicomputer.

INTERPRETATION OF THE DATA

THE INITIAL SINUSOIDS - The positive-pressure direction of the CAM record can be identified by analyzing the vowels of any speech present on the recording, from which the positive-going breath impulses of the larynx can be recovered. The initial pressure change, or phase, of the first sinewave at the CAM is related to the direction of initial motion - outward or inward - at the source. For example, a decompression in the passenger space decreases fuselage radius above the floor, and this inward motion will be transduced as a positive-going initial pressure excursion at the CAM. One can identify which variant of the ring mode is being observed by its frequency, and it is usually the antisymmetric one. This means that an explosion in the cargo space below the floor will also give a positive CAM excursion. It is not possible to sort out, from this datum alone, which event occurred.

---

*Only one spectrogram is shown in the written paper, because of the difficulty of reproduction. Others will be shown in colour during the verbal presentation.

FREQUENCY TRENDS OF THE SPECTROGRAM - It will be noted that the locus of first arrivals of the successive waves in Figure 4 rises in frequency; in other lengthier spectrograms it then falls. This is directly related to the internal pressure within the fuselage, since the frequency of the waves, or of the contours of Figure 3, depends directly on the pressure difference across the skin. A localized zone of pressure increase or decrease likewise translates into a frequency increase or decrease. In the event of Figure 4, the fuselage initially suffered a rapid rise in pressure, clearly indicating the detonation of an explosive device. The subsequent fall of frequency, hence pressure, present in other bomb spectrograms, indicates fuselage perforation and pressurization loss. Spectrograms of structural failures causing decompression are marked by a monotonic fall in frequency right from the start, with no initial rise. Both these trends are shown in Figure 5 for three "bombs" and two decompressions. The two types of event are clearly distinguishable.

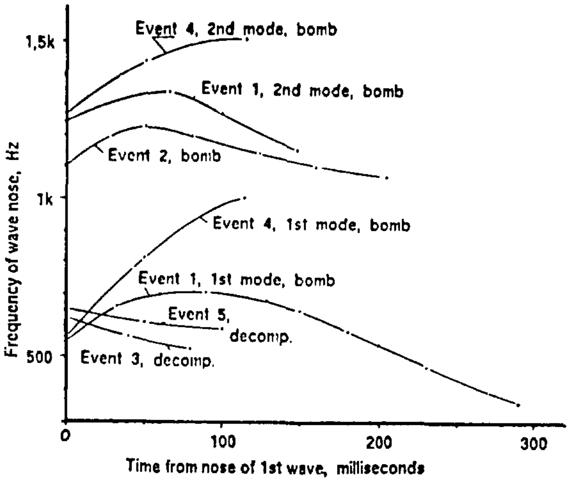

FIG. 5: Spectrogram frequency shifts for various events

Note that the pressure:frequency relationship is the same for events either below or above the floor. Thus this evidence, combined with the initial phase of the ring mode sinusoids, allows us to locate the event above or below the floor. It remains to determine its fore and aft position.

WAVE SPACINGS AND CURVATURE - If/when the propagation speeds of the various vibration modes become known by experiment, then the curvature of the first wave arrival contour would indicate the distance to the source (it began as a straight vertical line). However, in the absence of measured speeds, the axial location of the source can still be determined from the time-spacing of the successive reflections. For example, the time between first and second contours is the time taken by the waves to propagate to the rear, then reflect forward to the source point. The time between first and third waves is that of a full round trip. The ratio of the two times is thus the fractional distance of the event forward of the rear of the aircraft. Corrections must be applied for wave speedup in the nose and tail tapers, and in the stiff wing box area, and the time ratios must be measured repeatedly from various parts of the spectrogram and averaged, to eliminate wave contour position errors. When this is done, the event can be located fore-and-aft to a precision of less than one metre.

The techniques described above have now been applied to five aircraft disasters - three "bombs" and two explosive decompressions, and the analyses have always agreed with known data, or in one case, with the results of other lines of investigation. A series of nine test explosions aboard a Boeing 707 aircraft, using accelerometers and pressure sensors, have confirmed the maximum propagation speeds of fuselage vibration observed during the disaster analyses. It is intended to apply to these records the new computer programs for spectrogram generation, to obtain further information on propagation speeds of all the modal frequency components.

FUTURE DEVELOPMENTS

A new algorithm for spectrogram generation - the Wigner distribution (2), is being examined with a view to improving spectrogram readability. The spectrogram method is being combined with the "In-blast" computer model (4) to permit estimations of the size of the explosive charge (for bomb events), and/or the size of fuselage perforation. It is intended to apply the method to events originating in a wing, for which the vibration wave pattern is more complicated.

It is to be hoped that the next generation of CAMs and CVRs will retain, and possibly enhance, the ability to use cockpit microphone records for vibration spectrogram analysis.

CONCLUSIONS

1. The CAM recording of an aircraft which is subjected to the impulsive forces of a decompression or an explosion, contains structure-borne sound signatures associated with the radial vibration of the fuselage.
2. These radial vibrations may be non-dispersive (ring mode) or dispersive (other modes).
3. Analysis of the recording in the form of a spectrogram of amplitude versus both frequency and time reveals repeated wave passages up and down the aircraft at speeds from three to eight times the speed of airborne sound.
4. Analysis of frequency trends and time spacing of the waves provides extensive information on the nature, origin, strength and effects of the event which caused them.

ACKNOWLEDGEMENTS

The author acknowledges with appreciation the encouragement and support of Mr. Bernard Caiger of the NRC Flight Recorder Laboratory, and of Mr. Michael Poole of the Flight Recorder/Computer section of the Transportation Safety Board of Canada. The work has been financed by the National Research Council of Canada, and the guidance of Dr. W. Wallace and of Dr. G.F. Marsters of the Institute for Aerospace Research (NRC) has also been very helpful.

REFERENCES

1. Slingerland, F.W. Aircraft damage analysis by vibration spectrograms. Nat. Res. Council of Canada, Inst. of Aerospace Research, Lab. Tech. Report LTR-ST-1572, 21 Feb. 1986. See also Jour. Sound Vibration, Vol. 110(1) 1986, p. 166.
2. Wahl, T.J., Bolton, J.S. Identification of structure-borne noise components by the use of time-frequency filtering. AIAA 13th Aeroacoustics conference, Talahassee Fl. Oct. 22-4, 1990, Paper AIAA-90-3967.
3. Avery, J.G. Design manual for impact-damage-tolerant aircraft structures. AGARD report AG-238, Oct. 1981 (Unclassified). See Fig. 2-14, pg. 33. Impact-damage tolerance design technology research (overview), incl. "H.E. blast and fragment model".

Reprinted with permission from SAE paper No: 912041 ©1991, Society of Automotive Engineers Inc.

ADDENDUM

Identification of "Events"

Event	Description
1.	Air India Boeing 747 flt. 183 lost west of Ireland June 3, 1985 - bomb.
2.	Briefcase bomb aboard a Boeing 727-200 on flight Rome - Athens, March 1986.
3.	(Nameless!) Aft pressure bulkhead failure.
4.	Pan Am Boeing 747 flt. 103 lost over Lockerbie, Scotland, December 21, 1988 - bomb.
5.	Mac-D. DC 10 (Turkish) rear cargo door loss near Paris France, March 3, 1974.

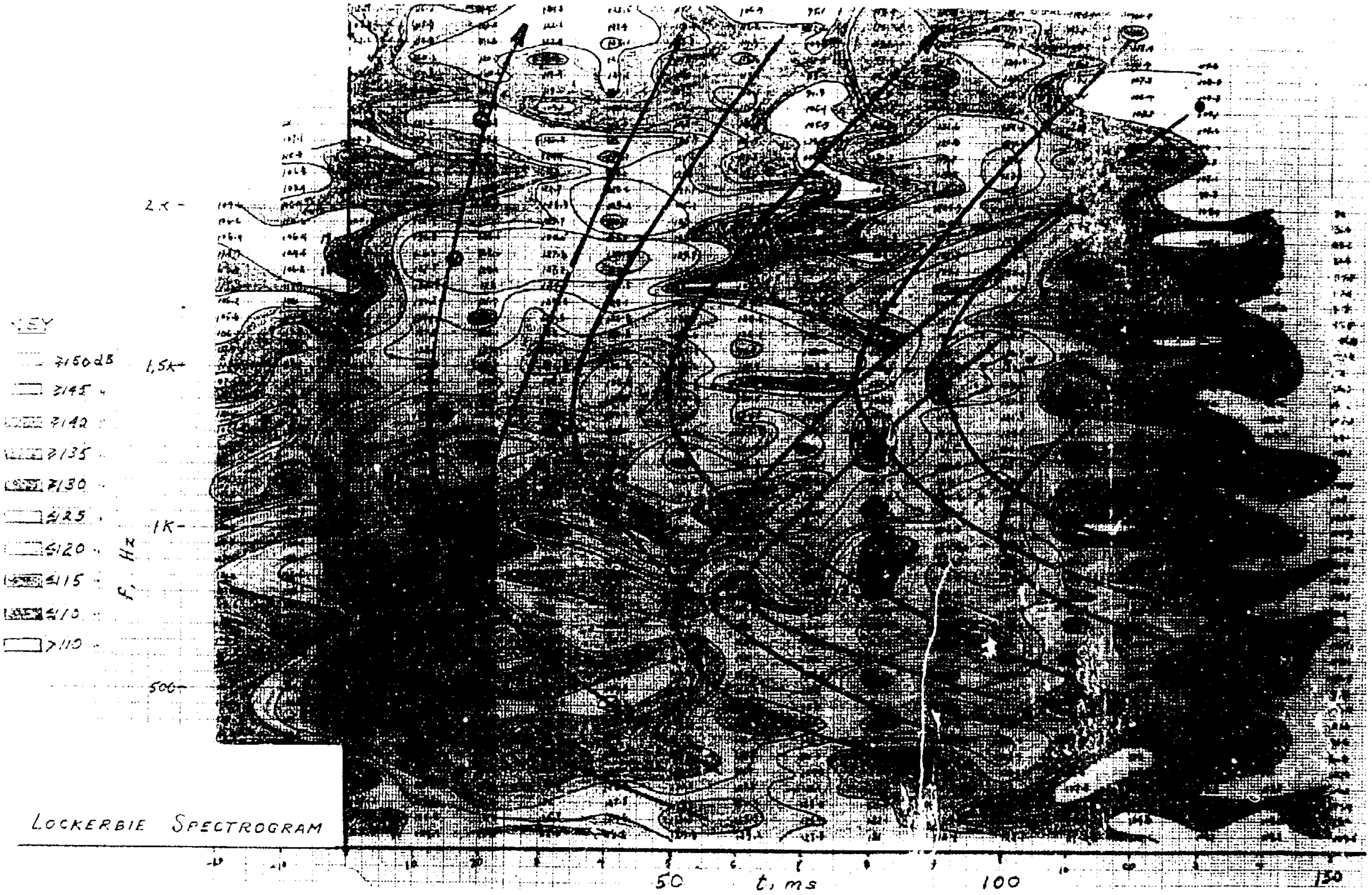

LOCKERBIE SPECTROGRAM

REPORT DOCUMENTATION PAGE

1. Recipient's Reference	**2. Originator's Reference** AGARD-CP-549	**3. Further Reference** ISBN 92-836-0001-0	**4. Security Classification of Document** UNCLASSIFIED

5. Originator
Advisory Group for Aerospace Research and Development
North Atlantic Treaty Organization
7 rue Ancelle, 92200 Neuilly-sur-Seine, France

6. Title

Impact of Acoustic Loads on Aircraft Structures

7. Presented at

A Symposium on "Impact of Acoustic Loads on Aircraft Structures" held in Lillehammer, Norway, May 1994.

8. Author(s)/Editor(s) Multiple	**9. Date** September 1994
10. Author's/Editor's Address Multiple	**11. Pages** 282

12. Distribution Statement

There are no restrictions on the distribution of this document. Information about the availability of this and other AGARD unclassified publications is given on the back cover.

13. Keywords/Descriptors

Structural design
Structural analysis
Acoustic fatigue
Thermal fatigue
Sub-sonic flow
Super-sonic flow
Hyper-sonic flow
Aerodynamics

14. Abstract

A broad band of different activities was addressed in the Specialists' Meeting held by the Structures and Materials Panel of AGARD in May 1994 :

Topics dealing with the acoustic environment in sub-, super- and hyper-sonic flow regimes, innovative structural design techniques and materials for fatigue resistant structures. Experimental and analytical tools for evaluation of the behaviour of structures in an acoustically and thermally adverse environment.

AGARDograph Conference Proceedings 549
Advisory Group for Aerospace Research and
Development, NATO
IMPACT OF ACOUSTIC LOADS ON
AIRCRAFT STRUCTURES
Published August 1994
282 pages

A broad band of different activities was addressed in the Specialists' Meeting held by the Structures and Materials Panel of AGARD in May 1994:

Topics dealing with the acoustic environment in sub-, super- and hyper-sonic flow regimes, innovative structural design techniques and materials for fatigue resistant structures. Experimental and analytical tools for evaluation of the behaviour of structures in an acoustically and thermally adverse environment.

ISBN 92-836-0001-0

AGARD-CP-549

Structural design
Structural analysis
Acoustic fatigue
Thermal fatigue
Sub-sonic flow
Super-sonic flow
Hyper-sonic flow
Aerodynamics

AGARDograph Conference Proceedings 549
Advisory Group for Aerospace Research and
Development, NATO
IMPACT OF ACOUSTIC LOADS ON
AIRCRAFT STRUCTURES
Published August 1994
282 pages

A broad band of different activities was addressed in the Specialists' Meeting held by the Structures and Materials Panel of AGARD in May 1994:

Topics dealing with the acoustic environment in sub-, super- and hyper-sonic flow regimes, innovative structural design techniques and materials for fatigue resistant structures. Experimental and analytical tools for evaluation of the behaviour of structures in an acoustically and thermally adverse environment.

ISBN 92-836-0001-0

AGARD-CP-549

Structural design
Structural analysis
Acoustic fatigue
Thermal fatigue
Sub-sonic flow
Super-sonic flow
Hyper-sonic flow
Aerodynamics

AGARDograph Conference Proceedings 549
Advisory Group for Aerospace Research and
Development, NATO
IMPACT OF ACOUSTIC LOADS ON
AIRCRAFT STRUCTURES
Published August 1994
282 pages

A broad band of different activities was addressed in the Specialists' Meeting held by the Structures and Materials Panel of AGARD in May 1994:

Topics dealing with the acoustic environment in sub-, super- and hyper-sonic flow regimes, innovative structural design techniques and materials for fatigue resistant structures. Experimental and analytical tools for evaluation of the behaviour of structures in an acoustically and thermally adverse environment.

ISBN 92-836-0001-0

AGARD-CP-549

Structural design
Structural analysis
Acoustic fatigue
Thermal fatigue
Sub-sonic flow
Super-sonic flow
Hyper-sonic flow
Aerodynamics

AGARDograph Conference Proceedings 549
Advisory Group for Aerospace Research and
Development, NATO
IMPACT OF ACOUSTIC LOADS ON
AIRCRAFT STRUCTURES
Published August 1994
282 pages

A broad band of different activities was addressed in the Specialists' Meeting held by the Structures and Materials Panel of AGARD in May 1994:

Topics dealing with the acoustic environment in sub-, super- and hyper-sonic flow regimes, innovative structural design techniques and materials for fatigue resistant structures. Experimental and analytical tools for evaluation of the behaviour of structures in an acoustically and thermally adverse environment.

ISBN 92-836-0001-0

AGARD-CP-549

Structural design
Structural analysis
Acoustic fatigue
Thermal fatigue
Sub-sonic flow
Super-sonic flow
Hyper-sonic flow
Aerodynamics

Best Available Copy

NATO ✛ OTAN

7 RUE ANCELLE • 92200 NEUILLY-SUR-SEINE

FRANCE

Télécopie (1)47.38.57.99 • Télex 610 176

DIFFUSION DES PUBLICATIONS
AGARD NON CLASSIFIEES

Aucun stock de publications n'a existé à AGARD. A partir de 1993, AGARD détiendra un stock limité des publications associées aux cycles de conférences et cours spéciaux ainsi que les AGARDographies et les rapports des groupes de travail, organisés et publiés à partir de 1993 inclus. Les demandes de renseignements doivent être adressées à AGARD par lettre ou par fax à l'adresse indiquée ci-dessus. *Veuillez ne pas téléphoner.* La diffusion initiale de toutes les publications de l'AGARD est effectuée auprès des pays membres de l'OTAN par l'intermédiaire des centres de distribution nationaux indiqués ci-dessous. Des exemplaires supplémentaires peuvent parfois être obtenus auprès de ces centres (à l'exception des Etats-Unis). Si vous souhaitez recevoir toutes les publications de l'AGARD, ou simplement celles qui concernent certains Panels, vous pouvez demander à être inclu sur la liste d'envoi de l'un de ces centres. Les publications de l'AGARD sont en vente auprès des agences indiquées ci-dessous, sous forme de photocopie ou de microfiche.

CENTRES DE DIFFUSION NATIONAUX

ALLEMAGNE
Fachinformationszentrum,
Karlsruhe
D-76344 Eggenstein-Leopoldshafen 2

BELGIQUE
Coordonnateur AGARD-VSL
Etat-major de la Force aérienne
Quartier Reine Elisabeth
Rue d'Evere, 1140 Bruxelles

CANADA
Directeur du Service des renseignements scientifiques
Ministère de la Défense nationale
Ottawa, Ontario K1A 0K2

DANEMARK
Danish Defence Research Establishment
Ryvangs Allé 1
P.O. Box 2715
DK-2100 Copenhagen 0

ESPAGNE
INTA (AGARD Publications)
Pintor Rosales 34
28008 Madrid

ETATS-UNIS
NASA Headquarters
Code JOB-1
Washington, D.C. 20546

FRANCE
O.N.E.R.A. (Direction)
29, Avenue de la Division Leclerc
92322 Châtillon Cedex

GRECE
Hellenic Air Force
Air War College
Scientific and Technical Library
Dekelia Air Force Base
Dekelia, Athens TGA 1010

ISLANDE
Director of Aviation
c/o Flugrad
Reykjavik

ITALIE
Aeronautica Militare
Ufficio del Delegato Nazionale all'AGARD
Aeroporto Pratica di Mare
00040 Pomezia (Roma)

LUXEMBOURG
Voir Belgique

NORVEGE
Norwegian Defence Research Establishment
Attn: Biblioteket
P.O. Box 25
N-2007 Kjeller

PAYS-BAS
Netherlands Delegation to AGARD
National Aerospace Laboratory NLR
P.O. Box 90502
1006 BM Amsterdam

PORTUGAL
Força Aérea Portuguesa
Centro de Documentação e Informação
Alfragide
2700 Amadora

ROYAUME-UNI
Defence Research Information Centre
Kentigern House
65 Brown Street
Glasgow G2 8EX

TURQUIE
Milli Savunma Başkanliği (MSB)
ARGE Dairesi Başkanliği (MSB)
06650 Bakanliklar-Ankara

Le centre de distribution national des Etats-Unis ne détient PAS de stocks des publications de l'AGARD.

D'éventuelles demandes de photocopies doivent être formulées directement auprès du NASA Center for AeroSpace Information (CASI) à l'adresse ci-dessous. Toute notification de changement d'adresse doit être fait également auprès de CASI.

AGENCES DE VENTE

NASA Center for
AeroSpace Information (CASI)
800 Elkridge Landing Road
Linthicum Heights, MD 21090-2934
Etats Unis

ESA/Information Retrieval Service
European Space Agency
10, rue Mario Nikis
75015 Paris
France

The British Library
Document Supply Division
Boston Spa, Wetherby
West Yorkshire LS23 7BQ
Royaume-Uni

Les demandes de microfiches ou de photocopies de documents AGARD (y compris les demandes faites auprès du CASI) doivent comporter la dénomination AGARD, ainsi que le numéro de série d'AGARD (par exemple AGARD-AG-315). Des informations analogues, telles que le titre et la date de publication sont souhaitables. Veuiller noter qu'il y a lieu de spécifier AGARD-R-nnn et AGARD-AR-nnn lors de la commande des rapports AGARD et des rapports consultatifs AGARD respectivement. Des références bibliographiques complètes ainsi que des résumés des publications AGARD figurent dans les journaux suivants:

Scientific and Technical Aerospace Reports (STAR)
publié par la NASA Scientific and Technical
Information Division
NASA Headquarters (JTT)
Washington D.C. 20546
Etats Unis

Government Reports Announcements and Index (GRA&I)
publié par le National Technical Information Service
Springfield
Virginia 22161
Etats-Unis
(accessible également en mode interactif dans la base de données bibliographiques en ligne du NTIS, et sur CD-ROM)

Imprimé par le Groupe Communication Canada
45, boul. Sacré-Cœur, Hull (Québec), Canada K1A 0S7

Best Available Copy